ISBN 978-987-45833-0-7

SPCI 10 Proceedings

10th International Symposium on the Science and Processing of Cast Iron

10th International Symposium on the Science and Processing of Cast Iron Proceedings

Boeri, Roberto

10 th International Symposium on the Science and Processing of Cast Iron / Roberto Boeri ; Juan M Massone ; Graciela Rivera ; compilado por Roberto Boeri ; Juan M Massone ; Graciela Rivera. - 1a ed. - Mar del Plata : INTEMA, 2015.

E-Book.

ISBN 978-987-45833-0-7

1. Ciencias . I. Massone, Juan M II. Rivera, Graciela III. Boeri, Roberto, comp. IV. Massone, Juan M, comp. V. Rivera, Graciela , comp. VI. Título

CDD 507

SPCI 10: PROCEEDINGS
241 pages © published 2015 by
INTEMA-UNMdP-CONICET

Mar del Plata, Bs. As., Argentina

ISBN 978-987-45833-0-7

SPCI 10

10th International Symposium on the Science and Processing of Cast Iron Proceedings

Compilers

Roberto Boeri
Juan M. Massone
Graciela Rivera

CONTENTS **PAGE**

BACKGROUND AND SCOPE.....**1**
THE ORGANIZING AND SCIENTIFIC COMMITTEES.....**2**

Understanding Compacted Graphite Iron Solidification through Interrupted Solidification Experiments.....**6**
G. Alonso, D.M. Stefanescu, P. Larrañaga, R. Suarez

Non-Metallic Inclusions in Lamellar Graphite Iron.....**7**
V. Fourlakidis, J. Ekengård, A. Diószegi

Crystallography of Graphite Spheroids in Cast Iron.....**12**
K. Theuwissen, L. Laffont, M. Véron and J.Lacaze

The Occurrence and the Effect of Casting Skin in Compacted Graphite Iron.....**13**
S. Boonmee and D.M. Stefanescu

On Microstructure-Based Mechanical Behaviour of a Ductile Iron Component.....**14**
Ingvar L Svensson and Jakob Olofsson

Crash Behavior of ADI Steering Knuckles.....**15**
L. Reissig, A. Nofal, W. Boehme, T. Reichert and I. H. Al Masry

High-Temperature Corrosion Fatigue of a Ferritic Ductile Cast Iron in Inert and Corrosive Environments at 700°C **20**
M. Ekström, S. Jonsson

Cast Iron Alloys for Exhaust Applications.....**21**
K. Papis, S. Tunzini and W. Menk

Local Chill as a Mean of Increasing Strength in Grey Cast Iron.....**28**
Fredrik Wilberfors, Ingvar L Svensson, Jessica Elfsberg, Kerstin Richnau and NuliferIpek

Austenite Dendrite Morphology in Lamellar Cast Iron.....**29**
Attila Diószegi, Vasilios Fourlakidis and Ruben Lora

Effect of Electric Current Pulse on Solidification Microstructure of Hypereutectic High Chromium Cast Iron Cooling from the Temperature between Liquidus and Solidus.....**30**
R.F. Zhou, Y.H. Jiang, R. Zhou, L. Zhang

Study of Shrinkage Porosity in Spheroidal Graphite Cast Iron.....**35**
N. Tenaglia R. Boeri, G. Rivera and J. Massone

A Review of Side-Lined Chunky Graphite Phenomena.....**36**
H. Borgström and V. Fourlakidis

New Concepts and Characterization of Gradient Castings Composed by low Alloyed White Cast Iron and Spheroidal Graphite Cast Iron.....**43**
Primož Mrvar, Mitja Petrič, Danijel Mitrovič and Jožef Medved

Trace Elements and the Control Limits in Ductile Iron.....**50**
L. Magnusson Åberg, C. Hartung and J. Lacaze.

Inoculant Ehancer to Increase the Potency of Ca-FeSi Alloy in Ductile Iron Produced from the Low Rare Earth Containing Master Alloy.....**58**
I. Riposan, V. Uta, S. Stan, M. Chisamera, M. Firican, R. Naro, D. Williams

Distribution of Some Active Elements in Primary Graphite Precipitates.....**66**
K. Theuwissen, T. Duguet, J. Esvan and J.Lacaze

Damage Evolution in Compacted Graphite Iron During Thermo-Mechanical Fatigue Testing.....**67**
V. Norman, P. Skoglund and J. Moverare

Corrosion Mechanisms in ADI Parts.....**68**
A.D. Sosa, C. Rosales, R. Boeri and S.N. Simison.

The Current Status of the Metallurgy and Processing of Austempered Ductile Iron (ADI).....**69**
A.A. Nofal

Environmental Embrittlement of Austempered Ductile Iron (ADI)– A Review.....**83**
R. Boeri and R.A. Martínez

Numerical Simulation of Dimensional Change during Austempering Heat Treatment in Ductile Cast Iron.....**91**
A.D. Boccardo, A.D. Sosa, M.D. Echeverría, P.M. Dardati,D.J. Celentano, and L.A. Godoy

Selected Aspects of the Use of Thermal & Derivative Analysis to Improve Macro Modeling of Solidification for Casting Iron. Comparison of Chosen Simulation Codes.....**100**
Zenon Ignaszak, Esteban Codina, Jakub Hajkowski, Paweł Popielarski and Pedro Roquet

A Computational Micromechanics Approach to Evaluate Effective Properties of Ductile Cast Iron.....**108**
F. J. Rodriguez, P. M. Dardati, L. A. Godoy and D. J. Celentano

Analytical Functions Describing Solidification of Gray Cast Iron based on Thermodynamic Calculations.....**118**
S. Jonsson

Effect of Cooling Rate and of Titanium Additionson the Microstructure of Thin-Walled Compacted Iron Castings.....**119**
Marcin Górny, Magdalena Kawalec, Gabriela Sikora, Hugo Lopez

Effect of Cu, Mn and Sn on Pearlite Growth Kinetics in As-Cast Ductile Irons.....**120**
J. Lacaze and J. Sertucha

Effect of Thermo-mechanical Processing Parameters on Phase Transformation and Hardness of Dual Matrix Ductile Iron.....**121**
M. Soliman, H. Ibrahim, A. Nofal and H. Palkowski

Occurrence and Behavior of Mo-Containing Precipitations in Nodular Cast Iron at High Temperatures.....**122**
Lutz Dekker, Babette Tonn

Quenching and Partitioning Process in Ductile Cast Irons.....**123**
A.J.S.T. da Silva, M.F. de Campos, A.S. Nishikawa, W.L. Guesser and H. Goldenstein

Boron Effect on the Precipitation of Secondary Carbides During Destabilization of a High-Chromium White Iron.....**131**
A. Bedolla-Jacuinde, F. V. Guerra, I. Mejía, J. Zuno-Silva, C. Maldonado

Metallographic Investigation of Nd: YAG Laser Processed Ductile Iron Surfaces.....**132**
A. Nofal, H. El-Gazzar and M. Ibrahim

Fe-C-V Alloys With Precipitates of Spheroidal Vanadium Carbides VC.....**140**
M. Kawalec and M. Górny

Cast Iron and the Self-Lubricating Behaviour of Graphite Under Abrasive Wear Conditions.....**141**
R. Ghasemi and L. Elmquist

Effects of Microstructure and Strength on Tool Wear in Rough Milling of Austempered Ductile Iron **148**
A. Sinlah, D. Handayani, C. Saldana, R. C. Voigt, K. Hayrynen, R. M'Saoubi

Characterization of Primary Dendrite Morphology in Complex Shaped Lamellar Cast Iron Castings.....**149**
P. Svidró, L. Elmquist, I. Dugic and A. Diószegi

A Study of the Oxygen Activity Before Start of Solidification of Cast Irons.....**156**
J.Ekengård, A.Diószegi and P.G. Jönsson

The System for Evaluating Fluidity and Solidification Characteristicof Alloy Melt.....**164**
D. Li, X. Ma, D. Shi and L. Wang

Solidification Macrostructure of Compacted Graphite Cast Iron and its Relationship with Shrinkage Porosity.....**171**
M. López, G. Rivera, J. Massone and R. Boeri

Automatic Vapour Sorption Analysis as New Methodology for Assessing Moisture Content of Water Based Foundry Coating and Furan Sands.....**179**
G.L. Di Muoio, N. Skat Tiedje and B. Budolph Johansen

Influence of Chromium and Molybdenum in Solidification and Shrinkage Defects for High Resistance Grey Iron Alloys.....**186**
L.Stuewe, A.P.Tschiptschin W.L.Guesser and R.Fuoco

Influence of the Furfury lmoulding Sand on the Flake Graphite Formation in the Surface Layer of Ductile Iron Castings.....**195**
M. Holtzer, R. Dańko and M. Górny

Feeding Against Gravity with Spot Feeders in High Silicon Ductile Iron.....**196**
N.K. Vedel-Smith and N.S. Tiedje

Mechanical Properties of Solid Solution Strengthened CGI.....**203**
Rohollah Ghasemi, Lennart Elmquist , Henrik Svensson , Mathias König , and Anders E. W. Jarfors

Determination of the Crack Propagation Direction of Fractured Ductile Cast Iron Based on the Characteristic Features of the Surface.....**204**
D.Fernandino, R.Boeri

Modeling Capabilities of Phenomena in Over-Moisture Zone Existing in Porous Medium Using the Simplified Simulation Systems Applied in Foundry.....**212**
P. Popielarski and Z. Ignaszak

Production of a Heavy Section Ductile Iron Grinding Table.....**220**
Ming You, Xiaogang Diao

Modelling of Density Changes of Nodular Cast Iron During Solidification by Cellular Automaton.....**226**
D. Gurgul, A. Burbelko, E. Guzik, D. Kopyciński and M. Królikowski.

Averaged Voronoi Polyhedron in the Equiaxed Solidification Modelling.....**234**
A.A. Burbelko, J. Począteк, W. Kapturkiewicz, and M. Wróbel

ORGANIZED BY:

(INTEMA) ***Institute for Research in Materials Science and Technology***

Av. Juan B. Justo 4302
CP (B7608FDQ)
Mar del Plata
Buenos Aires – Argentina
http://www.intema.gob.ar/

(UNMdP) ***National University of Mar del Plata***
(CONICET)***National Research Council of Argentina***

INTEMA
CONICET
UNMDP

BACKGROUND AND SCOPE

The Institue for Research in Materials Science and Tecnology (INTEMA) hosted the tenth International Symposium on the Science and Processing of Cast Iron (SPCI 10), from 10 to 14th of November 2014.

This symposium continues a series which began in Detroit, USA (1964), and was followed by meetings held at Geneva, Switzerland (1974), Stockholm, Sweden (1984), Tokyo,Japan (1989), Nancy, France (1994), Birmingham, USA (1998), Barcelona, Spain (2002), Beijing, China (2006), and Luxor, Egypt (2010).

SPCI 10 gathered some of the world leading researchers in the field of Cast Iron. Representatives of the academic and the industrial sectors from Sweden, China, France, Germany, USA, Russia, Mexico, Brazil, Egypt, Poland, Italy, Spain, Romania, Slovenia, Denmark, Switzerland, Norway, Thailand, Chile, Ukraine and Argentina have submitted their work to SPCI10. It has been an excellent forum where scientists, metallurgists, producers as well as users discussed the state of the art of cast iron science and processing and exchanged ideas and experiences. Nowadays Cast Iron, as most engineering materials on earth, faces a strong competition from other materials. Thanks to the joint efforts of producers, technologists and researchers, Cast Iron has not just maintained a strong position in the cast metals market over the last troubled years, but has also gained new markets and increased its applications. SPCI 10 provided an excellent opportunity to learn about the latest developments and to foresee the near future in this field.

TOPICS

- Fundamental research on solidification and solid state transformations of cast iron
- Recent technologies of melting, casting, heat treatment and process control.
- Computational modeling of cast iron transformations and processing.
- Novel developments and applications of cast iron.
- Mechanical properties of Cast Iron.

The Opening Ceremony will included talks by Prof. Ingvar Svensson (Jönköping University, Sweden), Dr. Jacques Lacaze (Université de Toulouse, France) and Prof. Doru Stefanescu (The Ohio State University, USA). During the four days of conference nearly 50 research articles were be presented on plenary sessions. In additon, a panel presentation was held on November 12th. In this panel, distinguished representatives from casting industries, technical organizations and research institutions discussed about the future needs in research and development in the cast iron field.

THE ORGANIZING AND SCIENTIFIC COMMITTEES

Chairman

Dr. Roberto Boeri (UNMdP)

Co-Chairman

Dr Juan M. Massone (UNMdP)

Members

Prof. Graciela Rivera (UNMdP-CONICET)

Prof. Ricardo Martínez (UNMdP-CONICET)

Prof. Martín Caldera (UNMdP-CONICET)

Prof. Alejandro Basso (UNMdP-CONICET)

Prof. Ricardo Dommarco (UNMdP-CONICET)

Dr. Sebastián Laino (UNMdP-CONICET)

SCIENTIFIC COMMITTEE

M. Nili Ahmadabadi	*University of Tehran,* ***Iran***
Sarum Boonmee	*Suranaree University of Technology,****Thailand***
Andriy Burbelko	*AGH Univ of Science and Technology,* ***Poland***
Manuel Castro	*CINVESTAV,* ***Mexico***
Jeong-Kil CHOI	*KITECH,* ***Korea***
Attila Diószegi	*Jönköping University,* ***Sweden***
Hasse Fredriksson	*KTH,* ***Sweden***
Marcin Górny	*AGH Univ of Science and Technology,* ***Poland***
Wojciech Kapturkiewicz	*AGH Univ. of Science and Technology,* ***Poland***
Jacques Lacaze	*CIRIMAT, ENSIACET,* ***France***
Frans Mampaey	*Sirris,* ***Belgium***
Vladimir Naydek	*PTIMA,* ***Ukraine***
Adel Nofal	*CMRDI,* ***Egypt***
Von Richards	*Missoury Univ of Science and Technology,* ***USA***
Iulian Riposan	*Univ Polytechnica of Bucharest,* ***Romania***
András Roósz	*University of Miskolc,* ***Hungary***
Oleg I. Shinsky	*PTIMA,* ***Ukraine***
Carlos Silva Ribeiro	*University of Porto,* ***Portugal***
Torbjørn Skaland	*Elkem,* ***Norway***
Doru M. Stefanescu	*Ohio State Univ; Univ. of Alabama,* ***USA***
Ramón Suárez	*Azterlan,* ***Spain***
Guoxiong Sun	Southeast University, ***China***
Ingvar Svensson	*Jönköping University,* ***Sweden***
Edis Ten	*MISIS, Moscow,* ***Russia***
Niels Skat Tiedje	*Technical University of Denmark,* ***Denmark***
Adian Udroiu	***Italy***
R. C. Voigt	*Pennsylvania State University,* ***USA***
Jiandong XING	*Xi´an Jiaotong University,* ***China***
Roberto Boeri	*UNMdP-CONICET,* ***Argentina****, Chairman*
Juan M. Massone	*UNMdP-CONICET,* ***Argentina****, Co-chairman*

REVIEW PROCESS

All papers included in these Proceedings have been reviewed and accepted by members of the Scientific Committee. A number of manuscripts were selected by the Scientific Committee based on their scientific and technical relevance, and were submitted for publication in a special number of the International Journal of Cast Metals Research. In those cases, only the abstract of the manuscript is included in the proceedings.

10th International Symposium on the
Science and Processing of Cast Iron Proceedings

Understanding Compacted Graphite Iron Solidification through Interrupted Solidification Experiments

G. Alonso[1], D.M. Stefanescu[2], P. Larrañaga[1], R. Suarez[3]

[1]Área Ingeniería, I+D y Procesos Metalúrgicos, IK4-Azterlan, Durango, Spain

[2]The Ohio State University, Columbus, OH and The University of Alabama, Tuscaloosa, AL

[3]Veigalan Estudio 2010 SLU, Askatasuna Etorbidea 16, E-48200 Durango (Bizkaia), Spain

While the manufacture of compacted graphite (CG) iron castings has seen significant expansion over the recent years, the growth of CG during iron solidification is still not fully understood. In this work effort was expanded to experimentally reveal the evolution of graphite shape during early solidification and its relationship to the solid fraction. To this purpose, interrupted solidification experiments were carried out on hypereutectic irons with three magnesium levels. The graphite shape factors were measured and analyzed as a function of chemical composition and solid fraction. Scanning electron microscopy was carried on to establish the fraction of solid at which the transition from spheroidal to compacted graphite occurs. It was confirmed that solidification started with the development of spheroidal graphite (SG) for all CG irons. The SG-to-CG transition was considered to occur when the spheroidal graphite developed a tail (tadpole graphite). The findings were integrated in previous knowledge to attempt an understanding of the solidification of CG iron.

Keywords: solidification, compacted graphite iron, interrupted solidification, graphite growth

Article available in the International Journal of Cast Metals Research

Non-metallic inclusions in lamellar graphite iron

V. Fourlakidis[1*], J. Ekengård[2] and A. Diószegi[3]
[1]Swerea SWECAST AB, P.O. Box 2033, SE-550 02 Jönköping, Sweden
[2]Sandvik SRP AB, Svedala, Sweden
[3]Jönköping University, Dept. of Mechanical Engineering/Material and Manufacturing Casting, Box 1026, SE-551 11 Jönköping, Sweden

Cast iron melts with two different carbon contents were used in this experiment. Quenched chill coins were extracted directly from the melting furnace and the size, the number and the composition of the non-metallic inclusions was examined using scanning electron microscopy (SEM), energy-dispersive X-ray spectroscopy (EDS) and an automate inclusions analysis system (EDAX). Large number of non-metallic inclusions was found in the chilled samples. Most of these inclusions are compounds of MnS with other elements. The number of the detected inclusions was found to increase with decreasing quenching temperature, while the number of large inclusions increases with the increase of the quenching temperature. This work provides supplementary data that helps a better understanding of the dependency between solidification rates, carbon composition, eutectic cells size, and constitutional undercooling in lamellar graphite iron.

Keywords: Lamellar graphite iron, MnS particles, graphite nucleation, non-metallic inclusions

Introduction

During the solidification of lamellar graphite iron the primary austenite is nucleated first and grows until the liquid metal attains the eutectic composition and the eutectic solidification occurs according to the stable austenite-graphite eutectic or the metastable austenite-iron carbide (cementite) eutectic. The equilibrium eutectic temperature for the austenite graphite reaction is tens of degrees higher than that of the austenite-carbide reaction in lamellar graphite iron. However the graphite nucleation usually requires significant undercooling below the eutectic temperature. When the undercooling becomes very high due to rapid cooling rates or low number of graphite nuclei, carbides formed instead of graphite [1-3].

In lamellar graphite iron the graphite phase nucleates heterogeneously from an un-dissolved graphite particle or from a complex substrate. The driving force for the graphite nucleation is the minimization of the free energy of the system consisting of the nuclei, the graphite and the melt. It has been shown that the value of the critical free energy is not available but is related to the lattice disregistry between nucleus and graphite. Therefore the disregistry can be used to indicate the ability of a surface to initiate the graphite nucleation [1].

Numerous research works investigate the phenomenon of graphite nucleation and the nature of the active nuclei at which the graphite nucleation can take place. Depending on the type of elements used for the treatment of the liquid iron, or the type of the inclusions which observed at the center of the graphite cells, several different graphite nucleation theories have been developed to explain the phenomena of heterogeneous nucleation of graphite in solidifying cast iron [5-12].

Lux [5] proposed that the addition of small amount of inoculation elements, such as Ca, Ba, Sr or Ce, in an iron melt promote the formation of salt-like carbides which constitute good nucleation sites for the participation of the graphite. Other researcher's [6] suggested that in flake graphite iron, CaO inclusions are nucleated first and they serve as embryo for the formation of SiO_2 oxide which possess as good nucleation site for the graphite.

Velichko [11] reconstructed a 3D visualization of the inclusions in a lamellar graphite iron sample. The performed EDS analysis indicated that those inclusions are precipitates of MnS. Wallace et al.[8] pointed out that the graphite flakes apparently grows from different sulfides inclusion. This theory is supported by Sommerfeld et al.[9] who analyzed the inclusions at the center of some eutectic cells and found that they consisting mainly by MnS. In another research work Riposan et al. [10] suggested that Al_2O_3 inclusions acting as nucleation sides for the precipitation of complex Mn(X)S compounds (where X is different elements such as Si, C, Ti, Ca, Al and others). These inclusions consider by the authors suitable sites for the nucleation of the graphite.

On the other hand the calculated lattice disregistry between the MnS inclusions and the graphite is very high (12.1%) and probably for this reason Tartera [5] consider that the MnS can serve as nucleation sites only in the absence of inoculation. Nevertheless the investigation results of other research works identified MnS as nucleus of flake graphite [9-10].

Sommerfeld et al. [9] used the software Thermo-Calc to calculate the fraction of stable phases in gray iron melts. The results of this work shows that in thermo-dynamical equilibrium condition the graphite is formed prior the MnS

* Corresponding author, e-mail: vasilios.fourlakidis@swerea.se

inclusions. MnS predicted to precipitate at temperature higher to graphite nucleation temperatures (1220°C), at high content of Mn and S (0.8% Mn and 0.12% S).

Recently [12], thermodynamics were used to analyze the nucleation of oxides and sulfides in lamellar graphite iron. This investigation shows that homogeneous nucleation of oxides/sulfides particles occurs when the concentration of oxygen/sulfur in the melt exceeding the supersaturation limit.

The aim of this experiment was to examine the number, the chemical composition and the size distribution of the non-metallic inclusions that forms in rapid solidify cast iron samples, produced at different quench temperatures.

Experimental Procedure

The experiment performed in an induction furnace having capacity of 6.000 Kg. The liquid iron was superheated up to 1500°C and then the melt left to cool down inside the furnace. Several chill samples were extracted from the melt during the cooling, until the liquid iron reaches the temperature of 1270°C.

The test samples are chilled coin shape specimens and they extracted directly from the melting furnace with the help of a resin bonded sand sampler. The rapid solidification of the samples it was provided by two steel plates which are positioned in the top and the bottom of the inner cavity of the sampler. The dimension of the experimental sample is ∅34.5x5.5 mm.

Two different carbon contents were used. The first melt had a carbon content of 2.8% and the second 3.2% C. Table 1 shows the chemical composition of the experimental alloys.

Table 1: Chemical compositions of the alloys, %wt.

Melt	**C**	**Si**	**Mn**	**P**	**S**	**Cr**	**Cu**	**Al**
1	3.4	1.7	0.5	0.04	0.05	0.2	0.7	0.003
2	3.7	1.7	0.6	0.05	0.05	0.2	0.7	0.003

The quenched specimens were ground and polished and number, size and chemical composition of the non-metallic inclusions measured by using SEM (Scanning Electron Microscope), EDS (Energy Dispersive Spectroscopy) system and an automate particles analysis program (EDAX Genesis software). Schamber [13] gives a detailed description of the methods used for the automated particle analysis in a SEM. An area of 0.026 mm² investigated in each specimen. The number of the analyzed micro-inclusions range from 130 to 870 particles per specimen.

Results and Discussion

The chemical composition of the alloy 1 in Table 1 has been used in JmatPro software for the calculation of the precipitated graphite and MnS, se Figure 1. The thermodynamic calculation shows that the graphite phase formed prior the precipitation of MnS in the specific alloy.

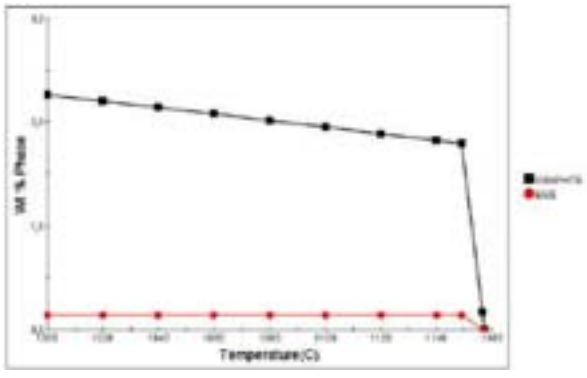

Fig. 1: Result of JmatPro calculation.

Large numbers of non-metallic inclusions were detected on the chilled samples. The majority of these inclusions are complex compounds of manganese and sulfur together with other elements such as O, Si, Ti, Ca, Al and others (Mn(X)S). Inclusions that contain manganese and sulfur alone (MnS) as well as oxides of various elements such as Ti, Si, Mn, Al and Ca were also detected. Figure 2 shows the number of the inclusions at various quenching temperatures and carbon compositions.

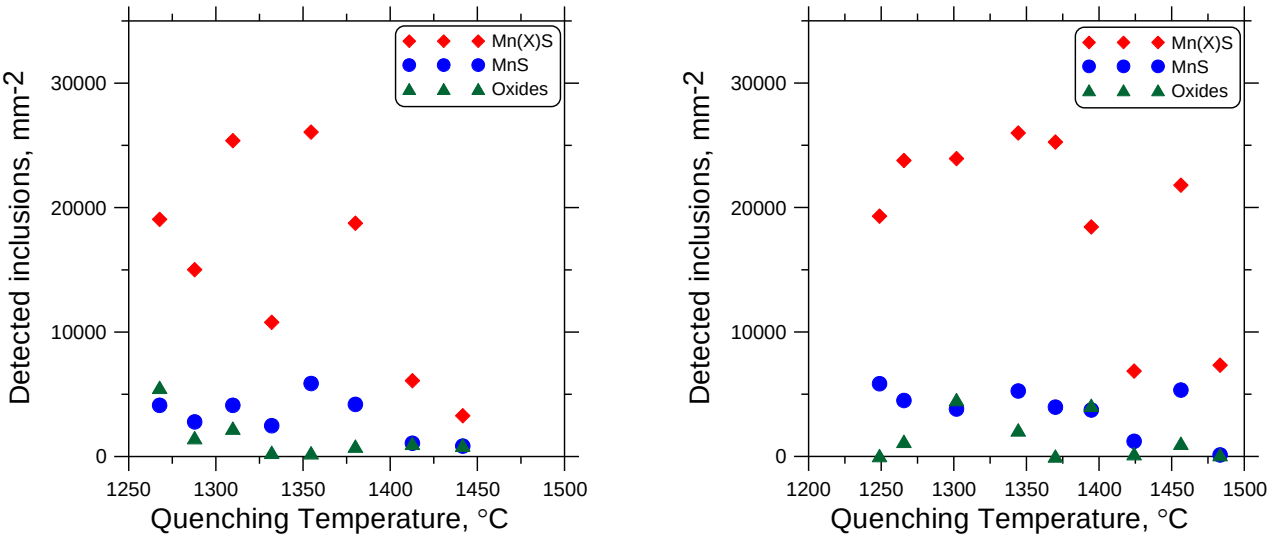

Fig. 2: Distribution of the MnS, Mn(X)S and oxides at different quenching temperatures. 3.4%C (left), 3.7%C (right).

The investigated samples have a fully martensitic microstructure. It is believed that the majority of the MnS and Mn(X)S inclusions were not existed in the melt at high superheat temperatures but these inclusions were formed in the chilled samples due to the non-equilibrium solidification conditions.

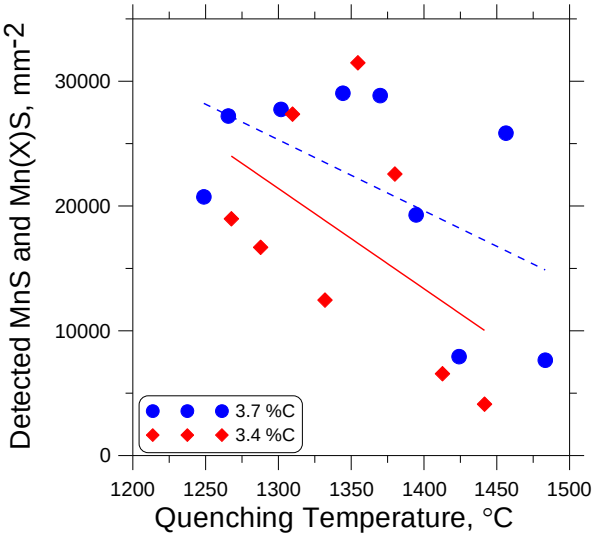

Fig. 3: The number of MnS and Mn(X)S inclusions at different quenching temperatures and carbon composition.

Lower quenching temperatures provide higher cooling rates. The number of the detected MnS and Mn(X)S inclusions is found to increase with increasing carbon content and decreasing cooling rates (lower quenching temperatures), see Figure 3. Due to the fact that MnS and Mn(X)S inclusions can serve as nucleation sites for the graphite can be concluded that as the number of these inclusions increases, earlier precipitation of graphite can occur, resulting to larger eutectic cells. This observation can explain partly the results of a previous work [14] where the eutectic cell size was found to increases with increasing carbon content.

It should be noticed that the graphite nucleation is a complex process which involves many different parameters and phenomena. For example the size of the eutectic cells depends on numerous parameters such as the secondary dendrite arm spacing (SDAS) [15] or the chemistry of the formed inclusions [7]. The present work aims to provide supplementary data to the existing knowledge.

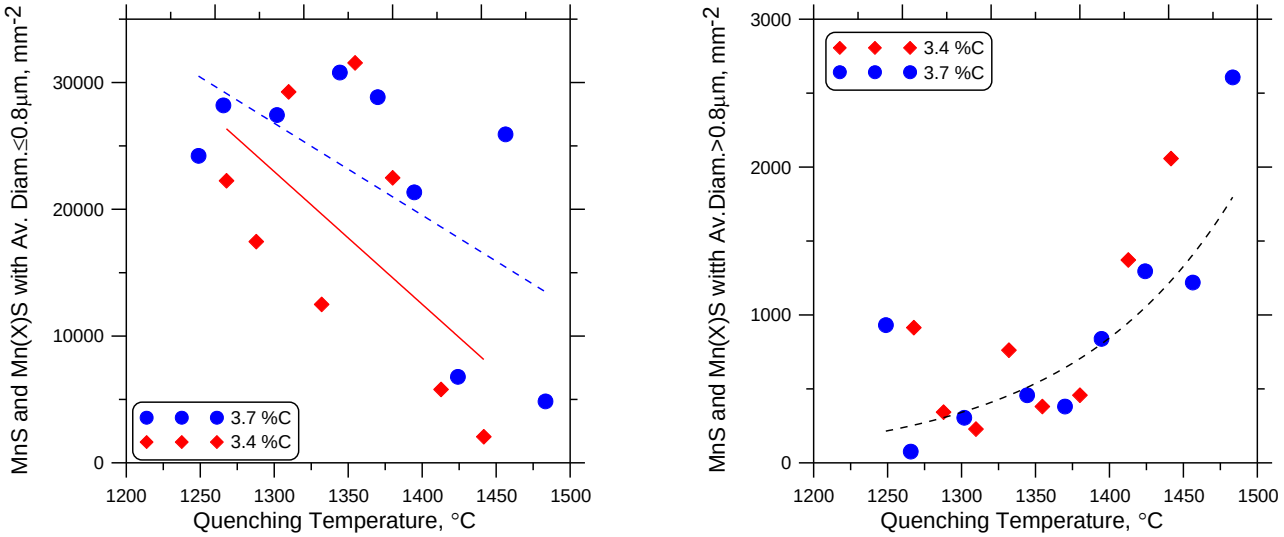

Fig. 4: Distribution of the MnS and Mn(X)S with size smaller or equal to 0.8µm (left) and with size larger of 0.8µm (right) at different quenching temperatures.

The average diameter of each inclusion was calculated as the diameter of a circle having area equal to the inclusion area. The increasing quenching temperature leads to a higher number of MnS and Mn(X)S inclusions with diameter smaller or equal to 0.8µm, see Figure 4 (left). On the other hand the higher number of MnS and Mn(X)S inclusions, having an average diameter larger than 0.8µm, were detected at high supercooling temperatures (lower cooling rates), Figure 4 (right). The later observation indicates the effect of cooling rate on the number of the of the large MnS and Mn(X)S inclusions. It has been proposed [16-17] that inclusions with radius larger than a critical radius can act as effective nucleation sites. Additionally in lamellar graphite iron the constitutional undercooling decreases with the reduction of the solidification rate [18]. Thus it appears that the absence of adequate number of large inclusions probably contributes to the increasing undercooling at high solidification rates in lamellar graphite iron.

Conclusions

1. Large number of MnS and Mn(X)S particles was found to exist at temperatures much higher than the predicted from the thermodynamic calculation. It is thought that these inclusions are the result of non-equilibrium cooling conditions.
2. Higher carbon content gives higher number of MnS and Mn(X)S particles and hence provides more potential nucleation sites for the precipitation of the graphite.
3. In view of the fact that higher quenching temperature provides lower cooling rates, the observed dependency between quenching temperatures, number and size of MnS and Mn(X)S, suggests that at lower cooling rates the number of the relatively large (>0.8µm) particles increases and thus the number of the particles that can act as effective nucleus for the graphite precipitation also increases.

References

1. I. Minkoff: ´The physical metallurgy of cast iron´, Jonh Wiley and sons, NY, 1983.
2. D.M. Stefanescu: *Materials Science and Engineering A*, 2005, 322-333.
3. R.B. Gundlach, J.F. Janowak, S. Bechet, K. Röhrigt: International symposium on the physical metallurgy of cast iron, ´The physical chemistry of inoculation of cast iron´, Stockholm 1984.
4. J. Tartera: *AFS International Cast Metals Journal*, 198, 7-14.
5. B. Lux, Recent research on Cast Iron, Edward Arnold Ltd, London, 1968, 241-288.
6. W. Weis: The Metallurgy of Cast Iron. St. Saphorin: Georgi Publishing Co, 1974, 69-79.
7. T. Skaland, O. Grong, T. Grong: Metallurgical Trans. A, 24A, 1993, 2321-2344.
8. J. F. Wallace, R. D. Rosemont: Conference on Modern Inoculating Practices for Gray and Ductile Iron, Illinois 1979, 41-73.
9. A. Sommerfeld, B. Tonn: *International Journal of Metalcasting*, vol 3, issue 4, 2009, 39-47.
10. I. Riposan, M. Chisamera, S. Stan, T. Skaland: AFS Cast Iron Inoculation Conference, Schaumburg Illinois, 2005, 31-41.
11. A. Velichko: Quantitative 3D characterization of graphite morphologies in cast iron using FIB microstructure tomography, Dissertation thesis work, University of Saarlandes, 2008, 103-110.
12. H.M. Mohmond, H. Fredriksson: *Metall. Trans. B*, 2012.

13. F. Schamber, Introduction to automated particle analysis by focused electron beam, Aspex Corporation, 2004.
14. V. Fourlakidis, L.V. Diaconu, A. Diószegi: Solidification and Gravity V, Trans Tech Publications, Switzerland, Materials Science Forum 649, 2010, 511-516.
15. A. Diószegi, K.Z. Liu, I.L. Svensson: *Int. J. Cast Met. Res*., 20.2, 2007, 68-72.
16. W. Kurz and D. Fisher: Fundamentals of solidification, 3rd edition, Trans Tech Publications, Switzerland, 1989.
17. A.L. Greer, A.M. Bunn, A. Tronche, P.V. Evans, D.J. Bristow: *Acta mater*., 2000, 48, 2823.
18. I. L. Svensson, A. Millberg; A. Diószegi, *Int. J. Cast Met. Res*., 2003, 16, 29-34.

Acknowledgements

The present work is a part of the research project JÄRNKOLL within the Casting Innovation Centre, financed by the Swedish Knowledge Foundation. Cooperating parties in the project are Jönköping University, Swerea SWECAST AB, Scania CV AB and Volvo Powertrain AB. Participating persons from these institutions/companies are acknowledged.

Crystallography of graphite spheroids in cast iron

K. Theuwissen[1], L. Laffont[1], M. Véron[2] and J.Lacaze[1]

[1]CIRIMAT, Université de Toulouse, ENSIACET, CS 44362, 31030 Toulouse cedex 4, France

[2]SIMAP Laboratory, CNRS-Grenoble INP, BP 46 101 rue de la Physique, 38402 Saint Martin d'Hères, France

To further understand graphite growth mechanisms in cast irons, this study focuses on the cristal structure of a graphite spheroid in the vicinity of its nucleus. A sample of a graphite spheroid from a commercial cast iron was characterized using transmission electron microscopy. The chemical composition of the nucleating particle was studied at the local scale. Crystal orientation maps of the graphite spheroid revealed misorientations and twist boundaries. High resolution lattice fringe.images showed that the basal planes of graphite were wavy and distorted close to the nucleus and very straight further away from it. These techniques were complementary and provided new insights on spheroidal graphite nucleation and growth.

Keywords: graphite growth, heterogeneous nucleation, crystal orientation, transmission electron microscopy

Article available in the International Journal of Cast Metals Research

The Occurrence and the Effect of Casting Skin in Compacted Graphite Iron

S. Boonmee[1] and D.M. Stefanescu[2]
[1]School of Metallurgical Engineering, Suranaree University of Technology, Thailand
[2]Department of Materials Science and Engineering, The Ohio State University, US

Most iron castings retain their as-cast surfaces because of their geometric complexity and to minimize the machining costs. However, the mechanical properties that are documented in standards (*i.e.* ASTM) are tested on fully machined test bars. Therefore, the effect of the as-cast surface and sub-surface features (commonly referred as "casting skin") on mechanical properties should be evaluated.
Preliminary works have shown the negative effect of the casting skin on mechanical properties of grey and ductile irons. This paper reviews the recent works on the casting skin effect on tensile and fatigue properties in compacted graphite and ductile irons. It was found that the tensile and fatigue strength were reduced by 9% and 40% respectively because of the presence of the casting skin. In addition, the correlations between processing parameters (*e.g.* nodularity and section thickness) and the casting skin features were presented. The experimental results suggest that the Mg depletion because of metal-mould and metal-air interactions was the main reason for the formation of the casting skin.

Keywords: Compacted graphite iron, Ductile Iron, Casting Skin, Formation Mechanism, Casting Surface.

Article available in the International Journal of Cast Metals Research

On microstructure-based mechanical behaviour of a ductile iron component

Ingvar L Svensson and Jakob Olofsson
Jönköping University, School of Engineering, Materials and Manufacturing - Casting
P.O. Box 1026. SE-551 10 Jönköping. Sweden

Castings are produced by a manufacturing method which gives the components properties that are depending on design, metallurgy and casting method. The aim is to explore and model the local properties in a cast iron component where the properties can vary in the casting volume, which makes it difficult to optimize the castings with good accuracy.
This paper presents modelling and simulation of local microstructure-based mechanical behaviour. The mechanical behaviour can be shown as stress-strain curves at different locations of the cast iron component. A careful evaluation of tensile tests are made of three industrial components to characterize the stress – strain curves for regions holding different microstructures. This data will be used to determine the local properties and how they will influence the component behaviour at service.

Keywords: ductile iron, microstructure, stress-strain curves, simulation, elastic deformation, plastic deformation.

Article available in the International Journal of Cast Metals Research

Crash Behavior of ADI Steering Knuckles

L. Reissig[1], A. Nofal[2*], W. Boehme[1], T. Reichert[1], I. H. Al Masry[3]

[1]Fraunhofer Institute for Mechanics of Materials IWM, Woehlerstrasse 11, Freiburg, Germany
[2]Central Metallurgical R&D Institute (CMRDI), P.O. Box 87, Helwan, Cairo, Egypt
[3]The German University in Cairo (GUC), El Tagamoa El Khames, New Cairo City, Egypt

Within a German Egyptian Research Fund (GERF) project, prototypes of steering knuckles with varying heat treatments were produced and their crash behavior was compared to a standard type steering knuckle. Therefore, high strain rate tensile tests were performed with round bar specimens, which were extracted from steering knuckles. The ADI materials achieved tensile strength values of up to 1400 MPa and an elongation at fracture of about 1 %. Lower strength ADI qualities attained tensile strengths of about 900 MPa and 1110 MPa with elongations at fracture of about 9 % and 14 %, respectively. For comparison a standard ductile cast iron for steering knuckles achieved a tensile strength of approximately 500 MPa and an elongation at fracture of about 23 %. These results demonstrate that ADI materials may exhibit a good potential for crash loaded automotive components. The TRIP effect which leads to high strength in combination with relatively high elongation at fracture was investigated by metallographic examination and X-ray-diffraction analysis.

Keywords: Austempered Ductile Iron, ADI, TRIP, phase transformation, crash

Introduction

Within the GERF research project »Introduction of Advanced Austempered Ductile Iron (ADI) Technologies to the Egyptian Industry« prototypes of ADI steering knuckles [1, 2, 3], which denotes an automotive component containing the wheel hub and connecting it to the suspension, in three different heat treatment conditions were produced in a pilot foundry of the Department of Metal Casting at the Central Metallurgical Research and Development Institute (CMRDI). As a part of this project the potential of this ADI material under misuse and crash conditions was investigated by tensile tests with high strain rates at Fraunhofer IWM and the results were compared to a standard type steering knuckle of a German passenger car which was made of ductile cast iron. To investigate the Transformation Induced Plasticity (TRIP) effect of the ADI material under misuse and crash load conditions, additional microstructure investigations and X-ray diffraction analyses were carried out before and after the high strain rate tensile tests.

Experimental Procedure

For the investigation of ADI steering knuckles six prototypes were casted in comparable dimensions of a standard type steering knuckle of a German passenger car. All ADI steering knuckles had the same chemical composition. The chemical composition of the ADI knuckles is given in table 1 and compared to the one of the standard type steering knuckle. After casting, three different heat treatments were applied to the ADI steering knuckles. Two steering knuckles (in total six) were available for each of the three ADI heat treatment conditions, see table 2. In comparison to the standard type steering knuckle which shows a ferritic/pearlitic microstructure, see fig.1a, ADI steering knuckle #1 has a fine ausferritic matrix (acicular ferrite and 21.6 vol. % retained austenite) which is caused by the low austempering temperature of 275 °C, see fig.1b. The higher austempering temperature of 375 °C of steering knuckle #2 leads to a coarser ausferrite structure with 38.3 vol. % retained austenite, see fig.1c. A mixture of fine ausferrite with 18.4 vol. % retained austenite and colonies of proeutectoid ferrite is caused by an intercritical annealing (partial austenitization) [7] of steering knuckle #3, see fig.1d.

The content of retained austenite was determined by X-ray diffraction analysis. This method is the most common method to determine the amount of retained austenite in steels. For a polycrystalline sample, the integrated intensity from any diffraction peak is proportional to the volume fraction of that phase. The austenite fraction is determined on basis of the ratio of the austenite and ferrite diffraction peak intensities.

* Corresponding author, email: adelnofal@hotmail.com

Table 1: Chemical composition of standard type and ADI steering knuckles.

Alloying element	C	Si	Mn	P	S	Cu	Mo	Mg	Fe
Standard type steering knuckle	3.73	2.62	0.3	0.026	0.01	0.67	0.194	0.06	Bal.
ADI steering knuckles	3.5	2.6	0.26	0.01	0.001	0.5	0.3	0.05	Bal.

Table 2: Heat treatment of ADI steering knuckles.

Steering Knuckle	Heat Treatment		Targeted Properties
	Austenitization	Austempering	
#1	900°C - 1 hr	275°C - 1.5 hr	Excellent strength, low ductility
#2	900°C - 1 hr	375°C - 1.5 hr	High strength, improved ductility
#3	820°C - 1 hr	300°C - 1.5 hr	Lower strength and hardness good ductility and machinability

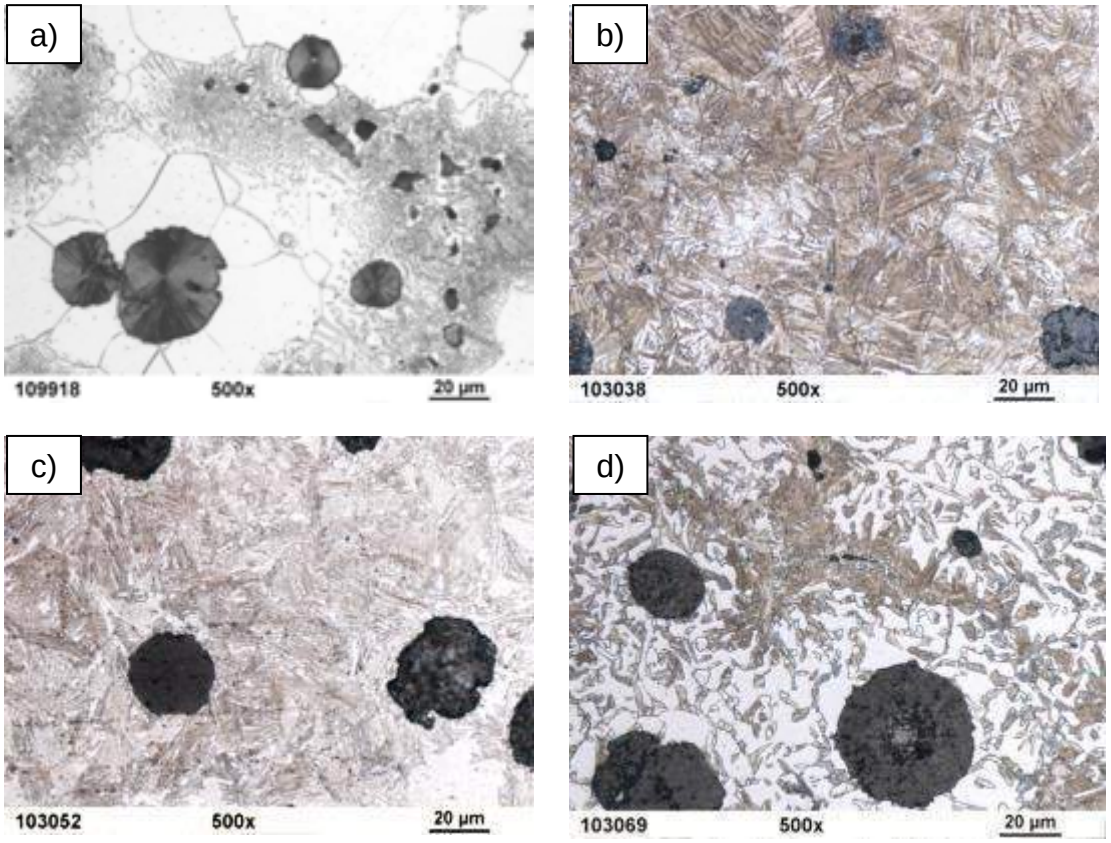

Fig.1: Microstructure of the steering knuckles: a) ferrite/pearlite and spheroidal graphite of the standard type steering knuckle, b) fine ausferrite (acicular ferrite and retained austenite) and spheroidal graphite of ADI steering knuckle #1, c) coarser ausferrite and spheroidal graphite of ADI steering knuckle #2, d) fine ausferrite, proeutectoid ferrite and spheroidal graphite of ADI steering knuckle #3

To be able to assess the material behavior under misuse and crash load conditions high strain rate tests are necessary as the mechanical properties are likely to be strain rate dependent. Therefore tensile tests were performed in a servo hydraulic testing machine at crash-like strain rates of $\dot{\varepsilon} = 50\ s^{-1}$. High speed measurement techniques were utilized in accordance with [4]. The force measurement was performed with a patent registered low vibration load cell [5] and the

elongation of the gauge length of the specimens was measured by a high speed video camera [6] with a time resolution of 70.000 frames.s^{-1}. The tests were carried out at room temperature (24 ± 2 °C).

Round bar tensile specimens, see fig.2, were machined from the steering knuckles as shown in fig.3.

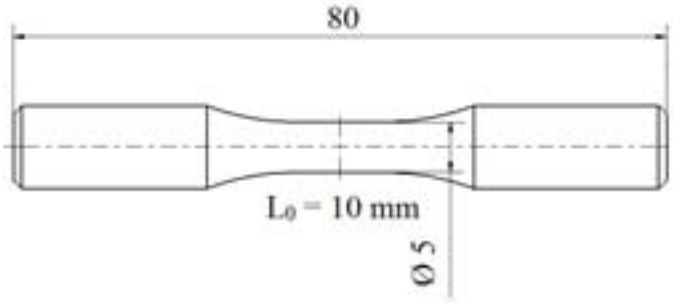

Fig.2: Geometry of the round bar specimens, which were used for the high strain rate tests.

Fig.3: Standard type steering knuckle and position of the round bar specimens.

Two ADI steering knuckles were available for each of the three heat treatment conditions. In total seven specimens have been machined from the ADI and two specimens have been machined from the standard type material for the high strain rate tensile tests.

Results and Discussion

The results of the high strain rate tensile tests are summarized in fig.4 and table 3. Here, the standard type steering knuckle shows an average tensile strength of approximately R_m = 500 MPa and an average elongation at fracture of approximately A_{10} = 23 %. The ADI material of steering knuckle #1 with a fine ausferritic microstructure (austenized at 900 °C and austempered at 275 °C) shows the highest average tensile strength of the investigated steering knuckles of R_m = 1447 MPa but the lowest elongation at fracture of A_{10} = 0.7 %. Steering knuckle #2 with a coarser ausferritic microstructure (austenitized at 900 °C and austempered at 375 °C) exhibits the best combination of tensile strength of R_m = 1110 MPa and a relatively high average elongation at fracture of 14.0 % caused by the high amount of retained austenite. The lowest tensile strength of the ADI materials was measured at steering knuckle #3 with an ausferritic / proeutectoid ferrite microstructure (intercritical annealed) with an average tensile strength of R_m = 880 MPa caused by the presence of proeutectoid ferrite. This steering knuckle showed also a relatively high elongation at fracture in the range of 8.8 - 12.2%, which is related to the effect of the presence of both proeutectoid ferrite and retained austenite..

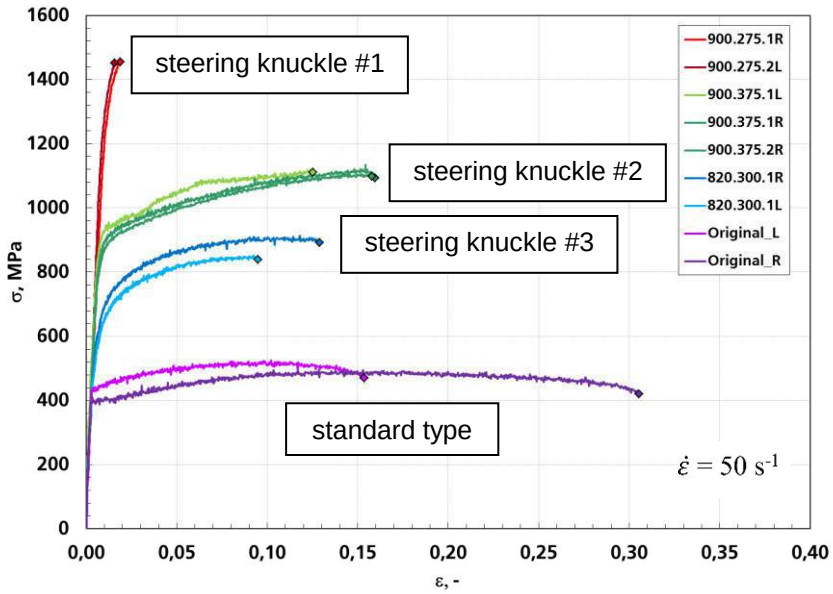

Fig.4: Results of the high strain rate tensile tests.

Table 3: Results of the high strain rate tensile tests at a strain rate of 50 s^{-1}.

Specimen	Test speed [m s^{-1}]	Strain rate [s^{-1}]	$R_{p0,2}$ [MPa]	R_m [MPa]	A_{10mm} [%]
#1, spec. 1	0.7	50	1300	1454	0.7
#1, spec. 2	0.7	50	1336	1440	0.6
average values			**1318**	**1447**	**0.7**
#2, spec. 1	0.7	50	874	1115	15.1
#2, spec. 2	0.7	50	852	1103	15.0
#2, spec. 3	0.7	50	900	1111	11.8
average values			**875**	**1110**	**14.0**
#3, spec. 1	0.7	50	620	907	12.2
#3, spec. 2	0.7	50	579	846	8.8
average values			**606**	**880**	**9.4**
standard type, spec. 1	0.7	50	395	486	30.3
standard type, spec. 2	0.7	50	436	515	15.5
average values			**416**	**501**	**22.9**

Following the high strain rate tensile tests, microstructural investigations were carried out with a light optical microscope. In comparison to the microstructure determined before the testing, see fig.1, no significant changes can be observed. Probably this is caused by the fact that the transformed martensite has a comparable etching behavior as the retained austenite. Further investigations are necessary to clarify this. By X-ray diffraction analysis, a significant reduction of the amount of retained austenite at the fracture surface of the ADI specimens was measured after the tests, see table 4. This is caused by the transformation of the metastable retained austenite under mechanical load into martensite (TRIP effect [8, 9]). This TRIP effect leads to a combination of high strain rate tensile strength and a relatively high fracture strain of the ADI material investigated. These results are in accordance with results of previous investigations under similar conditions, see [6].

Table 4: Values of retained austenite content in absolute vol. % measured by X-ray diffraction analysis before and after high strain rate tensile tests.

Steering knuckle type	Before high rate tensile test	After high rate tensile test
#1	21.6%	< 3%
#2	38.3%	3.9%
#3	18.4%	< 3%

Conclusions

1. In comparison to a standard type steering knuckle the investigated ADI steering knuckles austempered at 275°C reveal a much higher average tensile strength of R_m = 1447 MPa and a comparably low elongation at fracture A_{10mm} = 0.7 % under high strain rate test conditions (steering knuckle #1).
2. ADI material austenized at 900 °C and austempered at 375 °C (steering knuckle #2) shows a high average strength of R_m = 1110 MPa in combination with relatively high elongation at fracture of A_{10} = 14.0 %. Thus this material has a high potential for crash loaded car components also with regard to weight reduction in comparison to a standard type steering knuckle made of ductile cast iron.
3. Steering knuckles #3 partially austenitized in the intercritical temperature range at 820°C and austempered at 300°C showed lower tensile strength in the range of 846-907 MPa and a relatively high elongation in the range of 8.8-12.2%. The lower strength is due to the presence of proeutectoid ferrite, which is expected to lead to better machinability and lower production cost of the component.
4. The combination of a high strength and a relatively high elongation at fracture is caused by the TRIP effect, where retained austenite transforms into martensite under mechanical load. This reduction of retained austenite could only be verified by X-ray diffraction analysis. It could not be determined by microstructural analysis by light optical microscope.
5. Since higher deformations are recommended for suspension parts, in particular for legal reasons in context of accidents, both heat treatments used for steering knuckles #2 and #3 lead to high strength and ductility levels, which renders the resulting two ADI grades potential materials for the production of steering knuckles.

References

1. J. Aranzabal, G. Serramoglia, C.A. Goria, A. Rousiere: *Int. J. of Cast Metals Research*, 2003, 16, 185-191.
2. A. Nofal: Proc. of 10th Int. Conf. on 'Mining, Petroleum and Metallurgical Engineering', Assuit, Egypt, March 2007.
3. K. M. Ibrahim, M. M. Ibrahim, A. Nofal, A. H. El-Sawy: *Materials Science and Technology*, 2007, 15, no 4, 225-244.
4. W. Böhme: *Materialprüfung, Materials Testing*, 2008, Carl Hanser Verlag, München, Vol. 50 (4), 199-205.
5. W. Böhme, M. Hug: *European patent: EP 1 466 157 B1 (03.08.2005)*, Nov. 7, 2006.
6. W. Böhme, L. Reissig: *Giesserei 99 07*, 2012, 34-40.
7. N. Nofal: *Journal of Metallurgical Engineering (ME)*, Jan. 2013, Volume 2 Issue 1, 1 – 18.
8. J. L. Garin, R. L. Mannheim: *Journal of Materials Processing Technology*, 2003, no 143-144, 347-351.
9. H. Berns, W. Theisen: 'Eisenwerkstoffe, Stahl und Gusseisen', 4th edn., 170, 2008, Springer Verlag.

Acknowledgement

This German Egyptian Research Fund (GERF) project with the title »Introduction of Advanced Austempered Ductile Iron (ADI) Technologies to the Egyptian Industry« project was funded by the German Federal Ministry of Education and Research (BMBF), funding code 01DH12014. The responsibility for the contents of the publication is with the authors.

High-temperature corrosion fatigue of a ferritic ductile cast iron in inert and corrosive environments at 700°C

M. Ekström[1*], S. Jonsson[1]

[1] Division of Mechanical Metallurgy, Materials Science and Engineering, Royal Institute of Technology, SE-100 44, Stockholm, Sweden

In the present work, low-cycle fatigue testing of a ferritic ductile cast iron named SiMo51 has been carried out in three atmospheres: argon, air and a synthetic diesel exhaust-gas at 700°C. The fatigue life was reduced up to 80% in the worst case. Two crack growth mechanisms were observed and directly linked to oxidation. At weak oxidation, a nodule-to-nodule crack growth occurred. At strong oxidation, crack growth occurred through oxidized material in front of the crack tip.

Keywords: high-temperature LCF, corrosion fatigue, ductile cast iron, crack growth mechanisms

Article available in the International Journal of Cast Metals Research

Cast iron alloys for exhaust applications

K. Papis[1], S. Tunzini[1] and W. Menk[1*]

[1]Georg Fischer Automotive AG, Schaffhausen, Switzerland

Downsizing of engines – gasoline as well as Diesel - helps to reduce CO2-emissions. Smaller engines at the same or even raised power levels result in higher exhaust gas temperatures. In personal cars, these are raised to above 850°C in Diesel engines and up to 1,050 °C for turbocharged gasoline engines. Ferritic Si- and Mo-alloyed ductile iron grades are standardised in Europe in EN-16'124. However, these materials are not sufficient for highly turbo charged engines. Based on SiMo ductile iron, new ferritic materials have been developed to raise ferrite/austenite transition temperature, high temperature strength and scaling resistance. The paper describes the development of new ferritic high temperature ductile iron grades, their properties, serial applications and newest achievements in realizing even higher working temperatures.

Keywords: ductile iron, SiMo, temperature resistance, exhaust manifold, turbocharger, ferrite/austenite transformation.

Introduction

The omnipresent public discussion about climate warming and the required drastic reduction of CO2 emissions forces the car producers to develop new cars with lower gasoline consumption and reduced emissions as soon as possible. The raise of specific power and mean pressure of downsized engines leads to a raise of exhaust temperatures. These are in the region of 850 to 900 °C for Diesel engines. For turbocharged gasoline engines, a value of 1,050 °C is mentioned.[1] Additionally, the downsizing concept leads to rising transferred energy amounts with respect to the cylinder volume.
These actual engine developments lead in summary to a remarkable increase of thermal demands of components which are in contact with exhaust gas such as exhaust manifolds or turbochargers. Conventional materials hit their limitations therefore and new solutions have to be found. In general, the component temperatures remain 50 to 80 °C below the exhaust gas temperature, but at exposed positions – e.g. thin walled areas in contact with exhaust gas from several sides, or areas with thermal insulation – the temperature of the material can reach values close to these of the exhaust gas.

Materials for exhaust applications

Depending on exhaust temperatures, various materials are used for these applications. For exhaust manifolds, welded steel sheet constructions are in competition with castings, while turbocharger housings are cast in almost all cases. Ferritic cast iron with 4 to 5 % Silicon and 0.5 – 1.0 % Mo, compacted graphite cast iron (GJV) as well as nodular iron (GJS) is used for component temperatures up to 820 °C. Along with standard SiMo materials, variants with additional Cr or Ni in the range of 0.5 to 1.0 % are available (SiMoCr and SiMoNi, respectively), which are said to have a higher scaling resistance. At higher exhaust temperatures up to 950 °C, either austenitic ductile iron grades, such as GJSA-XNiSiCr35-5-2, known also as Ni-Resist D5S, or highly Cr alloyed ferritic steels are used. At temperatures up to 1'000 °C or slightly higher, only highly alloyed austenitic steels are able to fulfil the requirements. At even higher temperatures, Ni-based alloys have to be used.

Superior grade materials often need a higher amount of alloying elements. Thus, material costs rise continuously with rising temperatures of the application. Especially Nickel, which exhibited a volatile market price in the near past, is used in large amounts. From an economic point of view, it is advantageous to develop lower alloyed and therefore cheaper materials to be used at elevated temperatures and to substitute more expensive materials

Because of these facts, we decided to further develop ferritic SiMo materials several years ago, and thus to extend the range of use of such material to higher temperatures. The aim of this development was to reach properties close to the austenitic ductile iron GJSA-XNiSiCr35-5-2, which is predominantly used at component temperatures of 820 °C up to 930 °C.

Requirements for materials for exhaust applications

Materials for exhaust manifolds and turbocharger housings are exposed to heavy thermal and thermo-mechanical loads. The most important properties of such materials are therefore: [2]

- Scaling resistance

* Corresponding author, email: werner.menk@georgfischer.com

- Tensile strength, especially at elevated temperatures
- Temperature stability of the microstructure
- Thermal fatigue

Thermal fatigue or the resistance against thermo-mechanical fatigue are not singular material properties, but depend on various material characteristics. With each heating cycle of the component, temperature gradients are created which induce tension due to different thermal elongation at different positions and temperatures respectively. By mounting this component to another, such as the cylinder head, free thermal expansion is restrained, causing additional stress.

History of the development of ferritic ductile iron for temperatures above 800 °C

Si-Mo-alloyed ductile iron is known since more than 30 years – e.g., in 1980, Georg Fischer distributed documentation about such materials. [3] In the late 80s, French scientists did a lot of work to find a ductile iron material applicable at higher temperatures, adding some Aluminium. [4, 5] Due to massive problems caused by the very high tendency of this material to build oxide slags during the pouring process, the development was not successfully introduced on the market. We do not know an industrial application of this material. At the end of the 90s, we pursued the French work and developed the patented material 'SiMo1000®'. [6] In 2008, with further development of this material and especially the casting process, it was possible to go into serial production of exhaust manifolds and turbocharger housings for exhaust temperatures close to 900 °C:

Fig.1: Examples of a serial exhaust manifold and turbocharger housings made of GJS SiMo1000.

Further development of GJS SiMo materials

First experiments consisted of casting samples with various chemical compositions, measuring their ferrite/austenite transformation temperatures by dilatometry and evaluating the influence of the alloying elements on the transformation temperature. It could be shown that Molybdenum, Silicon and Aluminium increase the transformation temperature. The combination of Silicon and Aluminium by a Si-equivalent (Si-eq. = % Si + 0.8 x % Al) results in a much better correlation to the transformation temperature than with the two elements separately:

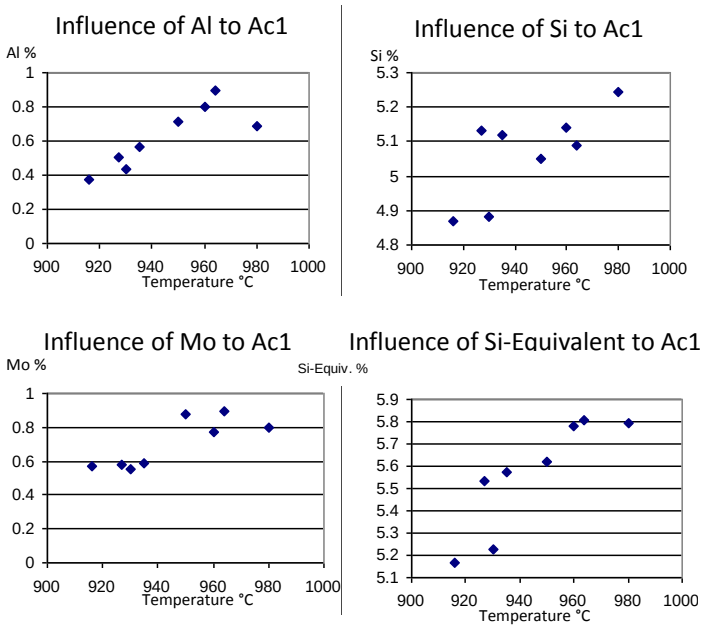

Fig.2: Influence of different alloying elements on the ferrite/austenite transformation temperature

Using multiple regression analysis, a formula to predict transformation temperatures was developed. A comparison of calculated and measured transformation temperatures is given in Fig. 3:

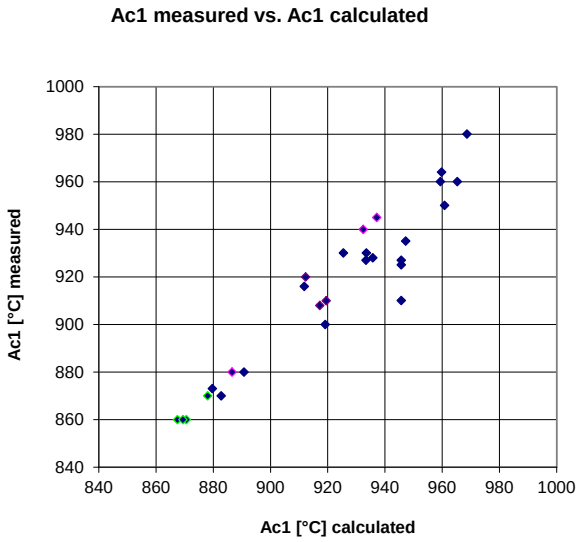

Fig.3: Correlation between calculated and measured ferrite/austenite transformation temperatures

However, a ferrite/austenite transformation temperature which is higher than the exhaust gas temperature is only one criterion for the applicability of a material. Furthermore, strength, creeping behaviour and scaling at elevated temperature have to be considered. Scaling still has to be improved by empirical trials by varying chemical composition and measuring the behaviour at elevated temperatures. Fig. 4 for example shows the scaling of different materials: compared to conventional materials, the GF SiMo 1000® exhibits a much better resistance to high temperature oxidation.

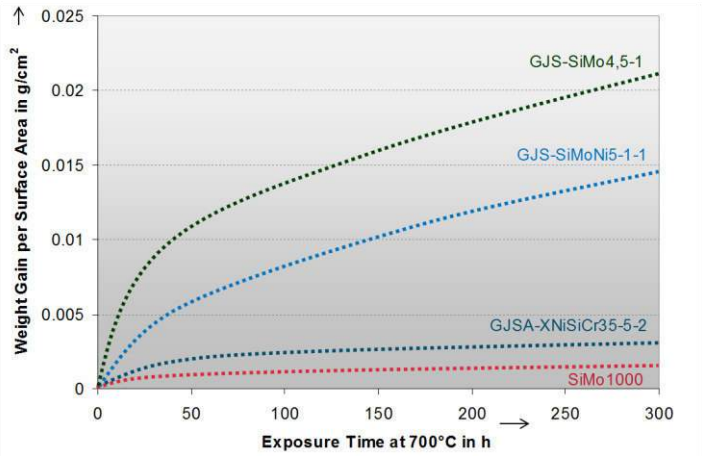

Fig.4: Scaling of different high temperature materials in unmoved air at 700 °C.

But for the prediction of transition temperature and possible precipitations and phases to improve high temperature strength and creeping, we do have simulation tools today.

Results and Discussion

Influence of Vanadium

Fig. 5 and 6 show a comparison of simulation results using the software JMatPro. Two chemical compositions with a variation of the Vanadium content were simulated, one without V, the other one with 0.4 wt-% V:

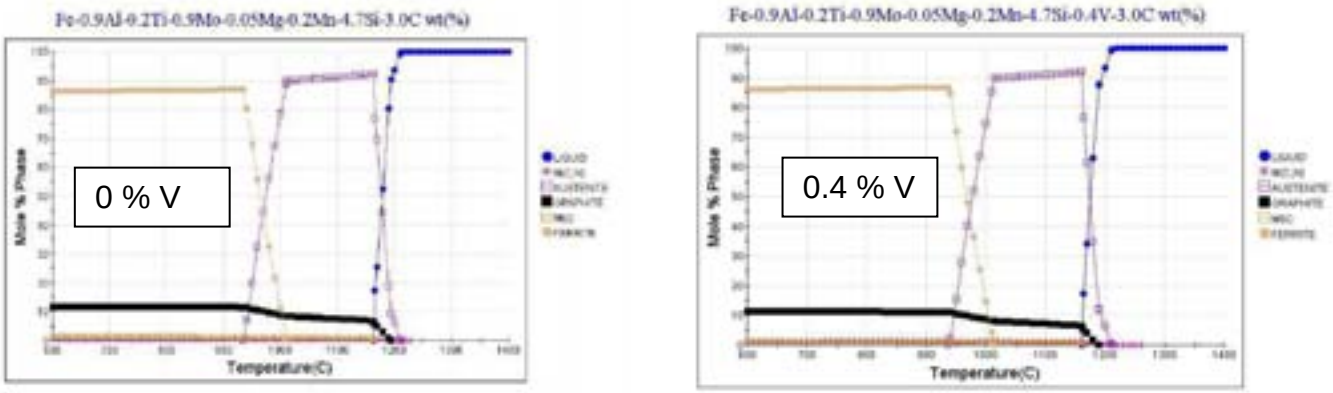

Fig.5(left) and 6 (right):
JMatPro-Simulation of two compositions with variations in the Vanadium content: Fig. 5 without, Fig. 6 with 0.4 % V. The simulation shows a ferrite/austenite transformation temperature of 935 °C without V and 938 °C with 0.4 % V. The addition of 0.4 % V leads to a raise of 0.42 % M(C, N) to 1.2 % and a drop of 2.21 % M6C to 0.86 %. M(C,N) consists of VC, where as M6C consists of Mo6C and Fe6C.

The experiment results in an increased total amount of carbides in the microstructure:

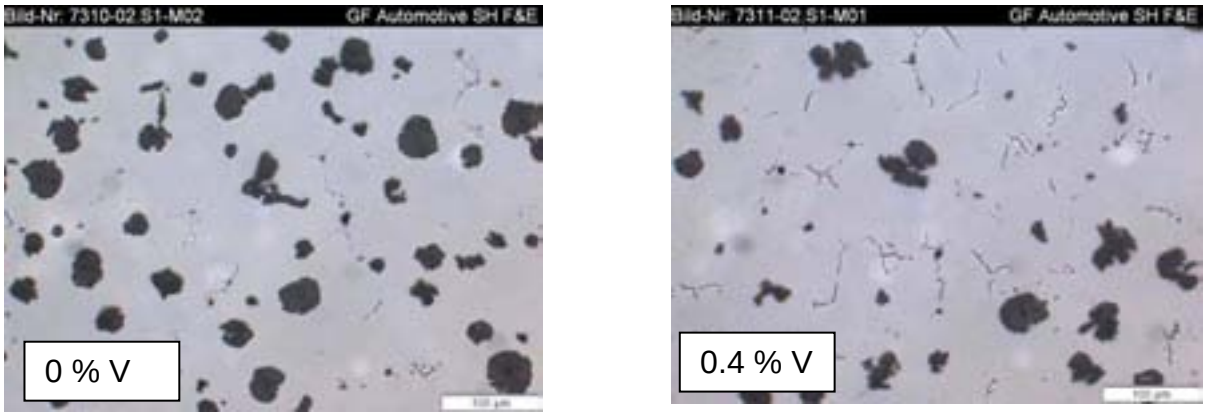

Fig.7(left) and 8 (right): Micrographs of the two variants without V (left) and with 0.4% V (right). The experiment confirms the predicted higher amount of carbides with 0.4 % V.

The effect of the higher carbide content was an increase of tensile strength at 800 °C from 52 MPa to 63 MPa (+20%).

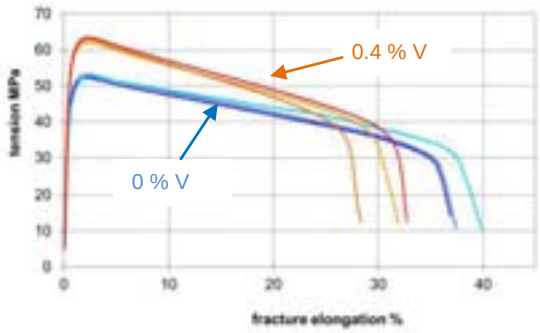

Fig.9: Result of tensile tests at 800 °C: significantly higher tensile strength with 0.4 % V (measured at ÖGI with a speed of 0.3 mm/min, according to ISO 6892-2:2011 .)

However, not every simulation result can be reproduced by experiment: According to the simulation, the variant with 0.4 % V should exhibit a ferrite/austenite transformation temperature of 938 °C, compared to 935 °C without V. The result of the experiment is shown in figure 10:

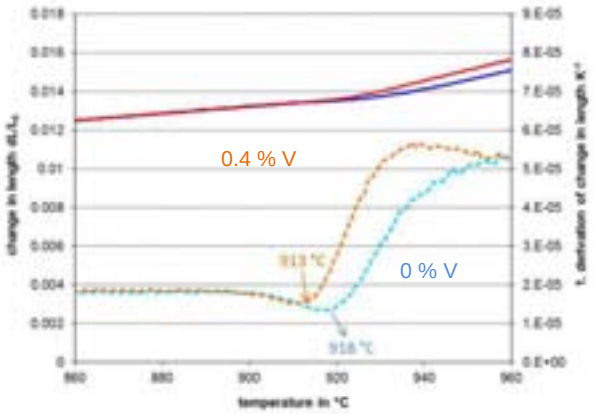

Fig.10: Result of measuring the ferrite/austenite transformation temperature by dilatometer.

The dilatometric measurement shows that 0.4 % V reduced the ferrite/austenite transformation temperature by 5 °C instead of increasing it by 3%. But both differences - simulation and experiment - are very small and can be interpreted as insignificant.

One limitation of simulation methods is the lack of data on some elements of interest, e.g. the solid solution strengthening element Co, which is known to raise transformation temperature and tensile strength at elevated temperatures.

Further Experiments

The element Cobalt is known as a ferrite stabilizer and a ferrite strengthener by solid solution. Adding Co to a SiMo iron could thus be a possibility to raise ferrite/austenite transformation temperature and high temperature strength. Unfortunately, our simulation tools have no Co implemented. To characterize the influence of Co, its effect on transformation temperature was measured empirically:

Melt No. 1 was prepared with the following composition:

2.5 % C, 5.2 % Si, 0.25 % Mn, 0.21 % Cu, 0.6 % Al, 1.8 % Co.

The composition of melt No. 2 was:

2.5 % C, 5.2 % Si, 0.24 % Mn, 0.21 % Cu, 0.4 % Al, 4.0 % Co.

Using our empirical formula the calculated ferrite/austenite transformation temperature was around 930 °C and 920 °C for melt No. 1 and melt No. 2, respectively (10% lower due to the influence of Al) – without considering Cobalt in the calculation.

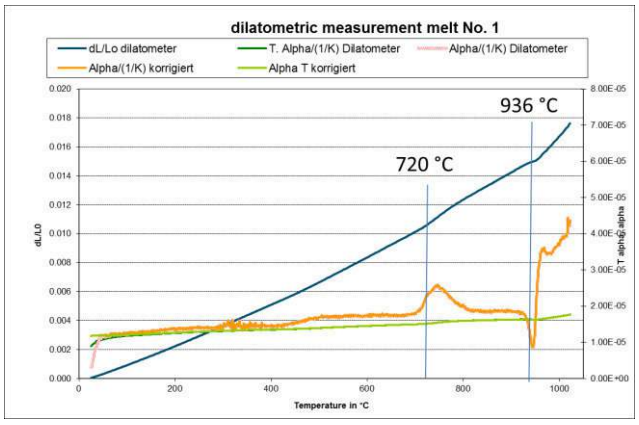

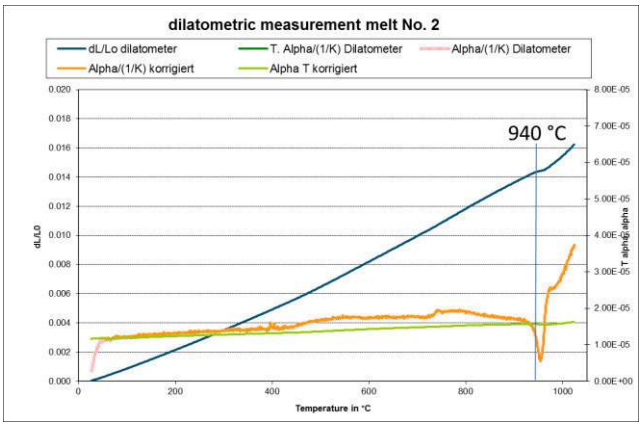

Fig.11 (left) and 12 (right): Dilatometry measurement graphs, indicating the ferrite/austenite-transformation temperature of melt No. 1 with 1.8 % Co, and melt No. 2 with 4.0 % Co. The first peak of melt No. 1 at 720 °C is probably due to solution of remaining pearlite.

The difference between calculated and measured transformation temperature is increased from plus 6 to plus 10 °C by raising the Cobalt content from 1.8 to 4.0 %. It seems therefore, that Co has a moderate raising effect on the transformation temperature. Considering the insignificant effect of Co on high temperature strength (see Fig. 13 and 14), the importance of this element as an alloy is negligible both from technological and commercial points of view.

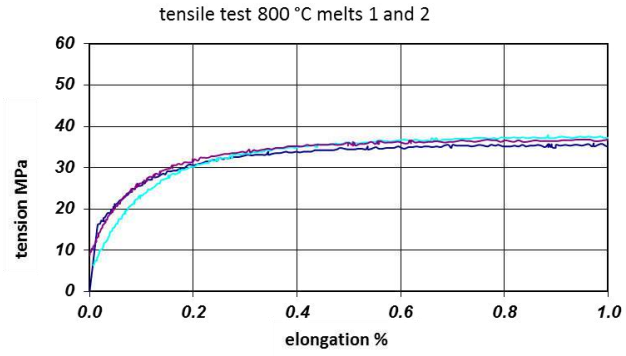

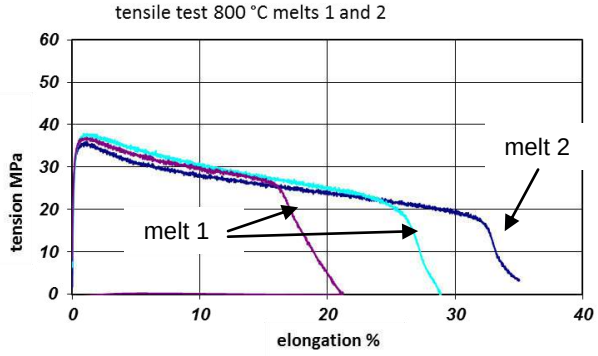

Fig.13 (left) and 14 (right): Result of tensile tests at 800 °C. The tensile strength Rm of melt No. 1 with 1.8 % Co and melt No. 2 with 4.0 % Co is 36 MPa and 38 MPa, respectively.

4. At the end of the 90s, Georg Fischer pursued the idea and developed a new GJS SiMo material on the basis of the French idea. This material can be used at exhaust gas temperatures up to 900 °C, which is suitable for exhaust manifolds and turbocharger housings of downsized Diesel engines, but not enough for turbocharged gasoline engines.
5. Recent investigations on as-cast ductile iron materials with Cobalt as alloying element showed, that this element slightly raises the ferrite/austenite transformation temperature, but has no significant effect on high temperature strength. The price of Co is too high to see an advantage in using this element.
6. Therefore, ductile iron materials with increased Si-, Al-, Cr-, V-, Ti-, N-contents show a big potential for a new as cast ductile iron with moderately higher element costs compared to conventional SiMo, but with a ferrite/austenite transformation temperature above 1,000 °C and a high temperature strength similar to the much more expensive austenitic ductile iron. This new material provides a potential for being used for exhaust manifolds and turbocharger housings of charged gasoline engines.
7. According to the experience we made with the development of the GF SiMo 1000® material, we have to assume, that still a lot of work has to be done until this new material is optimized so far for industrial production.

References

1. R. Krebs et al.: *MTZ 66,* 2005, 11, 844-856
2. W. Kallen, K. Röhrig, *konstruieren + giessen*, 26, 2001, 17-39.
3. Warmfeste Werkstoffe (SiMo5.1): Georg Fischer AG, Oct.24, 1980. (Documentation)
4. European patent EP 0 534 850, registered 24.9.1992
5. A. Reynaud, J.-L. Roberge: *Fonderie – fondeur d'haujourd'hui,* 1999, 182, 37-41.
6. European patent EP 1 386 976, registered 30.04.2003

Acknowledgement

The assistance of Ms. F. Friso and Mr. R. Kubiz is gratefully acknowledged.

Local chill as a mean of increasing strength in grey cast iron

Fredrik Wilberfors[a] Ingvar L Svensson[b], Jessica Elfsberg[c], Kerstin Richnau[d] and Nulifer Ipek[e]

[a]Scania CV AB, Engine development, SE-151 87 Södertälje Sweden

[b]Jönköping University, School of Engineering, Material and Manufacturing – Casting P.O. Box 1026, SE-551 11 Jönköping Sweden

[c,d,e]Scania CV AB, Materials technology, SE-151 87 Södertälje Sweden

The influence of a chill on the mechanical properties and microstructural features in grey cast iron has been studied. Some of the main findings were that the chill refined the microstructure and modified the graphite distribution from A to D/E. Eutectic cell size was reduced by 60-70 %. The Brinell hardness increased while the Vickers hardness, measured in dendrite arms, was unaffected. Fatigue testing in four point bending showed that the fatigue limit was increased by 20-30 % in the chilled samples. An increase in tensile strength, proof strength and Young's modulus was also observed in the chilled samples. The increase in fatigue limit was approximately twice as high as the increase in tensile strength. A possible explanation could be that the eutectic cell size had a more pronounced effect on the fatigue limit than on the tensile strength.

Keywords: grey cast iron, mechanical properties, chill, eutectic cell size, fatigue limit

Article available in the International Journal of Cast Metals Research

Austenite Dendrite Morphology in Lamellar Cast Iron

Attila Diószegi[1], Vasilios Fourlakidis[2] and Ruben Lora [1]
[1]Jönköping University, School of Engineering,
Materials and Manufacturing – Foundry Technology
P.O. Box 1026, SE-551 10 Jönköping, Sweden
[2]Swerea SWECAST AB, P.O. Box *2033,* SE-550 02 Jönköping, Sweden

Primary austenite has been underestimated in general when the theories of nucleation, solidification, microstructure formation and mechanical properties was established for cast iron and particularly for lamellar cast iron. After extensive use of colour etching during the last two decades it has been found that primary austenite dendrites can be characterized using general morphology parameters like those used for other technical cast alloys with dendritic structure. The present work aims to investigate the primary austenite morphology of as-cast samples of a hypoeutectic lamellar cast iron produced with different cooling rates. Morphological parameters as the area fraction primary austenite, the secondary dendrite arm spacing, the dendrite envelope surface, the coarseness of the primary dendrite expressed as the relation between the volume of the dendrite and its envelope surface and the coarseness of the interdendritic space also known as the hydraulic diameter are measured. Furthermore the role of the size of investigation area is revealed be sequential investigation. A strong relation between all measured morphological parameters and the solidification time have been established excepting the volume fraction of primary austenite which is constant for all cooling conditions.

Keywords: austenite, primary dendrite, dendrite envelope, interdendritic phase.

Article available in the International Journal of Cast Metals Research

Effect of Electric Current Pulse on Solidification Microstructure of Hypereutectic High Chromium Cast Iron Cooling from the Temperature between Liquidus and Solidus

R.F. Zhou*, Y.H. Jiang, R. Zhou, L. Zhang
Faculty of Materials Science and Engineering, Kunming University of Science and Technology, Kunming, Yunnan, PR China

In this paper, the solidification course of the hypereutectic High Chromium Cast Iron (HCCI) was treated by the Electric Current Pulse (ECP). Effects of treating time, initial temperature applying ECP and its parameters (voltage, frequency, pulse width) on the microstructure were researched. The results showed that the ECP can promote refining of primary and eutectic carbides significantly. As the result of strengthening role on the solute fluctuation by ECP, the larger effect of nucleation and refinement promoting of carbides was displayed at the initial temperature closer to the liquidus. The more obvious refinement effect was showed under longer treating time. Huge differences in microstructure were shown under different combination of the three ECP parameters. Some combinations promoted primary carbide refinement and eutectic carbide number reduce obviously, and fine granular primary carbides with the size of ~20μm could be obtained. Some other combinations led to a trend of eutectic carbide granulating.

Keywords: hypereutectic high Chromium cast iron, solidification microstructure, electric current pulse, carbides, grain refinement.

Introduction

Hypereutectic HCCI is considered to have higher volume fractions of the hard (hardness about 1600 Hv) and wear resistant M_7C_3 carbides than hypoeutectic HCCI [1], and is thus often the preferred alloy for many hardfacing applications [2, 3]. However, hypereutectic HCCI generally is not favored for casting, due to high scrap and rejection rates which are mainly caused by the coarser and larger primary carbides [2] with the size of 100~300μm.

It is valuable to find a new and more practical technique for refinement of primary carbides. The Electric Current Pulse (ECP) treatment for the solidification course has attracted more attention in the nonferrous metal [4-8]. However, for different processing metal especially ferrous metal in China, and different ECP waveforms, there are considerable differences in the refinement and the understanding of its refinement mechanisms [9-18]. In this work, a constant amplitude sharp ECP treatment for primary M_7C_3 carbide refinement in hypereutectic HCCI solidification microstructure from liquid-solid range is presented.

Experimental Procedure

The chemical composition of hypereutectic HCCI used in the present study is 4.21wt%C, 22.41wt%Cr, 1.61wt%Si, and Fe the balance. The liquidus and solidus temperature are 1357°C and 1289°C obtained by the DSC test, respectively. As cast cylinder hypereutectic HCCI samples (□□18 mm × 150 mm) were firstly prepared in sodium silicate bonded sand.

The ECP treatment was performed under liquid-solid temperature range by sharp ECP generator. The experimental arrangement for ECP treatment is shown in Fig. 1(a). The □□18 mm × 150 mm sample was sealed in an alundum tube by sodium silicate bonded sand and two nickel electrodes. It was soaked at a temperature in liquid-solid range for 3min in the muffle furnace, and then ECP treatment applied on it for certain minutes during the course of furnace cooling to the room-temperature. The temperature history of the furnace chamber and melts was monitored by two thermocouples and a temperature recording instrument. The waveform of ECP was detected in situ by a digital storage oscilloscope and it is a constant amplitude sharp pulse (see Fig. 1(b)).

The cross-section microstructures of the samples were investigated by optical microscope. For optical microscope analysis, the samples were etched in the reagent of 5g $FeCl_3$+100 ml H_2O.

* Corresponding author, email: zhourfchina@hotmail.com

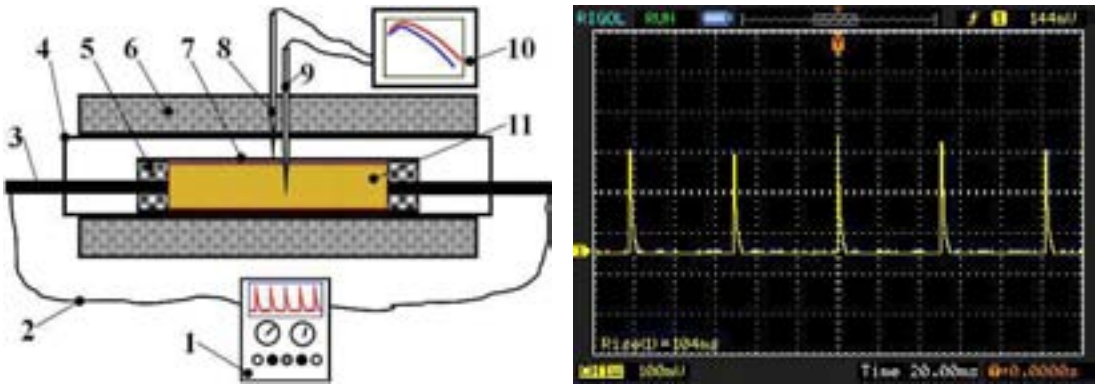

Fig. 1: schematic of ECP experiment: (a) experimental arrangement; (b) typical ECP waveform
1- ECP generator, 2 – copper wire, 3 – nickel electrode, 4 and 7 - alundum tube, 5 - sodium silicate bonded sand, 6 - muffle furnace, 8 and 9 – thermocouple, 10 - temperature recording instrument, 11 – HCCI melt or sample

Results and Discussion

Temperature history of the melts during the course of ECP treatment

The muffle furnace with samples was heated to the furnace chamber temperature of 1350 °C, 1360 °C for two ECP treatments, respectively. Fig. 2 shows temperature history of two samples soaking for 3 min, and then furnace cooling plus ECP treating in the muffle furnace. The ECP voltage, frequency and pulse width were 1400V, 30Hz and 30□s. It shows that the actual melt temperatures of the two samples were 1335 °C, 1343 °C before soaking and 1346 °C, 1353 °C after soaking, respectively. The increases of the melt temperature during the course of soaking were because of the release of latent heat of fusion. After soaking of the samples, they were applied furnace cooling plus ECP along the length direction immediately. The initial temperatures of ECP applying were 1346 °C and 1353 °C for two samples, respectively. After ECP treatment for 5min, the melts temperatures were still higher than the solidus one of 1289 °C. It was indicated obviously that the furnace cooling plus ECP treating of this study were in the liquid-solid temperature rang, and the ECP did not have any direct effects on the eutectic reaction of the melt.

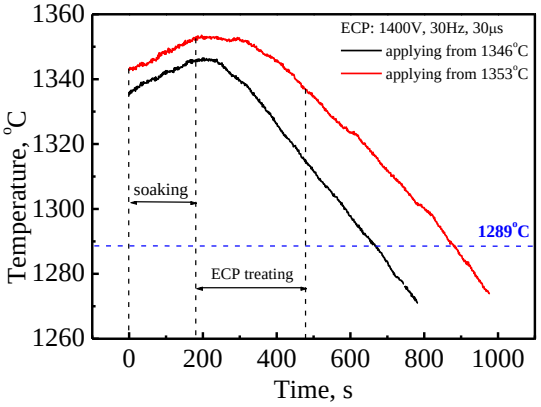

Fig. 2: Temperature history of the samples during soaking for 3 min, and furnace cooling plus ECP treating in the muffle furnace

Effects of initial temperature and time span of ECP treatment on the carbide refinement

The solidification microstructures from 1346°C and 1353°C of the melts ECP treated for different time are shown in Fig. 3 and Fig. 4, respectively. And the melt temperatures after ECP treatment obtained from Fig. 2 are also listed in the figures.

From the microstructures, some treatment effects are shown obviously. Firstly, with increasing ECP processing time, primary carbides and eutectic carbide have been refined significantly. The primary carbides were refined into granular from rod-like, and the eutectic carbide clusters became fine; thickness and length of the flaky eutectic carbide were shortened obviously in 3.5 min (see Fig. 3c and 4c). However, ECP treatment for too long time will make the carbides coarsening trend appeared, the rod-like primary carbides and long flaky eutectic carbides were reemerged again (see Fig. 4e). Secondly, carbide refinement effect is more obvious when the initial temperature of ECP applying is higher. As mentioned above, the samples were still in the liquid-solid temperature range when they were heated to 1346°C and 1353°C. The primary carbides did not melt down completely. The lower the heating temperature is, the larger the size

and the number of primary carbides are, which is shown in Fig. 3a and Fig. 4a. The chief effect of ECP is to promote solute atoms fluctuating uniformly in the hypereutectic HCCI melt by its magnetic contraction, and then the primary carbide nuclei number increasing significantly, which is benefit for getting fine primary carbides. Although the temperature T_e of the melt under ECP treatment for 3.5min was higher than that for 2.5min, the size of the primary carbide in the former (Fig. 4c) are finer than that in the later (Fig. 3c). Thirdly, the refinement of the primary carbides is benefit for the refinement of the eutectic carbides. It shows the strong evidence that the more refinement effect of eutectic carbides in the Fig. 4c than that in the Fig. 3c.

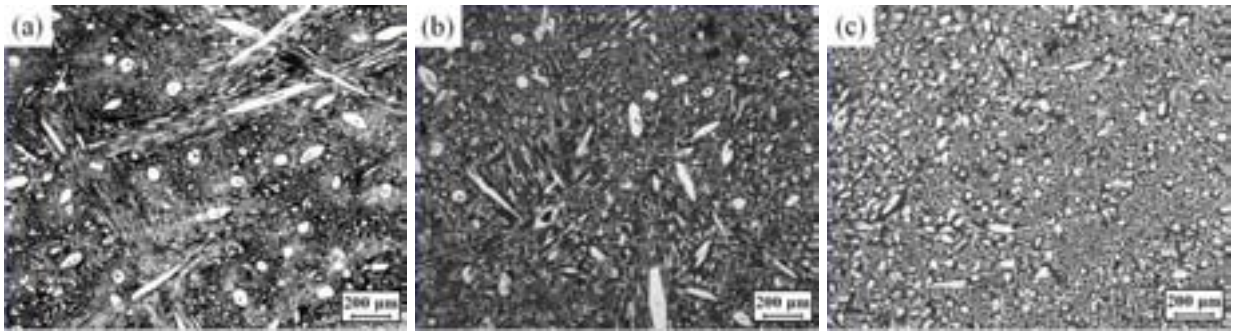

Fig. 3: Solidification microstructures from 1346 °C to T_e of the melts ECP treated for different time: (a) 0 min, T_e =1346 °C, (b) 1 min, T_e =1337 °C and (c) 2.5 min, T_e =1327 °C

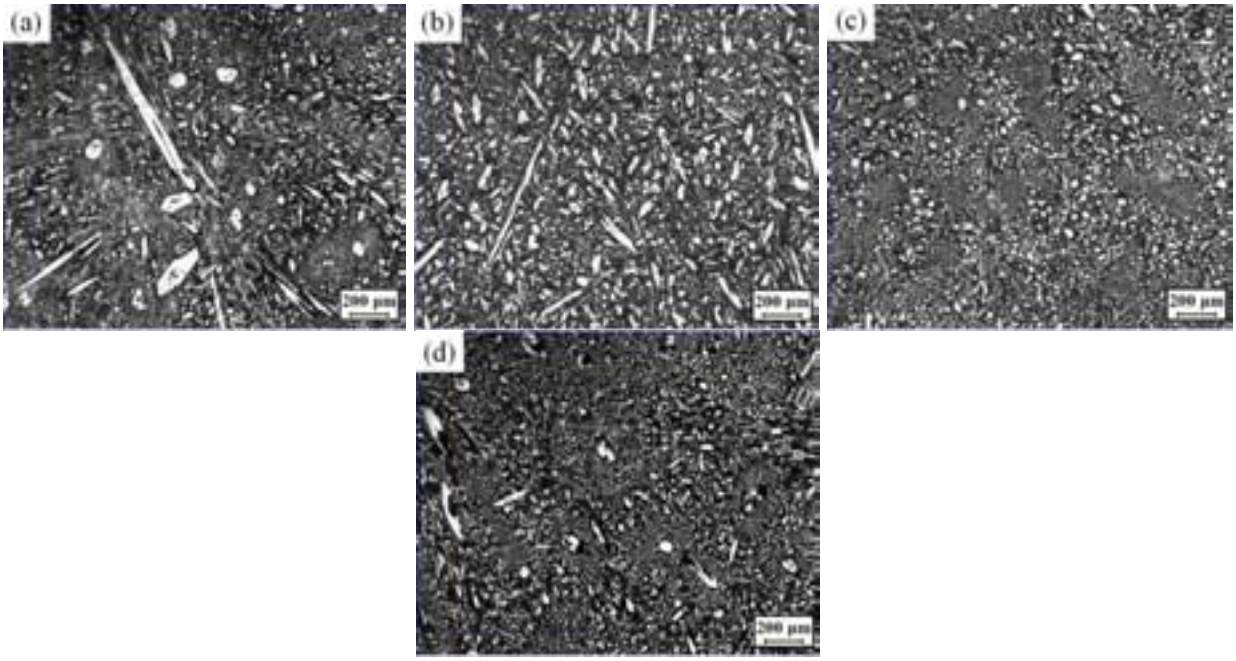

Fig. 4: Solidification microstructures from 1353 °C to T_e of the melts ECP treated for different time: (a) 0 min, T_e=1353 °C, (b) 2.5 min, T_e =1351 °C, (c) 3.5 min, T_e =1346 °C and (d) 5 min, T_e =1336 °C

Effects of ECP parameters on the solidification microstructure

Fig. 5 shows the solidification microstructures from 1353 °C of the melts treated for 3.5 min under different ECP parameter combination of voltage, frequency, pulse width. Huge differences in microstructure were shown under different ECP parameter combination. Two kinds of microstructure characteristic can be summarized. First, certain ECP parameter combination promoted the formation of much more primary carbides, which reduced the number of eutectic carbides. It was shown in Fig. 5c, f and g. Under the ECP parameter combination as 500V, 45Hz and 100μs, the size of the primary carbide was the least, and the number of the eutectic carbide was the smallest (see Fig. 5c). So the number of the eutectic carbide is related to the size of the primary carbide. Second, certain ECP parameter combination promoted eutectic carbide granulating, shown as Fig. 5a, b, d and e. Under these combinations, the size of the primary carbide is a little bit lager than that mentioned as the first one.

Among the three parameters of the ECP, the role of voltage responses in the effect of electro migration [4] on solute atoms, the role of frequency responses in the effect of magnetic contraction [4] on melt, and the role of pulse width responses in the effective treat time. High voltage condition such as 1400V, the ECP frequency should be reduced to

offset the effect of electro migration (see Fig. 5g). Low voltage condition such as 500V or 1000V, the ECP frequency should be increased to strengthen magnetic contraction to achieve good melt stirring effect (see Fig. 5c and f).

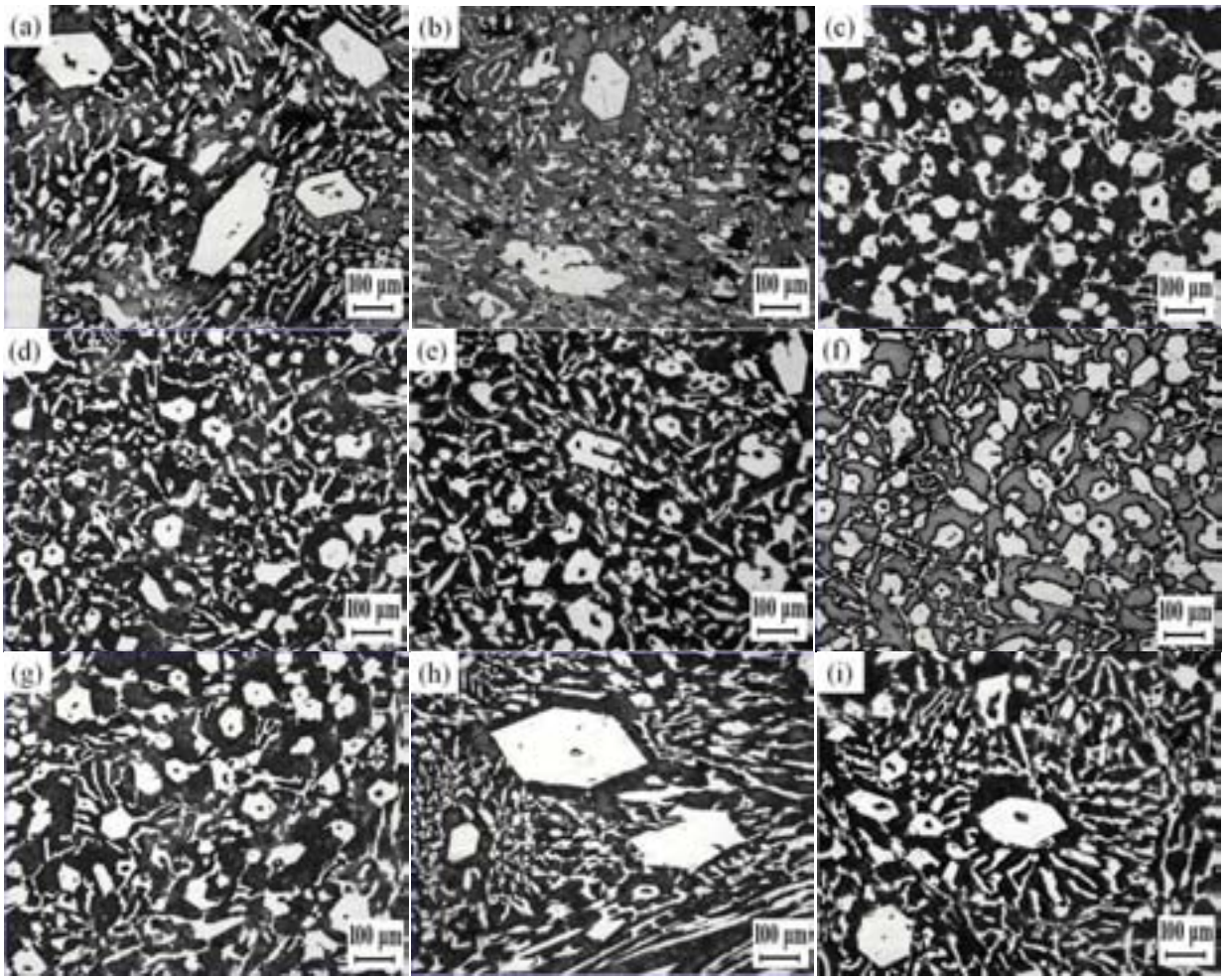

Fig. 5: Solidification microstructures from 1353 °C of the melts after treatment for 3.5 min at different ECP voltage, frequency, pulse width: (a) 500V, 15Hz, 10μs; (b) 500V, 30Hz, 30μs; (c) 500V, 45Hz, 100μs; (d) 1000V, 15Hz, 30μs; (e) 1000V, 30Hz, 100μs; (f) 1000V, 45Hz, 10μs; (g) 1400V, 15Hz, 100μs; (h) 1400V, 30Hz, 10μs and (i) 1400V, 45Hz, 30μs

Conclusions

1. The solidification microstructure evolution of hypereutectic HCCI under ECP treatment has been characterized. The ECP applied temperature near the liqudus and longer ECP treatment time are benefit for the refinement of the carbide. But the carbide will be coarsened under too long treatment time.
2. The ECP parameters such as the voltage, frequency, pulse width have a huge influence on the solidification microstructure. Some combinations of the three ECP parameters promoted primary carbide refinement and eutectic carbide number reduce, and fine granular primary carbides with the size of ~20μm could be obtained. Some other combinations led to a trend of eutectic carbide granulating.

References

1. R. J. Chung, X.Tanga, D. Y. Li, B. Hinckleyb, and K. Dolman: *Wear*, 2011, 271, 1454-1461.
2. R. J. Llewellyn, S. K. Yick, and K. F. Dolman: *Wear*, 2004, 256, 592–599.
3. Vickers Australlia Limited: *Patent* 1984, International WO84/04760, 1–12.
4. Hans Conrad: *Mater. Sci. Eng. A*, 2000, 287, 205–212.
5. J. G. Qi, J. Z. Wang, X. J. Liu, et al.: *Trans. Mater. Heat Treat*., 2006, 27, 36–39.
6. X. L. Liao, Q. J. Zhai, J. Luo, et al.: *Acta Mater*., 2007, 55, 3103–3109.

7. Y. Fang, X. L. Liao, C. H. Gan, et al.: *Special Cast. Nonferrous Alloy*, 2006, 26, 141–143 (in Chinese).
8. Q. C. Li, R. X. Li, X. D. Yue, et al.: *Materials Chemistry and Physics*, 2008, 112, 402-406.
9. M. Zhang, X. F. Ren, J. H. Li, et al.: *Journal of iron and Steel Research*, 2006, 18, 50-54 (in Chinese).
10. X. F. Ren: 'Effect of high density pulse current on Solidification Microstructure and wear resistance of high manganese steel', master thesis, Yanshan University, China, 2005 (in Chinese).
11. J. H. Fan, Q. Hua, X. Hou, et al.: *Iron and steel*, 2003, 38, 44-48 (in Chinese).
12. J. H. Fan, R. X. Li, Q. Hua, et al.: *Journal of iron and Steel Research*, 2004, 16, 59-62 (in Chinese).
13. Y. Chen, Y. Y. Gong, J. H. Fan, et al.: *Cast*, 2004, 53, 611-613.
14. L. Z. Li, Y. B. Zong, H. Cui, et al.: *Journal of University of Science and Technology Beijing*, 2004, 26, 478-481.
15. W. B. Wang, D. Q. Cang, W. Kong, et al.: *Shanghai Metal*, 2011, 23, 48-52
16. X. F. Zhang, S. Q. Yuan, Y. J. Wei, et al.: *Special Steel*, 2009, 30, 10-12.
17. J. J. Wang, L. Zhou, Y. L. Jin, et al.: *Journal of iron and Steel Research*, 2007, 19, 49-53.
18. P. Hong, H. C. Wang, X. Li, et al.: *Chinese Journal of process engineering*, 2011, 11, 79-84.

Acknowledgement

The assistance of PhD student H. CHEN is gratefully acknowledged. This research was supported by the National Natural Science Foundation of China grants 51261011.

Study of Shrinkage Porosity in Spheroidal Graphite Cast Iron

N. Tenaglia[1] R. Boeri[1], G. Rivera[1] and J. Massone[1]
[1]INTEMA, UNMdP – CONICET, Mar del Plata, Argentina

This study aims at identifying the relationship between the shrinkage cavities and the solidification structure in spheroidal graphite cast iron. Cast samples specially designed to contain shrinkage cavities were used. The solidification macrostructure was revealed by using the DAAS method while the solidification microstructure was revealed by using color etching. At the midsection of the pieces the shrinkage cavities and the solidification structure were observed jointly. Disperse porosity develops inside the solidifying austenite grains, in coincidence with the location of the last to freeze melt. The study showed that the classification of shrinkage porosity found in literature does not correspond to the ductile iron solidification model recognized by most of the scientific community. Early solidification models, and therefore shrinkage formation mechanisms, were proposed in instances when there was not a thorough knowledge of the morphology of the solid phases during solidification. At the present time, defects formation mechanisms can be described with higher accuracy. Therefore, an updated classification of shrinkage porosity for spheroidal graphite iron is proposed in this study.

Keywords: Ductile Iron, Solidification Structure, Shrinkage Porosity.

Article available in the International Journal of Cast Metals Research

A Review of Side-lined Chunky Graphite Phenomena

H. Borgström and V. Fourlakidis[1*]
[1]Department of Materials and Process Technology, Swerea SWECAST, Jönköping, Sweden

Considerable insight into Chunky graphite formation models and their corresponding mechanisms can be derived from revisiting graphite nucleation mechanisms in ductile iron. In particular, several unified theories related to the nucleation and growth of nodular graphite, need to be considered before Chunky graphite formation models and their corresponding mechanisms can be derived. This is justified by high resolution microscopy of quenching experiments, which elucidates that the formation of unwanted graphite forms like chunky occur shortly after graphite nucleation during eutectic solidification. Therefore it is the intension of this review to tie a number of nucleation theories stronger to events that have been shown to promote Chunky graphite formation. In particular a number of studies including radiography and spectroscopy will be reviewed that will shed new light into the Chunky graphite formation mechanism.

Keywords: Chunky graphite, ductile iron, nucleation.

Introduction

Even if certain in roads have been made in the understanding of Chunky graphite formation [1,2,3,4,5,6] and control in ductile iron [7], a systematic definition of remedies and adequate process control limits remain elusive. Furthermore, many times works on chunky graphite have been too complacent and too general in its execution. An example of this is how the role of Sb in the ductile iron microstructure has been investigated. The extensive use of Scanning electron microscopy is the reason for the lack of progress in describing the role of micro alloying components like Sb, which are commonly used to suppress Chunky Graphite if the right amount is used. Only with advanced auger electron spectroscopy is it possible to elucidate the 1-4 nm thin layer of Sb (and Sn) on the graphite nodule [8]. Furthermore, only a very few studies [9,10,11] have addressed the development of the primary structure's morphology with respect to cooling rate and thermodynamic conditions. In addition, our understanding of the graphite nucleation mechanisms in ductile iron remains incomplete [12]. This in turn is due to that there are several unified/alternative theories related to the nucleation and growth of nodular graphite, which need to be considered before Chunky graphite formation models and their corresponding mechanisms can be derived.

General overview of nucleation and growth of nodular graphite

The formation and development of precipitates, but also their lattice mismatch parameter with graphite in both nodularization and inoculation is what dictates whether nodular graphite will form [7,13]. Experimentally it has been difficult to verify the theory, but later studies [12,14] have included images of graphite nodule cross-sections with a clear 0.2 to 1μm MgO nuclei surrounded by MgS, CaS and Ca•Al2O3•SiO2 precipitates. This implies that MgO forms first and provides a nucleating site for the later forming MgS and other precipitates [12].

There are also cases where no MgO has been observed [15]. Instead various precipitates/inclusions like sulphides, oxides, oxy-sulphides, silicates, nitrides have been found in graphite nodule centres [15]. The notable exception is carbides that have not been found in nodule centres but this is realistic owing to the fact that those oxides and sulphides are thermodynamically more stable [15]. The principal role of all these inclusions is to reduce the undercooling required for the heterogeneous nucleation, by e.g. reducing the lattice disregistry [15]

Central for the silicate theory [15] is the reduction in lattice disregistry by formation events that occur during nodularization (i.e. Mg treatment) and inoculation, where the lattice disregistry constitutes a measure of the epitaxial fit between the nucleant particulate/inclusion and the graphite nodule. The main formation mechanism during the nodularization is the realization of Enstatite and Forsterite with reasonably high lattice disregistries of about 6 to 30% with graphite [15] as seen in equation 1. *

$$\xrightarrow{Nodularization} MgO \cdot SiO_2 \text{ or } 2MgO \cdot SiO_2 \xrightarrow{Inocululant} XO \cdot SiO_2 \text{ or } XO \cdot Al_2O_3 \cdot 2SiO_2 \quad X = Ca, Sr, Ba \tag{1}$$

*Corresponding author, email: henrik.borgstrom@swerea.se

These phases are then transformed into more faceted hexagonal silicate phases (seen in equation 1) during inoculation, yielding reduced lattice disregistries of about 1 to 8% with graphite [15]. The reduced lattice disregistries facilitate the formation of coherent/semi-coherent low energy interfaces between the nucleant and the graphite, which reduces the undercooling [15]. The implication of the silicate theory on Chunky graphite is tied to the coherency of the interfaces and the possible crystallographic growth direction of the nucleating graphite [15], which is affected by the presence of trace elements [15]. In fact an excess amount of trace elements was found to increase the formation of detrimental type C inclusions in the graphite nodulus core during nodularization, which coincided with an increased amount of Chunky graphite [13,15]. Here it is postulated that the impurities hinder the curved graphite growth necessary for graphite nodule formation in the austenite-liquid mushy zone, which has been discussed in view of chunky graphite formation. [15]. It is also believed that the formation of chunky graphite was tied to graphite growing with sufficient spherodizing ability in the direction where the basal plain expands predominantly [6]. An example of what is believed to be the initial stages of Chunky graphite formation is when two Ca rich precipitates were close to the commonly found MgO nuclei in the graphite nodule centre [16], had alterned the solidification path of the graphite, which caused the graphite to branch out to chunky Graphite [17].

In contrast to the silicate theory, there is in high purity Fe-C-Si systems a natural transition from plate like to nodular graphite morphologies [15]. If this is to occur the required purity for S is very high, but also entwined with a critical cooling rate. For slow (<40K/min), Intermediate (>40 K/min & <100K/min) and high (>100 K/min) cooling rates the required S purities are; 0.2 ppm, 1.5 ppm and 11 ppm, respectively [15sic]. For these high purities no impurities could be found in the graphite nodule centres, in essence, favouring conditions for Gorschkov's gas bubble to prevail. Historically, Gorschkov's gas bubble theory has evolved into "the pore filling theory" by Karsay [15] and finally into site theory proposed by Itofuji [5]. The theory postulates that graphite precipitates and grows inward into nodules on small pores/bubbles created during the nodulizing treatment 5. A more elaborate description for the site theory [6,9] dictates that unwanted graphite morphologies like Chunky graphite can be avoided if issues affecting the availability of enough Mg-gas bubbles are controlled during nucleation [18]. However, the occurrence of Mg-gas is highly questionable. Experimentally the pore filling effect has been observed after 12 hour dwells at 1150'C in a study on powder forging of Fe-C-Si [19]. Another study on liquid phase sintering of a similar Fe-C-Si system observed a partially graphite filled pore during a 90 min dwell at 1150°C in conjunction with cooling in vacuum, empowering the pore-filling effect [20]. Noteworthy, is that in both these studies the impurity levels could be considered very low as gas atomized powders contain very small amounts of impurities [20].

Another mechanism occurring during the solidification process for ductile iron, is Vacancy Diffusion [11]. This seems to occur when the austenite shell needs to deform plastically to grow around the graphite. Evidently wedge theory [21] dictates that the plastic deformation of the austenite should directly cause Chunky Graphite. For this to occur, the chemical potential for the austenite and the graphite needs to be the same. However, situations have been elucidated where the austenite is in contact with the graphite without being able to form a shell, when the nodules are smaller than 14 microns [11,22]. Here the underlying interface kinetics was affected when the graphite precipitated from the liquid. [11]. This could cause defects in the graphite that changes its chemical potential during growth. Of particular interest is the combination of large growth rates and large interface kinetics when the nodules are small [11].

Generalized Chunky Graphite Formation Model

Chunky graphite formation models and mechanisms often built on quenching experiments and high resolution microscopy seem to agree on that the formation of unwanted graphite forms like chunky occur shortly after graphite nucleation during eutectic solidification [9], even if there are discrepancies between the alternative theories. Theories proposed by Liu, Zhou and Gagné and Argo believe that the main chunky graphite formation mechanism is related to the dendrite growth of the austenite phase during solidification, [1,3,4]. It is also postulated that Chunky graphite is formed at the austenite/graphite interface, in the middle or at the end of the eutectic solidification before growing into the remnant liquid through a melt channel [3,23]. The main steps of these models essentially entail:

1. *Spheroidal graphite precipitates and is surrounded by austenite shell*
2. *Spheroidal graphite nucleation finishes and chunky graphite precipitates at the austenite-residual melt interface.*
3. *Chunky graphite growth is fuelled by its thin channel connection with the residual melt.*

Discussion

The role of Graphite nodule core precipitates

In the first step, is it really enough to only consider the direct meta physics of the precipitating graphite and austenite? I believe that in order to make progress it is necessary to split the first mechanism into:

1. How does the graphite precipitate and grow?
2. How does the austenite develop?

The shortcomings in compounding the graphite and austenite became evident when one delves a little deeper into the mechanisms behind the silicate theory [13,15]. In particular it is possible to question the nucleation of the silicates themselves. In an almost congruent way to *that graphite is a good nucleant to austenite, but austenite is a poor nucleant to graphite*. [13] In particular, too little attention has been made to investigate the thermodynamic conditions surrounding the precipitation of the silicates independently from the nucleation of the graphite nodules. In the above treatment of the

silicate theory it is clear that the lattice mismatch of the silicates with respect to the graphite is reduced by successful inoculation. Furthermore, work on S has shown that sulphides can have both hexagonal and cubic structures [10]. For Sulphides having a hexagonal the unit cell structure it has been found that these can be good nucleation sites for graphite directly. However, small sulphides have been found encapsulated in silicates, which indicates that under certain conditions the unit cell structure for the sulphides could be a poor match for graphite, but a good one for silicates that are with proper treatment and inoculation good nucleation sites for graphite [15]. Further evidence of this is found in work on SiC additions to ductile iron, where it was demonstrated that the nucleation potential of the melt increased when the amount of silicates increased [24]. It could well be that these studies presents an opening for understanding how to improve the inoculation and thus the nucleation of graphite during the latter part of the eutectic solidification, where evidently chunky graphite is precipitated.

Importance of Carbon Floatation

For the development of austenite dendrites the selection of a suitable carbon equivalent is critical since it is influenced by the alloying, dictates the melt viscosity, the risk for flotation, risk for carbide formation, the extent of micro-cavities, pearlite, carbides and denodularization etc. To avoid chunky graphite a slightly hypoeutectic composition is recommended for heavy sections [7]. Unfortunately, even if common logic would lead one to assume that graphite flotation would aggravate chunky graphite no specific study has been identified where this has been done systematically. However, the stability of the graphite spheroid is reduced at high CE (related to high carbon) and increased Ce/RE contents [7,25], conditions where graphite flotation is expected. Furthermore, the eutectic solidification time in a 200x200mm thick section can also increase from about 350 to 500 s when the carbon equivalent is increased from 4 to 4.3%, respectively [26]. The stability of the precipitating graphite spheroid is also related to how strongly it is coupled to the austenite. [16]. Here controlled spheroid growth possibly degenerates, by the co-precipitation of austenite, where the nodule is exposed to the melt or to temperature and compositional gradients occurring during flotation of the nodule. Consequently, the key point for Chunky graphite formation is to know what is happening in the last remaining liquid and micro-area around the dendrites during eutectic solidification.

Distribution of Ce in ductile iron

Fascinating insight on the role of Ce and Mg in ductile iron is found in an earlier study [25] entailing the radiographic evaluation of a Ce141 isotope in a ductile iron microstructure, from which a number of intriguing observations relating to chunky Graphite formation could be made. In the study, Ce distributes unevenly and preferentially in the grain boundaries of the primary dendrites of austenite [25]. Here the Ce concentration was about 2 to 5 times higher than in the "ordinary" cast iron microstructure, in which Ce in the metallic phase was 1.5 to 3 times higher than in the graphite phase [25]. The proposed mechanism for this is as follows [25]:

1. *Mg is preferentially absorbed on boundaries of growing graphite crystals during cooling and solidification, since Mg is more surface active than Ce with respect to graphite.*
2. *Ce absorbed on the graphite between dendrites (owing to being less horophillic than Mg) is forced back by the growing dendrites of austenite-graphite eutectic, where chemical compounds formation can occur [27]*
3. *The preferential Mg absorption on graphite crystal boundaries having the lowest reticular density leads to quasispheroidizing of the graphite crystals, owing to that the surface tension coefficients αi of select graphite boundaries are levelled in conformity to the Gibbs-Wulff principle (αi → α') [25].*

In the above mechanism formation products surrounding the growing dendrites of austenite-graphite eutectic include: compounds like CeFe5, phases enriched in both Mg and Ce as well as crystallized Mg and Ce that can facilitate Mg_3Ce [25sic]. It could be that the wide melting range of Ce [28] is responsible for the low melting range of many of these compounds of around 800°C that this aggravates the issue. Consequently, it is the formation of compounds rich in Ce and Mg that reduce the concentration of free and surface active Mg below the level necessary to favour the formation of spheroidal graphite [25sic]. In addition, for Ce based nodulizers it is a clear that chunky graphite prevalence is increased when the oxide content exceeds >10 wt-% [29], which fuels the issue about secondary oxidation. Noteworthy is also that Mg and Ce are usually found in formations products like dross, which are often present close to chunky graphite [23]. Moreover, since re-melting and wet grinding often precede OES analysis; it is likely that the segregation of Mg and Ce compounds have been elusive. Even if advanced ICP analysis is used it is still difficult to determine a baseline content of Mg and Ce compounds. Perhaps the most striking theme here is the notion of Magnesium's gas-liquid transition with pressure. Here higher pressure than the equilibrium vapour pressure entailed that Mg liquefied, which caused chunky graphite like morphologies [5,9] It would seem that the required pressure only involved the interaction of a few atoms at near-solidification temperature [5,9], which is less than the about 50 atoms of eutectic composition involved during the eutectic expansion [9]. These conditions are likely to be fulfilled in the thermal centre in heavy castings where solidification times are long and the segregation severe.

Establishing a Cerium baseline to avoid Chunky Graphite in ductile iron

Returning to the aforementioned scenario for small graphite nodules without shells having large growth rates and large interface kinetics [11], it could well be that the above segregation of liquefied Mg and/or Ce on the austenite dendrite arms provide ideal conditions for Chunk graphite. Evidence to support this is found in a study on Ce effect on graphite

nodule count and distribution, where excessive Ce concentrations of around 0.02% *promotes the graphite to grow fast* leading to chunky graphite clusters in their microstructures and a drop in nodule count [30]. Furthermore, in a ductile iron composition with less than 0.5 wt-% Mn, the chunky graphite residual limit for light (Ce rich) and heavy (Y rich) RE alloys were about 0.003 and 0.018 wt-%,respectively in both laboratory and production of a 1.6T component [31], which corresponded to alloying additions of 0.05 and 0.2 wt-%.

Even if there are numerous studies on different RE additions [15] most other work have centred on Ce additions without primarily focusing on chunky griphite. In the initial patent by Morrogh on "Nodular Cast Irons and The Manufacture Thereof" Ce was paramount to desulfurize and stabilize carbides, but also to ensure sufficient nodularization [32]. However, if excess Ce is present in the microstructure, Exploded, Spiky and coral Graphite morphologies can be found [33,34,35]. When the solidification conditions for heavy castings were reproduced by keeping small quantity of molten metal at the eutectic temperature for a long time even the amount of Chunky graphite was increased for Ce contents above 500 ppm together or without increased holding times and/or decreased cooling rates [36]. In Figure 1 it can be seen that levels below 0.01% (100ppm) Ce could be tolerated if Chunky graphite was to be avoided [6]. However, there are examples where amounts up to 0.02% Ce could be tolerated elsewhere [7].

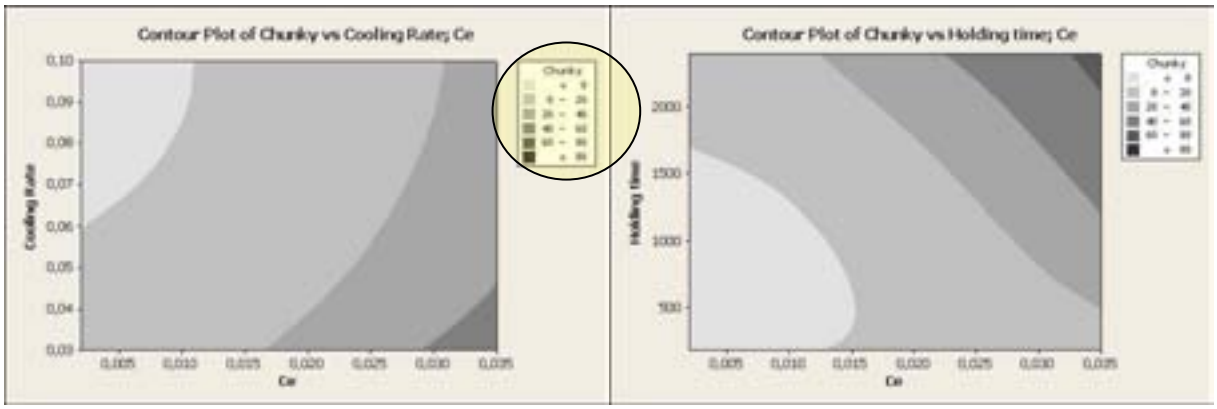

Fig.1: Effect of Cerium, cooling rate (left) and holding time (right) on the amount of chunky graphite. Adapted from [7]

The role of impurities and trace elements

In addition, Mg and Ce with other RE additions in the MgFeSi carrier are primarily used to deal with impurities and trace elements. The RE nodulizer additives whose primary function is to lessen the effect of subversive elements on the melt can be seen in Table 1 [1], which can be determined by the graphite denodularization factor, K_1, in equation 2 [35]. Theoretically the denodularization effect can be counteracted with RE (Ce, La, Nd, Pr etc) up to K_1=2. If K1>1.2 RE addition could be regarded as compulsory, for K_1<1.2 it is beneficial or could be avoided, if a high degree of process control prevails [35]. This is important when dealing with chunky graphite and clean charges, where the Ce required is often overrated.

$$K_1 = 4{,}4Ti + 2{,}0As + 2{,}4Sn + 5{,}0Sb + 290Pb + 370Bi + 1{,}6Al \quad (2)$$

Table 1: Chunky Graphite promoters and their subversive counterparts, adapted from [22].

Chunky Promoters	Ce	Ca	Ni	Si	Al	Cu	RE
Subversive counterparts	As	Bi	B	Sb	Sn	Pb	Cu

To limit the impact of RE and Ce on the final microstructure Sb is usually added. In practice, up to 0.005% Sb is used and related to a Sb:Ce ratio between 0.6 and 1.2 [37], with significantly less Chunky for a ratio higher than 0.8 [34]. Recently, ratios of 2 and above have been used in a theoretical study were the RE content was in in excess of 2.5% in the nodulizer [38]. Here Sb acts like a diffusion barrier around the graphite [8] and leads to higher nodularity and nodule counts, but it is obvious that the mechanism involved with Sb addition needs to be studied further. Especially since required the thickness of the diffusion barrier is stated as between till 1nm and 4nm [8,39] and the interaction with Ce and other RE is inclear.

The role of sulphur and magnesium

Fortunately, the chemical stability and availability of free Mg has received greater interest amongst the scientific community. Here issues governing availability and segregation of Mg are important. These include: secondary

oxidation during pouring, reaction with refractory, the evaporation/fading out of Mg gas bubbles and Mg segregation at the austenite-residual melt interface [5,9]. For the purpose of controlling the Mg-treatment the availability of free Mg and avoiding bound Mg related to inclusions is easiest. In practice oxygen, sulphur and trace elements need to be controlled to achieve a stable Mg-treatment process. Owing to S and O being surface active elements these will boost prism plane growth of the graphite leading to laminar and chunky graphite morphologies. However, if S, O, other surface active elements and trace elements are controlled the basal plane will be favoured, which favours nodular morphologies.

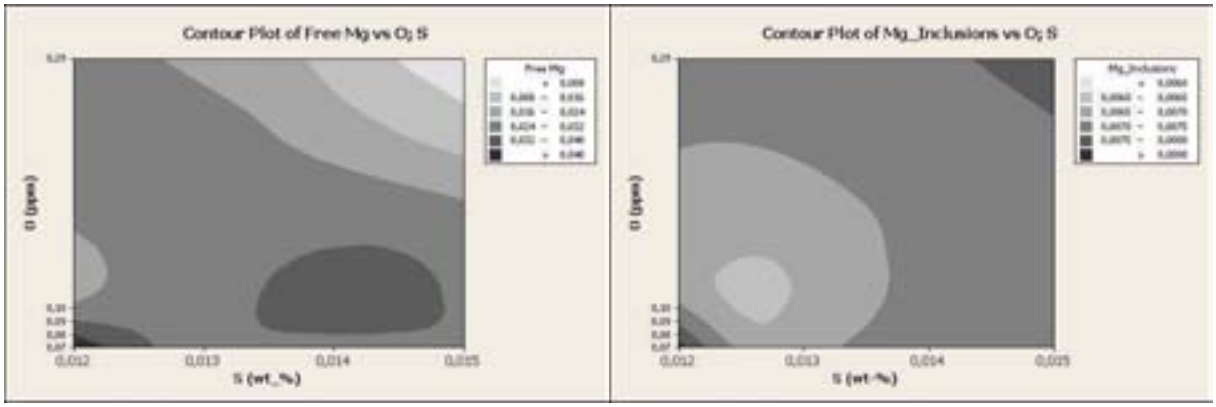

Fig.2: Optimum S, O and Mg levels in the Mg-treatment of ductile iron. Adapted from [16]

Unfortunately, it is only possible to distinguish between free and bound magnesium with advanced characterization methods like Inductively Coupled Plasma, ICP [16]. These are elucidated in Figure 2 [16]where it is seen that high amounts of S and O should be avoided, since excessive 0.05wt-% Mg amounts can favour the degeneration of graphite and increase the amount of intercellular carbide [35]. Regardless of total magnesium content, the bound content Magnesium has been determined to about 0.006 and 0.008 Wt-% Mg, [16], possibly due to few data points and a clean charge. In the same study it was more useful to look at O and S separately with the Mg-content. Here it was found that $0.012 < S < 0.013$, $0 < O < 0.2$ ppm and $0.035 < Mg < 0.045$ seem to be good interval to conduct the Mg-treatment in [16]. Generally 0.005 to 0.015wt-% S is beneficial to control Mg-treatment recovery, nodular graphite nucleation and the formation of inclusions [35]. Furthermore 0.0137 Wt-% S was found to minimize chill formation in the final microstructure of thin 2 mm strips [40]. The same study also found that Mg/s ratio >0.76 was necessary to ensure that nodularity was at least 80%. Moreover, reducing the Mg content in the Mg-alloy from 6% to 3% lead to higher solidification temperatures and lower amount of chill [41]. Furthermore, during the last decade, significant progress has identified an even narrower sulphur content range from 0.008 to 0.012 wt% S. Low Sulphur levels (<0.005 wt% S) increased the risk of exploded graphite and high Sulphur levels (>0.0135 wt% S) increased the risk of compacted graphite [6]. Here it was the Mg-rich inclusions in the graphite nucleus that lowered nodularity, either through a de-nodulizing hexagonal structure or due to the size of the S rich nucleus getting too big. Furthermore, the development of the oxygen activity meter has now made it possible to measure the transition between different graphite types. For example the transition from compacted graphite, CGI, to laminar graphite, LG, could be delayed by a factor of 5 if the S content was reduced from 0.0135 to 0.008 wt% S [42]. Hopefully this could be applied and reduce the likelihood for chunky graphite formation.

The increasing importance of surface tension

In fact, it is here that the surface tension of the liquid-graphite interface is receiving particular research focus today. The main obstacle so far is the complex chemistry, undefined interactions and oxidation potential of different elements in cast iron. Nevertheless, important relationships between temperature, surface tension and oxygen activity are beginning to emerge [43]. Moreover sensor technology is rapidly evolving to facilitate accurate measurement of temperature, surface tension and oxygen activity. It could be postulated that their concurrent measurement is what is needed to gain important insight in the control of the ductile iron production process. In particular key processes like liquid state after melting, extent of super heating, control of the nodularization treatment and the tailoring of the inoculation process are those that likely to benefit most from implementing sensor technology.

Today particular surface tension values are available [44,45] to demonstrate that it is possible to use surface tension to distinguish between different graphite forms. Below around 900-990 mN/m flake graphite occurs [44,45]. The vermicular region has been estimated to be between 1082 and 1360 mN/m [45]. The nodular region has been estimated at above 1465 mN/m [45]. Unfortunately, the reported surface tensions values for the intermediate vermicular and nodular transitions vary too much between researchers to be conclusive. The reason for this is that experimental conditions and the equipment have little resemblance to each other. Furthermore, the chemistries of the melts are inconsistent due to natural variation of the raw materials in terms of e.g. oxygen content. Another issue is that the content of surface active elements like Mg, Ce, Ba etc are different.

Conclusions

From the review a number of interesting observations could be made:

1. Under certain conditions sulphides could be a poor nucleant for graphite, but a good one for silicates that are with proper treatment and inoculation good nucleation sites for graphite
2. Ce distributes unevenly and preferentially in the grain boundaries of the primary dendrites of austenite
3. Ce concentrations of around 0.02% *promotes the graphite to grow fast* leading to chunky graphite clusters
4. Sulphur is very important for the graphite morphology in ductile iron

References

1. P. C. Liu, C. L. Li, D. H. Wu and C. R. Loper Jr.. AFS Transactions. 1983, Vol 91 No 83-51 pp. 119-126.
2. B. Prinz, et al. Giessereiforschung, 1991, Vol. 43, No. 3, pp. 107-115
3. J. Zhou, W. Schmitz and S. Engler. Giessereiforschung, 1987, Vol. 39, No. 2, pp. 55-70
4. M. Gagné and D. Argo: Proc. Int Conf. on Advanced Casting Technology, Kalamazoo, Michigan, USA, 12-14 Nov, 1989, ASM Int. pp231-256
5. H. Itofuji. AFS Transactions 1996, Vol 104 No 96-131 pp. 79-87.
6. Shoji Kiguchi; Masayuki Sintani; Haruyoshi Sumimoto and Kokichi Nakamura. Journal of Japan Foundry Engineering Society. 2000, Vol. 72, No. 5, p.311-316.
7. A. Javaid and C. R. Loper Jr. AFS Transactions 1995, Vol. 101 No 95-49 pp. 135-150.
8. W. C. Johnson and B. V. Kovacs, Metallurgical and Materials Transactions A, 1978, Vol. 9 (2), pp. 219-229.
9. H. Itofuji,, H. Uchikawa, AFS Transactions 1990, Vol. 98 No 90-42 pp. 429-448.
10. H. Nakae and Y. Igarashi, Materials Transactions, 2002, Vol. 43 (11), pp. 2826-2831
11. H. Fredriksson, J. Stjerndahl and J. Tinoco. Mat. Sci. Eng. A 413 (2005) pp. 363-372
12. S. Lekakh and C. R. Loper Jr. AFS Transactions 2003, Vol 111 No 03-103(05) pp. 885-894.
13. T. Skaland, A model for graphite formation in Ductile Cast Iron, PhD thesis. NTH 1992:33
14. Y. Igarashi and S. Okada. Journal of Japan Foundry Engineering Society. 1998, Vol. 70, No. 5, p.329-335
15. T Skaland. Nucleation Mechanisms in Ductile Iron. Proceedings of the AFS Cast Iron Inoculation Conference, American Foundry Society (AFS), Schaumburg, Illinois, 2005, Sept. 29-30, pp. 13-30
16. H. Itofuji. Journal of Japan Foundry Engineering Society. 2000, Vol. 72, No. 10, p.645-651 .
17. H. Itofuji and A. Masutani.. Journal of Japan Foundry Engineering Society. 2004, Vol. 76, No. 2, p.98-106 .
18. H. Itofuji and A. Masutani. International Journal of Cast Metals Research (UK). 2001,Vol. 14, No. 1, pp. 1-14.
19. K. Hanawa, K. Akechi, Z. Hara and T. Nakagawa,. Trans. J. Inst. of Metals, 1980, Vol.21 (12) pp. 765-772
20. W. Khraisat, H. Borgström, L. Nyborg, and W. A. Jadayil, Powder. Metall., 2009 Vol. 52 (4), pp. 291-29
21. A. Udroiu. Giesseri Rundschau 60 Heft 11/12 pp. 356-374
22. S-E. Wetterfall, H. Fredriksson and M. Hillert J. Iron Steel Inst. (1972) pp. 323-333
23. R. Källbom, K. Hamberg, M. Wessén and L.-E. Björkegren. Mat. Sci. and Eng. A, 2005, Vol. 413, pp. 346-351
24. H. Fredriksson Mat. Sci. Eng. 65 (1984) pp 137-144
25. V. A. Guiva, A. P. Lyubchenko and M. V. Mozharov Met. Sci. and Heat Treat., 1970, Vol. 12 (12), pp. 994-997
26. T. Kanno, I. Kang, Y. Fukuda, T. Mizuki and S. Kiguchi. Effect of Pouring Temperature and Composition on shrinkage Cavity in Sheroidal Graphite Cast Iron. AFS Transactions 2006, Vol 112 No 06-084 pp. 525-534.
27. H. F Fischmeister, A. D.Ozerskii and L.Olsson, Powder Metallurgy, 1982, Vol. 25 (1), pp. 1-9
28. Melting temp. 795°C &Boiling temp. 3257°C: www.chemicalelements.com/elements/Ce.html Accessed 2011-05-12
29. H. Löblich 2006, Giessereiforschung, Vol 58, No.3 pp. 2-11.

30. X. Diao et al. Int. J. Modern Physics B Vol. 23, No 6 & 7 (2009) pp 1853-1860
31. Y. Niu and Z. Zhang Foundryman. 1988 Vol. 81 (8), pp. 390-398.
32. H. Morrogh, Nodular cast iron and the manufacture thereof. US Patent 2488511, Nov. 15th, 1949
33. C. R. Loper Jr. and K. Fang. AFS Transactions 2008, Vol. 114 No 08-066(05) pp. 673-682.
34. P. Larrañaga, et al. Metallurgical and Materials Transactions A, 2009, Vol. 40, No. 3, pp. 654-661.
35. I. Risposan, M. Chisamera and S. Stan. China Foundry, 2010, Vol 7 No. 2 pp. 163-170
36. S. Méndez, et al. Experimental Investigation of Chunky Graphite Formation in Small-Section Ductile Iron Castings. Proc. of 69th World Foundry Congress, Hangzhou China 2010, Oct. 16-20, pp. 0387-0392
37. Rio Tinto Iron & Ti.. Chunk Graphite Defects in ductile Iron. The Sorelmetal Book of Ductile Iron, 2006 p 93
38. L. Zhe, C. Weiping and D. Yu, China Foundry, 2012, Vol. 9 No. 2 pp. 114-118
39. B. Kovacs, Method for Increasing Mechanical Properties In Ductile Iron by Alloy Additions. United States Patent 4363661, Dec 14th, 1982
40. Y. Igarashi and H. Nakae. Journal of Japan Foundry Engineering Society. 2002, Vol. 74, No. 1, p.30-35 .
41. H. Nagayoshi and K. Imanishi. J. J. Foundry Engineering Society. 1996, Vol. 68, No. 8, p.631-636 .
42. F. Mampaey, D. Habets, J. Plessers and F. Seutens, Int. J. of Metalcasting, 2010, Vol. 4 (2), Pp 25-43
43. K. Morohoshi, M. Uchikoshi, M. Isshiki and H. Fukuyam ISIJ International, 2011, Vol. 51 (10), Pp. 1580-1586
44. G. Paul, Journal of the Southern African Institute of Mining and Metallurgy, 1972, Vol. 72(1), pp. 165-170
45. D. Shi, D. Li, G. Gao and L. Wang, Materials Transactions, 2008 Vol. 49 (9), pp. 2163 to 2165

New Concepts and Characterization of Gradient Castings Composed by low Alloyed White Cast Iron and Spheroidal Graphite Cast Iron

Primož Mrvar[1,a] , Mitja Petrič[1,b], Danijel Mitrovič[1,d] and Jožef Medved[1,c]
[1] Department of Materials and Metallurgy, Faculty of Natural Sciences and Engineering, University of Ljubljana, Aškerčeva 12, 1000 Ljubljana, Slovenia;

This work deals with the problem of casting production regarding composed castings for rolls, also called gradient castings. The technology of production is a combination of the horizontal centrifugal casting of alloyed white cast iron (two sequences) and gravity casting of cores which occurs in third sequence. From the industrial casting, the systematic sampling for different investigation methods was done. The following examination methods were used: chemical analyses, thermodynamic calculation of equilibrium phases by TCW and Computerm programs, dilatometry in the solid state, calculation of density for extracted microstructural components by program TAPP 2.2, linear hardness measurements, determination of mechanical properties at room temperature and higher temperatures, optical and electron microscopy, FEM calculation of casting processes for all three sequences of casting.
The working layer of the roll is made from chromium alloyed white cast iron. The core is made of spheroidal graphite cast iron (SGI). The main focus was on the intermediate layer, which is made from flake graphite cast iron. Microstructural constituents were determined quantitatively and qualitatively.
Centrifugal casting is a highly complex process. With the help of the mentioned programs, the calculation of density was done for each microstructural constituent. It was discovered that austenite and M_7C_3 types of carbides have a difference in densities of approximately 0.3kg/dm^3 which influences the distribution of microstructural constituents in the roll cross-section due to centrifugal forces. The internal stresses in the casting were also calculated and measured. The explanations of the influences of inhomogeneous carbide distribution in the first and second layers, and the influence of core made by SGI on the mechanical properties of the casting were also made, together with internal stress.

Keywords: composed castings, centrifugal and gravity casting, white cast iron, spheroidal graphite cast iron, FEM casting and stress calculations, “in situ” experiments, characterization of microstructure

[a] Primoz.Mrvar@omm.ntf.uni-lj.si, [b] Mitja.Petric@omm.ntf.uni-lj.si,
[c]Jozef.Medved@omm.ntf.uni-lj.si, [d] danijel.mitrovic@gmail.com

Introduction

Centrifugal pouring technology is a casting process, where metal can be poured and solidified in a rotating permanent mold under the influence of centrifugal force. [1] The direction of solidification during the centrifugal process differs from the sand casting. Due to the rapid transfer of heat to the permanent mold, crystallization starts on the outer surface of the casting and progresses towards the inside. The result is a fine-grained surface crust, further solidification towards the interior takes place with the growth of dendrite crystals. [2]

A combination of centrifugal and gravity casting is used during roll production, where the working layer and intermediate layer are cast centrifugally and the core is gravity cast from spheroidal graphite cast iron. The working layer is made of chromium white cast iron to achieve hardness and wear resistance, the intermediate layer is sort of grey cast iron for producing good bonding of the working layer and core, whilst the core is made of spheroidal graphite cast iron to obtain toughness of the roll. [3]

In regard to the chromium white cast iron layer, it is desirable to have as little retained austenite as possible in the matrix and that it does not contain the pearlite phase within the microstructure.

In the as cast state, the matrix contains a substantial proportion of residual austenite (30–60 %), which is necessary to decompose with single or multistage heat treatment, in order to achieve the required microstructure, which contains small and evenly distributed $M_{23}C_6$ type carbides in α-metallic matrix. [4] Due to their high hardness and uniform distribution in the matrix, secondary carbides are of great importance for wear resistance.

The target mechanical properties are obtained by heat treatment, where casting is heated to austenitising temperature and control cooled to room temperature. Such treatment allows a good control over the segregation of secondary carbides within the temperature range from 800 to 1050 °C.

Experimental work

Analyses were carried out on samples taken from a working layer, intermediate layer, and the core. Optical microscopy was carried out using an Olympus BX61 microscope, scanning electron microscopy with a JEOL JSM–5600 electron microscope equipped with EDS-analysis, tensile tests at various temperatures by an Instron 1255 machine, hardness measurements by an Instron Tukon 2100 B machine, and dilatometric analysis by a BÄHR DIL 801 instrument. Densities of solidified phases were calculated using the TAPP 2.2 program and thermodynamic phase equilibrium calculations performed by Thermo-Calc software.
The chemical compositions of all three layers are presented in Table 1.

Table 1: Chemical analysis of gradient casting (mass. %).

	C	Si	Mn	P	S	Cr	Ni	Mo	Mg	Cu	Sn	Al	V	Ti	W	Co	Fe
Working layer	2,799	0,703	0,965	0,030	0,037	16,681	1,433	1,154	0,003	0,081	0,000	0,0000	0,296	0,000	0,000	0,000	75,818
Intermediate layer	3,118	1,034	0,342	0,026	0,010	0,129	0,247	0,029	0,000	0,039	0,005	0,0013	0,012	0,006	0,009	0,018	94,965
Core	3,002	2,734	0,366	0,031	0,007	0,131	0,247	0,029	0,009	0,039	0,007	0,0029	0,013	0,007	0,009	0,017	93,198

Results and discussion

Figure 1 presents the boundary layer of the working layer, intermediate layer and core of a roll. The microstructure of the working layer consisted of austenite and carbides as these alloys are rich chromium. The intermediate layer, which merges with the core, is highly rich with M_7C_3 carbides. At solidification of the intermediate layer melt in the first stage the formation of primary austenite crystals occurs which, by means of centrifugal force due to higher density than the rest of the melt, starts to impose towards the direction of the working layer. The melt of the intermediate layer re-melts a thin layer of a working layer and some carbide promoting elements, especially chromium, dissolves within the intermediate melt causing the formation of carbides, and due to the lower density compared with the γ begin to deposit on the interface of the intermediate layer and core. The large amount of carbides can be clearly seen in Figure 1. Sufficient solidification interval and a lower cooling rate are necessary to produce such a stratified intermediate layer that is an undesirable microstructure. Carbides, which are unevenly dispersed on the metal matrix, represent a brittle layer in the casting.

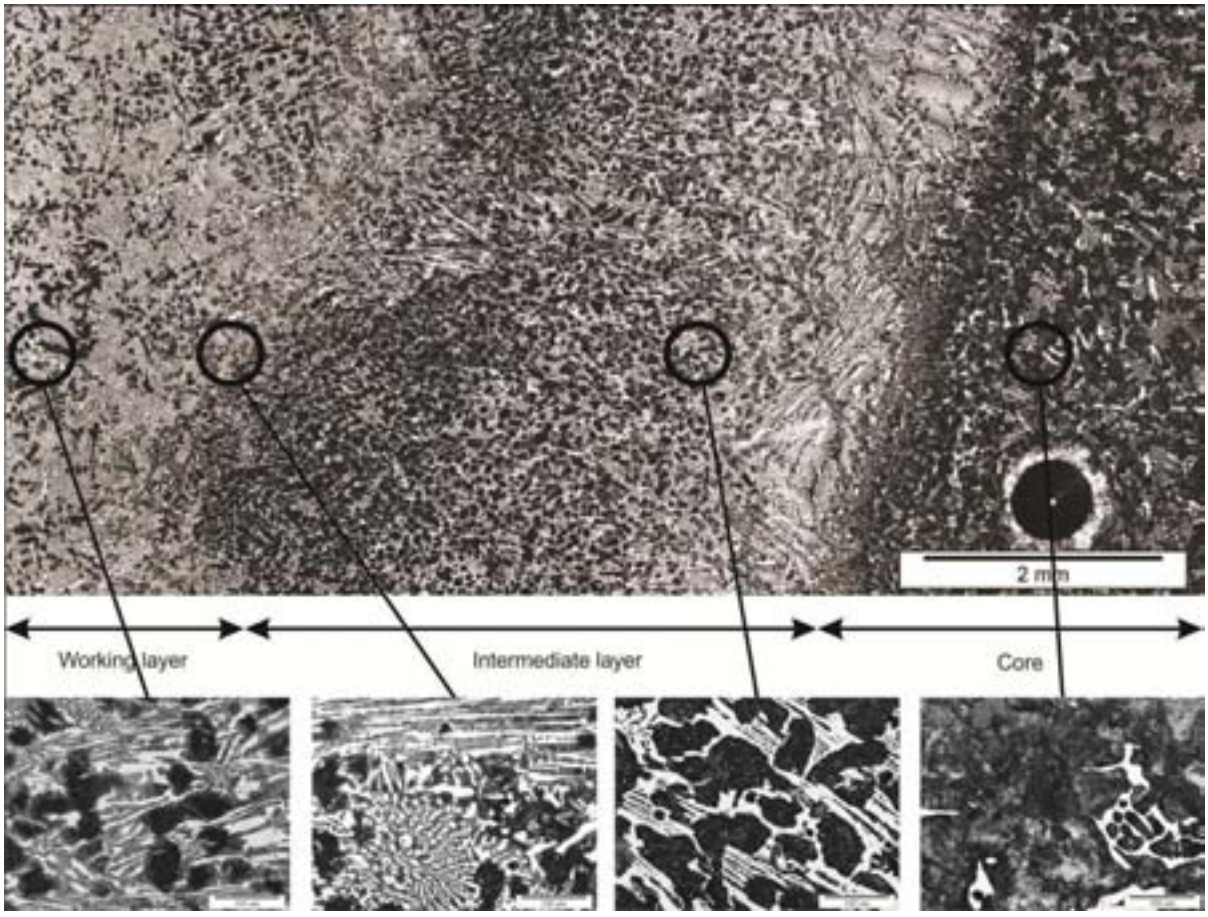

Figure 1: Macrostructure of a working layer, intermediate layer, and a core.

Figure 2 shows an isopleth phase diagram of the working layer material. Solidification starts with the solidification of austenite followed by eutectic reaction with the solidification of M_7C_3 type carbides between 1260 and 1230 °C. Precipitation of $M_{23}C_6$ type carbides takes place at 820 °C.

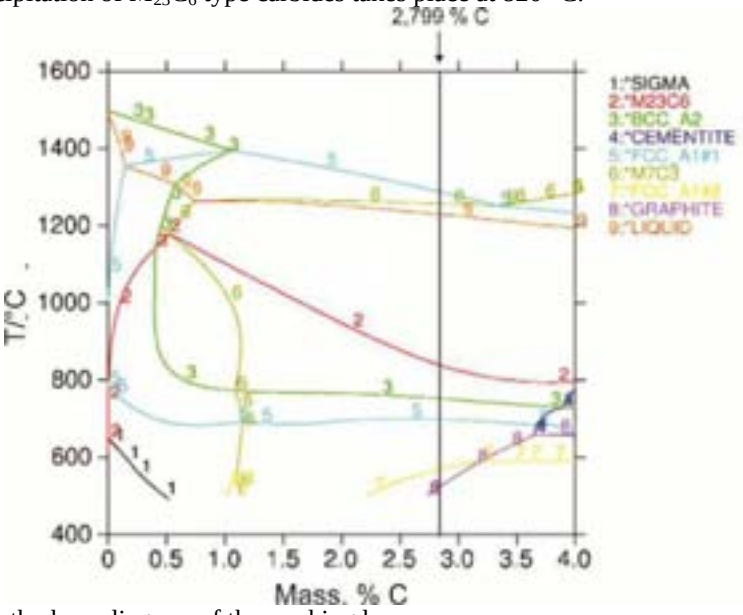

Figure 2: The isopleth phase diagram of the working layer.

With the help of the TAPP 2.2 program, the density of eutectic M_7C_3 carbides and austenite at the reference solidification temperature were calculated. The density of carbide M_7C_3 is 6.738kg/dm^{3}at temperature of precipitation; austenite has a density of a 6.99kg/dm^3 at a temperature of precipitation. Given the relative

differences in density between the austenite, carbides, and the melt during the solidification stage of the intermediate layer, it seems that stratification of both microstructural ingredients occurs. In the first stage austenite dendrites appear and are pushed by centrifugal forces and higher density in the direction near the working layer. When the temperature of the remaining melt falls within the scope of eutectic solidification, leading to the development of nucleation and growth of the carbides, they are pushed in the direction of the interface between the intermediate layer and core, as carbides have lower densities than austenite. The difference in density between the austenite and carbide is only 0,3kg/dm^3 but the difference is more significant at centrifugal forces of 120G leading to inhomogeneous microstructure development.

Figure3a shows the SEM-microphotograph of the working layer where the large particles are carbides solidified during eutectic reactions. EDS-analysis showed that these should be carbides of M_7C_3 type. The smaller particles in the matrix are carbides of $M_{23}C_6$ type precipitated in solid state from the solid solution of austenite. It is clear that practically all the austenite was transformed into martensite during heat treatment. The intermediate layer also contains carbides, determined by EDS-analysis to be M_7C_3 type, as seen in Figure 3b. There was a small amount of smaller particles of secondary carbides distributed in the martensite matrix but the amount was much lower as the concentration of carbide-promoting elements is much lower than for the working layer. Figure 3c shows an optic microphotograph of a core in a polished state where graphite is seen in the iron matrix. The graphite should be in nodule- like form but this is not because insufficient Mg-treatment and burn-off of Mg during the long solidification time of a core.

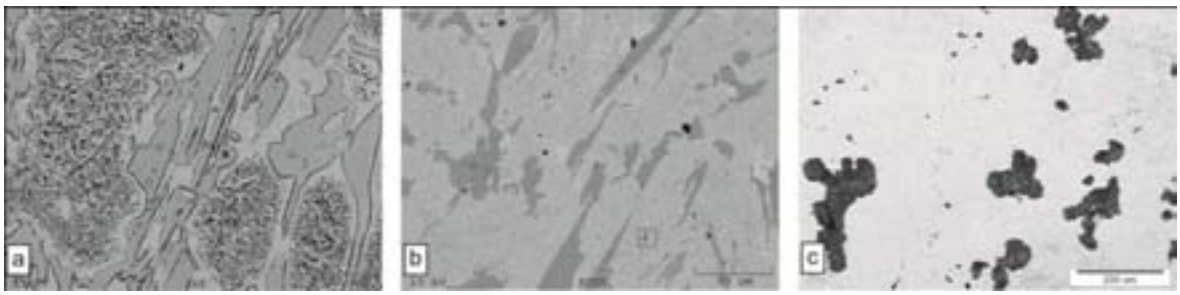

Figure 3: microstructures of all three layers: SEM microphotograph of the working layer (a), SEM microphotograph of the intermediate layer (b), and optic microphotograph of the core(c).

Figure 4 presents the EDS spectra of the analyzed microstructural constituents marked in Figures 3a and b.

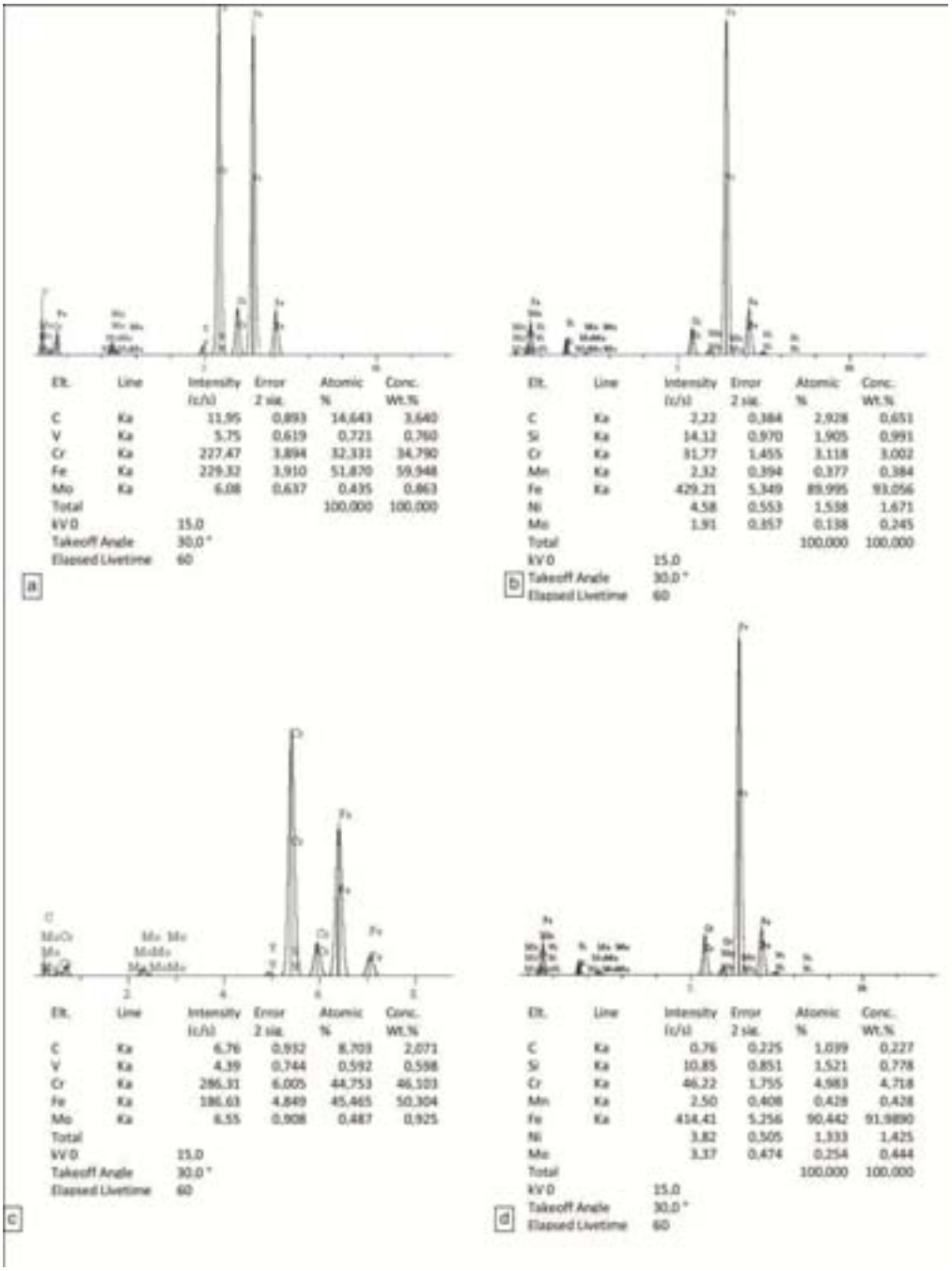

Figure 4: EDS-spectrums of phases: M_7C_3 carbide, spot 1 in Figure 3b (a), martensite spot 3 in Figure 3b (b), carbides $M_{23}C_6$, spot 6 in Figure 3a (c) and martensite with carbide $M_{23}C_6$, spot 4 in Figure 3b (d).

Rockwell Hardness measurements were carried out from the surface of the roll to an 80mm depth. Figure 5 presents the hardness of a working layer which is around 61HRC until 60mm in depth when the intermediate layer starts. In this layer hardness starts to descend and proceeds to descend into the core too where the hardness is only 32 HRC.

Tensile tests of the working layer at different temperatures showed that tensile strength is lowered by about 10% at 400 °C and at higher temperatures is lowered even faster and reaches only 200MPa at 700 °C. This means that the working layer has a tendency to form a crack formation during cooling after casting as the core has much higher temperature and causes tensile stresses in the working layer.

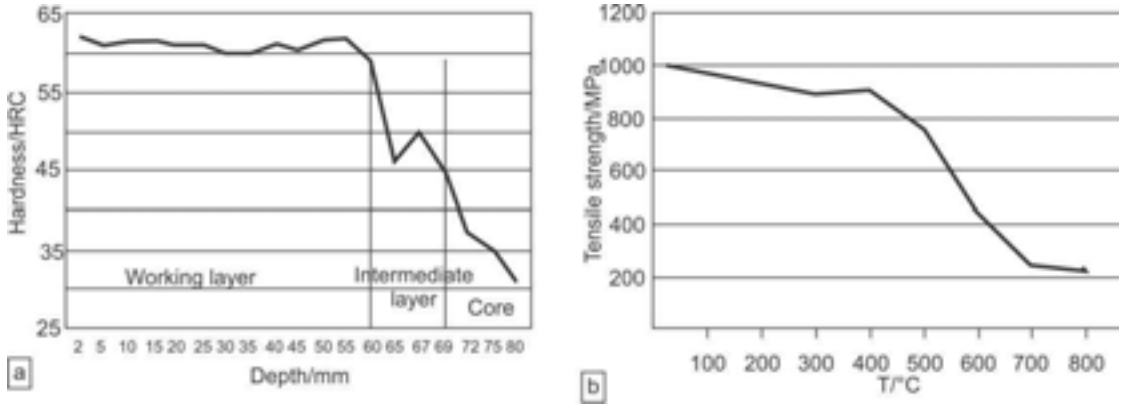

Figure 5: Mechanical properties: Hardness (a) and Tensile strength at different temperatures (b).

Figure 6 presents the dilatometric analysis of the samples, two from the working layer, one from the intermediate layer, and one from the core. It can be seen that the working layer had the lowest dilatation within the temperature range from room temperature up to 1100 °C. The Intermediate layer had slightly higher dilatation at the highest temperature but the core had the highest dilatation. These differences in dilatation cause high internal stresses during cooling of the gradient casting. It is clear that when the casting is cooling the surface – the working layer in this case shrinks faster than the core which causes tensile stresses in the working layer that might lead to a crack formation. A similar situation is met during heat treatment of the role, where the whole casting is heated to austenitising temperature and the core expands more than the working layer thus causing tensile stresses again. From Figure 6 it can be seen that the quantitative difference in dilatation of the samples is 0.055mm at 1000 °C which is not an insignificant value.

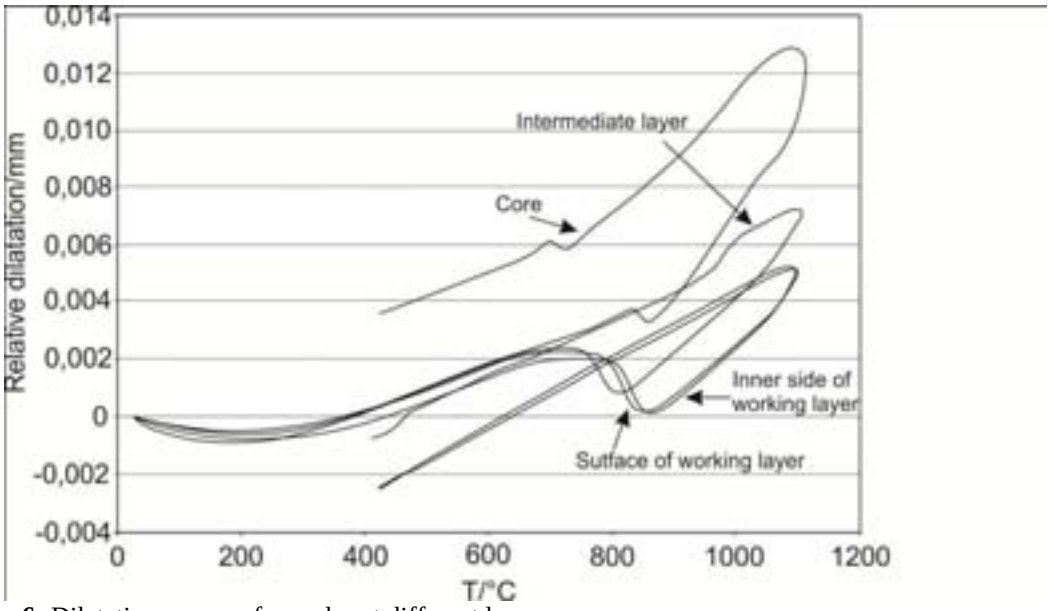

Figure 6: Dilatation curves of samples at different layers.

Stresses caused by different dilatations of layers during solidification and cooling of the casting were also calculated by Procast software and are presented in Figure 7. It is seen that the highest tensile stresses are reached just at the interface between intermediate layer and the core, which can lead to a crack formation and a failure of a role such as spall. [5]

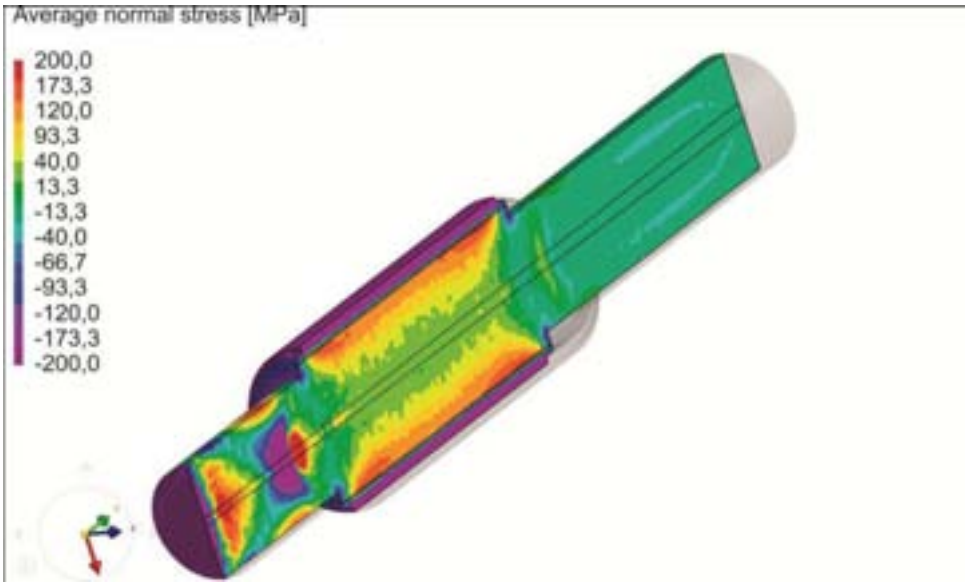

Figure 7: Simulation of normal stresses at the end of solidification.

Conclusions

1. Solidification of different layers was determined. It is clear that the intermediate layer re-melts the working layer and some carbide-promoting elements dissolve in an intermediate layer melt, which cause the formation of M_7C_3 type carbides. The working layer consists of secondary carbides too of a $M_{23}C_6$ type.
2. M_7C_3 type carbides have lower densities than austenite which are the reason that at slow solidification of the intermediate layer the formed carbides are pushed by high centrifugal forces into the inner side of the layer. Inhomogeneous microstructure is obtained in this way.
3. The tensile strength of a working layer is not changed until 500 °C, then it rapidly lowers which can lead to role failure if such working temperatures are reached.
4. The hardness of the roll's cross-section is lower in the intermediate layer and in the roll as a result of lower concentrations of primary and secondary carbides.
5. Dilatometric analysis showed big differences in the linear expansion coefficients of different layers. The difference in the dilatation of a working layer and a core is 0,055 mm at 1000 °C. Such differences may have already caused problems during cooling of the casting after solidification or during the following heat treatment.

References

1. Valji d.o.o., Manual for centrifugal casting of rols: Valji Štore d.o.o., 1986.
2. Jean-Pierre Breyer, Gisele Walmag, Metallurgy of High Chromium-Molybdenium White Iron and Steel rolls. Liege.
3. G.Rivera, P.R.Calvillo, R.Boeri, Y.Houbaert, J.Sikora Examination of the solidification macrostructure of spheroidal and flake graphite cast irons using DAAS and ESBD, Materials Caracterization, vol. 59, 1342-1348. s.l. : Elsevier Science Publishing Company, 2008.
4. Franc Gologranc, Preoblikovanje 1. Ljubljana: s.n., 1991.
5. Roll Failures Manual - Hot Mill Cast Work Rolls, 1st Edition, The European foundry association – Roll selection, 2002.

Trace elements and the control limits in ductile iron

L. Magnusson Åberg[1,*], C. Hartung[1] and J. Lacaze[2]
[1]Elkem AS, Foundry Technology Products R&D, Norway
[2] CIRIMAT, Université de Toulouse, France

Since the invention and start of production of ductile iron in the 1940's people working in the area have tried to find a way to easily control the final properties of the cast product. For this several different equations calculating the effect of trace elements have been developed. There are equations trying to predict nodularity, pearlite percentage (and thus ferrite), segregation, balancing harmful trace element content and so on. This paper reviews some of these equations and discusses their appropriate fields of use. Equations for predicting the appearance of degenerate and chunky graphite and how to balance the harmful trace elements are also discussed.

Keywords: ductile iron, trace elements, pearlite, segregation

Introduction

Ductile iron is composed of elements that can be divided into four groups: major, minor, trace[1,2] and alloying elements. The major elements are iron, carbon and silicon, minor elements are magnesium, oxygen and sulphur, alloying elements are typically copper, manganese and nickel (excluding Ni-hard and Ni-resist) while the rest of the elements are called trace elements. Trace elements are also often called tramp elements as in the ASM casting handbook[3]: "Contaminant in the components of a furnace charge, or in the molten metal or castings, whose presence is thought to be either unimportant or undesirable to the quality of the casting", while the Indian handbook defines trace elements as of such small quantity, usually too small for quantification.[4] Not all trace elements can be classified as deleterious as some of them have a beneficial influence on the mechanical properties of the final casting. The common trace elements in ductile cast iron (Ce, Bi, As, Sb etc) appear in amounts appropriate for chemical determination while others are hard to determine (Sr, Ba) due to their segregation behaviour. Some of the elements have an additive effect (Bi, Sb, As, Pb)[3,5] while others do seem to act alone (Zr, Sr).

Examples of typical trace elements and the change in the maximum amount found in ductile cast iron during a period of 30 years are given in Table 1. The content is based on Thielemann for years 1967 and 1998[6] in Germany while the numbers (average values) from 2009 are from Europe, based on samples processed by Elkem AS. The empty boxes in the table are due to no values reported. For some elements, like Mo, the value is reported for ductile cast iron not intended for high temperature use (i.e. SiMo cast irons are excluded). Thielemann reported concentration limits for avoiding the detrimental influence of trace elements, as found in literature.[5] These limits are listed in Table 2, where they are complemented with the maximum amount as recommended by Elkem AS.[7]

Equations developed for predicting nodularity are presented in the two next sections while those dealing with matrix structure as function of both trace elements and alloying elements are described in the following two sections.

Trace element effects on graphite structure

During the 1960's Thielemann[5] studied the influence of different elements by using raw material from different suppliers and adding the elements he was interested in. The different melts were cast into samples with thicknesses 8-45 mm. He specifically studied the influence of Pb, Bi, Al, Sb, Sn, As, Ti, Cu, Mg and the rare earths since the rest of the trace elements were present in such small amounts that they were found to have no noticeable influence on the final ductile iron casting. He found that Pb and Bi are additive i.e. together they have a higher negative influence on the graphite morphology, while Bi alone in small amounts will have a positive influence on the nodule number. Pb and Bi have negligible solubility in iron while Sb, Sn, As and Cu have a low solubility in austenite while decreasing the carbon solubility in liquid iron.[3,5] These latter elements have an additive effect as well. Ti and Al are depending on the cooling rate for their detrimental influence.

Thielemann developed a trace element evaluation number S_b for assessing the ability of the charge (i.e. this equation is only valid for calculations on the steel scrap, pig iron and returns used for producing the base iron) to give well-formed nodules:[5]

$$S_b = 4.4 \cdot w_{Ti} + 2.0 \cdot w_{As} + 2.3 \cdot w_{Sn} + 5.0 \cdot w_{Sb} + 290 \cdot w_{Pb} + 370 \cdot w_{Bi} + 1.6 \cdot w_{Al} \quad (1)$$

where w_i stands for the content in i elements, expressed in wt.%.

* corresponding author, e-mail: lena.magnusson.aberg@elkem.no

Table 1: Reported typical maximum amounts of trace elements (wt.%) for 1967, 1998 and 2009

Element	1967 Thielemann[5]	1998 Thielemann[6]	2009 (Elkem AS)
Ti	0.2	0.013	0.017
Cr	0.08	0.177	0.121
Ni	0.07	0.843	0.073
V	0.11		0.010
W	0.012	0.026	0.004
Te	0.005		0.002
Mo	0.05		0.061
Co	0.012		
Nb		0.007	0.003
Al	0.014	0.041	0.008
Sb	0.009		0.004
As	0.038		0.006
Sn	0.012	0.041	0.005
Zn	0.006	0.093	0.005
Bi	0.0009	0.008	0.004
Pb	0.005	0.008	0.001
B		0.005	
Ce		0.008	0.006

Table 2: Concentration limits for detrimental influence of trace elements (wt.%) according to Thielemann[5] and Elkem AS.

Element	Concentration	Elkem recommended maximum
Ti	0.04-0.10	0.2
Cr		0.1
Ni		0.2
V	0.05	0.02
W		0.03
Te	0.002-0.08	0.005
Mo		0.1
Co		
Nb		0.01
Al	0.08-0.3	0.2
Sb	0.002-0.026	0.01
As	0.02-0.125	0.01
Sn	0.005-0.13	0.15
Zn	0.01-0.10	0.05
Bi	0.001-0.03	0.01
Pb	0.002-0.011	0.005
B	0.005-0.01	0.01
Ce	0.02	0.02
Cu	0.5-4.0	1.5
Cd	0.01	
Se	0.03	0.002
Mg	0.08-0.10	0.03-0.06
Zr	0.01-0.10	0.01

Equation (1) is valid for residual Mg content 0.04-0.08 wt.% while the maximum concentration for the other elements is shown in Table 3. Comparing the maximum concentration limits for the validity of equation 1 with the numbers shown in Tables 1 and 2 the following can be remarked: lead is the only element where Elkem has a higher recommended maximum level in ductile cast iron. The other elements listed in Table 3 have a higher upper limit for the validity of equation 1 than the typical maximum levels listed in Tables 1 and 2 and thus equation 1 should still be valid for calculations for modern castings. When S_b=1±0.0625 no correction of the charge is necessary for obtaining a ductile iron with a nodularity above 85%. As earlier mentioned the equation was developed during the 1960's by experiments on castings with wall thicknesses 8-45 mm for different pig irons (37 different variants, where 17 were specifically aimed for production of ductile iron, from around the world) in combination with returns and steel scrap. The work is based on 200 industrial heats and 163 laboratory melts. Within the different groups, containing either Bi and Pb, or Sn and As and Sb, or else Ti by itself, the effect of the elements was found to be additive. This synergy and the effect between the different groups were taken into account when equation (1) was developed.

Table 3: Concentration limits (wt.%) of the various elements for the use of equation (1).[5]

Element	Maximum
As	0.14
Sb	0.10
Sn	0.15
Pb	0.002
Bi	0.002
Ti	0.12
Al	0.27

Equation (1) is sometimes found in literature with the denomination "anti-nodularising"[8] and almost always used for a final composition instead for a charge composition.[9] For some publications it is difficult to assess the calculations of S_b due to insufficient information, and it is sometimes unclear what the trace element evaluation equation is used to assess.[8] When the trace element evaluation number S_b is high (>~1.1) balancing the amount of deleterious elements is necessary. Javaid and Loper, Jr. did extensive work in this area,[10] since somewhat modified by Hansen et al.,[11] balancing the deleterious elements with the help of rare earths. The number of deleterious elements considered in the work by Javaid and Loper, Jr.[10] has been increased by Labrecque and Cabanne.[9]

Using rare earth elements to control nodularity

It was quite early clear that it is possible to balance the deleterious trace elements by rare earth additions. Most of this work has been concentrated on Ce or Ce in combination with La. Javaid and Loper, Jr.[10] and Lacaze et al.[12] investigated the ratios (Ce+La)/(Sb+Bi+As+Pb+Te+Ti) and (Ce+La)/Sb respectively, and found the balancing ratio to be 1 in the first case and 0.8 in the latter. Javaid and Loper, Jr. report the optimum amount of RE to be ~1.5 of the amount of added subversive elements or ~1 of the residual level of the final iron.[10] Lacaze et al. present a developed expression as (Sb+La)/(Mg+Ce)≈0.05.[12] None of these seems to be able to give a reasonable result when checked against foundry trials. This might be due to the difficulty in determining the low level of Sb, as well as the rare earths. Looking back at Table 1 it is seen that a typical maximum level of Sb is in the range of 0.004. Often the reporting limit for this element is set at 0.003 meaning the detection limit is around 0.0003. The difficulty is obtaining calibration standards for the lower concentration range. The numbers for the rare earths/trace elements ratio are very often misquoted in literature i.e. the number mostly quoted is 1.5 for Javaid and Loper, Jr.[10] while for Lacaze et al.[12] only 0.8 is mentioned. Javaid and Loper, Jr. pointed out the problem in using published work for reviews:[10] incomplete data on processing, incomplete chemistries, etc, but still managed to produce balancing equations for subversive elements. Note however that there was a drawback in their reasoning in one point: the trace elements considered have an additive effect and thus the amount of rare earths needed for balancing should not decrease but increase, as pointed out by Hansen et al.[11] According to these latter authors, the equation describing balancing of trace elements by rare earths should write:

$$w_{RE} = 0.5037 \cdot \sum w_{sub,i} + 0.0037 \quad (2)$$

where w_{RE} is the sum of added RE (wt.%) and $w_{sub,i}$ is the content in subversive element i (wt.%). The subversive elements are Sb, Pb, As and Ti, whereas it is unclear in the work by Javaid and Loper, Jr. if Bi and Te should be included.

Javaid and Loper, Jr. did also calculate a more complex equation where wall thickness ϕ (expressed in inches) is taken into account:[10]

$$\frac{w_{RE}}{\sum w_{sub,i}} = 2.083 + 65.896 \cdot w_P + 0.783 \cdot w_{Si} - 39.09 \cdot w_{Mg} - 1.963 \cdot w_{Ni} - 0.176 \cdot \phi \quad (3)$$

Both of these equations give reasonable results as shown by Hansen et al. when calculated for a ductile iron.[11] It may be also worth mentioning that Wray found in his experiments that 0.1%Ti=0.7%Si, somewhat implicating that Ti could be tolerated if the Si content is decreased.[13] Equation (3) could be amended accordingly.

Already in 1970 Thielemann[5] found that overcompensation with Ce-mischmetal gave exploded graphite, as also recently reported by Ghergu et al.[14] A simple evaluation of cerium adsorption on a graphite nodule is shown in the appendix. When comparing this calculation and assumptions with what seems to be a limiting amount of cerium in reality, when using charge material with low amounts of trace elements, the critical amount of cerium above which exploded or chunky graphite could appear seems to be of the order of 0.0029 wt.%. If the assumption that coverage of graphite by adsorption is the main mechanism for exploded or chunky graphite development, then a more precise calculation should account for all elements that can adsorb on it. Note however that chunky graphite does not evolve from exploded graphite, as seen in the paper by Ghergu et al.[14]

Löblich finds that Si, Cu, Ni, Ca and Ce will give chunky graphite in heavy section castings.[15] Ni will give chunky graphite even in thin sections, while Ca will only give chunky graphite if added late in the melting process. Ce-mischmetal added to a heavy section casting free of Ce in the charge will give chunky graphite in the centre of the casting. Löblich also found that chunky graphite will always appear when the undercooling of the eutectic reaction is 4-10 K while normal nodules will be formed at an undercooling of 1-2 K.[15] This is contradictory to the findings by Lacaze et al.[16] Löblich concludes that the following factors influence the formation of chunky graphite:[15] level of trace elements, number of nuclei, Si, Mn and S segregation, Ni level and long solidification time. The specific elements studied were Ce, Ca, Pb, Sb and As. It was concluded that these elements do not segregate at the casting scale. Finally, Löblich finds that Ce will be compensated by the presence of Pb, Sb and As and that the Si content (wt.%) in a 200x200 mm casting should be limited to a maximum value $w_{Si,limit}$ according to:[15]

$$w_{Si,limit} = \frac{2.26 - 1.5 \cdot \dfrac{w_{Ce}}{w_{Pb} + w_{Sb} + w_{As}}}{1.0 - 0.64 \cdot \dfrac{w_{Ce}}{w_{Pb} + w_{Sb} + w_{As}}} \quad (4)$$

This equation is valid for solidification times up to 50 minutes when the silicon content is lower than $w_{Si,limit}$. If the Si content is above this limit there is a danger for formation of chunky graphite. When checking this equation with other castings with or without chunky graphite no correlation between Si content and the appearance of chunky graphite can be found. Section size has an influence on acceptable limits of trace elements so that the level of cerium has to be lower in thick sections to avoid degenerated graphite.

Effect of trace and alloying elements on the matrix structure of ductile iron

A number of relations have been proposed to relate the composition of cast irons with the amount of ferrite or pearlite, at given cooling conditions. Björkegren[17] has reviewed some of the works available at the beginning of the 1980's, listing those by Weis,[18] Motz and Orths,[19] Campomanes and Goller[20] and Thielemann.[5] The first two works seem to have been dedicated to ferritic-pearlitic grades. Weis looked at the effect of low level elements on the mechanical properties of a standard nodular cast iron and tried to optimize the composition so that the product $A^{\bullet}(R_m)^2$ –where R_m is the rupture strength and A elongation at rupture - would be either lower than 41,000 or higher than 48,000.[18] As the ratio of ferrite and pearlite changed depending on the alloying content, Weis proposed the following expression for the pearlite fraction (%, with reference to the matrix only as all following relationships) in the matrix:[18]

$$f_{pearlite} = -2.45 + 768 \cdot w_{Sn} - 5.2 \cdot w_{Si} + 106 \cdot w_{Mg} - 142 \cdot w_{Co} + 138 \cdot w_{Cr} - 549 \cdot w_N + 101 \cdot w_{Al} + 51.6 \cdot w_P \quad (5)$$

Motz and Orths studied the detrimental effect of some elements on the ferrite fraction and obtained:[19]

$$f_{ferrite} = 92.3 - 96.2 \cdot w_{Mn} - 211 \cdot w_{Cu} - 14270 \cdot w_{Pb} - 2815 \cdot w_{Sb} \quad (6)$$

In a later work, Motz and Röhrig complemented their first study and provided the following relationship based on more than 100 heats:[21]

$$f_{ferrite} = -19.9 + 1.37 \cdot OGr - 3.01 \cdot [\%SiO_2] + 52.7 \cdot w_{Si} - 18.5 \cdot w_{Mn} + 814 \cdot w_S - 1818 \cdot w_{Cr}^2 - 11110 \cdot w_{Pb} \quad (7)$$

where O_{Gr} is the specific surface area of graphite and $[SiO_2]$ is the fraction of silica in the withdrawn slag.

For studying the effect of alloying elements in the case of ferritic grades, it has been suggested to use the product $w_{Si}.S_C$, where S_C is called the degree of carbon saturation and is given by the product of the alloy content in carbon and the carbon equivalent CE: $S_C = w_C \cdot CE$.[22] To the best of the knowledge of the authors, this suggestion has not found useful applications.

Campomanes and Goller studied the effect of carbide promoters on the microstructure of bars with different diameters.[20] They analysed 46 heats, using a small sized bar for evaluating the amount of carbide and a medium sized bar (1 in) for ferrite fraction. In this latter case, three bars showed an amount of carbide at 1% or less while all others were carbide free. Statistical analysis was first performed to look at the main effect of each element, and then multiple analyses were performed to characterize interactions. Though these latter analyses got a better correlation coefficient at 0.82 instead of 0.77 for the former, further use of their results will be made easier by considering the simpler linear analysis that gave:[20]

$$f_{ferrite} = -7.565 - 13.187 \cdot w_{Mn} + 11.293 \cdot w_{Si} - 68.546 \cdot w_{Ti} - 13.546 \cdot w_{Cr} - 16.37 \cdot w_V \quad (8)$$

In the same lines of looking at the effect of pearlite promoting elements on ferrite fraction, some more recent works are worth of mention. Yu and Loper, Jr. investigated the effect of Cu, Mo and Ni on the formation of ferrite in as-cast nodular cast iron containing 0.5 wt.% Mn.[23] For this, they cast bars with diameters D ranging from 0.5 to 2.5 in, and their results show that no bainite or martensite was observed in any bars with diameter equal or larger than 1.5 in. Regression analysis showed a high sensitivity to the cooling rate leading to the following equation:

$$f_{ferrite} = 15.6 + 19 \cdot D - 11.9 \cdot w_{Mo} - 13.6 \cdot w_{Cu} - 8.1 \cdot w_{Ni} \cdot D - 15.9 \cdot w_{Cu} \cdot D \quad (9)$$

Yu and Loper, Jr. noticed that Cu is the most efficient of these three elements to decrease ferrite fraction, followed by Ni the effect of which increases significantly with section thickness as for Cu. Mo is seen to favour pearlite, but close examination of Yu and Loper, Jr. data shows this effect slightly decreases with section thickness. The effect of Mo on ferrite fraction is indeed controversial, as mentioned by Yu and Loper, Jr.[23] and later by Venugopalan and Alagarsamy.[24] These latter authors studied the effect of the same elements plus Mn and P on the microstructure of 15 heats of nodular cast iron. These alloys were cast in keel blocks (1x1.5x8 in) and were all found free of carbides in the as-cast state. The authors report two regression analyses, with or without accounting for P, which both show some cross terms. The regression including P writes:[24]

$$f_{ferrite} = -86 + 66 \cdot w_{Si} + 721 \cdot w_P + 226 \cdot w_{Mo} - 29 \cdot w_{Mn} - 100 \cdot w_{Cu} - 16.5 \cdot w_{Ni} - 234 \cdot w_{Mo} \cdot w_{Ni} - 113 \cdot w_{Cu} \cdot w_{Mo} \quad (10)$$

It is here seen that Mo favours ferrite, in contradiction with the finding by Yu and Loper, Jr.[23] According to Venugopalan and Alagarsamy, this complex effect of Mo is related to the fact it increases temperatures for both ferrite and pearlite formation and shifts also both reactions to longer times. As a consequence, Mo favours ferrite at low cooling rate and pearlite at high cooling rates. It was very tempting to check if the two above works on Cu, Mo and Ni could be analysed together. Following Venugopalan and Alagarsamy, only their 12 first castings were used because their last melts had much larger nodule count. Their results were added to those obtained by Yu and Loper, Jr. for the 2.5 in bars. Multi-variable analysis was performed that gave a very high correlation factor $R^2=0.98$ but with several cross terms that decreased significantly the number of freedom of the analysis. It was thus decided to restrict the analysis to cross terms invoking Cu which, as already stressed, is the most efficient element effecting ferrite fraction. This procedure again led to a high correlation factor $R^2=0.98$ with the following equation:

$$f_{ferrite} = 135.8 + 18.1 \cdot w_{Si} - 1566 \cdot w_{Mg} - 52.1 \cdot w_{Mo} - 30.7 \cdot w_{Mn} - 27.6 \cdot w_{Ni} - (260 - 81.1 \cdot w_{Cu} - 1703 \cdot w_{Mg} - 62.0 \cdot w_{Mo} - 30.9 \cdot w_{Ni}) \cdot w_{Cu} \quad (11)$$

Measured versus predicted values are plotted in Fig. 1 where it is seen that both series of results span a large domain of ferrite fractions, and are thus intertwisted. Looking at equation (11), it is seen that the apparent first order effect of all elements but Si is to decrease the amount of ferrite. However, writing the cross terms as done shows that Cu, Mg, Mo

and Ni do level off the effect of Cu. In other terms, adding several pearlite promoter elements will rapidly saturate the effect. Also, it is seen that at low level of Mg, Mo or Ni, the cross term invoking either of these elements may overtake the first order term if the Cu content is high enough. In a simple analysis this would lead to conclude that these elements are ferrite promoters, but this will not be true if the Cu content is low enough.

The works presented so far were mostly concerned with the effect of alloying additions on ferrite fraction. Other works as the one by Thielemann were more focused on pearlitic grades and the effect of impurities. Thielemann expressed the residual ferrite fraction (%) as:[5]

$$f_{ferrite} = 961 \cdot \exp(-Px) \quad (12)$$

with:

$$Px = 3.00 \cdot w_{Mn} - 2.65 \cdot (w_{Si} - 2.0) + 7.75 \cdot w_{Cu} + 90.0 \cdot w_{Sn} + 357 \cdot w_{Pb} + 333 \cdot w_{Bi} + 20.1 \cdot w_{As} + 9.60 \cdot w_{Cr} + 71.7 \cdot w_{Sb} \quad (13)$$

Note that this evaluation is meaningful for grades with some pearlite as it should be ensured that $f_{ferrite}$ is lower than 100%, or equivalently that P_x is larger than about 2.3. Furthermore, if a fully pearlitic structure is considered to be obtained when the cast contains a maximum of 2% ferrite, the equation shows that Px should be higher than 6.2.

Predicting the matrix structure of ductile iron

The relationships listed above have been most often obtained for given cooling conditions which however may vary from one work to another. The effect of cooling rate and of nodule count on the amount of ferrite or pearlite is well documented, and it is in particular known that the ferrite fraction is much less sensitive to cooling rate at high nodule count than at low nodule number. In analysing literature data as done below, it appeared possible to show the effect of cooling rate and then to illustrate the effect of alloying or trace elements by selecting data corresponding to similar cooling conditions. However, it appeared hardly possible to separate the effect of nodule count.

The information included in equation (13) could be complemented by data from literature, where use is often made of Sn equivalent and Mn equivalent. Eventually, the coefficients giving the Sn or Mn equivalent of an element are obtained as the ratio of the corresponding coefficients in the listed equations. Table 4 shows the values for the Sn-equivalent obtained from the equation by Weis[18] and by Thielemann,[5] as well as other data proposed by Else[25] and Lacaze et al.[26] It is seen than apart for As, the proposed Sn-equivalent values are generally of the same order. Also, Neumeier et al. used 0.10 for Cu which is well in the range of the values reported in table 4.[27]

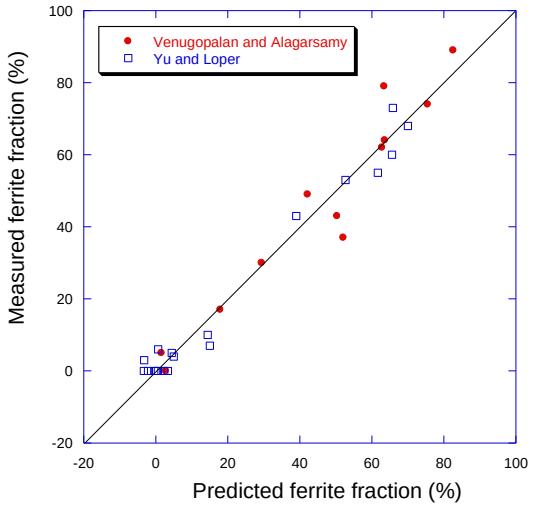

Fig.1: Measured[23,24] versus predicted ferrite fractions. The line is the bisector.

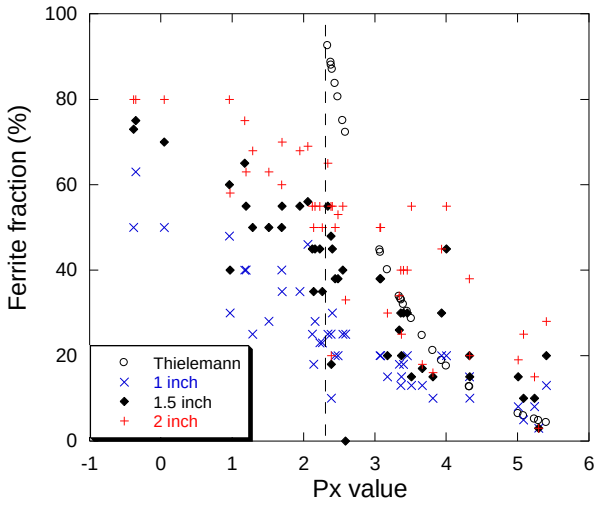

Fig. 2: Comparison of experimental ferrite fraction[20] with prediction equation (12) plotted versus amended Px parameter, equation (14).

The same data and other[28] can be used to evaluate a Mn-equivalent as shown in Table 5. It is seen that the values of some coefficients are scattered, with a factor of 8 for V. This scattering may be understood because some of the studies were focused on pearlitic irons while others investigated ferritic irons. Accordingly, linear relationships that have been used between composition and matrix structure fail to describe the transition between mainly ferritic and mainly pearlitic matrices. On the contrary, the exponential function used by Thielemann predicts that addition of any of the pearlitic-promoter elements above a critical level leads to an abrupt decrease of the ferrite fraction down to a value at which the effect of further additions levels off. This result has been confirmed recently for the case of Cu, Mn and Sn. At given cooling conditions, the critical level was found to be 0.6 wt.% for copper[29] and 0.05 wt.% for tin.[26]

Table 4: Sn-equivalent for several elements favouring (+) or preventing (-) pearlite.

Al	As	Bi	Co	Cr	Cu	Mg	Mn	N	P	Pb	Sb	Si	Reference
0.132			-0.185	0.180		0.138		0.715	0.067			-0.007	[17]
	0.22	3.7		0.107	0.086		0.033			3.97	0.797	-0.029	[5]
	2				0.083		0.042						[25]
					0.125		0.075						[26]

Table 5: Mn-equivalent for several elements favouring (+) or preventing (-) pearlite.

As	Bi	Cr	Cu	Mo	Ni	Pb	Sb	Si	Sn	Ti	V	reference
6.7	111	3.2	2.6			119	24	-0.9				[5]
48			2.0						24			[25]
		1.0						-0.9		5.2	1.2	[20]
			2.2			148	29					[19]
		4.0	0.5		1.5						10	[28]
			1.7						13.3			[26]
				1.7	0.9			-0.6				Equation (11)

It appeared then of some interest to attempt to use the data in tables 4 and 5 to complement the proposal by Thielemann and check predictions against results from literature. Merging information from both tables, a tentative amended Px value could be written:

$$\begin{aligned} Px = 3.00\cdot[w_{Mn} + 1.5\cdot w_{Ni} + 5.2\cdot w_{Ti} + 1.2\cdot w_{V} + 1.7\cdot w_{Mo}] - 2.65\cdot(w_{Si} - 2.0) + 7.75\cdot w_{Cu} \\ + 90.0\cdot[w_{Sn} - 0.185\cdot w_{Co} + 0.138\cdot w_{Mg} + 0.75\cdot w_{N} + 0.067\cdot w_{P}] \\ + 357\cdot w_{Pb} + 333\cdot w_{Bi} + 20.1\cdot w_{As} + 9.60\cdot w_{Cr} + 71.7\cdot w_{Sb} \end{aligned} \quad (14)$$

The first attempt was performed using the results by Campomanes and Goller,[20] plotting the reported ferrite fraction values for 1, 1.5 and 2 inches cylindrical bars against predictions made with the amended Thielemann's Px expression. As expected, it is seen in Fig. 2 that the experimental ferrite fraction does increase with the diameter of the bar, though the scattering of the data is quite significant. When compared to the predictions (open circles), which should be limited to values of Px higher than 2.3 (vertical interrupted line in the graph), it is seen that the agreement is within ±20% of ferrite, for ferrite fractions lower than 40%.

The next attempt concerned data reported by Pan et al. on the effect of Cu, Sn and Mn on the pearlite fraction measured in keel-block legs cast with both nodular and flake cast iron grades.[30] Their results are reported in Fig. 3 against the amended Px value, and compared with predictions made with Equation (12) using the corrected Px value given by equation (14). Data from Venugopalan and Alagarsamy[24] and Yu and Loper[23] used for plotting Fig. 1 have also been reported in Fig. 3, as well as results reported by Kovacs for 2 in thickness of a step casting in which 20 heats have been cast to study the effect of Mn, Sn and Sb on pearlite fraction of nodular and flake cast irons.[31] Though the scatter in the experimental results is here also quite high, it is seen that the transition from a ferritic-pearlitic matrix to a nearly fully pearlitic matrix is well reproduced. This has been emphasized by drawing the solid line corresponding to Thielemann's approach with around a greyed area (Px±2) that is intended to account for differences in nodule count, cooling conditions and uncertainties in chemical analysis. Two remarks are relevant here: i) it has been noticed that accounting for Mg content is of importance, the agreement would have been otherwise much worse with higher scatter, at least for the results by Pan et al.[30]; ii) data for lamellar graphite are all located in the fully pearlitic area so that it can hardly be concluded if they agree or differ from results for nodular iron. It is however worth mentioning that Pan and Loper showed convincingly that flake graphite irons are more pearlitic than compacted/nodular cast iron of similar composition.[33]

Buhr[32] studied the effect of low level elements Pb (up to 0.013 wt.%), Sb (up to 0.023 wt.%) and Bi (up to 0.009 wt.%) in 5 inch thick castings of nodular iron inoculated with three inoculants differing by their Ce content (high, medium and nil). Buhr used the sum of the contents in residual elements (Pb, Sb and Bi) to discuss the results and found their effect varies with the Ce content. Reanalysing these results shows that the pearlite content decreases when the nodule count increases at low level of residual elements, as expected. High levels of residuals increases the amount of pearlite for both nil and medium Ce contents, while it decreases it at high level of Ce. It may thus be inferred that this high Ce content was enough to counteract the effect of residuals, when this was not the case for the two lower levels. Buhr's results are plotted as function of the amended Px values in Fig. 4. Again, it was noticed that accounting for Mg and P through the amended Px expression is of importance. In fig. 4, it is thus seen that the results for nil and medium Ce contents do overlap and show the same trend when this was not the case when using the sum of the residuals as done by Buhr.[32] Excluding the high Ce series, this means that the weighting factors proposed by Thielemann are appropriate in the present case as well. Also, the curve calculated with equation (12) has been drawn in Fig. 4 and shows a trend similar to experimental data for low Ce levels. At high Ce level, a totally different process takes place that was not explained by Buhr.

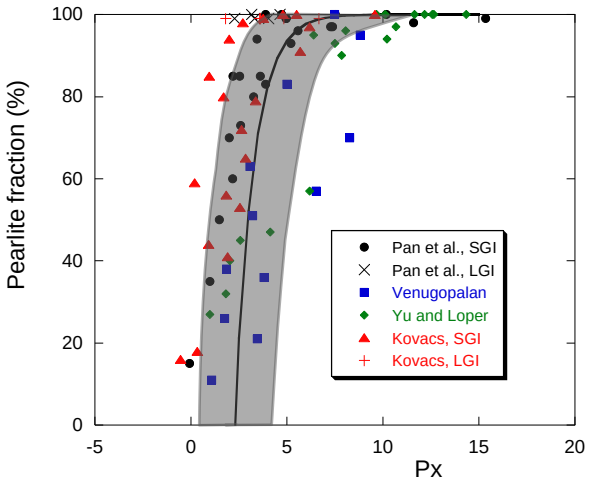

Fig. 3: Comparison of measured pearlite fractions for nodular (closed symbols) and lamellar (crosses) irons[23,24,30,31] with predictions made with Thielemann's approach (solid line), reported versus the amended Px value.

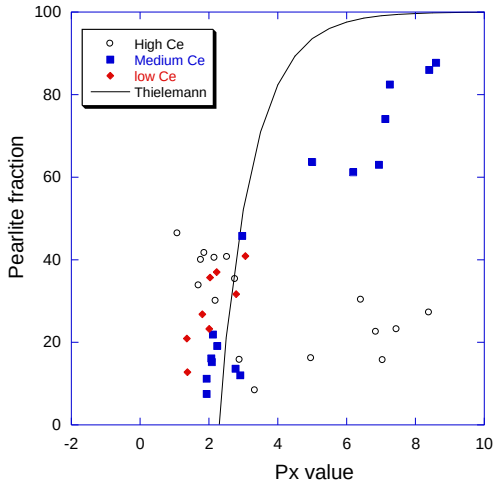

Fig.4: Plot of Buhr's data and predicted pearlite fraction as function of the amended Px values.[32]

Discussion - Conclusion

Thielemann's trace element evaluation equation for the charge of pig iron, steel scrap and returns is giving an indication of if the base iron will have to be adjusted for production of nodular cast iron. The trace element evaluation equation is however not made for evaluation of a final casting, as often seen in publications, and the equation has defined limits for its validity, as shown in the original paper and in Table 3.

Several of the trace elements used to develop equation 1 have drastically decreased, as seen in Table 1, during the 40 odd years covered in the table. The most detrimental element, Bi, has however increased. When the trace element evaluation equation indicates a value above 1, typically when the amount of returns increases, corrective actions by adding rare earth elements to the melt have to be taken. Thielemann did experiments with corrective additions of cerium-mischmetal but unfortunately did not produce any equations for this.

The balancing equations are found in the thorough work by Javaid and Loper, Jr., who analysed large amounts of data. The result is a simple equation easily used in a foundry. This equation, somewhat corrected by Hansen et al., gives reasonable results for modern ductile iron.

Javaid and Loper, Jr., as well as Lacaze et al. developed simple equations (ratios of rare earths to subversive elements) for correction of subversive elements. None of these equations did give any reasonable result when checked against foundry trials. This could, however, be due to the difficulty in determining the low levels of the trace elements.

Löblich tried to correlate the amount of subversive elements and cerium to a limiting level of silicon. The equation was developed for castings of size 200•200 mm^2 with a solidification time lower than 50 minutes. When calculating this silicon limit for foundry castings, comparing with actual silicon level and checking against defects like chunky graphite no correlation could be found.

When calculating the possible amount of cerium adsorbed on a graphite surface and comparing with foundry trials an upper cerium limit of 0.0029 wt.% seems reasonable to avoid the formation of chunky graphite in a cast iron with low level of trace elements.

Thielemann's equation expressing the fraction of ferrite as a function of a parameter which is a linear function of composition variables has been found to describe in most cases properly, though semi-quantitatively, the transition from ferritic-pearlitic to fully pearlitic microstructures. Some of the discrepancy may come from the fact that this equation does not account for casting size. The equation for Px has been here extended using Sn and Mn equivalents to account for elements that have not been studied by Thielemann. This may explain part of the scattering as well, but most of it certainly comes from interactions between alloying and trace elements for which very little is known and would be worth of further study. Also, check of a few results on lamellar graphite irons seems confirming these alloys are more prone to give pearlitic matrix than nodular cast irons, and this would certainly be worth of further study as it could give some valuable insight about the mechanisms by which trace elements affect solid-state graphite growth.

References

1. R. Elliott 'Cast Iron Technology', 2nd edn, 2004, Jaico Publishing House
2. Smithells Metals Reference Book, 7th edn, (Ed. E.A. Brandes), G.B. Brook, Buttherworth Heinemann
3. ASM Handbook volume 15 'Castings', 4th edn, 1998
4. Handbook of metal terminology, 62nd Indian foundry congress, 2014, Gandhinagar, India

5. Th. Thielemann: *Giessereitechnik*, 1970, 16, 16-24.
6. Th. Thielemann: *Giessereitag* 1.10.1998
7. Technical Information sheet 12, Elkem AS
8. I. Riposan, M. Chisamera and S. Stan: *Int. J. Cast. Met. Res*., 2007, 20, 64-67.
9. C. Labreque and P.-M. Cabanne: Proceedings of 69th WFC October 16-20, 2010, Hangzhou, China, 411-418.
10. A. Javaid and C.R. Loper: *AFS Trans.*, 1995, 103, 135-150
11. G.M. Hansen, C. Hartung, L. Magnusson Åberg and D.S. White: *AFS Trans.*, 2012, paper 12-020
12. J. Lacaze, S. Armendariz, P. Larrañaga, I. Asenjo, J. Sertucha and R. Suárez: *Materials Science Forum*, 2010, 636-637, 523-530.
13. R. Wray: *Castings*, 1962, November-December, 19-27.
14. R. Ghergu, L. Magnusson Åberg and J. Lacaze: *Materials Science Forum*, 2014, 790-791, 435-440.
15. H. Löblich: *Giesserei*, 2006, 93, 28-41.
16. J. Lacaze, L. Magnusson Åberg and J. Sertucha, 2013 Keith Millis Symposium on Ductile Cast Iron, AFS, 232-240.
17. L.E. Björkegren: *Gjuterinytt*, n°445, 1981
18. W. Weis: *Gjuteriet*, 1981, 71, 18-24.
19. J. Motz and K. Orths: *Giessereiforschung*, 1967, 19, 109-124.
20. E. Campomanes and R. Goller, *AFS Trans.*, 1979, 87, 619-626.
21. J. Motz and K. Röhrig: *Giessereiforschung in English*, 1970, 22, 141-151.
22. E.N. Pan, W.S. Hsu and C.R. Loper, *AFS Trans.*, 1988, 96, 645-660.
23. S.K. Yu and C.R. Loper: *AFS Trans.*, 1988, 96, 811-822.
24. D. Venugopalan and A. Alagarsamy: *AFS Trans.*, 1990, 98, 395-400.
25. G.E. Else, BCIRA Int. Conf, 1980, cited by Björkegren.[17]
26. J. Lacaze, J. Sertucha, P. Larrañaga and R. Suárez: Proc."Word Foundry Congress", Mexico, Monterrey, 2012.
27. L.A. Neumeier, B.A. Betts and D.H. Desy: AFS Trans., 1974, 82, 131-138.
28. M. Decrop, AFS Int. Cast Metals J., 1979, December, 18-20, cited by Björkegren.[17]
29. J. Sertucha, P. Larrañaga, J. Lacaze and M. Insausti: *Int. J. Metalcasting*, 2010, 4, 51-58.
30. E.N. Pan, M.S. Lou and C.R. Loper: *AFS Trans.*, 1987, 95, 819-840.
31. B.V. Kovacs : *AFS Trans.*, 1980, 89, 79-96.
32. R.K. Buhr: *AFS Trans.*, 1971, 80, 247-252.
33. E.N. Pan and C.R. Loper: *AFS Trans.*, 1986, 94, 545-556.
34. I. Minkoff and W.C. Nixon: *J. Applied Physics*, 1966, 37, 4848-4855.

Appendix

Let assume that nodules have precipitated with a density N_V around nuclei having a radius r°. The graphite fraction when the nodules have reached a radius r^g is:

$$V^g = \frac{4}{3}\cdot\pi\cdot\left[\left(r^g\right)^3 - \left(r^\circ\right)^3\right]\cdot N_V \qquad \text{(A-1)}$$

The number n_i of atoms of element i that were in the volume now occupied by graphite is $n_i = C_i \cdot V^g$, where C_i is the molar concentration of i in the initial liquid, which writes:

$$C_i = \frac{\rho_i}{M_i} = \frac{\rho\cdot w_i^0}{M_i} \qquad \text{(A-2)}$$

with ρ_i the mass concentration (kg.m^{-3}) of i in the liquid, ρ the density of the liquid, w_i^0 the nominal mass fraction of element i in the material and M_i the atomic mass of element i. Assuming that all i atoms in the V^g volume adsorb at the surface of the growing graphite nodules, the coverage is given by:

$$\Gamma_i = \frac{n_i\cdot\left(r_i\right)^2}{4\cdot\pi\cdot\left(r^g\right)^2\cdot N_V} = \frac{\rho\cdot w_i^0}{M_i}\cdot\frac{\left[\left(r^g\right)^3 - \left(r^\circ\right)^3\right]\cdot\left(r_i\right)^2}{3\cdot\left(r^g\right)^2} \qquad \text{(A-3)}$$

where the surface occupied by a i atom has been taken as $(r_i)^2$, where r_i is the atomic radius of element i. With ρ set at 7200 kg.m^{-3} and r° at 0.5 µm, M_i set at 140 g.mol^{-1} and r_i at 2 Å as for cerium, one gets the solid curves shown in Fig.A-1 for three values of w_i^0, 10, 100 and 1000 ppm per mass. As growth proceeds, more and more i element accumulates at the surface of the nodules until full coverage is achieved. This is readily done for 1000 ppm at the very start of growth while this will be achieved for a radius of 8 µm for 100 ppm and even larger for 10 ppm. The case where some of i element gets incorporated in graphite is illustrated with the dotted lines that assumes a "partition" coefficient of 0.25 as reported for lanthanum.[34]

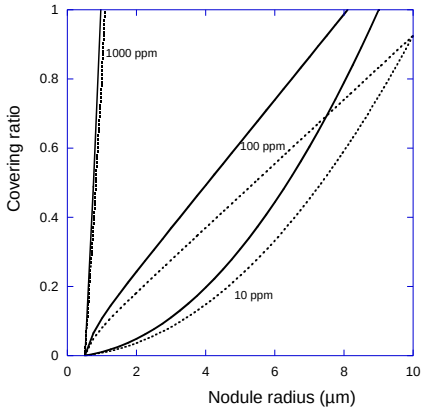

Fig.A-1: Calculation of graphite nodule coverage for various nominal amounts of adsorbed element.

Inoculant enhancer to increase the potency of Ca-FeSi alloy in ductile iron produced from the low rare earth containing master alloy

I. Riposan[1*], V. Uta[1], S. Stan[1], M. Chisamera[1], M. Firican[1], R. Naro[2], D. Williams[2]
[1]POLITEHNICA University of Bucharest, Bucharest, Romania
[2]ASI INTERNATIONAL LTD, Cleveland, Ohio, USA

The world rare earth elements [REE] crisis will continue at least in the short and medium term. With less REE available, their future use in foundry alloys should be carefully thought out and other inoculation methods need to be investigated. The use of an inoculant enhancer [OS-IE] led to a substantial increase in the potency of a 75% Ca-bearing FeSi alloy in low REE produced ductile irons, as this [Ca-FeSi + OS-IE] inoculation variant led to the lowest chill tendency, the highest nodule count and graphite nodularity. This combination of inoculant was more effective than an equivalent addition of 1) a REE-bearing, Ca-FeSi alloy, or 2.) a Ca,Ba-FeSi alloy, or 3.) the standard Ca-FeSi alloy variant, but with 60% or 77% lower alloy consumption, respectively. The enhancement of the 75% Ca-bearing FeSi alloy by the contribution of an addition of sulphur, oxygen and oxide-forming elements, appears to be a better and more effective inoculation solution compared to using more expensive inoculating elements, such as the REE or Ba containing alloys.

Keywords: ductile iron, magnesium, rare earths, inoculant enhancer, in-mould inoculation, chill, graphite nodularity, nodule count, shape factors

Introduction

Oxy-sulphide forming elements appear to have a very important role in graphite nucleation in cast irons. Complex (Mn,X)S compounds (where X = Fe, Al, O, Ca, Si, Sr, Ti, Zr, etc.) nucleated on Al_2O_3-based sites[1-5] and were the primary sites for graphite flake growth in both un-inoculated and inoculated grey irons (Fig. 1a).[4] Generally considered as inoculating elements, calcium and strontium were found to distribute differently in the inclusion volume. Calcium was distributed evenly throughout the inclusion while strontium was found mainly in the core of the inclusions. Particles associated with graphite had a lower Mn/S ratio than the matrix-embedded particles. The Ca-FeSi and Sr-FeSi inoculated irons had a lower Mn/S ratio than high-purity (HP) FeSi treated irons.[1-5]

According to M.H. Jacobs et al,[6] graphite nodules nucleate heterogeneously on particles formed in the melt, and exhibited a duplex sulphide/oxide structure. These nucleating particles consisted of a central seed, surrounded by an outer shell of different crystal structure and chemical composition. For Ca-FeSi and Sr-FeSi inoculated, FeSiMg treated iron, it was found that the central seed consisted of (Ca,Mg)S *versus* (Sr,Ca,Mg)S compounds, while the outer shell was a (Mg,Al,Si,Ti)Oxide having a spinel structure. It appears that Mg, Ca, and Sr play two important roles in ductile iron nucleation: 1) to combine with and remove the free S from the melt and 2) to form of sulphide particles, both roles

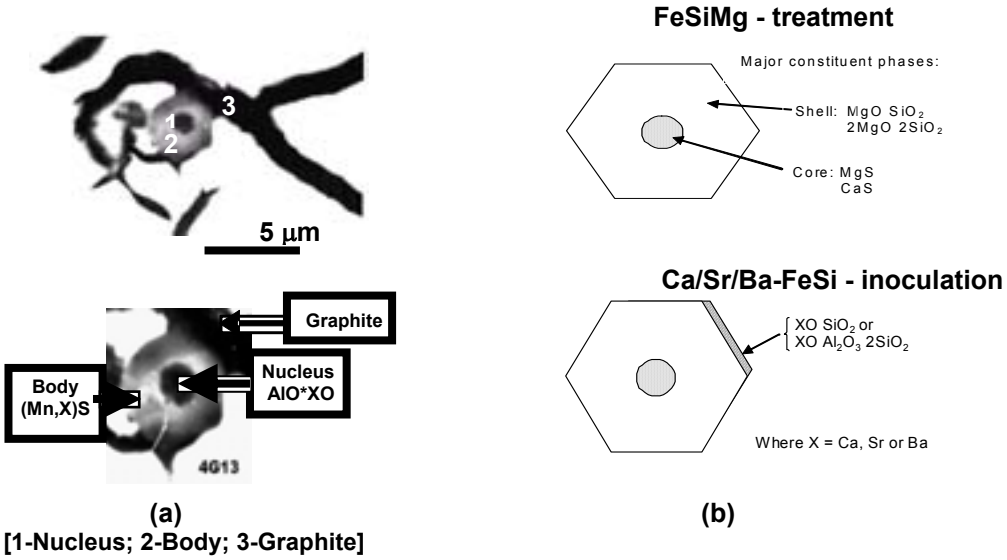

Fig. 1: Graphite nucleation mechanism in grey iron (a)[4] and ductile iron (b)[7]

* Corresponding author, email: i_riposan@rectorat.pub.ro

being important and necessary steps in graphite nucleation. T. Skaland found complex hexagonal silicate phases of XO-SiO_2 or XO-Al_2O_3-$2SiO_2$ on the surface of the previously formed Mg-silicates (Fig. 1b) making them more favourable sites for subsequent graphite nucleation. In post-inoculated ductile irons, X can be either Ca, Ba, or Sr. All of these phases will serve as favored sites for graphite inoculation.[7]

The simultaneous addition of sulphur with potent oxy-sulphide forming elements was first demonstrated by Naro and Wallace,[8] who showed that balanced ratios of rare earths and sulphur, without the presence of ferrosilicon, drastically reduced undercooling, completely eliminated chill and promoted favorable graphite shapes in grey irons (Fig. 2). Strande[9] showed that using CaSi-based inoculants along with increased direct sulphur additions to the metal vastly improved machinability in grey iron castings. Chisamera and Riposan[1-5] also illustrated the importance of sulphur content and inoculant effectiveness in grey irons.

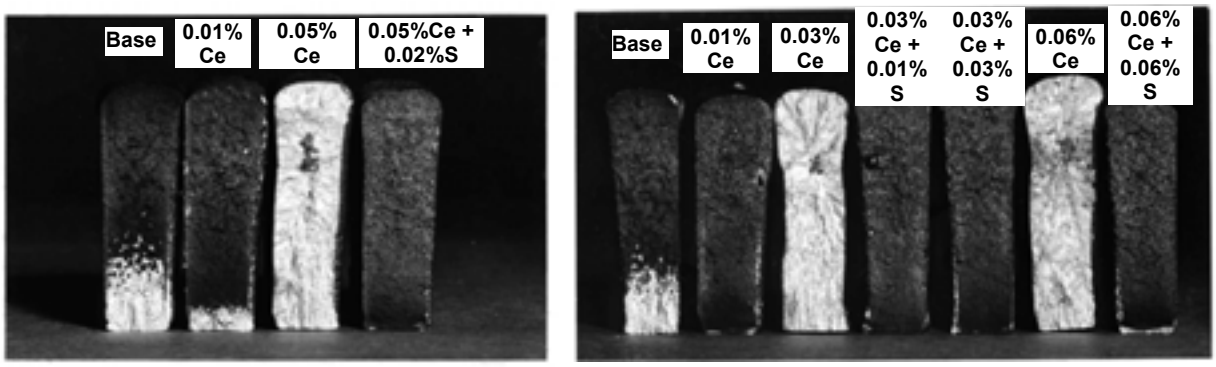

Fig. 2: Effect of oxy-sulphide forming elements (Ce and S) on the chilling tendency of grey iron[8]

In ductile irons, Chisamera and Riposan[10-14] demonstrated that less than 0.01wt.%S added concurrently with CaSi-based inoculants or/and rare earth elements, increased graphite-nucleation potential without affecting graphite nodularity. It was found that the strong sulphide-forming tendencies of Ca and rare earth, when used with controlled sulphur additions, strongly promoted the formation of sulphide compounds, assisting in their effectiveness as nodular graphite nuclei. Later, Skaland[15,16] developed an inoculant concept based on adding small and controlled amounts of sulphur and oxygen coated onto the surface of a Ca/Ce-FeSi alloy that could react with calcium and cerium when introduced into liquid iron.

Aluminum also appears to play an important role in nodular graphite nucleation in ductile irons. Aluminum has been found in nodular graphite as a complex nitride, such as AlMg2.5Si2.5N[17] and (Mg, Si, Al)N,[18] and as an oxy-nitride (Mg, Si,Al)ON at very low sulphur contents in the base iron (< 0.01wt.% S).[19] Aluminum, together with Mg and Ca as a constituent in sulphide and silicate inclusions has been observed in induction and cupola melted iron.[20] Recent work has also shown that a specific low level of aluminum has a beneficial impact on the properties of ductile iron.[21-23]

To exploit the important role that S, O, Al and oxy-forming elements play in the nucleation of graphite, new complex alloys have been developed.[24-25] These alloys contain potent nuclei (or oxy-sulphide) forming elements in a concentrated, easy-to-use form. They contain up to 20 times the level of oxy-sulphide forming elements normally found in other ladle or in-stream inoculants, or in cast and/or sintered in-mould inserts. They are useful as a solo inoculant or can be added as separate additions with conventional inoculants, acting as an inoculant enhancer, to increase the potency of Ca-FeSi alloys. As a result, greater efficiencies during inoculation treatment have been obtained at significantly lower addition rates, in both grey iron[26] and ductile irons.[27-29]

Generally, rare earth elements (REE) are used in ductile iron to 1.) neutralize tramp elements that interfere with the nodulizing effect of Mg, 2.) assist in nodulizing by providing a supplementary boost to Mg and lastly, 3.) assist in the inoculation effect of nucleating graphite. The use of REE's and the amount needed is dependent on charge materials quality and castings requirements. The unique properties of REE have caused them to be crucial to a number of emerging, growing technologies, as REE are important and critical to hundreds of other high-tech, non-foundry applications. The world REE crisis will continue, at least in the short and medium term, and less REE will be available for use in cast iron graphite morphology control, and their future foundry use must be carefully considered.[28,29]

A previous paper[28] pointed out that the anti-nodularising action of residual elements up to a level corresponding to a Thielman factor K[30] equaling 2.0 could be counteracted by REE additions. Such additions could also be beneficial for K values less than 1.2 and in some applications, can be regarded as compulsory for K values greater than 1.2. On the other hand, it was found that in relatively pure base iron with lower anti-nodularising trace elements (having Thielman Factor K less than 0.8), the microstructure was affected by solidification cooling rate, REE_{res} content, post-Mg-treatment and inoculant type. Without the role to neutralize the anti-nodularising trace elements, increased REE_{res} contents from 0.005 up to 0.025% increased carbide tendency and decreased nodular graphite compactness degree.[28,29]

The main objective of the present paper is to examine the effects of in-mould inoculation, using commercially available FeSi-based inoculants, in relatively pure base irons having low levels of anti-nodularising trace elements

(Thielman Factor K less than 0.8) and less than 0.01%REE_{res} (produced from the low REE-containing master alloy). Another inoculation variant consisted of adding a proprietary oxy-sulphide inoculant enhancing alloy [(OS-IE) based on a patented blend of CaSi, Al and proprietary oxy-sulphide elements][24] to a conventional Ca-bearing 75% FeSi alloy.

Experimental Procedure

The experimental heat was melted in an acidic refractory lined, coreless induction furnace (100kg, 2400Hz). The base iron melt was heated to 1500-1520^{0}C and then tapped into a 30kg nodulizing ladle. A tundish cover Mg-treatment technique was used along with a 2.5 wt.% Mg-bearing FeSi master alloy [wt.%: 44.7Si, 5.99Mg, 1.02Ca, 0.26TRE-Total Rare Earth (0.15Ce, 0.11La, 0.008Nd), 0.91Al, 0.35Mn, 0.048Ti, 0.10Cr, 0.035Ba, balance Fe] addition.

Three commonly used post-inoculants were evaluated, 1.) Ca-FeSi, 2.) Ca,Ba-FeSi and 3.) Ca,RE-FeSi, all having similar Si (72.6-73.8wt.%), Ca (0.87-1.02wt.%) and Al (0.77-0.96wt.%) levels. The main difference was the presence of 1.68wt.%Ba or 1.86wt.%TRE (Total Rare Earth), respectively, compared to the Ca bearing FeSi alloys. The above inoculants were added to an in-mould reaction chamber. After careful consideration of typical addition rates for in-mould, ductile iron inoculation, (typically 0.04 to 0.20wt.%), different inoculants consumptions were selected, depending on their presumed inoculating ability: 1.) 0.18wt.%Ca-FeSi, 2.) 0.10wt.%Ca,Ba-FeSi and 3.) 0.04wt.%CaRE-FeSi. Another inoculation variant consisted of adding an oxy-sulphide inoculant enhancing alloy [(OS-IE) based on a proprietary, stoichiometric blend of CaSi, Al, Mg and oxy-sulphide elements].[24] The inoculant enhancer was added as a separate addition to the reaction chamber with 75% Ca-bearing FeSi at the following rate: standard Ca-bearing 75% FeSi at 0.03 wt.% consumption level (75%) and Inoculant Enhancer (OS-IE) at 0.01 wt.% consumption level (25%), or more simply, a 3 to 1 ratio.

The specially designed test mould included a central downsprue, which supplied Mg-treated iron simultaneously to four separate reaction test chambers (one as an un-inoculated reference and three to test the different alloys).[28,29] W_3 chill wedge samples [ASTM A367-85 specification, 19.1 x 38.1 x 101.6 mm) dimensions, CM = 3.5 mm cooling modulus], plate specimens (4.5mm thickness) and round bar cooling specimens (25mm diameter) were gated off the inoculation reaction chamber. This allowed for evaluation of chemistry and microstructure characteristics after treating the ductile irons with the different inoculants [using 1450^{0}C pouring temperatures, pouring 3 minutes after Mg-treatment, into furan resin bonded moulds].

The wedge test samples were used to evaluate the influence of cooling rate on the structural characteristics of un-inoculated and inoculated irons. These samples were polished to determine graphite parameters on un-etched samples and then etched with Nital to determine free carbide percentages and the ratio of pearlite/ferrite. The structure variation on the centerline direction from the apex up to the base of wedge sample was evaluated at three points (the center and 1.0 mm distance left and right of the centerline). For each distance from the apex, the following conditions were used: 5μm trap size, 100x magnification, 3 fields were analyzed (more than 500 nodules) and the averages of the structure parameters were determined. The graphite characteristics were evaluated with Automatic Image Analysis [analySIS® FIVE Digital Imaging Solutions software].

$$\text{Sphericity Shape Factor (SSF)} = 4\pi A_G / P_G^2 \qquad \text{Equation 1}$$

$$\text{Graphite Nodularity (NG-SSF)} = 100\,[\Sigma A_{\text{particles-SSF}} / \Sigma A_{\text{all particles}}] \qquad \text{Equation 2}$$

Where:

$A_{\text{all particles}}$ is the area of all graphite particles greater than 5 μm; $A_{\text{particles-SSF}}$ is the area of particles for a specific SSF range; A_G is the area of the graphite particle in question; and P_G is the real perimeter of the graphite particle in question [the sum of the pixel distances along the closed boundary].

Results and Discussion

The final composition of the ductile irons (wt.%: 3.20-3.45C, 2.6-2.7Si, 0.57-0.64Mn, 0.016-0.017S, 0.0165-0.0182Al, 0.046-0.058Mg, 0.0045-0.0054Ce, 0.0010-0.0014La) lies solidly in the eutectic range, expressed by carbon equivalent (CE values between 4.1-4.4%) and carbon saturation degree (S_c values between 0.95-1.02). Typically, these irons have relatively low anti-nodularising Thielman factors (K values between 0.6 to 0.8) and a medium level of pearlite promoting factor P_x values between 2.2 to 2.5.[30] It was determined that the content of anti-nodularising elements in both Mg-treated irons was so low (K values less than 0.8), that the role of rare earths to counteract these elements was not necessary. The pearlite factor P_x, for conventional solidification conditions, would indicate a pearlite forming tendency.

The metal matrix and graphite phase characteristics are affected by the following: the solidification cooling rate (as the distance from the apex of wedge castings increases, corresponding to wall thickness increasing, the cooling rate is reduced); post-Mg-treatment application (un-inoculated versus inoculated ductile irons); inoculant type.

Examination of all chill wedges showed that free carbides were mainly present in the wedge sample apex area (Fig. 3), which solidified at the highest cooling rate, independently of the ductile iron state (un-inoculated or inoculated), and inoculating element type. As the distance from the apex increases, cooling rates decrease, leading to important changes in the solidification pattern, duly noting all of the other influencing factors that are important contributors to stable or

meta-stable solidification conditions. Typically, larger amounts of free carbides in un-inoculated irons occurred, with the amount decreasing as the distance from the apex increases. The presence of free carbides was avoided only when the wedge casting section thicknesses was greater than 10mm (more than 20mm distance from the apex).

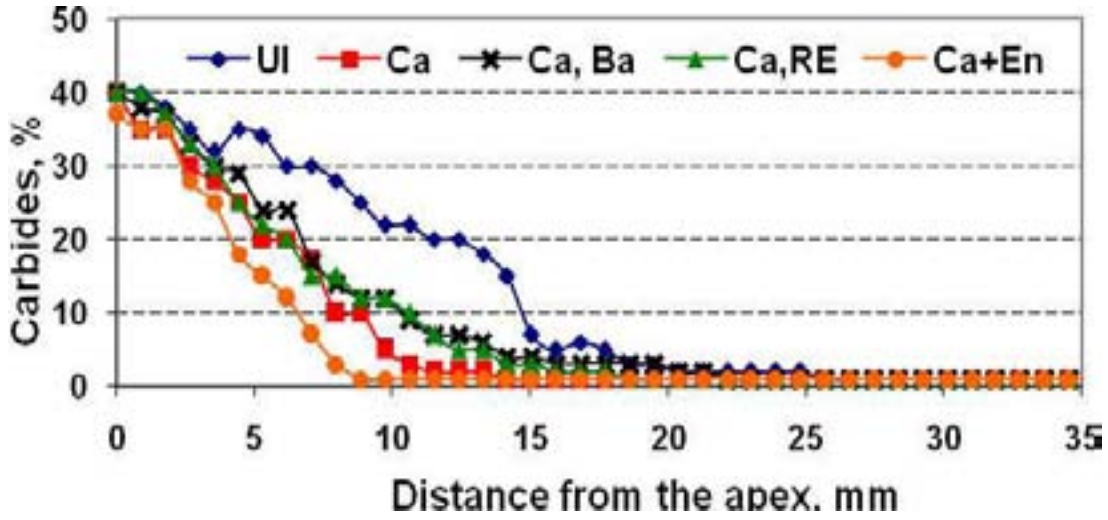

Fig. 3: Influence of the distance from the apex [W_3 wedge samples, ASTM A367] and inoculating elements on the carbides amount, in tested ductile irons [UI – un-inoculated; Inoculation: Ca – 0.18%Ca-FeSi; Ca,Ba – 0.10%Ca,Ba-FeSi; Ca,RE – 0.04%Ca,RE-FeSi; Ca+En – 0.04% [3/4Ca-FeSi + ¼ Enhancer (OS-IE)]

Inoculation of all the ductile irons decreased the carbide forming sensitivity, but at different magnitudes, depending on inoculant type and consumption level. All of the modified Ca-bearing FeSi alloys show improved inoculation capability, and incorporating either Ba or REE in the alloys contributed to increased inoculating potency. These active elements allowed a lower consumption level of inoculants, namely allowing the use of 0.10wt.%Ca,Ba-FeSi or 0.04wt.%Ca, RE-FeSi; the chill tendency was essentially at the same level as when standard additions of 0.18wt.%Ca-FeSi were made.

The use of the inoculating enhancer [OS-IE] significantly increased the effectiveness of the standard Ca-bearing FeSi alloy. The [Ca-FeSi + Enhancer] inoculation variant led to the lowest chill tendency. When compared to Ca,Ba-FeSi variant, 60% less alloy was needed to obtain the same chill reduction (0.10wt.% versus 0.04wt.%). When compared to the standard Ca-FeSi variant used by itself, 77% less alloy was needed to obtain the same level of chill reduction (0.18wt.% versus 0.04wt.%). The combination of [Ca-FeSi + Enhancer] was also more effective than an equivalent addition of the REE-bearing Ca-FeSi alloyed used at the 0.04wt.% level.

The metal matrix of W_3-ASTM A367 samples was mainly pearlitic (more than 90% pearlite), as predicted by the P_x factor (P_x = 2.2 to 2.5) for all of the tested irons. Although ferrite formation is favoured by lowering the cooling rate (thicker wall section castings), the amount of ferrite that formed was also dependent on the inoculation variants. All inoculated ductile irons showed a larger amount of ferrite, compared to un-inoculated irons. When comparing inoculation capability, the [Ca-FeSi + OS-IE Enhancer] variant appeared to have the greatest ferrite forming effect (starting at 5mm wedge casting section size), despite being used at the lowest consumption level.

Figure 4a shows a general view on the graphite phase, at different distances from the apex of wedge sample, or casting section size. Graphite particles are clearly visible in un-inoculated irons when the section size was in the range of 1.0 to 2.0mm [or 1.6-3.0mm distance from the apex]. With these very high solidification cooling rates, all of the inoculant variants led to increased graphite amounts and nodule counts. This was especially true for the 0.18wt.% [Ca-FeSi] variant, but also for the 0.04wt.% [(Ca-FeSi + (OS-IE)] alloy variant, again noting that it was used at a 77% lower consumption level.

As the cooling rate decreased and as the distance from the apex and the section size increased, increasing amounts of graphite formed in both the un-inoculated and inoculated irons. The largest difference in graphite percentage and nodule count was observed when the distance from the apex was 10 to 12 mm (corresponding to a section size of 5-6mm) or corresponding to thin walled castings having wall thicknesses of 5 to 6 mm (Figures 4b and 4c). When the distance from the apex was 10 to 12 mm, the large addition of the Ca-bearing FeSi alloy (0.18wt.%Ca-FeSi) resulted in the lowest carbide levels, and the highest graphite amounts and nodule counts. Although the 0.10wt.%Ca,Ba-FeSi and 0.04wt.%Ca, RE-FeSi inoculant variants were used at significantly reduced consumption levels, the beneficial effects of Ba and REE were only modest at these addition levels.

For the upper part of W_3 wedge casting, when the distance from the apex was more than 20mm, [corresponding to a section size greater than 10mm], the presence of free carbides was essentially eliminated in all of irons. The graphite amount was relatively constant at 8 to 10%, with minimal or limited effects of inoculant type and consumption.

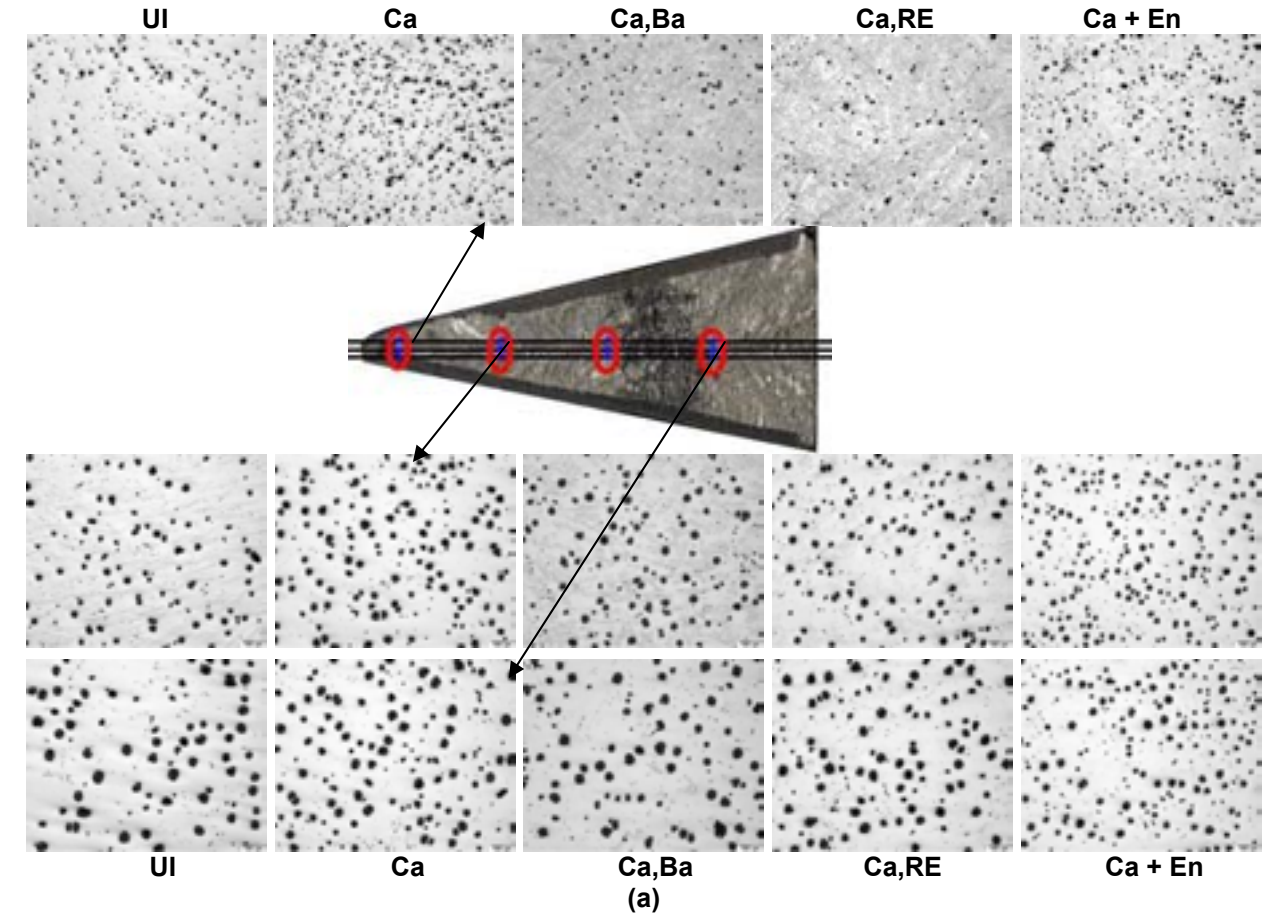

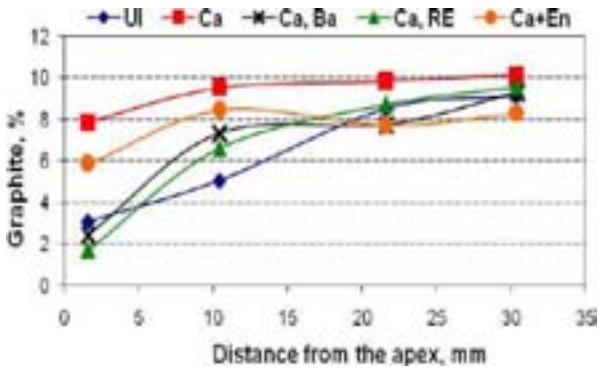

(b) Graphite Percentage

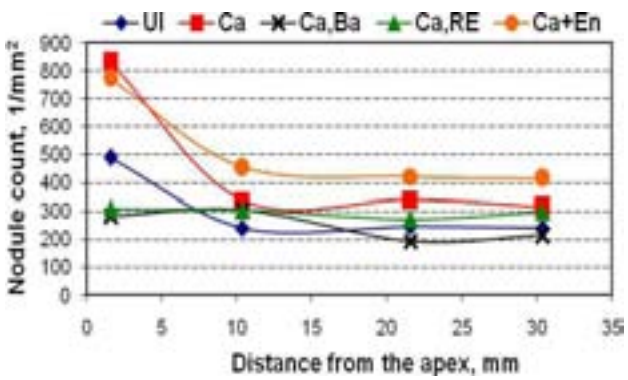

(c) Nodule Count

Fig. 4: Influence of the distance from the apex [W_3 wedge, ASTM A367] and inoculating elements on the structure (a), graphite amount (b) and nodule count (c), in tested ductile irons [UI – un-inoculated; Inoculation: Ca – 0.18%Ca-FeSi; Ca,Ba – 0.10%Ca,Ba-FeSi; Ca,RE – 0.04%Ca,RE-FeSi; Ca+En – 0.04% [0.75 Ca-FeSi + 0.25 Enhancer (OS-IE)]

The apparent contradiction of Fig. 3 and 4b, as the (Ca-FeSi + Enhancer) inoculation variant led simultaneously to the lowest amount of carbides and graphite, could result from the difficulties associated with the automatic image analysis. The probable cause was the result of trying to evaluate a ductile iron structure characterized by graphite nodules having a small size (Fig. 4a), that was typical for this inoculation variant. For this reason, when using a trap size of 5μm for graphite particles, it is highly possible that an important amount of nodules less than 5μm size were not included in this analysis.

Nodule counts are a complex parameter that can be greatly affected by cooling rate. Increased cooling rates typically produce higher graphite nodule counts, but conversely, free carbides are also promoted by high cooling rates. This investigation found that at the highest cooling rate in the wedge apex area, large amounts of free carbides formed. Also found was that high cooling rates had a significant effect on graphite nodule count (Figures 3 and 4).

The high level of carbides that formed in the apex for Ca,Ba and Ca,RE inoculation systems resulted in low nodule

counts. Higher graphitizing capacity was universally found for the Ca-FeSi and [Ca + Enhancer] inoculation variants. The Ca-FeSi and [Ca + Enhancer] inoculation variants both showed higher nodule counts in the high solidification cooling rate apex zone.

Decreasing the cooling rate as the distance from the apex increased (section size), led to decreased carbide levels and increased graphite amounts on all casting wedge sections. Nodule count also decreased at distances up to 10 mm from the apex (5mm section size). At distances greater than 10 mm from the apex, nodule count remained relatively constant, but within a wide range of 200 to 450 Nodules mm^{-2}, depending on the inoculation variant. In these experiments, the highest nodule count characterizes ductile iron inoculated with the lowest inoculant addition, the (Ca + Enhancer) variant, followed by the highest inoculant addition, the Ca-bearing 75% FeSi alloy. It appeared that the enhancing of the standard Ca-bearing 75% FeSi alloy inoculation intensity by the contribution of an addition of S, O and oxide-forming elements, in the form of the proprietary OS-IE alloy, was a better solution than the using of more expensive inoculating elements, such as REE. It was especially reflected by the obtained lowest carbides amount and the highest nodule count in the present ductile irons, characterized with REE_{re} levels less than 0.01% after Mg-treatment.

In actual foundry practice, graphite nodularity is typically used as a true measure of ductile iron quality. Over time, different expressions of graphite nodularity have been used. Generally, most all expressions refer to the ratio of nodular (spheroidal) particles compared to total particles in ductile iron structure. As flake (lamellar) graphite amounts are exempted, traditionally graphite nodularity is expressed as the ratio of nodular (spheroidal)/compacted (vermicular). As automated image analysis is used more and more to quantify the quality of ductile iron, determination of nodularity and nodule count has become very important. A recent publication[31] on the determination of nodularity and nodule count using image analysis pointed out the effect of several varying analytical parameters. This research showed important differences in graphite nodularity and nodule count can arise depending on the shape factors that are selected.

The graphs shown in Figure 5 compare the graphite nodularity (NG-SSF) values, calculated from Equation 2, for three levels of sphericity shape factors [SSF, Equation 1]. The data in all three graphs are for nodular (spheroidal) structures having SSF values between 0.5 to 1.0. Normally, as SSF values increase, the corresponding NG-SSF values decrease. Using a minimum sphericity shape factor SSF value of 0.5, more than 90% nodularity was observed for all of the tested irons, as shown in Figure 4. If the minimum limit of the shape factor is increased to a SSF value of 0.625, the nodularity appears to fall in the range of 80 to 95%, which would be typical of most ductile iron castings. Using the highest minimum shape factor SSF value of 0.8, corresponding to the highest compactness degree level for the graphite particles, the nodularity range fell to a 60 to 90% range. In many cases, this would be insufficient for some of the inoculated irons to be accepted as high performance ductile iron.

Solidification cooling rate, depending on the section size, had a complex action on the graphite nodularity. Generally, the lowest nodularity characterized graphite phase in the apex area, which solidified at the highest cooling rate, while the highest level of nodularity resulted for 5 to 6mm section size [10 to 12mm distance from the apex]. After that, the lowering of the cooling rate to the upper part of wedge casting affected graphite nodularity, but was dependent on the claimed graphite shape factor and inoculation variant. When the minimum value of SSF was 0.5, nodularity was not visibly influenced by the cooling rate, with only a slight dependence on the inoculation variant. When the minimum SSF values were 0.625 and 0.8, both the cooling rate and inoculant variant became important influencing factors, especially for SSF values of 0.8. Decreasing of the cooling rate generally decreased the graphite nodularity, becoming more pronounced for the highest level of graphite shape factor.

Inoculation can have a significant effect on graphite nodularity, especially if the minimum value of the Sphericity Shape Factor is 0.8 or higher. The experimental results showed that the highest nodularity resulted from inoculation with the 0.04wt.% [(Ca-FeSi + (OS-IE)] alloy variant (Fig. 6). Adding the proprietary inoculant enhancer (OS-IE) as a separate addition with the conventional Ca-FeSi alloy yielded reduced inoculant consumption levels [0.04wt.%] [Figs. 5

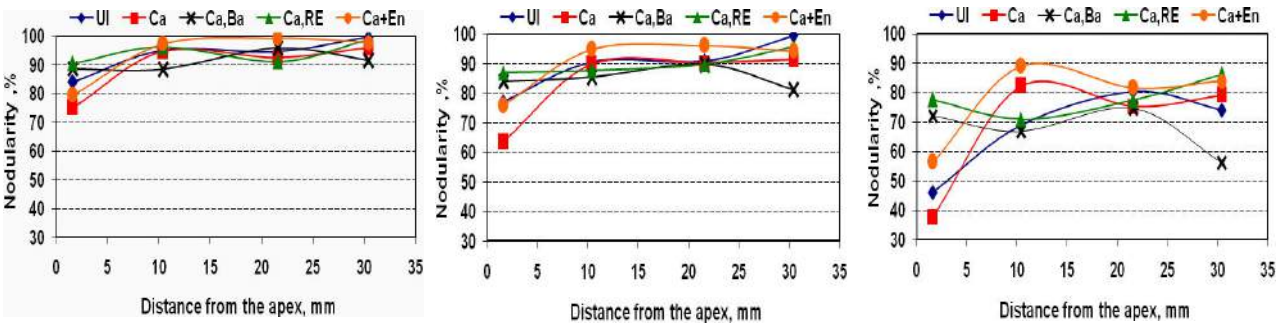

Fig. 5: Influence of the distance from the apex [W_3 wedge samples, ASTM A367] and inoculating elements on the graphite nodularity, depending on Sphericity Shape Factor [(a)-SSF=min. 0.5; (b)-SSF=min. 0.625; (c)-SSF=min.0.8] [Ca–0.18%Ca-FeSi; Ca,Ba–0.10%Ca,Ba-FeSi; Ca,RE–0.04%Ca,RE-FeSi; Ca+En–0.04% [3/4Ca-FeSi + ¼ OS-IE)]

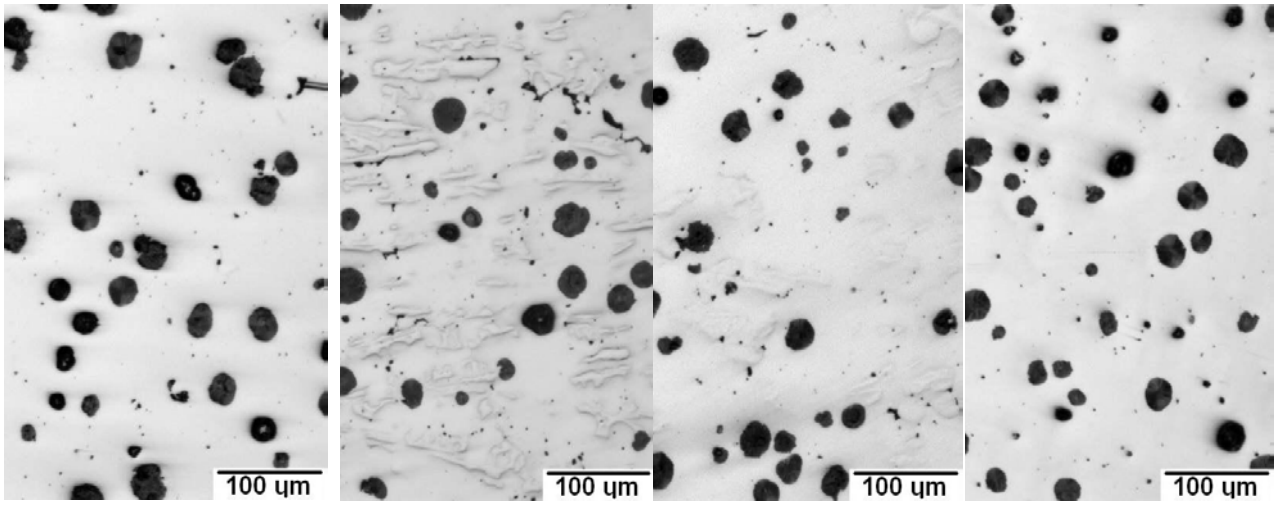

Fig. 6: Typical nodular graphite view at 10mm from the apex [5mm section size], W_3 wedge, ASTM A 367 [Ca – 0.18%Ca-FeSi; Ca,Ba – 0.10%Ca,Ba-FeSi; Ca,RE – 0.04%Ca,RE-FeSi; Ca+En – 0.04% [3/4Ca-FeSi + ¼ OS-IE)]

and 6]. Depending on which ever graphite shape factor was selected, the [(Ca-FeSi + (OS-IE)] inoculant variant produced 1.) 95% nodularity for SSF values were 0.5 minimum, 2.) nodularity was greater than 90% nodularity when SSF values were 0.625 minimum, and 3.) nodularity was greater than 80% nodularity when SSF values were 0.8 minimum.

It should be noted that the ability of this inoculation variant [(Ca-FeSi + (OS-IE)] to produce a graphite phase of maximum compactness is extremely beneficial for high ductility properties. Although excellent inoculation behavior was found for the Ca-FeSi inoculant variant, it required 450% larger in-mould additions to achieve results almost as good as the [(Ca-FeSi + (OS-IE)] variant. The Ca,Ba-FeSi inoculant variant provided the least chill reduction capability and produced satisfactory nodularity results only when SSF was less than 0.625. Intermediate chill reduction capability and nodularity results were obtained with the RE–0.04%Ca,RE-FeSi alloy variant.

The efficiency of the inoculation enhancer (OS-IE) used with Ca-FeSi, [(Ca-FeSi + (OS-IE)] has been substantiated with actual foundry production experience.[27] International Foundry X is a high-production automotive foundry that became concerned about rare-earth metal availability and the subsequent effect on the sky-rocketing cost of the rare earth-containing inoculant it had been using. Prior to changing the inoculation practice by adding separate additions of the inoculation enhancer (OS-IE) with Ca-FeSi, the tundish treated-Mg iron is transferred into unheated stopper rod pouring vessels where post-inoculation was performed using a proprietary rare earth inoculant containing sulphur and oxide surface treatments. After numerous qualification tests, which included 1.) in-depth thermal analysis, 2.) pouring test castings that had both thin sections and an isolated heavy section prone to shrinkage, and 3.) fading tests, this foundry made a complete change in their inoculation practice. Post inoculation is now done with the same alloy quantity, but the REE-inoculant has been replaced with a Ca-bearing FeSi alloy and OS-IE inoculant enhancer, used in a ratio of 3 to 1 respectively (the OS-IE is added separately to the un-heated pouring vessels). This combination of inoculants produced identical results to the more costly rare-earth inoculant. This foundry pours 400 tons ductile iron castings per day and estimates it is saving over US$8.00 per ton with the new inoculation procedure. On an annual basis, savings are estimated to be US$750,000 and the foundry reduced the need for REE addition.

Conclusions

1. It was found that in a relatively pure base iron, with low anti-nodularising trace elements (Thielman Factor K less than 0.8) the metal matrix and graphite phase characteristics are affected by (a) the solidification cooling rate, (b) post-Mg-treatment application and (c) inoculant type.
2. All of the modified Ca-bearing FeSi alloys showed improved inoculation capability, as incorporating either Ba or REE allowed a lower consumption of inoculants. For an in-mould technique and 0.10% Ca,Ba-FeSi or 0.04%Ca,RE-FeSi alloys, the chill tendency is practically at the same level as for 0.18%Ca-FeSi treatment.
3. The highest inoculation efficiency occurred when adding an oxy-sulphide inoculant enhancer alloy with 75% Ca-bearing FeSi [1:3 ratio]. This combination of additions was more effective than an equivalent addition of a REE-bearing, Ca-FeSi alloy or compared to the Ca,Ba-FeSi variant, but with a 60% lower alloy consumption, or the Ca-FeSi variant, with a 77% lower alloy consumption.
4. The [Ca-FeSi + OS-IE] inoculation variant resulted in the highest graphite nodularity, based on the imposed Sphericity Shape Factor SSF: greater than 95% for SSF values of 0.5 minimum, greater than 90% for SSF values of 0.625 minimum, and greater than 80% for SSF values of 0.8 minimum, despite being used as the lowest consumption level.

5. The enhancement of Ca-FeSi alloy inoculation potency by contributions of S, O and oxide-forming elements, proved to offer a better solution than the using of more expensive other inoculating elements, such as REE.
6. Should the level of REE in Mg-FeSi master alloys decrease because of price or availability in the future, modifying the basic charge along with selection of the proper inoculants will insure the production of high quality ductile irons castings. Inoculation enhancing by adding S, O and oxide-forming elements [such as OS-IE Enhancer] to commercial simple inoculants could be an alternative solution to REE presence in treatment alloys in ductile iron castings production.

References

1. M. Chisamera, I. Riposan, S. Stan and T. Skaland: Proc. 64th World Foundry Congress, Paris, France, CIATF, Sept. 2000, Paper R0 62.
2. I. Riposan, M. Chisamera, S. Stan, T. Skaland and M. Onsoien: *AFS Trans.*, 2001, 109, 1151-1162.
3. I. Riposan, M. Chisamera, S. Stan and T. Skaland: *Int. J. Cast Met. Res.*, 2003, 16 (1-3), 105-111.
4. I. Riposan, M. Chisamera, S. Stan and T. Skaland: Proc. AFS Cast Iron Inoculation Conference, Schaumburg, IL, USA, September 2005, AFS, 31-42.
5. I. Riposan, M. Chisamera, C. Hartung and D. White: *Mater. Sci. Technol.,* 2010, 26 (12), 1439-1447.
6. M.H. Jacobs, T.J. Law, D.A. Melford and M. Stowell: *Metal Technol.*, 1974, 490-500; 1976, 98-108.
7. T. Skaland: 'Nucleation Mechanism in Ductile Iron'. PhD Thesis, Trondheim, Norway, 1992.
8. R.L. Naro and J.F. Wallace: *AFS Trans.*, 1969, 77, 311; 1970, 78, 229.
9. K. Strande: Proc. 51st. Intern. Foundry Congr., Lisbon, Portugal, 1984.
10. I. Riposan, M. Chisamera and G. Simionescu: RO Patent No. 101339, 1988.
11. M. Chisamera and I. Riposan: *Advanced Materials Research,* Trans Tech. Publ., 1997, 4-5, 293-300.
12. M. Chisamera, I. Riposan and M. Liliac: Proc. INFACON7, Trondheim, Norway, 1995, 742-749.
13. M. Chisamera, I. Riposan and M. Barstow: Proc. AFS Cast Iron Int. Inoculation Conf., Chicago, IL, USA, April 1998, Paper no. 3.
14. I. Riposan, M. Chisamera, L. Sofroni, S. Stan and M. Liliac: Proc. 63rd World Foundry Congress, Budapest, Hungary, 1998; Kohaszat, 1999, 1, 11-18; 1999, 2, 59-65.
15. T. Skaland: U.S. Patent No.6,102,983, (August 15, 2000), International Patent W099/29911.
16. T. Skaland: Proc. 105th AFS Casting Congress, Dallas, USA, 2001, Paper 01-078.
17. J.K. Solberg and M.I. Onsoien: *Mater. Sci. Technol.*, 2001, 17, 1238–1242.
18. V. Igoraski and S. Okade: *Int. J. Cast Met. Res.*, 1998, 11, 83–88.
19. H. Nakae and Y. Igarashi: *Mater. Trans.,* 2002, 43(11), 2826–2831.
20. M.J. Lalich and J.R. Hitching: *AFS Trans.*, 1976, 84, 653–664.
21. I. Riposan, M. Chisamera, S. Stan and D. White: *AFS Trans.,* 2007, 115, 423-433.
22. M. Chisamera, I. Riposan, S. Stan and D. White: *Int. J. Cast Met. Res.*, 2009, 22(6), 401–410.
23. I. Riposan, M. Chisamera, S. Stan, P. Toboc, G. Grasmo, D. White, C. Ecob and C. Hartung: Proc. Keith Millis Symposium on Ductile Cast Iron, Las Vegas, NV, USA, Oct. 2008, DIS/AFS, 206–214; *J. Mater. Eng. Perform.*, 2011, 20 (1), 57-64.
24. R.L. Naro: U.S. Patents No. 6,293,988 B1, (September, 2001), No. 6,733,565 B1, No. 6,866,696B1.
25. R.L. Naro: *Foundry Management Technol.*, 2002, 20.
26. M. Chisamera, I. Riposan, S. Stan, C.B. Albu and R.L. Naro: *AFS Trans.*, 2007, 115, 481- 493.
27. R.L Naro, D.C. Williams, M. King and L. Basaj: *Foundry Manag. Technol.,* January 23, 2012.
28. I. Riposan, M. Chisamera, V. Uta, S. Stan, R.L. Naro and D.C. Williams: Proc. 2013 Keith Millis Symposium on Ductile Cast Iron, Nashville, TN, USA, October 2013, DIS/AFS, 256-275; *Int. J. Metalcasting,* 2014, 8 (2), 65-80.
29. I. Riposan, V. Uta, S. Stan, R.L. Naro and D.C. Williams: *AFS Trans.*, 2014, 122, Paper 14-004.
30. T. Thielman: *Giessereitechnik*, 1970, 1, 16-24.
31. S. Grenier, A. Bhattacharjee, R.B. Gundlach, B. Kroka, C. Labrecque and M. Riabow: Proc. 2013 Keith Millis Symposium on Ductile Cast Iron, Nashville, TN, USA, October 2013, DIS/AFS, 1-13.

Acknowledgment

The work has been funded by the Sectoral Operational Programme Human Resources Development 2007-2013 through the Financial Agreements POSDRU/159/1.5/S/132395 and POSDRU/159/1.5/S/134398. The authors would like to recognize and thank Dr. Rod Naro, ASI International Ltd, for partially supplying funding for the experiments and presentation at the SPCI10 Int. Symposium on the Science and Processing of Cast Iron, Mar del Plata, Argentina, 2014.

Distribution of some active elements in primary graphite precipitates

K. Theuwissen, T. Duguet, J. Esvan and J.Lacaze
CIRIMAT, CNRS-Université de Toulouse, ENSIACET, BP 44362, 31030 Toulouse cedex 4, France

The distributions of cerium and oxygen in the matrix and in graphite precipitates of a pure Fe-C-Ce cast iron sample have been studied using scanning Auger microscopy. It is shown that there is no accumulation of any element at the graphite-matrix interface. Cerium was detected in some cases in spheroidal graphite precipitates, most often associated with oxygen. Various non-spheroidal graphite precipitates proved to contain cerium and oxygen suggesting a correlation between cerium content and graphite degeneracy.

Keywords: ductile iron, graphite growth, Auger analysis, cerium, oxygen

Article available in the International Journal of Cast Metals Research

Damage Evolution in Compacted Graphite Iron during Thermo-Mechanical Fatigue Testing

V. Norman[1], P. Skoglund[1,2] and J. Moverare[1]
[1] Division of Engineering Materials, Department of Management and Engineering, Linköping University, SE-58183 Linköping, Sweden
[2] Scania CV AB, Materials Technology, SE-15187 Södertälje, Sweden

Thermo-mechanical fatigue (TMF) properties of a compacted graphite iron (CGI) in an out-of-phase (OP) configuration are investigated for different maximum temperatures and mechanical strain ranges. Furthermore, the stress-strain hysteresis loops are analysed and in particular the unloading modulus, i.e. the elastic modulus measured during specimen unloading, is obtained from each cycle. This material parameter has earlier been explicitly related to the amount of microcracking in cast irons. The results show that the unloading modulus linearly declines with the numbers of cycles in all tests performed. In addition, the rate of change of the unloading modulus is closely related to the number of cycles to failure. Accordingly, it is concluded that microcracks are independently propagated by fatigue until a point of rapid crack-linking resulting in the ultimate failure. This is supported by microstructural analyses consisting of optical microscope images taken at different stages throughout the life of a specimen.

Keywords: Thermo-mechanical fatigue, compacted graphite iron, microcracking, damage, unloading elastic modulus

Article available in the International Journal of Cast Metals Research

Corrosion mechanisms in ADI parts

A.D. Sosa[1,2], C. Rosales[1], R. Boeri[1,2] and S.N. Simison[1,2]
1 School of Engineering, Universidad Nacional de Mar del Plata, Mar del Plata, Argentina
2INTEMA, UNMdP – CONICET, Mar del Plata, Argentina

The objective of this research is to study the influence of microstructure and grinding on the corrosion resistance of ADI in salt water. Immersion and electrochemical tests were performed on samples austempered at two different temperatures and ground. The results indicate that the dissolution rate increases as the nodule count does, and depends on the microstructure and on the surface changes introduced during grinding. A porous layer is formed on ADI corroded surface due to the selective dissolution of ferrite, and a preferential dissolution of the matrix around graphite is noticeable. Ground surfaces are less corrosion resistant than polished ones.

Keywords: Austempered ductile iron, Corrosion, Ausferrite, Plastic strain.

Article available in the International Journal of Cast Metals Research

The current status of the metallurgy and processing of austempered ductile iron (ADI)

A.A. Nofal*
Department of Foundry Technology, Central Metallurgical R&D Institute, Cairo, Egypt

In the last three decades, the revolutionary material; the austempered ductile iron (ADI) with its unique combination of mechanical properties, has been offering the design engineer alternatives to conventional material process combinations,
This review is an attempt to compile the results of the worldwide explosion of research and development that followed the announcement of the first production of this material, meanwhile, reference is made to the work that has been carried out at CMRDI over the past decade. This paper is not designed to provide an in-depth investigation of any specific technology, but is rather a macro-analysis of the current state of metallurgy and processing of ADI.
Better understanding of the strengthening mechanisms of ADI led to the development of new techniques such as ausforming, squeeze casting as well as two-step austempering, which contributed to enhanced strength of the alloy. Abrasion resistance could be markedly increased through the development of carbidic ADI (CADI), bainitic/Martinsitic (B/M) ADI, locally austempered ductile iron using induction hardening techniques, as well as laser surface hardening.
Machinability problems of ADI, which have limited its mass production for long, have been solved through the development of new machinable types of ADI as IADI with mixed ferrite/ausferrite structures.
Production of thin wall ADI components may offer potentials for applications, and this could be achieved through casting or cold rolling, where strain hardening phenomena seems to be of special interest. Thin wall ADI castings are capable to build complex thin wall parts of high strength.

Keywords: ADI, strengthening mechanism, ausforming, dual-phase, machinable ADI, CADI, abrasion resistance, squeeze casting, laser treatment.

Introduction

The as-cast mechanical properties of ductile iron can be significantly improved through an austempering heat treatment. This has led to the birth of a new member of the cast iron family; the austempered ductile iron (ADI), with its unique microstructure; spheroidal graphite in an ausferritic matrix[1].

The austempering transformation in ADI can be described as two-stage reaction:

Stage I Reaction: $\gamma_c \rightarrow \alpha + \gamma_{HC}$ (toughening)

Stage II Reaction: $\gamma_{HC} \rightarrow \alpha + \varepsilon$ - carbides (embrittlement)

The morphology of the final two-phase matrix microstructure is determined by the number, shape and size of the initially formed ferrite platelets in the first stage austempering reactions. The control of this stage of transformation will, therefore, ultimately control the final microstructure and mechanical properties. The rate of ferrite formation during stage I austempering may be controlled by chemical, thermal or mechanical processing variables.

The mechanical properties of ADI depend on a number of interlinked factors, including primarily the austenitizing and austempering temperatures and times together with the as-cast microstructure, the composition and the section size. Of these, the austempering temperature is the most important. These variations in properties can be related to the changes in microstructure. At low austempering temperatures, an acicular (needle-like) ferritic phase is formed with only a small amount of retained austenite. At the very lowest austempering temperatures, the structure may also contain some martensite. This type of microstructure can provide high tensile strength and hardness but only limited ductility and poor machinability. With increased austempering temperatures, the ferrite becomes coarser with increased amounts of retained austenite (up to ~ 40%); with a typical "ausferrite" structure. This results in a substantial increase in ductility and machinability with a reduction in strength and hardness.

Since the announcement of the first production of ADI in the last decades of the last century, a worldwide explosion in research started, which provided a sound foundation for expanding the production and applications of this prospective material[2-5]. However, the practice of ADI production seems to be ahead of the theory; the strengthening mechanisms of ADI are still not very clear. The main constituents of ADI matrix are acicular ferrite and carbon enriched austenite (with the possibility of some martensite formations at low austempering temperatures), both main constituents are of low or

* Corresponding author, email: adelnofal@hotmail.com

medium strength. The "mystery" of the high strength of ADI, and how it may result from these constituents have been earlier related to the precipitation hardening arising from the formation of very tiny precipitates such as M_6C type carbides and others[6]. The density of these precipitates, however, seems to be too low to result in such superior strength properties. Recently, extensive use of TEM has shed more light on the strengthening mechanisms of the main structural constituents of ADI.

The following mechanisms have been proposed:

- The strengthening mechanism of ferrite was related to strain hardening caused by very high dislocation density, accompanied by high density very small dislocation loops.
- In the same time austenite strengthening is caused by solution hardening mechanism supported by grain refining due to twinning, which results in some extra coherent grain boundaries. Moreover, stacking faults representing obstacles for dislocation movement may play some strengthening role.
- Moreover, the austenite to martensite transformation at low austempering temperature is accompanied with high lattice distortion and consequently high strain energy. The martensite grains would be divided into a very large number of ultra thin microtwins. The resulting huge amount of coherent grain boundaries will impede the dislocation movement

Thanks to the extensive efforts made over the past few years, new processing techniques have opened even more opportunities for this excellent engineering material to acquire better combinations of strength, ductility, toughness, wear resistance and machinability. It is the objective of this paper to review the advances in the metallurgy of ADI that led to such properties improvement. Moreover, the novel techniques of surface engineering and welding of ADI will be shortly mentioned. Whenever possible, a reference will be made to the previous work conducted at CMRDI, where the first ADI pilot production line in Egypt has been established few years ago.

ADI with Enhanced Wear Resistance

In any material, improved tribological properties are usually enhanced by ensuring high hardness values. Higher grades of ADI austempered at low temperatures (230-260°) usually have high hardness of ~480-550 BHN and, therefore are selected when good wear resistance is the main requirement. With the increase of austempering temperature, the hardness decreases typically (290-320 BHN) leading to more wear. The increased retained austenite contents in these soft grades can work harden and/or transform to martensite when subjected to mechanical strain at the surface, resulting in significantly better wear resistance than would be expected. This effect is a disadvantage when machining, but can be very beneficial for ADI components as the worn away surfaces would be continuously replaced by a freshly formed hardened layer. The strain-hardening characteristics of ADI influence the total life cycle of components subjected to substantial plastic strains during service (e.g. fatigue, wear, machining) and, therefore, has recently attracted more attention[8-15].

Carbidic ADI (CADI)

CADI is ductile iron containing carbides that is subsequently austempered to produce an ausferritic matrix with an engineered amount of carbides. Volume fraction of carbides may be controlled by partial dissolution during the subsequent austenitization process and hence the proper abrasion resistance/toughness combination may be reached. CADI exhibits excellent wear resistance and adequate toughness. The abrasion resistance of this new material is superior to that of the ADI and increases with increased carbide content. In a number of wear applications, it can compete favorably with high Cr-abrasion resistant irons with improved toughness[17-24].

Several methods have been suggested to introduce carbides to the structure of ADI.

(a) As cast carbides can be introduced to the structure of ADI through alloying with carbide promoting elements such as Cr, Mo, Ti, etc., controlling the cooling rate during solidification, adjusting the carbon equivalent to produce hypoteutectic composition or through surface chilling.
Recently, it has been reported that good balance between wear resistance and impact toughness could be achieved through the selection of Cr-content/austempering temperature combination. The wear resistance as a function of Cr-content in CADI are illustrated in Fig.1-a[25]. It should be noted that both primary as well as eutectic austenite in CADI is transformed to very fine ausferritic structure[25] (Fig.1-b). Some examples of plow points produced at CMRDI pilot foundry are illustrated in Fig.1-c.

(b) Carbides precipitated during austempering: extending the second stage austempering will result in the precipitation of fine carbides from the high carbon austenite: $\gamma_{HC} \rightarrow \alpha + \varepsilon$.

(c) Mechanically introduced carbides; crushed M_x C_y carbides are strategically placed in the mold cavity at the desired location. The metal then fills in around the carbides resulting in a continuous iron matrix with discrete carbides mechanically trapped. This method allows the engineer the option of placing carbides only where needed resulting in conventional ductile iron matrix throughout the rest of the casting. These particular carbides are essentially affected by subsequent austempering process. This technique is currently only practiced by license

to Sadvik corporation and the specific method used to contain the carbides "in place" during mold filling needs further investigation.

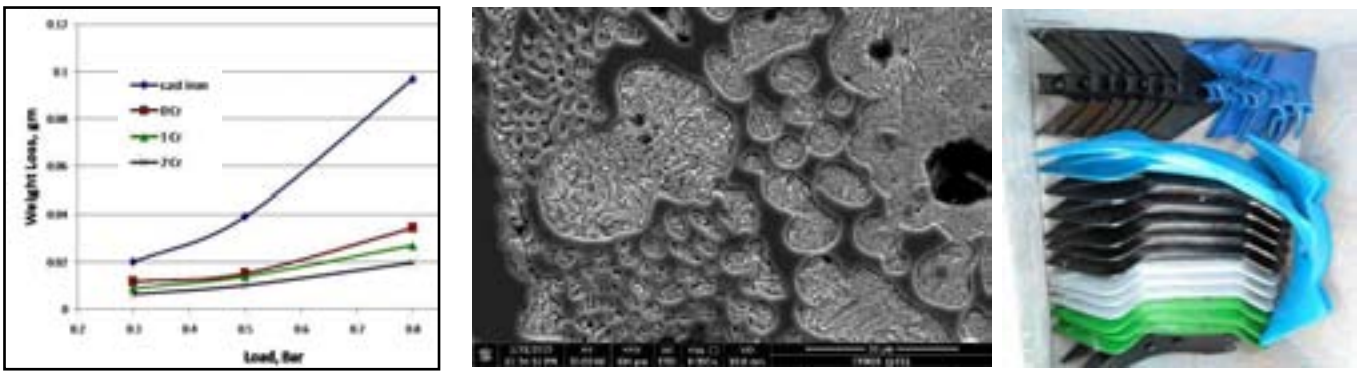

(a) (b) (c)

Fig.1[25]**:** (a) effect of Cr% on the wear resistance of CADI
(b) primary and eutectic austenite transformed to fine ausferrite
(c) plow points produced at CMRDI

Other surface treatment techniques adopted to enhance the wear resistance of ADI are introduced under section (Surface Hardened ADI) of this report.

Recent research work indicates increasing interest in developing CADI microstructure and properties by adding boron[26], studying the multi-response optimisation of production parameters using Taguchi Method[27], investigation of the influence of cooling rate from the austenitization temperature[28], enhancement of mechanical properties and abrasive wear resistance by modification with nano ceria particles[29,30].

Current applications of CADI include automotive, agricultural, railroad, construction and mining as well as other engineering application, e.g. pump components, wear housing, and plates, rollers and blast parts, etc.

Bainitic/Martensite (B/M) Dual-phase ADI

A new grade of wear resistant ductile iron, with properties similar to those of ADI was recently developed by combining less expensive alloying with a controlled heat treatment to produce a bainitic-martensitic dual-phase structure[31-33]. Alloying elements such as Si and Mn that promote bainitic transformation were added in the range of 2.5-3.0% each. Moreover, such alloying facilitates the separation of bainitic transformation from martensitic one. Manganese significantly reduces the Ms temperature, dissolves unlimitedly into austenite and improves hardenability. At Mn-contents higher than 3.0%, austenite increases on the account of bainite and carbides start to precipitate. Manganese carbides formation is restrained effectively by silicon, which promotes the formation of bainitic ferrite and the enrichment of asutenite with carbon. The resulting increase in austenite stability will reduce the possibility of manganese carbides formation and manganese dissolves in austenite and ferrite. The pearlite formation is avoided by controlled cooling heat treatment; consisting of three stages:

(1) Water spraying quenching is applied for rapid cooling from austenitization temperature to about 300°C in a few minutes which suppress any pearlite transformation.
(2) Soaking in a heat preservation setting for bainitic transformation over a range of temperature form the spraying end temperature to 200°C for 2 hrs.
(3) Air cooling to room temperature for martensitic transformation.

The resulting microstructure containing bainite, martensite and 8-10 vol. % retained austenite along with the graphite spheroids will give an excellent combination of hardness and toughness which reach 51.5 HRC and 21.7 $J.cm^{-2}$ respectively and this could be attributed to the following factors[31-33]:

i) The bainite needles split the undecompensed austenite and effectively decrease the size of martensite leading to improved strength and toughness.
ii) High toughness of bainite restricts the propagation of cracks originating mainly at the graphite/matrix interface and hence toughens the iron.
iii) The presence of retained austenite (8-10 vol. %) contributes to the toughening effect.

The impact wear resistance of the B/M ductile iron was found to be comparable with that of the high chromium cast iron and twice that of manganese steel. Under conditions of low impact load, such as that in the case of grinding balls and liners in the small and medium diameter ball mills, the B/M ductile iron can replace the manganese steel as a wear resistant material. In such application, the B/M ductile iron shows good work-hardening effect due to the presence of the

retained austenite. The surface work-hardening effect can considerably improve the wear resistance of the hardened surfaces, while the core of the balls remains tough.

Surface Hardened ADI

Fully or mostly ferritic matrix may be hard face welded in the area of greatest wear, which results in a carbidic weld and heat affected zone at the weld/casting interface. Subsequent austemper heat treatment was found to have little or no effect on the weld structure, depending on the chemical composition of the weld material chosen, whereas the heat affected zone is eliminated and a fully ausferritic matrix results in all areas except the weld area itself. In some weld applications, powdered metal carbides can be purged into the molten weld to provide additional wear resistance[17].

Limited number of publications may be cited in the literature, where the ADI surfaces were processed by laser to enhance the wear resistance properties[34-38]. Laser processing may lead to surface hardening (LSH) or surface melting (LSM) depending on the incident laser power and scanning speed; with the depth of the processed layer directly propotentional to the power and inversely related to the linear scanning speed. LSM produces a predominantly austenitic[35] or ledeburitic microstructures with almost complete dissolution of graphite. The LSM ADI surface layer revealed a near gaussian distribution of microhardness as a function of depth, so that the microhardness is lower near the surface and higher at the central part of the laser irradiated zone[35]. LSH resulted in a primarily martensitic microstructure with almost constant microhardness values across the irradiated layer higher than that in the LSM samplers.

Laser surface treatments, especially LSH significantly increase the wear resistance of ADI which was related to the fine microstructures of austenite, ledeburite or martensite obtained after LSM or LSH, giving hardness values up to 800 H_v, work hardening of the structure as well as stress induced phase transformation of retained austenite to martensite[30-38]. Moreover, such increase in wear resistance was correlated with the lower probability of micro-cracks initiation caused by sub-surface fatigue or deformation constraints at the interface between austenite and martensite produced by the stress induced austenite transformation to martensite[37]. It should be noted that the same transformation may produce compressive stresses if the ADI are subjected to surface treatments involving cold working operations such as controlled shot peening or fillet rolling which can improve the fatigue properties rather than the tribological ones[39,42].

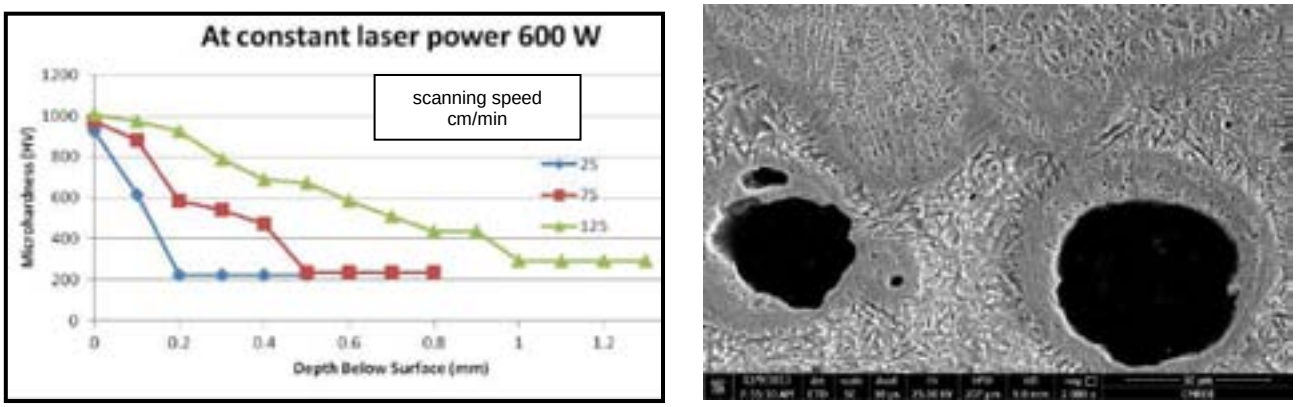

(a) (b)

Fig. 2: microhardness profile (a) and microstructure at the HAZ of an ADI sample irradiated with 600 W cw laser at different scanning speeds

In a current research at CMRDI, the hardness and the depth of the hardened layer were shown to increase with the laser scanning speed at constant power level. Fig. 2-a shows the microhardness profile across the transverse section of ADI laser surface processed with 600 W cw laser as a function of the laser scanning speed. Fig.2-b illustrates the microstructure of the irradiated sample at scanning speed of 75 cm/min. The upper part of the microstructure indicates that the hardened zone consists of retained austenite and martensite with all the graphite spheroids completely dissolved during laser melting of that area. The lower part of the microstructure shows the original graphite spheroids surrounded with a halo of retained austenitic dendrites as the C-content in this layer is relatively increased due to diffusion of carbon from the graphite spheroid at higher temperature. Graphite spheroids are contained in the original ausferritic matrix of ADI.

Locally Austempered Ductile Iron (LADI)

The currently available methods for "surface austempering" of ductile iron are often expensive and not as well controlled. Some components could benefit from austempering only a certain location of the component and leaving the remaining part as as-cast ductile iron with its excellent machinability. The LADI could improve the component's

abrasive wear resistance, bending or contact fatigue strength in a localized area. When selecting the proper material for an engine camshaft, one must balance the needs of a hard, strong and wear resistant material for the camshaft lobes with the better machinability of the component. LADI has been found to replace the use of assembled camshaft, which is usually an expensive solution[41]. LADI is obtained by a two step proprietary process:

- The surface of the camshaft is heated using computer controlled induction technology to the austenitization temperature and held for a time sufficient to ensure uniform C-content.
- The surface is then, cooled to a temperature range of 205-230°C by spraying with a liquid polymer quench. The camshaft is then held at this quench temperature until a surface layer of 3-5 mm of ausferrite is formed.

Enhancement of Strength Properties of ADI

Ausformed Austempered Ductile Iron (AADI)

It has been shown[42,43] that the rate of ferrite formation during stage I austempering may be controlled by the following processing variables:

- ***Chemical*** **-** including alloy content selection for hardenability purposes together with the austenitization temperature selection which controls the matrix carbon content
- ***Thermal*** **-** including austempering temperature and time
- ***Mechanical*** **-** including mechanical deformation introduced into the austempering schedule just after quenching, but before any asubstantial transformation of austenite (ausforming), Fig. 3.

Naturally, an optimum final microstructure could be produced by including elements of all three processing variables. It has been shown[44-46] that mechanical processing of ADI can act as a control valve for the stage I austempering reaction. In ausformed austempered ductile iron (AADI), mechanical deformation is utilized to affect the microstructure and, consequently, the mechanical properties of ductile iron due to acceleration of ausferrite reaction, refining the microstructure and increase of the structural homogeneity.

It has been shown[47] that ausforming up to 25% reduction in height during a rolling operation contributed to add a mechanical processing component to the conventional ADI heat treatment, thus increasing the rate of ausferrite formation and leading to a much finer and more homogeneous ausferrite product (Fig. 4). The effect of ausforming on the strength values was quite dramatic (Fig. 5) (up to 70 and 50% increase in the yield and ultimate strength respectively). A mechanism involving both a refined microstructural scale as a result of enhanced ferrite nucleation together with an elevated dislocation density was suggested[48]. Hardenability elements such as Ni and Mo are usually added to increase hardenability of thick section castings, and ausforming to higher degrees of deformation was found necessary to alleviate the deleterious effects of alloy segregation on ductility[49].

It is more practical that the advantage of ausforming would be taken by forging rather than by rolling. The forging process may be performed on cast preforms, austenitized and quenched to the austempering temperature, inserted into a die, pressed or forged to the final shape and then returned back into the austempering bath to complete the accelerated transformation. Minimal deformation degrees by conventional forging standards, i.e. an average strain of 25% would be sufficient for the forming part of the processing sequence. It has been reported[49] that in situations where very severe deformation occurs, the work-piece may not need to be returned to the austempering bath to complete the transformation to ausferrite, as the latter will have been completed by the time the work-piece is extracted from the die.

The idea of creating preforms in ductile iron and then ausforming them to final shape could be quite effective for relatively simple shaped castings that must meet high demanding strength and ductility requirements, e.g. connecting rods for automotive applications. It is understood that certain deviations in design elements of both preform as well as the die set should be involved compared to the design of conventional ADI process. The abovementioned concept has been utilized to produce tank track center guides[50] using a finite element simulation technique to match both the preform design and the die design so that a uniform equivalent stain throughout the casting averaged ~20%. No inclination - to fracture or cracking has been reported.

Squeeze Casting of ADI

ADI was produced without an austenitizing step based on a patent published in 1985 by P.B. Magalhaes[51]. In this process, casting in a permanent mold allowed the ejection of the part at a temperature level above 850°C where a completely austenitic range could be guaranteed. Subsequent quenching in a salt bath would lead to the ADI ausferritic microstructure.

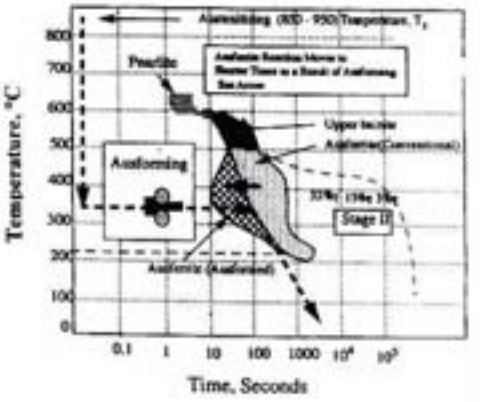

Fig. 3: Schematic representation of the ausforming process[42]

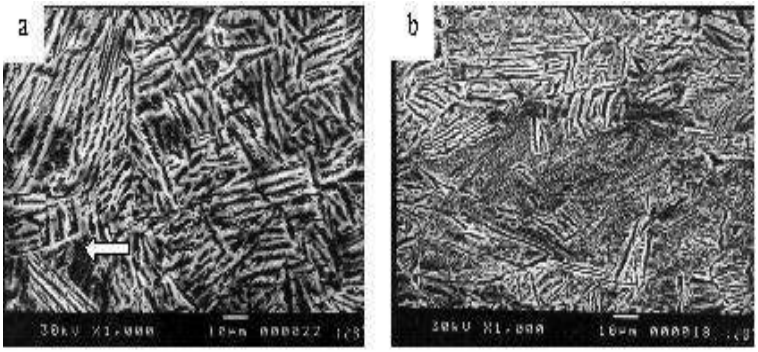

Fig. 4: SEM micrographs of ADI alloyed with 2% Ni austempered at 375°C for 1 minute. (a) Conventionally processed; (b) Ausformed to 25% reduction arrows indicate the brittle martensite formed in many zones in the conventionally processed ADI[47]

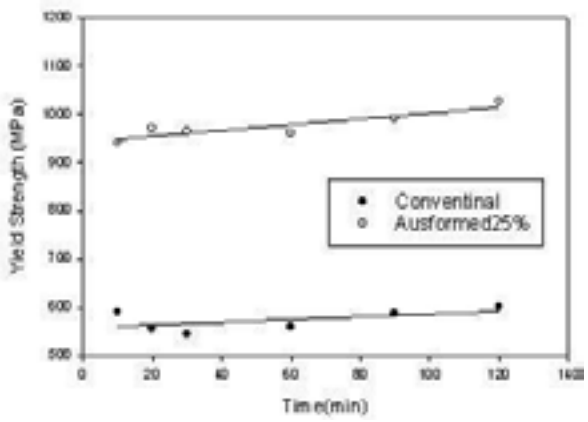

Fig. 5: Yield strength vs austempering time and ausforming reduction for adis alloyed with 2% Ni[47]

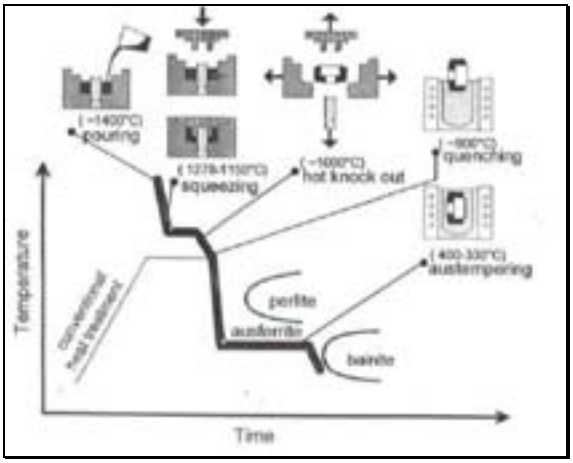

Fig. 6: Process steps and temperature regime of the SQ process and the in-situ heat treatment[52]

Based on this process, a novel technique has been simultaneously developed at TU-Aachen Foundry Institute [52] and component CPC - Finland[53] to produce superior quality ADI castings, using squeeze casting of molten metal in permanent mold, followed by in-situ heat treatment of the hot knock-out casting in the austenite range, followed by normal austempering in a salt bath. Figure 6 shows a schematic representation of the process[52].

This technique seems to have some unique advantages, such as:

- Sound castings can be produced without feeders or gating system as the solidification expansion was used to counteract solidification shrinkage.
- Increased heat transfer avoids formation of macro- and micro-segregation, which decreases the mechanical properties of ADI.
- Chemical composition of ductile iron can be selected to avoid any metastable solidification in spite of the extremely fast solidification.
- The production process is shorter and less energy consuming as the elimination of sand from the process would allow the hot castings coming out from the permanent mold to be directly introduced to the heat treatment furnace.
- The structure of the SQ ADI is much finer (the graphite as well as the ausferrite), which means better mechanical properties (ultimate tensile strength, elongation and fatigue strength).
- The casting surface is entirely free from any surface defects, which again means higher fatigue strength.
- The machinability is better.
- More environmentally friendly.

Table 1[52] shows some tensile test results of a squeeze casted ring gear test samples compared to EN standard. Fiat suspension fork was tested for fatigue strength and amazing results were achieved. This component had to pass the test without cracks loaded with 2500 KN after lifetime of 300,000 cycles. The squeeze cast forks could pass the test with 5000 KN without failure up to 3-10 million cycles. The tensile properties were much higher than pearlitic ductile iron or even better than microalloyed steels as shown in Table 2[53], yield strength was much higher than steel and elongation about the same.

Table 1: Some tensile test results of squeeze cast test samples compared to EN standard[52]

	Test 1	EN	Test 2	EN
Tensile strength, MPa	1238	1200	1115	1000
Yield strength, MPa	968	850	839	700
Elongation, %	13.4	2	15.3	5
Hardness, HB	388	340/440	363	300/360

Table 2: Comparison of different suspension fork materials[53]

	GJS-600-5	SQ ADI (Tested)	Microalloyed Steel
Tensile strength, MPa	600	950	1000
Yield strength, MPa	370	750	550
Elongation, %	10	11	12

Two-step Austempering of ADI

The mechanical properties of ADI are mainly dependent on:

- The fineness of ferrite and austenite in ausferrite
- The austenite carbon (X_γ,C_γ) where:
  X_γ is the volume fraction of austenite
  C_γ is the austenite C-content

Both these factors depend on the austempering temperature. Higher undercoolings enhance the nucleation of ferrite from the parent austenite and hence promotes finer ausferrite structure with higher yield and tensile strength but lower ductility. On the other side, higher austempering temperatures result in coarser feathery ferrite and austenite with lower strength but higher ductility properties. Moreover, higher austempering temperatures lead to higher (X_γ,C_γ) parameter which, in turn, increases fracture toughness and fatigue strength of ADI.

It is possible, therefore, to optimize the mechanical properties of ADI by ausferrite refinement as well as increasing the austenite carbon. Hence, the novel concept of two-step austempering was conceived[54], which involves first quenching the alloy to a lower temperature (250-270°C) after austenitization, thus increasing the undercooling, and then, once the nucleation of ferrite is complete, immediately raising the temperature of the quenching media to a higher temperature to enhance faster diffusion of carbon and increase austenite carbon (X_γ,C_γ) in the matrix.

The two-step austempering process has resulted in higher wear resistance in ADI compared to the conventional single-step austempering process. An analytical model for the abrasion wear behavior of ADI revealed the dependence of wear behavior of ADI on the microstructural parameters, especially the parameter $X_\gamma C_\gamma / \sqrt{d}$ where d is the ferritic cell size as well as the strain hardening exponent (n-value). The major wear resistant mechanism in ADI was shown to be the microstructural refinement in ausferrite and solution strengthening effect (high C-content in austenite) along with strain hardening effect of the austenite phase[55,56].

Meanwhile, the two-step austempering process resulted in higher crack growth rate and lower fatigue threshold than the single step ADI proces. The crack growth rate increment due to the two-step austempering process increases with the austempering temperature[57]. Moreover, it has been shown in a recent publication carried out at (CMRDI) that the two-step austempering process increases the fracture toughness of ADI, where the increment in the fracture toughness by the two-step process is more pronounced in unalloyed irons[58].

The improved toughness was correlated to reduced ferrite grain size, increased carbon content of the retained austenite as well as its stability.

Cold Rolling of ADI

ADI was subjected to cold rolling (CR) at different reduction percentages to produce as thin as 3 mm sheets without showing any evidence of cracking[59].

Increasing the cold rolling (CR) reductions, the amount of retained austenite (γ_r) was decreased due to partial transformation of retained austenite (γ_r) to martensite, (Fig. 7-a) indicate that the amount of mechanically generated martensite increases with increasing the CR reduction[59].

As can be seen from Fig. 7-b&c, the elongation and impact toughness decrease, while the ultimate tensile strength and hardness increase with increasing CR reduction. This is attributed to increase of the hardening of the investigated ADI with cold deformation processes (deformation bands and twins) and deformation - induced martensite. It must be mentioned that the observed changes in the mechanical properties at light cold deformation (7% reduction) are mainly attributed to the hardening of this alloy by plastic deformation concentrated in γ_r. At this light deformation the amount of mechanically formed martensite is very small (Fig. 7-a)[60].

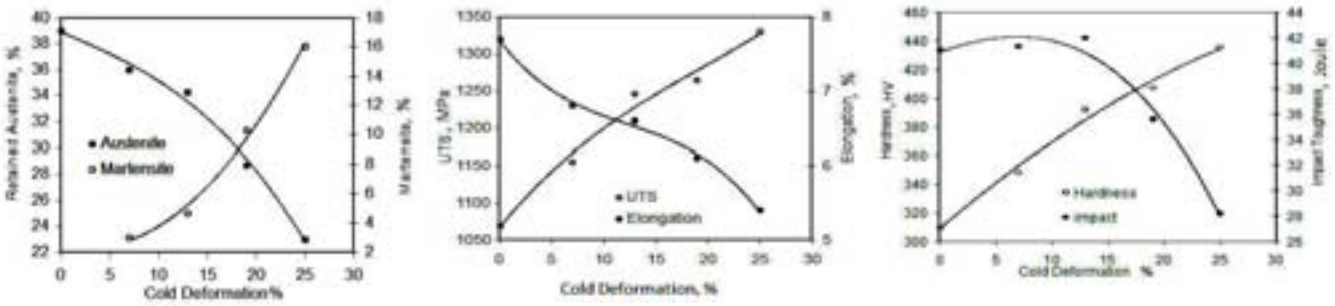

(a) (b) (c)

Fig.7[59]: Effect of cold reduction pct on:
(a) volume fraction of retained austenite and mechanically formed martensite
(b) elongation and ultimate tensile strength
(c) Vickers hardness and impact toughness

Two types of martensite induced by deformation have been reported[61], the first is of the lath type, which nucleates at twin boundaries or twin intersections, the second has a plate morphology and seems to form in regions affected by the homogeneous precipitation during the austempering treatment of quasi-coherent epsilon carbides in austenite. This latter martensite is of tempered type, containing epsilon carbides of sizes larger than those found in the parent austenite before deformation.

Improved toughness of ADI results from:

- reduced ferrite particle size
- increased carbon content in the retained austenite, which increases the strain hardening ability and strain hardening coefficient
- stability of the retained austenite

Formation of strain induced martensite is known to enhance the toughness in TRIP steels. In ADI, due to the high C-content, the martensite formed is brittle and it is debatable if the formation of strain induced martensite can improve the toughness. The contribution of strain induced martensite to the toughness of ADI has been recently discussed[62]. The martensite containing ADI can be visualized as fiber reinforced ductile material. Even if the fiber is brittle, it will not make the composite brittle, as long as the fiber is shorter than a critical length, as it will not be loaded to its maximum strength and will not, therefore, fracture. According to this argument, if the retained austenite regions are not massive, then only very short-length of thin martensite will form and will improve the toughness of ADI.

Thus, ADI austempered at lower temperature and having finer ausferritic structure should benefit from the martensite formation, while that treated at higher temperatures and consisting of massive retained austenite together with coarse ferrite will not. The retained austenite in upper bainite can easily transform to strain induced martensite[62].

Thin-Wall ADI Castings

To achieve fuel economy in automotive industry, reducing the vehicle weight has been a major research area of interest over the last few decades. Although the general trend has been to use low density materials (aluminum, magnesium and composites) instead of cast iron and steel in the automotive industry, numerous examples have been recently noted in the literature where iron castings started again to replace aluminum in the industry. This is encouraged by the increased strength, ductility, stiffness, vibration damping capacity, as well as reduced cost[63-65]. If the yield stress/cost ratio of the various materials is compared, the new member of the ductile iron family, the ADI, is most of the time the winner. When mechanical properties, density and cost are included in material evaluation, ductile iron may offer more advantages than aluminum, particularly if thin wall ductile iron parts could be produced without further heat treatment processes. The potentials for ductile iron applications for lightweight automotive components have been limited by the capability to

produce as-cast free carbide thin wall parts (2-3 mm)[66,67]. Production of thin-wall ductile iron castings still represents a daily challenge in modern foundries. Review of the recent literature shows that thin-wall ductile iron has been successfully produced for many years, thanks to the optimization of some critical production parameters: pouring temperature, chemical composition, thermal conductivity of the molding materials, type and amount of inoculating material in combination with the spheroidizing method adopted, casting design and other foundry basic practices[68,69].

When the commercial introduction of ADI in 1972, consistent efforts have been made to identify new applications of this new emerging material, however, difficulties have been encountered in producing ADI thicker than 100 mm due to the segregation of hardenability elements added to prevent pearlite formation. Such difficulty in obtaining the required austemperability and the heterogeneous microstructures do not represent a real problem when producing thin wall ADI castings due to the insignificant segregation tendency associated with rapid solidification of those thin wall castings. The use of ADI in thin-wall and high strength parts has, however, been mentioned in a very limited number of reference[70,71]. Successful case was recently reported[69], where a hollow connecting rod for a two-cylinder car engine and a front upright for a racing car were successfully made of thin wall ADI, which confirms the capability of ADI to build complex thin walled parts of high strength. With recent development in inoculation theory and practice, it became possible to cast thin-wall ductile iron parts completely free from carbides. Consequently, further improvements in the properties of thin wall ADI castings could be achieved with the austempering process. The results of a R&D program on the effect of wall thickness (3-10 mm) and silicon content (2.4-2.7%) on the properties of ADI has been reported[71]. It has been shown that thin-wall ADI castings austempered at 360°C and containing low silicon can exhibit ultimate strength exceeding 1100 MPa with more than 10% elongation. This is an indication that austempered thin-wall ductile iron is becoming a logical choice for the production of small, light weight and cost effective automotive components. However, more data about the metallurgy of thin-wall ADI castings seems to be of practical interest.

ADI 2 mm plates with a homogeneous ausferritic and nodule count of 300 nodules/mm^2 were produced at CMRDI[72]. It was found that decreasing the wall thickness leads to reduced amounts of retained austenite and structure refinement, which in turn increase the hardness. Increasing the austempering temperature from 350°C to 400°C resulted in reduced tensile strength values (950 and 1000 MPa for 8 and 2 mm wall thickness, respectively) to (775 and 875 MPa for the same wall thickness), increased impact strength from 40 to 80 and from 100 to 125 J at wall thicknesses of 2 and 8 mm, respectively, apparently due to increased amounts of retained austenite at higher austempering temperatures.

Machinable ADI

When ADI first started to be used for engineering applications, there were many difficulties experienced in trying to machine it, and some of these doubtlessly persist to this day. The hardest grades of ADI reach a hardness of ~50 HRC which would pose a challenge for any high volume machining operation. Although the softer grades of ADI have a typical hardness of 300-350 BHN, their matrix structure contains up to 40% retained austenite. When subjected to strains in service, as was mentioned in section (Cold Rolling of ADI) of this survey, this phase rapidly work hardens and can transform to martensite, this can thereby reduce the machinability compared with a steel of equivalent hardness. The volume fraction of high carbon austenite present in the microstructure of austempered ductile iron (ADI) is one of the important factors that influence the mechanical and physical properties of the alloy. Formation of martensite by TRIP (transformation induced plasticity) mechanism during the machining operation, in which a large amount of stress is applied to the microstructure, results in decrease in machinability of ADI. It is considered that the limited use of ADI for high volume applications is partly due to machining difficulties. This was one of the motivations in the recent developments of a machinable ADI[73-79].

A lack of experience of the high volume machining of ADI adds uncertainty to the costs and production rates and the early experiences of ADI exposed some inconsistencies in the machinability. These problems, however, can be minimized by collaboration between a knowledgeable foundryman, heat treater and machining expert.

The influence of austenitizing and austempering temperatures on the machinability of ADI was reported[80,81]. The production of machinable ADI has attracted the attention of many researchers in the last few years by optimizing the composition and heat treatment cycles of cast iron. Muhlberger developed[73] and patented[74] a machinable grade ADI by careful selection of the composition (low Mn) and heat treatment variables and this development was exploited in at least one European foundry[75,76]. More recently, two other grades of machinable ADI have been developed in the US[77,78], specifically aiming at increasing the use of ADI for automotive applications such as chassis components and crankshafts.

There are some differences between the two approaches, but the common feature is that the matrix structure contains a considerable amount of ferrite in both cases. The new grade, referred to as MADI™ is claimed to have unique machining characteristics and lower machining costs than as-cast ductile iron or regular ADI under appropriate conditions of speed and feed. In-plant machining trials have shown that MADI at 243 BHN could be machined on existing machine lines designed for ductile iron grade 65-45-12.

In a continuing effort to address the deficiencies of regular ADI, extensive efforts have been recently made to develop the dual-phase (ferritic-ausferritic) grades of ADI with enhanced machinability properties to compete with forged steel for power train applications[82-89]. The properties of dual phase matrix (DPM) ADI have been the subject of extensive studies.[16,55,90-99]

ADI offers an excellent compromise between the values of proof stress and elongation; both are very highly appreciated in the field of suspension parts in the automotive industry[100]. Many potential uses of ADI in competition with forged steel and aluminum alloys can be opened due to strong possibilities of weight and volume reductions.

The automotive industry has been showing a significant interest in the dual-phase intercritically austenitized ADI, several interesting publications can be cited recently in the literature.[101-109]

The optimum parameters of maching practice have been recently drawing increasing attention.[110-113]

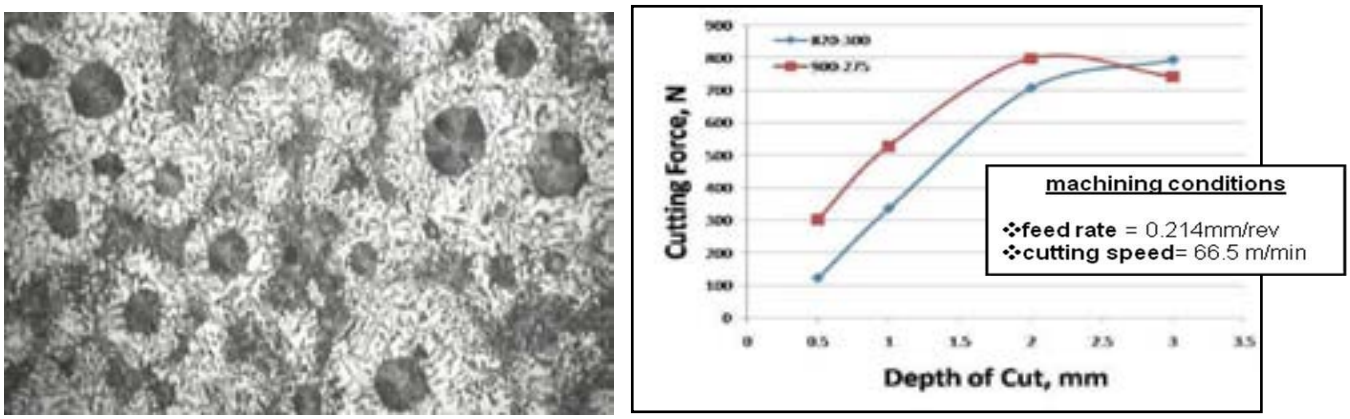

(a) (b)

Fig. 8: (a) The microstructure of IADI austenitized at 820°C and austempered at 375°C.
(b) The cutting force reduction of IADI compared to the conventional ADI[25]

Fig. 8-a shows the microstructure of intercritically austenitized ADI sample (IADI) and the resulting decrease in machining force of this material compared to the conventional ADI (Fig. 8-b)[25].

Conclusions

1. Extensive research work over the past decade has helped to develop the property combination of ADI in three directions:
   - increased strength, ductility and toughness
   - enhanced wear resistance/toughness combination
   - improved machinability
2. Carbidic, bainitic/martensitic locally austempered as well as laser surface processed ADI offer opportunities for superior wear resistance, combined with reasonable toughness, which may open new applications for ADI.
3. ADI offers high levels of mechanical properties at a competitive cost. When the high strength of ADI is taken into account, it could successfully compete with lightweight alloys, as the additive weight required to give unit strength is lower. Moreover, when the relative cost of ADI required to give unit strength is considered, ADI seems to be one of the cheapest alloys. These points have yet to be fully appreciated by many design engineers. Currently, novel processing techniques adopted to achieve better strength and toughness properties include ausforming, cold-rolling, two-step austempering, as well as squeeze casting.
4. The current research work aiming at improving machinability of ADI looks rather vital for the future of this material. The available machining techniques required for forging steel are not always suitable for ADI components, particularly on a high volume machining line dedicated to the production of one specific product. This problem can be minimized with the development of ferritic + ausferritic ADI structures.

References

1. R. A. Harding: Asia-Europe Environment Forum Conf., Jakarta Indonesia.
2. K.L. Hayrynen, K.R. Brandenberg and J.R.Keough: AFS Transaction, 2002, paper 02-084, 925-938.
3. A. Nofal: Proceedings of the World Foundry Congress, 19-21 May 2014, Bilbao, Spain.
4. J.R. Keough, K.L. Hayrynen, and V.M. Popovski: World Foundry Congress, 2012.
5. J. Lefevre and K.L. Hayrenen: In proceedings of the 26th Heat Treating Society Conference, 2011, ASM International, 99-107.

6. A. Krzyńska and M. Kaczorowski: *Achieves of Foundry Engineers*, 2007, vol. 7, Issue 4/2007, 111-114.
7. M. Kaczorowski and D. Myszka: Prace ITMat, 2003, 10-16.
8. J. Aranzabal, I. Gutierrez, J. M. Rodriguez-Ibabe and J. J. Urcola: *Metall. and Mater. Trans. A*, May 1997, vol. 28 A, 1143-1156.
9. A. Nofal, H. Nasr El-din and M. Ibrahim: *J. of Mater. Sci. and Techn*., 2003, vol. 11, No. 2, 86-96.
10. H. Nasr El-din, A. Nofal, A. Ramadan and M. Ibrahim: *Canadian Metallurgical Quarterly*, 2004, vol. 43, No. 2, 203-218.
11. J. L. Garin and R. L. Mannheim: *Mater. Process. Tech*., 2003, 143-144, 347-351.
12. Z. Zhongkui, S. Quingzhou, M. Hailong and Z. Junxian: Proceedings of the 8th International Symposium on Science and Processing of Cast Iron, 2006, Beijing, China, 464-467.
13. S. Chatterjee and H. K. D. H. Bhadeshia: *Mater. Sci. Tech*., 2006, vol. 22, No. 6, 695-699.
14. K. S. Ravishankar, K. Rajendra Udupa and P. Prasad Rao: The Proceedings of the World Foundry Congress, Chinnai 7-10 Feb. 2008, Chinnai, India, 35-40.
15. S. Daber and P. Prasad Rao: *J. Mater. Sci*b., 2008, 43, 357-367.
16. V. Kilicli and M. Erdogan: *J. of Materials Engineering and Performance*, April 2008, vol. 17(2), 240-249.
17. K. Mayrynen and K. Brandenberg: *Trans. AFS*, 2003, vol. 111, paper No. 03-088, 845-850.
18. J. R. Keough and K. L. Hayrenen: DIS Meeting, Nov. 14, 2000.
19. M. Chisamera, I. Riposan, C. Ionascu and S. Stan: International Scientific Conference on "ADI-Foundry's Offer for Designers and Users of Castings", Nov. 2000, III/25 - III/32.
20. S. Laino, J. A. Sikora and R. C. Dommarco: Wear, 2008, 265.
21. L. Jin-Lai, Y. Xuexian, Z. Hui and L. Guolu: Modern Cast Iron, 2008, 28, 4.
22. L. Jinhai, L. Guolu, Z. Huiyou, B. Boqian, X. Xingchuan, Y. Zhaoyu, Z. Yicheng and Y. Xuexian: Proceedings of 69th World Foundry Congress, Oct. 16-20 2010, Hangzhou, China, 423-426.
23. Z. Yi-Cheng, L. Kerui and Z. Zhong-Chou: Modern Cast Iron, 2007, 27, 10.
24. S. Laino, J. Sikora and R.C. Dommarco: Proceedings of the Ninth International Symposium on Science and Processing of Cast Iron (SPCI-9), 10-13 Nov. 2010, Luxor, Egypt, 187-192.
25. A. Nofal and L. Reissig: Introduction of Advanced ADI Technologies to the Egyptian Industries, Final Report of Joint German-Egyptian Research Fund (GERF) Project, 2014.
26. Y-C. Peng, H-J. Jin, J-H. Liu and G-L Li: *Material Science and Engineering A*, 2011, 529, 321-325.
27. Y-C. Peng, H-J. Jin, J.H. Liu and G-L. Li: *Material Characterization*, 2012, 72, 53-58.
28. P. Dhanapal, S. S. M. Nazirudeen and A. Chandrasekar: *J. Inst. Eng. India Ser D*, April-September 2012, 93(1), 23-29.
29. X. Sun, Y. Wang, D. y> Li and G. wang: Wear, 2013, 301, 116-121.
30. X. Sun, Y. Wang, D.Y-Li, Ch. Wang, X. Li and Zh. Zou: Materials and Design 2014, 62, 367-374.
31. R. Zhou, Y. Jiang, D. Lu, R. F. Zhou and Z. Li: Wear, 2001, 250, 529-534.
32. S. M. Lee, S. S. Park and B. M. Moon: Proceedings of the 65th World Foundry Congress, Gyeongju, Korea, 2002, 252-258.
33. Z. Ning, S. Ren, J. Sun and Y. Feng: Proceedings of Science and Processing of Cast Iron, SPCI-8, Beijing, China, 2006, 134-138.
34. Y. H. Tan, S. I. Yu, J. L. Doong and J. R. Wang: *Journal of Material Science*, 1990, 25, p. 4133.
35. A. Roy and I. Manna: *Materials Science and Engineering*, 2001, A297, 85-93.
36. S. K. Putatunda, L. Bartosiewicz, R. J. Hull and M. Lander: Material Manufacturing Processes, 1997, 12(1), 137-151.
37. K. M. Adel, A. S. Dhia and M. J. Ghazali: *International Journal of Mechanical and Materials Engineering (IJMME)*, 2009, vol. 4, No. 2, 167-171.
38. C. Soriano, J. Leunda, J. Lambarri, V. Garcia Navas and C. Sanz: Applied Surface Science, 2011, 257, 7101-7106.
39. R. J. Warrick, P. Althoff, A. P. Druschitz, J. P. Lemke, K. Zimmerman, P. H. Mani and M. L. Rackers: In Proceedings Casting Solutions for the Automotive Industry (SP-1504), SAE 2000 World Congress, Detroit, MI SAE Technical Paper 2000-01-1290.
40. K. Brandenberg, K. L. Hayrynen and J. R. Keough: Gear Technology, 2001, 18, p. 42.

41. Ch. Bixler, K. Hayrynen, J. Keough, G. Pfaffmann, and S. Gledhill: Technical Report of SAE, 2010, No. 2010-01-0652, 15 p.
42. K. B. Rundman: Casting 1997 – International ADI and Simulation Conference; Helsinki Univ. of Technology, Finland, 1997, ed. K. Holmberg, paper 2, 42 pp.
43. D. J. Moore, K. B. Rundman and T. N. Rouns: First International Conference on ADI, ASM, 1985, 13-31.
44. J. D. Dela'O, C. M. Bruke, B. Lagather, D. J. Moore and K. B. Rundman: In "Thermomechanical Processing and Mechanical Properties of Stels and Cast Irons", The Minerals, Metals and Materials Society, 1997, 79-100.
45. J. Aachary and D. Venugopalan: *Metall and Mater. Trans* A. 2000, vol. 31, 2575-2585.
46. B. N. Olson, Ch. Brucke, J. Parolini, D. J. Moore and K. B. Rundnan: International Conference on ADI, DIS and AFS, Louisville, KY, USA, 29-60 Sept. 2002, 25-27.
47. M. Nasr El-din, A. Nofal and M. Ibrahim: *International J. of Cast Metals Research*, 2006, vol. 19, No. 3, 137-150.
48. A. Nofal, H. Nasr El-din and M. Ibrahim: In "Proceedings of the 8th Symposium on Science and Processing of Cast Iron, SPCI-8, Beijing, China, 2006, 397-402.
49. B. N. Olson, D. J. Moore, K. B. Rundman and G. R. Simula: *AFS Trans.*, 2002, vol. 110, 02-118, 965-980.
50. X. Lei and C. J. Lissenden: *Trans. Of the AIME*, 2001, vol. 12, 420-425.
51. P. B. Magalhaes: Processo de Prodancao de Ferrous Fundidos Bainiticos por Austempera Directa, Patent no. 85046, Portugal, 1985.
52. R. W. Kaiser and P. R. Sahm: In "International Scientific Conference on "ADI-Foundry's Offer Designers and Users of Castings", Crackaw-Poland, 23-24 Nov. 2000.
53. M. Johanson: In: "World Conference on ADI, DIS and AFS, Louisville, KY, USA, 29-30 Sept. 2002.
54. J. Yang and S. K. Putatunda: Materials and Design, 2004, 25, 219-230.
55. J. Yang and S. K. Putatunda: *Materials Science and Engineering*, 2004, A382, 265-279.
56. J. Yang and S. K. Putatunds: *Materials Science and Engineering*, 2005, A406, 217-228.
57. J. Yang and S. K. Putatunda: *Materials Science and Engineering*, 2005, A393, 254-268.
58. K. M. Ibrahim, A. A. Nofal and M. M. Ibrahim: The 9th Int. Conf. on Mechanical Design and Production (MDP-9), Cairo, Egypt, Jan. 8-10, 2008.
59. H. Nasr El-din, A. Nofal, A. Ramadan and M. Ibrahim: *Canadian Metallurgical Quarterly*, 2004, vol. 42, No. 2, 203-218.
60. A. Nofal, H. Nasr El-din and M. Ibrahim: *J. of Mater. Sci. and Techn.*, 2003, vol. 11, No. 2, 86-96.
61. S. Chatterjee and H. K. D. H. Bhadeshia: *Mater. Sci. Tech.*, 2006, vol. 22, No. 6, 695-699.
62. K. S. Ravishankar, K. Rajendra Udupa and P. Prasad-Rao: In "The Proceedings of the World Foundry Congress" Chinnai, India, 7-10 Feb. 2008, 35-40.
63. D. M. Stefanescu and R. Ruxanda: In "Proceedings of the 65th World Foundry Congress (WFC)" Gyeonigiu, Korea, 2002.
64. E. Fras, M. Gorny and H. F. Lopez: *International Foundry Research:Giessereiforschung*, 2009, vol. 61, No. 3
65. G. Vidyarthee and K. K. Singh: *Int. J. Mech. Eng. & Rob. Res.*, 2014, vol. 3, No. 3, 465-473.
66. E. Fras and M. Gorny: In "Proceedings of the 8th International Symposium on Science and Processing of Cast Iron (SPCI-8):, Beijing, China, Oct. 16-19 2006, 157-162.
67. C. Labrecque and M. Gagné: AFS Trans., 2000, vol. 104, 31-38.
68. D. M. Stefanescu, L. P. Dix, R. E. Ruxanda, C. C. Coburn and T. S. Piwonks: *AFS Trans.*, 2002, vol. 187, 1149-1156
69. R. A. Martinez, R. E. Boeri and J. A. Sikora: World Conference on ADI, Louisville, Oct. 2004, 143-148.
70. C. Labrecque, M. Gagné and A. Jawid: *AFS Trans.*, 2005, St. Louis, vol. 109
71. M. Gagné, C. Labrecque, M. Popescu and M. Sahoo: *AFS Trans.*, 2006, vol. 110
72. M. M. Mourad, K. M. Ibrahim, M. M. Ibrahim and A. A. Nofal: In "Proceedings of the 68th World Foundry Congress (WFC)", Chinnai, India, 2008, 161-166.

73. H. Muhlberger: ASME and Amax Inc., 2nd Int. Conf. on ADI: Your Means to Improved Performance, Univ. of Michigan, Ann. Arbor, 1986, M1, 17-19 March, Illinois, 55-93.
74. K. Schmidth GmbH and others: German Patent/2853870, field 13 Dec. 1987.
75. F. Zandardi: 2002 World Conference on ADI, DIS and AFS, Louisville, KY (USA), Sept. 26-27, 2002.
76. F. Zanardi: *AFS Trans.*, 2005, paper 05-209(05), 13 p.
77. A. P. Druschitz and D. C. Fitzgerald: Non-Ferrous Casting (SP-1734), SAE World Congress, Detroit, Mitchigan, 3-6, 2003 SAE Technical Paper 2003-01-0831.
78. A. P. Druschitz and D. C. Fitzgerald: International Patent Application WO 2004/022792 A2, 18 March 2004, Also US Patent Application: 2004112479, June 17, 2004.
79. F. Zandardi: La Metallurgia Italiano, 10/2005, 27-32.
80. J. R. Keough and K. L. Hayrynen: Proceedings of the 8th International Symposium on Science and Processing of Cast Iron, Beijing, China 2006, 474-479.
81. M. C. Cakir, A. Bayram, Y. Isik and B. Salar: Materials Science and Engineering, 2005, A407, 147-153.
82. T. Kobayashi and S. Yamada: *Metall. Mat. Trans. A*, 1996, 27A(7), 1961-1971.
83. D. Rousiere and J. Aranazabal: *Metall. Sci. and Technol.*, 2000, vol. 18(a), 24-29.
84. A. M. Rashidi and M. Moshrefi-Torbati: *Materials Letters*, 2000, vol. 45, 203-207.
85. J. Aranzabal, G. Serramoglia, C. A. Goria and D. Rousiere: *Int. J. of Cast Metals Research*, 2003, 16(1-3), 185-192.
86. K. Kocatepe, M. Ceroh and M. Erdogan: Materials and Design, July 2005.
87. M. J. Pérez, M. M. Cisneras, M. F. López, S. Rodriguez and V. Vózquez: In "Proceedings of "the 8th Int. Symposium on Science and Processing of Cast Iron (SPCI-8), Beijing, China, Oct. 16-19, 2006, 139-144.
88. C. Valdes, M. J. Peres Lopez, M. Figueroa and L. E. Ramirez: Revista Mexicana De Fisica, 2009, S55, 1, 48-51.
89. M. Figueroa, M. J. Pérez, K. L. Fraga, C. V. Valdés and E. Almanza: Revista Mexicana De Fisica S55(1), May 2009, 105-109.
90. M. Cerah, K. Kocatepe and M. Erdogan: *J. Mat. Sci.*, 2005, 40(13), 3453-3459.
91. M. Erdogan, K. Kocatepe and M. Cerah: *Int. J. Cast Met. Res*., 2001, 19(4), 248-253.
92. Y. Sahin, M. Erdogan and V. Kilicli: *Materials Science and Engineering*, 2007, A444, 31-38.
93. V. Kilicli and M. Erdogan: *Int. J. Cast Met. Res.*, 2000
94. M. Erdogan, V. Kilicli and B. Emir: *J. mat. Sci.*, 2007
95. J. K. Chen, J. S. Tsai and B. T. Chen: Supplemental Proceedings, vol. 3, General Paper Selections, The Minerals, Metals and Materials Society, 2011.
96. R. Aristizabal, A. P. Druschitz, E. Druschitz, R. Bragg, C. R. Hubbard, T. R. Watkins and M. Ostrander: *AFS Transactions*, 2011, vol. 119, 407-413.
97. A. P. Druschitz, R. E. Aristizabal, E. Druschitz, C. R. Hubbard, T. R. Watkins, L. Walker and M. Cstrander: *Met. Trans. A*, 2012, vol. 43, No. 5, 1468-1476.
98. F. Zanardi: 2013 Keith Millis Symposium on Ductile Iron, 2013, 200-222.
99. F. Klocke, M. Arft and D. Lung: Prod. Eng. Res. Devel, 2010, 4, 433-441.
100. J. R. Keough: SAE Int. Off-highway and Powerplant Congress, Sept. 2000, SAE Technical Paper 2000-01-2563.
101. A. P. Druschitz and D. C. Fitzgerlad: SAE Technical Paper 2003-01-0187, Society of Automotive Engineers, Warrendale, PA, 2003.
102. A. P. Druschitz, H. Folz, D. Devor, S. Kapoor, A. Balasubramanian, K. Bronk, J. Bussema, M. Glowik, N. Malkewicz, S. Etling and P. Hedge: SAE Technical Paper # 2005-01-1684, Society of Automotive Engineers, Warrendale, PA, 2005.
103. A. P. Druschitz and D. C. Fitzgerald: US Patent No. 7, 070,666, July 4, 2006.
104. A. P. Druschitz, D. C. Fitzgerald and I. Hoegfeldt: SAE Technical Paper # 2006-01-0016, Society of Automotive Engineers, Warrendale, PA, 2006.
105. A. P. Druschitz and D. C. Fitzgerald: US Patent No. 7,497,915, March 3, 2009.
106. A. P. Druschitz, R. Aristizabal, E. Druschitz, C. R. Hubbard, T. R. Watkins and M. Ostrander: *SAE International Journal of Materials and Manufacturing*, June 2011, vol. 4, No. 1, 111-118.

107. M. Tadyon Saidi, N. Baghersaee, N. V. Varahram, M. Hanumantha Roa, G. V. S. Nageswara Rao: Metal, 2007.
108. A. P. Druschitz, R. Aristizabal, and M. Ostrander: SAE Technical Paper # 2013-01-0950, Society of Automotive Engineers, Warrendale, PA, 2013.
109. A. P. Druschitz, M. Ostrander and R. Aristizabal: In "The Proceedings of 71st World Foundry Congress:, 2014, Bilbao, Spain.
110. M. Vasconcelos de Carvalho, D. M. Montengro and J. d-Oliveira Gomes: *J. of Materials Processing Technology*, 2013, 213, 560-573.
111. K. M. Kumar and P. Hariharan: Procedia Engineering, 2013, 64, 1495-1504.
112. M. Arft and F. Klocke: Procedia CIRP, 2013, 8, 129-134.
113. A. Meena and M. El Mansori: *Int. J. Adv. Manf. Technol.*, 2013, 69, 2833-2841.

Environmental embrittlement of austempered ductile iron (ADI) – A review

R.E. Boeri[1], R.A. Martínez[1*]

[1]División Metalurgia, Facultad de Ingeniería, Universidad Nacional de Mar del Plata, INTEMA – CONICET, Mar del Plata, Argentina

In this article, the authors revise the advances in the understanding and characterization of the unusual embrittlement phenomenon. The phenomenon affects the behavior of austempered ductile iron (ADI) while stressed in contact with water and other liquids, reducing its strength, elongation and fracture toughness.

The different investigations carried out by the authors include the characterization of the embrittlement by means of tensile, fracture toughness and cyclic load tests taking into account the influence of selected liquids. The use of electrochemical potentials during testing and the surface protection by different coatings are also discussed.

These results show that there have been significant advances in the characterization of the embrittlement phenomenon since it was first reported.

Based on the examination of the fracture surfaces, a fracture model, called "Localized slip process induced by adsorption in aqueous environments" is proposed.

Keywords: ductile iron, ADI, embrittlement, water, properties.

Introduction

The family of ductile cast alloys (DI) can show different matrix microstructures and can cover a wide range of mechanical properties. As an example, ferritic matrices are used in parts, such as automotive suspension components, where high impact strength is the main requirement. On the other hand, pearlitic and martensitic matrices are used when hardness, strength and wear resistance represent a major issue.

DI production has maintained a sustained rate of growth over the last decades substituting cast and forged steels in a large number of applications. At present, researchers and producers are developing new applications for DI, and targeting the market of safety critical parts when combinations of strength and toughness are required.

The strength of nodular graphite ductile iron increases after an austempering heat treatment process, obtaining the so-called austempered ductile iron (ADI). The microstructure of the resulting matrix is a combination of acicular ferrite and high carbon austenite, also known as ausferrite.

However, ADI suffers a noticeable embrittlement when its surface is in contact with liquids during slow monotonic tensile load application [1-7]. The first reports of embrittlement by contact with water were published by Shibutani et al [1,2]. Martínez et al [3] verified the existence of the phenomenon when obtaining similar results after testing several ADI grades (ASTM A 807M-06). Such studies showed that reductions in tensile strength and elongation could reach 30% and 70%, respectively.The origin of embrittlement remains to be comprehensively unexplained. Nevertheless, the presence of this effect has not stopped the increasing application of ADI in the construction of high strength mechanical components. The very low incidence of brittle failure of ADI in service could be explained by two distinctive characteristics of this effect: it is fully reverted after the part surface is dried, and it is unnoticed at high loading rates. As a result, failure in service requires a relatively slow overloading (initial stages of plastic deformation) when the part is in contact with liquids, which does not occur very frequently.

Embrittlement phenomena by contact with liquids are not unusual. In some cases different groups of materials that regularly have a ductile behavior, among which some metallic alloys are included, show lower ductility and strength when their surfaces are in contact with a specific liquid while stressed over the yield limit. The fracture surface characteristics change from those observed when testing the same material in air [3].

A brief review of the most extensively studied environmentally induced cracking (EIC) processes for this kind of phenomenon includes hydrogen embrittlement (HE), together with stress corrosion cracking (SCC) and liquid metal embrittlement (LME)[10-12]. EIC process is characterized by brittle failures in which cracks propagate at stress intensity (K) levels lower than the critical values in air or vacuum, because of the combined effect of a tensile stress field and the presence of a corrosive media. Corrosion rates are usually quite low. The mechanisms involved in this type of failure are very complex and remain under discussion. In consequence, the occurrence of EIC failures in service is still difficult to predict.

LME causes the catastrophic brittle failure of normally ductile metal alloys in contact with a liquid metal and stressed in tension[13]. The fracture mode changes from a ductile to a brittle intergranular or brittle transgranular

* Corresponding author, email: rimarti@fi.mdp.edu.ar

(cleavage) mode. It has been shown that the stress needed to propagate a sharp crack or a flaw in liquid is significantly lower than that necessary to initiate a crack in the liquid metal environment. In most cases, the initiation and the propagation of cracks appear to occur instantaneously, with the fracture propagating through the entire test specimen. The velocity of crack or fracture propagation has been estimated to be 10 to 100 cm/s. LME is not a corrosion, dissolution or diffusion–controlled intergranular penetration process. The embrittlement is severe, and the propagation of fracture is very fast in the case of LME as compared to that in SCC.

The authors have studied the embrittlement of ADI over the last years. The general features of this embrittlement shares some common features with LME. The objective of this manuscrip is to present a critical review of the general features of ADI embrittlement and to introduce some recent results about the influence of cyclic loading.

Experimental Procedure

Several ductile cast iron melts were prepared in a medium frequency induction furnace. Steel scrap and foundry returns were used as raw materials. Nodulization was carried out using the sandwich method with 1.5 Wt% of Fe-Si-Mg (6% Mg) and inoculated with 0.6 Wt% Fe-Si (75% Si). The chemical compositions of the melts were determined by using a Baird DV6 spectrometer. (Table 1).

Table 1: Chemical composition of the melts.

Melt	C	Si	Mn	Mg	Cu	Ni	Mo	P	S
A	3.20	3.30	0.2	0.03	1.00	0.68	0.09	0.01	0.01
B	3.35	2.74	0.32	0.062	1.05	0.44	---	0.02	0.01
C	3.32	1.77	0.18	0.05	0.06	---	---	0.06	0.02
D	3.20	3.30	0.2	0.03	1.00	0.68	0.09	0.01	0.01
E	3.58	1.95	0.18	0.046	1.08	0.38	0.18	0.02	<0.01
F	3.45	2.3	0.25	0.65	---	---	---	0.01	<0.01

One inch "Y" blocks were cast in sand molds and used to prepare different specimens such as those shown in Fig. 1.

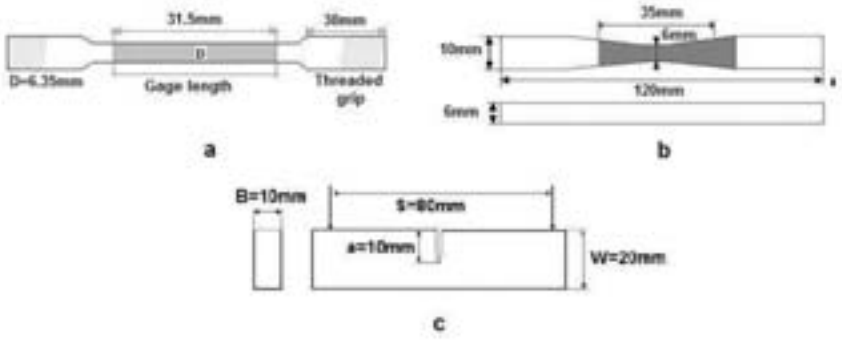

Fig.1: Samples used for mechanical tests

The experimental setups used to carry on the tests in wet condition are shown in Fig. 2 a and b. The first shows the arrangement in the case of tensile test using samples such as shown in 1a and 1b, the second is a sketch of the double eccentricity machine used to apply cyclic loads to samples SEN(B) /ASTM E399). This machine, producing a displacement-controlled cyclic load, was used with a constant eccentricity e = 0.145 mm, which resulted in stable crack propagation under small-scale plasticity condition.

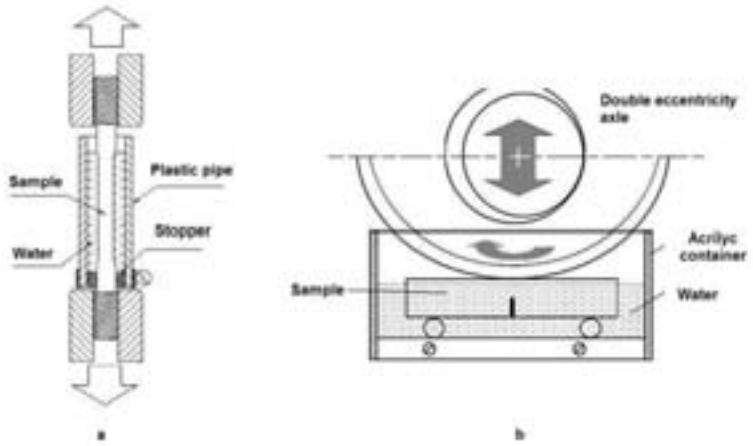

Fig.2: Experimetal set up used for wet tensile and cyclic load tests

Test samples of the different melts were heat treated to obtain different ADI grades. The heat treatments applied to each melt are detailed in Table 2.

Results and Discussion

1. Tensile tests

1a. Different ADI grades

Table 2 lists the results of tensile testing of samples of melt A of different ADI grades. In all cases, significant drops in UTS and elongation are caused by the presence of water in contact with the surface of the sample.

Table 2: Tensile tests

Material		U.T.S.[MPa]/δ[%]	Heat tretment
ADI 150-110-7 (grade 2)	Dry	1168/16	60´@900°C+90@360°C, air cooling
	Wet	852/2.8	
ADI 175-125-4 (grade 3)	Dry	1340/11.3	60´@910°C+90@320°C, air cooling
	Wet	1030/3	
ADI 200-155-2 (grade 4)	Dry	1526/6.3	60´@910°C+90@280°C, air cooling
	Wet	1071/1.2	
Ferritic matrix	Dry	517/25	24hs@680°C, furnace cooling
	Wet	516/26	
Pearlitic matrix	Dry	1100/7.3	60´@910°C , air cooling
	Wet	900/3.1	

Melt A (Table 1), sample a (Fig. 1), ADI standard ASTM A 897-06

1b. Crack develoment

The process of cracking and failure under tensile stresses has been studied by the metallographic inspection of the polished and etched surfaces of the samples shown in Fig. 1-b. A careful inspection of the samples showed that above certain stress levels, cracking begins at certain locations of the microstructure, as shown in Fig. 3

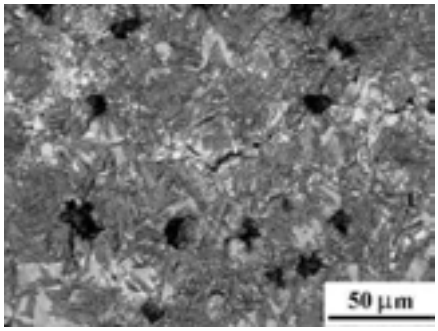

Fig.3: Crack developed in LTF zone after small plastic deformation.

A careful analysis of the location of the first cracks showed that they form at some specific portions of the microstructure usually called Last To Freeze (LTF). LTF distribution and chemical composition are the result of the solidification process. The solidification of spheroidal graphite iron involves the nucleation and growth of relatively large austenite dendrites. The microsegregation of the alloy elements takes place between the dendrite arms, therefore, the distribution of the LTF regions is intradendritic and its dispersion depends on the dendrite coarseness. Given the fact that LTF zones solidify at the end of the process, they can show a higher or lower concentration of some alloy elements and impurities as well as small shrinkage cavities [6,7]. The chemical composition of DI always includes Mg, C, Mn, Si, S, and P; while elements like Mo, Cu, and Ni are frequently added as alloying elements. Therefore, LTF regions can show varied chemical compositions and properties for different ductile iron alloys. In general terms, the higher the alloying content, the larger the microsegregation. Hence, the ADI fracture process should be analyzed on a material that can be considered to be formed by an ausferritic metallic matrix that shows spherical cavities of different sizes (the strength of the graphite occupying these sites is negligible), and certain sites in the matrix (LTFs) where microporosity, non-metallic inclusions and phases such as phosphides, carbides etc. may be present. Indeed these zones present adverse characteristics from a mechanical properties viewpoint.

1c Influence of Different liquids

The presence of water in contact with the surface of the samples causes the formation of surface cracks at lower stress levels. A stress level above 850 Mpa, barely larger than the yield strength, is enough to begin cracking in the presence of water. Other liquids show similar behavior to that of water, but induce higher critical cracking stress [9]. The influence of liquids on the surface crack initiation was determined by using the samples shown in Fig. 1b. Those samples allow investigating the surface integrity after a given stress or strain has been applied. Fig. 4 shows the stress threshold for the formation of cracks determined for the different liquids used. It is very clear that the presence of the liquids facilitates the initiation of surface cracks.

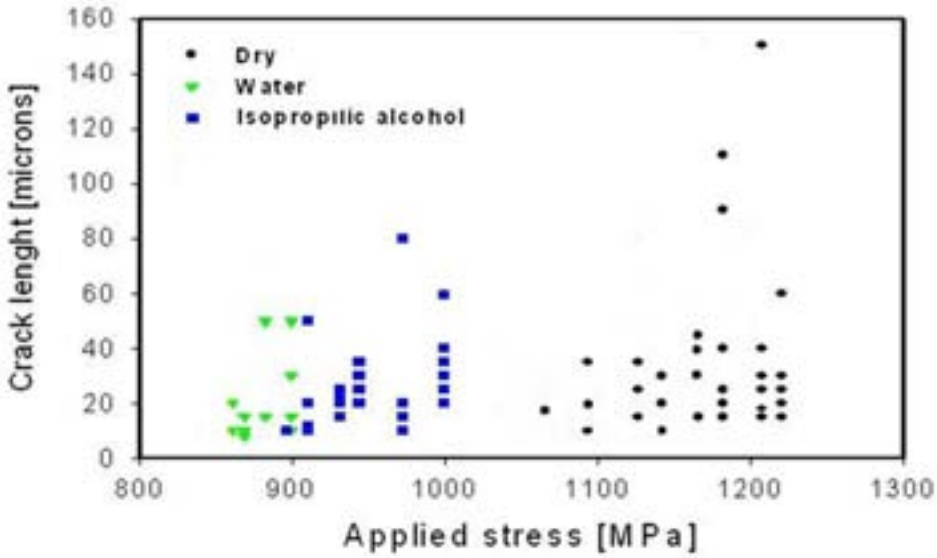

Fig.4: Crack development using different liquids. Melt B. Sample b. ADI grade 2

The obtained threshold values results are summarized in Table 3.

Table 3: Crack initiation threshold values.

Media	Air	Heptane	Ethanol	CCl_4	Water	Isopropyl alcohol
Threshold stress [MPa]	1020	910	903	923	851	880

Melt B. Sample b, ADI grade 2.

In addition, Different liquids cause different degrees of embrittlement. The degree of embrittlement could not be clearly related neither to polarity, nor to surface tension.

2. Fracture toughness and hardness

The fracture toughness tests were performed using blunt notched (BN) and precracked (P) samples. The results are listed in Table 4. For both stress concentrators, the values of K_{IC} in wet condition were nearly half of the values obtained when the samples were tested in dry condition. The critical flaw size is also calculated and displayed in the table.

Table 4: Fracture toughness

Sample	Condition	K_{IC} [MPa.m$^{1/2}$]	$\{K_{IC}/\sigma_{YS}\}^2$ [mm]
BN	Dry	72.5	0.6
BN	Wet	34.2	0.15
P	Dry	53.4	0.36
P	Wet	26.8	0.09

Melt C, sample c.ADI grade 2

The hardness measurements show small but consistent changes because of wetting. The hardness of ADI Grade 2 of melt C measured in dry condition reaches 318HB, while it increases to 335HB when the tests are carried out in contact with water. These results suggest that the strain hardening increases when the surface of the ADI is wet.

The observation of the inner surface of the hardness test indentation by optical microscopy showed a flat surface with signs of plastic deformation and scratches produced by the friction between the ball and the material when the measurement was done in dry condition. On the other hand, the inner surface of the indentation when the test was carried out on samples submerged in water showed a very different aspect including striations, which contain small cracks observable at high magnification, and preferentially located at cellular boundaries (LTF zones).

3. Cyclic loads

The behavior of samples tested after applying cyclic loads to samples a of melt C on ADI Grade 2 is summarized in Fig. 5 where the crack length is plotted against test time and number of cycles. It can be noticed that cracks nucleate earlier in submerged samples than in samples tested in dry condition, and also that the crack growth rate is greater for the submerged samples, as shown by the slope of the curves.

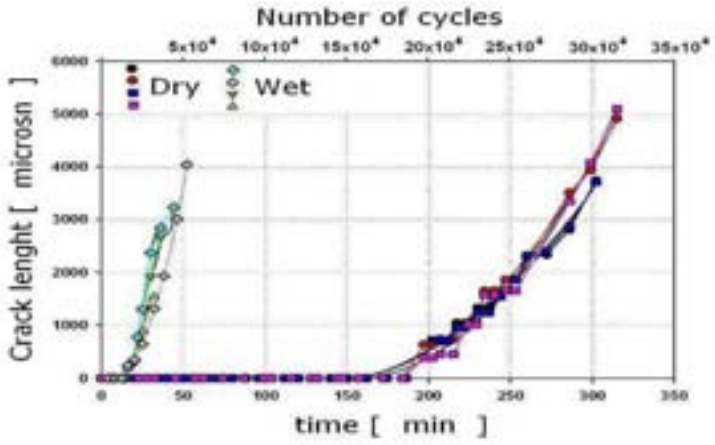

Fig. 5: crack length as a function of test time and number of cycles.

The values measured for nucleation time and growth rate showed very low dispersion. The results shows that the application of cyclic loads under wet conditions severely affects the fatigue resistance of ADI, facilitating the nucleation of cracks and increasing the fatigue crack growth rate.

4. Influence of testing under controlled electrochemical potential

The application of controlled potential during tensile testing of ADI in contact with water neither enhances nor inhibits the embrittlement effect observed under free potential testing conditions, as shown by the results listed on Table 6. This has been the case for both anodic and cathodic conditions. This result supports the hypothesis that H atoms are not responsible for the embrittlement.

Table 5: Results of tensile testing of ADI under free and controlled electrochemical potential.

Test condition	U.T.S.[MPa]	Elongation %
E_{CORR}=-0.69/-0.72(SCE)	863	3
Wet cathodic potential=1.45V(SCE)	857	3
Wet anodic potential=-0.55V(SCE)	868	3
Dry	1168	16

Melt D. Sample a. ADI grade 2

These result were also supported by tests performed by Caballero et al. [7]

5. Efficiency of protective coatings.

Despite the apparent lack of practical incidence of the embrittlement effect, the identification of technical means to alleviate its influence is highly desirable. A first look into the problem would indicate the convenience of painting or coating the surface of ADI parts to isolate it from the environment. The ability of different paints and metallic coatings to protect ADI against embrittlement by contact with liquids has been examined experimentally. The results are listed in Table 7. Only an acrylic coating reinforced by fibers worked against embrittlement. It is apparent that for a coating to be effective, it must be able to withstand relatively large elastic deformations. The protection is effective only when the surface layer integrity is not affected by the deformation undergone by the substrate, and then, the contact of water with ADI surface is prevented. Additionally, the efficiency of a water repellent agent was tested. After spraying the samples with WD40 ®, they were submerged in water and tested. No signs of embrittlement were observed.

Table 6

Sample ID/test condition	U.T.S. [MPa]	δ [%]
Uncoated/Dry	1050	14.8
ASTM 897M-06	900	9
Uncoated/Wet	843	1.2
H-Epoxy/Wet	837	1.4
S-Epoxy/Wet	873	3
Polyester/Wet	823	3.4
Polyester-U/Wet	807	4
E-Zinc/wet	817	1.3
M-Zinc/wet	833	2.8
E-Tin/Wet	795	3.3
Acrilyc w/fibers/Wet	1010	13.8
WD40®/Wet	1040	14.6

Melt E. Sample a. ADI grade 2

6. Influence of Chemical Composition and fracture model

Evaluation on unalloyed samples

Since, as discussed in section 1-b, LTF zones are the main spots for crack initiation when the material is loaded, it is important to assess the influence of the characteristics of the LTF zones on the embrittlement of ADI. With this aim, grade 2 ADI samples of the unalloyed Melt F, which show very low microsegregation at the LTF, were tested in wet conditions, resulting in drops of 15% in UTS and 80% in elongation, while yield stress remained at the same level. As opposed to what was hypothesized, the use of non-alloyed ductile iron with minimized LTF zones neither inhibited nor reduced the embrittlement phenomenon.

The microscopical study of the lateral surface after loading the samples at higher magnification reported nucleation and growth of cracks in LTF zones. These observations demonstrate that the initiation of cracks in unalloyed DI proceeds in the same manner as that previously verified in low alloy DI, thereby indicating that suppressing the alloy elements in the melt does not improve the strength of LTF zones nor prevents crack initiation.

Fracture mechanism model

It has been shown that microsegregated regions of the ADI microstructure, usually referred to as Last To Freeze (LTF), cracked during testing after plastic deformation starts, acting as initiation sites of the embrittlement process (Fig. 3).

The ductile fracture process is sketched in Fig. 6a, where the classic mechanism of growth and coalescence of voids opperate in nodule cavities and inclusion possibly located at LTF.

A different mechanism is proposed for liquid submerged samples (Fig. 6b). In this case, the first few atomic layers at the crack tip adsorb water molecules that weaken the metal interatomic bonds and facilitate the dislocation nucleation. Alternated dislocation injection from the crack tip on planes D1 and D2 produces a crack tip growth Δa. New voids

generation produce further crack growing by alternate slip coalescence. In this manner, the macroscopic fracture bisects the active slip planes.

Compared with the ductile process less blunting occurs at crack tip, strains ahead of crack tip are lower and voids form only just ahead of cracks. Therefore, the fracture surface displays small shallow dimples as shown in Fig 6b.

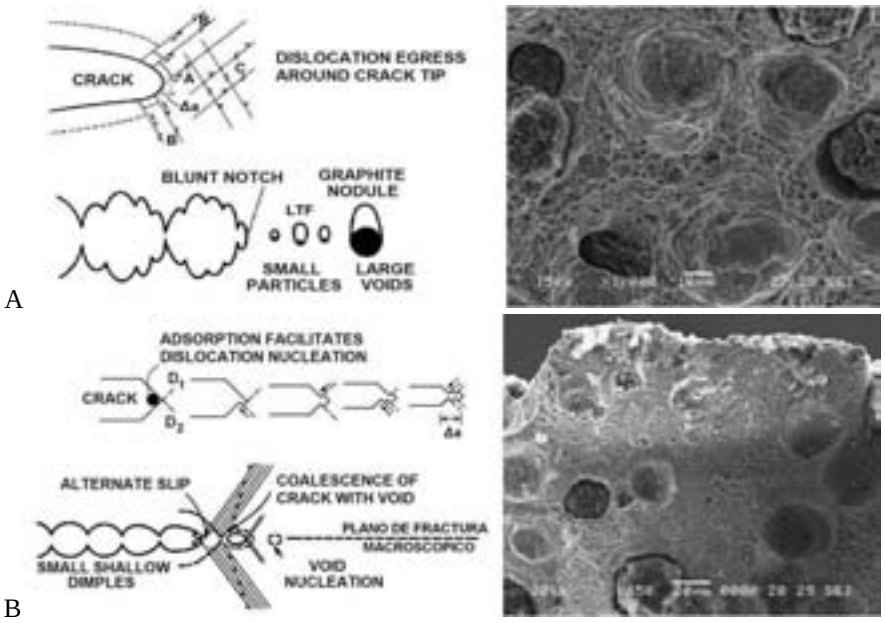

Fig.6: Ductile growth (A) and water assisted growth (B).

The fracture surface of a sample submerged is shown in Fig. 7. The enclosed area at the top is the zone where the crack started to grow with water assistance. It is shown that after reaching a critical size the fracture continues with the ductile mechanism (area outside the white line).

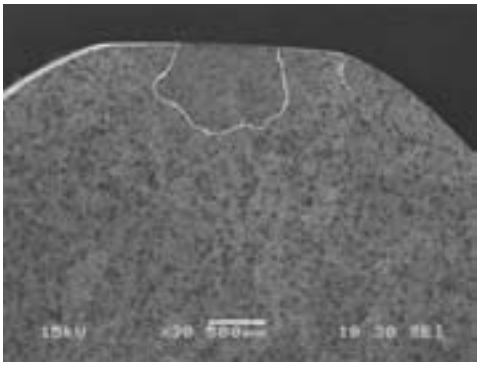

Fig.7: Fracture surface of a tensile sample.

Final Remarks

The research on the embrittlement of ADI over the last years has proven that:

1. Significant drops in UTS and elongation are caused by the presence of water and other liquids in contact with the surface of the sample. Different liquids cause dissimilar degrees of embrittlement.
2. The presence of liquids facilitates the initiation of surface cracks. Cracks nucleate at the microsegregated last to freeze portions of the metal matrix.
3. The presence of water on the surface of ADI causes also drops on fracture toughness and increase of hardness values.
4. The application of cyclic loads under wet conditions severely affects the fatigue resistance of ADI, facilitating the nucleation of cracks and increasing the crack growth rate.
5. The strategy of protecting the surface by coatings to avoid embrittlement is effective only when the integrity of the coating surface layer is not affected by the deformation undergone by the substrate, and then, the contact of water with ADI surface is prevented.
6. The amount of alloy elements present in the alloy does not influence the embrittlement degree of ADI, i.e., a stronger microsegregation at the LTFs does not affect the amount of embrittlement.

References

1. S. Komatsu; C.Q .Zhou; S. Shibutani; Y Tanaka, Int. J. Cast Metals Res., **11,** 1999. p. 539-544
2. S Komatsu, Y. Osafune, Y. Tanaka, K. Tanigawa, S. Shibutani, H. Kyogoku, Int. J. Cast Metals Res. **16**, 2003 p. 209-214
3. R. A. Martínez, R. E Boeri, J. A Sikora,, Int. J. Cast Metals Res., **13,** 2000 p. 9-15
4. R. A. Martínez, S. N. Simison and R. E. Boeri, 2002 World Conference on ADI, pp. 91-96, 26-27 September 2002, Louisville, KY. USA
5. R. A. Martínez, S.N. Simison and R .E. Boeri, Int. J Cast Metals Rev. 2003 Vol. 16 no. 1-3, pp. 251-256
6. L. Masud, R. A. Martínez, S. Simison and R. E. Boeri ,Journal of Material Science.38 (2003) 2971-2977
7. L. Caballero, M Elices and R.N. Parkins. Corrosion. Vol. 61, No.1. 2005 pp. 51-57
8. B. Daga, R. A. Martínez, S. Simison, R. E. Boeri, Annals of the Seminar SAM / CONAMET Congress/ MATERIA Symposium 2003, San Carlos de Bariloche, Argentina. pp. 647-650
9. B. Laine, S. N. Simison, R. A. Martínez, R. E. Boeri, Annals of the Congress CONAMET/ SAM – SIMPOSIO MATERIA 2002, Santiago de Chile, Chile. pp. 121-126
10. T. Lemme, R. A. Martínez, S. N.- Simison, R. E. Boeri, Conference SAM –CONAMET 2004, La Serena, Chile. pp. 457-462
11. R E. Boeri; R A. Martínez; Materials Science and Technology, Volume 29, Number 6, June 2013 , pp. 665-671(7)
12. R.A. Martinez ,Engineering Fracture Mechanics 77 (2010) 2749–2762
13. P. Zanotti, S. Simison, R. A. Martínez, R. E. Boeri, Annals of the Binational Congress SAM/CONAMET 2005, Mar del Plata, Argentina. ISBN 987-2243-0-8
14. S. Lynch, Mater. Forum, 11, 268-283, 1988.
15. Anderson, T. L. (1994) Fracture Mechanics. Fundamentals and Applications. Chapter 12. 2nd edition, CRC Press; Boca Raton, Florida, USA. (book)

Numerical Simulation of Dimensional Change during Austempering Heat Treatment in Ductile Cast Iron

A.D. Boccardo[1*], A.D. Sosa[2,3], M.D. Echeverría[2,3], P.M. Dardati[1], D.J. Celentano[4], and L.A. Godoy[5]

[1]Departamento de Ingeniería Mecánica, Universidad Tecnológica Nacional, Facultad Regional Córdoba. Maestro M. Lopez esq. Cruz Roja Argentina, Córdoba, Argentina.

[2]School of Engineering, Universidad Nacional de Mar del Plata, J.B. Justo 4302, Mar del Plata (B7608FDQ), Argentina.

[3]Metallurgy División, INTEMA, J.B. Justo 4302, Mar del Plata (B7608FDQ), Argentina.

[4]Departamento de Ingeniería Mecánica y Metalúrgica, Pontificia Universidad Católica de Chile. Av. Vicuña Mackenna 4860, Santiago de Chile, Chile.

[5]Facultad de Ciencias Exactas, Físicas y Naturales, Universidad Nacional de Córdoba, CONICET. Av. Velez Sársfield 1611, Córdoba, Argentina.

Changes in the form and dimensions of ductile iron parts occur during the austempering process, and this poses a challenge whenever tight tolerances need to be satisfied. Thus, it is important to be able to predict the deformation which occur under heat treatment to evaluate the minimum and maximum stock material required to perform the final machining. Moreover, parts could be machined before heat treatment under better machinability condition. This paper presents a thermo-mechanical-metallurgical formulation to predict the dimensional changes and final microstructure of a ductile cast iron part as a consequence of the austempering heat process. A coupled thermal, mechanical and metallurgical problem is solved using a finite element method, to take into account different coupled and complex phenomena present in this process. As an illustration, the heat treatment of a specimen is considered and results are validated by comparison with experimental data.

Keywords: austempered ductile iron, dimensional change, numerical simulation, finite element analysis.

Introduction

Nodular cast iron is currently employed in industry because of its improved mechanical properties and facility to cast. Its microstructure is formed by graphite nodules which are inserted in a metal matrix. In an as-cast nodular cast iron, the matrix may be ferritic, ferritic-perlitic, or perlitic. The mechanical properties of nodular cast iron may be improved by means of an austempered heat treatment, which is the subject of this paper.

The ever growing use of austempered ductile iron (ADI) in manufacturing high strength parts, such as gears and other elements and devices of the agricultural and transport industry, has incresed the interest of ADI researchers and users in several aspects of metallurgy and optimal sequence of parts manufacturing.[1-5]

To perform an austempering treatment, the material is initially heated and kept at a temperature between 1123K and 1223K in order to obtain a matrix which is completely austenitic and with the appropriate carbon contents. Next, the material is suddenly cooled down to a temperature between 523K and 723K to initiate the austempering process. The chosen temperature for the treatment depends on the desired microstructure (lower or upper bainitic ferrite). Finally, the part is cooled until ambient temperature is reached.[5,6]

As a consequence of the heat treatment process, there are changes in the part dimensions.[4,7] In several experimental reports, the influence of chemical composition, part shape, austenized and austempered temperature, initial matrix, and density of graphite nodules on the change of dimensions have been observed.[2,4,7,8] Parts with ferritic initial matrix undergo smaller changes in dimensions that those based on an initially perlitic matrix. Therefore, in some applications, parts with an initial perlitic matrix are subjected to a ferritic treatment prior to an austempering treatment.[4] Parts with high graphite nodule density experience large changes.[8]

The quantitative prediction of dimensional change (DC) plays a key role in the mass production of parts, because it allows not only performing final machining before heat treatment under better machinability conditions but also allows obtaining parts with the required dimensional tolerances.

Taking the data from experimental studies into account, Dai Pra *et al*. developed a fuzzy model to predict DC% values, involving ten typical parameters corresponding to chemical composition and thermal cycle. The predictions confirmed the experimental information; and relevant data concerning the individual effects of the alloying elements and

* Corresponding author, email: aboccardo@mecanica.frc.utn.edu.ar

relative compositions were obtained, not available in systematic studies previously reported.[9] There are models which allow predicting residual stresses and the final shape of nodular cast iron parts following solidification and subsequent cooling down to the ambient temperature[10-12], but no models have yet been developed for the parts which have been subjected to austempering treatment.

This paper presents a thermo-mechanical-metallurgical formulation to represent the austempering heat treatment process of a nodular cast iron. The model allows predicting phase fractions, final shape, and residual stresses in a part, by taking into account the initial microstructure, chemical composition, temperature of the thermal process, and initial shape of the part.

The thermo-mechanical-metallurgical formulation is first presented, followed by results of experiments carried out to validate the computational tools. Details of the implementation of the model are provided.

Thermo-mechanical-metallurgical formulation

The heat treatment process to obtain an ADI may be modeled by taking into account thermal, mechanical, and metallurgical problems. The thermal problem considers the temperature evolution; the mechanical problem accounts for strain and stress evolution due to heating, cooling and phase change; whereas the metallurgical problem deals with the evolution of the phase in the material. Those are interdependent problems, as shown in Fig. 1.

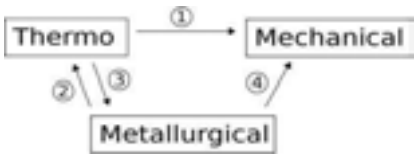

Fig.1: Interactions between thermal, mechanical and metallurgical problems.

The mechanical model receives information concerning temperature and phase change through interactions 1 and 4 in Fig. 1, which is used in the computation of strains and stresses. Interaction 2 accounts for the thermal problems, the heat liberation or absorption produced during phase change. The phase change is related to temperature through interaction 3.

Thermo-mechanical model

A fully coupled thermal-stress analysis in ABAQUS standard was used in this work. The temperatures are integrated using a backward-difference scheme, and the nonlinear coupled system is solved using Newton's method.[13] An exact implementation of Newton's method involves a non-symmetric Jacobian matrix, where the coupled equations are:

$$\begin{bmatrix} k_{uu} & k_{u\theta} \\ k_{\theta u} & k_{\theta\theta} \end{bmatrix} \begin{Bmatrix} \Delta u \\ \Delta\theta \end{Bmatrix} = \begin{Bmatrix} R_u \\ R_\theta \end{Bmatrix} \quad (1)$$

Solving this system of equations requires the use of the unsymmetric matrix storage and solution scheme. The mechanical and thermal equations must be solved simultaneously.

Implementation of interactions 1 and 4 was archived by using the general formulation for a fully solid material, which states that the total mechanical strain may be written as the sum of elastic, viscoelastic, thermal and phase change contributions[14]:

$$\varepsilon_{ij} = \varepsilon_{ij}^{el} + \varepsilon_{ij}^{vp} + \varepsilon_{ij}^{th} + \varepsilon_{ij}^{pc} \quad (2)$$

For an isotropic solid material, the thermal strain tensor is evaluated with equations 3. The strains due to reverse eutectoid transformation[14] and bainitic transformation[15] are evaluated with equations 4 and 5 respectively. These equations have been implemented in ABAQUS by means of a subroutine called UEXPAN.

$$\varepsilon_{ij}^{th} = \alpha_t \left(T - T_{ref}\right)\delta_{ij} \quad (3) \qquad \varepsilon_{ij}^{pc} = \beta_{pc} f_{pc} \delta_{ij} / 3 \quad (4) \qquad \varepsilon_{ij}^{pc} = \frac{1}{3}\left(1 - \frac{a_\gamma^3}{\beta + a_{e\gamma}^3}\right)\delta_{ij} \quad (5)$$

$$\beta = \frac{2a_\alpha^3 - a_{e\gamma}^3}{1 + \left(2V_\gamma a_\alpha^3\right)/\left(V_{\alpha b} a_{e\gamma}^3\right)} \quad (6)$$

The interaction 2 is taken into account through evaluation of phase change heat flow with equation 7, which is implemented in subroutine HETVAL.[16]

$$r = L\ \rho\ f_{pc} \quad (7)$$

Metallurgical model

A reverse eutectoid transformation occurs during heating of a part starting at ambient temperature up to the austenized temperature, during which an initial ferritic-perlitic matrix is transformer into austenite. As a following stage, during cooling from austenized to austemperized, as the temperature becomes lower than bainite start, there is a bainitic transformation. During this bainitic transformation, part of the austenite is transformed into a bainitic ferrite. Finally, during the subsequent cooling to ambient temperature, the possibility of the existence of a martensitic transformation is considered.

The model that takes the above mentioned transformations into account has been implemented in subroutine USDFLD in ABAQUS. Interaction 3 has been taken into account by means of subroutine GETVRM.

Reverse eutectoid transformation

The reverse eutectoid transformation is modeled by considering stable and metastable transformation.[17] The initial microstructure is formed by graphite nodules, ferrite halos and perlite colonies of diverse sizes. For the stable transformation, for each size of graphite nodules, a representative volume element (RVE) formed by a graphite nodule surrounded by a ferrite shell is considered.[18] In the metastable transformation, for each perlite colony, a RVE is formed by half layer of cementite and half of the ferrite[19] (see Fig. 2).

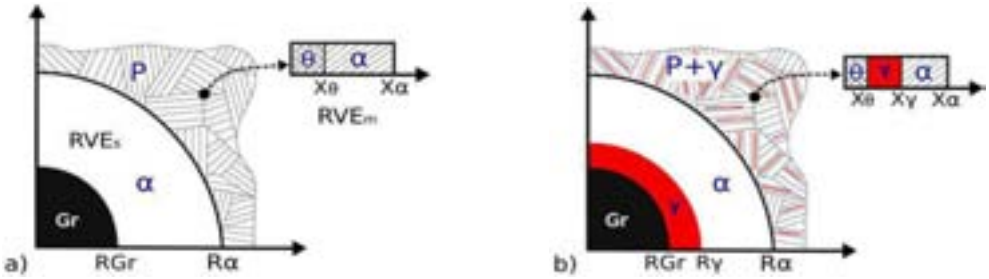

Fig.2: RVE employed to model the stable reverse eutectoid transformation (RVEs) and metastable reverse eutectoid transformation (RVEm). Schematic representation of phases (a) before transformation; (b) during transformation.

The model for stable reverse eutectoid transformation discussed above predicts the evolution of graphite, ferrite, and austenite fractions, by accounting for the graphite nodule size, ferrite shell, and chemical composition of the alloy. The transformation starts when the temperature reaches a value T_α^o.[20] Austenite nucleation occurs at the graphite-ferrite interphase.[18] Instantaneous nucleation of an austenite shell of radius 1% larger that the graphite nodule is considered. The mechanism of growth is governed by long range carbon diffusion from graphite to ferrite through the interfaces graphite-austenite and austenite-ferrite.

On account of the families of equal size graphite nodules, the graphite, austenite, and ferrite fractions may be written as:

$$V_{Gr} = \frac{4\pi}{3}\sum_{i=1}^{nfam} N_{nfam_i} r_{Gr_i}^3 \quad (8) \qquad V_{\gamma s} = \frac{4\pi}{3}\sum_{i=1}^{nfam} N_{nfam_i}\left(r_{\gamma_i}^3 - r_{Gr_i}^3\right) \quad (9) \qquad V_\alpha = \frac{4\pi}{3}\sum_{i=1}^{nfam} N_{nfam_i}\left(r_{\alpha_i}^3 - r_{\gamma_i}^3\right) \quad (10)$$

The increment of graphite and austenite radius for each family size are computed through the mass balance condition for carbon at the mobile interfaces graphite-austenite and austenite-ferrite is considered, together with carbon diffusion in steady state, and mass conservation of carbon in the RVE, in the form:

$$\frac{dr_{Gr_i}}{dt} = \frac{D_\gamma \rho_\gamma r_{\gamma_i}}{r_{Gr_i}\left(r_{\gamma_i} - r_{Gr_i}\right)} \frac{\left(C_{\gamma/\alpha} - C_{\gamma/Gr}\right)}{\left(C_{Gr}\rho_{Gr} - C_{\gamma/Gr}\rho_\gamma\right)} \quad (11)$$

$$\frac{dr_{\gamma_i}}{dt} = \frac{D_\alpha \rho_\alpha r_{\alpha_i}}{r_{\gamma_i}\left(r_{\alpha_i} - r_{\gamma_i}\right)} \frac{\left(C_{\alpha s} - C_{\alpha/\gamma}\right)}{\left(C_{\gamma/\alpha}\rho_\gamma - C_{\alpha/\gamma}\rho_\alpha\right)} - \frac{D_\gamma \rho_\gamma r_{Gr_i}}{r_{\gamma_i}\left(r_{\gamma_i} - r_{Gr_i}\right)} \frac{\left(C_{\gamma/\alpha} - C_{\gamma/Gr}\right)}{\left(C_{\gamma/\alpha}\rho_\gamma - C_{\alpha/\gamma}\rho_\alpha\right)} \quad (12)$$

$C_{\gamma/\alpha}$ and $C_{\alpha/\gamma}$ are evaluated using expressions given by Lacaze and Gerval.[21] $C_{\gamma/Gr}$ is computed with expressions given by Boeri.[22]

The model of the metastable reverse eutectoid transformation predicts the evolution of the perlite and austenite fractions, and takes into account the inter-laminar spacing of perlite colonies and the chemical composition of the alloy. The transformation starts when the temperature reaches the higher of T_P or T_α.[20] Nucleation and growth of austenite occurs at the cementite-ferrite interface[19]. Instantaneous nucleation is considered of an austenite layer with a thickness

equal to 1% of the cementite layer. The growth mechanism is governed by long-range carbon diffusion, from cementite to ferrite, through the interfaces cementite-austenite and austenite-ferrite.

Perlite and austenite fractions are calculated for different perlite colonies, as:

$$V_P = \sum_{j=1}^{ncol} V_{col_j}\left[1 - \frac{2\left(x_{\gamma_j} - x_{\theta_j}\right)}{sip_j}\right] \quad (13) \qquad V_{\gamma m} = 2\sum_{j=1}^{ncol} V_{col_j}\frac{\left(x_{y_j} - x_{\theta_j}\right)}{sip_j} \quad (14)$$

The mass balance condition for carbon at the mobile interfaces cementite-austenite and austenite-ferrite is considered, together with carbon diffusion in steady state, and mass conservation of carbon in the RVE, in order to evaluate the increment of position of interfaces in the form:

$$\frac{dx_{\theta_j}}{dt} = \frac{D_\gamma \rho_\gamma}{\left(x_{y_j} - x_{\theta_j}\right)}\frac{\left(C_{\gamma/\alpha} - C_{\gamma/\theta}\right)}{\left(C_\theta \rho_\theta - C_{\gamma/\theta}\rho_\gamma\right)} \quad (15)$$

$$\frac{dx_{\gamma_j}}{dt} = \frac{D_\alpha \rho_\alpha}{\left(x_{\alpha_j} - x_{\gamma_j}\right)}\frac{\left(C_{\alpha m} - C_{\alpha/\gamma}\right)}{\left(C_{\gamma/\alpha}\rho_\gamma - C_{\alpha/\gamma}\rho_\alpha\right)} - \frac{D_\gamma \rho_\gamma}{\left(x_{\gamma_j} - x_{\theta_j}\right)}\frac{\left(C_{\gamma/\alpha} - C_{\gamma/\theta}\right)}{\left(C_{\gamma/\alpha}\rho_\gamma - C_{\alpha/\gamma}\rho_\alpha\right)} \quad (16)$$

$C_{\gamma/\theta}$ is evaluated with an equation proposed by Kapturkiewicz *et al.*[19]

The total austenite fraction is computed by means of the sum of austenite fraction formed during the stable and metastable transformations:

$$V_\gamma = V_{\gamma s} + V_{\gamma m} \quad (17)$$

Bainitic Transformation

The model employed for the bainitic transformation allows computation of bainitic ferrite and residual austenite. The carbon mass in graphite nodule is assumed to by constant, with the consequence that the graphite volume fraction remains constant[23]. The kinetics of growth of bainitic ferrite is modeled by means of Avrami's equation[24], equation (18). The maximum fraction of bainitic ferrite is computed using the lever-rule[5], equation (19). The residual austenite fraction is computed from equation (20).

$$V_{\alpha b} = V_{\alpha b}^{max}\left[1 - \exp\left(-k_a t^{m_a}\right)\right] \quad (18) \qquad V_{\alpha b}^{\max} = \left(1 - V_{Gr}\right)\left(C_{\gamma To} - C_\gamma\right)/\left(C_{\gamma To} - C_{\alpha b}\right) \quad (19) \qquad V_\gamma = 1 - \left(V_{Gr} + V_{\alpha b}\right) \quad (20)$$

Martensitic Transformation

The martensitic transformation occurs when the temperature martensite start (M_s) is higher than the ambient temperature[5]. The temperature M_s depends on the concentration of alloy components in the residual austenite. The carbon concentration plays an important role because the latter increases as the bainitic transformation progresses. Thus, M_s is inversely proportional to austemperized time.

The model employed for the martensite transformation evaluates M_s once cooling starts from the austemperized temperature to ambient temperature. If M_s is higher than the ambient temperature, then part of the residual austenite is transformed into martensite. The residual austenite that did not become martensite is known as retained austenite. The volume fractions of martensite[25] and retained austenite are computed by equations (21) and (22).

$$-\ln\left(1 - V_{\alpha'}\right)/V_{\alpha'} = 1 + c_2\left(M_s - T\right) \quad (21) \qquad V_\gamma = 1 - \left(V_{Gr} + V_{\alpha b} + V_{\alpha'}\right) \quad (22)$$

Experimental Procedure

Twelve cylindrical coupons, having 10mm diameter and 100mm length, were tested as a part of this research. The chemical composition of the coupons is given in table 1.

Table 1: Chemical Composition [w%]

Melt	C	Si	Mn	Mg	Cu	P, S	EC
A	3.36	3.13	0.32	0.5	0.25	0.25	4.4
B	2.81	3.54	0.36	0.64	0.11	0.24	4
C	2.64	4.2	0.36	0.62	0.11	0.24	4

The temperatures of austenization were $T_{\gamma A}$=1173K, $T_{\gamma B}$=1193K y $T_{\gamma C}$=1213K for the three chemical compositions A, B y C respectively. In all tests, the austemperized temperature was T_{α}=633K, and the time was 90 minutes.

All dimensions were measured before and after heat treatment. A millesimal outside micrometer (0-25mm) of accuracy ±(1+L/75)μm was used to measure the cylindrical samples diameter. The length was measured with a Coordinate Measuring Machine of accuracy ±(1.2+ L/1000)μm. To achieve greater repeatability in measurements, special supports were used, which allowed fixing specimens in same position before and after heat treatment.

The metallographic characterization of the specimens before and after heat treatment was performed using conventional methods of inclusion and polishing. The polished surfaces were etched with nital 2%. The microstructures were analyzed using an Olympus PMG3 optical microscope; and the proportions of the phases in each sample were quantified by means of image software.

In all cases, castings displayed a nodule size 5, nodularity higher than 80%. The nodule count and phase fractions in as-cast condition are given in table 2. As expected, as Si content increased, the amount of ferrite in the as-cast microstructure also increased. Fig. 3 depicts the representative microstructures under as-cast condition for each melt under study.

Table 2: Nodule count [nodules m^{-3}] and phase fractions [%] in as-cast condition

Melt	nodule count	V_{Gr}	V_{α}	V_P
A	$1.563x10^{12}$	9	39.5	51.5
B	$2.164x10^{12}$	11.4	68.9	19.7
C	$1.822x10^{12}$	10.5	79.5	10

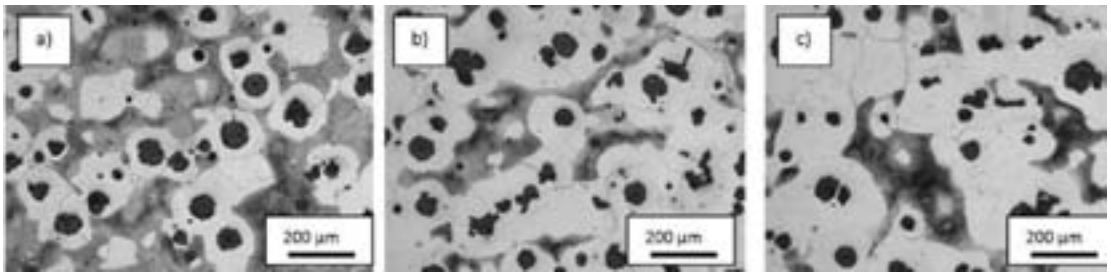

Fig. 3: Microstructures in as-cast condition: (a) melt A, (b) melt B, and (c) melt C.

The X-ray diffraction patterns (XRD) corresponding to the different {hkl} reflections in ferrite and austenite phases were measured in ADI samples to estimate the amount of austenite and its carbon content. Graphite-monochromated Co-Kα radiation (λ=0.1789nm) was the option of choice for such measurement. The X-ray tube was operated at 40kV and 30mA. Three XRD intensity patterns versus 2θ were obtained for each ADI sample, and a scan in the range of 47º to 62º with a 2θ step of 0.05º and 0.05 seconds by step was performed. Powder Cell software developed by Kraus and Nolz[26], for peak profile refinement was applied to analyze the XRD patterns and to obtain peak positions and intensities as well as austenite volume fraction and its lattice parameter.

The percentage variations of other phases, such as non-retained austenite and/or carbides, were disregarded as they are believed not to affect V_{γ} and C_{γ} estimations.

The percent dimensional change (DC_i) was calculated using the measured dimensions values before and after each austenitizing-austempering heat treatment based on expression (23). The arithmetic mean of DC_i (DC_{Mean}) and its dispersion (ΔDC) were calculated for each group of specimens from a melting-heat treatment batch using Equations (24) and (25).

$$DC_i = \frac{(l_f - l_o)}{l_o} 100 \quad (23) \qquad DC_{Mean} = \frac{1}{n}\sum_{i=1}^{n} DC_i \quad (24) \qquad \Delta DC = \sqrt{\frac{1}{n-1}\sum_{i=1}^{n}(DC_i - DC_{Mean})^2} \quad (25)$$

Numerical Procedure

The specimen described in the experimental procedure was heat treated using the proposed formulation. Owing to the symmetry, half sample was discretized using 250 axisymmetric elements of 8 nodes. The thermo-mechanical-microstructural properties of nodular cast iron are listed in table 3. The thermal properties of casting/bath salt interface are listed in table 4 and thermal properties of casting/furnace and casting/environment interfaces are listed in table 5.

Table 3: Thermo-mechanical-microstructural properties of nodular cast iron.[5,12,15,17]

Temp [K]	Young's Modulus [MPa]	Yield strength [MPa]
293	163500	260
773	110900	130
1273	28400	20

Poisson's ratio: 0.33

Thermal dilatation [K^{-1}]: $\alpha_{t\alpha p}= 14x10^{-6}$ (ferrite and perlite); $\alpha_{t\gamma}= 25.61x10^{-6}$ (austenite); $\alpha_{t\alpha b}= 13.5x10^{-6}$ (bainitic ferrite)

Lattice parameters at ambient temperature [$1x10^{-10}$m]: $a_{\alpha o}= 2.873$; $a_{\gamma o}= 3.555+0.04C_{\gamma o}$

Eutectoid reverse phase change volumetric deformation: $\beta_{pc}= -6.22x10^{-4}$

Temp [K]	Conductivity [W m^{-1} K^{-1}]	Specific heat [J kg^{-1} K^{-1}]	Density [kg m^{-3}]
293	44.1	500	7277
833	37.1	750	7120
1253	22.5	820	7070

Latent heat of reverse eutectoid transformation [J kg^{-1}]: $L_P= 9x10^4$(perlite); $L_\alpha= 4x10^4$ (ferrite)

Avrami's parameters: k_a=0.032617; m_a=1.2146

Table 4: Thermal properties of casting/bath salt interface.

Temp [K]	Heat transfer coefficient [J s^{-1} m^{-2} K^{-1}]
473	250
573	400
773	3000
1223	10

Table 5: Thermal properties of casting/furnace and casting/environment interfaces.[17]

Interface	Heat transfer coefficient [J s^{-1} m^{-2} K^{-1}]
Casting/furnace	70
Casting/environment	70

Results and Discussion

The formulation presented before was used to describe the thermo-mechanical-metallurgical response of the ADI used in the experiments. The evolution of computed phases for the melt A is presented in Fig. 5a. The phases at the end of the heat treatment are included in table 6. The model predicts that martensite is not present; this is in agreement with the experiments because the micrographs obtained following austemperized do not show martensite in the material. The matrix from micrographs is composed of ausferrite (96%) and retained austenite (4%).

Table 6: Computed phase fractions [%] obtained with the heat treatment.

Melt	V_{Gr}	$V_{\alpha b}$	V_γ	$V_{\alpha'}$
A	8.46	49.63	41.91	0
B	6.67	46.01	47.32	0
C	6.17	42.06	51.77	0

Effects due to Si content in phase fractions are observed: A decrease in the quantity of Si produces an increase in the fraction of bainitic ferrite, while the fraction of retained austenite decreases. This is due to (a) the concentration of carbon at equilibrium in austenite at the austenized temperature is virtually the same for all casts considered; and (b) the carbon concentration in residual austenite for which the bainitic transformation ($C_{\gamma To}$) is arrested, increases as the quantity of Si decreases.

The dimensional changes (length and diameter) of the coupon are shown in Fig. 4; both variations were obtained via testing and simulation. The evolution of computed longitudinal displacement of the end of half cylinder for the three melts is presented in Fig. 5b.

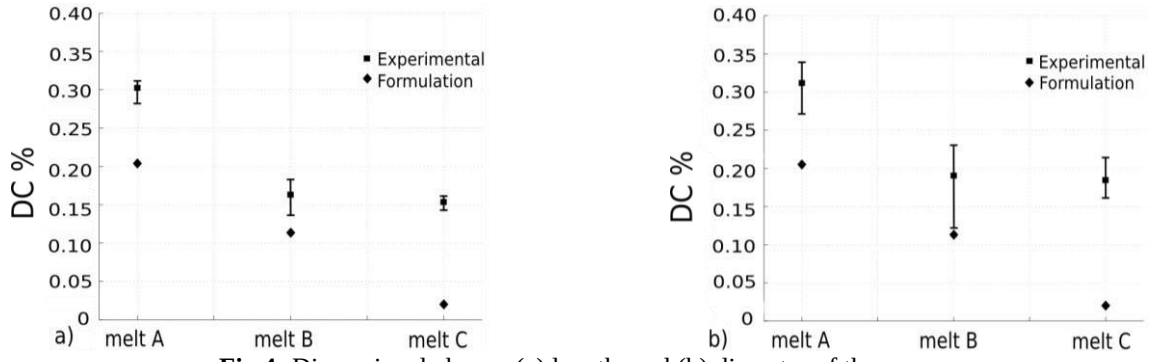

Fig.4: Dimensional change (a) length; and (b) diameter of the coupon.

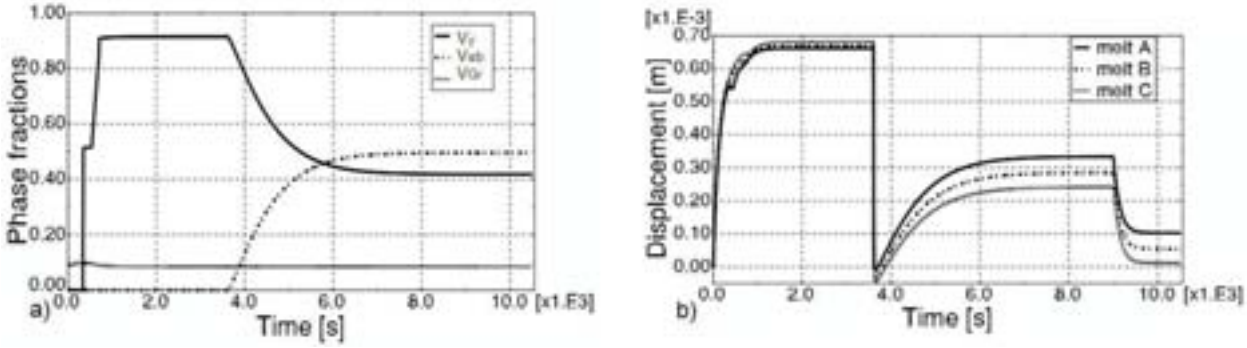

Fig.5: Evolution of computed phases for melt A (a) and evolution of computed longitudinal displacement of the end of half cylinder for three melts (b).

Next, the influences of the Si contents and initial geometry on the change in geometry were investigated. In the experiments it is possible to observe that an increase in Si concentration has the effect of reducing the changes in the geometry of the part. The Si content has an effect on the type of matrix of the cast material. By increasing the quantity of Si it is possible to obtain a matrix with higher ferrite contents. As mentioned before, other authors reported a less significant change in geometry in parts with ferritic matrix.[4] Other aspect to be taken into account is that an increase in Si contents yields a lower volume fraction of bainitic ferrite and lower carbon concentration in residual austenite during the bainitic transformation; this combination has the effect of a lower expansion in the part.[15]

The results of the computational simulation follow the same trend, with differences of 30%, 30% and 80% (for casts A, B, C, respectively) with respect to the experiments.

In the testing performed in this research the coupon diameter had larger relative changes than the length. The trend is not detected in the simulations. It may be convenient to perform new experiments with coupons of different geometries to better understand this effect.

Conclusions

A thermo-mechanical-metallurgical formulation has been presented to simulate the austempering treatment of a nodular cast iron. The model predicts phase fractions, final shape, residual stresses, taking into account the initial microstructure, chemical composition, temperature of heat treatment, and initial shape of the part.

The model was employed to simulate the results of an austempering heat treatment of cylindrical coupons. The response was investigated to account for different initial microstructures, chemical compositions and temperatures of the process.

Comparison between experiments and computations show that the model is sensitive to the parameters which were considered in the experiments. The calculated changes in geometric dimensions in the model are considered to be adequate for the melts A and B. For the melt C it is necessary a better model for take into account interactions 1 and 4.

As further work, testing new coupons with differences in geometry will be done to investigate the influence of the initial shape in more detail.

List of symbols

α_{ti}	coefficient of thermal expansion of ductile iron with matrix i (tangent), K^{-1}
$a_{\alpha,\gamma,e\gamma}$	lattice parameter of ferrite, austenite and carbon enriched austenite at the transformation temperature, m
β_{pc}	phase change volumetric deformation

$C_{\gamma/\alpha,\gamma/Gr,\gamma/\theta}$	equilibrium carbon concentration of austenite at austenite-ferrite, austenite-graphite and austenite-cementite interface respectively, wt%
$C_{\gamma,\gamma To,\alpha b}$	average carbon concentration of austenite prior to bainitic transformation, residual austenite when bainitic transformation stops and bainitic ferrite respectively, wt%
$C_{Gr,\theta}$	carbon concentration of graphite and cementite respectively, wt%
$C_{\alpha/\gamma}$	carbon concentration of ferrite at ferrite-austenite interface, wt%
$C_{\alpha s,\alpha m}$	carbon concentration of ferrite in r_α and x_α respectively, wt%
c_2	parameter of martensite transformation
$D_{\gamma,\alpha}$	diffusion coefficient of carbon in austenite and ferrite respectively, $m^2\ s^{-1}$
DC	dimensional change
Δu, $\Delta\theta$	corrections to the incremental displacement and temperature respectively
ΔDC	dispersion of dimensional change
δ_{ij}	Kronecker delta
ε, $\varepsilon^{el,vp,th,pc}$	mechanical, elastic, viscoelastic, thermal and phase change strain tensor respectively
ρ, $\rho_{\gamma,\alpha,Gr,\theta}$	density of nodular cast iron, austenite, ferrite, graphite and cementite respectively, kg m^{-3}
f_{ph}	phase change function
k_a, m_a	Avrami's parameters
k_{ij}	submatrices of the fully coupled Jacobian matrix
L	latent heat, J kg^{-1}
$l_{o,f}$	initial and final length respectively, m
M_s	temperature martensite start, K
ncol, nfam	number of colonies of perlite and number of families of graphite nodule
N_{nfam}	number of nodule for unit of volume of a family, nodule m^{-3}
$r_{Gr,\gamma,\alpha}$	radius of graphite nodule, austenite shell and ferrite halo respectively, m
$R_{u,\theta}$	mechanical and thermal residual vectors respectively
sip	inter pearlite spacing, m
T_{ref}	reference temperature, K
$V_{Gr,\alpha,P,\gamma,\alpha b,\alpha',col}$	volume fraction of graphite, ferrite, perlite, austenite, bainitic ferrite, martensite and a perlite colony respectively
$V_{\gamma s,\gamma m}$	volume fraction of austenite formed in the stable and the metastable reverse eutectoid transformation respectively
$x_{\theta,\gamma,\alpha}$	coordinate of cementite-austenite, austenite-ferrite and ferrite interface respectively, m

References

1. J.R. Keough: AFS Proceeding of the 3rd World Conference on ADI, 1991, 2, 638.
2. O.J. Moncada, R.H. Spicacci and J.A. Sikora: *AFS Trans.*, 1998, 106, 39-45.
3. M.D. Echeverría, O.J. Moncada and J.A. Sikora: *ISIJ International*, 2001, 41, 25.
4. A.D. Sosa, M.D. Echeverría and O.J. Moncada: *ISIJ International*, 2004, 44, (7), 1195-1200.
5. M.A. Yescas-Gonzalés: 'Modelling the microstructure and mechanical properties of austempered ductile iron', PhD thesis, University of Cambridge, Cambridge, UK, 2001.
6. D.C. Putman and R.C. Thomson: *Int. J. Cast. Met. Res.*, 2003, 16, (1-3), 191-196.
7. O. Moncada and J.A. Sikora: *AFS Trans.*, 1996, 104, 577-580.
8. A.D. Sosa, M.D. Echeverría, O.J. Moncada, N. Míngolo and J.A. Sikora. *Journal of Materials Processing Technology*, 2009, 209, 5545-5551.
9. A.L. Dai Pra, M.D. Echeverria, A. Scandurra, O.J. Moncada and J.A. Sikora: *Lat. Am. appl. res. (LAAR)*, 2005, 35, 197.
10. D. Celentano: *Int. J. Plast.*, 2001, 17, 1623-1658.
11. D. Celentano: *Mater. Manuf. Processes*, 2010, 25, (7), 546-556.
12. D.J. Celentano, P.M. Dardati, F.D. Carazo and L.A. Godoy: *Mater. Sci. Technol*., 2013, 29, (2), 156-164.
13. Abaqus analysis user manual. 6.5.4 Fully coupled thermal-stress analysis.
14. J. A. Dantzing and M. Rappaz: 'Solidification', 1st edn, 2009, Switzerland, EPFL Press.
15. H.K.D.H Bhadeshia, S.A. David, J.M. Vitek and R.W. Reed: *Mater. Sci. Technol*., 1991, 7, 686-689.
16. D.M. Stefanescu: 'Science and engineering of casting solidification', 2nd edn, 2009, New York, USA.
17. F.D. Carazo, P.M. Dardati, D.J. Celentano and L.A. Godoy: *Metallurgical and Materials Transactions B*, 2012, 43, (6), 1579-1595.

18. U. Batra, S. Ray and S.R. Prabhakar: *Journal of Materials Engineering and Performance*, 2005, 14, (5), 574-581.
19. W. Kapturkiewicz, E. Fraś and A.A. Burbelko: *Materials Science and Engineering A*, 2005, 413-414, 352-357.
20. R.M. Ghergu, J. Sertucha, Y. Thebault and J. Lacaze: *ISIJ International*, 2012, 52, (11), 2036-2041.
21. J. Lacaze and V. Gerval: *ISIJ International*, 1998, 37, (7), 714-722.
22. R. Boeri: 'The solidification of ductile cast iron', PhD thesis, University of British Columbia, Canada, 1989.
23. W. Kapturkiewicz, A.A. Burbelko and E. Fraś: *Int. J. Cast. Met. Res.*, 2003, 16, (1-3), 287-292.
24. U. Batra, S. Ray and S.R. Prabhakar: *Journal of Materials Engineering and Performance*, 2004, 13, (1), 64-68.
25. S.A. Khan and H.K.D.H Bhadeshia: *Materials Science and Engineering A*, 1990, 129, 257-272.
26. W. Kraus and G. Nolze. Powder Cell 2.3 version, 1998, CPD Newsletter, 20, 274.

Acknowledgement

A.D. Boccardo had a doctoral scholarship from CONICET during this research. L.A. Godoy and A.D. Sosa are members of the research staff of CONICET. D.J. Celentano gratefully acknowledges the support of Fondecyt Project 1130404.

Selected aspects of the use of thermal & derivative analysis to improve macro modeling of solidification for casting iron. Comparison of chosen simulation codes

Zenon Ignaszak[1*], Esteban Codina[2], Jakub Hajkowski[1], Paweł Popielarski[1], Pedro Roquet[3]

[1]Poznan University of Technology, 3 Piotrowo street, 60-965 Poznan, Poland
[2]UPC Labson, Campus Terrassa, Colom, 11, 08222 Terrassa, Barcelona, Spain
[3]Fundiciones de Roda, Disseminats, s/n, Roda de Ter, Spain

The article concerns the influence of grey cast iron density and different trials of fraction of solid curves (influencing latent heat generation) on the formation of shrinkage discontinuities. Two alternatives of density curves were considered (Rho=f(T)): the classical one, (usually applied in macro model simulation codes) and the modified one, which includes graphite expansion (based on compensation of primary shrinkage discontinuities during eutectic phase crystallization). Solid fraction curves applying Newtonian Thermal Analysis (NTA) were estimated. The experimental and numerical simulation tests were performed on the castings, which were made with Derivative Thermal Analysis (DerTA) standard cups and in furan-bonded sand cube mould of 250 mm side and a upper riser ϕ140x200 mm The numerical tests were realized using NovaFlow&Solid (NF&S) and ProCast codes. Also, some tests were realized using ProCast with a micro model (default value parameters). In this work, the coupled influence of both curves on the dynamics of the shrinkage-expansion phenomena and on shrinkage defects prognosis in grey cast iron castings has been revealed.

Keywords: cast iron, simulation codes, macro/micro models, heat source function, porosity defects

Introduction

The defects related to shrinkage remain one of the biggest quality problems. The application of foundry simulation codes in industrial conditions should, above all, ensure the most accurate predictions of casting quality. Only in this case, a proper assessment with criteria of minimum defects related to shrinkage can be stated. This item and the effectiveness of simulation codes using these criteria are the main challenges, regardless of its origin, discretization method and particular user's opinions.

Metal alloys crystallization phenomena simulation is based on mathematical models, which represent the complexity related with physical and chemical processes in a very diversified way. The corresponding simplifications are assigned to applied simulation code and must be taken into consideration in database. The coefficients for the database should be determined by experimental validation by comparing the real and virtual casting process. Sometimes, the analysis can be difficult because the applied simplifications are not usually revealed to the users or not well described in the trouble-shooter (manual or help window in simulation code)[1].

In the literature, problems of determination or validation of databases is named the inverse problem solution. The authors have devoted many of their previous publications on this topic.[1,2,3,4]. Other authors discussed the problem of using more complex models through introducing a new phenomena, which can lead to better formal physical description, for example, nucleation of particular phases, their growth, including intermetallic phases, segregation, shrinkage and stress, and flow in the solid-liquid zone. Despite getting a quasi-ideal model, it is necessary the use of some simplifications and/or empirical models.[1] This is strictly related to a need of disposing the new physical parameters and coefficients (contained in a set of boundary conditions in the material databases), as shown in papers[5,6]. Nevertheless, not all parameters used in simplified models can be used in the complex ones, which is supposed to describe a real casting-mould system in a better way e.g. macro/micro models.

The phenomena, which are the most important in casting processes models, are shrinkage phenomena, compensation (decreasing) by a liquid metal stream, and void micro spaces refilling, which are related to the following items: feeding shrinkage coefficient (shrinkage of overheating and solidification), feeding flow range from the riser head, chills on the oriented (directional) solidification and casting configuration (dimensions and shape). All them are well known by casting process designers. The basic expectation, formulated through virtual simulation models (using preliminary technology concept), is the validation of its correctness regarding the shrinkage defects. The prognosis of these defects and its

* Corresponding autor, e-mail: zenon.ignaszak@put.poznan.pl

comparison with acceptability criteria (formulated in the customer requirements), is a decisive factor in order to accept/refuse castings to be produced using the preliminary technology concept or after its optimization.

Shrinkage phenomena intensity is a result of density and crystallizing phases variability with temperature Rho=f(T). On the other hand, dynamics of the solid phase generation (particular phases), flow conditions (so-called critical fraction of solid phase – critical Fs) and gravity field will also decide the macro- and micro- shrinkage porosities (location and intensity).

This paper presents the application of the Derivative Thermal Analysis (DerTA) of the grey cast iron castings (EN-GJL-250), poured in a standard DerTA cup (single thermocouple), in order to determine the solid fraction curve, Fs=f(T) used in a basic model of generation of the latent heat (macro model). Cooling curve shape in this method is a relatively easy way to obtain information about the crystallization process evolution. Simplified crystallization model has been used by simulation codes for a long time (solidification interpreted as an accumulative growth of the solid phase). Someone still use them (e.g. NF&S). Other codes use a new micro model (alternatively with macro model). A question appears – can the phenomena description in the macro model and the solid fraction curve Fs=f(T) enhance the prognosis of the grey cast iron castings shrinkage defects?

The method evaluates crystallization latent heat effects on the basis of temporal cooling curve derivative and „zero curve", Z_N. For a real experimental sample, the difference between them explains the dynamics of the crystallization process. In this paper, „zero curve" has been estimated through a Newtonian Thermal Analysis (NTA). In NTA standard method, Z_N „zero curve" is arbitrarily defined by extrapolation of an exponential curve[7] $dT/dt=-A\ exp(-Bt)$, where dT/dt is cooling rate, A and B are experimentally determined constants and the assumption of null temperature gradient through the section of DerTA cup. „Zero curves" does not take into account the phase transition latent heat.

Liquid alloy temperature fields is described by the Fourier-Kirchhoff equation with internal heat sources: $\partial T/\partial t=\alpha\nabla^2 T+q_s/C_v$, where $\partial T/\partial t$ *is* metal cooling rate [K/s], α is thermal diffusivity [m^2/s], C_v is volumetric specific heat (J/m^3 K), q_s is volumetric heat generated during solidification resulting from NTA method [W/m^3]. Fourier-Kirchhoff equation can be transformed into the following form[7,8]: $q_s=C_v(\partial T/\partial t - Z_N)$ and the Newtonian zero curve has the form: $Z_N=q_{su}/C_vM$, where q_{su} is partial heat flow from casting surface to ambient, assigned to accumulative cooling of casting [W/m^2], M is thermal modulus [m] (ratio between volume and cooling surface).

Fras et al. paper[7], related with Newton (NTA) and Fourier (FTA) analyses indicates the differences in approximations of zero curves, assigned to solidifying casting particular points. FTA analysis requires that the nucleation and growth phenomena must be based on an empirical model[9,10,11,12] (e.g. the Oldfield model or similar e.g. Rappaz, Boeri or KGT), which means that it allows a different approximation of „zero curve", based on specific simplifications.

The installation of a second thermocouple in DerTA cup is not standard yet. This experimental version permits a simplified temperature gradient evaluation through the section of DerTA cup. Precise separation of both thermal effects: accumulation heat and latent heat, for diversified non-equilibrium solidification conditions is not feasible. That is why NTA analysis was assumed as standard in this paper.

Experimental and numerical studies

The experimental and simulation tests were performed on the castings samples, which were made with DerTA standard cups (Fig. 1a) and in furan-bonded sand cube mould of 250 mm side and a upper riser ϕ140x200 mm (Fig 1b). Table 1 shows average EN-GJL-250 cast iron chemical composition.

In developing a macro model, à priori, phase growth rate calculation in each solidifying micro region of the casting (assigned to a given node) is based on local temperature drop in the given time step (according to the Fs=f(t) curve) but, due to observed undercooling and recalescence effects, this calculation is not possible to be taken into account directly. So, if solid fraction Fs = f(T) curve estimation is based on experimental DerTA curve, we first need to approximate the curve as shown in Fig. 2.

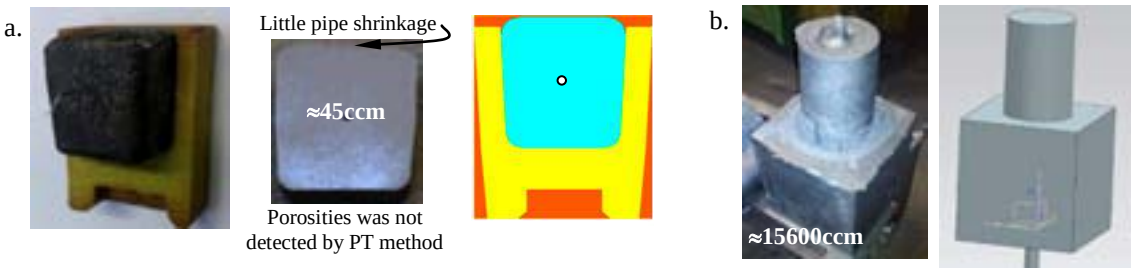

Fig.1: The views of the test EN-GJL 250 castings: a. standard DerTA cup (left), results of PT method after cutting (middle) and CAD geometry (right); b. real experimental cube casting (250 mm side) with upper riser ϕ140x200 mm (casting and CAD geometry).

Fig. 2a presents EN-GJL-250 alloy cooling curve and its first derivative selected from the test series carried out in Fundiciones de Roda facilities[13], using the ITACA system developed by Proservice[14]. With these experimental data, calorimetric curves („zero curve") were estimated using the NTA method, $q_s=f(t)$ values were calculated using trapezoid scheme and finally Fs=f(T) curves were obtained (Fig.2b). The curve 1 represents the heat flow release q_s, but it cannot be introduced directly inside the macro model as a generated latent heat curve (its shape is due to undercooling and recalescence effects). Curves 2 and 3 represent broken linear approximation curves of the real solid fraction evolution considering a monotonic trend (cumulative Fs value increases as temperature decreases). Fig. 2b also contains others Fs=f(T) curves: curve 4 from the NF&S code and curve 5 from the ProCast code, both based on chemical analysis presented in Table 1. The values of the characteristic temperatures: T_{liq}, T_{eut} and T_{sol} respectively by NF&S and ProCast own modules, were also calculated.

Table 1: Average chemical analysis [%] of the EN-GJL-250 cast iron used in the studies.

C	Si	Mn	Mg	P	S	Cu	Cr	Mo	Ni	V	Sn	Pb	Ti	Te	Ceq
2,93	2,01	0,82	0,00	0,02	0,06	1,24	0,04	0,00	0,02	0,00	0,00	0,00	0,02	0,00	3,61

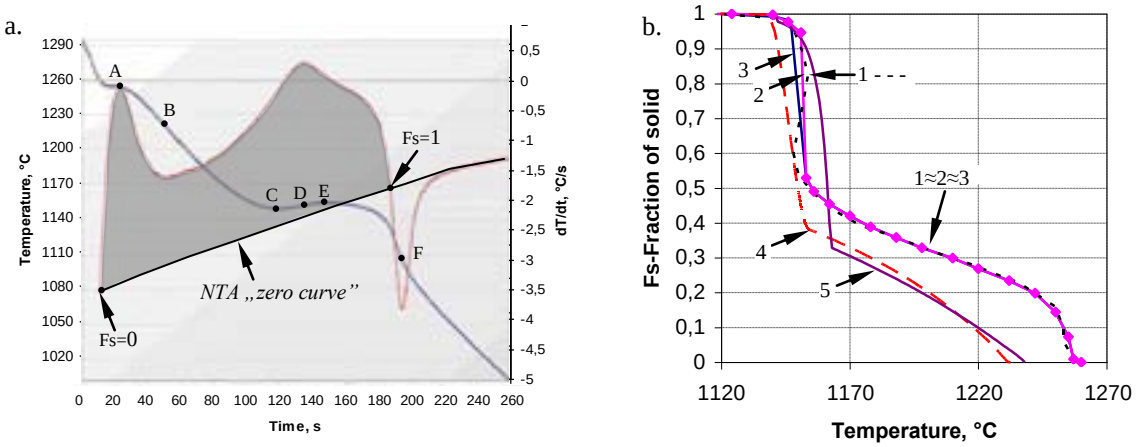

Fig. 2a: Cooling curve of grey cast iron type EN-GJL-250 and its first derivative obtained by DerTA cup method (ITACA[14]) with principle of „zero curve" determination. Characteristic temperature points [°C]: A- $T_{Liq.}$=1253; B- $T_{eut.Start}$=1219; C- $T_{eut.Min}$=1148; D- $T_{eut.Intermediate}$=1152; E- $T_{eut.Max}$=1154; F- $T_{Sol.}$=1107

Fig. 2b: Variation of solid fraction with temperature: 1 - curve (dashed) deduced from cooling curve showed in the Fig. 2a; 2 and 3 –simplified curves without the undercooling/recalescence; 4 and 5 – curves according to NF&S and ProCast databases respectively, both based on chemical analysis presented in Table 1. The maximal temperatures on the curves are the liquidus temperatures for cases 1 to 5.

Volume balance related to the shrinkage phenomena in a solidifying alloy is dependent on its density variation with the temperature. These phenomena in a liquid and solid-liquid state directly decide on the shrinkage defects formation. Most cast alloys are characterized by a continuous density increases as temperature decreases.

In the most databases regarding even the cast iron, the density variation character is preserved. However, it is known that the graphite crystallization as a graphite eutectic component is accompanied by the so-called graphite expansion (graphite volume growth), which must causes density decrease in defined temperature interval for case of the eutectic cast iron. This problem is rarely considered in the simulation system databases. Because of the above mentioned items, two Rho=f(T) curves were tested (the first considers a continuous density increases as temperature decreases-Fig.3b and the second considers a density decreases around of eutectic temperature due to eutectic graphite expansion-Fig.3c).

In relation with numerical tests for validation codes, critical liquid fractions parameters (CLF) limits for feeding flow have been formulated. In NF&S code, the limit levels are: mass feeding about 50% and inter-dendritic feeding (capillary) about 30%. Also, in ProCast code, mass feeding about 50% and inter-dendritic feeding about 70%.

In the numerical experiment tests, identical cast iron thermo-physical curves were assumed: heat conductivity and specific heat, (Fig. 3a). Also, constant latent heat value was considered (254 kJ/kg).

The thermo-physical parameters of sands (Croning sand cup and furan-bound sand cube) were assumed as constant values in temperature range of 20÷1500°C: heat conductivity were equal 0,8 and 1,04 W/m K respectively and the specific heat 1000 J/kg K and density 1540 kg/m^3 for both materials.

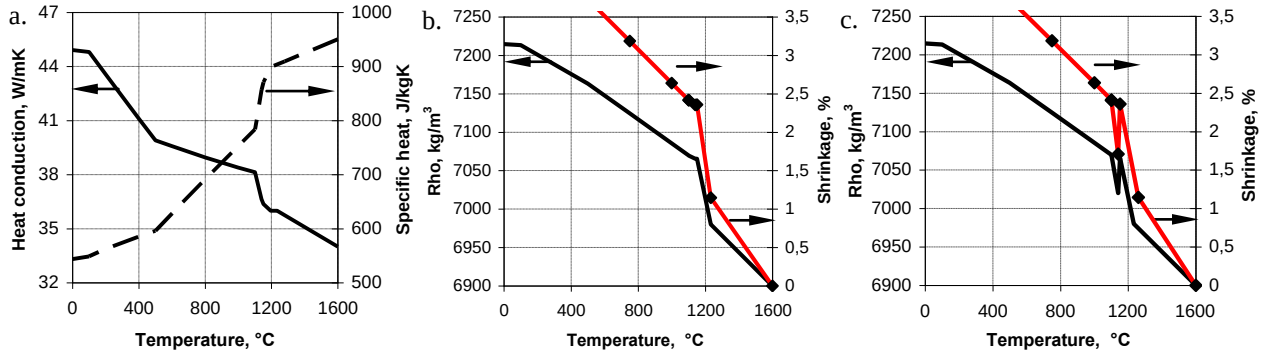

Fig.3: Chosen database parameters for EN-GJL-250 cast iron: a. heat conduction and specific heat, b. density and shrinkage curves in variant Rho 1 (without graphite expansion consideration), c. density and shrinkage curves in variant Rho 2 (with graphite expansion consideration).

Results and discussion

Tables 2, 3 and 4 show simulation results obtained using two simulation codes and its comparison for the casting geometries: NF&S with Macro model and ProCast with Macro and Micro models. They are presented in form of a sequence for selected cooling time. Specific simulation variants are denominated by its solid fraction curve number (Fig. 2b – Fs 2, Fs3 and Fs 4) and its density curve number (Fig. 3b – Rho 1 and Fig. 3c – Rho 2).

Table 2: Chosen results sequence obtained from NovaFlow&Solid CV for different variants: Fs & Rho.

Variant: Fs 4 & Rho 1

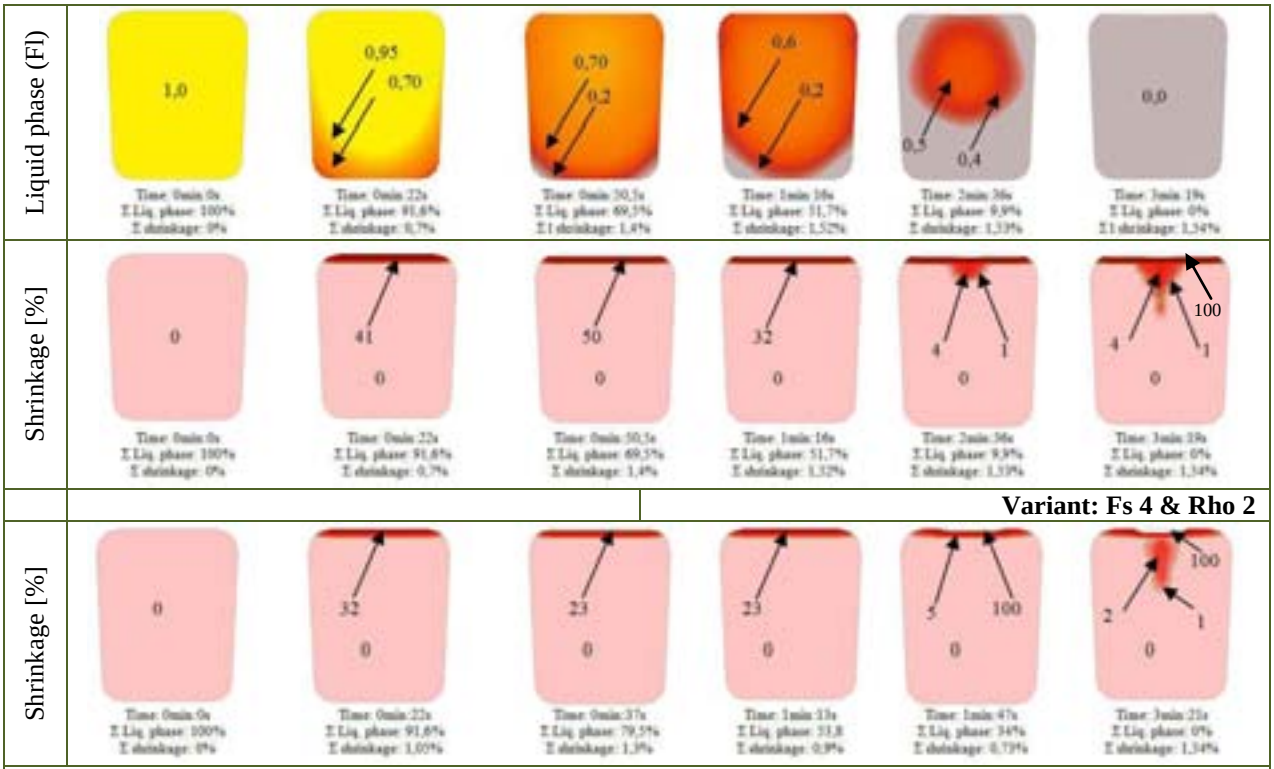

Local value (indicated by arrows) of liquid phase fraction (Fl): 1,0 is equivalent to 100% Fl and respectively 0 to 0% Fl (obviously 100% Fl corresponds to 0% Fs and 0% Fl to 100% Fs). Local shrinkage values are also indicated by arrows. The description of each sequence contains for indicated value of the time: the remaining fraction [%] of the liquid phase (Σ Liquid phase) and the relative total shrinkage volume [%], including the possible expansion of graphite phase (Σ shrinkage).

Table 2 shows NF&S numerical simulation test results obtained using Fs 4 solid fraction curve and two density curves (Rho 1 and Rho 2). It can be seen progressive shrinkage volume increase. Contribution of Rho 2 is lower than Rho 1, remember that Rho 1 doesn't consider the graphite expansion. It should be mentioned that similar dependency is present on

ProCast simulation tests results but, in this case, internal shrinkage discontinuities were finally completely compensated by graphite expansion. Only the primary shrinkage (pipe) formed before eutectic crystallization on casting top side will be not compensated (Table 3).

Comparing the results of Fs 4 & Rho 1 and Fs 2 & Rho 1 variants, we can see that second variant produces higher internal and pipe shrinkage. This is an evidence of solid influence on shrinkage defects. Also, these variants show full compensation of internal shrinkage defects but less shrinkage contribution can be observed before graphite expansion. Similar dependence occurs in Fs 3 & Rho 1 and Fs 3 & Rho 2 variants but with higher shrinkage contribution than variants before mentioned.

Results of ProCast numerical tests (Table 4), using its own micro model, show that its contribution in relation with internal shrinkage formation is much smaller than other variants. Also, compensation effect and highest primary shrinkage (pipe) intensity can be observed. Solid fraction variability with the temperature, assigned to a micro area (to a particular mesh node), has influence on the solidification process. If this Fs=f(T) variability is happening in the same temperature range $T_{liq} - T_{sol}$, there is practically no influence on simulated final solidification time. However, we need to make some assumptions about the use of the same database in relation to the remaining process parameters and materials, including the latent heat of solidification of the casting.

Changes of solid fraction curve profile, inside $T_{liq} - T_{sol}$ range, with the above mentioned assumption, have influence on the solid phase growth evolution, which in turn affects the shrinkage-expansion processes in cast iron and local liquid phase micro flows feeding shrinkage cavities than have appeared.

In this study, the influence of Rho=f(T) and Fs=f(T) on predicted shrinkage porosities (distribution and quantity) was identified. The best porosity prediction between numerical and experimental tests has been observed by comparing the surface of DerTA cup casting cross-section (result obtained by penetration test, PT), shown in Fig. 1a, and ProCast numerical simulation results for Fs 4 & Rho 2 variant (Table 3). This good accordance was also confirmed by ProCast Micro model results (Table 4). Other trials for both codes (with other variants Fs–Rho) using Rho 2 have also given good results (minimal internal porosity), unlike those obtained using Rho 1.

Table 3: Chosen results sequence obtained from ProCast Macro model for different variants: Fs & Rho.

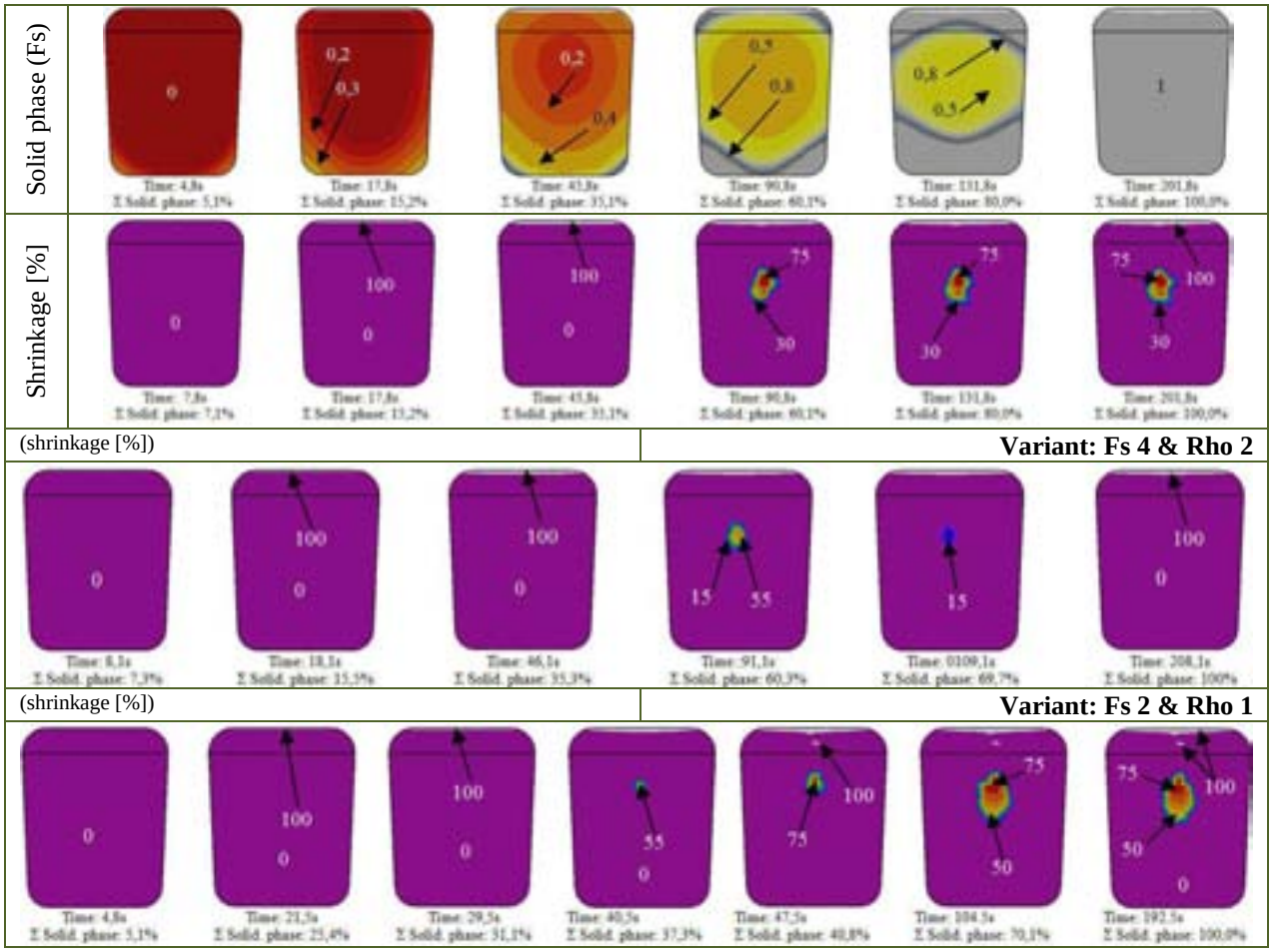

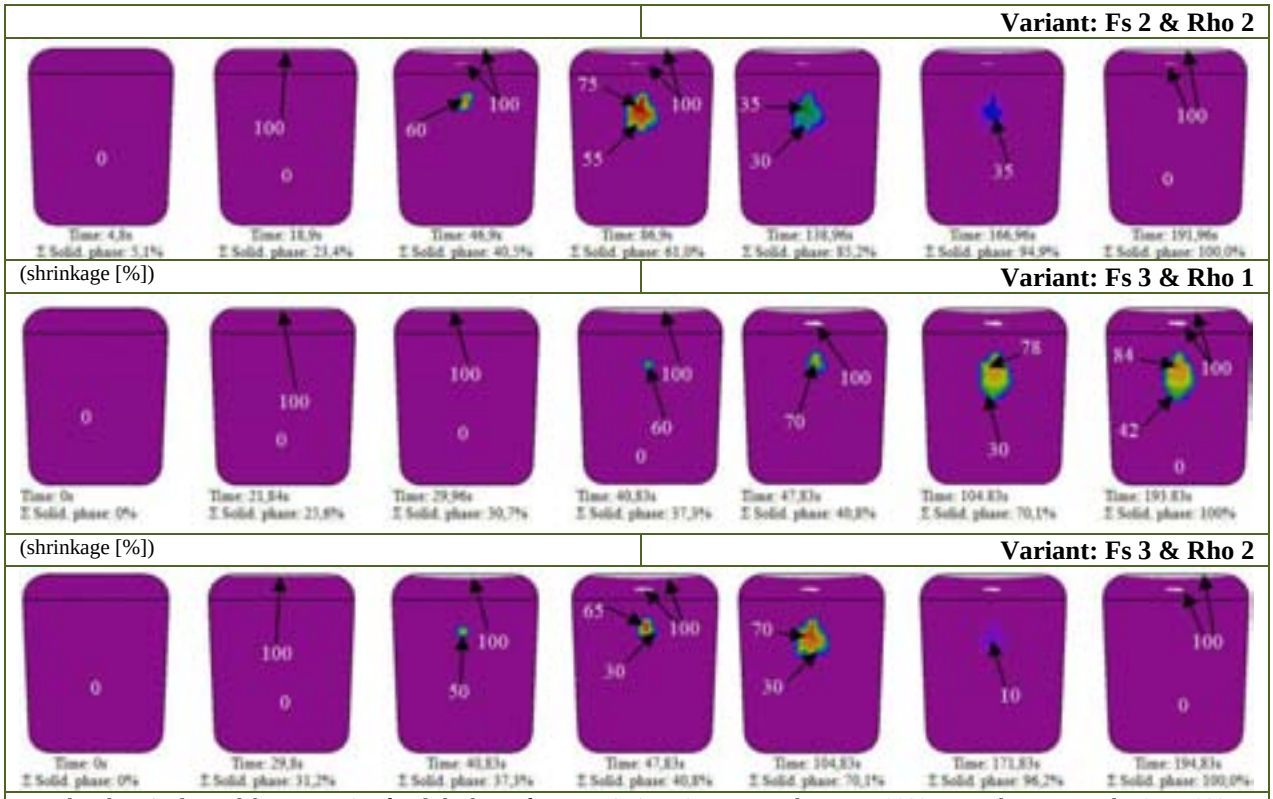

Local value (indicated by arrows) of solid phase fraction (Fs): 1,0 is equivalent to 100% Fs and respectively 0 to 0% Fs (obviously 100% Fs corresponds to 0% Fl and 0% Fs to 100% Fl). The relative total shrinkage volume [%] isn't calculated as sum regarding entire casting volume, but the expansion of graphite phase results from sequence of shrinkage local values (indicated by arrows). The description of each sequence contains for indicated value of the time: growing fraction [%] of the solid phase (Σ Solid phase).

Table 4: Shrinkage sequence obtained from ProCast Micro model (to compare with Macro models).

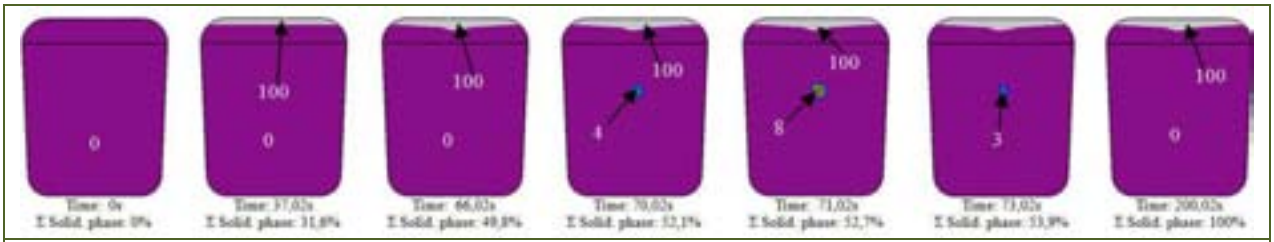

Local shrinkage values [%] are indicated by arrows. The description of the sequence contains for indicated value of the time: growing fraction [%] of the liquid phase (Σ Solid phase).

Moreover, the application of the same thermal database parameters in both codes (NF&S and ProCast with Macro model) results in a different image related to porosity prognosis. This could be due to the hidden algorithms used by these commercial codes and therefore not available to users.

The same methodologies and, experimental and numerical tests were applied to evaluate coupled influence of Fs=f(T) and Rho=f(T) curve variants, in the $T_{pouring} - T_{sol}$ range, over the shrinkage effects and expansion phenomena in relation with cube casting (approx. 15600 ccm) with the upper riser (Fig. 1b), so analogous to what was done with DerTA cup casting.

Table 5 shows final porosity prognosis results using both codes and selected variants. Shrinkage defects maps are different but when compared for example to Fs 4 and Rho 2 (cases c and e), we observed that these are unexpected. Some potential reasons were given in the previous deviation analysis realized for DerTA cup castings.

Fig. 4a shows the real surface of experimental cube casting cross-section (result obtained by PT test), which it is free of shrinkage defects. Pipe shrinkage occurred only in the top part of the riser. As can be seen from the results shown in Fig. 4b and 4c, only two variants of Fs & Rho showed an acceptable agreement with the experimental results (compare cases c and f from Table 5).

Table 5: Final shrinkage from NF&S CV (a,b,c) and ProCast (d,e,f) for chosen cases – cube casting (shrinkage %).

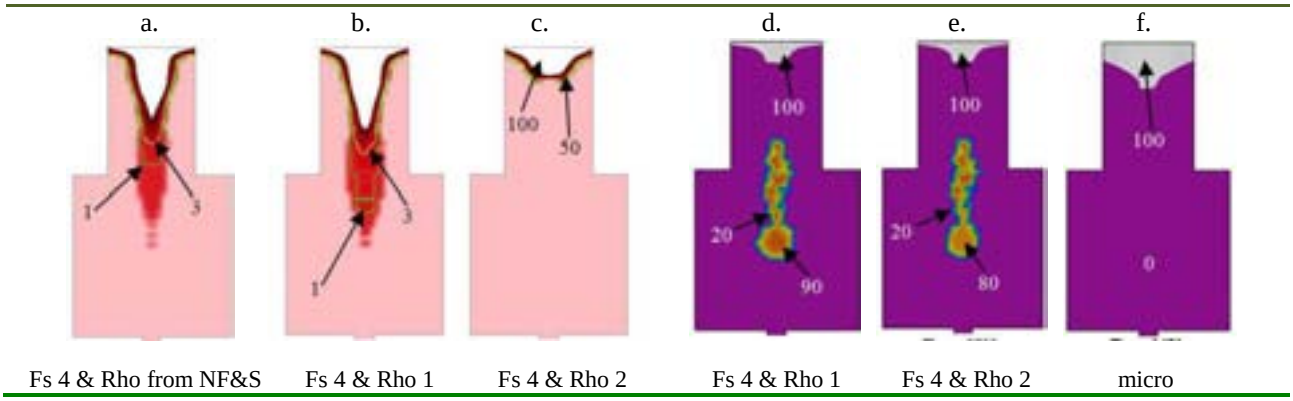

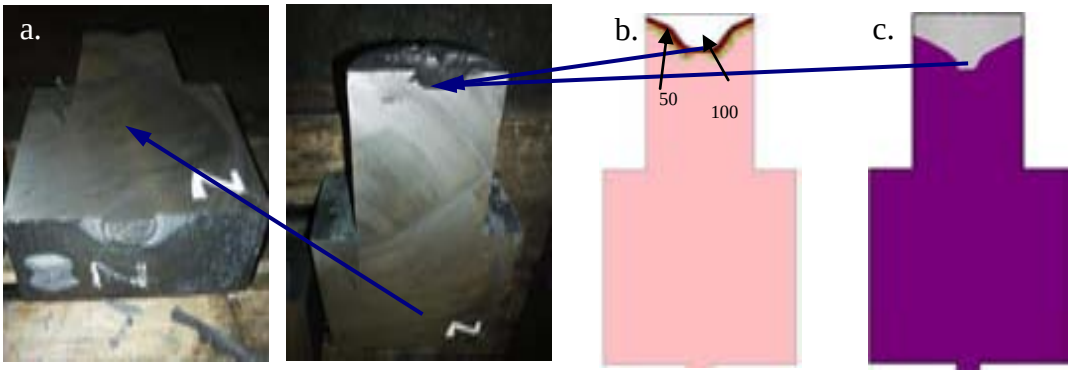

Fig.4: Correct soundness of real cube casting after cutting (a) compared with of shrinkage prognosis obtained from the NF&S CV Macro model (b) and from ProCast Micro model (c)

These results highlight the importance of the issues raised in this paper regarding a prognosis of shrinkage defects in cast iron castings. Also, one can recognize a certain influence on the castings size and shape.

Conclusion

The tests performed in this study are related with an important problem concerning formation of shrinkage discontinuities phenomena in gray cast iron castings. Coupled shrinkage-expansion phenomena due to graphite phase increase do not exist in other technical alloys (e.g. cast steel, Al and Cu alloys etc.). These phenomena lead to shrinkage discontinuities reduction. This is the reason why these phenomena have been analyzed in this paper. Simulation tests using two codes and its macro models have been carry out. Also, other tests applying micro model (only with ProCast code) were realized. Generally, they confirm that is necessary to consider expansion-shrinkage phenomena modeling as well as an appropriate interpretation about dynamic shrinkage evolution during solidification process, before predicting a final casting shrinkage map.
To summarize the realized studies, the following remarks can be made:

1. Two simple casting geometries are used during experimental validation processes. More complicated casting shapes wouldn't allow an unequivocal answer regarding sensitivity analyses of simulation codes based on adequate databases selection (including hard and soft models[1]). Hence, the tests described in this paper let to prove the hypothesis with higher probability
2. Coupled influence of different variants about Fs and Rho curves on the shrinkage defects prediction for EN-GJL 250 castings, was confirmed.
3. Taking into account graphite expansion effect (Rho 2 curve), expected responses of both Macro models were observed.
4. ProCast's Micro model (some important shrinkage-expansion parameters are not available for users), gives satisfactory shrinkage predictions according both experimental castings.

Evaluation of experimental simulation tests efficiency using the macro or macro-micro models should definitely include the totality of castings quality. In the scope of these issues, we want to reflect that published numerical simulation studies using micro models, with extremely small casting sample size (cubic samples whose side is a fraction of a millimeter or 2D simple sample, e.g.[15]), are an important research area from the scientific viewpoint, which could be a practical significance in some undefined future. Prof. Rappaz[16] relates this area with microelectronics and computing developments and, in a visionary manner, considers that a full symbiosis with castings modeling, including the atomic scale, is likely to happen. On the one hand, there is need to find a coherent physical description of phenomena from the macro to atomic scale: basic differential equations (hard modeling) and empirical equations approach (soft modeling), but also, and on the other hand, maybe mostly, there is need to microelectronic developments and new computers generation (calculation speed and memory size). It should be considered that there are prognosis models[16] with working times even as long as 100 years.

References

1. Z.Ignaszak: *Key Engineering Materials*, 2011, 457, 305-311.
2. Z. Ignaszak, P. Popielarski: *Archives of Foundry*, 2003, 3 (in Polish).
3. Z. Ignaszak, P. Popielarski, J. Ciura: *Archives of Foundry*, 2005, 5, 157-163.
4. Z. Ignaszak, P. Popielarski: *Archives of Foundry*, 2006, 6, 224-231 (in Polish).
5. Z. Ignaszak, J. Hajkowski, P. Popielarski: *Defect and Diffusion Forum*, 2013, 334-335, 314-321.
6. Z. Ignaszak, P. Popielarski, J. Hajkowski: *Defect and Diffusion Forum*, 2013, 336, 135-146.
7. E. Fras, W. Kapturkiewicz, A. Burbielko, H.F. Lopez: *AFS Trans.*, 1993, 101, 505-511.
8. A. Diószegi, I.L. Svensson, *Material Science and Engineering A*, 2005, A 413-414, 474-479.
9. D.J. Celentano, P.M. Dardati, L.A. Godoy, R.E. Boeri: *Int. J. Cast Met. Res.*, 2008, 21, 416-426.
10. Ch.-A. Gandin, M. Rappaz: *Acta Metall. Mater.*, 1994, 42, 2233-2246.
11. M. Rappaz, A. Jacot Ch.-A. Gandin: published in Raabe D.(editor) et all, Continuum Scale Simulation of Engineering Materials Fundamentals - Microstructures - Process Applications, Wiley-VCH 2004.
12. D.M. Stefanescu: *ISIJ Int.*, 1995, 35, 637-650.
13. M. Castro, P. Roquet, R. Castilla, E.Codina: Industrial requirement for melting (Flexicast report, 2013)
14. Thermal Analysis Software. ProserviceTechnology. http://www.proservicetech.net
15. D. Gurgul, A. Burbelko, E. Fras, E. Guzik: *Archives of Foundry Engineering*, 2010, 10, 35-40.
16. M. Rappaz: *ESI Conference EUROPAM*, Mainz, 2003.

Acknowledgements

The research was partially supported by 7FP-2012-7-NMP-ICT-FoF-314540 FLEXICAST project

A computational micromechanics approach to evaluate effective properties of ductile cast iron

F. J. Rodriguez[2*], P. M. Dardati[1], L. A. Godoy[2] and D. J. Celentano[3]

[1]Departamento de Ingeniería Mecánica, Universidad Tecnológica Nacional, Facultad Regional Córdoba

[2]Universidad Nacional de Córdoba, Facultad de Ciencias Exactas, Físicas y Naturales – CONICET.

[3]Departamento de Ingeniería Mecánica y Metalúrgica, Pontificia Universidad Católica de Chile.

Ductile iron has excellent mechanical properties. The properties of SGI are mainly controlled by the type of matrix and by the size, shape, and distribution of graphite nodules. Thus, knowledge of the relation between microstructure and mechanical properties becomes important to design parts made with SGI. Micromechanical modeling of materials is a new approach recently employed to evaluate such relations while taking the topology of the constituent phases and the properties of each into account. The macroscopic mechanical behavior of a mixed ferritic/pearlitic matrix cast iron is investigated in this work by means of a micro-mechanical model, in which asymptotic homogenization is applied to computationally generated multi-particle cells in two and three dimensions. The displacement field inside the cells is computed via finite elements. From these cells, the size of the Representative Volume Element is determined, and the effective response is obtained for this element.

Keywords: ductile iron, homogenized propertied, computational micromechanics

Introduction

Most cast metal materials are microscopically heterogeneous, being formed of different constituents and phases, which are distinguishable on an appropriate scale. The constituents of a cast material have different topologies and mechanical properties, so that the macroscopic response is actually a result of the cooperative mechanical behavior of its various elements. Since in most cases the difference between the dimensions of the macrostructure (D) and that of the forming microstructure phases and constituents (d) is large, it is not possible to make a direct representation of the microstructure on the macroscopic scale of a part. For this reason, until recently, Mechanics of Materials has only used a macroscopic characterization of the materials. According to this characterization, the material is considered to be homogeneous and the coefficients needed to describe phenomenologically the macroscopic mechanical behavior of the material are determined by testing performed on relatively large specimens. However, such description cannot explain certain macroscopic behaviors of the material without additional information of microstructure.

Extensive research has been conducted since the early nineteenth century in order to address this problem. The increase in capacity of computational calculation and the development of numerical methods of recent decades have given an important impetus to research that has extended the area of multiscale studies to different materials and different physical phenomena. In this context, the ductile cast iron, also known as nodular cast iron or spheroidal graphite iron (SGI), can be considered as an heterogeneous material formed of a metallic matrix composed of ferrite, perlite or a combination of both, in which graphite nodules are embedded. Given these microstructural features, ductile iron can be analyzed as a heterogeneous material with an array of matrix-inclusion.[1]

The properties of ductile iron are controlled mainly by the type of matrix, the presence of defects into it, and the size, shape and distribution of graphite nodules. Therefore, it is very important to investigate the relationship between microstructure features and mechanical properties in order to obtain parts with specified mechanical properties.

One of the approaches to the study of the relationship between the microstructure and the mechanical properties is based on phenomenological models which depend on experimental data. Guo *et al.*[2] studied the relationship between the characteristics of matrix and graphite and different mechanical properties of the SGI, and proposed expressions to determine Brinell hardness, yield strength and ultimate stress based on the microstructural characteristics analyzed.

Wenzhen and Baicheng[3] predicted the mechanical properties of microstructures by means of a solidification model, employing experimental expressions developed by Lundback *et al.* [4]

Another approach employs multiscale modeling and on the micromechanics of a continuum. Pundale *et al.*[5] investigated the influence of volume fraction of graphite and of shape, size and distribution of nodules on the effective Young modulus. They analyzed cells, in which the graphite nodules are assumed to be voids, with two models: a plane stress model and an axisymmetric model. Collini and Nicolleto[6] proposed a unit cell model to predict constitutive law

* Corresponding author, email: rodriguez-fj@hotmail.com

and failure of a nodular cast iron. They considered a unit cell with a mixed matrix of ferrite and pearlite; this allowed analyzing the influence of the volume fraction of these micro-constituents on the mechanical properties.

Collini[7] implemented different micromechanical computational models, using the finite element method to determine the elastic-plastic behavior of the material and to identify failure initiation mechanisms. He compared the results obtained by different models and performed validation with experimental results.

According to the literature review, there are no studies in which multi-particle three-dimensional cells with mixed matrix have been analyzed for determining effective properties using micromechanical analysis. For this reason and because of the limitations of two-dimensional models, a comparison between 2D and 3D models becomes important. However, meaningful 2D-3D comparisons can only be made by preserving some similar features between both models. As will be shown next, the procedure commonly used to obtain multiparticulate plane cells is from micrographs. So in order to obtain comparable models, the procedure presented here to obtain a plane model attempts to reproduce the same procedure used to obtain a micrograph.

The micromechanical requires an appropriate representation of the material through what is called a representative volume element (RVE). Obtaining the RVE can be done using two main methodologies[1], one of them uses "synthetic" microstructures generated by computer algorithms. A second methodology is based on micrographs obtained experimentally, using acquisition and image processing to produce digital images and with these the micro-geometries. This second approach has the disadvantage of only allowing the generation of planar geometry and thus only a two-dimensional analysis of the problem.

The appropriate choice of RVE is an essential ingredient, from which the effective properties of the material shall be determined using the principles and laws of micromechanics and the multiscale theories. A RVE must (a) be statistically representative of the macroscopic response analyzed, and (b) have a dimension greater than the minimum size of the heterogeneity that characterizes the microstructure of the material. A RVE can be considered as the minimum volume of material whose performance is equivalent to the macroscopic behavior of the material. To define the size of the RVE, two important issues must be considered: the desired accuracy and the computational cost to solve the model; both of them increase with increasing volume.

Drugan and Willis[8] and Drugan[9] concluded that RVE should have a size equal to or greater than twice the diameter of the spheres to get a 5% error in the modulus of elasticity, being able to reduce this error to less than 1% when the size is increased to 4.5 times the diameter.

To define the RVE it is possible to adopt a geometric or a physical criterion[1,10]. According to the geometric criterion, the RVE must be statistically representative of the microstructure of the material, thus being independent of the physical property to be studied. The physical criterion defines the RVE based on the requirement that, for a given physical behavior, their overall response is not dependent on the applied boundary conditions.

The main objective of this work is to obtain Young's modulus and yield strength of a nodular cast iron using homogenization techniques. To achieve this goal, multiparticulate cell models, in two and three dimensions, are used. Nodules are considered as voids which are embedded in a matrix with different percentages of ferrite. The size and the volumetric density of graphite nodules are the result of the computer simulation of a solidification process, specifically of a block Y (1in).

Experimental Procedure

The assessment of the effective mechanical properties of ductile iron using a micromechanics approach with a synthetic representation of the microstructure of the material is presented in this paper. For the generation of a representative material geometry at microscale level, density and size distribution of graphite nodules and the volume fraction of each microconstituent are taken as data.

In order to provide information related to the volumetric nature of the spheres of graphite, a computer simulation for the solidification of a block-type Y (1in) test is carried out. The model considers thermal and metallurgical problems of solidification of ductile iron, making the coupling between both by the latent heat method. The thermal problem is macroscopically treated, solving the heat equation in the complete domain (part and mold) by the finite element method. The microstructural model used for solidification, due to Boeri[11], simulates the stable equiaxed solidification of a nodular cast iron, of eutectic composition, according to the plurinodular theory. The nucleation of graphite nodules is considered as a continuous process, so that in each time step of the numerical resolution and while certain conditions are satisfied, the nucleation of a set of nodes occurs. Each set is called a family of nodules. In the model used, all nodes belonging to the same family are assumed to have the same radius. Thus, at the end of the simulation, each family will possess a density and a size of nodules that characterizing it, as shown in Fig. 1. The implementation of the solidification model was performed in the general purpose finite element program ABAQUS.[12]

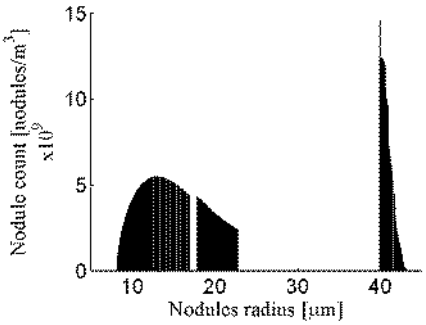

Fig. 1: Simulated nodule size distribution

On the other hand, to define the constitution of the matrix, several cases with different percentages of pearlite and ferrite are considered in order to explore the influence of different matrix compositions on the mechanical properties analyzed.

Using as input data the size and density of nodules of each family and the total volume fraction of graphite resulting from the simulation, and after setting the fractions of ferrite and pearlite in the matrix, the multi-particle cells are generated: (a) a three-dimensional cubic and (b) a two-dimensional square shape. The latter is the result of performing a section of the three-dimensional cell with a plane parallel to one face of the cell and at a random distance from that face.

The two-dimensional model is analyzed as a plane stress problem. From the above, it follows that all cells are formed of a matrix composed of ferrite and pearlite, and nodules of different sizes embedded into it. A perfect elastic-plastic behavior of the matrix elements is assumed. The equality of the Young's modulus to ferrite and pearlite is assumed, accordingly to [13-17]. The microconstituent properties are shown in Table 1.

The nodules are modeled as voids in order to reduce the number of degrees of freedom of the finite element model, and because they do not constitute a reinforcement of the matrix due to its low Young's modulus.[5,7] In order to define the mixed matrix of ferrite and pearlite, first percentages of each microconstituent are chosen, and then it is assumed that all nodes are surrounded by a spherical shell of ferrite such that its predefined percentage is reached. To determine the thickness of the ferrite layer, it is assumed, for simplicity, that the relationship between the radius of each ferrite layer and its corresponding node is constant and equal to a given value that depends on the ferrite fraction.

Table 1: Properties of microconstituents of the matrix[7]

Constitutent material	E [GPa]	ν	σ_0 [MPa]
Ferrite	209	0.3	427
Pearlite	209	0.3	552

The cell used for homogenization should be large enough to have all the information necessary to describe the behavior of the heterogeneous material.[18] The cell that meets this requirement is a RVE. The macroscopic response obtained with these models shows a strong dependence on the size of the volume element. Thus, it is very important to find an optimal size for the volume element that is large enough to adequately capture the physical behavior of the material studied but simultaneously involving the least possible computational cost.

Using a definition of the RVE by geometrical criterion, the appropriate size is obtained based on the characteristics of the micro-geometry regardless of the physical property. The appropriate size of the RVE is that which possesses geometric features equivalent to the analyzed material. The use of this criterion for choosing the size of the RVE, according to some researchers[1], is suitable for micromechanical models used to estimate the elastic behavior of heterogeneous materials. Drugan and Willis[8] demonstrated that, for isotropic heterogeneous materials comprising a matrix and spherical particles of equal size, with size cells between two and five times the diameter of the particles, representative results of macroscopic elastic stiffness are achieved with errors smaller than 5% and 1%, respectively.

As can be noted, according to these authors, the RVE size is independent of the volume fraction of particles.

According to the physical criterion, the size of the cell is appropriate when an increase of the size does not produce change in the physical property analyzed.

In this paper, to obtain a cell size that can be considered representative of the material, a series of cells with increasing volumes were analyzed up to the percentages of phase (geometric criterion) and mechanical properties (physical criteria) converge to a value;

$$\xi = \frac{|A_{i+1} - A_i|}{A_{i+1}} \cdot 100 \qquad (1)$$

where A_i and A_{i+1} are the analyzed property values for cell size i and for next higher cell size $i+1$. A cell is assumed to be representative, i.e. a RVE, when the error ξ is less than 2%.

Based on the results of the works by Drugan and Willis[8] and Drugan[9], the absolute size of the cell, hereinafter cell size L, is the side length of the square cell for bi-dimensional models and the edge length of the cubic cell for three dimensional models. A relative size of cell is also defined by the ratio between L and the radius of the largest nodes, which are those belonging to the family of nodules which is the first to nucleate.

All three-dimensional equal-sized cells include the same number of nodes of each family and the same volume fraction of voids. However, the methodology for obtaining two-dimensional cells entails that the geometric characteristics are particular to each of them, that is, not unique for each cell size. This is because both the number of voids intersected by the plane and the position for which the plane intersects them, are variable. The variability of the geometrical characteristics of the two-dimensional cell leads to a high dispersion of the results, which does not allow convergence of the results with increasing cell size for any of the two criteria. To reduce scatter in the results the concept of averaged of a sample or ensemble averaging is used.[10] The location of the centers of the nodules in the three-dimensional cell is made with the RSA algorithm, thereby generating different cell geometries in each run. In this way it is possible to generate different three-dimensional cells and from them to obtain M two-dimensional cells, each of these plane cells (called *realization*[10]) is a member of what, taken together, is called sample. The response of each realization in the sample $Q^{(K)}$ is generally different, being able to define an average response of the sample $\langle\langle Q\rangle\rangle$ with the following expression:

$$\langle\langle Q\rangle\rangle = \frac{1}{M}\sum_{K=1}^{M} Q^{(K)} \tag{2}$$

Considering an increasingly larger number of realizations and computing a new ensemble average each time a new realization is added to the set, results in an average response $\langle\langle Q\rangle\rangle^k$ computed from K samples. The successive increase of a sample size gives origin to a sequence of $\langle\langle Q\rangle\rangle^k$. This sequence shows a convergence which will decrease the randomness of the results. Then, to define a characteristic value of response for each two-dimensional cell size, the sample size is increased successively until the marginal value of the property studied is negligible. When this occurs, it is assumed that this average value is a characteristic response of this cell size.

For both bi and tri-dimensional cells, determining the mechanical behavior is performed using the asymptotic method of homogenization[19] by solving the displacement field within the cell, produced by subjecting the cell to a set of prescribed macroscopic deformations, by the finite element method. These deformations are imposed by prescribing appropriate displacements to the degrees of freedom of a set of control nodes NC.[20,21]

For the computation of the effective mechanical properties analyzed in this work, it is necessary to obtain the solution of a single boundary value problem. For this, the cell is subjected to a set of prescribed macroscopic strains, in accordance to the indicated in the strain tensor of expression (3), imposed as displacements to the control nodes NC.

$$\varepsilon_{11}^0 = \begin{bmatrix} \varepsilon_{ij}^0 & 0 & 0 \\ 0 & 0 & 0 \\ 0 & 0 & 0 \end{bmatrix} \tag{3}$$

The use of this methodology leads to a homogenization called external[21], in which the stress tensor is calculated as the rate between the reactions in the control node and the cell volume. The homogenization process is performed for each increment of deformation to obtain the stress-strain curves and, from them, the Young's modulus E and the yield stress σ^0.

The model is implemented in ABAQUS using a script developed in Python that generates the different components of the finite element model. The developed program allows: generate cells with periodic geometries, assign the constitutive properties of materials, ensure the periodicity of the finite element mesh (see next section), impose periodic conditions to the opposite faces of the cell and apply the macroscopic strains to the degrees of freedom of the control nodes. For the post-process a specially developed script that reads the results and executes the homogenization is used.

Multiparticulate Cells

For the three-dimensional cell, the graphite nodules are represented by spherical voids having different radii that are obtained from the numerical simulation of the solidification. In each cell, a certain amount of nodules of each family is included. Such amount of nodules is determined by taking in account the volumetric density of nodules of the family and the total volume of the cell:

$$N = \Omega_C N_{vol} \tag{4}$$

where N is the number of nodules pertaining to a family included in the cell, N_{vol} is the volumetric density of nodules obtained from the solidification simulation and Ω_C is the volume of the cell. The value obtained by expression (4) is rounded, because the number of nodes should be a natural number.

For a given volume fraction of ferrite, the radius of the envelope of ferrite is determined by considering the volumetric density and the size of nodules of each group as:

$$\zeta = \sqrt[3]{\frac{f_f}{f_{gr}} + 1} \tag{5}$$

where ζ is the ratio between the radius of the outer sphere of ferrite (r_f) and the radius of the graphite nodule (r_g), f_f is the volumetric fraction of ferrite and f_{gr} is the volumetric fraction of graphite; see Fig. 2.

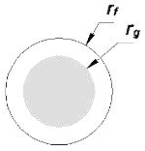

Fig.2: Scheme of the nodule surrounded by the envelope of ferrite.

The three-dimensional multiparticle cell is generated by the Random Sequential Addition method, RSA. This method generates the coordinates of the centers of the spheres in a sequential and random mode. The condition that the nodules should not interpenetrate and must be completely contained within the cell without intersection with the edges of it (see Fig. 3.c) is imposed. This condition is relaxed for the ferrite spheres in such a way that a free contact between them and between a sphere and the faces of the cell is allowed. The only condition is that regions generated among spheres and cell faces have not a reduced volume because this situation makes it difficult to obtain an appropriate finite element mesh.

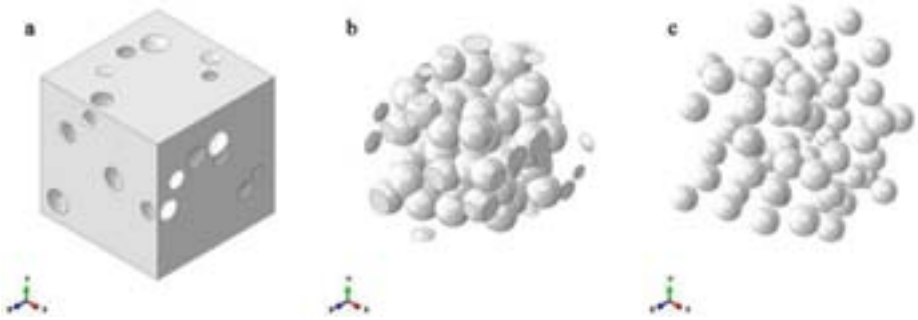

Fig. 3: Parts of the RVE: (a) pearlite, (b) ferrite envelopes, (c) nodules (voids in the simulation)

The two-dimensional cell is obtained by sectioning the final three-dimensional cell through a plane parallel to one face located at a random position. For this, once chosen the plane with which the section will be made, nodules and envelopes of ferrite that are cut are identified and then, the radius of the circles that are the intersections between the plane and each of the parts are determined; see Fig. 4.

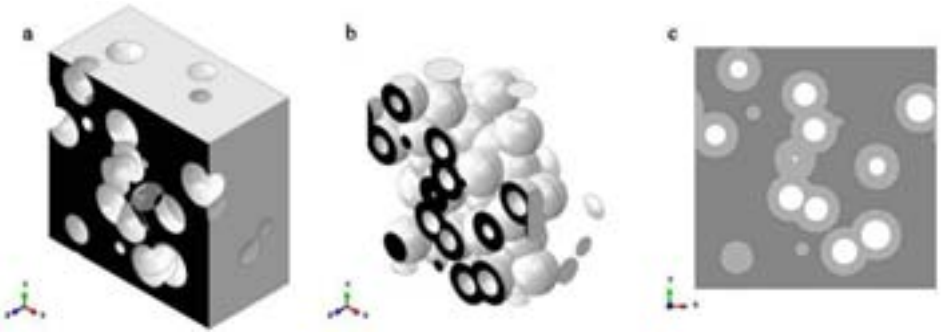

Fig. 4: Scheme of the sectioning to generate two-dimensional model.

To define the macroscopic behavior of the material, the homogenizing asymptotic method is used. It enables the replacement of a heterogeneous medium by an equivalent homogeneous one, allowing obtaining the macroscopic laws using microesctructural information. Some researchers [22, 23] have applied this technique to the modeling material with a not exactly periodic microstructure. Taking this into consideration, the nodular cast iron can be modeled by a periodic repetition of a cell.

This homogenization model requires implementing periodic boundary conditions which require, in turn, that both the geometry of the RVE, Fig. 3 and 4, and the mesh of finite elements be periodic Fig. 5.
The periodicity conditions of the cell is guaranteed if it holds that

$$u_k = \varepsilon_{kl}^0 L + u_k \tag{6}$$

ε_{kl}^0 is the tensor of macroscopic deformation, u_k the displacement of node *k*, and u_k the displacement of its correspondent periodic node. Since u_k is unknown, for numerical implementation of these conditions, some expressions that relate the movement of a pair of points located on opposite sides must be posed. To ensure the periodicity, the boundary conditions to impose on the faces, edges and vertices of the cell are determined by considering the vectors of periodicity of the cell analyzed.[23, 24]

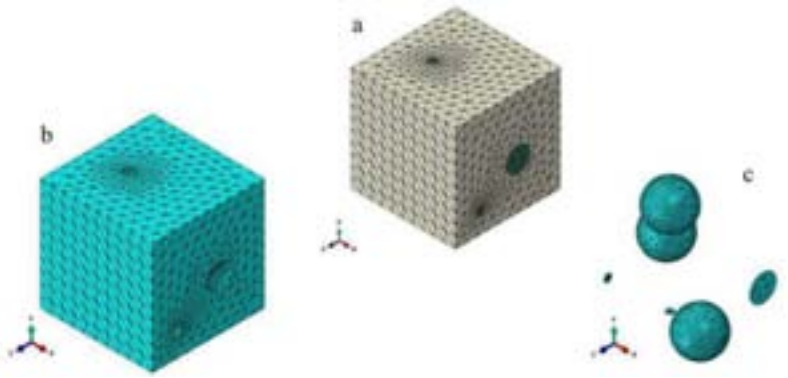

Fig.5: Boundary mesh of parts included on FEM model: (a) assembly of pearlite and ferrite envelope, (b) pearlite and (c) ferrite envelopes.

Results and Discussion

The RVE size determination is performed according to the geometric and physical criteria. Through a series of independent analysis of increasing size cells, first a three-dimensional RVE size is defined according to both criteria and, second, the same is done for the two-dimensional model.

In this work, the geometric analysis focuses exclusively on the convergence of the ferrite volume fraction and the results of a geometric analysis for graphite fraction, reported by Rodríguez *et al.*[25], are used.

Fig. 6 shows the evolution of the ferrite fractions in the cell with increasing relative size thereof; it shows that it is not possible to achieve the convergence to the searched ferrite fraction values in the cell for high fractions of ferrite of matrix. This is because the RSA method used to generate the random distribution of graphite nodules has difficulty in generating distributions with high volume fraction.[10] Because the ferrite is assumed distributed with spherical shells around the graphite, their distribution is coincident with that of the nodules and therefore it is governed by the same distribution method. For this reason in this work we analyze matrices with ferrite fractions of 10, 20 and 30%, values that can be achieved with the method used. The cell sizes finally adopted for each percentage of ferrite are shown in Table 2.

Fig. 7 shows the evolutions of the Young's modulus and the yield strength as functions of relative size of the cell. By this criterion, different sizes of RVE for each percentage of ferrite in the matrix is also obtained, showing that this approach results in larger cell sizes (Table 2) relative to those determined according to the geometric criterion.

In order to defining the size of the two-dimensional RVE, cells with increasing relative size are analyzed. Both for the geometric definition as for physical definition of the RVE size, a dispersion of the results is observed. This is because of the way the cells are generated and that causes a variation in the geometrical characteristics for each cell, as it indicated above.

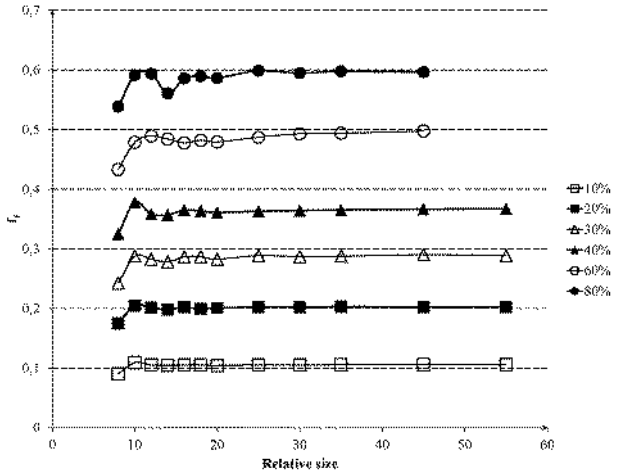

Fig.6: Volume fraction of ferrite in the three-dimensional cells for different percentages of ferrite in the matrix and different relative sizes of the cell.

Table 2: Geometric and physical criteria: RVE relative sizes for different ferrite volume fractions

		f_f [%]		
Model	Criterion	10	20	30
2D	Geometric	18	20	20
	Physical	35	20	22
3D	Geometric	12	12	12
	Physical	15	15	15

In Fig.8 (a) the evolution of the fraction of ferrite for relative size 10 and 20 and 10, 20 and 30% of ferrite in the matrix is observed. Convergence was achieved by increasing the number of realizations in the sample; it can be further noted that the results dispersion decreases with increasing size of the cell used. The characteristic behavior for each cell size is obtained from the average of a set of at least 25 realizations.
In Fig.8 (b) the convergence of the characteristic values by increasing the size of the cell, for the different analyzed percentages of ferrite is observed. The RVE sizes adopted with this criterion, for 2D models, are listed in Table 2.

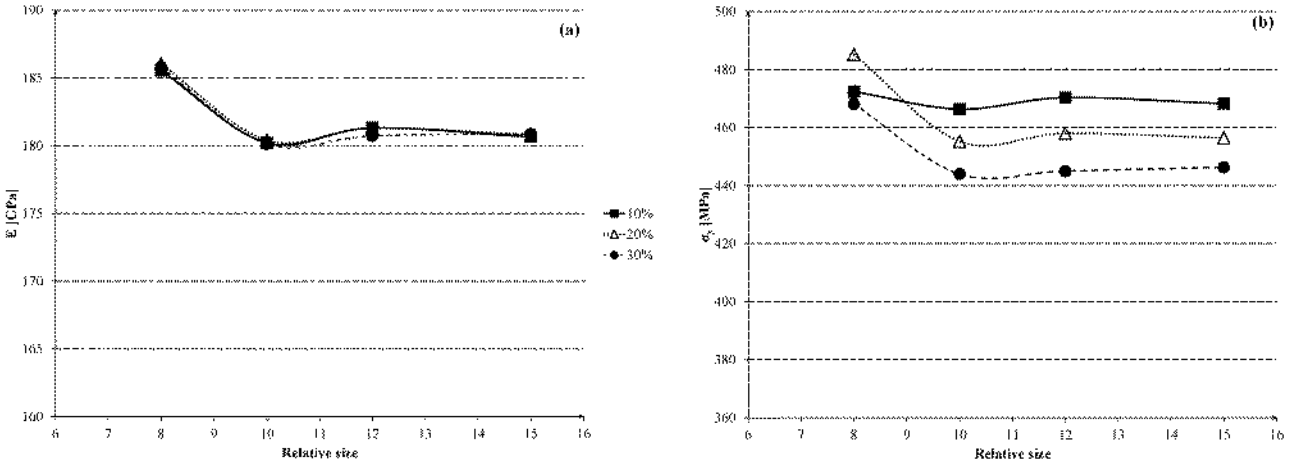

Fig.7: Material properties of three-dimensional RVE with 10, 20 y 30% of ferrite in matrix for each cell size analyzed: (a) Young's modulus E, (b) yield strength σ_y.

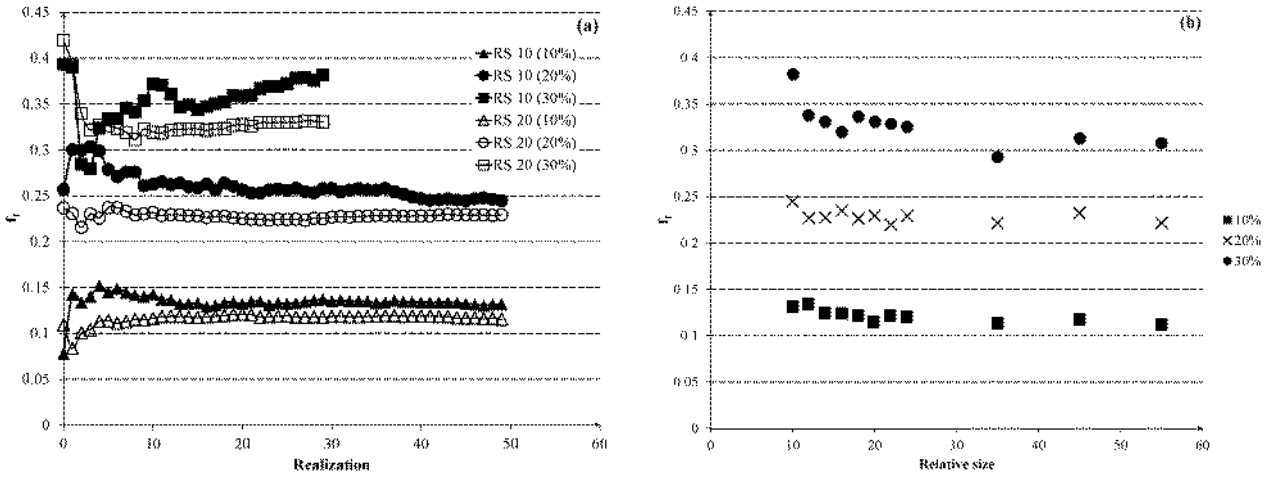

Fig.8: (a) Volume fractions of ferrite for two-dimensional RVE of relative size 10 and 20 with increasing number of realizations, (b) ferrite fraction averaged for each analyzed cell size.

The characteristic results for each two-dimensional cell size, according to the physical criterion, are plotted in Fig. 9. The characteristic values of the properties analyzed show convergence with increasing cell size considered, slower convergence for the values of yield stress is observed. The Young's modulus tends to be equal for all three analyzed ferrite percentages, accordingly to the assumption of equal Young's modulus for ferrite and pearlite. On the contrary, the yield stress decreases with the increase of the fraction of ferrite.

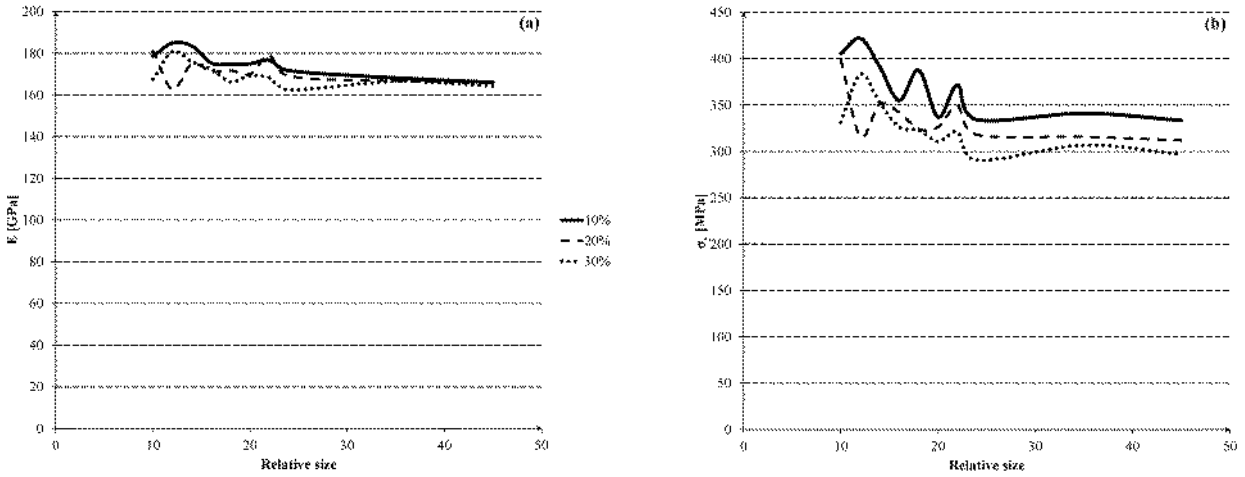

Fig.9: Average material properties of two-dimensional RVE with 10, 20 and 30% of ferrite in matrix for each cell size analyzed: (a) Young modulus averaged, (b) yield strength averaged σ_y.

Given that the physical criterion requires larger cells to achieve convergence, this criterion is used to define the final size of RVE in both models. In Fig. 10 the strain-stress curves for two-dimensional and three-dimensional RVE with 10, 20 and 30% of ferrite in matrix are shown. The 2D model demonstrates greater stiffness [25] as well as a lower yield point. As expected, the increase of volume fraction of graphite causes a reduction of the yield point. No hardening was observed in any of the two models because a perfect elasto-plastic constitutive model was used.

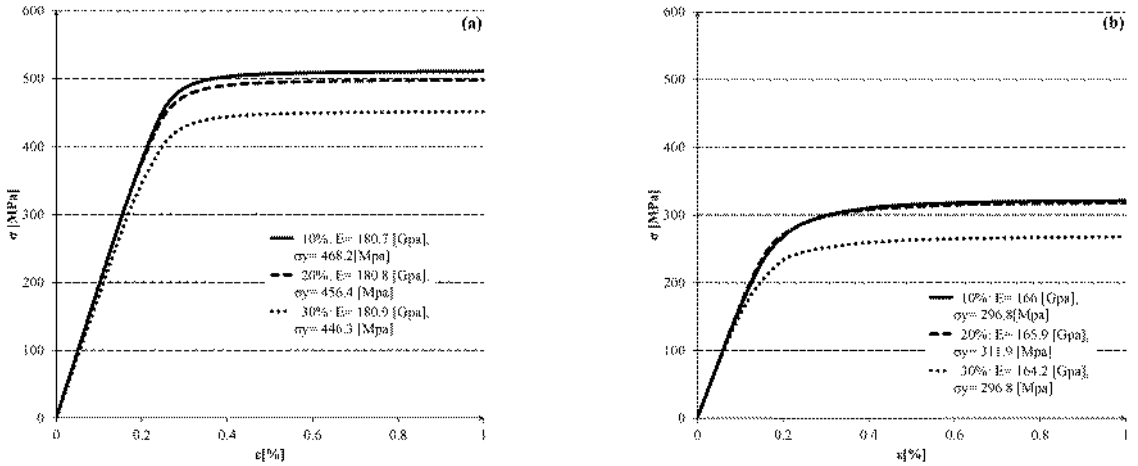

Fig.10: Stress-strain curves for RVE with 10, 20 y 30% de ferrite in matrix: (a) three-dimensional, (b) two-dimensional RVE.

In Fig. 11 the fields of von Mises equivalent stresses calculated for two-dimensional and three-dimensional RVE with ferrite fraction of 20% are shown.

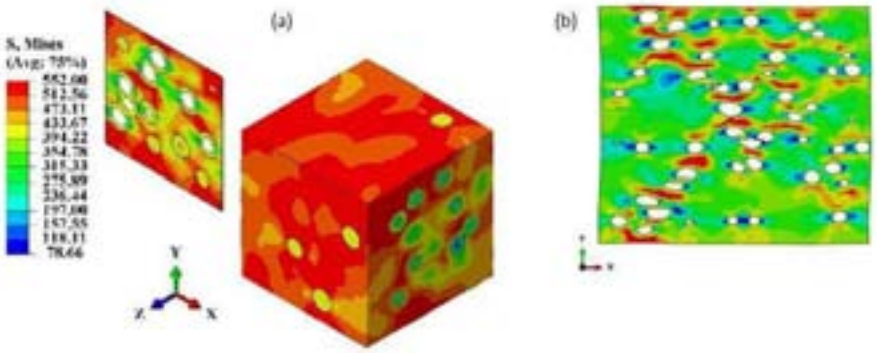

Fig.11: von Mises equivalent stresses for RVE with 20% ferrite fraction in matrix and strain of 0.25% (a) three-dimensional and (b) two-dimensional RVE.

Conclusions

Macroscopic Young's modulus and yield stress for nodular cast irons using the method of asymptotic homogenization for multiparticle models, have been obtained in this work. The generated cells are formed by a mixed matrix with different proportions of ferrite and pearlite and nodules embedded therein. The nodes are represented as voids; the ratio between the radii of the spherical layers of ferrite and the radii of the corresponding nodules is assumed constant.

The RSA method used to obtain the distribution of nodes limits the maximum fraction of ferrite in the matrix that can be achieved.

The different criteria for defining the RVE give different results, being in general the geometric criterion which gives the smaller sizes. With regard to the cells in two or three dimensions, it is noted that lower representative values are obtained for the last. This might be because the three-dimensional models provide a more complete description of the material structure. However, the use of three dimensional models has a much higher computational cost even when compared with that of the two-dimensional RVE of higher relative sizes.

Three-dimensional models have stiffer behavior than two-dimensional models. This is attributed to the assumptions that are made by considering the problem as a plane stress problem. The perfect elastic-plastic constitutive model used for the microconstituents does not allow the macroscopic representation of the strain hardening of the material.

Given the limitations identified in the work, it is considered appropriate to analyze, in future works, other methods to generating cell that would achieve higher ferrite fractions. It is also considered necessary to evaluate other forms of distribution of the ferrite whose characteristics may be, for example, the simulation result of the cooling of the material in the mold.

References

1. H. J. Böhm: 'A Short introduction to basic aspect of continuum micromechanics', Report, Institute of Lightweight Design and Structural Biomechanics (ILSB), Vienna University of Technology, 2012.

2. X. Guo, D.M. Stefanescu, L. Chuzhoy, M.A. Pershing and G.L. Biltgen: AFS Transactions, 1997, 105, 47–54.
3. L. Wenzhen and L. Baicheng: International Proceedings of 62nd World Foundry Congress, Philadelphia, Pennsylvania, USA, April 1996, 2-10.
4. E. Lundback, I.L.Svensson, I.L. and P. Person: Proceedings of the Euromech 233, Colloquium 'Modelling of metal forming processes', Sophia Antipolis, August France, 1988, 37–46.
5. S.H. Pundale, R.J. Rogers and G.R. Nadkarni: *AFS Transactions*, 2000, 102 (98), 99–105.
6. L. Collini and G. Nicoletto: *J. Strain Anal. Eng. Des.*,2005, 40 (2), 95–106.
7. L. Collini: 'Micromechanical modeling of the elasto-plastic behavior of heterogeneous nodular cast iron', PhD thesis, Università degli Studi di Parma, Italia, 2004.
8. W.J. Drugan and J.R. Willis: *J. Mech. Phys. Solids*, 1996, 44, 497–524.
9. W. Drugan: *J. Mech. Phys. Solids*, 2000, 48, 1359-1387.
10. I. Temizer: Micromechonics: Lecture Notes 'Analysis of Heterogeneous Materials', Department of Mechanical Engineering. Bilkent University, Ankara, Turquía, 2012.
11. E.R. Boeri: 'The Solidification of Ductile Cast Iron', PhD thesis, University of British Columbia, Canadá, 1989.
12. F.J. Rodriguez, A.D. Boccardo, P.M. Dardati, F.D. Carazo, D.J. Celentano and L.A. Godoy: *Mec. Comput.*, 2012, XXX, 2093-2118.
13. Angus H.T.: 'Cast Iron: Physical and Engineering Properties', 2nd edn, 1978, Butterworths & Co.
14. Anand L.: Scripta metalúrgica, 1982, 16, 173-177.
15. Centre d'Information des Fontes Moulées: 'Manuel des Fontes Moulees', 705, 1983, Paris, Éditions Techinques des Industries de la Fonderie.
16. Metzloff K.E. et al.: AFS Transactions, 1996, 104, 721-728.
17. Ohashi T., Roslan L., Takahashi K., Shimokawa T., Tanaka M y Higashida K.: Materials Science and Engineering A, 2013, 588, 214-220.
18. L.A. Godoy: *Mec. Comput.*, 2003, XXII, 1964-1984.
19. E. Sanchez-Palencia: *Rend. Sem. Mat. Univ. Politec. Torino*, 1986, 44, 1-45.
20. C. Miehe, J. Schotte and J. Schröder: *Comput. Mater. Sci.*, 1999, 16, 372–382.
21. J. A. Zahr Viñuela: 'Comportamiento mecánico de materiales compuestos de matriz metálica y refuerzo de partículas. Un enfoque basado en celdas multipartícula', PhD thesis, Universidad Carlos III de Madrid, España, 2010.
22. J. Pinho-da-Cruz, J.A. Oliveira and F. Texeira-Dias: *Comput. Mater. Sci*., 2009, 45, 1073-1080.
23. A.A Ibarra Pino and A.P. Cisilino: *Mec. Comput*., 2011, XXX, 3413-3430.
24. S. Li and A. Wongsto: *Mec. Mat.*, 2004, 36, 543-572.
25. F.J. Rodriguez, P.M. Dardati, L.A. Godoy and D.J. Celentano: *Mec. Comput.*, 2013, XXXII, 453-463.

Analytical Functions Describing Solidification of Gray Cast Iron based on Thermodynamic Calculations

S. Jonsson
Department of Materials Science and Engineering, Royal Institute of Technology,
SE-100 44, Stockholm, Sweden

Thermodynamic calculations and Scheil-Gulliver simulations are used for simulating solidification of gray cast iron, systematically varying the composition around Fe-3.35C-2Si by adding Cr, Ni, Mn, Mo, Cu, S, P, and in some cases, Al, V, and B. By adding Ti and N, the competition between Ti(C,N) and N_2-gas precipitation is thoroughly studied.
The simulated results are assessed by regression analysis producing many explicit formulae for predicting solidification of gray cast iron. The agreement between thermodynamic calculations and regression formulae is generally very good.

Keywords: gray cast iron, solidification simulations, Scheil-Gulliver simulations, liquidus projections, analytical functions.

Article available in the International Journal of Cast Metals Research

Effect of Cooling Rate and of Titanium Additions on the Microstructure of Thin-Walled Compacted Iron Castings

Marcin Górny[a], Magdalena Kawalec[b], Gabriela Sikora[c], Hugo Lopez[d]
[a-c]AGH-University of Science and Technology, Reymonta Str. 23, 30-065 Krakow, Poland.
[d]UWM University of Wisconsin-Milwaukee, P.O. Box 784, Milwaukee, WI 53201, U.S.A

This article addresses the effect of cooling rate and of titanium additions on the exhibited microstructure of thin-walled compacted graphite iron (TWCI) castings as determined by changing molding media, section size and Ferro Titanium. Various molding materials were employed (silica sand and insulating sand "LDASC") to achieve different cooling rates. This study shows that the cooling rates exhibited in the TWCI castings varies widely (70-14^{o}C/s) when the wall thickness is changed from 2 to 5 mm. In turn, this is accompanied by a significant variation in the compacted graphite fraction. The resultant cooling rates were effectively reduced by applying an insulating sand in order to obtain the desired graphite compactness. Ti additions in combination with LDASC sand molds were highly effective in promoting the development of over 80% compacted graphite in castings with wall thicknesses of 2 and 3 mm as evidenced by quantitative metallographic analyses.

Keywords: Compacted Graphite Iron, Cooling Rate, Thermal Analysis, Microstructure.
.

Article available in the International Journal of Cast Metals Research

Effect of Cu, Mn and Sn on pearlite growth kinetics in as-cast ductile irons

J. Lacaze[1] and J. Sertucha[2]

[1] CIRIMAT, Université de Toulouse, ENSIACET, Toulouse, France

[2] Área de Ingeniería, I+D y Procesos Metalúrgicos, IK4-Azterlan, Durango (Bizkaia), Spain

In a previously published work, pearlite growth in cast irons was investigated and it was claimed that growth kinetics of pearlite in nodular cast iron does not depend on alloying elements and that only the start temperature for the transformation is modified. Since then, the authors have investigated the effect of copper at low level of manganese and the combined effect of copper and tin at intermediate manganese contents. In the first case, thermal records confirmed that copper decreases the formation temperature for both ferrite and pearlite. In the second work, an optimised content for tin, manganese and copper was found so as to improve mechanical properties while keeping fully pearlitic structures. The thermal records obtained during this latter study are here used to estimate the pearlite growth kinetics and the effect of copper and tin on it. Tin has been shown to reduce pearlite undercooling (increase of start transformation temperature) and thus to favour the formation of this constituent.

Keywords: ductile irons, pearlite growth, copper, manganese, tin, eutectoid transformation

Article available in the International Journal of Cast Metals Research

Effect of Thermo-mechanical Processing Parameters on Phase Transformation and Hardness of Dual Matrix Ductile Iron

M. Soliman[1], H. Ibrahim[1], A. Nofal[2] and H. Palkowski[1]
[1]Institute of Metallurgy, Clausthal University of Technology, D38678 Clausthal-Zellerfeld, Germany
[2] Central Metallurgical Research and Development Institute - CMRDI, Helwan, 11421 Cairo, Egypt

The microstructural changes and hardness exhibited by ductile iron with dual matrix structure (DMS) are investigated. In particular, DMS microstructures are obtained by continuous cooling in the (ferrite + austenite) region followed by quenching to transform the austenite into martensite or by austempering at 375 °C, so as to transform the austenite into ausferrite. Additionally, two deformation steps are applied in the austenite-region. The structure was produced in a thermo-mechanical simulator equipped with a dilatometry system. The dilatometry is used to monitor the structure development throughout the thermo-mechanical processes. The structure was investigated using light optical microscopy and scanning electron microscopy. The influence of introducing ferrite to the microstructure and the deformation magnitude on the structure development and hardness properties are explored.

Keywords: ductile iron, thermo-mechanical processing, dual matrix, phase transformations, dilatometry.

Article available in the International Journal of Cast Metals Research

Occurrence and behavior of Mo-containing precipitations in nodular cast iron at high temperatures

Lutz Dekker[1], Babette Tonn[2]
[1] Stahlwerk Bous GmbH, Saarstraße, D-66359 Bous, Germany
[2] Institute of Metallurgy, Clausthal University of Technology, Robert-Koch-Str. 42; D-38678
Clausthal-Zellerfeld, Germany

In nodular cast iron molybdenum is alloyed in the range of 0.5 wt.-% to 1.5 wt.-% to increase the mechanical properties for high temperature application, especially for thick-walled castings like housings of gas or steam turbines. The behaviour of Mo-precipitations in the as cast state as well as under long exposure to heat was the object of this investigation. In the as-cast state Mo forms metastable carbidic grain-boundary precipitations with iron, silicon and carbon. These transform into stable MoC precipitations during sustained temperature influence. Furthermore, there are finely dispersed Mo-containing precipitations found in the matrix. These increase the high temperature strength of Mo-alloyed cast iron due to the Orowan mechanism and the occurrence of additional grain boundaries. However, it has been shown that these Mo-containing precipitations underlie Ostwald ripening under continuous heat exposure and a precipitation free area occurs along the ferritic grain boundary.

Keywords: ductile iron, high-temperature application, molybdenum, Ostwald-ripening

Article available in the International Journal of Cast Metals Research

Quenching and Partitioning process in Ductile Cast Irons

A.J.S.T. da Silva[1,2], M.F. de Campos[3], A.S. Nishikawa[1], W.L. Guesser[4] and H. Goldenstein[1*]
[1]Department of Metallurgical and Materials Engineering, Escola Politécnica da USP, São Paulo, Brazil
[2]Tupy Fundições S.A., Mauá, Brazil
[3]Universidade Federal Fluminense,Volta Redonda, Brazil
[4]Center of Technological Sciences, Universidade do Estado de Santa Catarina, Joinville, Brazil

A commercial ductile iron alloy was submitted to Quenching and Partitioning (Q&P) process. Samples were austenitized at 900ºC for two hours, quenched at 170ºC and held at this temperature for 2 minutes and finally were re-heated in temperatures between 300 and 450ºC in time intervals between 2 and 180 minutes. The microstructure evaluation was performed with SEM and X-ray diffraction and mechanical properties were measured using uniaxial tensile tests and Charpy tests. In general, the Q&P process is suitable to achieve large fractions of retained austenite in ductile cast irons. The combination of properties thus obtained is very interesting from the engineering point of view, and if the elongation can be increased will provide an alternative to the austempered ductile irons.

Keywords: Quenching & Partitioning, Q&P, ductile iron, solid state transformations, austenite, bainite, ADI.

Introduction

The production of Austempered Ductile Iron (ADI) takes advantage of the effects of the high Si content on the austenite decomposition in the bainitic range, in order to obtain a carbide-free matrix microstructure (ausferrite), where sheaves of bainitic ferrite laths are separated by films or islands of metastable high carbon retained austenite. In ferrous alloys containing Si (or Al), the carbide precipitation step of the bainite transformation is slowed down or suppressed for a time long enough for the carbon from the transformed regions partition and diffuse into the austenite, leading to (meta)stable austenite at room temperature. Similar phenomena occur in TRIP steels, high Si (or Al) low alloy high strength steels containing ausferrite microstructures and also islands of MA (martensite/austenite) microconstituent. In all those material, longer heat treatments lead to carbide precipitation, causing abrupt loss of elongation and fracture toughness, signaling the existence of a finite "process widow".

Recent developments in steels containing small fractions of retained austenite introduced a new heat treatment route, namely *Quenching and Partitioning* (Q&P). This heat treatment cycle is an alternative route for obtaining multi-phase steel, in which the volumetric fraction of retained austenite is controlled by carbon partition from supersaturated martensite into austenite, allowing the stabilization of austenite[1].

The concept of Q&P involves transforming partially the austenite to martensite, by quenching to temperatures between Ms (martensite start temperature) and Mf (martensite final temperature), followed by a thermal partitioning treatment, which allows the carbon to diffuse from the supersaturated martensite to the non-transformed austenite. The increased carbon in the austenite lowers its Ms temperature promoting its stabilization[2]. Fig. 1 shows a schematic of the Q&P process. In order to obtain a volume of carbon stabilized austenite, a certain amount of non-transformed austenite after quenching is necessary and also the suppression of carbide precipitation by the presence of silicon or aluminum alloy additions, for a time period long enough for partition to occur[1].

Studies conducted by several researchers[4–9] proved to be possible to achieve substantive amounts of retained austenite through Q&P heat treatments in silicon containing steels. In these studies it was possible to see the dependence between the fractions of retained austenite (as well as its final carbon content) and the heat treatment conditions. These studies demonstrate that with increased partitioning temperature, the kinetic of the reactions is accelerated, obtaining higher fractions of retained austenite in a shorter period of time. From one point on, this austenite fraction starts decreasing, indicating the beginning of transformation to other type of products (carbide containing phases). Transmission electron microscopy dark field images confirmed that the final structure is composed of thin flakes of austenite between martensite platelets. Furthermore, they evidenced that the Q&P heat treatment cycle is a feasible route for the achievement of combinations of high tensile strength with reasonable tenacity or toughness, using relatively simple Si containing commercial steels. The carbide suppression improves the toughness of steels while the retained austenite will protect the bainitic or martensitic ferrite from the detrimental effects in mechanical properties caused by carbide dispersion.

At the early stage of the development of Q&P, Speers recognized the potential for Q&P ductile cast iron, due to the usual high level of Si found in those alloys, and made preliminary experiments[1]. Undergraduate students at Colorado School of

* Corresponding author, email: hgoldens@usp.br

Mines conducted the work in 2004, with a commercial 3.7%wt C, 2.5%wt Si, 0.34%wt Mn, 0.17%wt Cu ductile cast iron. A limited number of Q&P parameters were assessed in this work, while austenitizing temperature and partitioning time were held constant. The results showed that substantial fractions of carbon-enriched austenite could be retained via Q&P processing, although the austenite levels were found to be lower than obtained via austempering under the processing conditions evaluated. The strengths were greater in the Q&P condition, while the ductility and room temperature impact properties were lower. Speers' group did not pursue this work, though.

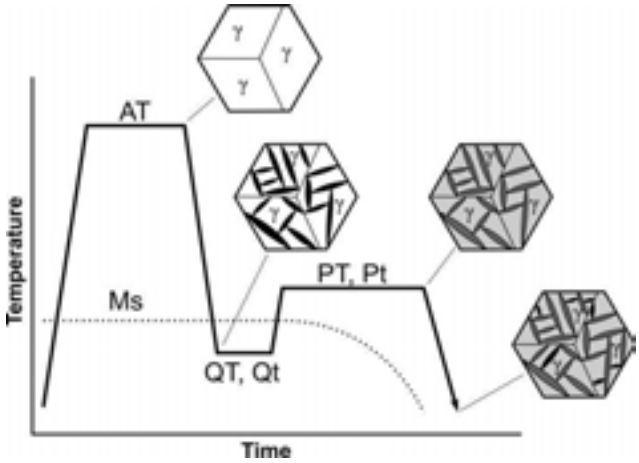

Fig.1: Schematic of the Q&P process for production of austenite-containing microstructures. Adapted from Matlock et al[3].

The main objective of this work is to obtain further knowledge about the behavior of nodular cast irons heat treated in a Q&P cycle. We expected to understand the evolution of the microstructure during the heat treatment in order to identify the existence of a process window, which can be used to obtain improved mechanical properties. The major contribution expected by applying this route in ductile iron is the development of a class of heat-treated nodular cast iron, which can be a technological alternative in applications where the austempered ductile iron are consolidated materials.

Experimental Procedure

A commercial ductile iron alloy, used in components for the automotive industry, was cast as Y-blocks, following the Brazilian standard NBR 6916. Composition, presented at table 1, is not the optimum composition for ADI, as the Mn level is too high. Nodule counting was 163 nodules/mm², also not very high; a higher nodule count would be beneficial to alleviate the effects of the heterogeneity of the microstructure due to the segregation of chemical elements during solidification.

Table 1: Chemical composition of alloys studies in the present work.

Element	C	Si	Mn	P	S	Cr	Cu	Mg	Ni
Composition (wt %)	3.48	2.89	0.52	0.06	0.01	0.03	0.50	0.05	0.01

The Y-blocks were cut into pieces of 25mm thickness, 40mm width and 135mm length and processed under Q&P thermal cycle as described in the Fig. 1. The heat treatment consisted of austenitizing of the specimens at 900°C during 2 hours in a air muffle furnace, quenching into oil bath preheated at the temperature (QT) of 170°C, and reheating until partitioning temperatures (PT) of 300, 375 and 450 °C during various times in the range of 5-180min. The partitioning step was also performed in an air muffle furnace.

The austenitizing temperature was chosen on basis of the parameters typically used in the heat treatment of ADI. In this step carbon redistribute between austenite and graphite, approaching equilibrium levels, although substitutional alloying elements may still remain far from equilibrium compositions. Austenite composition at austenitizing temperature was calculated using computational thermodynamics calculations with Thermo-Calc® software and it is given in table 2. Minor impurities on chemical composition (P, S, and Mg) were not considered in this calculation. This result was coupled with Andrews empirical equation[10,11] (equation 1) and the Ms temperature was estimated as 189°C. Using Koistinen-Marburger[12] relationship (equation 2), the amount of athermal martensite formed at QT from austenite was estimated to be 35 %vol.

$$Ms\ (°C) = 539 - 423\%wtC - 30.4\%wtMn - 12.1\%wtCr - 7.5\%wtMo - 7.5\%wtSi \quad (1)$$

$$f_{\alpha'} = 1 - \exp\{-1.1 \cdot 10^{-2}\ (Ms - QT)\} \quad (2)$$

Table 2: Equilibrium austenite chemical composition at 900°C calculated using Thermo-Calc®.

Element	C	Si	Mn	Cr	Cu	Ni
Composition (wt %)	0.71	2.97	0.52	0.03	0.51	0.01

Samples were prepared using conventional metallographic techniques by mechanical polishing and chemical etching using 2% Nital reagent. Scanning electron microscopy (SEM) evaluations were performed using SEM Phillips model XL30 operating at 20kV. X-ray diffraction (XRD) analyses were performed using a Shimadzu model 6000 diffractometer with Co Kα radiation. Bragg-Brentano geometry was used and the scanning was made over the interval of 2θ = 30–110° at steps of 0.02º and 6 sec per step. Retained austenite volume fractions and carbon content were estimated by analysis of diffraction data *via* the Rietveld method using the software TOPAS ACADEMIC 4.1. The amount of carbon dissolved in austenite was obtained using the method developed by Dyson and Holmes[13] through an empirical equation (equation 3) which considers the volumetric changes of crystalline structure with the percentage of alloying elements in solid solution using the change in lattice parameter.

$$a_\gamma = 3.5780 + 0.033\%atC + 0.00095\%atMn + 0.002\%atNi + 0.0006\%atCr + 0.0031\%atMo + 0.0018\%atV \quad (3)$$

Mechanical evaluation was carried out by impact Charpy tests from samples machined from heat treated blocks. Impact tests were carried out in a 30 KPM Wolpert machine, model PW 20/30K according to NBR 6157 standard. Tensile tests samples were also machined from heat treated blocks. Uniaxial tensile strength tests were conducted in an EMIC universal machine model DL 20000 at a loading speed of 1 mm/min.

Results

Analyses of microstructures

The analysis of the microstructure *via* SEM method showed that the microstructure of almost all treated samples presents pronounced differences between the intercellular zones and the areas around graphite nodules, as can be seen in Fig. 2. In the areas surrounding the nodules, it was observed the presence of partitioned martensite (i.e., martensite formed during quenching step and tempered during partitioning step) and ausferrite (bainitic ferrite + retained austenite). On the other hand, the intercellular areas were composed predominantly by fresh martensite, probably formed by the transformation of unstable austenite during final cooling. Due to segregation, the intercellular area presented lower Ms value and thus remained austenitic during quenching step. In the absence of athermal martensite, the only way to carbon-enrich austenite in these areas would be the formation of ausferrite. In shorter partitioning times there was not enough time for substantial formation of ausferrite and, consequently, during the final cooling the unstable austenite transformed into martensite. For longer partitioning times the intercellular austenite fully decomposes into ausferrite, as can be seen in Fig. 3.

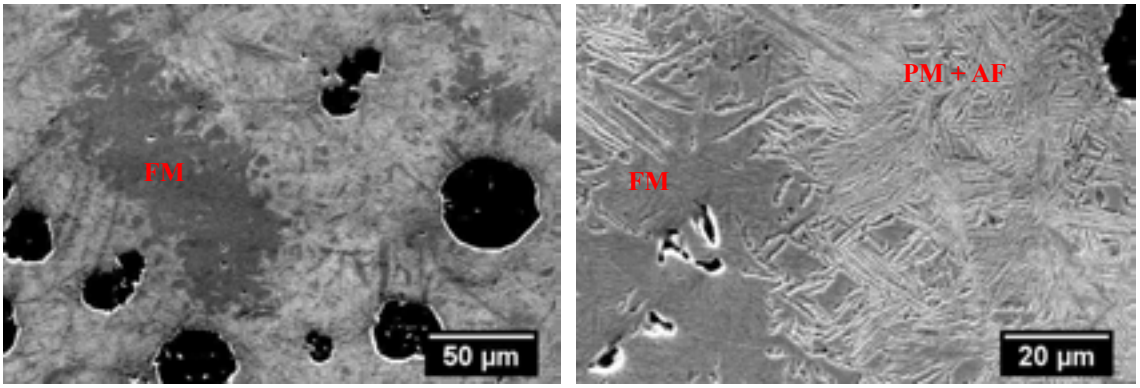

Fig.2: Microstructure of the sample partitioned at 300ºC during 2 minutes, showing the differences of microstructures around the nodules (PM = partitioned martensite, AF = ausferrite) and around the eutectic cells (FM = fresh martensite).

Chemical elements such as manganese, molybdenum and chromium segregate towards eutectic cell boundaries. In practice, areas around the nodules and intercellular areas behave almost as two different alloys, with different compositions. Therefore, the kinetic of transformations resulting from heat treatment will differ on both areas[14]. This phenomenon will possibly allow that, in the same heat treatment, austenite will be stabilized by carbon in areas close to the graphite nodules whereas in the intercellular areas there is still austenite with low carbon content, which will transform to fresh martensite during final cooling. It's known that differences in substitutional elements chemical composition will not relax on the relatively short austenitizing times applied in this study. Thus different percentages of carbon and substitutional elements will be present, either in equilibrium with graphite or in intercellular areas and around the nodule at the end of the austenitizing process. As a consequence the Ms temperature and the amount of martensite (either the real values and those predicted by equations 1 and 2) will be different in these areas.

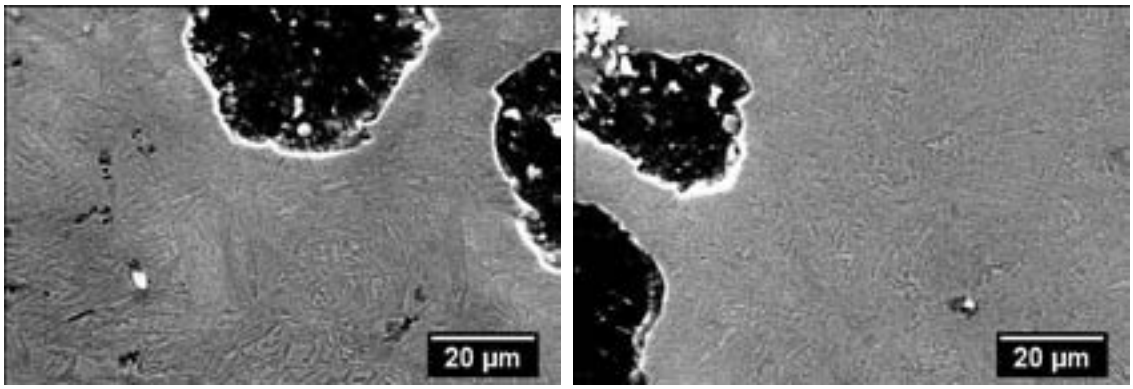

Fig.3: Sample partitioned at 300 °C during (a) 60 minutes and (b) 120 minutes. It's possible to observe that intercellular areas were fully transformed into ausferrite.

SEM micrographs presented in Fig. 4 show the matrix microstructure near a graphite nodule. As pointed earlier, it's possible to distinguish ausferrite (thin needle-like product) from partitioned martensite (PM) that was formed during first quenching and whose carbon was partitioned during the isothermal heat treatment. The carbon of the plate martensite observed around the nodule diffused to the remaining austenite, eliminating martensite supersaturation. In this way, this product is plate martensite (morphologically) but with low carbon content and body centered cubic structure, similar to ferrite. It's worth noting that the amount of partitioned martensite seems to be lower than the predicted amount estimated by Koistinen-Marburger (KM) equation. There are two possible explanations to this observation: KM equation adjusting coefficients are sensitive to alloy chemical composition and thus may introduce an error to the estimative. Moreover, the sample holding time at quenching temperature may not have been long enough to allow the thermal stabilization between the sample and the oil bath, leading to a lower amount of martensite.

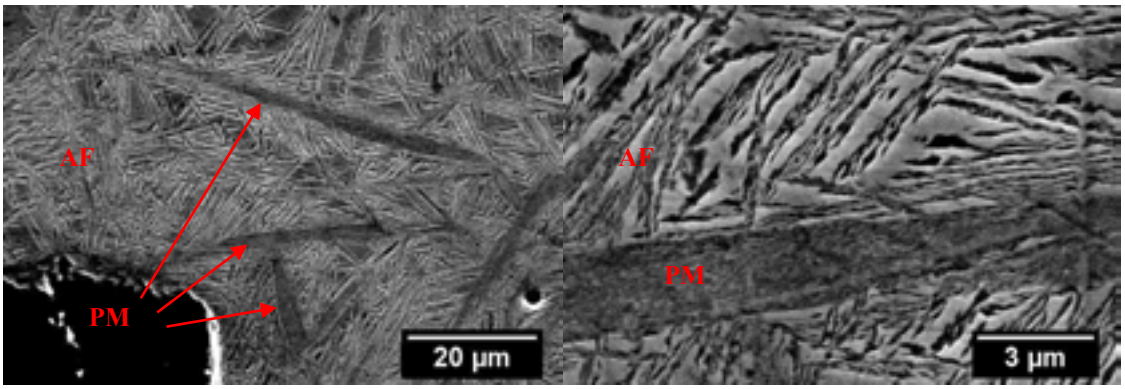

Fig.4: Sample partitioned at 300 °C during 5 minutes, showing ausferritic structure (AF) as well depleted carbon martensitic areas formed during quenching (PM).

The two martensitic areas presented in Fig. 2 and Fig. 4 have distinct morphology and mechanical properties due to different carbon contents in solution. The low carbon content of the martensite present around graphite nodules allows this

phase to present lower hardness. On the other hand, martensite in the intercellular areas has higher carbon content; therefore, this phase is potentially brittle due to its high hardness, tetragonality and level of residual stresses.

Summarizing, the final microstructure obtained through quenching and partitioning in ductile cast irons is composed of graphite nodules formed during solidification and a mixture of ausferrite (bainitic ferrite free of carbides and retained austenite) with high and low carbon (carbon depleted) martensite.

Analyses of XRD results

X-ray diffraction tests were carried out with the purpose of measuring the fractions of retained austenite in the samples. The charts in Fig. 5 show that is possible to obtain sizeable fractions of retained austenite with considerable carbon content dissolved in it, depending on the partitioning conditions. The transformation kinetics during the partitioning step shows strong dependence on temperature. In general, the kinetics is accelerated at higher partitioning temperatures. Samples partitioned at 300°C presented retained austenite fractions with increasing tendency during the 180 minutes of the partitioning cycle, while the samples partitioned at 450°C shows the retained austenite peaking in the first minutes of the partitioning cycle followed by fast subsequent decreasing contents, indicating a minimal or nonexistent process window for this temperature.

Fig. 5b shows that higher austenite carbon content was obtained faster when higher partitioning temperatures were used. In all conditions, carbon content increases during the initials heat treatment times. After certain time, it is noticed that the carbon content dissolved in austenite decreases. This behavior is evidence that after certain time intervals the austenite decomposes into other types of products, probably carbides of the second stage of bainitic reaction, the same phenomenon that occurs in ductile cast iron subjected to long austempering times.

It also can be noted that for the sample partitioned at 300 °C in the shortest time (2 min) austenite carbon content calculated from the lattice parameter is smaller than the expected austenite initial composition. This might be due to the fact that at this partitioning time austenite is not sufficiently carbon-enriched to stabilize itself. Hence, fresh martensite may have formed at the final cooling, exerting compressive stresses on the austenite surrounding regions, thus explaining the smaller lattice parameter observed. Similar results were reported by Golovchiner[15] in Fe-Ni alloys, and Toji et al[16] for a Q&P steel.

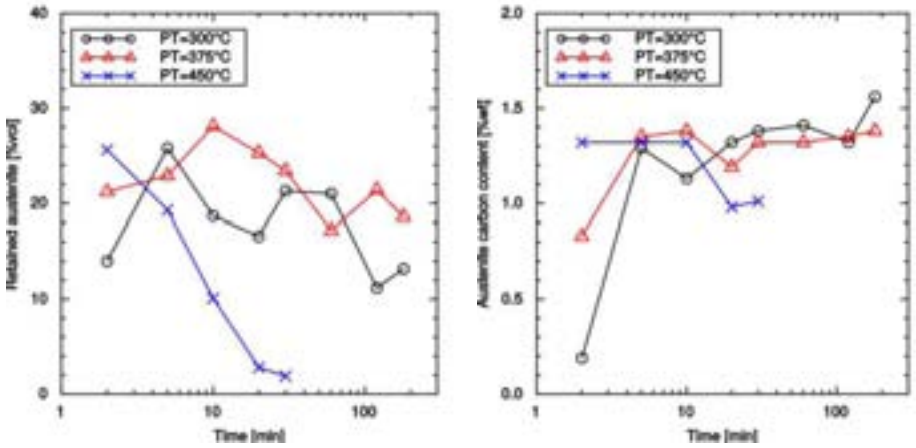

(a) **(b)**

Fig.5: (a) Retained austenite fractions obtained in all partitioning conditions. (b) Carbon content in solid solution in retained austenite obtained in all partitioning conditions.

Mechanical properties

Impact tests were performed to provide an estimate of the toughness of this new class of material. The data presented in Fig. 6 shows that the impact energy initially increases and after some time of partitioning treatment starts to decrease, characterizing a process window. For 300ºC the energy decreases after 120 min, for 375ºC after 20 minutes and for 450ºC after only 10 minutes. The initial increase is explained by the presence of stabilized retained austenite, confirmed by X-ray diffraction. The maximum impact energy results obtained were 87.2 J on samples partitioned at 300°C for120 minutes, 92.2 J on samples partitioned at 375°C for 20 minutes and 58.8 J on samples partitioned at 450°C for 5 minutes. A time interval that produces optimized properties can be observed for each heat treatment temperature used in this study. If the heat treatment time is longer or shorter than the process window, the mechanical properties will be decreased.

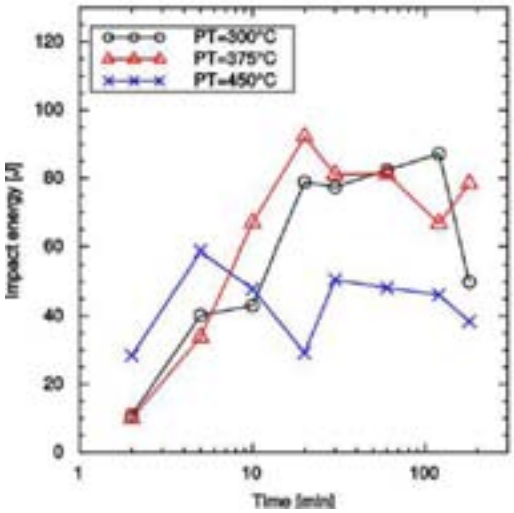

Fig. 6: Impact energy (Joules) of all heat treatment conditions.

Analyzing Fig. 7 it is possible to observe that both Ultimate Tensile Strength (UTS) and Yield Strength (YS) presents a tendency to increase during the partitioning heat treatment. This result is in agreement with the kinetic of ausferrite formation in the intercellular areas. For all tested conditions, the higher values of tensile/yield strength were observed after longer partitioning times. In the sample partitioned at 300 °C, there was a large increase of the mechanical properties only after 60 minutes of treatment, presumably because of the slow kinetics of ausferrite formation at this temperature. After 120 min, the impact energy and total elongations started to fall even for the 300° C treatment.

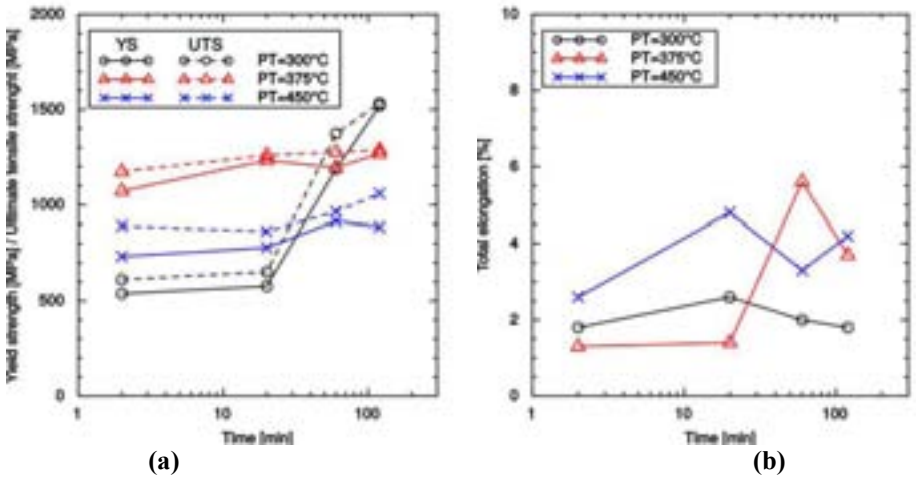

Fig. 7: Tensile properties of all conditions tested. (a) Yield strength (YS) and ultimate tensile strength (UTS). (b) Total elongation.

Discussion

The concept of process window is widely used on the austempered ductile irons and consists of the time intervals and temperatures in which it is possible to obtain optimal mechanical properties[14]. If the holding time at the austempering temperature is too short, it is possible that certain portion of austenite will not be enriched enough by carbon to be able to reach thermal stability and will transform to fresh martensite during cooling to room temperature, decreasing the material toughness (decrease on elongation and impact energy). On the other hand, if the time is too high, the second stage of bainitic reaction will be reached, in which the austenite, supersaturated in carbon, will decompose precipitating carbides. This phenomenon will also decrease the toughness of material. In this way, for each austempering temperature used in heat treatment, it exists a time interval where the material present optimal properties. In general, higher austempering temperatures will produce more tight process windows, because the transformations during heat treatment will be accelerated[14].

Fig. 8 presents a comparison between the mechanical properties of the samples used in this study with the mechanical properties of austempered ductile iron presented in ASTM A897 standard[17]. It is possible to see that the Q&P heat treatments were not able to obtain the elongations specified for austempered ductile irons (ADI), with the exception of one sample treated at 375ºC for 60 minutes.

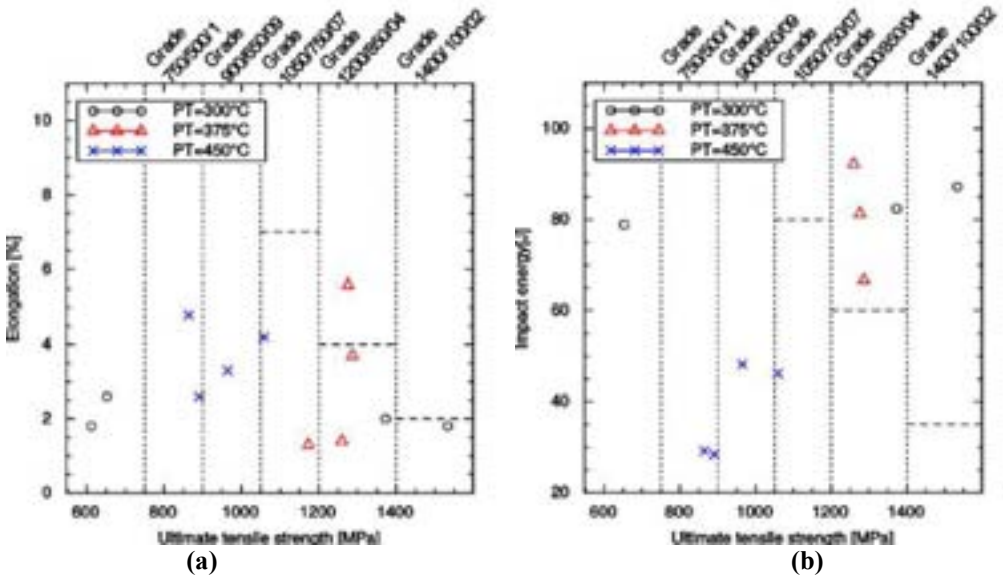

Fig. 7: Mechanical properties map comparing ADI with quenching and partitioning ductile cast iron. Dashed lines represent ASTM A897 specifications.

A possible explanation for this failure is suggested by the difference in microstructure between the regions near the nodules and the intercellular regions, an indication of chemical heterogeneity between the two regions, due to segregation during the solidification. As discussed earlier, the segregation of chemical elements will change the local kinetics of transformation mainly at intercellular areas, richer in elements such as manganese and molybdenum that segregate to the last region to solidify. In the specific case of the alloy used in this study, the formation of fresh martensite during the final cooling in the segregated intercellular areas was due to two main effects: the Ms temperature of the intercellular areas is reduced below the quenching temperature, blocking the formation of martensite during the first step of heat treatment; secondly, the formation of ausferrite in the intercellular areas will be difficult, producing large areas of cell boundary containing non-stabilized austenite, which will be transformed into martensite in the final cooling. Thus, high manganese contents shortens the process window, making less probable the stabilization of the intercellular austenite for smaller partitioning times. At the same time, the end of the process window is accelerated near the nodules, for the same reasons. This difference causes the process window of one region to have a minimal overlap with the process window of the other; one region starts to precipitate carbides before the other has stabilized the austenite, in the same sample. This is probably what happened at 450ºC causing the low elongation and fracture energy obtained for partitioning at this temperature. Using as initial material a cast iron with a higher nodule count through advanced inoculation techniques and lowering the Mn content could help minimize intercellular segregation, thus improving significantly the elongation.

The application of Q&P to thicker parts will eventually require the use of alloying elements (Mo, Mn) in order to increase hardenability and therefore the effect of segregation of these elements tends to be potentiated. In addition to their effects on the kinetics of isothermal transformations, both manganese and molybdenum tend to form eutectic carbides at the end of the solidification, which are difficult to dissolve during the austenitizing step. These carbides will act as nucleation sites for cracks, harming the mechanical properties. An option is to use nickel and copper additions, as these alloying elements do not tend to segregate in intercellular areas. Another way to minimize the segregation effect is to increase the amount of eutectic cells through inoculation. An effective inoculation can significantly increase the number of eutectic cells in the ductile cast irons and consequently improve the distribution of segregation in the microstructure[14].

The precipitation of carbides can occur owing to the use of too long times or too high temperatures during isothermal treatment. The experimental data of volumetric fraction of retained austenite and carbon content in the austenite that were presented in this study shows that higher partitioning temperatures will accelerate the kinetics of reaction causing higher percentages of retained austenite and carbon content in solution for shorter times. This provides evidence that higher temperatures accelerate the partition of carbon into the austenite, and also the precipitation of other products, such as ausferrite or carbides from second stage of bainitic reaction, the last one with embrittlement effect. In this way, the correct

selection of partitioning temperature is the key to obtain the best combination of mechanical properties. The silicon content also has a role, preventing carbide formation in austempered ductile irons. So the correct selection of the silicon content added to the base alloy is an important way to optimize the process window and therefore the mechanical properties.

Conclusions

1. Q&P is a viable route to obtain ductile irons with considerable volumetric fractions of retained austenite.
2. The microstructural analysis showed that the microstructure resulting from quenching and partition heat treatments of a conventional ductile iron is composed of a mixture of partitioned martensite (low carbon) + fresh martensite + ausferrite (bainitic ferrite free of carbides + retained austenite).
3. In intercellular areas, fresh martensite formed from unstable austenite is predominant. In other areas, the presence of ausferrite formed in the partitioning cycle will predominate. These differences are originated from the gradient of chemical composition between these areas.
4. The process window concept can be applied to ductile cast irons heat treated with a Q&P cycle.The heterogeneities between the intercellular region and the neighborhood of the nodules cause a difference on the kinetics, which can
5. The combination of properties thus obtained is very interesting from the engineering point of view, and if the elongation can be increased will provide an alternative to the austempered ductile irons in applications in which the latter has already been consolidated.

References

1. J.G. Speer, D.V. Edmonds, F.C. Rizzo F.C. and D.K. Matlock: *Curr. Opin. Solid State Mater. Sci.*, 2004, 8, 219-237.
2. G.A. Thomas, J.G. Speer and D.K. Matlock: *Iron Steel Technol.*, 2008, 10, 209-217.
3. D.K. Matlock, V.E. Bräutigam and J.G. Speer: *Mater. Sci. Forum*, 2003, 426-432, 1089-1094.
4. A.M. Streicher, J.G. Speer, D.K. Matlock and B.V. Edmonds: Proc. Int. Conf. on 'Advanced High Strength Sheet Steels for Auto Applications', Warrendale, USA, 2004, 51-62.
5. D.V. Edmonds, K. He, F.C. Rizzo, B.C. De Cooman, D.K. Matlock and J.G. Speer: *Mater. Sci. Eng. A*, 2006, 438-440, 25-34.
6. N. Zhong, X. Wang, Y. Rong and L. Wang: *J. Mater. Sci.*, 2006, 22, 751-754.
7. E. De Moor, S. Lacroix and L. Samek: Proc. 3rd Int. Conf. on 'Advanced Structural Steels', Gyeongju, Korea, August 2006.
8. S.S. Nayak, R. Anumolu, R.D.K. Misra, K.H. Kim and D.L. Lee: *Mater. Sci. Eng. A*, 2008, 498, 442-456.
9. A.J.J. Clarke, J.G. Speer, D.K. Matlock, F.C. Rizzo, D.V. Edmonds and M.J. Santofimia: *Scr. Mater.*, 2009, 61, 149-152.
10. K.W. Andrews: *Iron Steel Inst. J.*, 1965, 203, 721-727.
11. I.A. Yakubtsov and G.R. Purdy: *Metall. Mater. Trans. A*, 2011, 43, 437-446.
12. D.P. Koistinen and R.E. Marburger: *Acta Metall.*, 1959, 7, 59-60.
13. D. Dyson and B. Holmes: *J. Iron Steel Inst.*, 1970, 208, 469-470.
14. W.L. Guesser: in 'Propriedades Mecânicas dos FerrosFundidos'; 2009, São Paulo, Edgar Blücher Ltda.
15. K.Y. Golovchiner: *Phys. Met. Metallogr.*, 1974, 37, 126-130.
16. Y. Toji, H. Matsuda, M. Herbig, P.P. Choi and D. Raabe: *Acta Mater.*, 2014, 65, 215-228.
17. ASTM International: 'ASTM A897/A897M-06 - Standard Specification for Austempered Ductile Iron Castings', 2011.

Acknowledgement

The authors acknowledge the support of CAPES – Coordenação de Aperfeiçoamento de Pessoal de Nível Superior and CNPq – Conselho Nacional de Desenvolvimento Científico e Tecnológico through grants for some of the authors. The authors thanks Tupy Fundições S.A., Mauá, Brazil for providing the cast iron samples and access to facilities.

Boron Effect on the Precipitation of Secondary Carbides During Destabilization of a High-Chromium White Iron

A. Bedolla-Jacuinde[1], F. V. Guerra[1], I. Mejía[1], J. Zuno-Silva[2], C. Maldonado[2]
[1]Universidad Michoacana de San Nicolás de Hidalgo, México
[2]Universidad Autónoma del Estado de Hidalgo, México

This work analyses the secondary carbides precipitation during the destabilization of a 17%Cr white iron containing 195 ppm Boron. The experimental iron was characterized in the as-cast conditions to have comparable parameters with the heat treated samples. Destabilization heat treatments were undertaken at temperatures of 825, 900 and 975ºC for 25 minutes; each sample was air cooled after this soaking time. Characterization was undertaken by optical and electronic microscopy, image analysis and EDS microanalysis; hardness and microhardness were also evaluated. It was found that the volume fraction of secondary carbides precipitated is always higher for the lowest destabilization temperature (825ºC) due to the lower carbon solubility in austenite at low temperatures. A much higher precipitation for the irons containing boron than that for the iron without boron at any destabilization temperature was also noticed.

For the iron containing boron, a density of 23 carbide particles per square micron was measured when destabilized at 825ºC, and it decreased to about 10 particles per square micron when destabilized at 975ºC. In the case of the alloy without boron additions, about 10 carbides per squared micron were counted when destabilized at 825ºC and about 5 when destabilized at 975ºC. Higher volumes of carbide precipitation implies higher values of bulk hardness and microhardness in the alloys. The results suggest that boron works as nuclei for the precipitation of secondary carbides; this is discussed in terms of the limited solubility of boron in iron and the formation of boron rich precipitates found in the iron in the as-cast conditions.

Article available in the International Journal of Cast Metals Research

Metallographic investigation of Nd: YAG laser processed ductile iron surfaces

A. Nofal*, H. El-Gazzar and M. Ibrahim
Department of Foundry Technology, Central Metallurgical R&D Institute, Cairo, Egypt

Ductile cast iron is finding increased applications in parts subjected to different types of wear due to sliding contact and hence novel hardening techniques of mating surfaces need to be investigated. Laser hardening has proved to be very effective in enhancing the tribological properties of ductile iron surface.
In this work, high power CW-Nd:YAG 600 W laser was used for the processing of ductile iron surfaces at different scanning speeds. The depth and hardness of the processed surface were found to be dependent on the scanning speed. At lower speeds of 25 cm/min, remelting and rapidly solidified layer resulted in the formation of carbidic and graphite free surface layer of microhardness around 1200 HV. Increasing the scanning speed to 125 cm/min results in heating of the surface layer to the austenitic region with the formation of martensitic layer upon rapid cooling.
Some microstructural features associated with the laser processing were noticed at the hardened/HAZ transition layer and suggestions were made for their formation. Microhardness profile across the hardened zone were plotted, where different scanning speeds were shown to affect the hardened case depth and hardness.

Keywords: ductile iron, laser processing, surface hardening, surface remitting, accelerated graphitization, microhardness profile.

Introduction

Ductile cast irons are still finding increasing applications in many industrial sectors, thanks to their good mechanical properties, excellent castability and machinability, high thermal conductivity as excellent noise and vibration damping capacity as well as reasonable price. The strength, wear and fatigue properties of ductile irons can be improved by means of different conventional surface treatments such as induction and flame hardening and more recently by electron beam and laser technologies. However, the laser surface hardening stands out for a number of reasons, some of them are:

- Possibility of accurate control the area where laser radiation should be delivered, as well as the amount and rate of energy deposition. The laser beam is finite in size; therefore, the process is ideally suited to conduct specific localized area treatment.
- The heated thin surface layers do not require external quenching since the bulk of the material serves as a thermal sink.
- Due to the small energy input received by the material, distortion of the treated components may be minimized or eliminated, rendering the final machining or refinishing unnecessary.

Laser processing is used to produce through rapid heating and cooling a thin hard layer on the surface of a bulk material, with enhanced abrasion and corrosion resistance. Both surface hardening and melting have been used to impart better tribological properties to the surface of grey and ductile iron.

Recently a comprehensive state-of-the-art of laser processing for material surface modification has been published[1], indicating that lasers provide unlimited possibilities for surface engineering, such as solid state hardening, melting, alloying, cladding, ablation, shot peening, cleaning and texturing.

In a recent investigation[2], solid-state phase transformation during the laser surface hardening of grey cast iron was induced using low power fiber laser of power 100 W in both continuous as well as pulsed modes in conjunction with a beam-integrator. The effect of process parameters, e.g. beam power, beam diameter, travel speed and bulk time on the geometry, dimensions and hardness of heat affected zone was studied. Application of low-power lasers was shown to be more favorable compared to expensive large-sized powerful CO_2 or Nd:YAG lasers usually used as the low power thermal process avoids post process machining with minimum distortion.

Evaluation of the Nd:YAG bulked laser surface hardening of cast iron used in automotive industry was reviewed[3].

Matsuyama and Shibata[4] reported in an earlier investigation that in the laser surface processed ferritic ductile iron, graphite spheroids were surrounded by a martensitic ring, which resulted in considerable increase in wear resistance, proportional to the amount of martensite in the matrix. On the other hand, the impact strength of laser processed iron

* Corresponding author, email: adelnofal@hotmail.com

was inferior to that of untreated ductile iron. However, the impact strength of the laser treated iron with a ferritic matrix was superior to that of untreated iron with a pearlitic matrix.

Chen et al[5,6] have studied the effect of LSM process parameter on the microstructure, hardness and wear resistance of ductile iron. The refined austenitic microstructure produced by LSM could induce better wear resistance as a result of deformation induced martensitic transformation. However, such phase transformation may develop microcracks at the martensitic-austenitic interface due to the volume change involved in austenite to martensite transformation and the deformation constraints at these interfaces.

In a recent work, Fernández-Vicente et al[7] have analysed the microstructures obtained from LSM and LSH of ductile iron of different compositions under different laser processing conditions. The mechanism explaining the formation of cracks during laser treatment was studied. Extensive cracking of the laser processed layer was related to thermal stresses generated under high-energy density conditions as well as to transformational stresses associated with retained austenite contents exceeding 40%.

Farias et al[8] in an attempt to find out the laser operating parameters which will lead to certain desired properties associated with laser surface hardening, conducted the metallurgical analysis, the thermodilatometric characterization of structural evolution during rapid heating and cooling involved in LSH together with microstructural analysis of laser treated specimens for ductile cast iron as well as plain carbon steel XC42.

Wang and Bergmann[9,10] have utilized LSM to improve the abrasion resistance of ductile iron by generating a rapidly solidified ultra-fine ledeburitic surface layer. A novel iron-base material containing both the rapidly solidified eutectic cementite and the ultra-fine graphite nodules could be produced by partial graphitization of the cementite. This material was expected to have excellent performance under dry or boundary lubrication wear conditions due to its combination of the excellent abrasion resistance of the rapidly solidified eutectic cementite and the superior self-lubrication, heat conducting and damping properties of the graphitic phase.

The effect of processing parameters (beam-substrate interaction time and power density) during laser surface processing of ductile iron was earlier studied.[11,12]. The microstructure of the melted zone depends mainly on the its solidification rate and two different microstructures were obtained; at lower solidification rate a dendritic microstructure with low hardness and a second with lamellar ferrite plus parallel cementite plates with high hardness at high solidification rate. Chen et al[12] proposed that excessive supercooling of the melt during laser processing can reduce the nucleation level in the molten iron, thus enhancing the undercooling during solidification leading to the formation of carbides.

Grum and Štrum[13-15] used a mathematical model to determine the temperature cycles in grey and ductile irons and the depth of the modified layer. The mathematically obtained results were critically assessed and compared with the experimental results. The optimum laser melt-hardening conditions for individual parts were determined with a reduced number of trial experiments.

Using 500 W Nd:YAG laser equipped with self-designed diffractive optical element, a novel surface layer having both rapidly solidified eutectic cementite, martensite and graphite particle was obtained on the surface of pearlite-ferrite matrix ductile iron. The microstructure along the layer surface and the layer depth had obvious gradient distribution consisting of fine austenite, martensite with residual austenite and deudritic austenite growing radially along the periphery of graphite, martensite with residual austenite and ledeburite shell around the graphite nodules.[16]

The erosion resistance of the laser treated ductile iron was claimed to be 110 times greater that the untreated material.[17] The erosion mechanism of the untreated ductile iron under normal and oblique angles was by severe plastic deformation and ploughing; whilst the treated material was eroded by fatigue cracking. The enhanced erosion resistance after laser treatment was related to the very fine structure, high microhardness (650 Hv0.1) with the resistance to plastic flow and to the dissolution of the graphite nodules.

Recently, it was reported that the matrix of the as-cvast ductile iron specimens shows three stages of wear[18]: mild, transition and severe, while the laser processed specimens show only two stages of wear: mild and transition. The increased wear resistance was related to fine microstructures, work hardening as well as stress induced phase transformation of retained austenite to martensite.

Throughout the abovementioned reports, a very wide spectrum of microstructures has been observed and used to explain different surface hardness values, microhardness profiles across the transverse sections of the treated samples, abrasion resistance as well as the tendency of the treated surface to develop cracks.

This paper reports the first results of a research project aiming at investigating the microstructural features of ductile iron (DI) and austempered ductile iron (ADI) subjected to Nd:YAG laser surface treatment using different power intensities at scanning speeds. The results shown are limited to ductile iron treated with one power intensity of 600 W and scanning speeds from 25 to 125 cm/min.

Experimental Procedure

The ductile iron and ADI used throughout this work was melted in 100 kg MF induction furnace to reach the nominal chemical composition of 3.6%C, 2%Si, 0.3%Mn, 0.01%S.

The molten iron was treated with 10% Mg FeSiMg alloy in a Vortex unit, inoculated with foundry grade ferrosilicon and poured in Y-blocks of 200*100*15 mm^3 dimensions. Rectangular specimens of 100*10*15 mm^3 were machined from the ductile iron stock. The microstructure of DI before subjecting to laser processing was ferrite/pearlitic.

Laser treatment was performed using a high-power (2 kW) diode pumped Nd-YAG laser (Rofin Sinar DY 022) in CW mode, equipped with a 3-axis computer numerical controlled work table and a 6-axis robot was used to process the DI specimens. The DI samples were processed with 600 W laser beam at scanning speeds of 25, 75 and 125 cm/min. Multipass overlap treatment was carried out, with overlap ratio of about 15%. The overlap ratio is defined as xxxx (L/W) x 100 pct, where L is the overlap width, i.e. the width which the succeeding processing track overlaps on the preceding processed track, and W is the width of the single processing track.

The incident laser beam was focused to a spot with a diameter of 3 mm. During laser processing, the sample surface was protected by argon gas (1 bar).

Microstructural analyses were carried out using both optical as well as scanning electron microscopy (SEM). Metallographic samples in the transverse section of the laser processed track were prepared using conventional metallographic techniques, then etched with 2 pct nital. The depth of the processed zone was measured using an optical microscope on as-polished surface for higher accuracy.

The hardness of the upper surface of the processed zone was measured at 0.1 mm below the irradiated surface. The microhardness profiles on transverse sections were measured and plotted as a function of the distance from the irradiated surface.

Results and Discussion

Microstructure of DI Processed with 600 W Laser

The microstructure of the DI irradiated with 600 W and scanned at 25 m/min speed laser beam is shown in Fig.1 at low magnification. The microstructure is homogeneous and free of any graphite nodules. The laser processed zone is of semicircular morphology due to the Gaussian distribution of incident power across the diameter.

This figure shows the variation of the case depth in a transverse section perpendicular to the laser treated surface and lasing direction as a function of laser scanning speed at 600 W power intensity. It is obvious that the higher the speed, the smaller the corresponding interaction time for laser-material interaction and hence the lower value of the case depth. SEM micrograph shown in Fig.2 reveals that the microstructure consists of eutectic lamellar carbides (cementite) and a mixed matrix of martensite and retained austenite. The eutectic structure is an indication of surface remelting, the molten metal pool will solidify under severe cooling rate, caused by the chilling effect of the underlying solid metal which acts as very powerful heat sink.

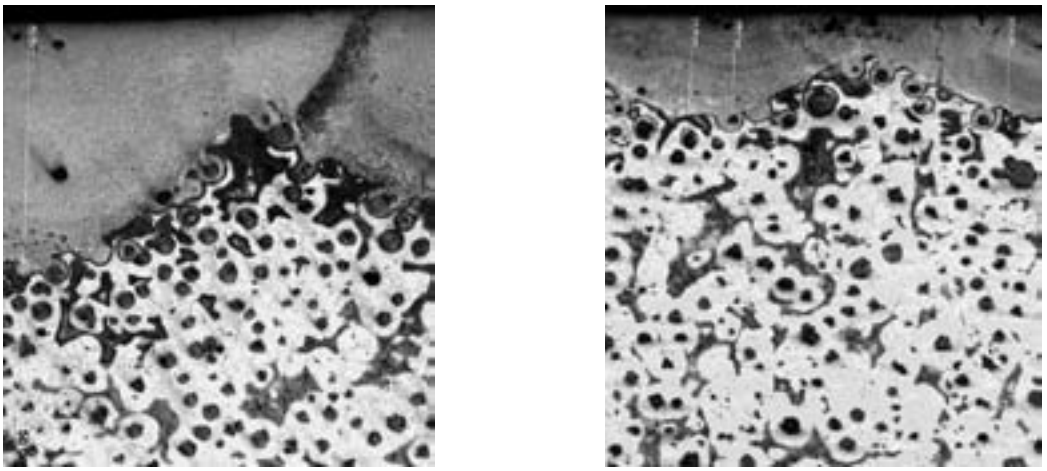

(a) (b)

Fig.1: microstructures of hardened layer of DI treated with 600 W laser at scanning speeds of a) 25 cm/min, b) 75 cm/min

Fig. 1-a shows that under the overlays, the volume fraction of cementite, which is the white etching phase, was significantly reduced after the overlap reheating by the subsequent track and the former rapidly solidified cementite almost decomposed.

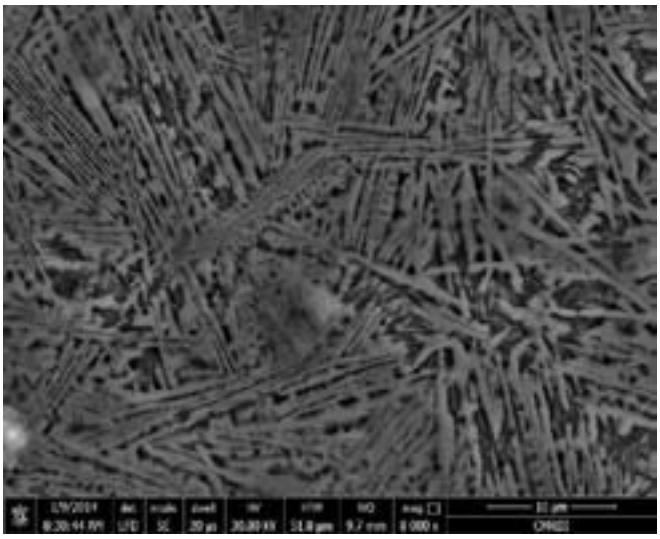

Fig.2: SEM micrograph of the remelted layer of DI processed by 600 W at scanning speed of 25 cm/min

SEM examination (Fig.3) reveals that the formerly solidified carbides had transformed into extremely fine graphite particles of approximately 1-2 μm in diameter with the formed austenite transformed on subsequent rapid cooling into martensite and retained austenite. The degree of graphitization seems to be maximum and decreases with the distance from the overlap lower surface. The graphitization almost disappears at 60-70 μm from the overlap boundary and the matrix is only tempered without any noticeable degree of graphitization. Careful examination of SEM micrograph of the partially graphitized zone (Fig.3-b) shows that some undissolved carbide phase still exists and that the graphite particles are in contact with the undissolved cementite. This may give indication that the cementite-matrix interfaces are preferential sites for the cementite-graphite phase transformation. Such accelerated graphitization of carbides may be related to different factors:

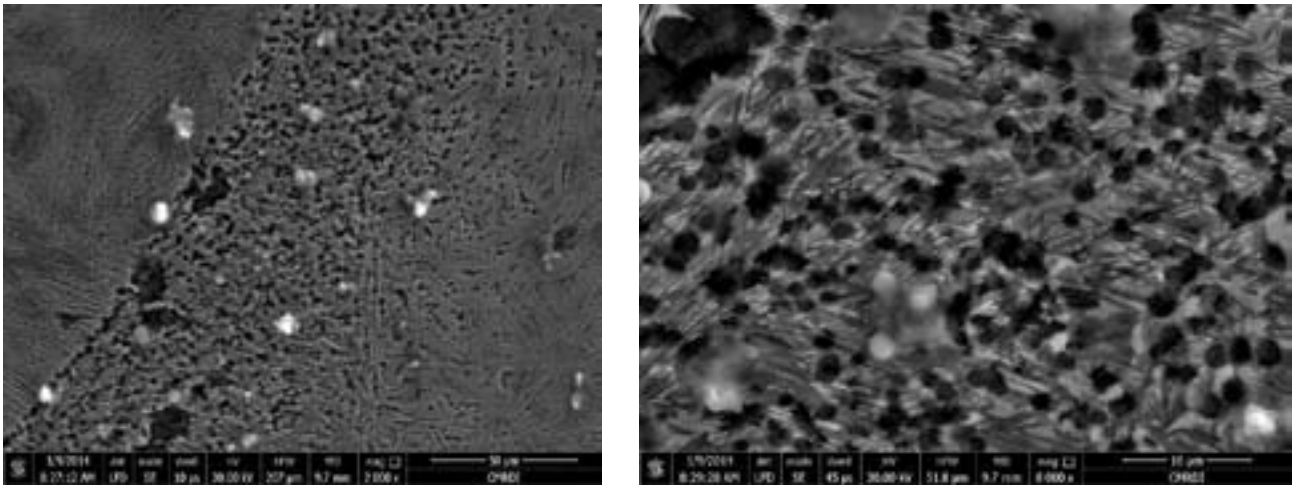

(a) (b)

Fig.3: microstructure of the overlap boundary layer showing the ultrafine graphite nodules precipitation
a) at lower magnification, b) at higher magnification

- Thermodynamic factors related to the composition of the iron, the relatively high C and Si contents, both are potent graphiting elements that are not usual for white iron composition, would significantly increase the graphitization potential of the iron and would, at least partly contribute to the unusually accelerated graphitization process in the laser remelted ductile iron.
- Kinetic factors related to the ultrafine structure of the microstructure of extremely rapidly solidified laser remelted pool. Such structure would provide enormous cementite-matrix interfaces, which are favorite heterogeneous nucleation sites for graphite. Moreover, the very short C-difusion path in such ultrafine structure would enhance the graphitization process.

- The extremely rapid solidification, and the resulting ultrafine structure, remarkably increase the density of crystal defects such as vacancies, dislocation, etc .. at the carbide/matrix interface, which would decrease the activation energy required for the graphite nucleation at those sites.
- Another mechanism has been earlier proposed[9], where pulsed Nd:YAG laser beam was used for remelting, the accelerated graphitization was related to the unique heating behavior of the pulsed laser beam to material. Such mechanism was quantitatively demonstrated based on simplified calculations of temperature profiles during pulsed Nd:YAG laser beam scanning. It was shown that temperature fluctuates very violently, with each cycle of temperature fluctuation regarded as a microannealing treatment, enhancing the cementite dissolution and the acceleration of ultrafine graphite nucleation. However, in our investigation, CW-mode of laser was used, hence, this mechanism may be excluded when considering reasons behind the precipitation of the ultrafine graphite nodules beneath the overlap boundary.

It is of interest to notice from Fig.1 that the graphitization zone disappeared when increasing the scanning speed, which indicates that at higher speeds, the heat input at the overlap is not sufficient to induce significant graphitization of carbides.

Fig. 4 shows the microstructure of the interface between the remelted zone and the substrate, i.e. the upper part of the heat-affected zone (HAZ). The temperature reached in this zone was not high enough to dissolve all graphite nodules and some nodules are still noticed surrounded by a matrix of plate martensite and retained austenite. The dendritic morphology of the solid/liquid interface of austenite suggests that the solidification velocity was rather high. It has been reported that with increasing the solidification rate of the laser remelted Fe-C-Si alloys, the austenite growth morphology would transform from planar to cellular to dendritic[19].

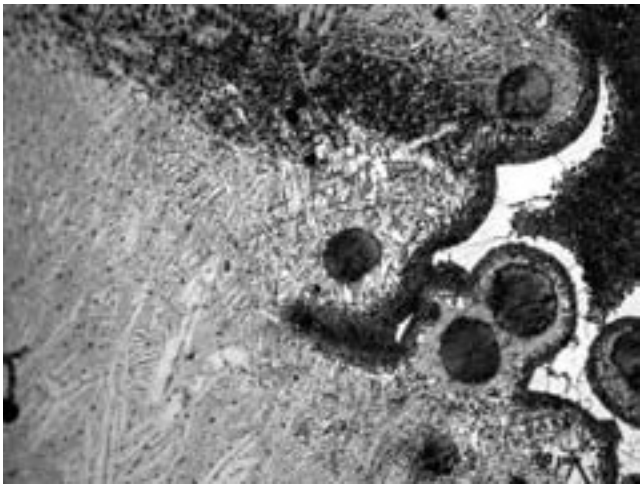

Fig.4: microstructure at the upper part of the HAZ or transition zone

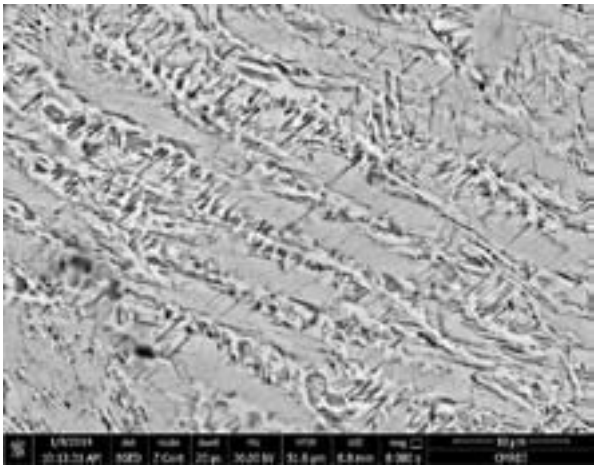

Fig.5: microstructure of the hardened layer using 600 W laser with scanning speed of 125 cm/min

Effect of Laser Scanning Speed

The microstructure of the surface processed zone considerably changes with increasing the scanning speed. Higher scanning speeds mean lower heat input received by the sample surface hence, lower probability of surface remelting and the subsequent formation of ledeburitic structure in the hardened layer. Fig.5 shows SEM micrographs of the surface layers of samples processed with scanning speeds of 125 cm/min. It seems that at the high scanning speed of 125 cm/min the heat input was not enough to remelt the sample surface which was only heated to the austenitic zone with the subsequent transformation of the austenitic dendrites to martensite as shown in Fig.5.

Moreover, in the samples processed with the lowest heat input at scanning speed of 125 cm/min, two interesting features have been noticed:

i) The substrate in the vicinity of the bottom of the hardened zone (i.e. the upper part of the heat affected zone) is characterised by the appearance of coarse plate martensite, typical of high-C martensite, together with retained austenite Fig.6. This may be explained by the rejection of carbon atoms by the C-saturated austenite upon cooling, which may create a C-enriched layer at the interface between the hardened and the transition or heat-affected zones. The formation of such coarse plate martensite in that area has been reported before[9], but without explanation.
ii) The originally ferritic halos in the as-cast samples are transformed to two layers, an inside one near the graphite spheroid consisting of austenitic dendrites and an outer shell with martensitic structure, Fig.7. If the applied power induces sufficient heat, the carbon of the graphite nodules may dissolve in the adjacent layer of the austenitic shell, thus leading to increased C-content and stabilising the austenite upon subsequent rapid quenching of that layer, austenite dendrites may be seen at the internal halo around the graphite spheroids. The carbon diffusion from the

graphite spheroid would lower the liquidus temperature of the adjacent layer due to increased C-content, leading to incipient fusion of that layer with the high-C molten layer solidifying in the form of dendritic retained austenite.

The C-content of the outer layer of the austenitic shell around the graphite spheroid may be not so highly enriched with carbon to stabilise the austenite and subsequent quenching will transform into a martensitic layer as shown in Fig.7.

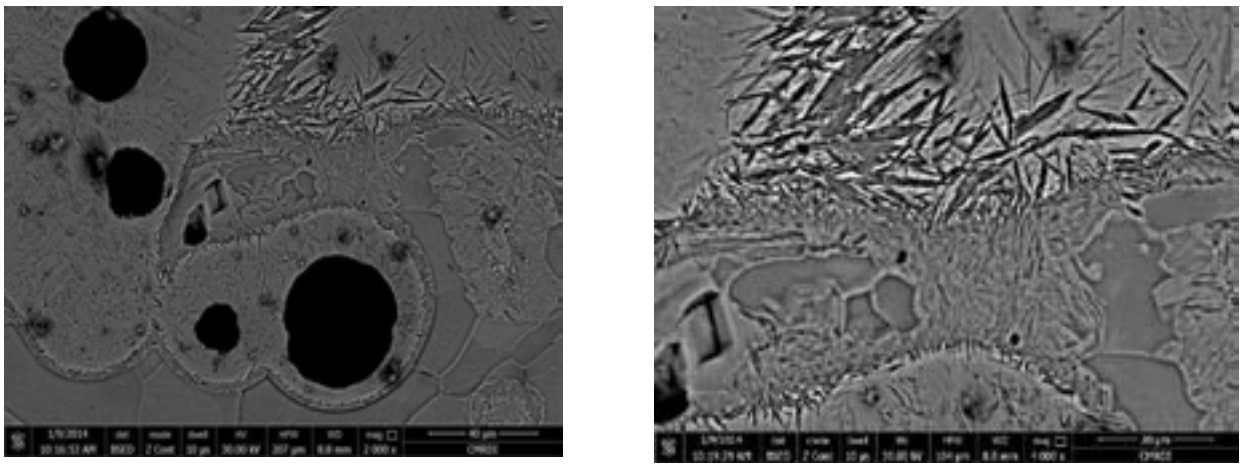

(a) (b)

Fig.6: Coarse martensite plates at the transition zone between the laser irradiated zone and the HAZ. a) at lower magnification, b) at higher magnification

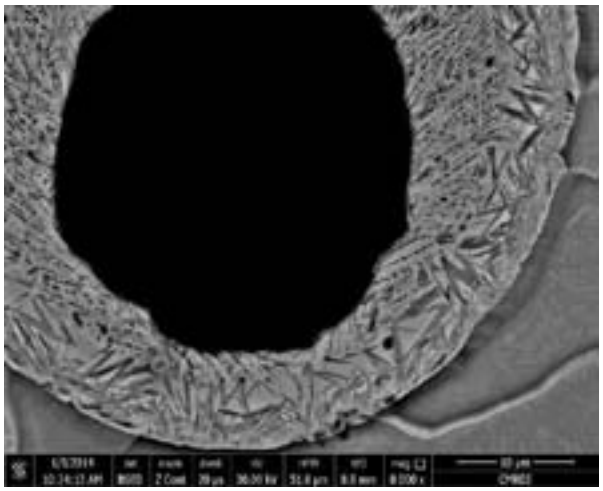

Fig.7: Outer shell around a graphite spheroid with an internal layer of austenitic dendrites and outer layer of martensite.

Microhardness Profile

As shown in Fig.1 and the microhardness profile of Fig.8, the thickness of the layer remelted and hardened zone decreases with increasing the laser scanning speed, apparently due to the lower heat input associated with higher scanning speeds.

The microhardness gradient from the sample surface to the lower part of the hardened zone drops more steeply with increasing the scanning speed. At 0.4 mm distance from the sample surface the microhardness drops from 1200 to 1000 to 400 HV when increasing g the scanning speed from 25 to 75 to 125 cm/min, respectively. Increased scanning speeds reduce both the thickness of the hardened layer as well as the hardness values achieved at fixed distance from the processed surface.

It should be noted that the surface hardness of that sample, processed at 600 W is around 960 HV, which is somewhat lower than the first recorded microhardness value at 0.2 mm beneath the melt surface, which may be related to slight surface decarburisation during remelting process.

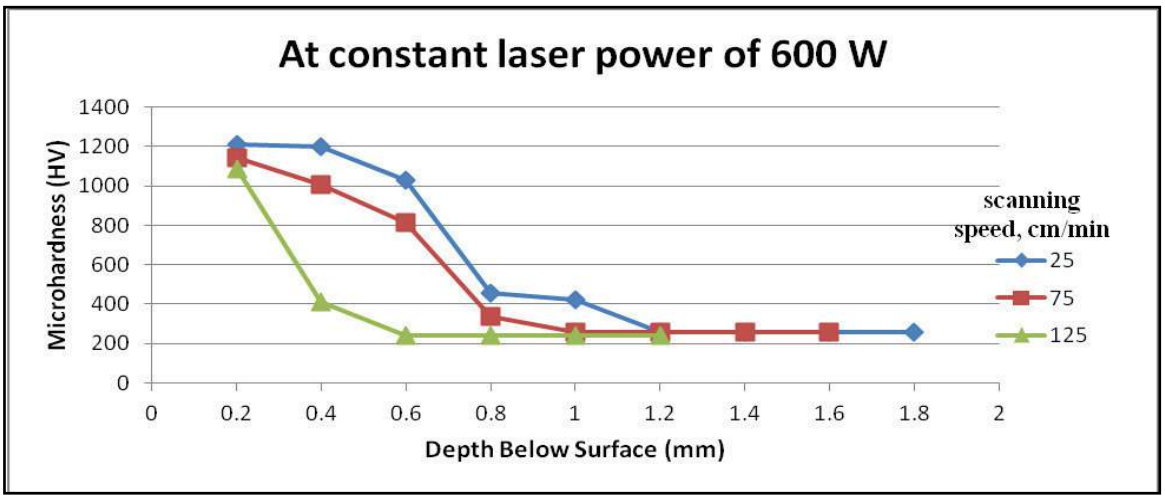

Fig8: Microhardness profile from the sample surface, as a function of scanning speed

Conclusions

1. The surface of ductile cast iron was processed with a high power 600 CW-Nd:YAG laser. The hardness depth of hardened layer as well as its microstructure were found to largely depend on the laser scanning speed.
2. At low scanning speeds of 25 cm/min, the surface layer was melted and then solidified at very high cooling rates. The microstructure of the hardened layer consisted mainly of carbides in a matrix of retained austenite and martensite.
3. As the scanning speed increased to 125 cm/min, the hardened surface did not reach the melting point and the austenite formed during heating was transformed to martensite.
4. The rapidly solidified carbidic structure with the low scanning speed of the underlying laser melted track experienced very accelerated graphitisation during the multipass overlap remelting process. Such accelerated graphitisation resulted in the formation of ultrafine graphite nodules and was related to thermodynamic, kinetic factors as well as increased level of crystal defects at the carbide/matrix interface.
5. Some interesting microstructural features were observed at the transition zone between the hardened zone at the HAZ such as the formation of coarse martensite plates and the formation of austenitic/martensitic double layer around the graphite spheroids. Mechanisms were suggested for those structural formations.

References

1. J. Kusinski, S. Kac, A. Kopia, A. Radziszewska, M. Rozmus-Gomkowska, B. Major, L. Major, J. Marczak and A. Lisiecki: Bulletin of the Polish Academy of Sciences, Technical Sciences, 2012, vol. 60, No. 4, 711-728.
2. S. S. Bhavikatti, S. S. Pardeshi and P. K. Mishra: International Journal of Engineering and Innovative Technology (IJEIT), 2012, vol. 2, Issue 2, 42-46.
3. W. A. Monteiro, E. M. R. Silva and W. de Rossi: 3rd International Conference on Integrity, Reliability and Failure, Porto/Portugal, July 2009, Paper Ref: S2403_P0409.
4. H. Matsuyana and K. Shibata: 8th International Congress on Heat Treatment of Materials, Heat and Surface, Kyoto, Japan, 1992, 2207-210.
5. C. H. Chen, C. J. Altstetter and J. M. Rigsbee: Metall. Trans. A, 1984, 719-728.
6. C. H. Chen, C. P. Ju and J. M. Rigsbee: Mater. Sci. Technol, 1988, 4, 161-166.
7. A. Fernández-Vicente, M. Pellizzari and J. L. Arias: Journal of Materials Processing Technology, 2012, 212, 989-1002.
8. D. Farias, S. Denis, A. Simon, Suardi, G. Vinsaro, J. C. Cherrier, J. Quesada, D. Boisselier, A. Cornet and Y. Pourprix: Second International Seminar of Surface Engineering with High Energy Beams, CEMUL (INIC), Lisbon (Portugal), September 25-27, 1989.
9. H. M. Wang and H. W. Bergmann: Metallurgical and Materials Transactions A, April 1995, Vol. 26 A, 793-800.
10. H. M. Wang and H.W. Bergmann: Scripta Metallurgica et Materialia, 1995, vol. 32, No. 8, 1147-1152.

11. C. H. Chen, C. P. Ju and J. M. Rigsbee: Mater. Sci. Technol., 1988, 4, 161-166.
12. C. H. Chen, C. J. Altstetter and J. M. Rigsbee: Metall. Trans. A, 1984, 15, 719-728.
13. J. Grum: In: G. E. Totten, K. Funatani, L. Xie (Eds.) Handbook of Metallurgical Process Design, 2004, Marcel Dekker Inc., New York, 659.
14. J. Grum and R. Sturm: J. Mater. Process. Technol, 2004, 147, 351-358.
15. J. Grum and R. Strum: International Journal of Microstructure Material Properties, 2005, 1(1), 11-23.
16. Y. Chen, C. H. Can, L. X. Wang, G. Yu and A. Kaplan: Applied Surface Science, 2005, 245, 316-321.
17. K. F. Alabeedi, J. H. Abboud and K. Y. Benyounis: Wear, 2009, 266, 925-933.
18. A. K. Mahmoud and M. Mohamed: Machines, Technologies, Materials, 2013, 12, 3-6.
19. M. S. F. Lima and H. Goldenstein: Journal of Crystal Growth, 2000, 208, 709-716.

Fe-C-V alloys with precipitates of spheroidal vanadium carbides VC

M. Kawalec[1] and M. Górny[1]
[1]Faculty of Foundry Engineering, AGH-University of Science and Technology, Krakow, Poland

The paper presents the results of tests on the spheroidising treatment of vanadium carbides VC done with magnesium master alloy and RE. The conducted metallographic studies have shown that introducing the magnesium master alloy to an Fe-C-V system of eutectic composition causes the crystallisation of spheroidal carbides. The content of these carbides is about 5.6%, representing 33% of all the crystallised vanadium carbides. Adding RE to the base alloy melt caused 31% of the vanadium carbides crystallise as dendrites. Testing of mechanical properties has proved that the spheroidising treatment of VC carbides in high-vanadium cast iron increases the tensile strength by about 60% and elongation 14 - 21 times, depending on the type of the spheroidising agent used. Tribological studies have shown that high-vanadium cast iron with eutectic, dendritic and spheroidal carbides has the abrasive wear resistance more than twice as high as the abrasion-resistant cast steel.

Keywords: Fe-C-V alloy, eutectic, vanadium carbide, spheroidisation, mechanical properties, wear resistance.

Article available in the International Journal of Cast Metals Research

Cast iron and the self-lubricating behaviour of graphite under abrasive wear conditions

R. Ghasemi*and L. Elmquist
Materials and Manufacturing - Casting, School of Engineering, Jönköping University,
P.O. Box 1026, SE-551 11 Jönköping, Sweden

Cast iron is assessed as a self-lubricating material under sliding conditions. This is due to the graphite particles distributed in the matrix, which come out from their pocket, and form a tribofilm between the mating surfaces, and by which improve the tribological characteristics. In this study, the directionality and the interaction between the graphite and matrix material was investigated by micro-indentation and micro-scratch techniques. The results showed that the graphite is fractured and pushed out from the middle of graphite lamellas as a result of indentation. It was also observed that the graphite orientation below the surface intensely influenced the pushing out behaviour. For the graphite oriented toward the indenter position, the effect was more pronounced. Moreover, it was found that a scratch test can be used to investigate and explain the graphite pushing out tendency. The result was used to explain the directionality and the closing tendency of the graphite lamellas during sliding.

Keywords: lamellar graphite iron, graphite self-lubricating behaviour, tribological performance, micro-indentation test, micro-scratch test.

Introduction

Cast iron as a metal matrix composite contains graphite particles which are distributed as embedded constitutes throughout the matrix. Due to its relatively low production cost, excellent thermal conductivity, and good tribological performance, it is widely used in applications where the component is exposed to wear and heat. One particular case is piston ring-cylinder liner system, where usage of the lamellar graphite iron is quite common. The foremost reason for good tribological properties is attributed to the presence of graphite as a solid phase self-lubricating agent in the matrix.[1] It is generally accepted that lamellar (also called flake) graphite has a layered crystal structure where carbon atom has a strong covalent bond to its three adjacent carbon atoms. The layers are linked by weak long ranged van der Waals forces.[2] This weak bonding between the interlayers allows the graphite layers to easily slide over each other when are subjected to the shear forces. It is well accepted that under sliding conditions, the graphite embedded in matrix; which are extremely softer than the matrix, is extracted as carbon atoms from the graphite pocket. This happens as a result of surface and subsurface deformation of matrix induced by shear stress. As a result, graphite particles are come out and distributed between the sliding surfaces.[2, 3] Previous investigations carried out by Eyre et al.,[4] and Hironaka et al.,[5] showed that formation of the graphite film improved the tribological properties significantly, and reduced the coefficient of friction. When the graphite is removed from the graphite flakes, empty pockets are left behind.[6] These pockets potentially act as oil reservoirs sites and that supplies oil at dry starts or similar conditions of oil starvation. It has also been observed that some of these pockets are covered earlier under sliding conditions as a result of matrix deformation.[6] This in turn deteriorates the expected behaviour, and might in worst case leads to scuffing issue. In addition, it has also been found that the graphite lamellas which closed earlier were oriented predominantly parallel to the sliding direction. Moreover, it is believed that the easier conditions for shearing and continuously supplying of graphite will result in substantial improvement in tribological performance.[7]

Presence of hard particles has explicitly pronounced impact on resulting abrasive wear. Besides the wear debris particles, some of these hard particles are external contaminants such as catalyst (CAT) fines (rich in aluminum, silicon and oxygen) in oil lubricant.[8, 9] Wear phenomenon in piston ring-cylinder liner application is considerably abrasive wear controlled. The worst scenario of abrasion wear could result in seizure of the piston ring-cylinder liner. From this standpoint, a single hard asperity can indent a mating elastic surface.[10] In addition to the importance of its abrasion effect, it was found that there exists a relationship between the lamellar graphite orientation and their covering resistance under sliding and abrasive wear condition, so that those graphite flakes were parallel or close to the sliding direction were covered earlier rather than the deviated ones.[6] Deformation of the metal matrix near the graphite was found as the main controlling factor on closing the graphite lamellas.

In the present work, this directionality and the interaction between the graphite and matrix material is investigated by means of a micro-hardness indenter. The results obtained from indentation and scratch tests presented are the attempts to better understanding of the graphite's smearing mechanism under abrasive and sliding wear conditions.

* Corresponding author, email: rohollah.ghasemi@jth.hj.se

Experimental Procedure

Test specimens used in the present study were selected from a pearlitic lamellar cast iron. Polishing was performed following the standard procedure down to 1 µm diamond polishing, to get a mirror like polished surface, and then the achieved surface was cleaned with ethanol prior to examination. To explain the interaction between hard abrasive particles and lamellar graphite under abrasion conditions micro-indentation and micro-scratch techniques were carried out on plenty of graphite lamellas. The conventional Vickers indenter was used for both experiments. Indentations were made under applying a load of 500 g sufficiently far relative to each other to prohibit the overlapping issues. Nano-indentation was also employed to make a grid of indentations on lamellar graphite to determine the hardness variation within the graphite structure. After micro-indentations, metallographic studies were conducted on residual indentation marks using optical microscopy and scanning electron microscopy (SEM) with the aim of determining the matrix deformation pattern and matrix-graphite interaction. In addition, the deep etched technique using Aqua regia (Nitro-hydrochloric acid) solution was selected to reveal the orientation of the lamellar graphite beneath the surface.

Results and discussion

Interaction between the micro-indentation and graphite lamellae

It has been accepted that the improvements in tribological performance is achieved when the graphite is continuously supplied into the sliding surfaces.[11] The graphite lubricating effects were investigated by Rohatgi et al.[7] on aluminium alloy-graphite particle composite, and Sarmadi et al.[12] on copper–graphite composites. They indicated that the surface and subsurface deformation, which occurred as a result of sliding; had a major influence on graphite film formation between the sliding parts. One of the main difficulties in describing the influence of matrix deformation and how it contributes to from the lubricating film is connected to the 3D complex configuration of the graphite which makes the present interpretation a little bit difficult. One of the most important factors in controlling the wear surface appearance during sliding is the hard particles. The significance of these particles was discussed elsewhere.[13] These particles are hard enough to indent and scratch the mating surfaces during the sliding condition. Therefore, micro-indentation tests were carried out close to the several graphite lamellas in order to better understanding of graphite film formation and its contribution to sliding wear.

As found earlier,[6] graphite lamellas with different orientations with respect to the abrasive wear particle showed dissimilar characteristics. Hence, it is believed that the orientation of the graphite play an important role on pushing out the behaviour of graphite under abrasive condition. To simplify the present explanation, it is necessary to specify the individual orientation of the lamellar graphite beneath the sliding surface. Fig. 1 (a) and (b) show two typical virgin graphite lamellas before indenting. Two indentations were made on both sides of the lamellar graphite.

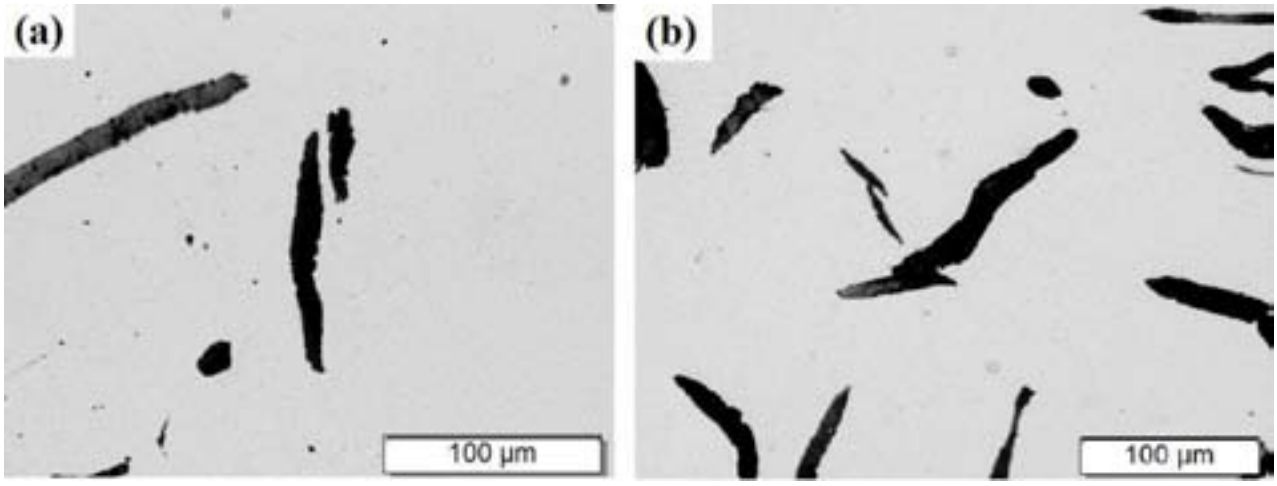

Fig. 1: Virgin graphite lamellas present in cast iron matrix**.**

Fig. 2 (a) and (b) illustrates the same graphite flakes after indentations. As being identified by comparing the images before and after indentations, graphite lamellae presented in Fig. 2 (a) compared with the virgin graphite showed no response to the indentation and was remained almost unaffected, although the indentations were made very close. However, SEM examinations revealed that the other graphite was squeezed and pushed out from its pocket as a result of indentation, clearly observed in Fig. 2 (b). Matrix deformation occurred around the indentation mark stimulated the graphite to be fractured and pushed out from its pocket. This particular tendency is simply recognizable from the shiny appearance of the pushed out graphite. A most likely reason for such difference may relate to the orientation of the lamellar graphite beneath the surface with respect to the indenter tip which strongly controls the pushing out tendencies of the graphite. A fast and simple way to reveal the flake graphite orientation is to remove the metal matrix by

aggressive solutions such as Aqua regia or Nital solution. This etching technique (also called deep etching) was performed to determine the 3D morphology of the interconnected cell structure and orientation of the graphite flake under the affected regions, illustrated in Fig. 2 (c) and (d). As shown in deep etched image microstructure mainly consisted of a pearlite constituent. Hard phases are least affected constituents during etching process and stand out throughout the matrix after etching, as shown in Fig. 2 (c).

The SEM studies conducted on deep etched samples provided valuable information on graphite responses under abrasive (here indentations) conditions. Fig. 2 (c) shows a particular case, where the graphite remained almost unaffected. It confirms that the graphite perpendicular to the projected area obtained maximum resistance without indicating any pushing out tendency, whereas for the graphite towards the tip of indenter pushing out behaviour is observed as a result of deformation of the matrix. Interestingly, such phenomenon occurs only for those graphite lamellas which had particular orientation with respect to the indenter tip.

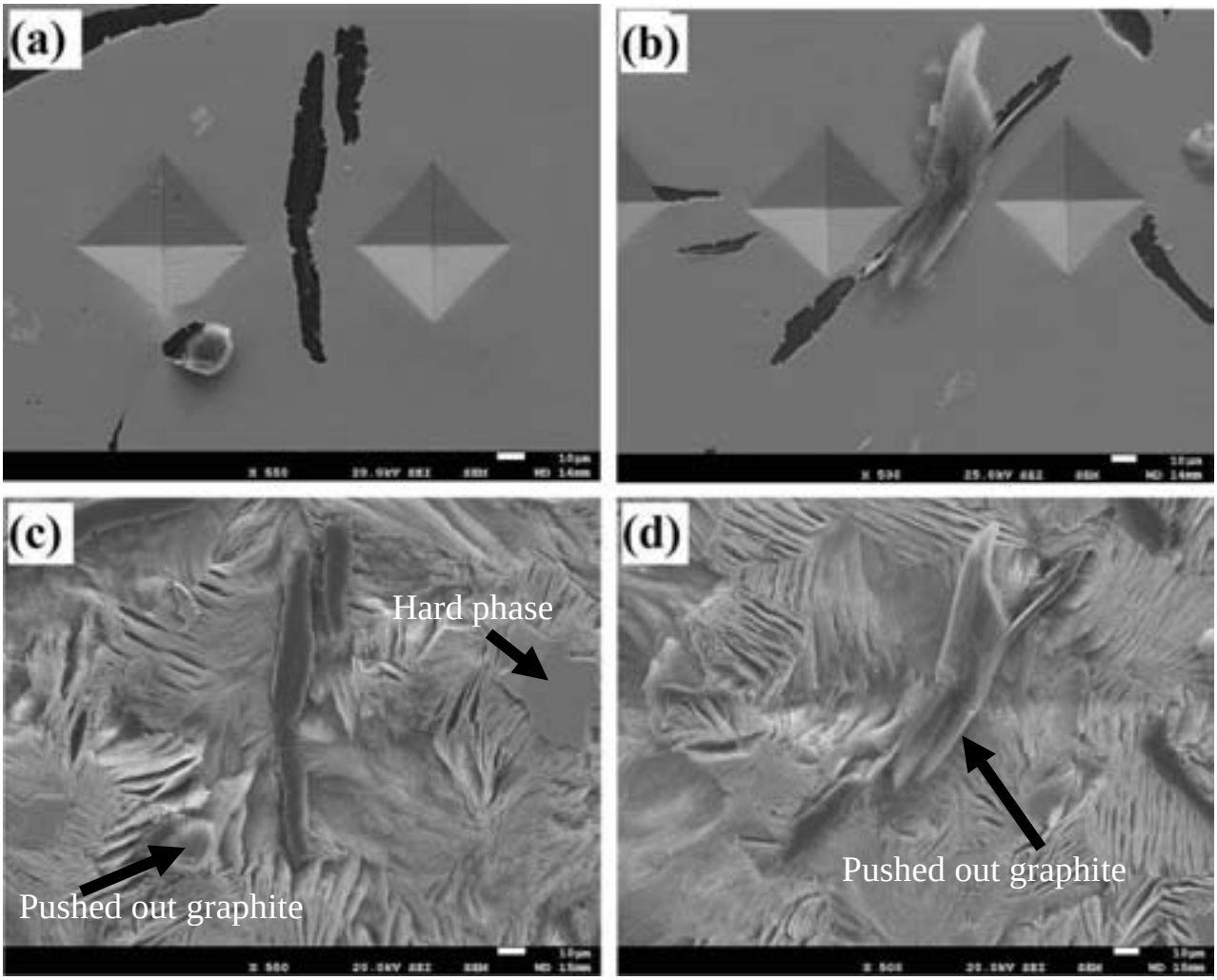

Fig. 2: SEM micrographs showing the graphite lamellas response when subjected to the indentation; (a) before etching, (b) after etching (deep etched by Aqua regia solution).

Fig. 3 illustrates two more cases where the graphite lamellas have been pushed out as a result of indentation made close to the graphite. Dissimilar behaviours are observed. These characteristics could represent that not only the applied load, but also the orientation of the graphite is an important factor to determine whether the graphite will be pushed out under a certain applying load or not. So that, two graphite flakes presented in Fig. 3 showed different responses when subjected to an individual indentation. These indicate that apart from the discussed variables (orientation and applied load), the size of the graphite seems to have a significant influence on observed phenomena. These parameters will be presented in details in upcoming studies.

Fig. 4 summarizes and illustrates schematically various positions of the graphite lamellas with respect to the indenter tip. In all cases, the indentation was made almost in the same distance from the graphite. Based on the observations on graphite lamellas responses when are subjected to similar indentation conditions such as load, dwell time and distance condition, case (a) shows the highest tendency due to less material under the indenter. Consequently, the deformation of the matrix is significantly higher compared to the other cases which stimulates the graphite to be compressed and pushed

out for the pocket. In this circumstance the displacement of the graphite is accompanied by severe matrix deformation followed by covering the graphite pocket. The present occurrence is confirmed by SEM image presented in Fig. 3 (a).

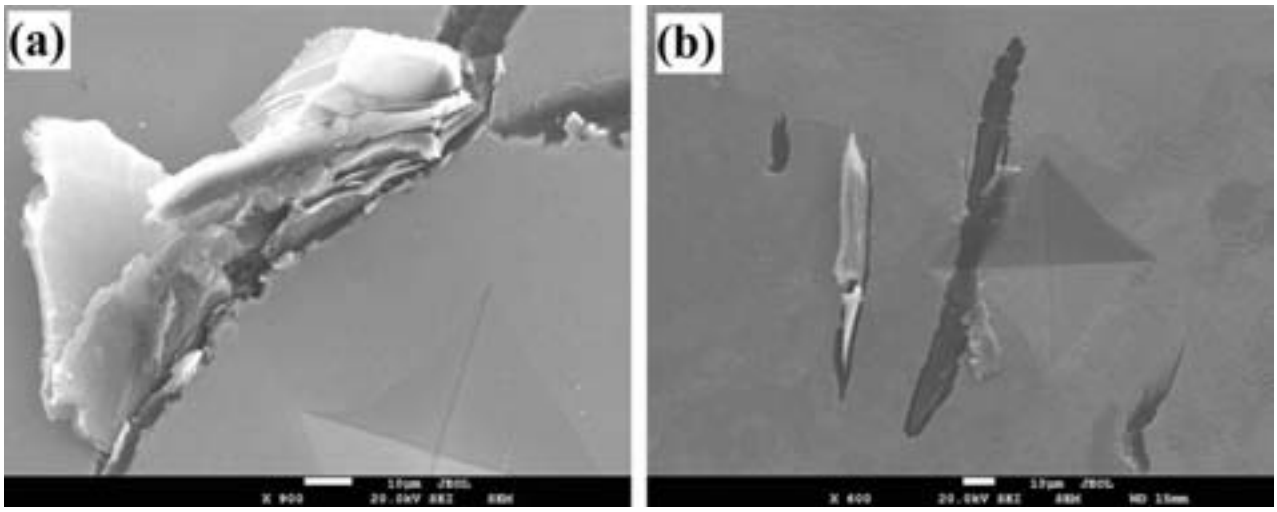

Fig. 3: Relationship between the graphite lamellas' orientation and their corresponding pushing out tendency.

As known strains are related to the stiffness of the material. Plastic flow appears when the stresses on the surface exceed the yield strength of the metal.[8] Consequently, in Fig. 4 (b) the highest resistance is resulted, as the stresses generated by indentation are carried by a larger volume of the matrix, and subsequently this reduces the net transferred strain to the graphite instead. As shown in Fig. 3 (b), under a sufficient load, the graphite is pushed out perpendicular to the indentation's projected area. However, the bigger graphite beside that did show an insignificant response to the same indentation which might be related to either its size or the orientation with respect to the indenter tip. Moreover, case (c) behaves between the cases (a) and (b). With regard to this matter that, however, there is much amount of matrix beneath the indenter carrying the applied load, when the load exceeds a certain limit (can be called threshold), the graphite will be subjected to the stress and fractured. In such instance, not the compressive stresses, but the tensile stress results in fracturing and extract the graphite form its natural state. However, but surprisingly, even in this situation the fractured area are located in centre of the flake graphite.

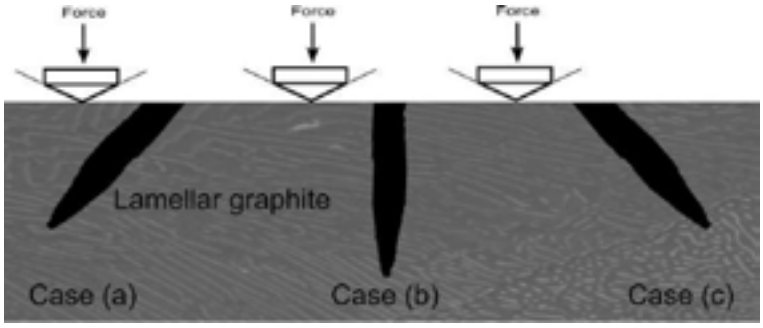

Fig. 4: Three possible cases of graphite lamellas' position in relation to the indenter tip.

From the above observations, and previous study,[13] it can be concluded that why the graphite lamellas are fractured and pushed out from the middle is mainly connected to either the presence of a soft area, together with a weak bonding in the centre of the graphite or the effect of the matrix which supports the graphite. The first assumption could be interpreted by the graphite flake nucleation theory. Based on that, the weak bonding between the graphite interlayers/or graphite and oxide particles in the middle of graphite may cause to this phenomenon. The nucleation mechanism of the lamellar graphite has been investigated for many decades. So, many theories have been proposed regarding the graphite nucleation mechanism. Warrick[14] proposed that the nucleation of lamellar graphite occurs on the complex oxides and sulfides particles. Campbell[15] proposed the concept of double films in order to highlight the role of silica-rich oxide (bifilms) in providing the substrates for the formation of oxysulfide particles as favored substrate for the graphite nucleating mechanism. There are also investigations, such as that performed by Riposan,[16] which have examined the influence of the MnS on the lamellar graphite nucleation theory. Considering the second claim, it is possible to show that the hardness gradually decreses reaching the minium in the center of the graphite. It might be directly connected to the fact that as closer the graphite to the matrix it is more supported by the surrounding matrix. This results in pushing the graphite out always from the center.

In order to verify this hypothesis, a gird includes (10×10) of nanoindents was performed on a typical lamellar graphite. A very low applied load of 10 mN with a 7μm distance was selected to hit the graphite. The results obtained in shown in Fig. 5, which was a bit contradictory with our expectation. The middle part of the graphite was found the softest area. The presence of the oxide particles or any other constituents (according to the graphite flake nucleation theory) should have shown a higher value which was not observed. The nano-hardness value is presented in GPa. The first indent (upper left corner of the pattern) showed a very high hardness which could be due to the hard phase such as carbides which distributed in the cast iron examined sample.

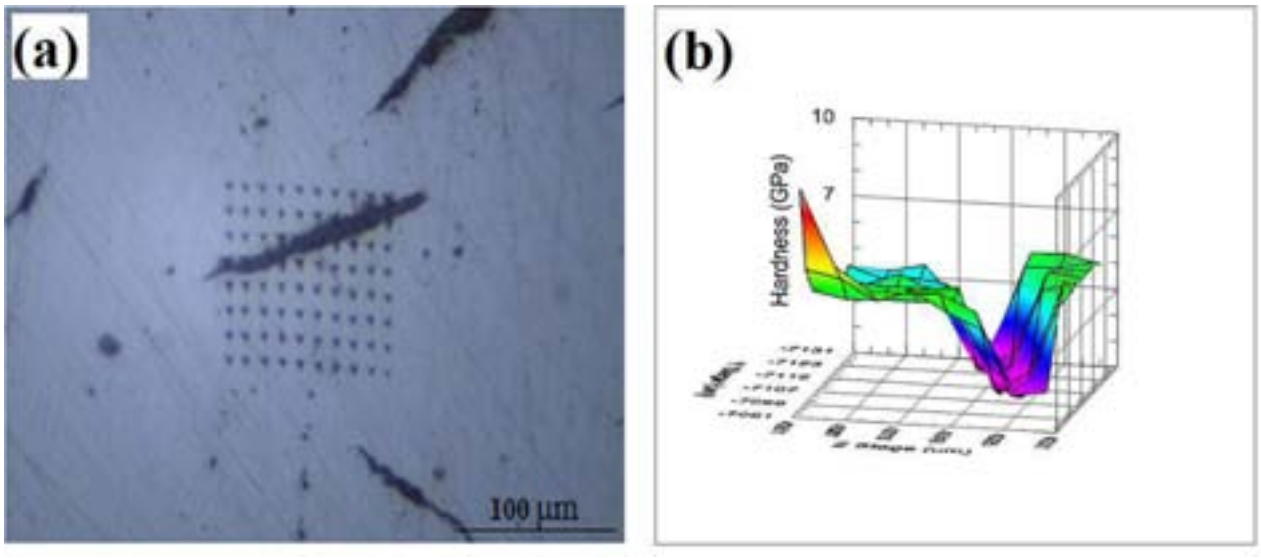

Fig. 5: (a) lamellar graphite with 10×10 nanoindents; (b) hardness value obtained from nano-indentation around and over the lamellar graphite

Interaction between the micro-scratch and lamellar graphite

The above demonstration could only give a crude clue about how the graphite lamellas with different orientation relative to the sliding direction contribute to forming the graphite solid lubricating film when are subjected to the abrasive sliding conditions. Meanwhile, it should be noted that the presented situation should only be considered as an extreme condition like sliding under dry conditions. To verify the ability of graphite to come out of their embedded state, the micro-scratch testing method was selected. Similar to the micro-indentation, different scenarios exist in scratching the matrix consisting of lamellar graphite with individual orientation in relation to the indenter tip.

As explained above, the lubricating behaviour of the graphite lamellas highly depends upon their orientation with respect to the sliding direction of the abrasive particles. On the interaction between a single hard particle, metal matrix and graphite lamellas, Fig. 6 demonstrates variant possible scenarios which may control the graphite film formation, simulated by scratching technique. In Fig. 6 (a), the indenter embedded into the graphite and scratched the graphite pocket. It resulted in chipping the graphites and in turn generating graphite particles. The current interaction is typically followed by smearing of graphite and lubricate both sliding surfaces by developing a very thin graphite later.

For those lamellas which were positioned parallel to the sliding direction, the deforming of the matrix caused by passing the particles along the lamellas lead to push out the graphite with similar mechanism which discussed above, as marked by white arrow in Fig. 6 (a). This was not the case for the graphites perpendicular to the sliding direction which behaved differently. The matrix near the graphite collapsed, and gave rise to cover the graphite pocket Fig. 6 (b). A slight pushed graphite was observed, indicated by arrows. The consequence is limiting further graphite supplying during the sliding. As observed in Fig. 6 (c) there was an appreciable difference in response of the graphite lamellas in which positioned with a particular angle relative to the sliding direction. No pushing out phenomenon was detected. With regard to the above discussion, this can be linked to the orientation of the lamellar graphite beneath the surface.

Fig. 6: Interaction between a single scratch pass made by Vickers micro-indenter, and graphite lamellas with different orientations with respect to the indenter tip.

A summarized possibilities of graphite lamellas' orientation when subjected to the scratching is schematically depicted in Fig. 7. In all cases only a 2D cross-sectional view of the graphite appears on the polished surface, therefore, it is fairly essential once more to emphasize on 3D feature of the graphite which makes the present interpretation more complicated. Fig. 7 (a) shows a case where the graphite in 2D is parallel to the scratch direction. In this situation the interaction includes the pushing out tendencies of the graphite controlled by both elastic and plastic deformation of the matrix during passing the particle along the graphite. Out of different graphite orientation potentials, only three possible occasions are illustrated with this consideration that in real case the graphite lamellas can position within range of -90° and +90°. Considering these three possibilities, the incorporation of each graphite would be individually different. With regard to the experimental evidence, during scratching the surface; case (a) has a higher tendency to the matrix deformation and pushing out tendency rather than cases (b) and (c).

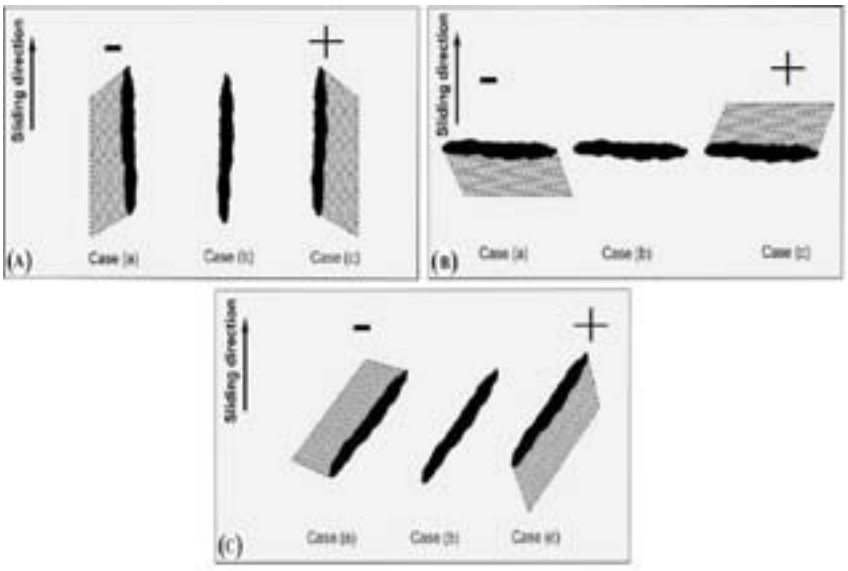

Fig. 7: Graphite lamellas with different orientations in relation to the sliding direction.

Furthermore, Fig. 7(b) shows a different case where the graphite is perpendicular to the scratching direction nevertheless different responses were detected for each. As studied in earlier work,[6] in general these graphite lamellas have higher resistance to be covered by deformed matrix than does the paralleled graphite, conformed by Fig. 6 (b). In the same study it was found that among graphite lamellas with different orientations those which had a certain range of orientation, i.e. around 60°, showed the highest covering resistance compared to the other ones.

Conclusions

The following conclusions are possible to make:

1. During a single scratch pass, it was observed that graphite lamellas were fractured and pushed out from the middle region similar to the micro-indentation test.
2. The orientation of the graphite lamellas controls the pushing out tendencies, so that if the graphite is oriented toward the position of the indenter the effect is more pronounced.

3. The graphite which is perpendicular to the micro-indentation projected area shows the highest pushing out resistance.
4. The nano-indentation test revealed that the centre part of the graphite is the softest part in lamellar graphite which could might the reason why the graphite starts to be pushed out from the centre.

References

1. J. Sugishita and S. Fujiyoshi: *Wear,* 1981, 66, 209-221.
2. J. A. Williams, J. H. Morris and A. Ball: *Tribology International,* 1997, 30, 663-676.
3. B. K. Prasad: *Mater. Sci. Eng., A* 2007, 456, 373-385.
4. T. S. Eyre, 'Friction and wear of cast irons', Vol. 18, 10th ed., 1992, 695-701.
5. S. Hironaka, *Boundary lubrication*. ASME Press, 2004, pp. 41.
6. R. Ghasemi and L. Elmquist: *Wear,* 2014, 317, 153-162.
7. P. Rohatgi, S. Ray and Y. Liu: *Int. Mater. Rev.,* 1992, 37, 129-152.
8. J. Nadel and T. S. Eyre: *Tribology International,* 1978, 11.
9. A. R. Riahi and A. T. Alpas: *Wear,* 2003, 255, 401-409.
10. R. L. Jackson and L. Kogut: *Journal of Tribology,* 2006, 128, 209-212.
11. Y. Liu, P. Rohatgi and S. Ray: *Metall. Trans. A* 1993, 24, 151-159.
12. H. Sarmadi, A. H. Kokabi and S. M. Seyed Reihani: *Wear,* 2013, 304, 1-12.
13. R. Ghasemi and L. Elmquist: Sumbitted to *Wear,* 'Examination of the self-lubricating behavior of graphite lamellas using micro-indentation and micro-scratch techniques', May 2014.
14. R. Warrick: *Int. J. Cast Met. Res.,* 1966, 2, 97-108.
15. J. Campbell: *Metall. Mater. Trans. B,* 2009, 40, 786-801.
16. I. Riposan, M. Chisamera, S. Stan and T. Skaland: Proceedings of the AFS Cast Iron Inoculation Conference, 'A new approach to graphite nucleation mechanism in grey irons', September 2005, pp. 29- 30.

Acknowledgment

The research leading to these results has received funding from the European Union Seventh Framework Programme (FP7/2007-2011) under grant agreement no. 265861 (Helios).

Effects of microstructure and strength on tool wear in rough milling of austempered ductile iron

A. Sinlah[1], D. Handayani[1], C. Saldana[1], R. C. Voigt[1], K. Hayrynen[2], R. M'Saoubi[3]
[1] Harold and Inge Marcus Department of Industrial and Manufacturing Engineering, The Pennsylvania State University, University Park, PA USA
[2] Applied Process Inc, Livonia MI USA
[3] Seco Tools AB, Fagersta, Sweden

The machinability of various grades of austempered ductile iron (ADI) has been investigated for rough milling operations. ADI 900, ADI 1050 and ADI 1200 grades were commercially produced, commercially heat treated, and machined under controlled conditions using coated carbide inserts with coolant in the laboratory. The milling performance of the various grades was compared to that of AISI/SAE 4340 with similar hardness. In this study, machinability characteristics relative to wear rate (ISO 8688-2) and machining forces were measured and related to initial microstructure and properties. These preliminary results have been used to establish initial rough milling machining guidelines for machining ADI with coated carbide milling inserts.

Keywords: austempered ductile iron, machinability, tool life, cutting forces

Article available in the International Journal of Cast Metals Research

Characterization of primary dendrite morphology in complex shaped lamellar cast iron castings

P. Svidró[1*], L. Elmquist[2], I. Dugic[3] and A. Diószegi[1]
[1]Department of Materials and Manufacturing - Foundry Technology, Jönköping University, Jönköping, Sweden
[2]SinterCast AB, Katrineholm, Sweden
[3]Department of Mechanical Engineering, Linnaeus University, Växjö, Sweden

Shrinkage porosity and metal expansion penetration are two fundamental defects appearing during the production of complex shaped lamellar cast iron components. Simplified test models simulating the thermal and geometrical conditions existing in complex shaped castings have been successfully used to provoke shrinkage porosity and metal expansion penetration. A stereological investigation of the primary dendrite morphology indicates a maximum intra-dendritic space in connection with the casting surface where the porosity and the penetration defects appear. Away from the defect formation area the intra-dendritic space decreases. Comparison of the simulated local solidification times and measured intra-dendritic space indicates a strong relation which can be explained by the dynamic ripening process. The slow local solidification time situated at the boundary between the casting surface and its surrounding is explained to be the reason for the formation of an austenite morphology which can promote mass flow between dendrites, thereby provoking shrinkage porosity or metal expansion penetration.

Keywords: lamellar cast iron, primary austenite, dendrite morphology, coarsening, shrinkage porosity, metal expansion penetration.

Introduction

Complex shaped lamellar cast iron castings are the most widespread application of cast iron materials. The automotive industry is the largest consumer of this type of cast component. Despite the advantages of good thermal conductivity, high damping capacity and good machinability, some recurrent defects like shrinkage porosity (SP) and metal expansion penetration (MEP) create additional expense for the casting producers and users. Shrinkage porosity can cause leakage through the casting wall when the component is pressurized. Metal expansion penetration can require additional and unhealthy cleaning procedures leading to "white fingers", an occupational disease. Great efforts have been made to investigate the mechanism of defect formation and to reduce the number of reject castings due to SP and MEP. Metal expansion penetration has been investigated in detail by Levelink et al[1,2] where they determined that liquid metal was squeezed out from the casting volume and forced between the molding sand grains and causing the defect. They attributed the driving force for MEP formation as the presence of phosphorus and late solidification of the phosphorus eutectic, hence the time for penetration was assumed to be the end of solidification. Later, Dugic et al[3] demonstrated that the time for penetration was in fact the beginning of the eutectic phase formation. Dugic and co-workers used non-welded thermocouples to detect when the liquid metal entered the penetrated zone. Formation of shrinkage porosity in foundry practice was believed to take place at the end of the solidification, which was a quite unreasonable statement because lamellar cast iron precipitates low density graphite during the late stage of solidification, providing a liquid surplus that should compensate for the liquid-to-solid contraction. The statements were based on the observation of porosity between the eutectic colonies in the last solidifying areas, with the porosity located between dendrite arms.

An important tool for investigation of SP and MEP was created when techniques for color etching[4] and Direct Austempering After Solidification (DAAS)[5,6] were introduced into cast iron research. Diószegi et al[7,8], using color etching revealed and distinguished a perfect eutectic composition or an intra-dendritic alloy in the penetrated layers between the sand grains while the original composition of the cast iron was a standard hypoeutectic alloy with minor addition of pearlite stabilizer elements. This was the first observation to show the presence of primary austenite grains and a flow path related to austenite grains observed on the DAAS treated samples. Elmquist et al[9], used the same method of color etching on samples showing SP. In the color etched samples it became clear that shrinkage porosity did not surround single eutectic colonies, but instead several groups of cells. Further investigation[10] based on DAAS revealed that shrinkage porosity was located at austenite grain boundaries. Later investigation[11] based on Electron Back Scattering Diffraction (EBSD) confirmed the locations of the pores at the grain boundaries. The internal surface of the

* Corresponding author, email: peter.svidro@jth.hj.se

shrinkage porosity was found to be oxidized, suggesting a connection to the surrounding atmosphere. Oxidizing gases from the surrounding atmosphere were assumed to flow into the intra-granular area, a material transport path opposite to the one observed during MEP.

Advances in characterization of the primary dendrite morphology[12] and recent demonstration of the dendrite coarsening phenomena during solidification of hypoeutectic lamellar cast iron[13], [14] motivates the present work, which aims to characterize the liquid flow paths during the formation of MEP and SP as a mean to clarify the mechanics of formation of these defects.

Experimental Procedure

The aim of the experiment is to carry out a quantitative analysis of the primary austenite morphology in regions affected by shrinkage porosity and metal expansion penetration. Samples taken from test castings previously developed to reproduce the thermal conditions in complex shaped castings, and showing the relevant casting defects were used. The casting alloy was hypoeutectic grey cast iron of similar composition to alloys used in the commercial production of automotive cast iron components.

Shrinkage porosity

A casting sample, here "Sample A", combining simple geometrical domains of cylinders and plates according to Fig. 1 was used[10] to create thermal fields comparable to those found in complex shaped cylinder heads. The chosen geometry is prone to form shrinkage porosity similar to that found in real castings. A lamellar cast iron alloy used in an industrial foundry process, with the composition presented in Table 1, melted in an induction furnace and treated according to the current production procedure was cast into a mold prepared using Epoxi-SO_2 hardened quartz sand. Sample A was cut as indicated by the dashed lines in Fig. 1. The cut surface including the lower cross section of the middle cylindrical domain (Fig. 2) shows shrinkage porosity of the same type as it is described in the literature[9], namely the porosity is formed in connection with the casting surface, and forms between eutectic colonies where primary austenite dendrites can be observed (Fig. 3).

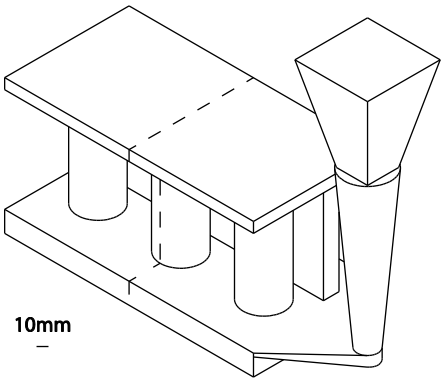

Fig.1: Sample A, combines a 10 mm top plate and a 20 mm bottom plate interconnected with three cylinders (Ø 40 mm) and a wall of 15 mm parallel to the cylinders. The minimum distance between the vertical plate and the cylinder is 7 mm.

Table 1: Chemical composition of Sample A.

Element	C [%]	Si [%]	Mn [%]	P [%]	S [%]	Cr [%]	Mo [%]
Sample A	3.28	1.96	0.64	0.03	0.06	0.26	0.05

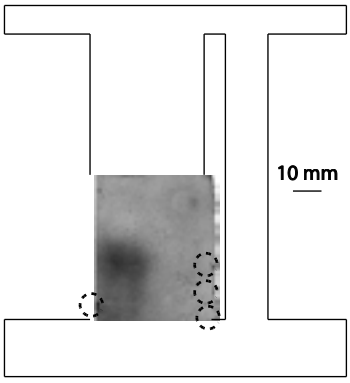

Fig.2: Sample A, investigated cross section. Circles of dashed lines indicate where shrinkage porosity connected to the casting surface was observed.

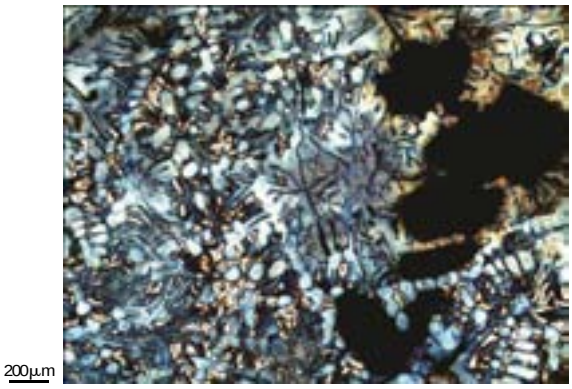

Fig.3: Sample A, color etched micrograph from the investigated cross section showing SP.

Metal Expansion Penetration

The casting sample used here "Sample B", is a combination of a cylindrical casting with diameter Ø80 mm x 80 mm tall with an internal cylindrical channel with Ø30 mm and an internal concave casting surface with R15 mm. The cross section of the mold used to produce Sample B is shown in Fig. 4, is identical with that discussed in the literature[7], [8] and is designed to promote metal expansion penetration. Similar molding materials and liquid metal from the same foundry process were used as for "Sample A" except for the chemical composition which is shown in Table 2.

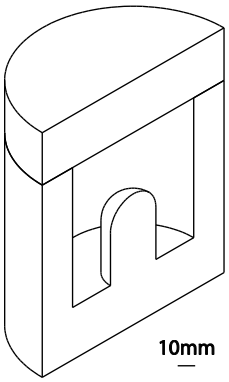

Fig.4: Sample B, a half section of the mold.

Table 2: Chemical composition of Sample B.

Element	C [%]	Si [%]	Mn [%]	P [%]	S [%]	Cr [%]	Mo [%]
Sample A	3.18	1.77	0.56	0.05	0.09	0.15	0.24

The Sample B casting was cut in half and prepared for metallographic observation as shown in Fig. 5. Sample B is rotational-symmetric and penetration defects appeared evenly distributed across the internal concave casting surface as marked on Fig 5. The exuded metal which penetrates the mold appears to contain a perfect eutectic composition as shown in the left lower corner of Fig. 6. The chemical composition (Table 2) is a hypoeutectic alloy, which implies that primary austenite should form under stable solidification conditions. The microstructure of the bulk material belonging to the sample connected to the concave casting surface (upper right corner of Figure 6) contains primary austenite dendrites (highlighted with red color) between the eutectic colonies. This is the evidence that the metal present in the region has solidified according to the stable solidification condition. The material in the lower left part of Fig. 5 is the penetrated material behind the casting surface and contains only individual graphite flakes embedded in the metallic matrix without any evidence of primary austenite dendrites. This particular combination was mentioned in the introduction to be previously discussed in the literature as indicating that the intra-dendritic liquid in the bulk material of the sample after the formation of the primary austenite dendrite and segregation up to a close eutectic composition has been forced into the interstices between the sand grains of the mold.

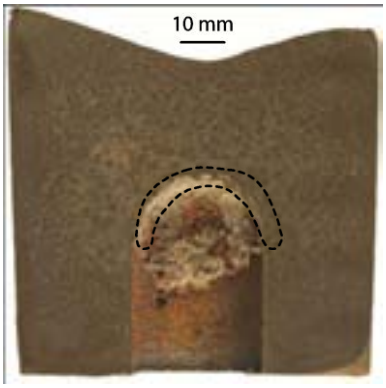

Fig.5: Sample B, a cross section of a cylindrical casting sample, dashed line indicates the penetrated area.

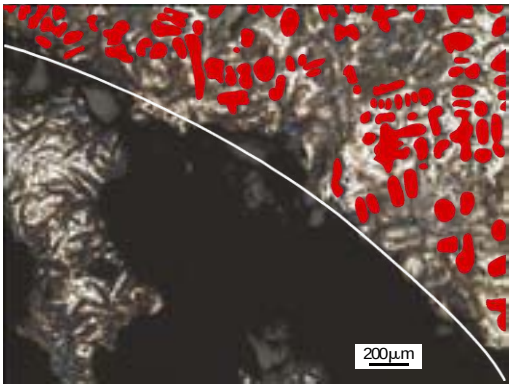

Fig.6: Sample B, a color-etched micrograph showing the microstructure in the penetrated zone. The upper right corner belongs to the casting while the lower left corner represents the penetrated metallic matrix.
Red – primary austenite dendrites.
White line is the mold-metal interface.

Image analysis and stereological definitions

The surfaces of samples A and B were color-etched using the standard picric acid-based technique[4] at elevated temperature. Characterization of the microstructure components has improved since digital image analysis has been introduced, which allows a more sophisticated examination of the morphology. In the case of cast iron the use of color etching in combination with image analysis opened up the characterization potential of the primary austenite network. The color distribution obtained by picric acid-based etching is strictly dependent on the silicon segregation pattern[15].

Positive segregation of Si (k>1) creates a well distinguished picture of the primary austenite only where the primary network is not superimposed on the eutectic colony. As a consequence it is necessary to consider the equal distribution of the primary austenite in the casting domain. For this reason a distinguishing procedure has been adapted by dividing the investigated area into clear primary austenite, clear intra-dendritic space and not distinguishable areas. The procedure is presented in Fig. 7 and Fig. 8. Fig. 7 shows the color-etched microstructure including the entire dendritic austenite network and the superimposed eutectic cells. Fig. 8 shows the pre-processed structure performed in combination between image analysis software and a manual touch-pad screen.

Fig.7: A color-etched micrograph from Sample A.

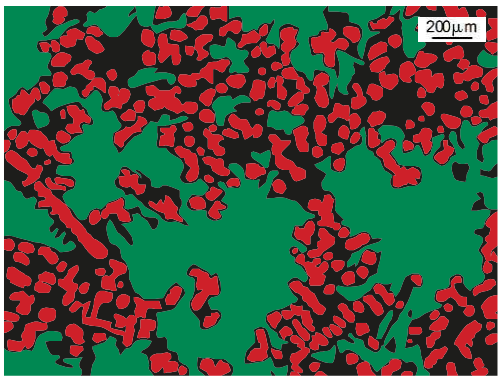

Fig.8: Pre-processed structure for image analysis.
Red – primary austenite
Black – intra-dendritic space
Green – excluded from the measurement, as it is obscure.

Three units showing primary austenite dendrites were investigated. Secondary dendrite arm spacing (SDAS) given in mm was measured as well the surface area A_i of the intra-dendritic phase and the perimeter P_i between the observed primary austenite phase and the intra-dendritic space. Recent research work[12] demonstrated a stereological parameter useful for the present research work to characterize the local intra-dendritic space as a measure to indicate the flow path direction during formation of MEP and SP. This parameter was called the *modulus of the intra-dendritic phase*, M_{IP} and relates the volumes of the intra-dendritic phase and its envelope. Invocation of stereological rules demonstrated that M_{IP} as a 3-D parameter can be approximated by comparing A_i and P_i obtained from a 2-D planar observation. The modulus of the intra-dendritic space is comparable with the hydraulic diameter used in fluid dynamics $M_{IP} = \frac{A_i}{P_i}$ with a unit of µm. Recent research[13], [14] in the field of lamellar cast iron solidification demonstrated the occurrence of dynamic

ripening of the primary austenite. This phenomenon is a superimposed effect of the dendrite coarsening process while the primary phase is continuing to precipitate. The dendritic network is continually changing shape during the coarsening, as surfaces with sharp curvature remelt and surfaces with low curvature increase. The consequence of this ripening process is a continuous decrease of the solid-liquid interphase with the scope to reduce the surface curvature related phase instability. Both stereological parameters SDAS and M_{IP} have a linear relation to the $t^{1/3}$ of local solidification time. Stereological parameters measured on as-cast samples when the sample is at ambient temperature are possible because the stereological parameters are considered identical with the ones obtained at the end of the solidification.

Surfaces intended for investigation in Samples A and B were divided into a lattice of squares of 5 mm^2 as represented in Fig. 9 and Fig. 10, and the local SDAS and M_{IP} of each square was measured at a magnification of 2,5x on pre-processed color micrographs. The average local solidification time for each square was calculated using MAGMAsoft©, considering the casting temperature and a kinetic model based on the chemical composition. The calculated local solidification time for samples A and B are plotted and represented in Fig. 9 and Fig. 10.

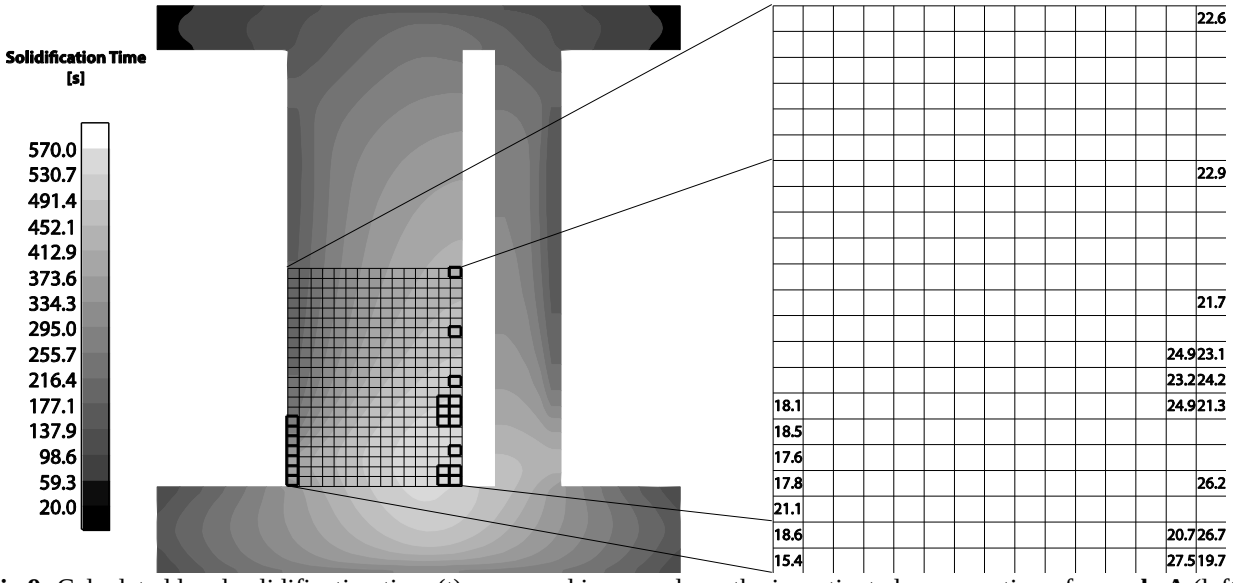

Fig.9: Calculated local solidification time (t) expressed in seconds on the investigated cross section of **sample A** (left) plotted together with the calculated modulus of the intra-dendritic phase $\boldsymbol{M_{IP}}$ expressed in µm (right).

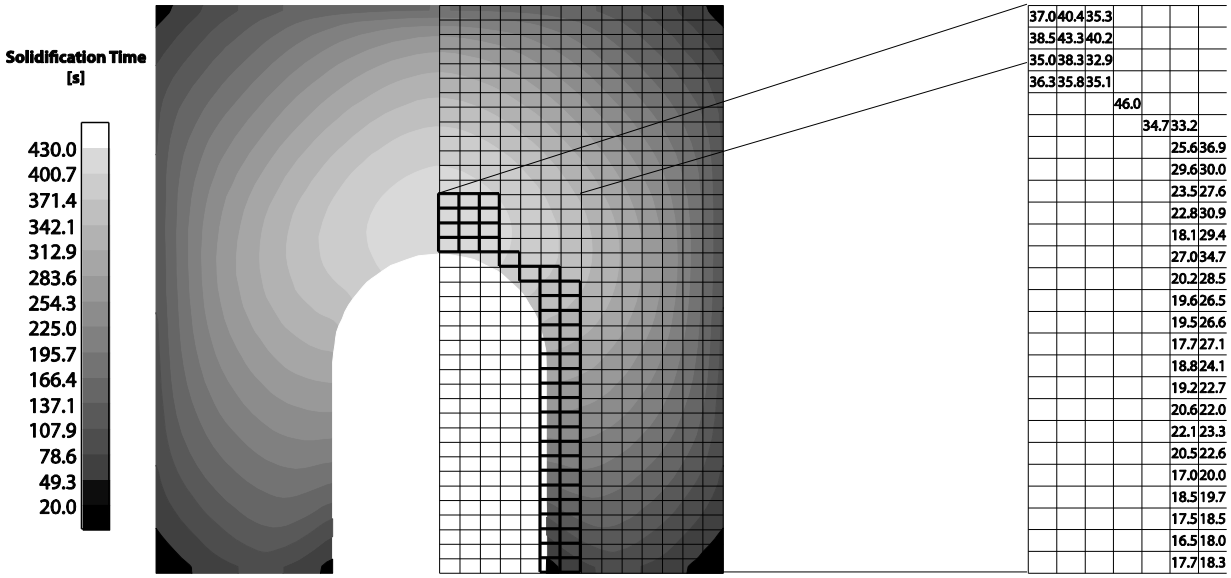

Fig.10: Calculated local solidification time (t) expressed in seconds on the investigated cross section **sample B** (left) plotted together with the calculated modulus of the intra-dendritic phase $\boldsymbol{M_{IP}}$ expressed in µm (right).

Experimental results and discussion

Solidification results in both cases presented in Fig. 9 and Fig. 10 indicate that the longest local solidification times are found at the casting-mold boundary where MEP and SP are formed in real castings. The same tendency can be observed for the calculated modulus of intra-dendritic space where the largest interspaces correspond to the longest simulated local solidification times Based on the calculated local solidification time it can be concluded that the largest intra-dendritic space in the casting is situated at the casting-mold boundary and decreases continuously as the local solidification time decreases. The gradient in M_{IP} is also an indication of how the inter-dendritic melt existing during solidification of the lamellar cast iron can serve as a transport path to the surroundings. This path can transport material in both directions as is described in the literature, from the surroundings into the casting as in the case of shrinkage compensation and inversely from the inner domains of the casting to the surrounding as in the case of metal expansion penetration.

Fig. 11 and Fig. 12 compare both the modulus of the intra-dendritic phase M_{IP} and the secondary dendrite arm spacing SDAS to the calculated local solidification time with literature data[16] obtained in previous work. The literature results were obtained as the average on cylindrical samples (Ø40mm x 40mm) cast separately from the same raw material at different cooling rates. In the present work the results were collected from the complex shaped samples A and B where the different cooling rates were created within the same sample.

Comparing the morphological parameters M_{IP} seems to give less scatter in the result than SDAS for both solidification cases in samples A and B. Apart from the influence of the local solidification time, which was calculated without taking into account the ripening phenomena - the differences in the scatter can be attributed to fragmentation of the dendritic network, which is reported in the literature[17]. Dendrite fragmentation is an obstacle to accurate SDAS measurement.

The relatively good correlations for both M_{IP} and SDAS with respect to the literature data presented in Figure 11 and Figure 12 are remarkable because the values from the literature were demonstrated to depend strictly on the coarsening process of the dendritic network during the columnar to equiaxed transition and the end of the solidification.

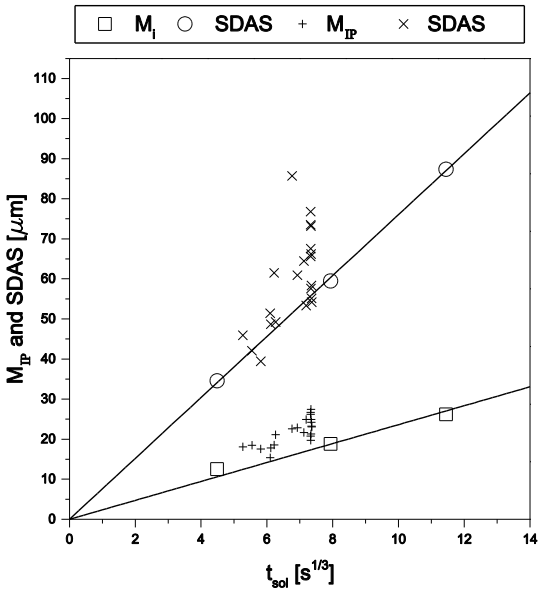

Fig.11: Measured SDAS and M_{IP} as a function of time compared to the literature data in sample A.

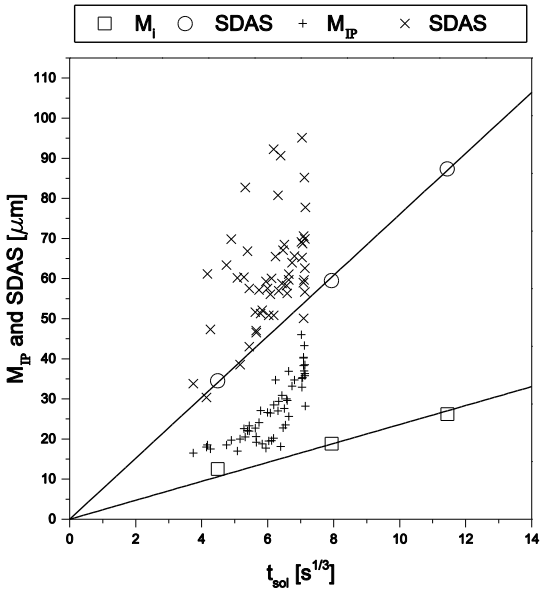

Fig.12: Measured SDAS and M_{IP} as a function of time compared to the literature data in sample B.

Conclusions

1. The local solidification time affects the austenite morphology in complex shaped castings.
2. When the local solidification time (t) increases, the modulus of intra-dendritic space M_{IP} and the secondary dendrite arm space (SDAS) also increase.
3. The increasing value of the modulus of the intra-dendritic phase can be explained by the dynamic coarsening process.
4. The presence of thermal conditions leading to the slowest local solidification time at the boundary between the casting surface and its surroundings cause the formation of an austenite morphology which can promote mass flow between dendrites, thereby provoking shrinkage porosity or metal expansion penetration.

References

1. H. G. Levelink and F. P. M. A. Julien: AFS Cast Met. Res. J., 1973, 9, 2, 56–63.
2. H. G. Levelink and F. P. M. A. Julien: AFS Cast Met. Res. J., 1973, 9, 2, 105–109.
3. I. Dugic and I. L. Svensson: Int. J. Cast Met. Res., 1999, 11, 5, 333–338.
4. A. Diószegi: 'On the microstructure formation and mechanical properties in grey cast iron', PhD thesis, Linköping University, Linköping, Sweden, 2004.
5. G. L. Rivera, R. E. Boeri, and J. A. Sikora: Scr. Mater., 2004, 50, 3, 331–335.
6. G. Rivera, P. Calvillo, R. Boeri, Y. Houbaert, and J. Sikora: Mater. Charact., 2008, 59, 9, 1342–1348.
7. A. Diószegi and I. Dugic: Proc. 'Science and Processing of Cast Iron VIII', Beijing, China, October 2006. 92-97.
8. A. Diószegi, I. Dugic, and I. L. Svensson: AFS Trans., 2007, 115, 609–615.
9. L. Elmquist, S. Adolfsson, and A. Diószegi: Proc. '112th Metalcasting Congress', Atlanta, GA, USA, May 2008, Paper 08-105(05).
10. L. Elmquist and A. Diószegi: Int. J. Cast Met. Res., 2010, 23, 1, 44–50.
11. L. Elmquist, K. Soivio, and A. Diószegi: Mater. Sci. Forum, 2014, 790–791, 441–446.
12. A. Diószegi, V. Fourlakidis, and R. Lora: Proc. '10th International Symposium on the Science and Processing of Cast Iron', Mar Del Plata, Argentina, September 2014.
13. A. Diószegi, R. Lora, and V. Fourlakidis: Mater. Sci. Forum, 2014, 790–791, 205–210.
14. V. Fourlakidis, R. Lora, and A. Diószegi: Mater. Sci. Forum, 2014, 790–791, 211–216.
15. S. Vazehrad, J. Elfsberg, and A. Diószegi: Int. J. Mater. Charact., 2014.
16. R. Lora and A. Diószegi: Metall. Mater. Trans. A, 2012, 43, 13, 5165–5172.
17. J. C. Hernando: 'Isothermal coarsening of primary austenite in Lamellar Cast Iron', Master thesis, Jönköping University, Jönköping, 2013.

Acknowledgements

The present work is a part of the research project JÄRNKOLL within the Casting Innovation Centre, financed by the Swedish Knowledge Foundation. Cooperating parties in the project are Jönköping University, Swerea SWECAST AB, Scania CV AB and Volvo Powertrain AB. Participating persons from these institutions/companies are acknowledged.

A Study of the Oxygen Activity before Start of Solidification of Cast Irons

J.Ekengård[1*], A.Diószegi[2], P.G. Jönsson[3]
[1] Sandvik SRP AB, Svedala, Sweden
[2] Jönköping University, School of Engineering, Dept. of Materials and Manufacturing – Foundry Technology, P.O. Box 1026, SE-551 10 Jönköping, Sweden
[3] Royal Institute of Technology, School of Industrial Engineering and Management, Material Science and Engineering, Div. of Applied Process Metallurgy, Stockholm, Sweden.

In the present paper the oxygen balance during a temperature decrease and especially at temperatures close to the liquidus temperature has been studied for lamellar, compacted and nodular cast irons. Extrapolated data from the full scale trial results show that there are significant differences in the level of dissolved oxygen before start of solidification. Earlier research suggest the influence of the dissolved oxygen on the graphite shape, while the present work draws the attention on how the different shaped lamellar-, compacted- and nodular graphite is incorporated in the austenite matrix based on the differences in the dissolved oxygen content. Predicted differences in the dissolved oxygen are also suggested to influence the growth mechanism of the eutectic colonies and the graphite morphologies in the lamellar cast irons.

Key words: austenite, primary dendrite, lamellar graphite, compacted graphite, nodular graphite, oxygen.

Introduction

General considerations of the total and dissolved oxygen in cast iron

Oxygen in liquid cast iron, can exist as dissolved oxygen or in oxides. The sum of these two contributions gives the total oxygen content. In addition, during a temperature decrease, the dissolved oxygen is also combined with alloying elements to form non-metallic or gaseous compounds[1]. The dissolved oxygen causes changes in the interfacial energy in the solid-liquid interface during solidification and therefore it also influences the crystal growth of graphite[2]. The oxygen combined as oxides is related to a heterogeneous nucleation and a slag formation[3]. This is both advantageous and disadvantageous, due to that oxygen first assists in the nucleation of graphite during solidification. Thereafter, if the poured melt is not raked or filtered properly, it can cause surface or internal defects in the cast product.

The formation of oxides during melting is influenced by a number of factors such as melt surface properties, refractory conditions, melt temperature and melt composition. In the processing of steel, oxygen activity measurements and slag analyses are used as a tool to refine the melt properties. Therefore, the question is if this also is the road towards cast irons with stable properties? One challenge is that industrial cast iron melts are more or less supersaturated with oxygen, due to a contact with the atmosphere. Therefore, the melt contains more oxygen than would otherwise be present at equilibrium.[4]

The influence of dissolved oxygen on the nucleation and growth morphology in cast iron.

The dissolved oxygen plays a decisive role in controlling the graphite morphology. According to [5.6] oxygen atoms and other surface active elements are absorbed on the prism plan of the graphite lattice which block growth in the c-direction. A consequence is a preferred growth in a-direction and a resulting lamellar morphology of the graphite. A removal of dissolved oxygen and other surface active elements like sulphur would enable a graphite growth in the c-direction.

The morphologies of compacted and nodular iron are controlled by surface active elements such as oxygen. Also, lamellar cast iron has a large variety of graphite morphologies and consequently a large variation of the thermo mechanical and thermo physical properties. From the literature [7] it is known that additions of small amounts of deoxidizing elements, less than necessary to form compacted graphite iron, causes the bended shape of the lamellar graphite to transform to a straight shape. Furthermore, to promote higher heat conductivity in the flake graphite iron.

Scope of the present paper

The scope of the present investigation was to measure the dissolved oxygen content during melting and preparation of the liquid iron to cast components, resulting in different graphite morphologies. Due to limitations on the measurement techniques for the temperature ranges close to the solidification temperature, the obtained values were extrapolated towards the liquidus temperatures. This enabled a prediction of the dissolved oxygen levels at nucleation and growth of different cast iron grades.

* Corresponding author, e-mail: johan.ekengard@sandvik.com

Experimental Procedure

Plant trials were performed at three occasions, two lamellar cast iron experiments at Foundry 1 (F1) and another experiment at Foundry 2 (F2) with lamellar, compacted and nodular iron melts.

Process and sampling descriptions

At F1, grey iron melts with different carbon contents were prepared in a six-tonne medium frequency induction furnace. Each trial started with a molten iron, a turned off power and a starting temperature of 1500^{o}C. The raw material for the charges at F1 was machined chip. Iron samples, top slag samples, oxygen activity measurement, and temperature were all taken during 10-15 sampling occasions. Iron samples were sampled with scoop and poured into a cleaned copper mould. Top slag samples were sampled with scoop and poured onto a clean steel plate. Oxygen activity measurements were conducted with a Heraeus ElectroNite MultiLab Celox with probes for cast iron. The temperature was measured with a Heraeus ElectroNite temperature probe. When the temperature was below 1250 ^{o}C to 1270 ^{o}C the measurement was finished and the power was turned on again.

At F2 a lamellar cast iron (LGI) melt was prepared in a six-tonne furnace. After a complete melting the power was turned off. The raw materials for the charges at F2 consisted of returned plate and cast iron returns. Sampling of the same type with same technique as in the F1 experiment were conducted every 10 minutes. The melt was reheated and used as a base iron for Mg-treatment. Four Mg treatments were carried out, two aiming to produce nodular (SGI) iron and another two aiming to produce compacted (CGI) iron. The same base iron melt was used for all four Mg treatments.

Results and Discussion

Primary results

Table 1 in the Appendix shows the sampling temperature range and the determined chemical compositions. The first four experiments called LGI 28, LGI 32, LGI 34 and LGI 37 were conducted at Foundry 1, and the LGI 35 together with the CGI and SGI experiments were conducted at Foundry 2.

Dissolved oxygen in non-treated liquid iron

The temperature dependence of the oxygen activity, $a_{\underline{O}}$, has been evaluated by a number of authors[1-3]. A linear relationship has been proposed as

$$\log a_{\underline{O}} = C_1 \frac{1}{T} + C_2 \qquad (1)$$

where C_1 is proportional to the standard enthalpy change of the reduction or oxidation reaction taking place and C_2 is dependent on the chemical composition[2]. Furthermore, T is the temperature. In Fig. 1 results from the present work are plotted together with results from some previous studies. One hypothesis from earlier work[1] was that a higher carbon equivalent (CE) would decrease the measured oxygen activity. This trend can be seen in Fig. 1 to some extent in the previous work, but cannot be confirmed based on the results from the present study. In Fig. 1 the Kusakawa results seems differentiated with respect to the oxygen activity when varying the carbon equivalent. Mampaey´s results have a similar CE range as Kusakawa´s experiments, but differ in slope. Elmqvist´s results are based on lower CE values and consequently according to[1] should give higher oxygen activities. In the results from the present work, the differentiation of oxygen activities due to carbon equivalent cannot be repeated.

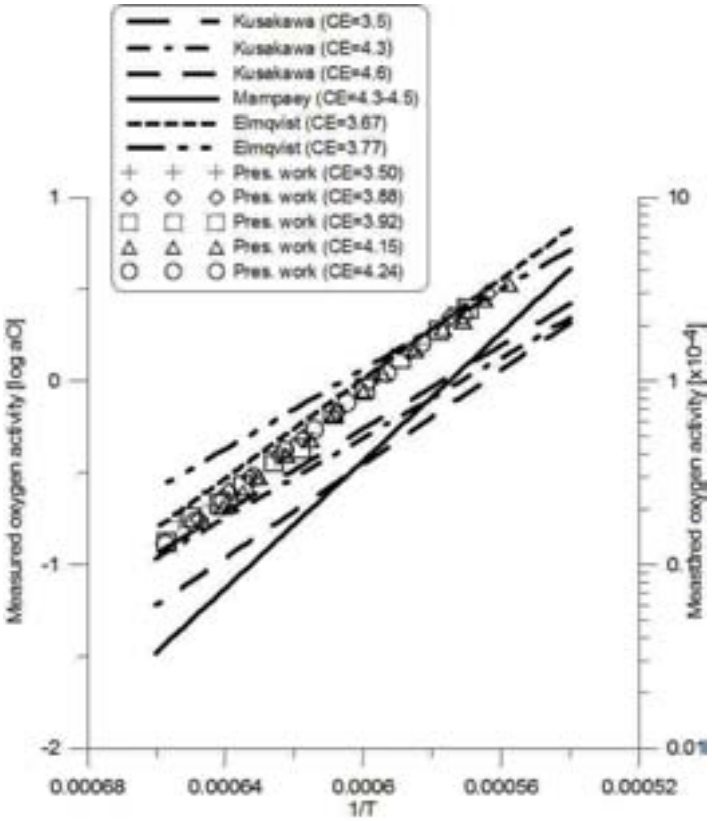

Fig. 1. Oxygen activity*) in non treated liquid iron.

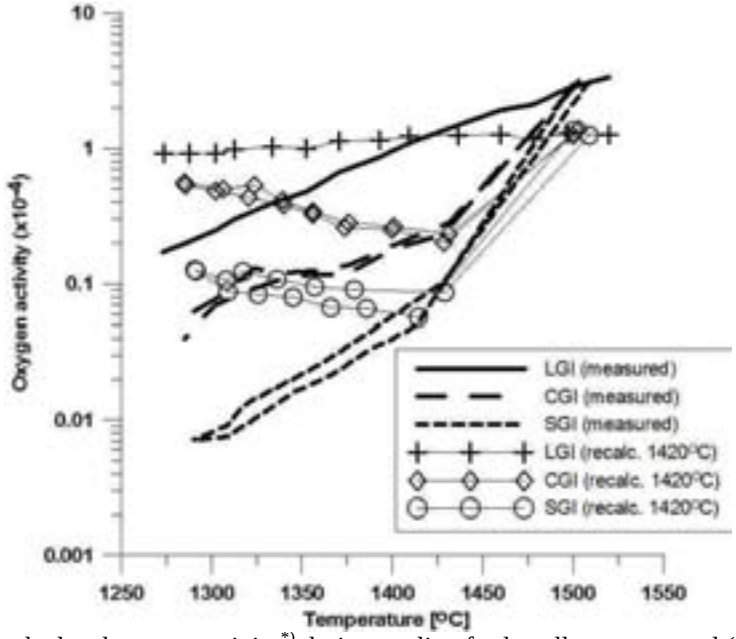

Fig.2. Measured and recalculated oxygen activity*) during cooling for lamellar, compacted (two series) and nodular (two series) cast iron melts.

Dissolved oxygen in treated liquid iron

Due to that the oxygen activity is strongly temperature dependent; Mampaey[2] recalculated measured oxygen activity values to a constant reference temperature of 1420°C. Then this value was chosen as a common casting temperature for nodular iron. The recalculated oxygen activity was retrieved using the coefficient C_1 at the measured temperature and iterating a hypothetical oxygen activity at 1420°C. This procedure was also performed in the present work as shown in Fig. 2, where the measured and the recalculated values of the oxygen activity are given. For lamellar cast iron (LGI), the recalculation only gives a view of how much the temperature influences the oxygen activity value. But for compacted graphite (CGI) and nodular iron (SGI), the recalculation reveals that the oxygen activity increases towards equilibrium as the treated melt is being cooler and at the same time the magnesium decreases in the melt. The recovery of oxygen activity due to a MgO flotation, or the effect of oxygen activity increases as the temperature decreases. In the

*) reference state 1% (by weight) hypothetical solution

everyday foundry practice this phenomena is called fading. After too long time spent between the treatment and casting the oxygen content increase. Therefore the obtained graphite morphology is different from the expected. The speed of the oxygen recovery is highly dependent on the temperature, shape and size of the ladle and whether the top slag is removed or not. The effect of a MgO flotation is partially demonstrated in Fig. 3a-b. Specifically this effect can be seen in the SGI 2 and CGI 2 series, where the MgO content in the top slag increases with a decreased temperature and the Mg content in the liquid iron decreases with a decreased temperature. Unfortunately, the SGI 1 and CGI 1 show the opposite results for MgO in the top slag, which could be due to difficulties at the top slag sampling.

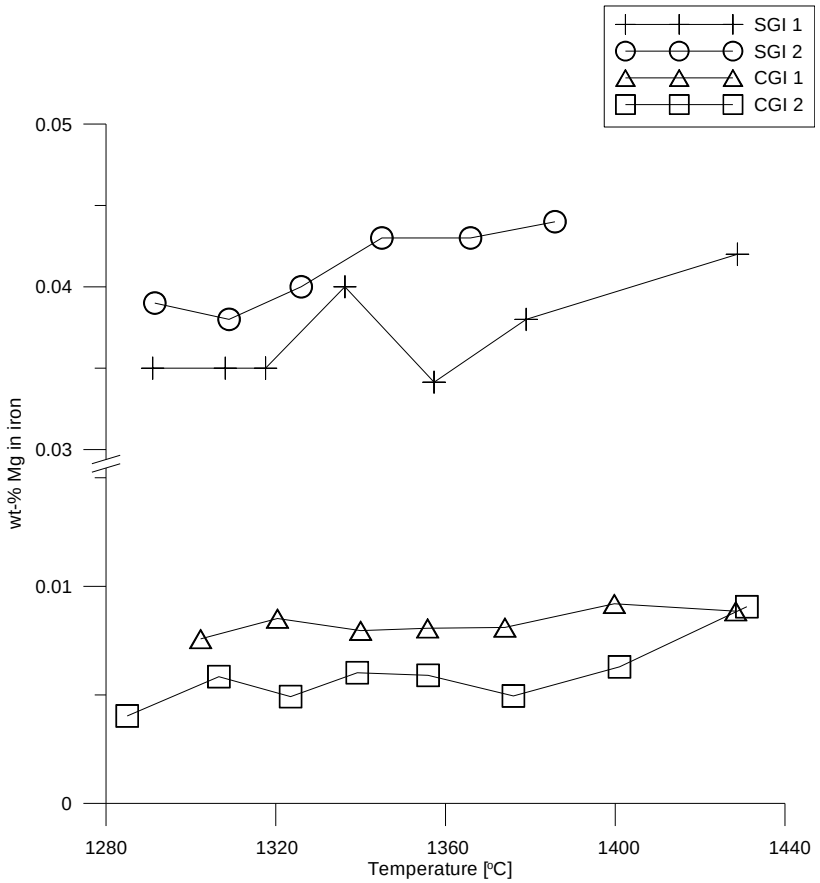

Fig.3a. Mg content in Mg treated iron in the ladle. Data are given for four trials, see Table 1.

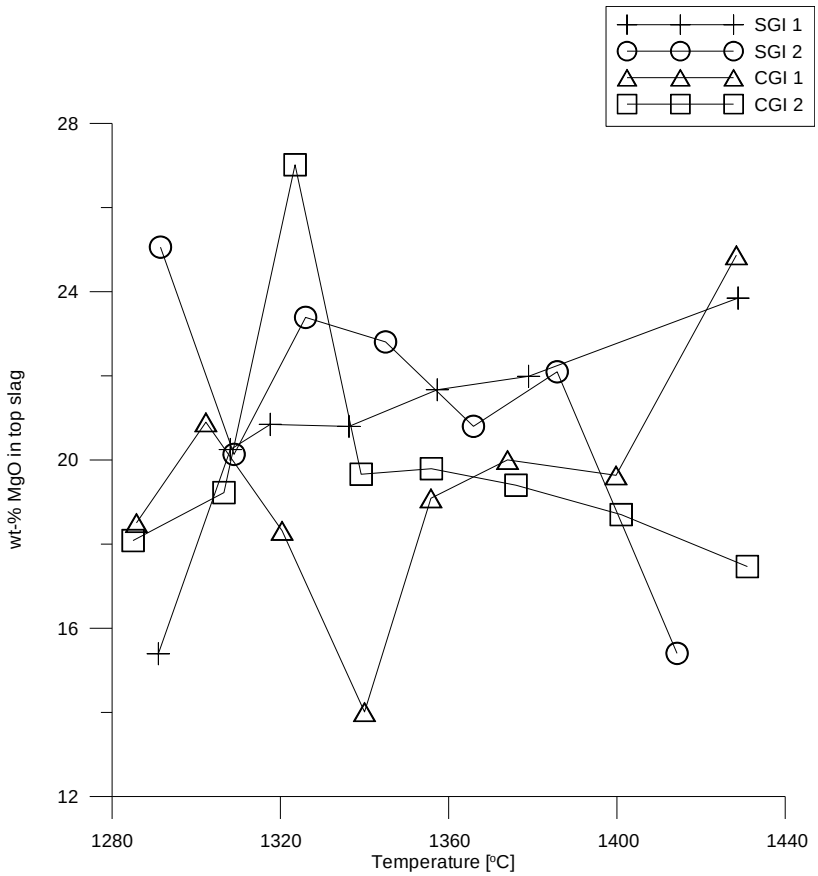

Fig.3b. MgO content in the top slag. Data are given for four trials, see Table 1.

Prediction of the dissolved oxygen content

In Fig. 4 the measured oxygen activity as function of temperature has been extrapolated towards the liquidus temperature for each iron composition. A very clear difference in oxygen activity is predicted for the different liquid irons aimed to produce nodular, compacted and lamellar cast iron. The predicted oxygen activity values support well the theories on the mechanism of graphite shape formation, where it is stated that the absence of oxygen allow the nodular graphite growth. Increasing oxygen activities contribute to a transition from nodular to compact and lamellar graphite shape.

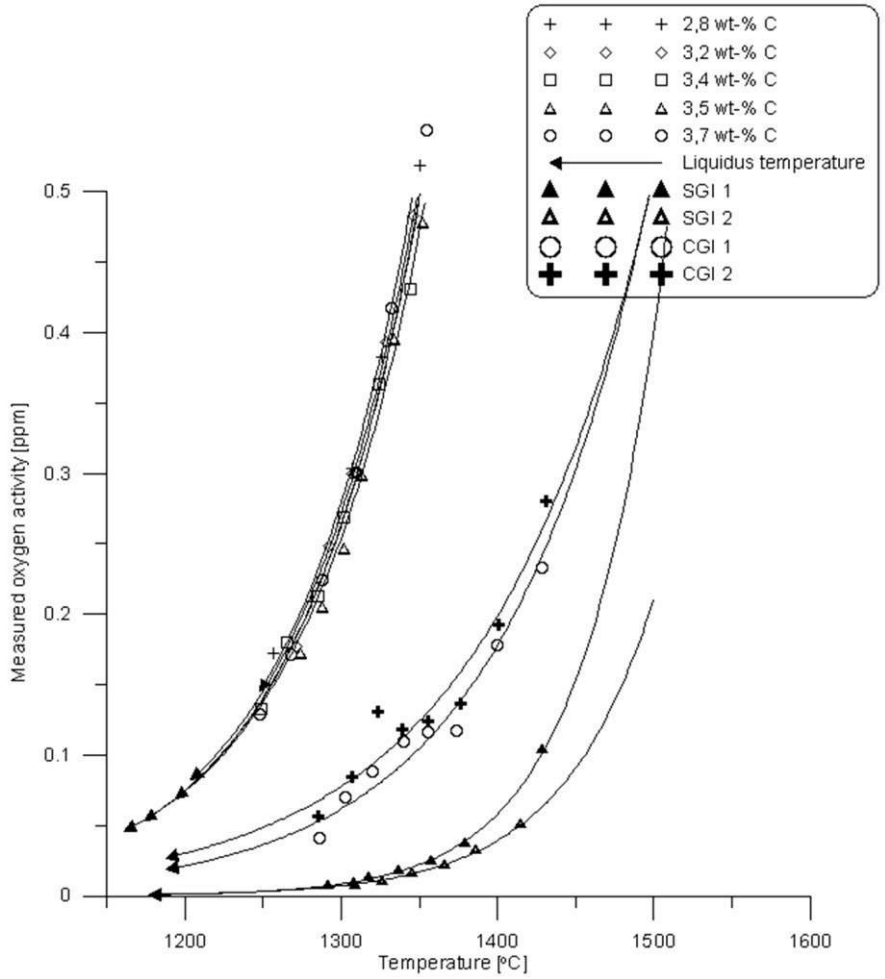

Fig.4. Extrapolated oxygen activities to liquidus temperatures.

Oxygen is considered as a surface active element, which influences the solid-liquid interfacial energy between the austenite and the liquid[8]. Consequently, it is suggested by the authors that the oxygen activity influences not only the shape of the graphite but also how the graphite particles are incorporated in the eutectic austenite during the eutectic growth. Here, nodular graphite is completely incorporated in the austenite shell[9] while compacted and lamellar graphite is incorporated only partially. That results in a cooperative growth between graphite and austenite, where the graphite remain in contact with the liquid iron.

This cooperative growth could be explained with the oxygen activity in the solidification front, where there is a gradient of surface active oxygen in the solidification range. This is due to the diffusion of carbon in the mushy zone, as can be explained with Fig. 5. A higher carbon content results in lower surface active oxygen content at the solidification front. In Fig. 4 the measured oxygen activity as function of temperature has been extrapolated to the respective liquidus temperatures. The oxygen activities almost coincide at these temperatures but the difference in the oxygen activity at the start of solidification for different carbon contents is up to 0.1 ppm. This can be seen more clearly in Fig 5. for the lamellar cast iron melts.

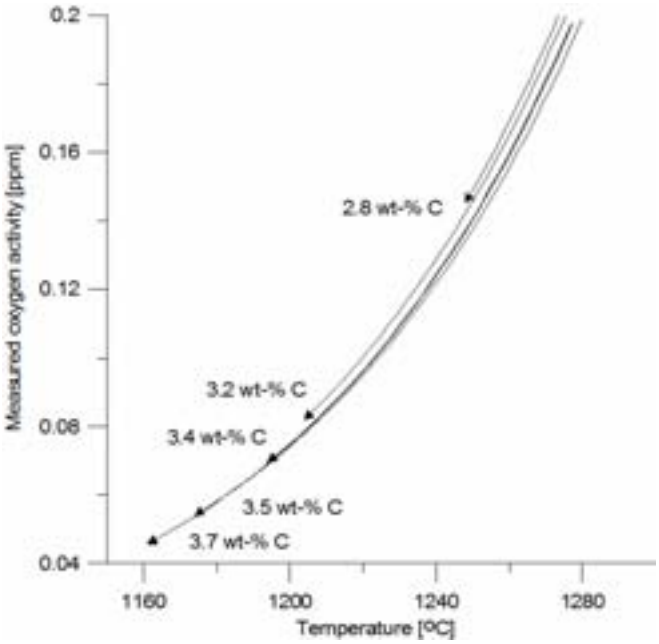

Fig.5. Extrapolated oxygen activities to liquidus temperature for lamellar cast iron melts.

The presented results of this paper were obtained from experiments where no additions of inoculants were made. In the daily foundry practice it is widespread the addition of inoculants with the scope to control the graphite nucleation[10]. Many of the inoculants include strong oxidizing element like Al, Zr, Ti, which promote oxide formation and a consequent change of the oxygen activity at the start of the solidification. In previous work[11] it has been demonstrated that the addition of inoculants containing oxidizing elements influence the number of nucleated eutectic colonies. Moreover, also the growth rate of the eutectic colonies is influenced in the case of casting of lamellar graphite iron. If we consider the growth rate of a eutectic colony proportional to the incorporation ability of graphite in to the austenite matrix, it is possible to conclude that the local oxygen activity in the solid –liquid interface control also the eutectic solidification of lamellar cast iron.

Differences in the lamellar graphite shape morphology can also be related to the oxygen content of the liquid phase. From the literature[7] it is known that additions of small amounts of deoxidizing elements, less than necessary to form compacted graphite iron, causes the bended shape of the graphite to transform to a straight shape and promote higher heat conductivity in the flake graphite iron. The present observations reveal that a lower oxygen activity can be the reason why the lamellar growth is promoted to an extreme, before the transition to a compacted shape takes place.

Conclusions

Measurements of oxygen activities indicate a large variety of dissolved oxygen levels during the processing of cast iron. In addition, clear differences in oxygen content can be predicted for different cast iron melts at temperatures close to the liquidus temperature. The lowest dissolved oxygen content is predicted for nodular cast iron melts, followed by the compacted and lamellar cast iron melts. The latter have the highest predicted dissolved oxygen level. Recalculations of the oxygen activity indicate an increase of the ”relative” oxygen activity and indicate when the treated liquid irons lose their ability to form compacted or nodular graphite. Considerable differences in oxygen activity are predicted at the liquidus temperature for different hypoeutectic iron compositions aimed for a lamellar graphite iron production. The predicted differences of the dissolved oxygen levels are suggested to be an influential factor for how graphite particles are incorporated in the austenite matrix. In the case of lamellar cast iron, the predicted differences of oxygen level are supposed to influence the morphology of the graphite lamella. Hence, the material properties like heat conductivity will be influenced.

References

[1] T. Kusakawa, X. Xu, and S. Okimoto, ‘Effects of oxygen in cast iron during melting and solidification process’, Report of the castings research laboratory, Waseda University, 1988.

[2] F. Mampaey et al.: *Giessereiforschung*, 2008, 60(1), 2-19.

[3] L. Elmquist, J. Orlenius, A. Diószegi: *Transactions of the American Foundry Society*, 2007, 115, 625-636.

[4] B. Marincek: 2nd International Symposium on ´The Metallurgy of Cast Iron´, Geneva, Switzerland 1974.

[5] B. Lux: *AFS Cast Metals Research Journal*, 1972, June, 49-65.

[6] R. Källbom: ‘Chunky graphite in heavy section ductile iron castings’, Report 16, Chalmers University of Technology, Sweden, 2006.

[7] D. Holmgren, A. Dioszegi, I.L. Svensson: *International Journal of Cast Metals Research*, 2006, 19, 6, 303-313.
[8] Z. Yuzhen, S. Yaowo and L. Yongping: *Metallurgical and Materials Transactions B*, 2006, 37B, 485–493.
[9] G.L. Rivera, R. Boeri and J Sikora: Proceedings of the Eight International Symposium on 'Science and Processing of Cast Iron', Beijing, China 2006.
[10] I.L. Svensson, A. Millberg, A. Diószegi: *Journal of Cast Metals Research*, 2003, 16, 29-34.
[11] A. Diószegi: 'On the Microstructure Formation and Mechanical Properties in Grey Cast Iron', Dissertation 871, Linköping Studies in Science and Technology, Sweden, 2004.

Acknowledgement

The present work was performed within the frame of IEC/CIC which is collaboration between Jönköping University, Swerea Swecast, and Swedish foundries. Special thanks are expressed for SKF Mekan AB and Volvo Powertrain AB hosting the experiments and Camelia Bondesson and Vasilios Fourlakidis for assistance during the experimental procedure.

Appendix 1

Table 1. Iron analyses and temperatures

		Temp [C]	C	Si	Mn	P	S	Cr	Ni	Mo	Cu	Sn	Al	Ti
								[wt-%]						
	min	1257	2,83	1,91	0,58	0,026	0,055	0,182	0,059	0,202	0,83	0,047	0,002	0,010
LGI 28	max	1473	2,87	1,96	0,59	0,027	0,061	0,184	0,061	0,205	0,85	0,047	0,002	0,011
	stddev		0,01	0,02	0,00	0,000	0,002	0,001	0,000	0,001	0,00	0,000	0,000	0,000
	min	1271	3,21	1,90	0,56	0,026	0,052	0,179	0,059	0,199	0,83	0,046	0,002	0,010
LGI 32	max	1500	3,26	1,92	0,57	0,027	0,058	0,181	0,061	0,202	0,83	0,047	0,002	0,010
	stddev		0,02	0,01	0,00	0,000	0,002	0,001	0,000	0,001	0,00	0,000	0,000	0,000
	min	1249	3,28	1,71	0,59	0,033	0,061	0,151	0,048	0,220	0,88	0,055	0,002	0,012
LGI 34	max	1483	3,40	1,72	0,60	0,035	0,073	0,153	0,049	0,226	0,88	0,057	0,002	0,012
	stddev		0,03	0,00	0,00	0,001	0,003	0,000	0,000	0,002	0,00	0,001	0,000	0,000
	min	1248	3,55	1,75	0,58	0,034	0,064	0,159	0,050	0,221	0,87	0,045	0,002	0,012
LGI 37	max	1478	3,72	1,78	0,60	0,036	0,073	0,161	0,051	0,226	0,88	0,046	0,002	0,013
	stddev		0,05	0,01	0,00	0,001	0,003	0,001	0,000	0,002	0,00	0,001	0,000	0,000
	min	1274	3,46	1,87	0,62	0,014	0,045	0,036	0,035	0,007	0,85	0,006	0,003	0,005
LGI 35	max	1534	3,57	1,89	0,63	0,016	0,052	0,036	0,036	0,008	0,86	0,007	0,003	0,005
	stddev		0,03	0,01	0,00	0,000	0,002	0,000	0,000	0,000	0,00	0,000	0,000	0,000
	min	1286	3,05	1,39	0,38	0	0,008	0,026	0,032	0,003	0,28	0,005	0,003	0,003
CGI 1	max	1503	3,56	2,16	0,39	0	0,009	0,026	0,033	0,006	0,28	0,006	0,005	0,005
	stddev		0,16	0,26	0,00	0	0,000	0,000	0,000	0,001	0,00	0,000	0,001	0,000
	min	1285	3,07	1,38	0,37	0	0,007	0,026	0,032	0,003	0,28	0,005	0,003	0,003
CGI 2	max	1500	3,51	2,12	0,39	0	0,009	0,026	0,033	0,003	0,28	0,005	0,005	0,004
	stddev		0,15	0,24	0,00	0	0,001	0,000	0,000	0,000	0,00	0,000	0,001	0,000
	min	1291	3,38	1,42	0,39	0	0,007	0,027	0,032	0,003	0,28	0,005	0,003	0,004
SGI 1	max	1509	3,55	2,10	0,40	0	0,008	0,027	0,033	0,003	0,28	0,005	0,009	0,005
	stddev		0,06	0,24	0,00	0	0,001	0,000	0,000	0,000	0,00	0,000	0,002	0,000
	min	1292	3,34	1,39	0,38	0	0,006	0,026	0,032	0,003	0,28	0,005	0,003	0,003
SGI 2	max	1500	3,49	2,16	0,40	0	0,008	0,027	0,033	0,003	0,28	0,005	0,009	0,005
	stddev		0,05	0,29	0,01	0	0,000	0,000	0,000	0,000	0,00	0,000	0,002	0,000

The System for Evaluating Fluidity and Solidification Characteristic of Alloy Melt

LI Dayong*, MA Xuliang , SHI Dequan and WANG Lihua

School of Material Science and Engineering, Harbin University of Science and Technology, P.R.China

The fluidity and solidification characteristic of alloy melt will affect the casting quality directly. It is necessary to build up a system to evaluate fluidity and solidification characteristic simultaneously. A new system, which consists of fluidity evaluation unit and solidification characteristic evaluation unit, is developed. The fluidity of alloy melt is evaluated by melt flow velocity and flow length in a special mould and the solidification characteristic of alloy melt includes solidification temperature range, linear shrinkage, thermal stress and hot tearing tendency. In the paper, the principle of measuring various parameters, the key techniques of hardware and software design are discussed and the application results are also analyzed.

Keywords: fluidity, solidification characteristic, evaluating system

Introduction

The casting quality, such as shape integrity, edge sharpness and acceptable properties, is attached much importance to the mold-filling capacity and solidification characteristic of alloy melt, the evaluation of which has accordingly attracted plenty of investigation in depth.

In the practice home and abroad, fluidity is always used to characterize the mold-filling capacity and to provide a basis for the determination of the processing parameters, like gating system, mold structure, etc.[1-4]. Flow length of the fluidity spiral sample or the vacuum fluidity test sample is conventionally adopted to evaluate the fluidity of alloy melt. Based on this, various methods and units have been developed to measure the fluidity more precisely and automatically. M.Di Sabatino reported higher precision acquired in fluidity test using plunger pouring to get good command of pouring temperature and pressure[5]. Xu Lin from Taiyuan University of Technology developed a new device named ALWY-1 to test the resistance change of the resistance wire wrapped by alloy melt[6], which could reflect the flow length change of the test sample. Making use of the conductivity of melt, Li Fengjun from Tsinghua University obtained instantaneous flow velocity and flow length of the melt in the mold-filling process by testing the breakover frequence and holding time of the contacts that burried into cavity in advance [7]. In addition, there are relevant reports on the application of high-speed photography method and X-ray-based observation[8-12].

In the design of casting structure and casting technology, the consideration of linear shrinkage, thermal stress and hot tearing tendency is very important. Over a few past years, scholars home and abroad have made profound investigation on various measurement methods and instruments and acquired certain success in the test of solidification temperature range, linear shrinkage, thermal stress and hot tearing tendency. The instrument function has developed from single-parameter to comprehensive multiple parameters, and data processing from X-Y recorder to SCM and to IPC [13-15]. The instrument developed by Li Mingdi et al from Shandong Institute of Architecture & Engineering has been applied in laboratory for teaching experiment of cast alloy[16]. Zhang Jiafeng et al from Tsinghua University have tested the stress change of aluminum alloy using self-made device[17]. On the basis of ZQS-2000 tester, Gao Xinsheng from Wuhan University of Science and Technology has developed a new system for measuring linear shrinkage and hot tearing tendency of cast alloys [18]. The foundry test and control lab in Harbin University of Science and Technology developed a new type tester for measuring the linear shrinkage, thermal stress and hot tearing tendency of cast alloys[19-20].

On the basic of analyzing the existing apparatus, the authors developed a new system, which consists of fluidity evaluation unit and solidification characteristic evaluation unit, to provide a reference for designing new casting material and optimizing foundry technology, and also supplying universities or colleges with an experimental platform.

Characterization parameters and testing methods for the fluidity of alloy melt

The fluidity of alloy melt refers to its flow length in the standard mold. The flow length, however, reflects only the final length under certain conditions but no instantaneous mold filling information. Actually, according to Reynolds, cast alloys with the same filling capacity under the identical filling velocity can either be turbulence or laminar flow because of their different viscosity. Therefore, an integrated data consisting of flow length and transient flow velocity is a desired

* Corresponding author, email:dyli@hrbust.edu.cn

parameter. For improving the deficiency of present testers, the authors developed a visual dynamic evaluation system within which the traditional drag flask was replaced by transparent heat-resistant quartz plate, and a common camera was used to record the flowing process of melt sample. Therefor the instantaneous velocity and flow length as well as the final flow length could be obtained by image recognition and analysis.

In traditional image acquisition and data processing system, CCD camera is used for capturing images, internal storage or screen for saving images and line scanning techniques for identifying feature points of the images, which requires a special image acquisition card and the corresponding software. As shown in Fig.1, the picture is progressively scanned from left to right and bottom to top, and the pixel values are recorded simultaneously. The characteristics of the image are ultimately depicted by feature points, which are determined by pixel values in discrepant gray scale that is recognized by special software. However, when the image is identified in this way, tiny change will take place, and the scanning for the whole image and the analysis point by point are needed, which increases the processing time undoubtedly.

During the overall visualization test process, there is an important available objective condition—the previous region of variation, that is to say, the only variation is the flowing track of the melt. The new method only recognizing the changed regions is distinguished from traditional methods scanning the whole region, which will accelerate the data processing and improve the precision.

After the origin coordinate is located, the flow-track equation of alloy melt can be drawn, and the length from every point of orbit to the origin can also be calculated in accordance with the Archimedean formula. Therefore, the common camera is easy to be used to capture the flow along certain track. Fig.2 is the sketch of the system being filled. Cycle detection of the initial point (point 1) is made at first when its pixel value is changed, and then the system begins to distinguish the next trace point(point 2) which has been calculated previously. Meanwhile, the instantaneous flow velocity and flow length are computed and the flow time and coordinate values of point 1 and point 2 are drawn simultaneously. To distinguish, and to calculate until no alteration in the current point could be observed or until the evaluation of point 31. It is the known locus equation that makes it convenient to extend the monitor point and to upgrade the calculation accuracy.

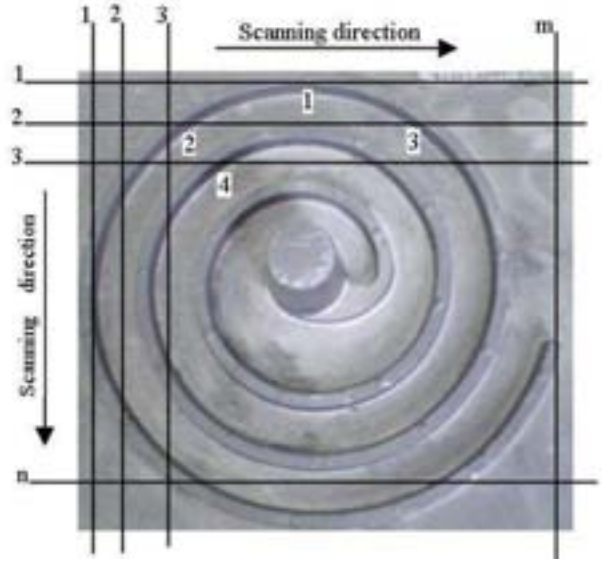

Fig.1: Order of the points based on scanning

Fig.2: Order of the points in filling process

Parameter and Method of Evaluating Solidification Characteristics of alloy melt

Solidification characteristics including solidification temperature range, linear shrinkage, thermal stress and hot cracking tendency are significant parameters for influcing the casting and solidification process. The solidification temperature range and velocity will determine the solidification mode. The narrow temperature range leads to skin solidification tendency and the wide volume solidification. To guarantee the casting quality under a given solidification temperature range, the solidification mode can be controled by optimizing the casting process and specific solidification velocity. Similarly, particular design of casting process is also an effective means for ensuring the size and properties of castings within the foregone information in melt shrinkage, thermal stress and hot cracking tendency.

Comprehensive multi-parameter analysis of alloy melt solidification characteristics includes traditional single parameter test for linear shrinkage, thermal stress, hot cracking tendency, and temperature range. The system structure based on the method mensioned above is shown in Fig.3. The hardware mainly comprises unloading unit, positioning unit, modeling unit, thermal analysis sampler, sensor group and the data acquisition and processing unit.

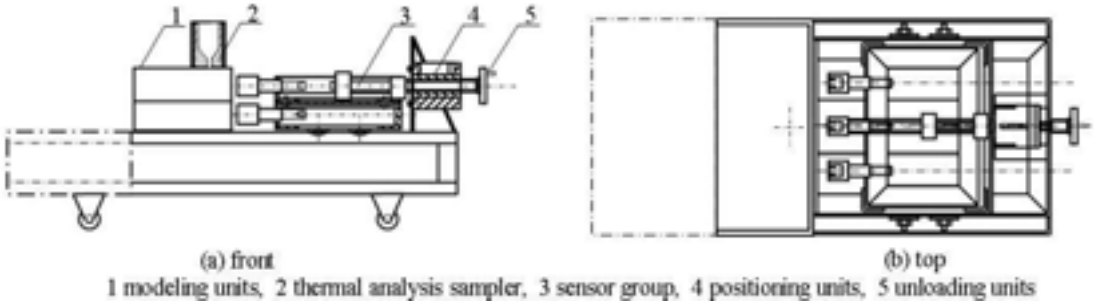

Fig.3: The structure of evaluating solidification characteristics

Positioning unit is used to fix position of modeling unit and sensor connector. Sensors are connected to the specimen through the connecting rod, within which thermal elements and signal transmission lines are embedded for measuring real-time temperature. Besides, positioning unit is also used to change test functions.

Unloading unit makes it easy to remove solidification specimen after testing. In hot cracking tendency testing position, the specimen is connected to the positioning unit and the fixed clamps at each end respectively. During solidification process, it is difficult to depart the specimen from either positioning unit or fixed clamps because of the contraction stress generated by linear shrinkage, however, it can be released easily by the rotating the hand wheel and the conjoint screw rod in the unloading unit.

Modeling unit is composed of flask and mould. The three detachable samples which can be fixed on the plate by the location pins are designed according to the test standard, and they are used for measuring the linear shrinkage, thermal stress and hot cracking tendency respectively. The horizontally parted flask is made up of the top and bottom. Various parameters can be tested using the same flask and plate by replacement of the corresponding samples. The thermal analysis sampler is also served as a sprue cup. The measurement for solidification temperature range is obtained after the thermal analysis curve is recorded.

Sensor group mainly includes three type BK-2Y pressure sensors and a type WDL25 displacement sensor, which convert the stress and displacement to electrical signals respectively. The measurement for linear shrinkage, thermal stress and hot cracking tendency are differentiated by different samples and sensors.

Data acquisition and processing unit is used to collect multiparameters including alloy solidification temperature range, linear shrinkage, stress and cracking tendency, and to analyze the acquired data and finally to display the testing results on the screen or save the database. Data acquisition module ADAM4017 and ADAM4018M are adopted to acquire the signals of displacement, stress and temperature. These signals will be sent to the computer through the communication interface module ADAM4520.

System Construction for Alloy Melt Fluidity and Solidification Characteristic Evaluation

Based on the testing principles and realization methods of testing alloy melt fluidity and solidification characteristics, a new system combined both fluidity tester and solidification tester was developed and a flexible software was designed. The mechanism structure of the system is shown in Fig.4. The left side is the fluidity test unit including gating unit, insulated gate, sand sample and image acquisition unit, and the right side is solidification characteristics evaluation unit.

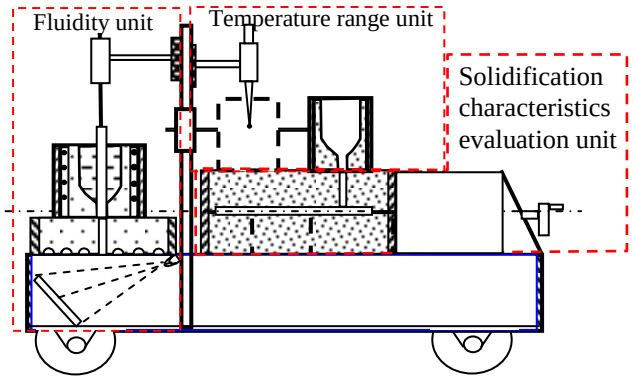

Fig.4: The diagram of system mechanism structure

In the fluidity test unit, the pouring temperature and static pressure of the sample melt can be effectively controled via an electronic lock and temperature measuring device. The substitute quarts glass served as bottom flask needs to be modified through a special treatment. The main program to evaluate the fluidity is shown in Fig.5.

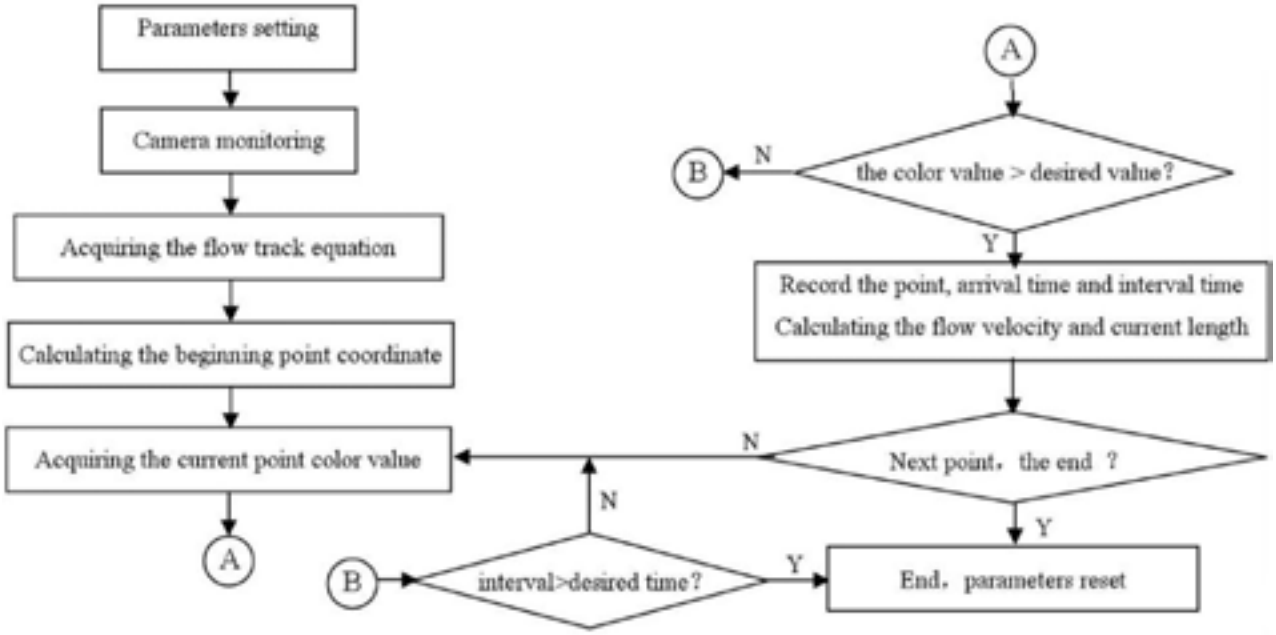

Fig.5: Main program of calculating the flow velocity and length based on flow track

The Solidification characteristics test unit is used to measure the solidification temperature range, linear shrinkage, thermal stress and hot cracking tendency simultaneously. Hereon, the sprue cup was also used to hold the thermal analysis specimen for the solidification temperature range test. After the alloy melt fulfilled the mould, the sprue cup is pushed to the preset position and the thermocouple is fallen into the cup to test the temperature range.

Delphi language is adopted to compile the software system, which mainly includes solidification characteristics test module and fluidity test module. Multi-thread technology is used in the program in order to display the real-time results and testing curve or image.

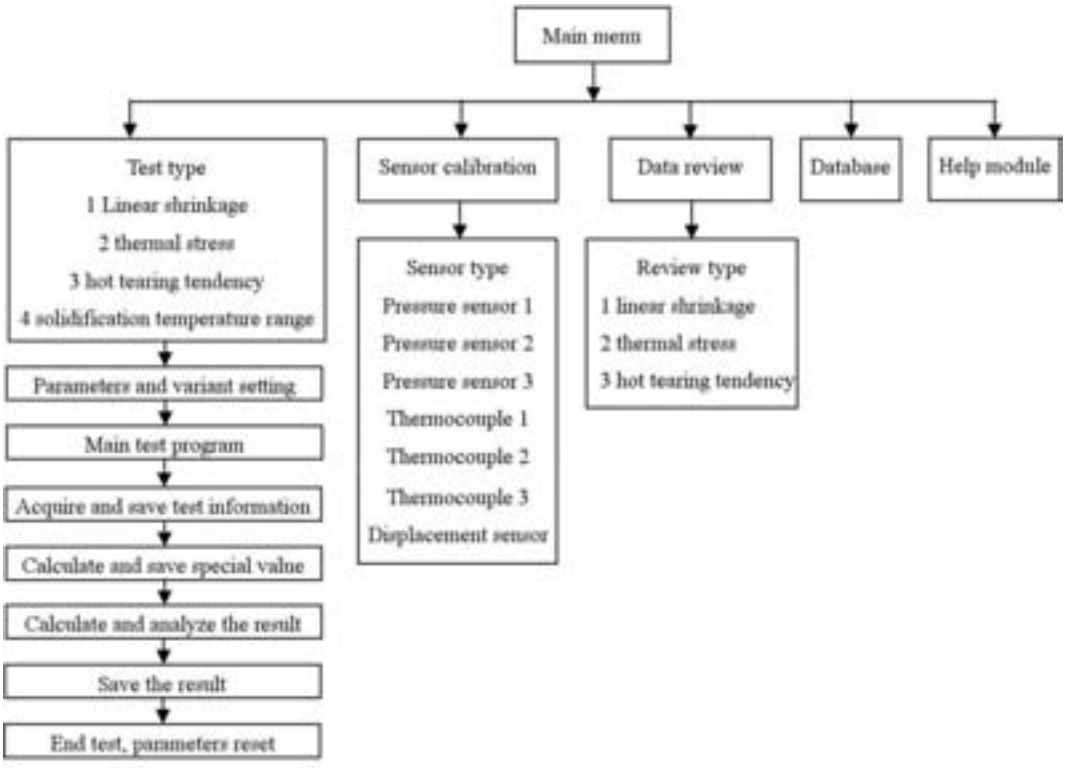

Fig.6: Framework of solidification characteristics test module

Fig.6 depicts the framework of solidification characteristics test module, which is mainly composed of five parts, namely the test module, sensor calibration module, historical data view module, database module and help module. The main interface of solidification characteristics is shown in Fig.7.

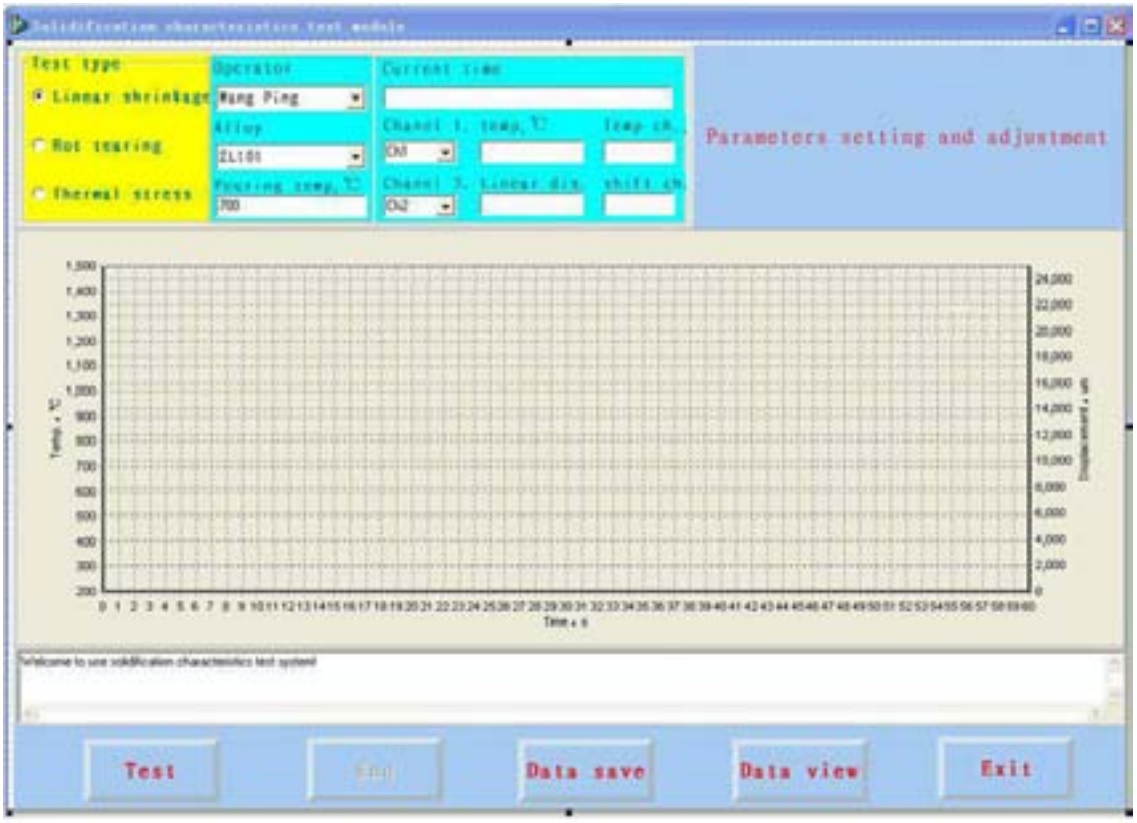

Fig.7: Main program interface of solidification characteristics test module

Practical Experiments on Evaluation System

A comprehensive system to evaluate the fluidity and solidification characteristics of alloy melt was adopted to test the fluidity, solidification temperature range, linear shrinkage, thermal stress and hot cracking tendency in the lab, and the experimental results are shown in Fig.8 and Fig.9. The results show that the developed evaluation system has the error of 2℃ in temperature range test, 0.5% in linear shrinkage test, 2% in thermal stress test, 2% in hot tearing tendency test and less than 1% in final flow length test comparing with the practical value.

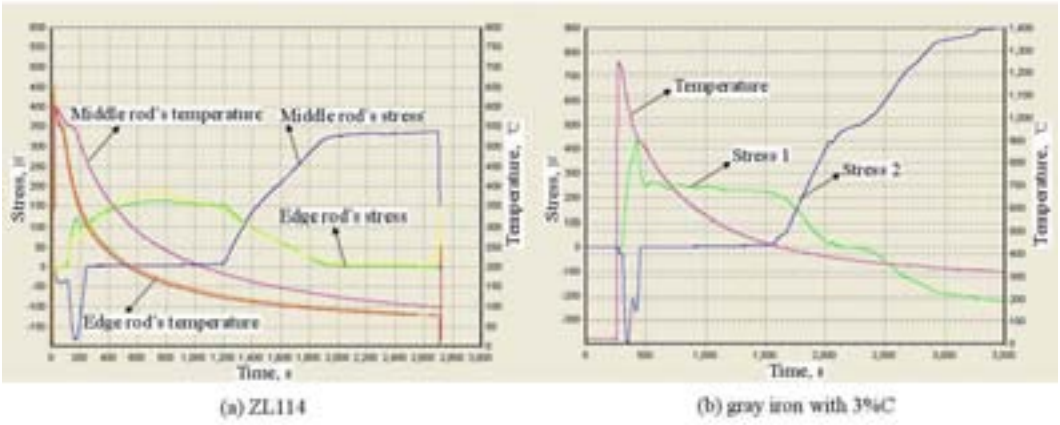

Fig.8: Stress-time relation of different alloys

Fig.9: Fluidity evaluation program interface

Conclusions

The comprehensive and accurate evaluation on fluidity and solidification characteristics of alloy melt is very important in practice. The experimental results indicate that the fluidity of alloy melt can be real-time and roundly evaluated by tracing track and computer recognition method. The high-precision comprehensive evaluation on the solidification characteristics can be realized by the novel desin of compound sampling structure, stress-unloading unit and dual purpose sprue cup.

References

1. Sabatino D.I., Marisa A. L., et al.: *Int. J. Metal Cast.*, 2008, 2, issue.3, 17-26.
2. Kwon Y.D., Lee Z.H.: *Mat. Sci. Eng. A-Struct.*, 2003, 360, 372-376.
3. Zhang Z., Chen X.G., Charette A.: *J. Mater. Sci.*, 2009, 44, 492-501.
4. Gourlay C.M., Nogita K., Read J., et al.: *J. Electro. Mater.* , 2010, 39, issue 1, 56-69.
5. Sabatino D.I.M., Amberg L.: I*nt. J. Cast. Met. Res.*, 2005, 18, issue 3, 181-186.
6. Zai L., Zhan J., Xu L.: *Computer development and application*, 2000, 13, issue 10, 11-12.
7. Li F., Lin Q., Liu B.: *Foundry*, 2002, 51, issue.11, 684-686.
8. Lee H.S., *AFS Cast Met. Res. J.*, issue 9, pp. 112-116 (1973).
9. Yao X., Shivkumar s.: *AFS Transactions*, 1995, 103, 761-765.
10. Xu D., Han L., Shen Q.: *Metal Materials and Heat Processing*, 1983, issue 1, 58-64.
11. Mirbagheri S.H.M., Silk J.R., Davami P.: *Mater. Design*, 2006, 27, issue 2, 115-124.
12. Wang K., Mo Y., Xia L. et al.: *Heat Processing*, 2009, 38, issue15, 63-65.
13. Warrington D., Mccartney D.G.: *Cast Met.*, 1989, 2, 134.
14. Zhang W., Qian G., Li W.: J*ournal of Shen Yang Institute of Mechanical and Electrical Engineering*, 1982, 2, 47-57.
15. Wang Y., Yu J., Wang Q., et al.: *Journal of materials*, 2003, 17, issue 11, 72-74.
16. Li M., Chu F., Zhang P.: *Research & Exploration in Laboratory*, 2006, 25, issue 3, 30.
17. Zhang J., Kang J., Liu B.: *Foundry*, 2007, 56, issue 9, 960.

18. Gao X.: 'Linear Shrinkage & Hot-Crack Detection System Cast Alloy', Master's degree thesis, Wuhan University of Technology, Wuhan, China, 2006.
19. Sun Q., Li D., Shi D. et al.: *Foundry*, 2006, 55, issue 6, 608-610.
20. Li D., Sun Q., Shi D., et al.: 'Multi-functional Device For Testing Linear Shrinkage And stress And Heat Check of Alloy liquid', *China*, 2004200639943[p]. 2006-03-01.

Acknowledgements

The research is financially supported by the National Natural Science Fund of China (project number: 50827403). The authors sincerely appreciate the national natural science fund committee.

Solidification Macrostructure of Compacted Graphite Cast Iron and its relationship with Shrinkage Porosity

M. López[1*], G. Rivera[1,2], J. Massone[1,2] and R. Boeri[1,2]
[1]Metallurgy Division, Faculty of Engineering, UNMdP, Mar del Plata, Argentina
[2]INTEMA, UNMdP – CONICET, Mar del Plata, Argentina

This work focuses on the study of the solidification macrostructure of compacted graphite iron and its relationship with shrinkage porosity formation. Cast samples especially developed to present shrinkage porosity were examined after applying the DAAS technique, which involves hot shake out of the castings at temperatures above the eutectoid, followed by an austempering. The samples were then sectioned, polished and etched with Nital 2%. The results were compared with those obtained earlier by Rivera et al on spheroidal and flake graphite cast irons. The results show that, similarly to spheroidal and flake graphite irons, the solidification of compacted graphite iron is dominated by the presence of relatively large grains of austenite that can be observed by the naked eye. Differences in the grain size were detected as a function of the position into the different volumes analyzed, observing a typical ingot structure. The dispersed shrinkage cavities formed were found inside the grains and located between the austenite dendrite arms.
The results allow the authors to propose a novel explanation of the solidification of compacted graphite irons that shares common features with spheroidal and lamellar graphite irons.

Keywords: solidification macrostructure, compacted graphite iron, DAAS technique, shrinkage porosity, solidification model.

Introduction

Compacted graphite cast irons are gaining increasing interest nowadays. Their main current applications include diesel engine blocks, turbo housings and exhaust manifolds for the automotive industry. Compacted graphite iron (CGI) is replacing lamellar graphite iron (LGI) in applications where greater mechanical strength is needed, as long as its lower thermal conductivity than flake graphite iron does not become a limiting factor. As the production of CGI is forecasted to increase over the next years, the basic understanding of its phase transformations becomes very important. Nowadays, the knowledge about the solidification behaviour of CGI is limited. The prediction and prevention of casting defects such as micro porosity demands a thorough understanding of the solidification of CGI.

Recent studies of the solidification micro and macrostructure of spheroidal graphite cast iron (SGI) carried out by Rivera et al[1,2] have provided new experimental results that gave support to an explanation of the solidification of eutectic SGI. This explanation postulates that each solidification unit is a grain of eutectic austenite that has a dendritic substructure and contains a very large number of graphite nodules.

Rivera et al[3,4,5] stated that in free graphite cast irons the process of solidification starts with an independent nucleation of austenite dendrites and graphite from the melt. As heat is extracted, austenite dendrites grow and interact with graphite precipitates. They claim that this interaction is quite different depending on the graphite morphology.

Flake graphite and austenite grow cooperatively with both phases in contact with the melt. Otherwise in SGI, spheroidal graphite particles are enveloped by an austenite layer soon after they get in contact with the growing austenite dendrites, and further growth of graphite is controlled by the diffusion of carbon from the melt to the graphite through the austenite shell. These authors proposed the term "eutectic colony" to describe the shapes formed during the solidification of free graphite irons.

In the case of CGI, a big step in the study of its solidification mechanism was carried out by Mampaey[6], who presented samples quenched during solidification which show that some of the compacted graphite particle tips remain in direct contact with the melt. Now it is important to complete this understanding by employing the new techniques and knowledge developed.

The objective of this investigation is to reveal and to characterise the macrostructure of compacted graphite iron in order to develop a theory explaining how solidification proceeds in compacted graphite cast irons and to correlate the solidification structure with shrinkage porosity, similarly as Elmquist et al made for LGI[7].

Experimental Procedure

All tests were carried out on samples especially designed to develop large and small shrinkage cavities. They were designed employing dimensions and geometric relationships that violate the basic design rules. The conditions that,

* Corresponding author, email: marcosl@fi.mdp.edu.ar

according to Campbell[8], give the most difficult feeding conditions were used, such as: right angles, hot spots, intricate areas, section changes, metallostatic low pressure zones, long feeders, thin sections, etc. The system was then simulated employing the software MagmaSoft, in order to make the necessary modifications in the geometry to maintain the presence of shrinkage porosity in the model.

The simulations were performed employing the properties of an eutectic ductile iron GJS-600 listed in the database of Magmasoft with the following characteristic temperatures:

- Liquidus temperature: 1169ºC
- Solidus temperature: 1166ºC

The parameters that were adopted to hold the simulations are as follow:

- Pouring temperature: 1360ºC
- Pouring time: 5 s
- Feeding efficiency: 70%
- Inoculation treatment: 70%
- Graphite precipitation: 7

Regarding to the mould material, Silica_dry sand at a temperature of 25ºC was used. It was also employed a uniform meshing along the whole moulding cavity with 200.000 elements.

Concluded this process the design showed in Fig. 1was reached.

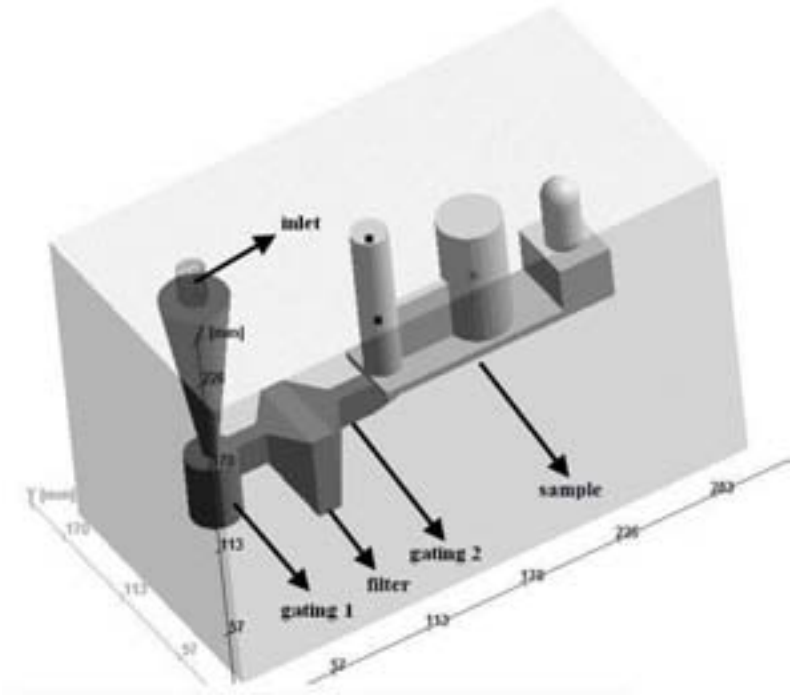

Fig. 1: 3D view of the model.

Fig. 2 indicates the velocity distribution after 2.65 seconds from pouring, showing that the velocity inside the piece is lower than the critical value of 1 m/s, avoiding turbulent flow.

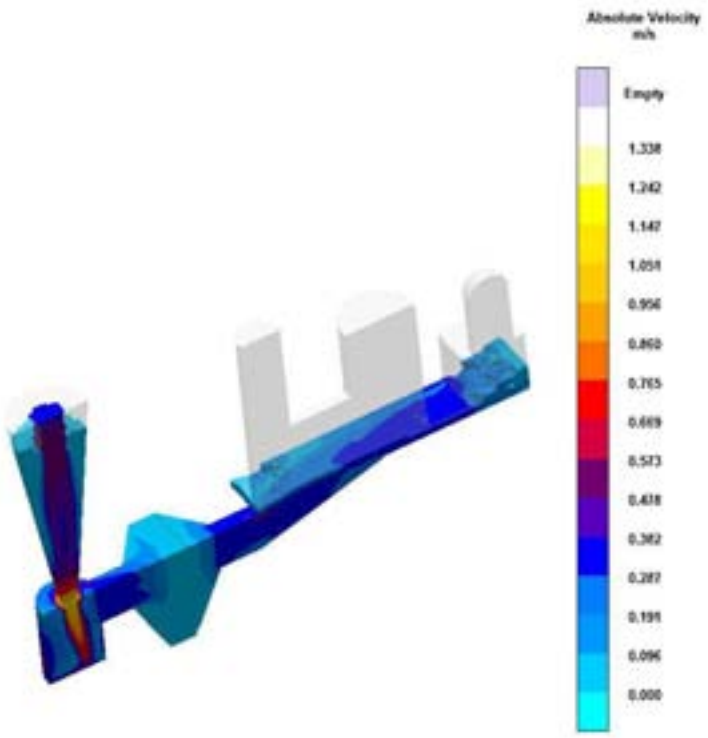

Fig. 2: Velocity distribution in the final design after 2.65 s.

Fig. 3 shows the temperature at the middle section of the mould cavity when the cavitie is completelly filled (5 seconds after pouring started). It can be observed that the minimum temperature in the piece is 1230 °C, which is higher than the liquidus temperature (1169 °C) .

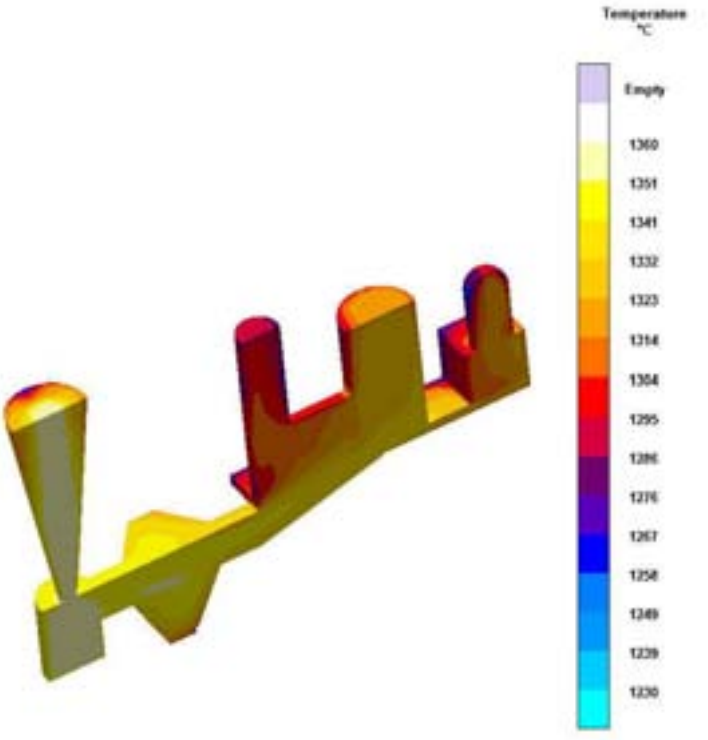

Fig. 3: Pouring temperature of the final design.

Lastly, Fig. 4 shows the porosity distribution at the middle section of the part predicted by the software once solidification has finished. Through this prediction, it can be confirmed the presence of shrinkage porosity in the experimental sample.

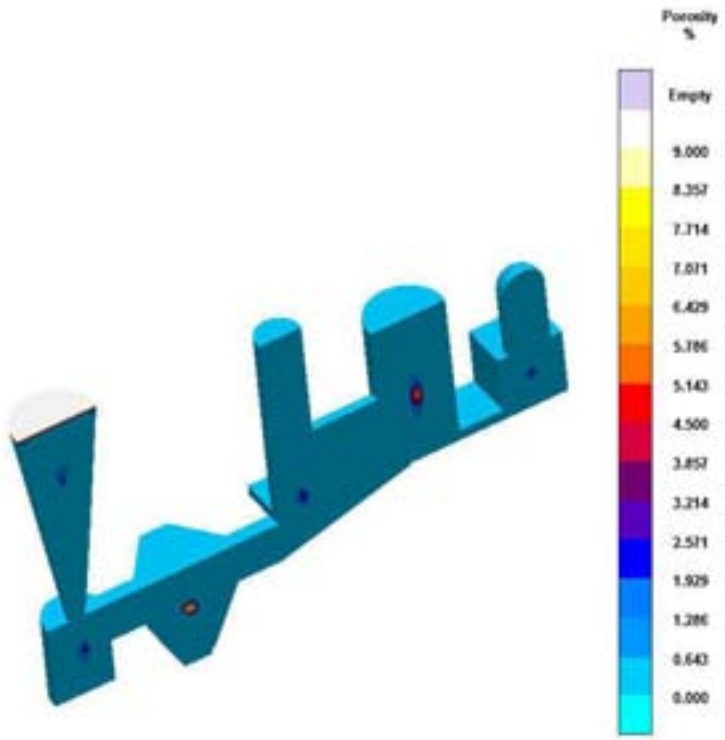

Fig. 4: Porosity at the middle section of the final design.

Once the final design was completed employing MagmaSoft, experimental meltings were carried out by using a medium frecuency induction furnace of 50 kg capacity at the foundry laboratory of INTEMA. The chemichal compositions of the heats are listed in Table 1. Melt A, with a CE of 4.29%, has eutectic composition, while Melt B is hypereutectic. The melts were nodularised by using between 0.6 and 0.67 wt-% of Fe-Si-Mg-Ca-Ce (6 wt-%Mg), and post inoculated with 0.5 wt-% of Fe-Si (80 wt-%Si). Compositions include small amounts of Cu and Ni that were added to reach the level of austemperability needed to carry out the DAAS procedure.

Table 1: Chemical Compositions.

Melt	% C	% Si	% Mn	% S	% P	% Mg	% Cu	% Ni
A	3.38	2.74	0.17	0.017	0.033	0.020	0.97	0.66
B	3.53	3.15	0.18	0.016	0.041	0.015	1.025	0.78

After the moulds were filled, the cast parts were shaken out when their minimum temperature reached approximately 950ºC, being then transferred to a furnace held at 920ºC, where they were kept during 30 min in order to allow their temperature homogenisation. The parts were then austempered in a molten salt bath held at 360ºC for 90 min. This relatively high austempering temperature was chosen in order to maximize the amount of retained austenite.
Later the samples were sectioned, polished and etched with Nital 2%. Nodularity was measured by comparison with standard charts.

Results and Discussion

Fig. 5 shows the graphite morphology obtained in both melts. These micrographies reveal that samples of Melt A show a nodularity of 30%, whereas samples of Melt B have a nodularity of 15%. These values were found from the average of five different fields analysed and are consistent with the amounts of Mg found in each melt.

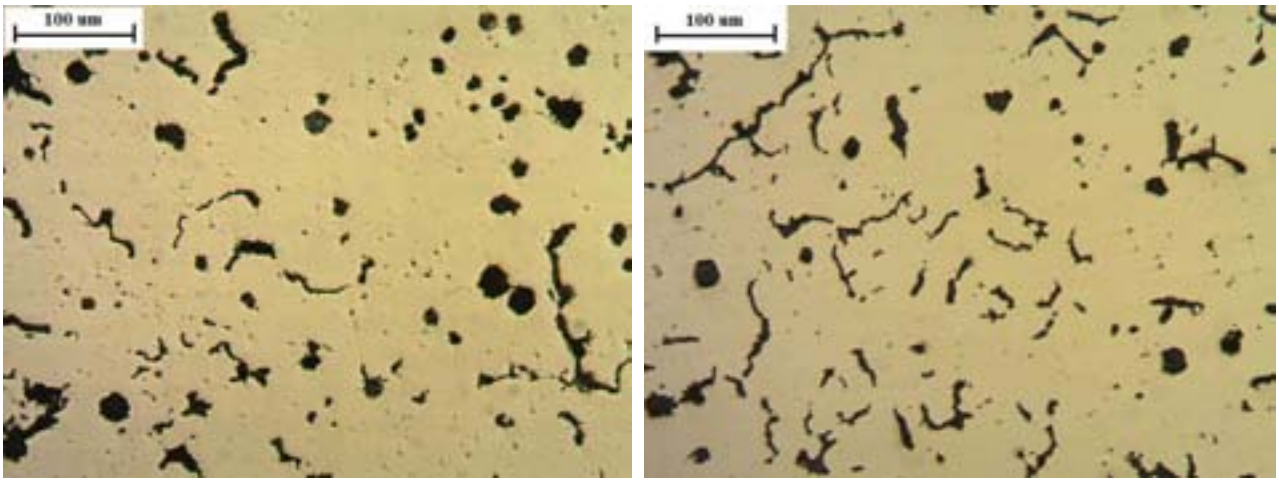

Fig. 5: Microstructure of Melt A (left) and Melt B (right). Unetched.

The microstructure of the metallic matrix after Nital 2% etching is shown in Fig. 6. The austempering heat treatment lead to a matrix microstructure formed by a fine mixture of acicular ferrite and austenite. This austenite is in fact the primary austenite, which has been retained in the matrix after the use of the DAAS technique.

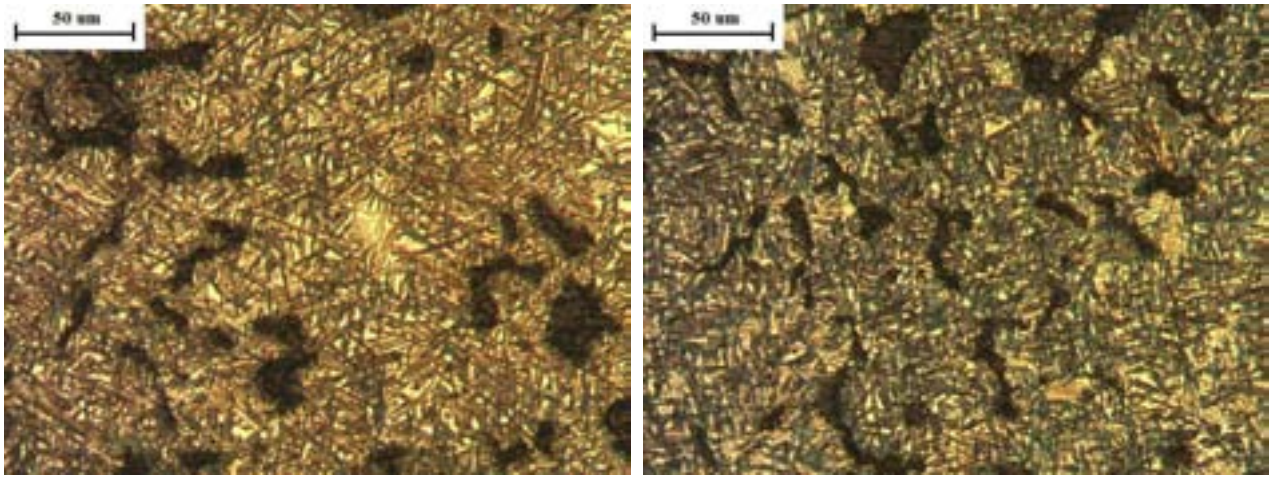

Fig. 6: Microstructure of Melt A (left) and Melt B (right) after etching with Nital 2%.

The retained austenite kept the crystalline orientation defined during solidification. Therefore, after standard chemical etching, the grained structure of the austenite can be observed macrographically. Fig. 7 and Fig. 8 show the macrostructures obtained after applying DAAS technique and etching with Nital 2% for Melts A and B respectively. These are some of the first pictures published to date in which the solidification macrostructure of CGI is simultaneously shown with shrinkage porosity. Small equiaxed grains are visible at the faster solidifying portions of the sample, while much larger, and sometimes columnar, grains are observed on other areas of the samples.

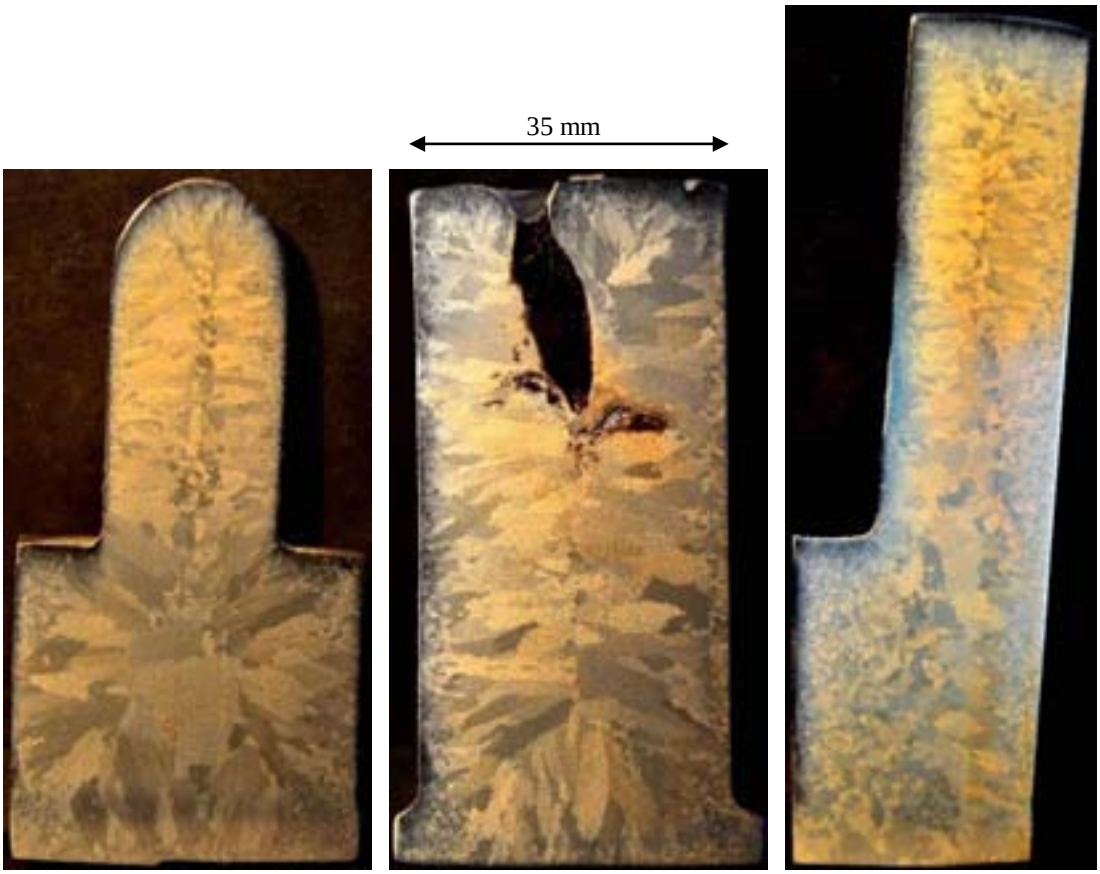

Fig. 7: Solidification macrostructures obtained for Melt A.

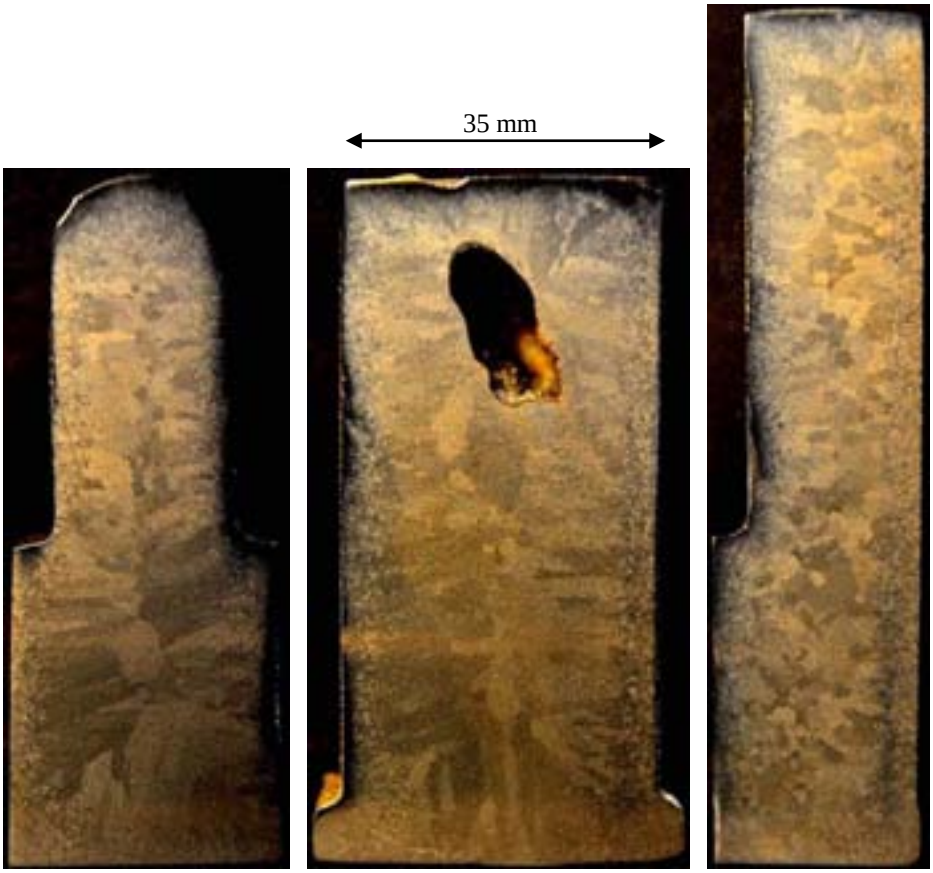

Fig. 8: Solidification macrostructures obtained for Melt B.

When comparing the results shown in Fig. 7 and Fig. 8 with those obtained previously by Rivera et al[3] for SGI and LGI, the similarity of CGI macrostructure is noticeable. Just as it was concluded earlier for SGI and LGI, the solidification of CGI is strongly dominated by the nucleation and growth of relatively large grains of austenite, each one including a large number of graphite particles. The use of EBSD by Rivera et al[3] for samples of SGI and LGI demonstrated that there is a clear correlation between the results obtained applying DAAS technique and EBSD analysis. EBSD technique proved that austenite grains can be properly observed by employing the procedure DAAS.

Based on the observation of the macrostructure and the previous experience exposed in the references[1-5], it is proposed that the solidification of CGI proceeds in a manner similar to that characteristic of LGI. The nucleation and growth of austenite and graphite proceed mostly independently in the melt. Austenite grows dendritically. The portions of the casting exposed to higher cooling rates reach larger undercoolings and show a relatively large density of austenite nucleae, resulting in small grain size. On the other hand, slower cooling portions show smaller density of austenite nucleae and therefore larger grain size. The graphite particles grow in the melt, most probably as spheroids during the first stages, but later, as the growing austenite dendrites collide with them, form eutectic colonies in which austenite and graphite grow cooperatively, with both phases in contact with the melt.

Concerning the location of porosity, Fig. 9 shows that dispersed shrinkage cavities from samples obtained in this research are mostly intragranular and locate between austenite dendrite arms. It can also be observed that there is no a linear arrangement of shrinkage porosity, as would be found if cavities were formed between the austenite grains.

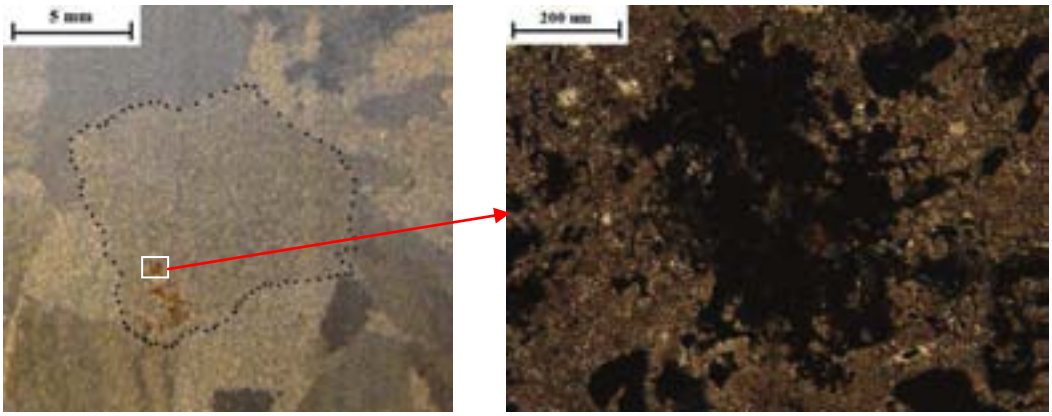

Fig. 9: Porosity in macro and microstructure.

The main features of the solidification of CGI revealed by this investigation are quite important for practical aspects. Nowadays, the computational packages aimed at the prediction of the filling and solidification of free graphite cast irons poured in moulds do not take into account the actual size and shape of the austenite dendrites, to the best of our knowledge. The prediction of fluid flow, filling, temperature evolution and defect formation should be improved by the adoption of more realistic solidification models.

Conclusions

1. The solidification of compacted graphite iron is dominated by the presence of relatively large grains of austenite that, after the use of the DAAS technique, can be observed by the naked eye, just as it was previously demonstrated for lamellar and spheroidal graphite cast irons. It is proposed that the solidification of CGI proceeds in a manner similar to that of LGI, this is with an independent nucleation and growth of austenite and graphite from the melt.
2. The dispersed shrinkage cavities form mostly inside the grains, and locate between the austenite dendrite arms.

Acknowledgements

This study made use of an academic license of MagmaSoft, which is gratefully acknowledged.

References

1. G. Rivera, R. Boeri and J. Sikora: 'Revealing and characterising solidification structure of ductile cast iron', *Materials Science and Technology*, June 2002, Vol. 18, 691-697.
2. G. Rivera, R. Boeri and J. Sikora: 'Research Advances in Ductile Iron Solidification', *AFS Transactions*, Vol. 111, 3-159, pp 1-11 (2003)
3. G. Rivera, P. R. Calvillo, R. Boeri, Y. Houbaert and J. Sikora*:* 'Examination of the solidification macrostructure of spheroidal and flake graphite cast irons using DAAS and ESBD', *Materials Characterization 59*, 2008, 1342-1348.

4. G. Rivera, R. Boeri, J. Sikora: 'Searching for a Unified Explanation of the Solidification of Cast Irons', *Eighth International Symposium on Science and Processing of Cast Iron*, Beijing, China, 2006, Vol 1. pp 45-50.
5. G. Rivera, R.Boeri, J. Sikora: 'Growth of eutectic austenite in free graphite cast irons', *Key Engineering Materials 457*, pp 67-72 (2011).
6. F. Mampaey: 'Influence of compacted graphite on solidification morphology of cast iron', *AFS Transactions*, 2000, Vol. 27, 11-17.
7. L. Elmquist and A. Diószegi: 'Shrinkage porosity and its relation to solidification structure of grey cast iron parts', *International Journal of Cast Metals Research*, 2010, Vol. 23, 44-50.
8. Campbell, J: 'Castings', Butterworth-Heinemann Ltd, Chapters 2 and 5. 1991.

Automatic vapour sorption analysis as new methodology for assessing moisture content of water based foundry coating and furan sands

G.L. Di Muoio[1,2*], N. Skat Tiedje[2] and B. Budolph Johansen[1]

[1]Global Castings A/S, Copenhagen, Denmark

[2]Technical University of Denmark, Copenhagen, Denmark

Gas generated during the casting process can cause defects that increase the cost of the components and possibly lead to scrapping the parts. Gases are produced during evaporation of water and by decomposition of organic materials present in the foundry coating and in the moulding sand.

This study investigates how equilibrium water content varies in foundry coating and in different furan based binding systems with the objective to determine what variables are critical for material moisture process control. The influence of relative humidity, temperature, dust levels and binder type are investigated**.**

Results show that highest effects are given by relative humidity and binder type. They can cause moisture level variations from 0.1% to about 0.8%. Temperature and dust levels play a minor role. Hysteresis effects between sorption and desorption curves are limited. Finally, the sorption curves are fitted with 3rd order polynomial equations.

Keywords: Water based coating, furan sand, automatic sorption analysis, sorption/desorption curves, drying process control, moisture control.

Introduction

When cast parts are produced, the molten metal in contact with the mould causes the production of gases that can lead to defects and scrapped items (Fig 1.a). Possible gas related defects are: hydrogen pin holes, blow holes, cracks and explosive penetrations.[1,2,3] These gases are composed by a mixture of water vapour, decomposition products of the coating and moulding materials and from gases dissolved in the molten iron.[1,2] Gas defects can be correlated directly to vapour generated in the mould and coating material due to a high level of residual moisture.[3,4,5] In particular for furan sands, water vapour is a significant component of the gases generated during the decomposition.[6] Moisture is present in furan sand as product of the binder and catalyst reaction but its amount can change over time.[5] Literature shows that gas defects probability can be predicted by simulation if models are calibrated with experimental data for the specific binding system used.[7,8,9] Other studies show that gas evolution rates can vary for different materials.[10,11,12,13]

All the current studies however focus on different classes of binding system and foundry material but do not provide information about the influence of parameters such as temperature, air humidity and dust levels and about different brands of furan binders used in Global Castings production facilities.

In this study the objective is to identify how the moisture contents in foundry coating and in sands bonded with different brands of furan binders (Fig.1.b) are affected by relative humidity, temperature and dust levels (Fig.1.c). In order to do this, we use an automatic vapour sorption analyser to determine the equilibrium sorption/desorption curves of the considered materials. The reason for choosing an automatic moisture analyser are: a shorter test time (due to the use of a small sample), the increased precision in weight measurement (due to eliminating manual handing operations of the samples during the tests) and easy and precise control of temperature and humidity.

Sorption/desorption curves are typically used in other industries (such as food, wood, paper) to design and optimise drying processes (by knowing the initial moisture and final moisture achievable at the drier's air humidity and temperature levels)[14], to provide limits for production processes control and monitoring, to predict shelf life by knowing what moisture level a material will reach in an environment at a given air humidity (i.e. shelf life prediction in food packaging depends on moisture content)[15] or to predict possible moisture migration between different materials.[14,15] These curves are a property of the material and show how its moisture levels vary as a function of relative humidity at a given temperature. In particular they will show the minimum possible level of moisture achievable in given environmental conditions for a given material.

These tests are normally not used in the foundry industry but are thought to be relevant by the authors for the following reasons:

- to understand which parameters have the highest effect on moisture levels in the considered material and therefore on the generation of water vapour and the risk of gas defects

* Corresponding author, email: gidmu@globalcastings.com

- to create a set of data that can be used for the design and control of driers of furan moulds and foundry coatings
- to support foundry engineers making the right choices when optimizing the production and drying process of coated furan sand moulds.
- to provide a new methodology for testing foundry coatings and binding systems

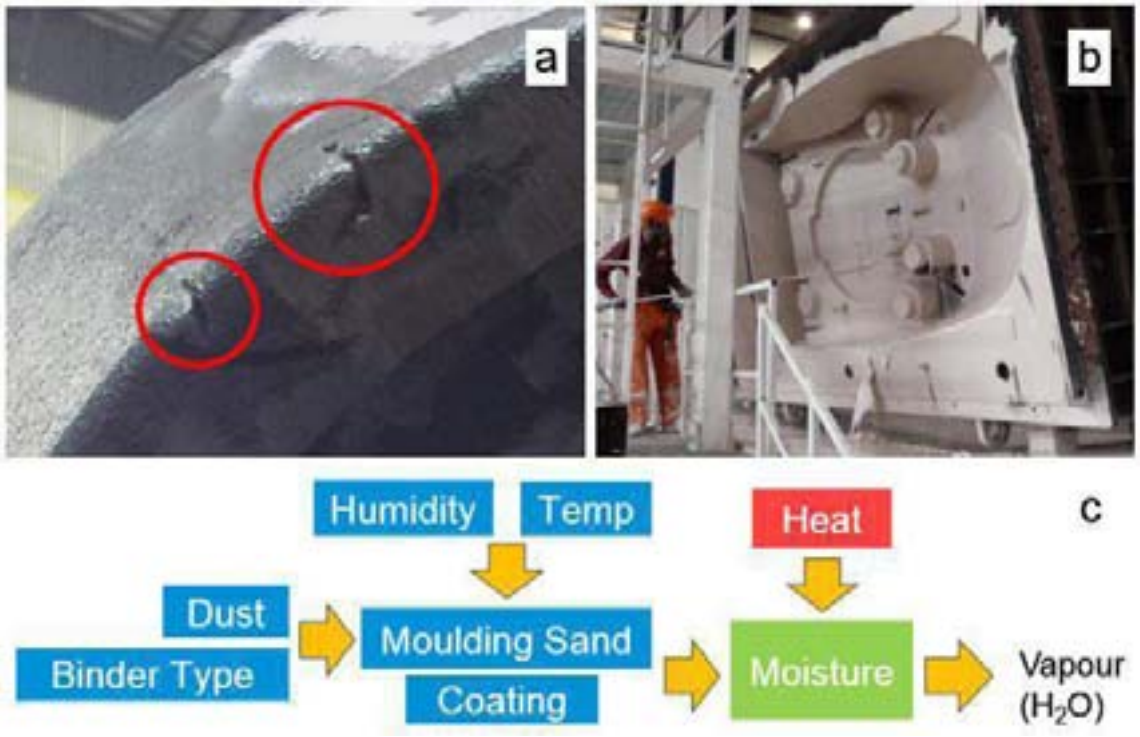

Fig.1: a) Example of moisture related casting defect, b) coating process of furan bonded sand mould, c) parameters affecting vapour generation in a castings process.

Experimental Procedure

In order to investigate the effect of different variables, the experimental plan described in Table 1 was designed. First, the effect of temperature on the two main classes of material is studied (coating and GCX F sand). Then the effect of dust levels are investigated (no dust and 2% dust) and different binder system brands (GCX S, GCM and GCGG). Finally pure dust and un-bonded sand were tested to provide baselines for comparison.

Table 1: Overview of Experimental Plan.

Material	Temperature [°C]		
	15	25	35
Coating	X	X	X
GCX F	X	X	X
GCK No Dust		X	
GCK 2% Dust		X	
GCX S		X	
GCM		X	
GCGG		X	
Pure Dust		X	
Un-bonded Sand		X	

The temperature levels were chosen as the minimum (15°C), typical (25°C) and maximum (35°C) temperature allowed in the produciton facilities. Similarly, dust levels representing the maximum allowed (2%) and the minimum (0%) possibly achievable levels were used. The binder brands are the same as used in the considered produciton facilities.

For the bonded sand, the sample preparation started by mixing of sand, binder and catalyst (Fig.2a), followed by curing for one week at 23-25 °C and 45-50% RH and finally manual crushing (Fig.2b) (for easier handling during tests).

Binder addition was 1% of sand weight and catalyst addition was 40% of binder weight. The coating samples were obtained by drying the liquid coating (typically containing an initial moisture of about 40% on wet basis) at same conditions and time used for the sand samples and then manually crushing the dry coating into powder (Fig.2c). Pure dust and un-bonded sand were taken directly from filter bags and silos in the factory and then let equilibrate at the same temperature and humidity conditions as described for the other samples.

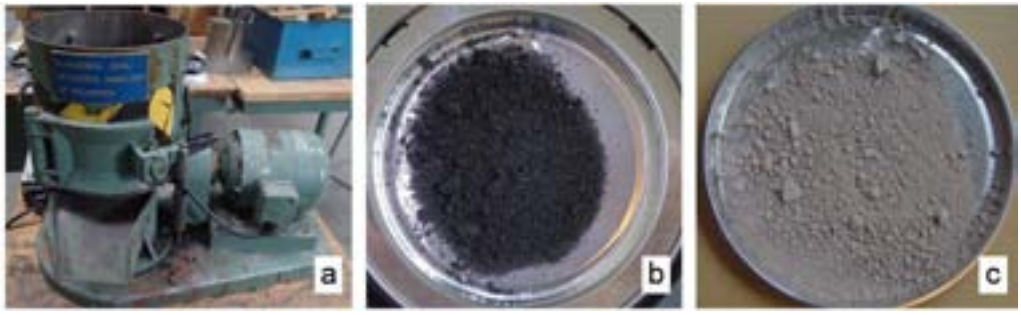

Fig.2: Materials preparation: a) mixing, b) crushed sand and c) crushed coating.

After sample preparation and equlibration at 23-25 °C and 45-50% RH for a week, a sample of each type was tested in an automatic moisture analyzer (Fig.3.a) with an accuracy of 0.05%. The automatic moisture analyzer was set to dry the sample at a temperature of 105 °C. The wet basis moisture (calculated as in equation (1)) values obtained are needed as input in the automatic vapor sorption analyser to compute the sample moisture values during the sorption tests since it is not possible for the automatic moisture analyzer to dry the samples at 105 °C.

$$InitialMoisture_{w.b.} = \frac{InitialWeight - DryWeight}{InitialWeight} 100 \quad (1)$$

The automatic vapor sorption analyser used for this study (Fig.3.c) is equipped with a precision scale with +/- 0.1 mg accuracy, a dew point sensor with 0.5 % RH accuracy and infrared sensor for temperature control. The moisture level can be controlled by supplying either wet air or dry air.

The sorption/desorption tests were carried out by loading a sample of about 10-12g in the automatic sorption analyzer and inputting the initial moisture of the sample at 23-25 °C and 45-50% RH (Fig.3.b) from the previous tests. After sealing the cover, the machine will start recording weight variation and changing temperature and relative humidity according to the test plan.

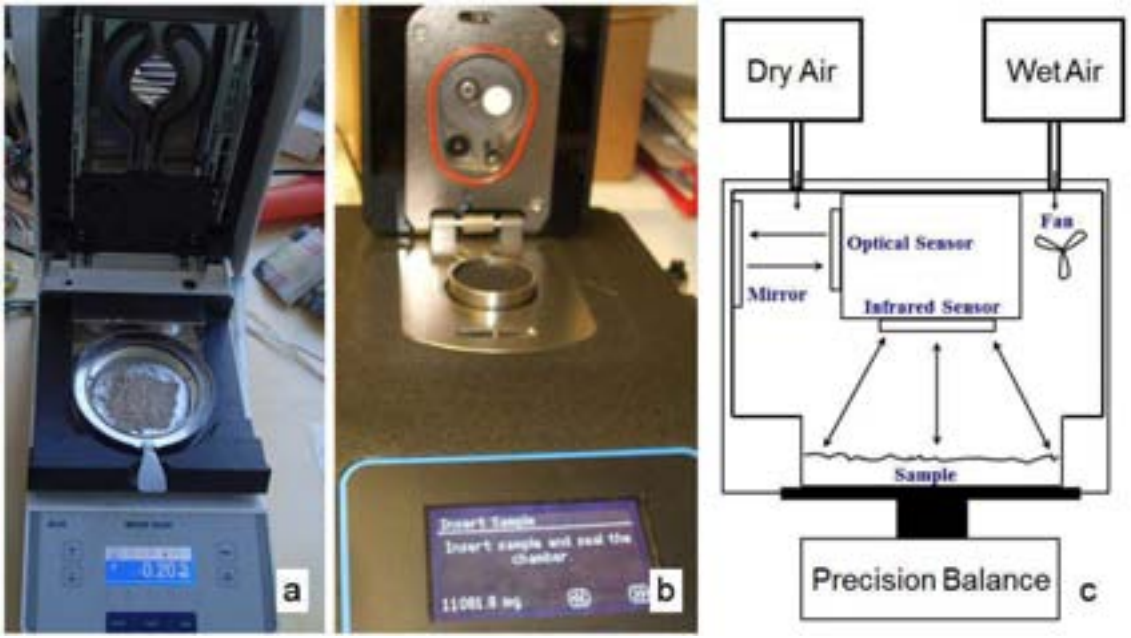

Fig.3: Test Setup: a) initial moisture level measurement, b) automatic vapour sorption analyser and c) schematic.

In order to abtain the sorption/desorption curves, the temperature is held constant at either 15 °C, 25 °C or 35°C while the air humidity is changed stepwise in 5% increments. The current moisture content of the sample is calculated as:

$$CurrentMoisture_{w.b.} = \frac{CurrentWeight - DryWeight}{CurrentWeight} 100 \quad (2)$$

Where dry weight is calculated from the initial moisture and weight as:

$$DryWeight = InitialWeight\left(1 - \frac{InitialMoisture_{w.b.}}{100}\right) \quad (3)$$

During the test, at each imposed air humidity level, the moisture level in the sample is calculated using equation (2). If the variation in moisture is less then 0.02% in one hour, the sample is considered equilibrated and the air humidity can be changed to the value required by the next step (Fig.4a).

Each test begins at 50% RH and the air humidity is incresed stepwise up to 95% to initialise the sample (Fig.4b), then the desorption phase starts (humidity is decresed step wise to 5% RH) and finally the adsorption phase is carried out (humidity is increased stepwise to 95% RH). In order to obtain the final sorption curve, the moisture level of each equilibrium point is plotted versus the air humidity. Sorption curves are plotted in the results section without the initialization steps.

Finally, 3rd degree polynomial equations are fitted to the experimentally obtained sorption and desorption curves (Fig.4c and equation (4)). The curves coefficients are reported in the result section for each material, as well as the coefficient of determination R^2 used to check how well the model fits the data (R^2 values close to 1 represent a good fit between the curve and the data).

$$MaterialMoisture_{w.b.} = a_0 + a_1 \frac{RH_{air}}{100} + a_2\left(\frac{RH_{air}}{100}\right)^2 + a_3\left(\frac{RH_{air}}{100}\right)^3 \quad (4)$$

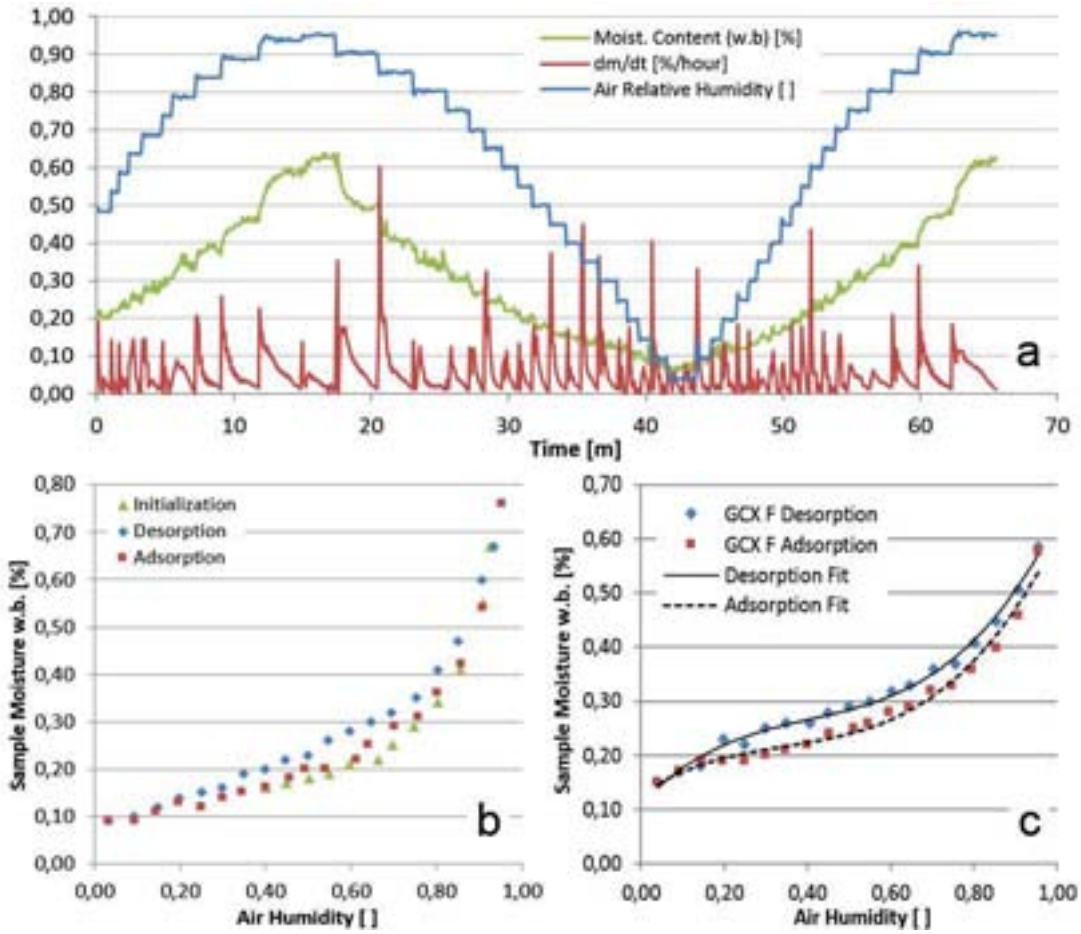

Fig.4: Example of: a) Sorption tests data, b) equilibrated points, c) fitted curves.

Results and Discussion

Table 2 summarises the results of the initial moisture tests carried out on the equilibrated samples at 23-27 °C and 45-55% relative humidity. We can see that pure filter dust has the higher initial moisture level (0.71%), un-bonded sand has the lowest moisture level (0.11%) and all the bonded sands have initial moisture levels between 0.17% and 0.24%.

Table 2: Initial sample moisture after and equilibration at 23-25 °C and 45-50% RH for a week.

Material	Initial Moisture w.b. [%]	Material	Initial Moisture w.b. [%]
Coating	0.20	GCX S	0.17
GCX F	0.24	GCM	0.18
GCK No Dust	0.21	GCGG	0.17
GCK 2% Dust	0.23	Un-bonded Sand	0.11
Pure Dust	0.71		

Figures 5a and 5b show the sorption curves respectively for GCX F furan bonded sand and for foundry coating at 15 °C, 25 °C and 35 °C. It can be seen that, for both materials, temperature does not have a significant effect. On the other hand, air humidity has a major effect. For both materials, moisture can be as low as 0.1% at 5% RH and become as high as 0.6% at 95% RH. Even though the absolute values seem small, we need to notice that from 0.10 % to 0.60% there is a variation of 600%. Additionally, large amounts of moulding sands are used in each mould. For example a 40 tons mould might contain as low as 40 kg of water at 0.1% moisture (if dried at 5% RH for enough time) or as much 240 kg of water at 0.6 % moisture (if stored for enough time at 95% RH). It is therefore important to be aware of this variation when designing the drying process, factory environment conditions and venting channels in the moulds.

Another important conclusion is that the hysteretic behaviour between adsorption and desorption is fairly limited especially for the coating. For the moulding sand, where there is slightly more hysteresis, the difference between sorption and desorption curve is typically less than 0.05% in moisture.

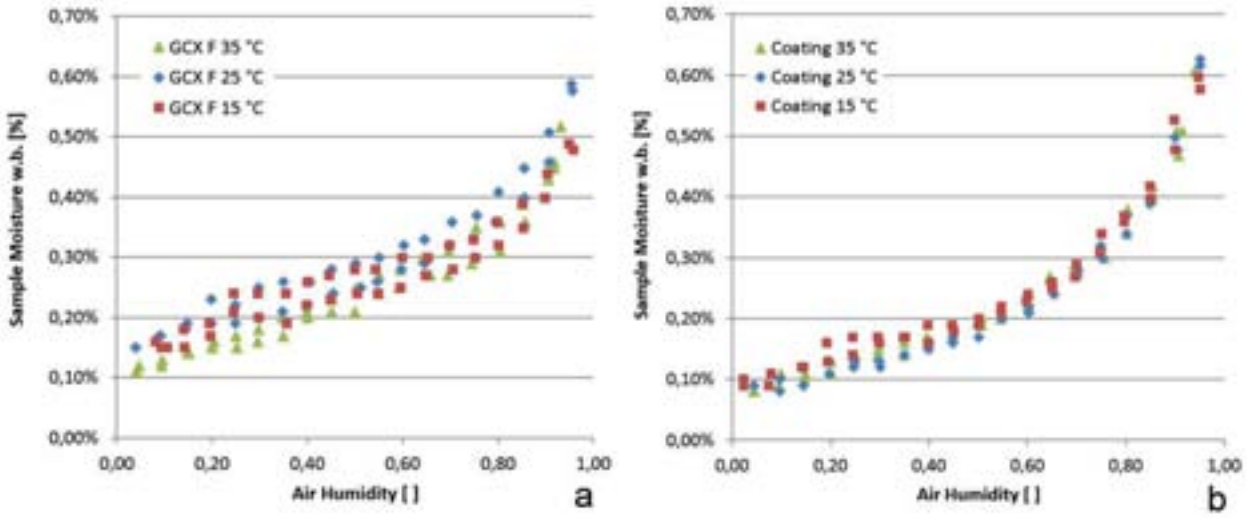

Fig.5: Sorption curves at 15 °C, 25 °C and 35 °C for a) sand and b) coating.

Figure 6a shows that the effect of a 2% dust addition causes a small increase in moisture levels, for example from 0.20% to 0.24% at 50% relative humidity. However, pure dust can contain from 0.30% to 1.70% moisture. It is therefore important to reduce dust segregation in silos to avoid lumps of dust in the moulds.

Figure 6b shows a comparison between moulding sands bonded with different binder types and un-bonded sand. It can be seen that un-bonded sand has the smallest moisture content (between 0.04% and 0.20%), it has no hysteresis between adsorption and desorption and moisture value is a linear function of air humidity. When adding binder the behaviour becomes nonlinear and the moisture level increases up to 4 times that of the un-bonded sand. This is a confirmation of the hydrophilic nature of furan binding systems.

Also we can see that a binder like GCM has significantly lower moisture level compared to the other binders, and it could therefore be used in moulds that are more prone to gas defects. For example, considering a 40 ton mould at 90 % RH where GCM binder is used, it will have a moisture of 0.30 % and therefore a water content of 120 kg. On the other hand if GCK or GCGG binders are used, the same mould will have a moisture content of about 0.55 % at 90% RH, which translates to a water content of 220 kg (almost double the one of VCM binder). Finally, the highest moisture

content is 0.75%, given by GCGG binder at 95% RH, this translates in a quantity of 300 kg of water for a 40 tons mould.

These results show that different amounts and brands of furan binders can have different performance with respect to moisture content. Sorption tests can help to quantify these performances and to choose the right material recipe.

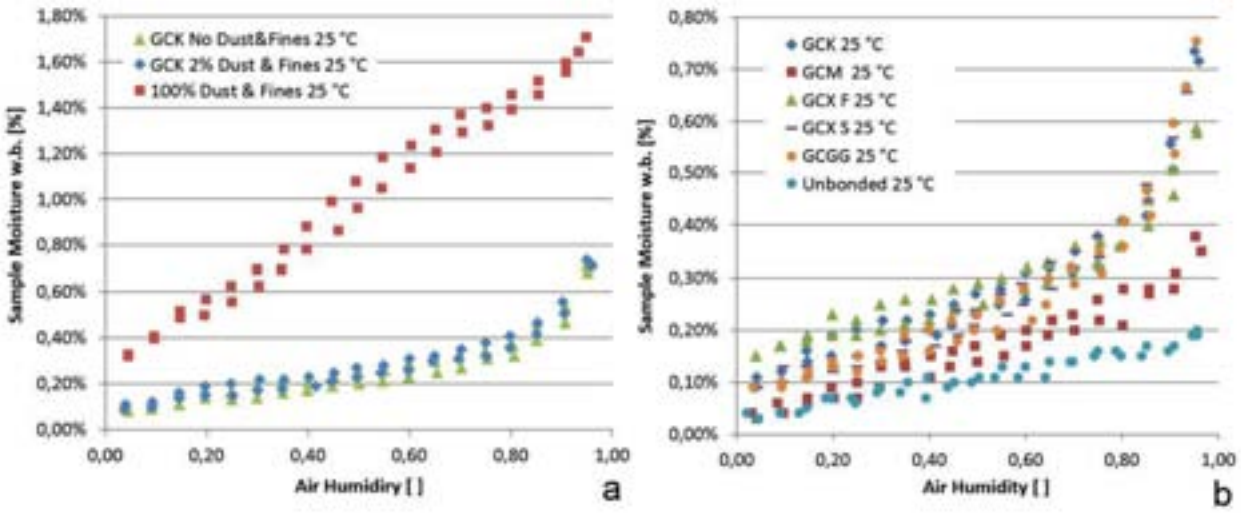

Fig.6: Sorption curves for a) dust, sand with 0% and 2% of dust and fines, b) sand with different binders and un-bonded sand.

Table 2 reports the coefficients of the 3rd degree polynomials used to fit the experimental sorption curves of the different materials as well as the coefficient of determination R^2. Coefficients are provided for the desorption and the sorption of each material tested but not for the different test temperature and dust levels since these two parameters were found to have little influence on the curves. Additionally, it was chosen to provide the same coefficients for the desorption and sorption curves of coating and un-bonded sand since hysteresis was found to be negligible. Finally, we can see that for un-bonded sand a_3 and a_2 coefficients have a value of 0 since its behaviour can simply be described by a linear curve.

As a final check, we can see that all the curves have good fit since R^2 values are always above 0.95 and above 0.97 for most of the curves.

Table 2: Coefficient of 3rd order polynomials fitted to sorption and desorption curves for furan bonded sands and foundry coating with corresponding coefficients of determination R^2

	Desorption					Sorption				
	a_3	**a_2**	**a_1**	**a_0**	**R^2**	**a_3**	**a_2**	**a_1**	**a_0**	**R^2**
Coating	1.5094	-1.4926	0.6256	0.0444	0.9869	1.5094	-1.4926	0.6256	0.0444	0.9869
GCK	2.1500	-2.5702	1.1754	0.0402	0.9807	2.0139	-2.3105	1.003	0.0371	0.9687
GCM	0.3853	-0.4522	0.4298	0.0215	0.9867	0.4665	-0.5090	0.3853	0.0168	0.9775
GCX F	1.2690	-1.5475	0.8048	0.1099	0.9932	1.0985	-1.1412	0.5195	0.1275	0.9831
GCX S	1.3006	-1.2949	0.6960	0.0484	0.9893	1.3734	-1.1971	0.5098	0.0683	0.9895
GCGG	1.6866	-1.7783	0.8256	0.0425	0.9882	2.2606	-2.4140	0.9222	0.320	0.9692
Un-bonded	0	0	0.1616	0.0284	0.9562	0	0	0.1616	0.0284	0.9562
Pure Dust	-0.6240	0.6183	1.4406	0.2623	0.9951	-0.8065	1.3640	0.8244	0.2958	0.9964

Conclusions

To summarise the main conclusions of the study we can say that:

1. We have shown that automatic vapour sorption tests are useful to detect differences between factors affecting moisture and can help the foundry engineer to choose binders that have lower moisture levels. As a consequence these tests could be used as an evaluation tool for new binding systems recipes and coatings to be introduced in production.
2. Dust effect and temperature effect are not critical in the ranges currently allowed in the factories, it is therefore not critical to tightly control their values as soon are they are within current specification.

3. Air humidity is a very important parameter, in particular drying at low air humidity can significantly reduce the moisture in the moulds
4. Binder type can heavily affect the moisture retention properties of the mould. It is therefore important to choose binding systems that can reduce the amount of moisture in the sand to reduce the generated vapour and therefore the probability of gas defects
5. Due to the weak hysteresis effect between sorption and desorption curves, moisture lost during drying can be regained when moulds are stored for enough time in an open environment at higher humidity. This might jeopardise the positive effects of expensive drying processes.
6. The data obtained from this study can be used as basis for the design of dryers and to help define control limits for the drying of moulds and cores in the foundry industry.
7. Simple calculation examples have been performed using the results from the experiments to show a possible use of this new test methodology
8. Coefficients of 3rd order polynomials fitted to sorption and desorption curves for the tested materials have been obtained.

References

1. J. Campbell, R.A. Harding: 'Solidification Defects in Castings', Lecture 3207, The University of Birmingham, 4-8, 1994.
2. L. Elmquist: 'Defect formation in cast iron', Presentation, School of Engineering, Jonkoping University, Sweden, 2012.
3. IKO: 'Description of Casting Defects', Chapters 04,10,12, S&B Industrial Minerals
4. A. Chojecki*, J. Mocek: 'Effect of atmosphere in a foundry mould on casting surface quality', Archives of Foundry Engineering, Volume 12, Issue 1/2012, 13-18.
5. D - Elkem: 'Hydrogen Pinholes', Technical Information 30, Elkem Foundry Products, Rev. 1.2, 2007.
6. A. Siewiorek, R. Nowak, A. Chojecki, J. Mocek: 'Gas evolution rate from heated moulding sands bonded with organic binders', Archives of Foundry Engineering, ISSN (1897-3310), Volume 11, Issue 1/2011, 87 – 92.
7. A.Starobin, C.W. Hirt, D. Goettsch: 'A Model for Binder Gas Generation and Transport in Sand Cores and Molds', Modeling of Casting, Welding, and Solidification Processes XII, TMS (The Minerals, Metals & Materials Society), 2009.
8. A.Starobin, T. Hirt, H. Lang, M. Rode: 'Core Drying Simulation and Validation', International Foundry Research 64 (2012) No. 1, 2-5.
9. P. Scarber, C.E. Bates: 'Simulation of Core Gas Production During Mold Fill', AFS, 2006.
10. N.Tiedje, R. Crepaz, T. Eggert, N. Bey: 'Emission of organic compounds from mould and core binders used for casting iron, aluminium and bronze in sand moulds', Journal of Environmental Science and Health, Part A, 45: 14, 1866 – 1876.
11. G. Samuels and C. Beckermann: 'Measurement of Gas Evolution from PUNB Bonded Sand as a Function of Temperature', University of Iowa, International Journal of Metal Casting, Spring 2012.
12. A. Shepherd: 'Understanding Emission Characteristics of a Foundry Sand Binder', Proceedings of The National Conference On Undergraduate Research (NCUR) 2012, Weber State University, Ogden, UT, March 29-31, 2012.
13. BCRA: 'Venting of mould and cores', BCIRA Broadsheet 188, 1980.
14. A.S. Mujumdar: 'Handbook of industrial drying', 3rd edition, Ch. 1-2, 2006.
15. Decagon Devices: 'Vapor Sorption Analyzer', Operator's Manual, Ver.5, Ch. 2.

Acknowledgement

This work was financed by Global Castings A/S, the Danish Agency for Science, Technology and Innovation (DASTI) and the Technical University of Denmark (DTU). LabCell Ltd. provided support in executing the tests on the AquaLab automatic vapour sorption analyser.

Influence of chromium and molybdenum in solidification and shrinkage defects for high resistance grey iron alloys

L.Stuewe[1], A.P.Tschiptschin[2] W.L.Guesser[3] and R.Fuoco[4]
[1]MAGMA Engenharia do Brasil, São Paulo, Brazil
[2]USP - São Paulo University, Department of Materials Engineering, São Paulo, Brazil
[3]UDESC – Santa Catarina University, Joinville, Brazil
[4]Metso Minerals, Sorocaba, Brazil

This paper presents an evaluation of Cr and Mo influence in solidification and shrinkage defects in grey cast iron. A series of five grey cast irons were produced with different Cr and Mo additions. A test casting was developed by casting process simulation to reproduce defects of an specific cylinder head.
Macroshrinkage cavities were detected in the top of the test parts and microshrinkage porosity defects were analyzed in the hot spots. Macroshrinkage volumes were measured by filling the cavities with water. The microshrinkage porosities were evaluated by liquid penetrant examination and image analysis. The solidification sequence and microstructure were evaluated by thermal analysis and metallography.
Combinations of 0,4%, 0,6% and 1,00 % of Cr + Mo presented a significant increase in macroshrinkage volumes and combinations of 0,6% and 1,00% of Cr + Mo presented an increase of microshrinkage porosity. In solidification Cr and Mo increased undercooling, austenite pro-eutectic fraction volume, intercellular carbides, reduced the eutectic cell size and fraction volume of graphite.

Keywords: grey cast iron, shrinkage defects, thermal analysis, chromium and molybdenum, simulation

Introduction

Continuous increasing demands for diesel engine performance resulted in higher peak operating temperatures, consequently increased cast irons requirements for components such as cylinder heads. Grey cast iron alloys are usually used for these applications due to their good combination of physical and mechanical properties, besides good machinability and cost. Unalloyed irons do not reach the necessary properties at these temperatures, therefore alloying is required to increase thermal fatigue resistance and stability[1]. Cr and Mo are usually used for this purpose, however the addition of these elements increases the tendencies of shrinkage defects[2,3], becoming a challenge to the foundry process engineers. Therefore it becomes necessary to improve knowledge about the influence of these elements on the solidification of grey cast irons, with the aim to better predict and control the factors that contributes to these defects.

Since the shrinkage defects terminology is ambiguous in the literature, in this paper the defects caused by primary shrinkage (liquid + primary austenite shrinkage) are called macroshrinkage cavities. And defects caused by secondary shrinkage (grain boundary liquid shrinkage) are called microshrinkage porosities.

Experimental Procedure

To evaluate the effect of Cr and Mo a test casting was developed using casting process simulation (MAGMAsoft®), as shown in Fig.1. The casting part should represent a cylinder head section which presented shrinkage porosity in the production. The section, size core and solidification times should be the same.

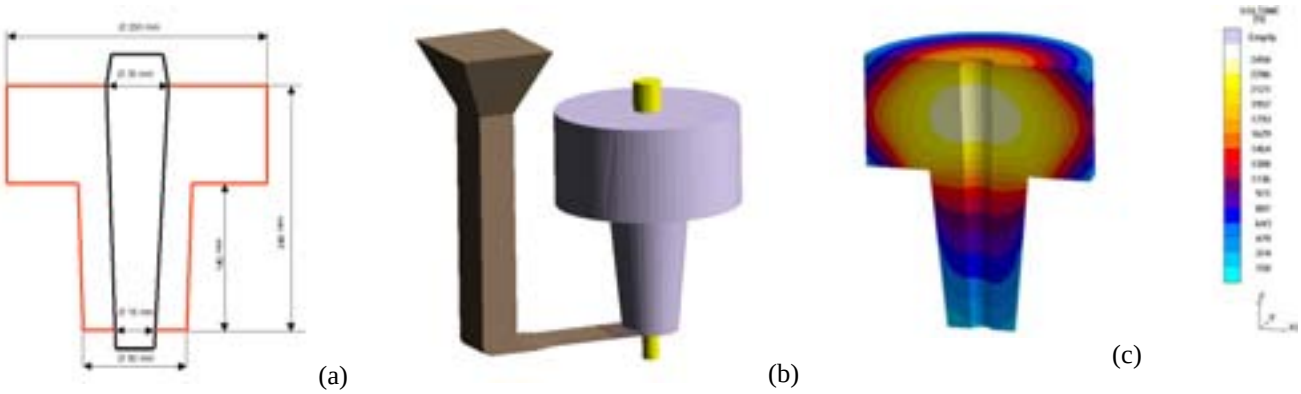

(a) (b) (c)

Fig.1: (a) Test casting dimensions. (b) Test casting isometric view with gating system. (c) Simulation result of solidification time of base alloy.

In this investigation six series of grey cast irons were planned to be produced. A base iron (alloy2), 0,2% Cr (alloy3), 0,2%Mo (alloy4), 0,2%Cr+0,2%Mo (alloy5), 0,3%Cr+0,3%Mo (alloy6) and 0,5%Cr+ 0,5%Mo (alloy8). The complete casting procedure is published in reference 4. Macroshrinkage defects were detected in the top of test casting and the volumes were measured by filling the cavities with a mixture of soap and water, as shown in Fig. 2 (a). The microshrinkage porosities were analyzed qualitatively by liquid penetrants and quantified by image analysis in the thermal center of the casting part, region C, as shown in Fig. 3. The microstructure was analyzed by optical microscopy and image analysis. The fraction volume of graphite – Vgraf (%), fraction volume of intercellular carbides - V_{carb} (%) and diameter of eutectic cel - $\varnothing_{CE}$ (mm) were investigated in the regions A and C as shown in Fig. 2(b).

(a) (b)

Fig.2: (a) Measurement of macroshrinkage cavities. (b) Microshrinkage and microstructure evaluation areas.

Thermal analysis was performed for each alloy using shell sand cups without tellurium. The analyzed parameters in cooling curves are shown in Fig. 3. The equilibrium temperatures of stable (TEEi) and metastable (TEMi) where calculated by the program Thermocalc® using equilibrium systems Fe-C-Mn-Si, Fe-C-Mn-Si-Cr, Fe-C-Mn-Si-Mo e Fe-C-Mn-Si-Cr-Mo

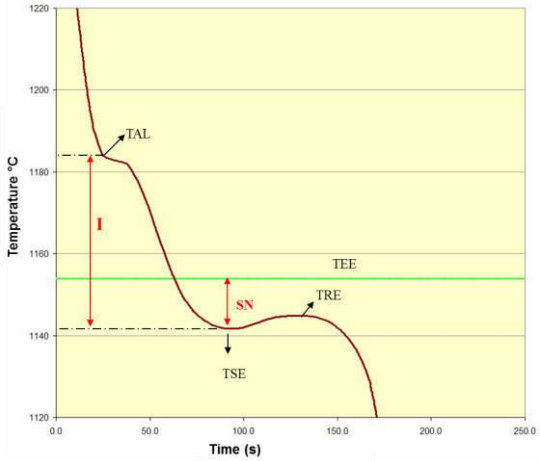

Fig.3: Analyzed parameters in the cooling curve: I = primary solidification interval (I = TAL – TSE), SN = undercooling (SN = TEE-TSE) ΔT = Recalescence (ΔT = TER – TSE).

Chemical analysis of carbon and sulfur were analyzed by direct combustion (infrared detection) and the other elements were analyzed by ooptical emission spectrometry.

Results and Discussion

Table 1 shows the results of chemical analysis and pouring temperatures of planned alloys.

Table 1: Chemical analysis results and pouring temperature.

Alloy	CE %	C %	Si %	Mn %	P %	S %	Cu %	Sn %	Cr %	Mo %	Pouring temp. °C
02	4,12	3,38	2,18	0,46	0,03	0,13	0,77	0,10	0,03	0,00	1400
03*	4,11	3,38	2,16	0,46	0,04	0,13	0,77	0,10	0,15	0,00	1380
04	4,15	3,42	2,16	0,45	0,04	0,13	0,77	0,10	0,04	0,18	1350**
05	4,17	3,42	2,20	0,45	0,04	0,13	0,77	0,10	0,20	0,18	1400
06	4,12	3,40	2,11	0,44	0,04	0,14	0,76	0,10	0,31	0,31	1400
08	4,15	3,39	2,25	0,44	0,04	0,13	0,76	0,10	0,52	0,52	1385

*The Cr yield in the ladle was lower than expected, resulting in a lower value compared with what was planned. **Alloy 4 was poured below the lower limit variation.

Influence of Cr and Mo in the volumes of macroshrinkage cavities and microshrinkage porosities:
All alloys presented macroshrinkage defects in the top of the casting parts. Fig. 4 shows the measured volumes of macroshrinkages and Fig. 5 shows the images of the defects in the top of the casting parts.

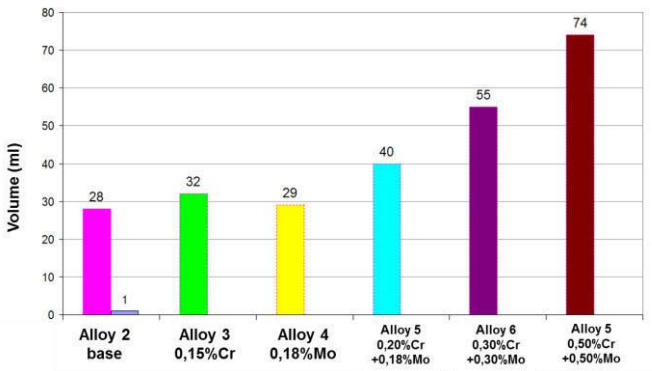

Fig.4: Macro shrinkage porosity volumes for alloys with growing addition of Cr and Mo elements.

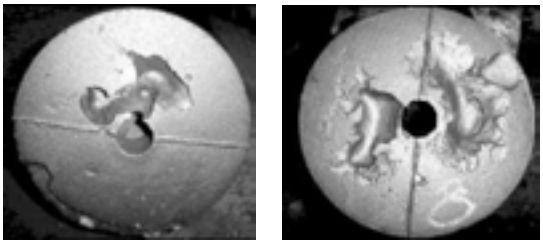

(a) Alloy 2 (b) Alloy 8

Fig.5: Macroshrinkages for alloys 2 and 8.

In alloys 3 and 4 was observed lower influence of Cr and Mo additions comparing with the unalloyed base grey cast iron (alloy 2). However when the elements are added together in alloys 5,6 and 8 the volume of shrinkage is significantly affected. Alloy 4 could show higher macroshrinkage volumes, because in this trial the metal was poured with lower temperate than planned. The casting process simulation was able to predict correctly the macroshrinkage tendency with growing Cr and Mo additions, as shown in Fig.6.

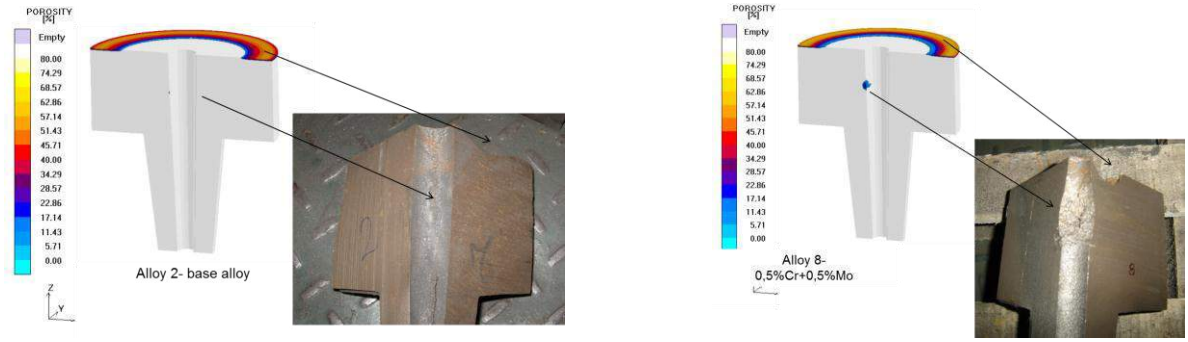

Fig.6: Simulation results of shrinkage prediction – alloy 2 (left), alloy 8 (right).

Higher additions of Cr and Mo also increased the microshrinkage porosities fraction volumes as shown in the Fig.7. Just alloy 6 and 8 presented significant effect in the microshrinkage porosity. The evaluation with liquid penetrants also revealed micro porosities only in the alloys 6 and 8 (Fig.8).

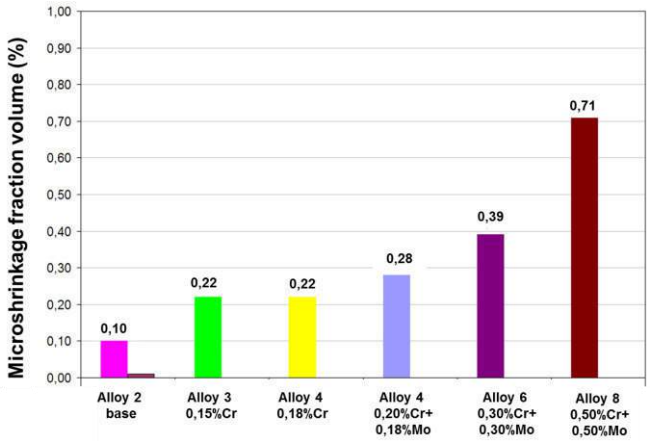

Fig.7: Microshrinkage fraction volume (%) for alloys with growing addition of Cr and Mo elements. Average of 20 optical fields measurement.

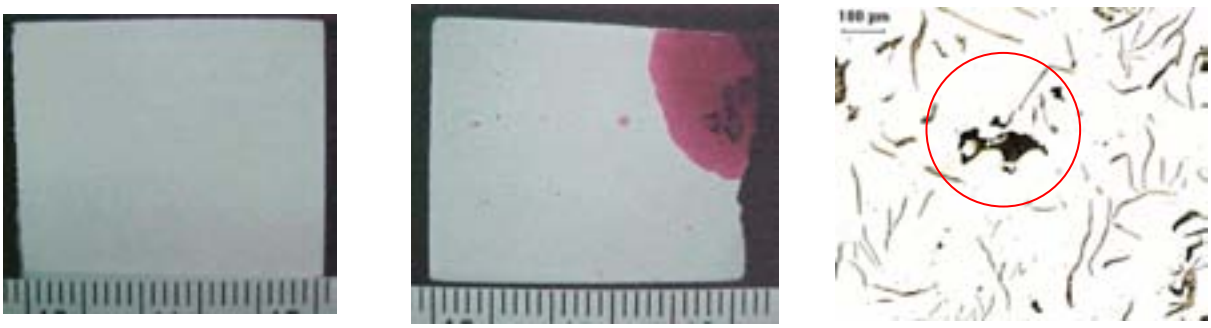

(a) Alloy 2 – base alloy (b) Alloy 8 – 0,5%Cr+0,5%Mo (c) Alloy 8 – 0,5%Cr+0,5%Mo

Fig.8: (a) – (b) Results of micro shrinkage revealed by liquid penetrants in area C of casting part. c) Microshrinkage example in alloy 8.

Influence of Cr and Mo in cooling curves parameters:
Table 3 shows the results of thermal analysis of the cooling curves. Fig. 10 shows the cooling curves for all alloys evaluated.

Table 3: Temperatures and cooling curve parameters for all casting alloys.

Alloy	TAL (°C)	TEEi (°C)	TEMi (°C)	DTE** (°C)	TE (°C)	TSE (°C)	TRE (°C)	SN (°C)	I (°C)
02	1185	1164	1124	40	1167	1151	1155	13	34
03	1185	1163	1125	38	1166	1149	1152	14	36
04	1184	1163	1123	40	1165	1149	1153	14	35
05	1180	1162	1124	38	1164	1147	*	*	*
06	1187	1161	1125	36	1164	1145	1150	16	42
08	1184	1160	1125	36	1159	1141	1145	19	43

* In the alloy five temperatures were not totally recorded due to a failed in thermocouple during the test
** DTE = TEEi – TEMi. Interval between stable (TEEi) and metastable equilibrium (TEMi) initial eutectic temperatures.

Analyzing the eutectic temperatures TEEi and TEMi in Table 3 is possible to observe that the DTE interval between stable and metastable equilibrium eutectic temperatures were reduced with the highest amounts of Cr an Mo as already studied by Kanno et.al[5]. During cast iron solidification the elements Cr and Mo segregates to the liquid and retard the eutectic cell nucleation[6,7], consequently reducing nucleation temperature (TE), undercooling temperature (TSE) and undercooling (SN = TEEi-TSE). The results presented in the Fig. 11 confirm this effect for alloys 6 and 8. The other alloys presented similar values compared with base alloy.

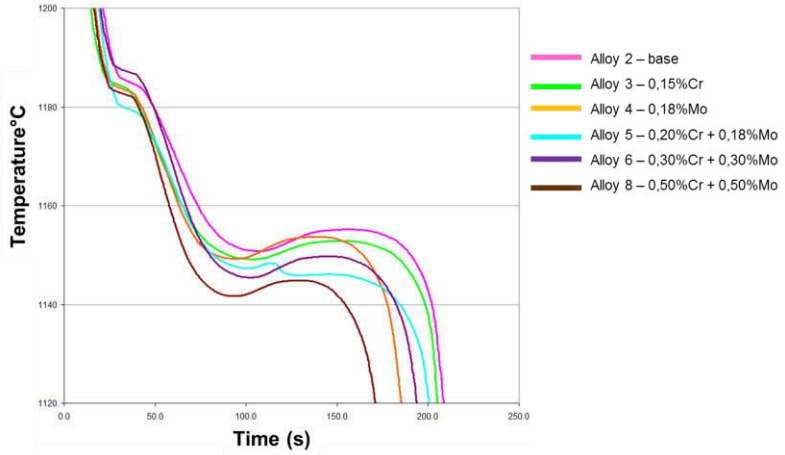

Fig.10: Cooling curves of all alloy castings.

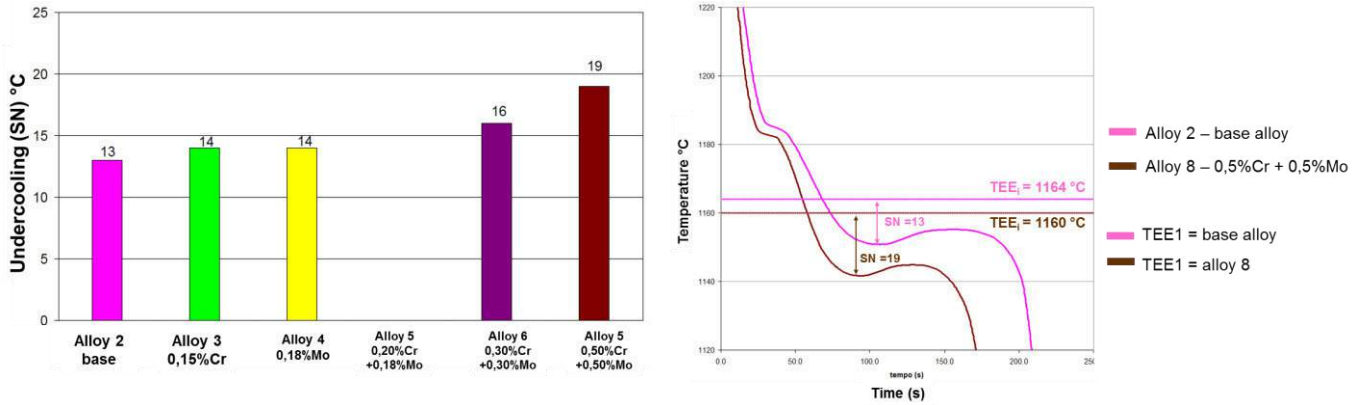

(a) (b)

Fig.11: (a) Undercooling values for alloys with growing additions of Cr and Mo. (b) Cooling curves, thermal equilibrium temperatures and undercooling values for base alloy 2 and alloy 8.

Higher undercooling leads to higher interval between TAL and TE (Fig.3a), increasing in this way the primary solidification interval (I = TAL – TSE), as shown in results of Fig. 12 (a). The higher the primary solidification range, the larger the expected fraction solid of pro-eutectic austenite. Pro-eutectic austenite increases macroshrinkage tendencies. Fig. 12 (b) shows a relation between macroshrinkage defects volumes with the primary solidification interval (I).

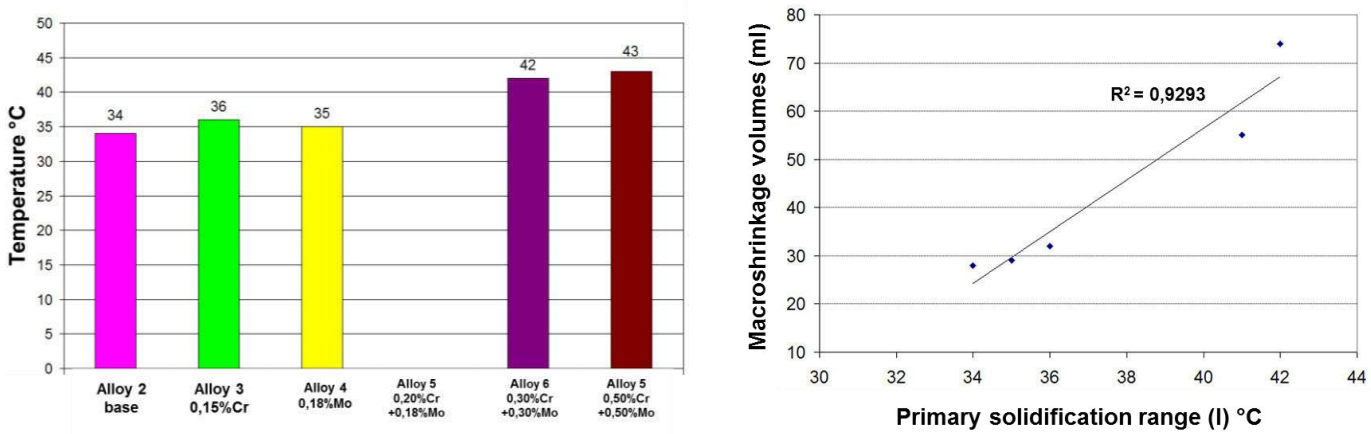

Fig.12: (a). Primary solidification interval for alloys with growing additions of Cr and Mo. (b) Relation between macroshrinkage defects volumes and primary solidification interval (I) for alloys 2,3,4,6 and 8.

All alloys were cast with equivalent carbon close to the eutectic point, making a metallographic analysis of primary austenite fraction solid volume more difficult. Nevertheless, foundry process simulation results show that higher Cr and Mo additions increases the austenite fraction solid volume, as shown in Fig.13. However the difference is not so significant and probably this is not the only factor to explain the increase of macroshrinkage tendencies with Cr and Mo additions.

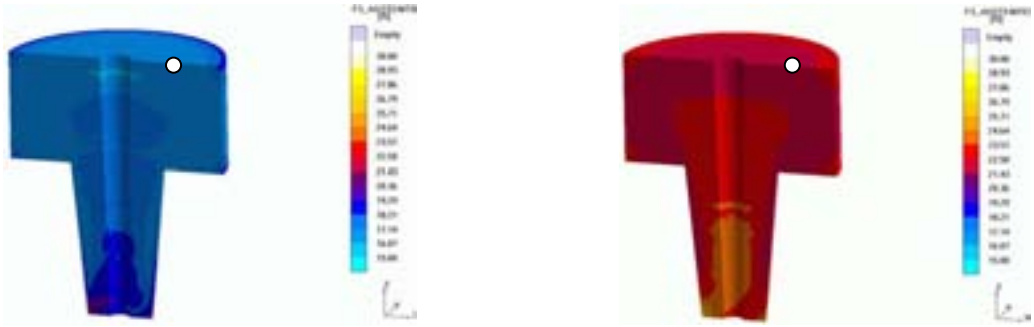

(a) Alloy 2 – base alloy – 16% austenite (b) Alloy 8 – 0,50% Cr + 0,50%Mo - 22% austenite

Fig.13: Simulation result – fraction volume of austenite (%). White dot indicates the local point of comparison results.

Influence of Cr and Mo in microstructure:

Fig. 14 (a) shows the results of fraction volume of eutectic graphite for alloys with growing additions of Cr and Mo. Just alloys 6 and 8 presented a significant reduction value of eutectic graphite fraction volume.

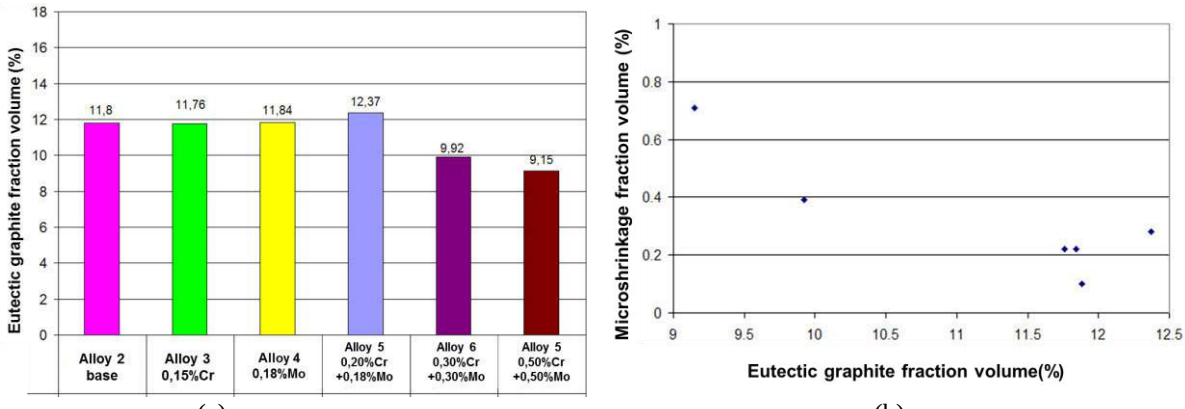

(a) (b)

Fig.14: (a) Eutectic graphite fraction volume for alloys with growing additions of Cr and Mo. (b) Relation between microshrinkage fraction volume and eutectic graphite fraction volume.

Lower eutectic graphite fraction volume leads to less eutectic expansion necessary to compensate secondary shrinkage, consequently more microshrinkage porosities are expected. Is possible to see in Fig. 14 (b) that there is a tendency to increase microshrinkage porosities with lower fraction volume of eutectic graphite, however it was not

possible to establish a direct relation between these results. Fig. 15 shows microstructures of alloys 2 and 8, highlighting the lower graphite fraction volume in the alloy with Cr and Mo.

(a) Alloy 2 – base alloy

(b) Alloy 8 – 0,5% Mo + 0,5%Cr

Fig.15: Microstructures: (a) base alloy 2 and (b) alloy 8. Optical microscopy, magnification 100x.

Due to the higher undercooling presented by alloys with higher Cr and Mo additions a higher number of eutectic cells and more refined structure is expected as shown in Fig. 16 and Fig. 17.

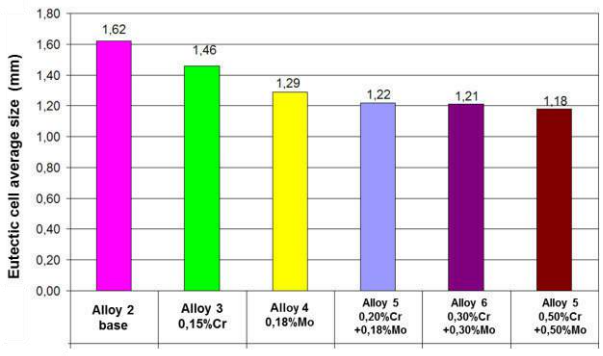

(a)

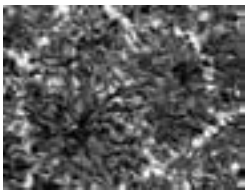

(b) alloy 2 – base alloy

(c) alloy 8 – 0,50%Cr + 0,5%Mo

Fig.16: (a) Average eutectic cell size (mm), measured in area C, for alloys with growing additions of Cr and Mo. (b) (c) Microstructure of eutectic cells. Stead's reagent. Magnification: 25x.

Comparing the graphs from Fig. 4 and Fig. 16 the alloys with higher levels of Cr and Mo presented higher volume of macroshinkage and smaller eutectic cell size. According with literarue[8] higher number of eutectic cells means higher number of nucleus in growing process, reducing in this way the directionality of solidification front, changing it to be more mushy morphology solidification. A more mushy solidification reduces the solidified shell thickness in the beginning of solidification process[8,9]. The shell is consequently less resistant to the external pressure, allowing in this way deeper macroshrinkage cavities in the top of the test part. Another effect that can explain higher volumes of macroshrinkage increasing the eutectic cell number is the effect of mass feeding cited by Campbell[10], where the slurry of solid metal and residual liquid is able to flow and feed closed regions. The alloys that presented smaller cell size or higher cell number also presented higher volume of microshrinkage, as can be seen comparing graphs of Fig. 7 and Fig. 16. The smaller eutectic size tends to increase the surface area of cells, increasing the number of intercellular liquid pockets and also reducing the channels thickness between cells reducing the feeding condition to intercellular regions.

Fig. 17 presents volume fraction of carbides for alloys with growing additions of Cr and Mo. As expected Cr and Mo segregate to eutectic cell boundaries and reduce the DTE interval (interval between stable and metastable eutectic temperatures) in this regions, consequently the solidification occurs below TEM (metastable eutectic temperature) through Fe-C metastable equilibrium system, generating eutectics austenite+carbides[11].

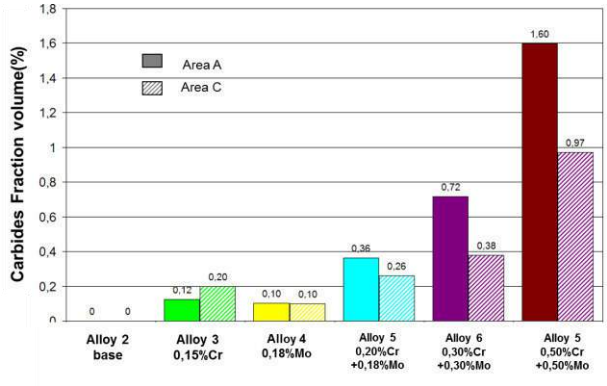

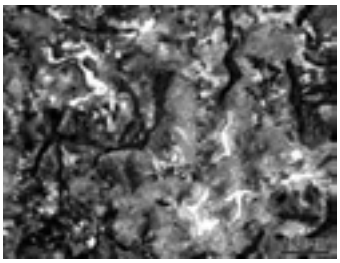

(a) (b)

Fig.17: **(a)** Carbides volume fraction (%) for alloys with growing additions of Cr and Mo for evaluation areas A and C. (b) microstructure of an intercellular carbide in alloy 8 with magnification of 100x. Nital 4% reagent.

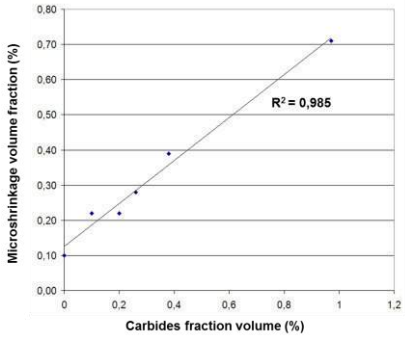

Fig.18. Relation between volume fraction of carbides and microshrinkage volume fraction (area C).

The shrinkage of carbides solidification in relation of the liquid is approximately –1,9 ΔV%, consequently it generates microshrinkage porosities, therefore it was possible to correlate directly the carbide volumes with microshrinkage volumes as shown in Fig. 18.

Conclusions

1. Growing additions of Cr and Mo in grey cast irons increased both macroshrinkage cavities and microshrinkage porosities. When the elements were added separately and in lower amounts (≅0,2%) the alloys did not present significant difference in macro and microshrinkage volumes comparing with the base alloy. However when the elements were added together 0,2%Cr+0,2%Mo, 0,3%Cr+0,3%Mo and 0,5%Cr+0,5%Mo occurred a significant increase in macroshrinkage tendencies. The combinations of 0,3%Cr+0,3%Mo and 0,5%Cr+0,5%Mo presented a significant increase in microshrinkage porosities tendencies.
2. In the solidification the elements Cr and Mo reduced the DTE interval (interval between stable and metastable equilibrium eutectic temperatures), reduced the nucleation temperature TE, increased the undercooling (SN) and primary solidification interval (I). Due to these factors the microstructure presented higher fraction volume of pro eutectic austenite, lower fraction volume of eutectic graphite, higher volume of intercellular carbides and higher number of eutectic cells. According with previous studies higher number of eutectic cells can shift the shell type solidification morphology to a more mushy solidificatiom morphology.
3. The factors that increased the macroshrinkage cavity volumes are higher fraction volume of pro eutectic austenite and a possible change in the solidification morphology. The factors that increased the microshrinkage porosities were reduction of eutectic graphite (necessary for expansion and secondary shrinkage compensation), increase of fraction volume carbides and a possible change in the solidification morphology. The results here presented and discussed did not allow to know what is the most important factor that contributes to higher shrinkage defects increasing Cr and Mo contents in grey cast iron.

References

1 W.L.GUESSER: Propriedades Mecânicas dos Ferros Fundidos 1st ed, p.170-175, 2009, São Paulo, Brazil, Edgard Blücher Ltda.

2 J.C HAMAKER; W. P. WOOK; F.B. ROTE: Internal porosity in gray iron castings. AFS Transactions, v.60, p.401-431, 1952.

3 R.B GUNDLACH; W.G. SHOWLZ: Phosphide eutectic in gray cast irons containing molybdenum and/or chromium. AFS Transactions, v.81, p.395-402, 1980.
4 L.STUEWE: Avaliação da influência do cromo e molibdênio na solidificação e formação de rechupes em ferros fundidos cinzentos. Master thesis, São Paulo University, São Paulo, Brazil, 2008.
5 T.KANNO, et al.: Effect of alloying elements on eutectic temperatures in cast iron. AFS Transactions. v.113, p.1-9, 2005.
6 J.F JANOWAK, et al.: Technical advances in cast iron metallurgy. International Cast Metals Journal. v.06 n.04, p.847-863, 1981.
7 H.D.MERCHANT, et al.: Structure delineation of eutectic cells in cast iron. AFS Transactions. v.70, p.973-992, 1962
8 H.D. MERCHANT: Solidification of Cast Iron – A review of literature. Recent Research on Cast Iron. Proceedings of a seminar held in Detroit, Michigan, ASM. 1968, New York: Gordon and Breach 831
9 I.C.H. HUGUES, et al. Factors influencing soundness of gray iron castings. AFS Transactions, v.67, p.149-165, 1959.
10 CAMPBELL J. Castings. 2.ed. p.191-192, 1993, Oxford, United Kingdom; Butherworth-Heinemann Ltd.
11 J.F.JANOWAk, R.B. GUNDLACH: A modern approach to alloying gray iron. AFS Transactions. v90 p.847-863, 1982.

Influence of the furfuryl moulding sand on the flake graphite formation in the surface layer of ductile iron castings

M. Holtzer[1], R. Dańko[1] and M. Górny[1]
[1]AGH-University of Science and Technology, Faculty of Foundry Engineering, Krakow, Poland

The results of investigations of the influence of molding sand with furan resin, prepared both with fresh sand and reclaimed matrix, on the formation of microstructure and flake graphite formation in the surface layer of ductile iron castings, are presented in this paper. A series of experimental melts of ductile iron in molds made of molding sand, characterised by different levels of surface-active elements (sulphur, oxygen) were performed. The effect of the wall thickness, and the initial temperature of the metal in the mould cavity on the formation of the flake (and compacted) graphite formation in the surface layer of the casting, is shown in the paper. Investigations carried out by Energy Dispersive Spectroscopy (EDS) and Wavelength Dispersive Spectroscopy (WDS), showed concentration gradient profiles of surface-active elements in the surface layer of castings which are responsible for their quality. Finally it has been shown that there exist a significant effect of the quality of the sand on the formation of the flake graphite layer and the surface characteristic of ductile iron castings.

Keywords: ductile iron, casting skin, graphite degeneration, moulding sand, reclaimed matrix.

Article available in the International Journal of Cast Metals Research

Feeding Against Gravity with Spot Feeders in High Silicon Ductile Iron

N.K. Vedel-Smith[1*] and N.S. Tiedje[1]

[1]Department of Mechanical Engineering, Technical University of Denmark, Kgs. Lyngby, Denmark

A test pattern, with three different moduli castings was developed to investigate methods to optimise feeding of high silicon ductile cast irons. Different feeder types, modulus, and locations were investigated using both an insulating and an exothermal sleeve material. Porosities were analysed and classified using X-ray imaging and ultrasound analysis. The effect of the different feeder configurations were classified in reference to defect location, sleeve material, and feeder type, modulus, and location.

The analysis showed that exothermal feeder sleeves with the right configurations can feed up-hill against gravity. This effect may contribute to the thermal expansion created by the exothermal reaction. It was also found that the optimum feeder size does not scale linearly with the casting modulus but that larger casting modulus requires relatively smaller modulus feeders. The thermal gradient created by the feeders made with the insulating sleeve material was not sufficient to significantly improve feeding.

Keywords: ductile iron, spot feeding, risering, solidification, high silicon, ram-up sleeves.

Introduction

Feeding complex castings with different moduli sections is a challenge for the foundries, as customers require improved yield, less machining, and sound castings. Optimisation of cast components is an essential driver for many industries in order to improve their products. Thus the foundries are met with an ever growing requirement to improve methods and increase yield. The location and orientation of the casting is determined by casting geometry, location of cores and feeders. However, new designs with great variation between thin and thick walled sections, and highly complex designs limit the use of traditional feeders.

In vertically parted moulds geometrical feeders are normally located at the top of the casting on the parting plane. All feeders require an unbroken feeding path from the feeder to the section that must be fed. This makes it difficult, if not impossible, to feed heavy sections that are disconnected from the feeding path by a low modulus section. Additionally, the feeder requires a driving force to move the melt from the feeder into the casting. Traditionally this driving force is gravity, but other forces also act on the melt during solidification. E.g. solutions like the William wedge and similar geometries are a part of almost all feeder designs to ensure that the feeder is kept open to the atmosphere (punctured) and thus prevent the negative pressure gradient retaining the melt inside the feeder. Other natural forces working on the melt can be the contraction and expansion of the melt itself as different sections of the casting goes through the different stages of solidification at different intervals depending on the modulus, cooling rate, and alloy composition. The movement, deformation, expansion, and the reduction in strength of the green sand mould also influence these factors.

Descriptions and guidelines to the application and effect of feeders that make use of these naturally occurring driving forces to move the melt from a feeder located at the bottom of the casting into a section at a higher elevation are sparse at best. The study presented in this paper represents an experimental design comprising 9 different feeder configuration tested on a scalable casting geometry in three different sizes of casting moduli—8 mm, 10 mm and 15 mm. The study quantified the effect of different modulus spot feeders for different modulus castings. The trial was made with different insulating and exothermic ram-up sleeves together with high silicon ductile iron castings.

Experimental Procedure

Casting Geometry and Pre-feeder Design

The casting geometry was designed to be parametric in order to represent different moduli sections with the same geometry (see Figure 1). The casting itself was a rectangular cuboid. A square footprint was chosen because the square design allow for a high geometrical modulus and was better suited than a round design for ultrasound and x-ray analysis. The height of the casting was chosen as 3 times the width and depth of the casting. The basic idea with the design was to have one uniform section that would create a significant amount of shrinkage by itself. The height of the casting should be great enough that a feeder at the top and a feeder at the bottom would influence the casting differently due to the difference in ferrostatic pressure. For steel bars cast in a horizontal orientation the maximum feeding distance between two feeders was reported as varying between 1-4 times the thickness of the bar[1]. Though the trial castings are

* Corresponding author, email: nikvs@mek.dtu.dk

cast vertically and in SGI, it was chosen to uphold as great a distance between the two feeders on the casting as possible. The height of the bar was governed by the pattern size and allowed for a bar length of 3 times the thickness (a). In turn this allowed for a feeder distance of approximately 2.5 times the thickness (a).

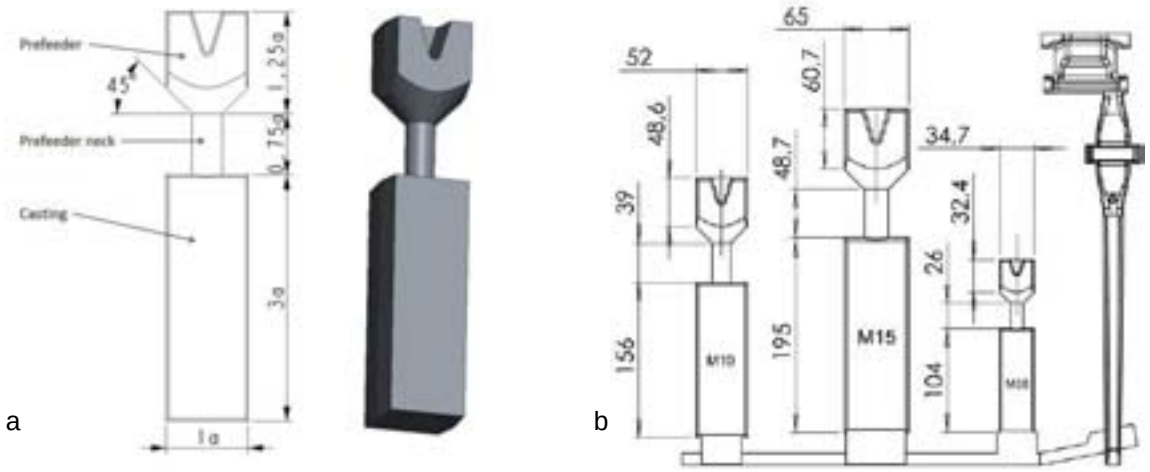

Fig.1: Schematic of the parametric casting design (a), and pattern layout (b). Measurements in mm.

A pre-feeder was placed on top of the casting—designed to compensate for the liquid shrinkage that occur as the casting cools from the pouring temperature to the solidus temperature, so that the variations in pouring temperature on total shrinkage are eliminated. The design had to ensure an identical amount of shrinkage in all castings, regardless of pouring temperature. If not done properly it would afterwards be impossible to prove that changes in porosities in the castings were related to changes in feeder configurations and not attributable to a smaller or greater liquid shrinkage caused by varying pouring temperatures.

The size of the pre-feeder neck was determined so that it closes and blocks feeding at the point in time where solidification begins in the casting itself. Based on Chvorinov's modulus law[2] equation (1) was derived:

$$D_{neck} = 4M_{neck} = \frac{c_p(T_{start}-T_{eut})}{(-\Delta H)+c_p(T_{start}-T_{eut})} M_{casting} \quad (1)$$

where D_{neck} was the diameter of the pre-feeder neck, M_{neck} was the modulus of the pre-feeder neck, and $M_{casting}$ was the modulus of the casting. H was the enthalpy of the system, c_p was the heat capacity, T_{start} was the pouring temperature and T_{eut} was the eutectic temperature for the given alloy. Equation (1) gives the diameter of the pre-feeder neck. However, the equation does not take into account the heat flux from the casting and pre-feeder but assume unidirectional solidification. To determine the optimum pre-feeder neck height, which would reduce the amount of liquid shrinkage as much as possible while still allowing for a timely solidification of the neck, numerical simulations of the different pre-feeder neck geometries were used (see Figure 2).

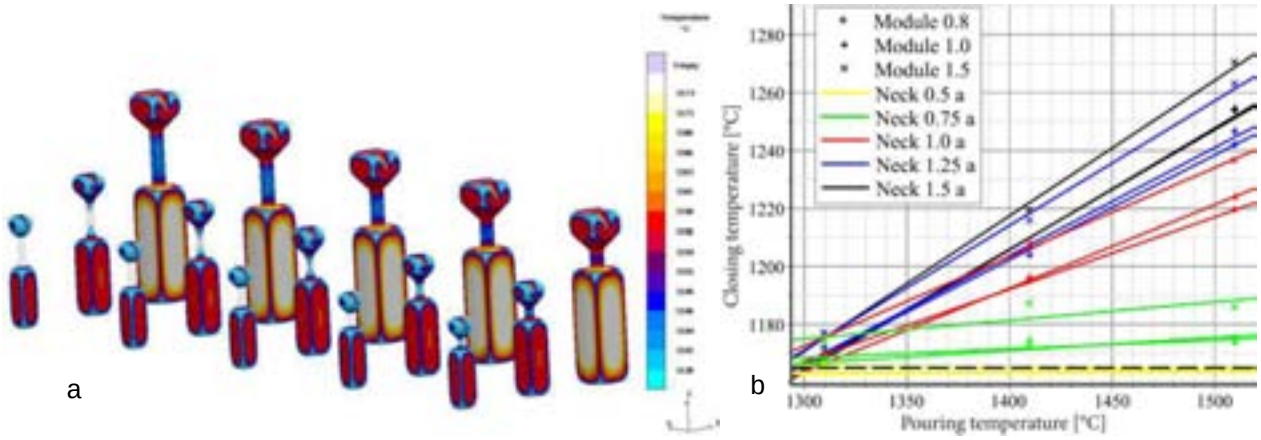

Fig.2: (a) Parametric study of varying pre-feeder neck lengths from 0.5a to 1.5a, and (b) a graph showing the temperature at the centre of the casting (Closing temperature) as a function of the pouring temperature for three different moduli castings and five different pre-feeder neck lengths. The dashed line indicates the eutectic temperature of the alloy.

The solidification times obtained from the numerical simulation of the different parametrical geometries, at different pouring temperatures, were plotted in Figure 2(b). The graph shows that the yellow line representing the shortest pre-feeder neck was below the eutectic temperature line. This means that the solidification of the casting had begun before the neck had closed off. All other pre-feeder neck lengths closed off before the casting centre reaches the eutectic temperature. Hence the pre-feeder neck length of 0.75a was chosen because that length allowed for the best prevention of liquid shrinkage and for the most uniform performance across all casting temperatures. Additionally, this analysis was repeated for another alloy with a different eutectic temperature to make sure the design would function with different alloy compositions.

Feeder Placement, Modulus, and Combinations

The trial setup consisted of 6 different feeder geometries, using either an insulating or an exothermic sleeve material, and applying feeders to two different locations on the casting—at the top near the pre-feeder neck (upper) and at the bottom near the ingate (lower). The possibility of placing feeders either at the top or bottom of the casting, or at both locations simultaneously, enabled an analysis of the feeders' performance in relation to the pressure height of the location. The feeders themselves were mounted horizontally, which minimises the feeders own influence on the ferrostatic pressure. The driving force for moving the melt from the spot feeder into the casting required other forces than gravity to act on the liquid in order to feed the casting. The horizontal orientation also minimised the difference between the upper and lower spot feeder location.

The different spot feeders were mounted onto the three different modulus castings as shown in Table 1. The first group (0) was a control group without any spot feeders. Groups 1 and 2 had only feeders at the upper location, groups 3 and 4 only at the lower location. The remaining groups (5-9) all had feeders at both the upper and the lower location. All combinations were cast in 2-3 duplicates to ensure repeatability.

Table 1: Trial combination overview. Numbers before the letter indicate melt volume [cm^3], letters indicate I for insulating and E for exothermic, and numbers after the letters indicate feeder modulus [mm].

	#	0	1	2	3	4	5	6	7	8	9	Feeder Types	
	Dup.	3	3	3	2	3	2	2	2	2	2	Ins	Exo
M08	U		28I08	28E10			28I08	07I05	28E10	08E08	07E06	07I05	07E06
	L				08E08	28E10	28E10	08E08	28E10	07E06	28E10	08I06	08E08
M10	U		22I10	22E12			22I10	08I06	22E12	28E10	08E08	28I08	28E10
	L				28E10	22E12	22E12	28E10	22E12	08E08	22E12	22I10	22E12
M15	U		121I16	121E19			121I16	22I10	121E19	82E15	22E12		82E15
	L				82E15	121E19	121E19	82E15	121E19	22E12	121E19	121I16	121E19

The spot feeders used in the study were so called ram-up sleeves which are mounted on a pin on the pattern before the moulding process begins. After the moulding process the ram-up sleeves are located inside the green sand mould as described by Vedel-Smith et.al.[3] Figure 3 show the spot feeders from group 6 mounted on the pattern, ready for moulding.

Fig.3: Spot feeders from group 6 mounted on the pattern, ready for moulding. Insulating spot feeders on the top. Exothermic spot feeders at the bottom.

Production, Alloy and Thermal Measurements

The castings were produced on a vertically parted moulding machine—Disamatic 240B—as part of a production run in an operating foundry. The mould size was 775 x 600 x 300 mm. The poured weight of the casting without any spot feeders was approx. 16 kg—whereof the M08 weights ~1.1 kg, M10 ~3.7 kg, and M15 ~7.3 kg. The pouring time was around 6 s. The castings were made with an EN-GJS-500-14[4] alloy and four alloy composition analyses were made during the duration of the trails. See Table 2.

Table 2: Alloy composition [wt%] and casting temperature [°C] variation during the trials.

	CE	C	Si	Mn	P	S	Mg	Cr	Ni	Mo	Cu	Sn	Temp [°C]
I	4.60	3.31	3.91	0.31	0.015	0.003	0.051	0.047	0.021	0.001	0.09	0.004	1,398 (±5)
II	4.57	3.31	3.81	0.31	0.015	0.003	0.045	0.046	0.023	0.001	0.09	0.005	1,387 (±5)
III	4.54	3.35	3.61	0.25	0.015	0.004	0.042	0.051	0.026	0.001	0.06	0.005	1,380 (±5)
IV	4.54	3.34	3.64	0.25	0.015	0.004	0.039	0.050	0.025	0.001	0.06	0.005	1,361 (±5)
Avg	4.56	3.33	3.74	0.28	0.015	0.004	0.044	0.049	0.024	0.001	0.08	0.005	1,382 (±5)

Four temperature measurements were made in one of the castings—4A—which was cast immediately before the series II castings listed in Table 2 were made. Three thermo couples were placed at the centre of each parametric casting, and a single thermo couple was placed at the lower spot feeder of the M15 parametric casting (see Figure 4). All thermo couples were K-type and the data were recorded at a sampling rate of 1 Hz with a stand-alone 4-channel thermo couple data logger.

The castings solidified and cooled in the mould for approx. 1½ hours, and were thereafter removed manually from the moulds at the shake-out station. This ensured that all spot feeders remained attached to the castings. When the castings had air cooled to room temperature they were cleaned by shot blasting.

Ultrasound Analysis and X-ray Analysis

All castings were analysed with ultrasound by the same, experienced operator using a Karl Deutsch Digital-Echograph. The location and size of the porosities were painted on the castings. This gave a detailed picture of the size, location, and direction of the porosities. All castings were photo documented for later analysis.

Following the ultrasound analysis selected groups of castings were analysed using x-ray imaging. The x-ray imaging focussed on confirming the results obtained by the ultrasound analysis, but also on documenting the porosities located in areas not suitable for ultrasound analysis—the pre-feeder neck and the spot feeders. Several images were taken of each of the castings and then assembled into an overview, allowing for a more holistic analysis of the x-ray imaging results.

Results

Ultrasound Analysis

The findings from the ultrasound analysis were classified with respect to porosity size (0-4 where 0 is no porosities and 4 is large porosities), porosity location (top, middle, bottom), and if porosities at different locations were connected or disconnected. Additionally it was also registered when the porosities had an opening out unto the surface of the casting (**bold**). See Table 3.

Table 3: Results of the ultrasound analysis

	#	0			1			2			3		4			5		6		7		8		9	
		A	B	C	A	B	C	A	B	C	A	B	A	B	C	A	B	A	B	A	B	A	B	A	B
M8	T	4	4	4	4	4	4	4	4	4	4	4	4	4	4	4	4	4	4	0	2	4	4	4	3
	M	2	2	2	2	2	0	0	0	0	2	2	2	2	2	2	2	0	0	2	2	4	4	4	4
	B	0	0	0	0	0	0	0	0	4	0	0	0	0	0	0	0	0	0	2	0	0	0	0	0
M10	T	4	4	4	4	4	4	4	4	4	4	4	4	4	4	4	4	4	4	4	4	4	4	4	4
	M	2	2	2	1	0	1	2	2	0	2	2	2	2	2	2	2	2	2	2	2	2	2	2	2
	B	0	0	0	0	0	0	0	0	0	0	0	0	0	0	0	0	0	0	0	0	0	0	0	0
M15	T	4	4	4	4	4	4	4	4	4	0	0	0	4	4	4	4	0	0	2	2	1	0	0	0
	M	0	4	2	0	2	1	0	0	0	1	3	2	4	4	0	2	2	1	0	0	0	0	1	0
	B	0	0	0	0	0	0	0	0	0	0	0	2	4	4	0	0	0	0	0	0	0	0	0	0

	Nomenclature
0	No porosity
1	Micro Porosities
2	Small Porosities
3	Medium Porosit.
4	Large Porosities
	Connected
	Disconnected
	Puncture at neck

The quantified results of the ultrasound analysis indicated that many of the different castings, especially the two smallest modulus castings, displayed the same amount of porosity as the reference casting groups (0) without any spot feeders. This was partly true, however it should be noted that the large porosity (4) indication has no upper limit, meaning that the same indication can cover great differences (see Figure 4).

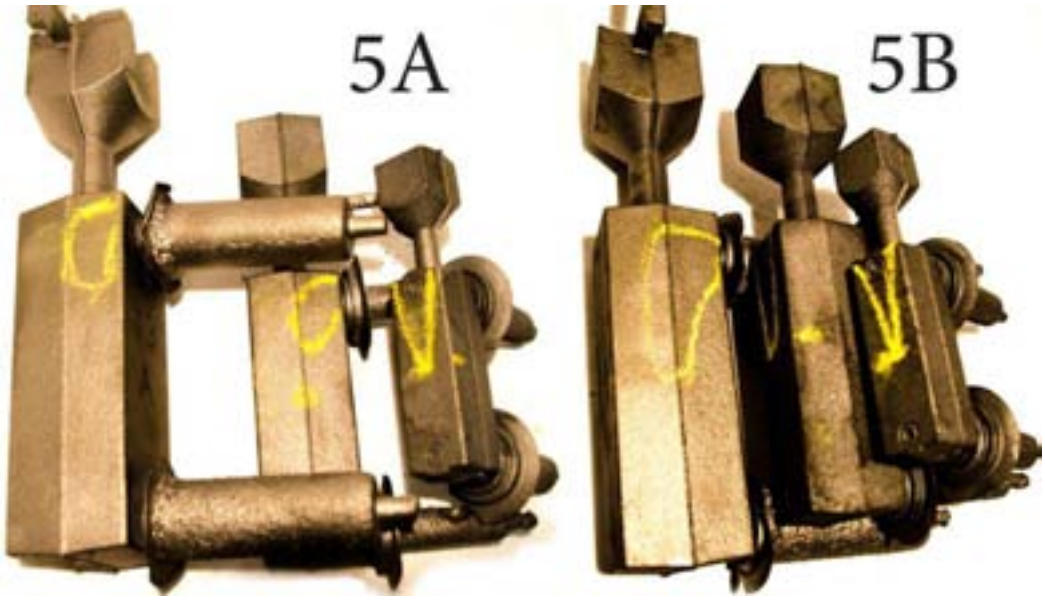

Fig.4: Porosity markings from the ultrasound analysis of casting groups 5A and 5B.

Additionally, some of the reference castings without spot feeder displayed clear signs of surface shrinkage, indicating that some of the shrinkage for these castings have occurred in location that have not been covered by this analysis. Surface shrinkage was not observed in any of the castings with spot feeders.

X-Ray Imaging and Analysis

The x-ray images are greyscale images produced by irradiating the casting from one side, and recording the radiation that reaches the sensor at the opposite side. This gives an image that in greyscale contrast show areas with little material in between (light), and areas with a lot of material in between (dark). Porosities show up because they are holes in the bulk material, and thus areas with porosities absorb less radiation, resulting in a brighter area of the image. However, the radiation does scatter and diffuse, rendering the images a little fuzzy at the edges. Because of this effect there was a limit to the difference between the size of the casting and the size of the porosity that could be imaged. This made it difficult to obtain good images of the defects in the M15 castings (see Figure 5).

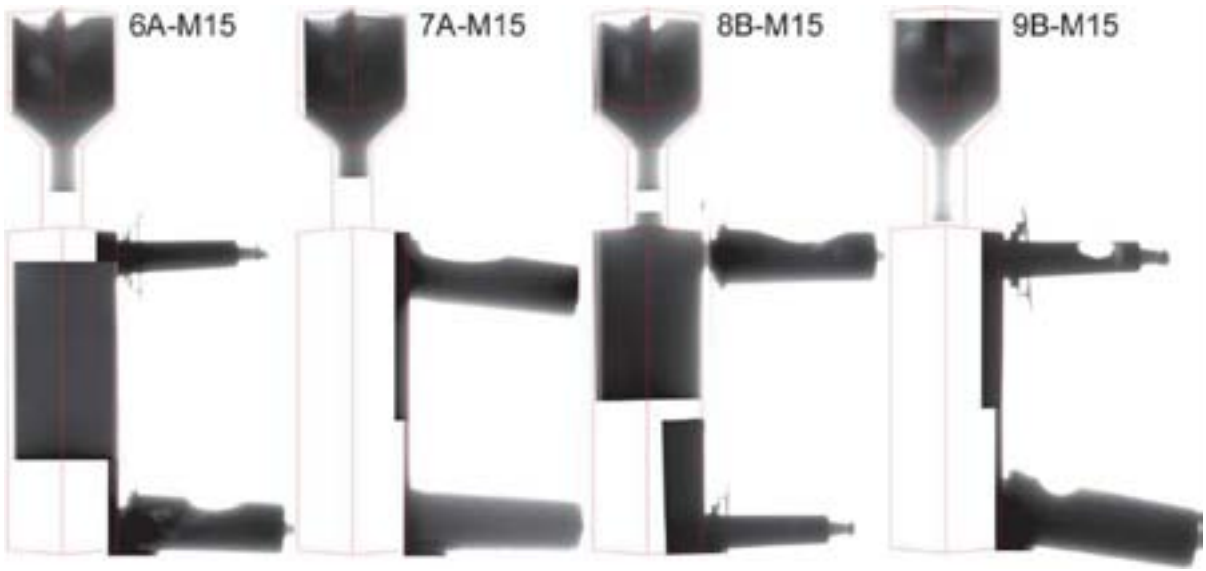

Fig.5: X-ray images of casting 6A, 7A, 8B, and 9B—all that largest casting with a modulus of 15 mm.

Thermal Measurements and Cooling Curves

The cooling curves showed that the three parametric castings solidified and cooled in a comparable manner, confirming that the parametric design provide the intended comparison between the different moduli castings (see Figure 6). The maximum temperature measured was 1,325 ±5 °C indicating that the gating filling of the mould has lowered the temperature of the melt by 62 ±10 °C from the pouring temperature of 1,387 ±5 °C. However, the specified temperature limit of 1.300 °C for the K-type thermo couples for short duration readings should be taken into consideration[5].

The cooling curves showed that in the bottom part of the M15 casting ended solidification approx. 320 s before the centre of the casting, albeit 400 s later the curves met again. This was caused by the thermal influence of the spot feeder, and the area between the two curves indicates the energy that the spot feeder provides transferred to the casting.

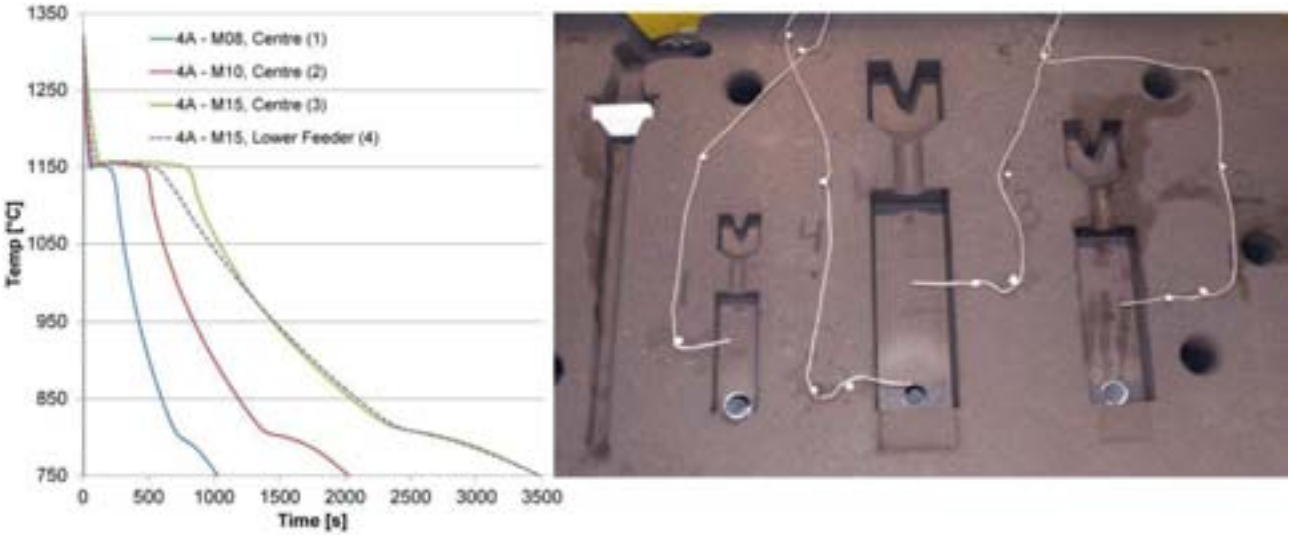

Fig.6: Thermal measurement of the casting, cooling, and solidification of casting group 4A.

Discussion

Examining Table 3 it was seen that most of the castings, regardless of modulus size and spot feeder combinations, had a large (size 4) porosity at the top and a small (size 2) porosity at the middle. As mentioned in the results section the large porosity characteristic was open ended, and covered many gradually increasing porosities. However, the consistent results show the stability of the model and the production conditions. Thus, the most interesting castings were the ones that differentiate from the stable and repeatable porosities formed in the other castings.

Castings 8B-M15 and 9B-M15 were classified as porosity free and the castings with the same spot feeder configuration—8A-M15 and 9A-M15—only displayed micro (size 1) porosities. 7A-M15 and 7B-M15 were classified with small porosities at the top, but no porosities at the middle. Finally, 3A-M15 and 3B-M15 only displayed porosities at the middle of the casting—ranging from micro (size 1) to medium (size 3) porosities.

The smaller castings—M08 and M15—did not show the same effect for these feeder configurations even though the modulus of the spot feeders were scaled according to the changes in casting modulus. This indicated that the solidification of the three different modulus castings was different as well. These changes in solidification can be caused by the slower solidification of the large modulus castings, which provide the longer time for the graphite nodules to grow and inhibit pearlite formation which would have reduced the effect of the graphite expansion. However, the high Si content of the alloy greatly limits pearlite formation already, and none of the three castings are small enough to be considered thin walled sections. Hence other factors were needed to fully explain the solidification differences between the different modulus castings.

Additionally several of the castings had ‘punctures’ at the bottom of the pre-feeder neck, opening into a large porosity in the casting. This effect seemed to have been dominant for the smaller modulus castings, but it also seemed to be unrelated to the amount of porosities recorded and the effectiveness of the spot feeders.

The most likely explanation was that the large modulus castings had a greater tendency to form a solid shell early during solidification, so that the low pressure that occurred inside the casting towards the end of solidification had enough force to move the melt from the spot feeders and into the casting itself.

Some melt may have been provided by the pre-feeder regardless of the intention that this should not happen. The x-ray images showed that the pre-feeders contained porosities. It was not possible to determine how much of the porosities in the pre-feeders that was a result of feeding and how much were related to the liquid shrinkage that the pre-feeders were designed to handle. However, it was noted that most pre-feeders displayed the some amount of porosities.

No correlation was found between the amount of porosities in the pre-feeder and the amount of porosities in the casting itself.

However, the negative pressure gradient from the casting itself could completely explain the results shown in Table 3. If group 3 and 4 were compared for the M15 castings it was noted that the first displayed a few and small porosities whereas the latter displayed more and larger porosities. However, it was the latter—group 4—that had the largest spot feeder. If the main driving force for feeding from the spot feeder into the casting was the negative pressure in the casting, then the larger spot feeder should have produced a porosity free casting. Instead it was seen that the smaller spot feeder reduced the porosities in the casting significantly compared to the large one.

To explain this phenomenon other forces than a negative pressure caused by shrinkage of the material in the casting must be taken into account. The graphite expansion was assumed to be the same for both configurations as they were cast with the same alloy, and only minor differences would occur as an effect of the small changes in solidification between the two spot feeder configurations. However, the timing of the graphite expansion, and particularly in relation to the timing of the negative pressure inside the casting, seemed to reach an optimum for this configuration. Thus, the two different forces come to act together, rather than against each other. If so, this could be seen as a special case of John Campbell's feeding rule no. 6 regarding the pressure gradient requirement[6].

External forces can also have occurred and gas development from exothermic feeder sleeves was a known concern. However, if gas development from the exothermic material was a significant driving force for the movement of the melt, then group 4 and 5 should have displayed fewer porosities than what was recorded.

Finally, examining the results of the M15 casting groups 3, 6, 8, and 9, in comparison with the other five groups, it was shown that a feeder located at the lower part of a casting section can feed the section with equal efficiency compared the same feeder located at the upper part of the casting section. This showed that the horizontally oriented spot feeders with exothermic sleeve material depend little upon the gravity as a driving force for feeding.

Conclusions

1. The optimum feeder size did not scale linearly with casting modulus. Larger casting modules required relatively smaller modulus feeders.
2. The timing of the negative pressure from solidification shrinkage combined with the timing of the graphite expansion seemed to be important in order to achieve the best possible feeding conditions. Similarly a larger feeder may shift the time enough for the effects to counteract each other and thus cancel most of the feeding effect if not directly developing more shrinkage.
3. The location for horizontally oriented spot feeders was relatively unaffected by the difference between the high and low location. The spot feeders that functioned at one location also functioned at the other location. The spot feeders that did not function at one location did not function at the other location either. In special cases it was possible to feed against gravity.

References

1. ASM International: Casting Design and Performance–Part II: Process Design, Riser Design, 2009, 61-72.
2. N. Chvorinov: Theory of the Solidification of Castings, *Giesserei*, Vol. 27, 1940, 177-186.
3. N.K. Vedel-Smith, N.S. Tiedje, K.T. Maza, and J. Sällström: Quantification of Feeding Effects of Spot Feeding Ductile Iron Castings made in Vertically Parted Molds, AFS Proceedings, 13-1310, 2013.
4. EN 1563:2012-3: Founding: Spheroidal Graphite Cast Irons, 2012.
5. L. Michalski, K. Eckersdorf, J. Kucharski, and J. McGhee: Temperature Measurements, 2nd Edn, 2001 John Wiley & Sons Ltd.
6. J. Campbell: 'Casting Practice – The 10 Rules of Castings', 120-156, 2004, Burlington, Elsevier Butterworth-Heinemann.

Acknowledgement

This work was funded by the Public Service Obligation (PSO) funds made available by the Danish Government. The project was made in collaboration with FOSECO Ltd., MAGMA GmbH, DISA Industries A/S, and Vald. Birn A/S. Rune Engelberth Hansen carried out the development of the parametric casting geometry.

Mechanical properties of solid solution strengthened CGI

Rohollah Ghasemi[1, a], Lennart Elmquist [1, b], Henrik Svensson [2, c], Mathias König [3, d], and Anders E. W. Jarfors [1, e]

[1]Jönköping University, School of Engineering, Materials and Manufacturing, P.O. Box 1026, SE-551 10 Jönköping, Sweden

[2]Swerea SWECAST AB, Materials and Process Development P.O. Box 2033, SE-550 02 Jönköping, Sweden

[3]Scania CV AB, Materials Technology, SE-151 87 Södertälje, Sweden

The development of high-performing components is crucial in applications such as heavy vehicle automotive powertrains. In these applications, strength, weight and thermal conductivity is essential properties. Key materials that may fulfil these requirements include cast irons of different grades where in terms of manufacturability and in particular machinability pearlitic grades are difficult due to hardness variation, where a fully ferritic matrix would provide an advantage. To achieve maximum strength a fully ferritic and solid solution strengthened compacted graphite iron (CGI) would provide an interesting alternative to the automotive industry. In the current study, the effect of Si level on mechanical properties in a fully ferritic material was investigated. The influence of section thickness on tensile properties and hardness was investigated. The resulting material was fully ferritic with limited pearlite content. Section thickness influence on nodularity and hence the mechanical properties were also investigated.

Keywords: compacted graphite iron, high Si ferritic CGI, mechanical properties, solution hardening, ferrite

Article available in the International Journal of Cast Metals Research

Determination of the crack propagation direction of fractured ductile cast iron based on the characteristic features of the surface

D.Fernandino[1*], R.Boeri[1]

[1]Metallurgy Division, National University of Mar del Plata
INTEMA- CONICET, Mar del Plata, Argentina

In this article, the characteristic fractographic features of ductile cast irons with different metallic matrices were analysed. Several heat treatment cycles were carried out on samples from the same cast iron melt in order to obtain ferritic ductile iron, pearlitic ductile iron and austempered ductile iron. The specimens were broken under impact and bending tests and the fracture surfaces were analysed by means SEM observation. Two methodologies to evaluate the main crack propagation based on some characteristic features of the fracture surface were proposed.
The investigation involves a systematic study of the fracture surfaces of ductile iron of different matrices. The authors propose methodologies suitable for identifying the main crack propagation direction of fracture processes of unknown origin applicable to brittle and ductile fracture cases.

Keywords: ductile iron, fracture surface, roughness, bending, crack propagation

Introduction

Ductile irons (DI) can cover a wide range of mechanical properties. Different matrix microstructures can be generated after heat treatments, such as ferritic, pearlitic, martensitic and ausferritc (austempered), among others[1]. Thanks to their good mechanical performance and relatively lower cost when compared to steels, ductile cast irons are increasingly applied in the construction of highly stressed parts of machines and vehicles. The relationship between microstructural features of the material and the working conditions on the DI fracture processes are analysed in the literature by different authors [2-8]. The fractographic characteristics identified for DI differ from those usual in steels and other metallic alloys [9, 10]. The presence of spheroidal graphite and the occurrence of microsegregation can have a strong influence on the morphology of the fracture surface [11, 12]. However, the fractographic analyses reported in most works are secondary to studies of mechanical properties. Few authors have carried out a systematic analysis focused on the interpretation of the DI fracture surfaces under different load conditions [13-15]. Therefore, there is limited information available to evaluate, for example, the crack propagation direction from the observation of some characteristic features of the fracture surface of a component failed in service. This lack of information can be considered to be an obstacle for the application of these alloys because, for example, it is very difficult to extract information from a fractographic analysis and, therefore, to obtain information from one of the more important diagnosis elements.
In consequence, this study is intended to identify the general features of fracture of different types of ductile irons broken under different loading conditions, and to correlate these features with the main crack propagation direction.

Experimental Procedure

The material used in this study was obtained from one-inch 'Y' blocks of DI. The chemical composition was determined by using a Baird DV6 spectrometer. Pearlitic DI was obtained from as-cast condition. 'Y' blocks were ferritised in order to improve the machinability and to standardise the initial microstructure before other heat treatments were carried out. Ferritizing consisted of an austenitizing stage at 920 ºC for 4 hours followed by a slow cooling stage down to room temperature. In addition, a conventional austempering heat treatment cycle consisting of an austenitizing stage at 920°C for 1 hour followed by an isothermal heat treatment at 360°C for 1 hour was made in order to obtain ADI. Metallographic samples were prepared by means standard polishing and etching methods using nital (2 %). The microconstituents as well as the as-cast characterisation were quantified by using an optical microscope OLYMPUS PMG3 and the Image Pro Plus software. V-notched Charpy impact specimens of 10x10x55 mm for impact and three point bending test (ASTM E23) were machined from the 'Y' blocks.

Impact and three point bending tests were carried out. Impact testing was carried out by using a pendulum AMSLER 130/688, with a maximum energy of 300J. Three-point bending tests under quasistatic loading were performed by using a universal testing machine Morh&Federhaff with a crosshead displacement rate of 8.4×10^{-3} mm/sec. The fracture surfaces of the broken specimen were observed by means of a scanning electron microscopy (SEM). Table 1 exemplifies the labelling used to identify the samples for each testing conditions.

* Corresponding author, email: dfernandino@fi.mdp.edu.ar

Table 1. Labelling used for each test condition.

Sample Label	Test type	Test temperature
PI-20	Impact	-20°C
FI-20		
ADI_{360}I-20		
PI20		20°C
FI20		
ADI_{360}I20		
PI60		60°C
FI60		
ADI_{360}I60		
Pflx	Bending	20°C
Fflx		
ADI_{360}flx.		

Results and Discussion

Chemical composition and microstructures

The chemical composition of the DI used is listed in table 2. The as-cast microstructure characterization according with the ASTM A 247 standard and the Brinell hardness are listed in tables 3 and 4 respectively. The nodularity was considered suitable for this study. The microstructures of the different types of samples used are shown in Fig. 1.

Table 2. Chemical Composition of DI used (Wt %)

C	Si	Mn	S	P	Mg	Cu	Ni	Cr
3.32	2.36	0.31	0.012	0.016	0.033	0.62	0.025	0.058

Table 3. Metallographic characterisation of as-cast samples

Nodule count [nod/mm^2]	Nodularity	Nodule size
100	>95%	6

Table 4. *Brinell hardness value*

F	P	ADI_{360}
149	272	350

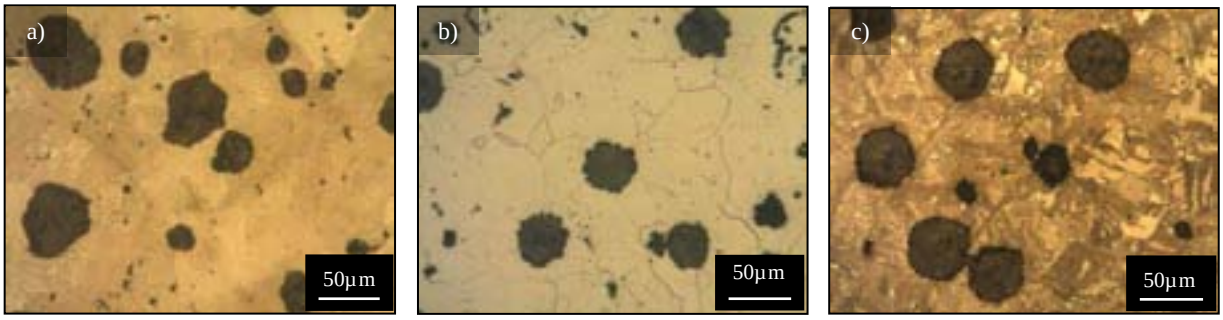

Fig. 1. Microstructures of the different types of DI investigated. (a) Pearlitic (As Cast); (b) Ferritic; (c) Ausferritic.

Analysis of fracture surfaces by SEM

Figures 2 to 5 show several fracture surfaces. A general feature of all fracture surfaces analysed is the presence of graphite nodules and empty cavities left by graphite nodules that were detached from the matrix during the fracture process.

Fracture surfaces from impact testing at different temperatures

Fig. 2 shows the fracture surfaces of ferritic DI impact tested at different temperatures. At low temperatures (-20 ºC, Fig. 2a) the surface shows cleavage facets with river patterns. The graphite nodule cavities show very little strain. Both observations support a predominantly brittle failure mode. At room temperature (Fig. 2b) a significant fraction of the surface shows ductile dimples, while the remaining surface shows cleavage facets. Furthermore, the nodule cavities show extensive deformation. As the test temperature rises to 60 ºC, Fig. 2c, cleavage facets are no longer present, but the fracture surface is dominated by dimples formed after microvoid coalescence.

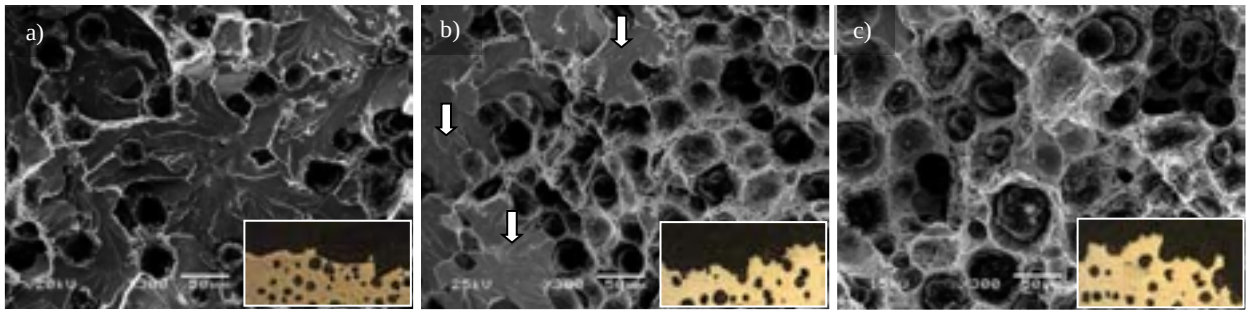

Fig. 2. Fracture surface of FDI broken at different impact test temperature. (a) FI-20; (b) FI20; (c) FI60

Fig. 3 shows the fracture surfaces of pearlitic DI generated by impact testing at different temperatures. A brittle fracture surface conformed by cleavage facets that show river patterns and cracks that break into the surface is observed at -20°C as is shown in Fig. 3a. As the test temperature increases, the predominant fracture mode remains unchanged and only a slight decrease in the number of cracks that break into the surface was found. Even for the samples tested at 60°C, the nodular contours showed little or no plastic strain (Fig. 3c). Only some very small ductile fracture regions were found both at high and low temperatures. Therefore, cleavage facets dominate the fracture surface of pearlitic DI broken under impact, with a minor presence of ductile fracture surfaces.

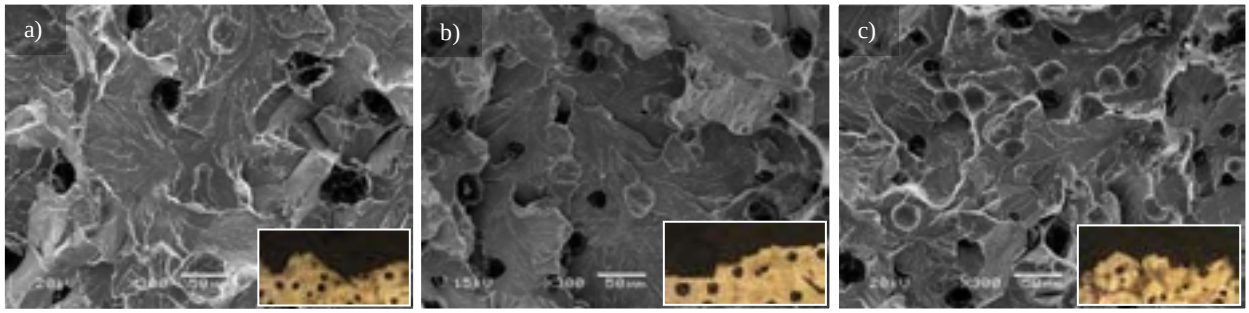

Fig. 3. Fracture surface of pearlitic DI broken by impact at different temperatures. (a) PI-20; (b) PI20; (c) PI60

Fig. 4 shows the fracture surfaces of austempered DI. At low temperature (-20°C, Fig. 4a), the predominant fracture mode is cleavage. Nevertheless, the cleavage facets are smaller than those found in pearlitic and ferritic DI. In addition, the contours of nodular cavities are strained and some disperse areas of ductile fracture can be found. The fracture mechanism combining cleavage facets and small ductile portions is called quasi-cleavage. As the test temperature increased, the nodular contours show greater plastic deformation and the contours of the inclusions, mostly concentrated at the last to freeze portions of the matrix, also show marked deformation. As the temperature further increases, the classical ductile fracture mechanisms begins to be predominant (nucleation, growth and coalescence of voids with the contours of nodular cavities deformed), and the main fracture mechanism changes from quasi-cleavage to ductile (with small areas of quasi-cleavage facets).

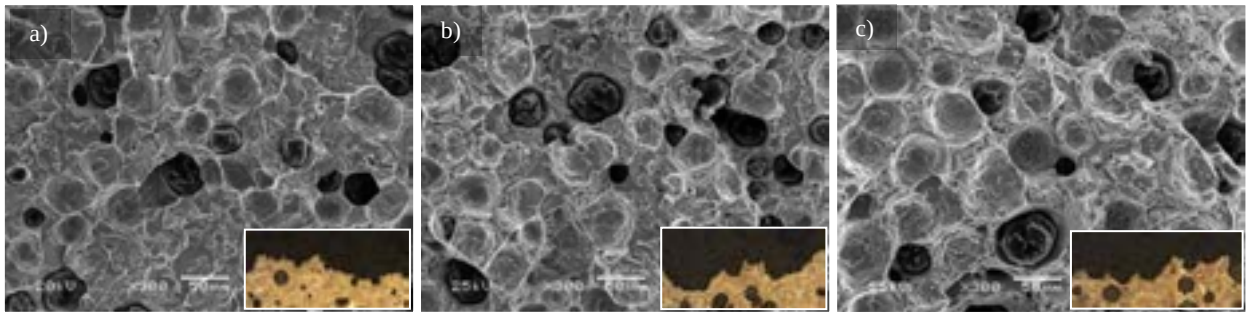

Fig. 4. Fracture surface of ADI broken at different impact test temperature. (a) ADII-20; (b) ADII20; (c) ADII60

Fracture surfaces from bending tests

Fig. 5a shows the fracture surface of ferritic DI. A fully ductile fracture micromechanism dominates the surface, as dimples and highly deformed graphite nodule cavities are found. No cleavage facets are seen. Noticeable differences in the predominant fracture mode are observed as the fracture surfaces broken at room temperature (20ºC) by impact and quasi/static bending loading are compared. After the three-point bending test, the fracture surface shows a very rough topography and a much higher apparent nodular density (i.e. the number of nodules per area) when compared to the fracture surface resulting from the impact testing, where some disperse cleavage facets can be found, as shown in Fig. 2b. This apparently higher nodular density is caused by the greater enlargement of the nodular cavities due to the plastic deformation that takes place when the loading is slow. When pearlitic DI fracture surfaces are analysed, Fig. 5b, brittle cleavage facets dominate the fracture surface and only little portions showing microplasticity features were evidenced along some cleavage steps and other disperse areas of the fracture surface. Consequently, as was reported for the samples broken under impact testing at room temperature, brittle fracture was the predominant failure mode. When fracture surfaces of austempered DI are analysed, several cleavage zones are evidenced (marked by arrows) as shown in Fig. 5c, mixed with ductile fracture portions, resembling the results of impact testing at 60ºC (Fig. 4c).

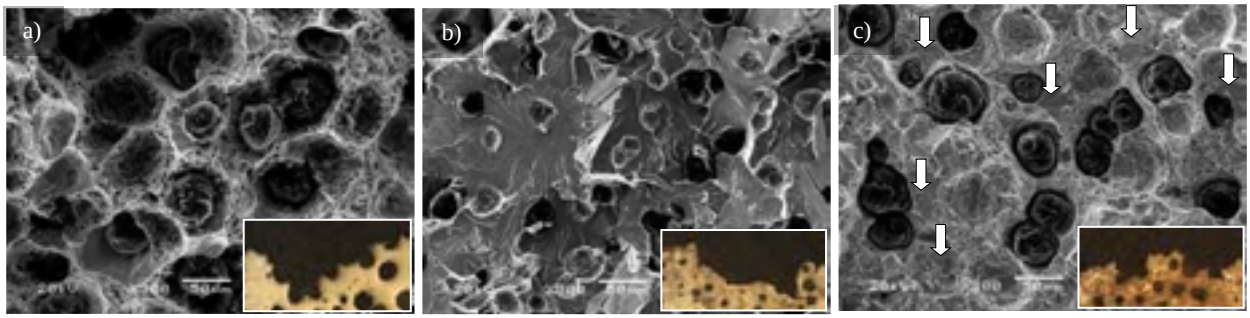

Fig. 5. Fracture surface of samples broken under slow bending testing. (a) Fflx; (b) Pflx; (c) ADIIflx

Main crack propagation direction and its relation with the topographic features

With the goal of identifying the propagation direction of fracture, the topographic features of the fracture surfaces were analysed carefully, for the different loading conditions investigated.

Brittle failure mode

The literature reports that the river patterns present on the cleavage facets converge into a single crack following the direction of the local crack propagation. Therefore, it should be possible to assess the main crack direction through the observation of the propagation on the cleavage planes or facets. The approach used in this study was to identify and to characterize the local propagation direction by means of the observation of the directions of the river patterns with respect to the main crack propagation direction, which is known. The methodology proposed used a local propagation vector that is defined at the point in which two river patterns join, as shown in Fig. 6. All measured local propagation vectors were characterised by the angle formed with respect to the main crack propagation direction. The large number of values of local angles measured were averaged and the resulting direction compared to the main crack propagation direction. In all situations, the main crack propagation direction was set at 0 º.

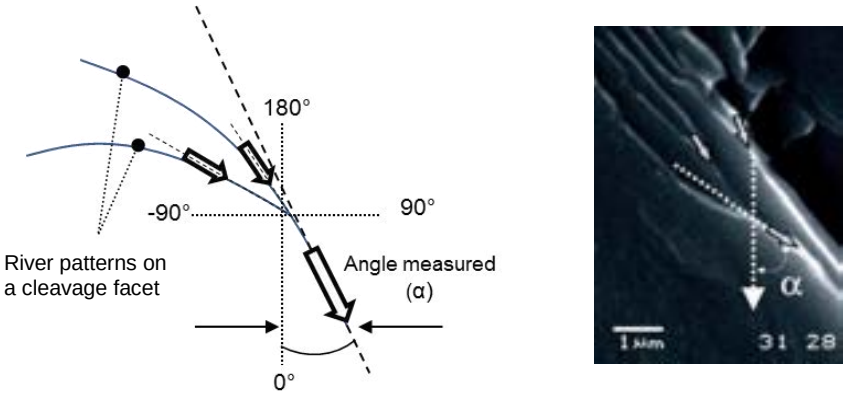

Fig. 6. Method used to define a local propagation vector on the cleavage fracture surfaces resulting of impact and bending test.

The results of the statistical dataset are listed in Fig. 7. The mean value (X) of the dataset was 9±2 and the mode value (Mo) of the distribution was 0º. These results not only show that the average of local propagation vectors reveals the predominant propagation direction with good accuracy, but also, a higher relative frequency was observed for the directions with little deviation from the main crack propagation. The local directions were grouped into 20 intervals ranging from -180º to 180º in concordance with the reference system used in the present methodology. A number of 1515 local crack propagation direction was analysed in five different fracture surface area.

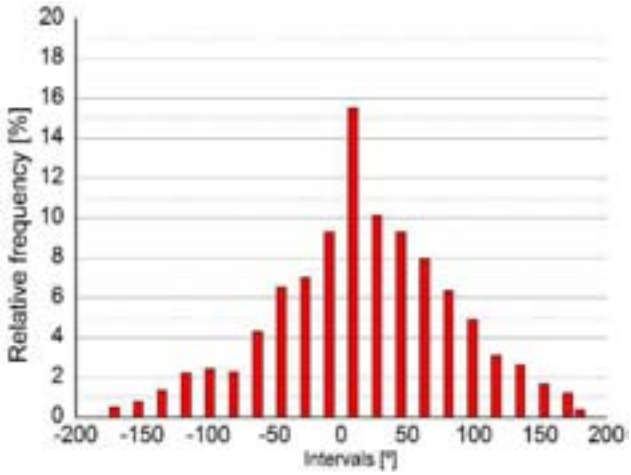

Fig. 7. Histogram obtained from the quantitative analysis on SEM fractographies of FI-20 sample.

Ductile failure mode

A different method was developed to determine the propagation direction when the ductile fracture is the predominant failure mode. The method is based on the measurement of the plastic deformation of the metallic matrix surrounding the graphite nodules. For each nodule present at the fracture surface an ellipse is manually defined with the best possible fit to the deformed nodular contour. Then, two different measurements were carried out. First, the length of the nodular contour in parallel (Y) and perpendicular (X) axes to the main crack propagation direction were measured, as shown in Fig. 8. In addition, the angle formed between the major axis of the ellipse and the main crack propagation direction was measured. The methodology demands time and care. The results of the measurements of the ratio Y/X and the angle (α) on several fields of the samples investigated are listed in table 4. The results are grouped depending on the value of the Y/X ratio. The larger proportion of the nodular cavities show values of Y / X greater than 1, i.e., the nodular cavities tended to strain according to the main crack propagation.

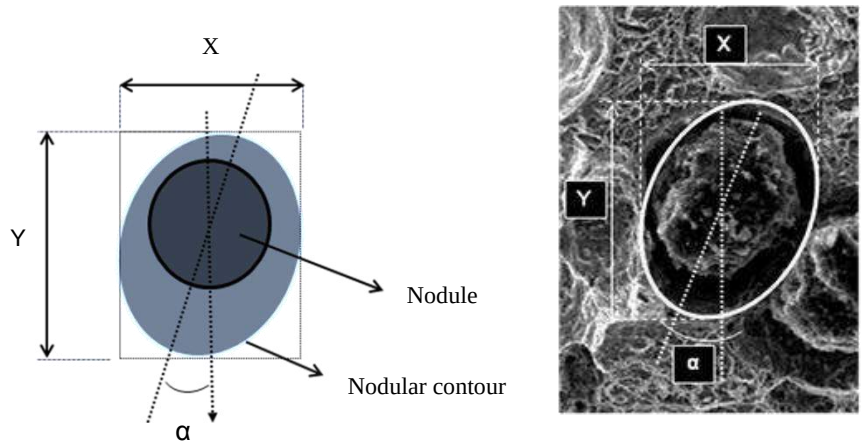

Fig. 8. Method used to measure the parameters that characterise the nodule contour deformation. Ductile fracture.

Table 5. Deformation of the nodular contour on the fracture surface

Sample	Y axe [%]	Equiaxial [%]	X axe [%]	Contours analysed	Angle (β)
FI60	66	23	10	254	2.70 ± 0.18º
Fflx	77	15	8	135	0.80 ± 0.14º
ADI_{360}I-20	72	6	23	74	1.90 ± 0.28°
ADI_{360}I60	68	7	24	111	2.20 ± 0.30°
ADI_{360}Flx	78	11	12	161	9.00 ± 0.20º

For a better interpretation of the dataset, a histogram and a function of cumulative frequency of the X/Y ratio is plotted in Fig.9. The results show that for the ferritic DI sample under impact testing at 60°C, 66% of the nodular cavities analysed had a ratio Y/X> 1, while for the bending case, this value increased to 77%. For ADI, in all test conditions, the ratio Y/X was greater than one for at least the 68% of the dataset. The fraction of the nodular contours showing greater deformation along the Y-axis increase as the impact test temperature increases, and as loading in quasistatic. The mean values of β show a maximum deviation respect to the reference Y- axe of 9.00 ± 0.20° for ADI_{360}I-20 sample. The average of β values obtained in each condition for each DI were plotted in Fig. 10. Taking into account that the reference Y-axis has been set along the main crack propagation direction, it can be concluded that this method allows to identify the main crack propagation direction with good approximation. It must be noted that the result will be independent from the reference axis chosen, as will be the case when a fracture surface of unknown crack propagation direction is examined.

a)

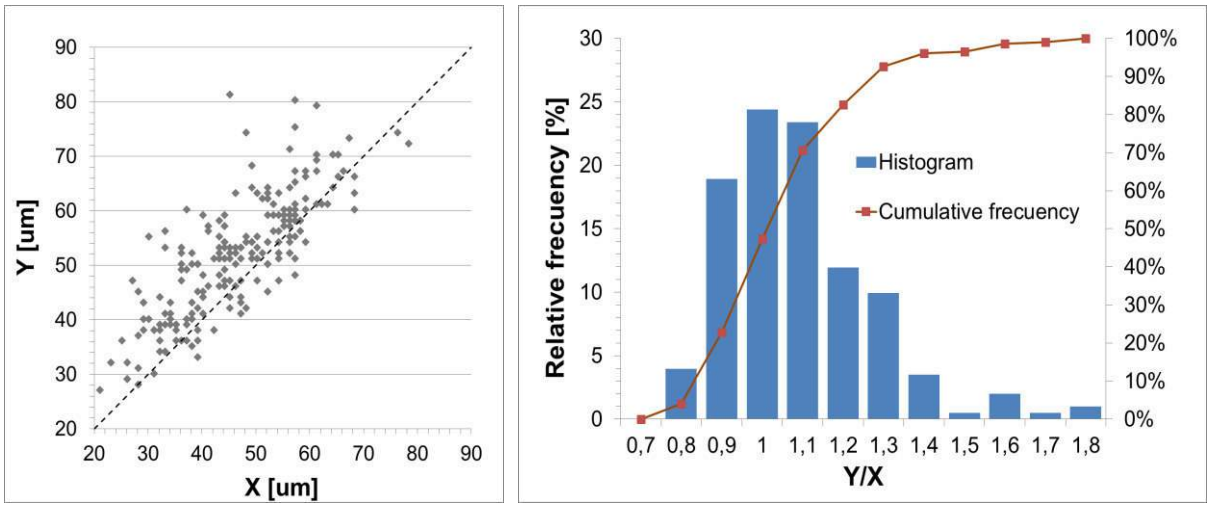

b)

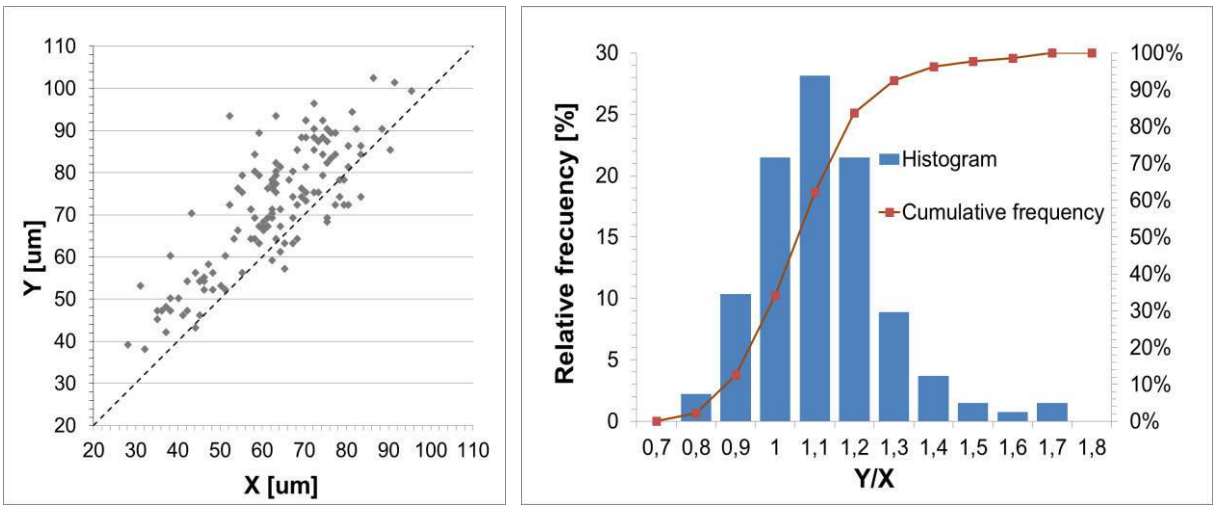

Fig. 9. Statistic plots from the experimental measurements of X/Y ratio on FDI. (a) FI60; (b) Fflx

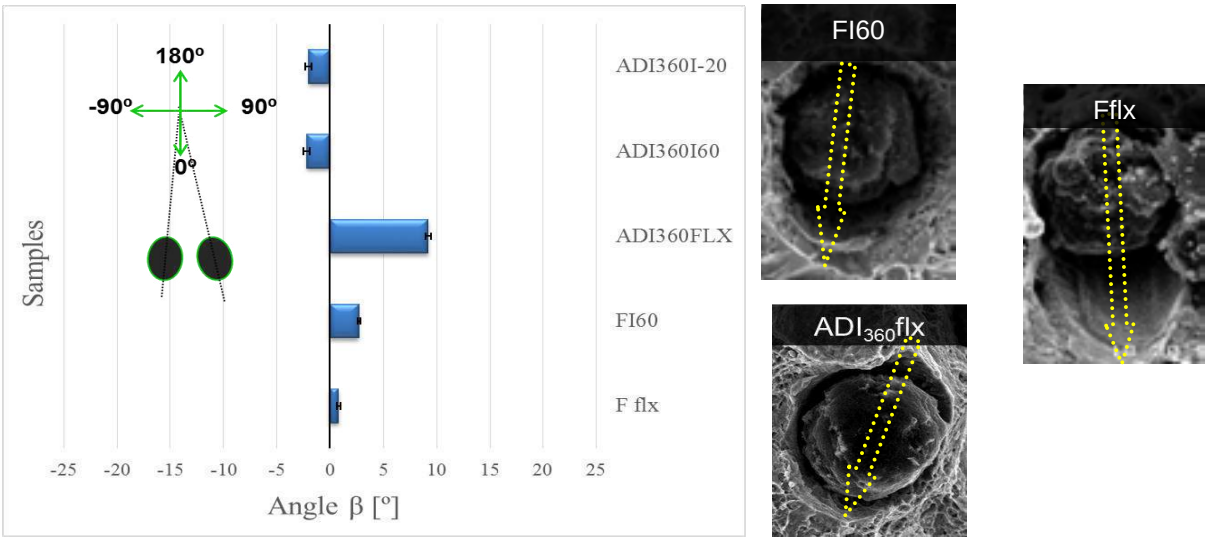

Fig. 10. Plot from the experimental measurements of angle $_{\beta}$

Conclusions

The investigation involves a systematic study of the fracture surfaces of DI with different metallic matrices and broken under different loading conditions.

1. In the case of ferritic ductile iron, the predominant failure mode shows noticeable changes as a function of the loading conditions and testing temperatures. The predominant fracture mechanism changes from brittle (cleavage) to ductile as the impact test temperature increases. When fracture surface from bending test was evaluated, a fully ductile behavior was evidenced.
2. In the case of pearlitic ductile iron the fracture surfaces resulting from both impact at different temperatures and bend loading, showed brittle fracture characteristics, as the surfaces were conformed by cleavage facets that show river patterns and cracks that break into the surface. Only some very small ductile fracture regions were found at both high and low testing temperatures.
3. In austempered ductile iron the predominant fracture mechanism change from quasi-cleavage to ductile (with little areas of cleavage facets) as the impact testing temperature was increased. For bending test, a mix of cleavage facets, nodular contours strain and microvoids coalescence were evidenced. The contours of the inclusions, mostly concentrated at the last to freeze portions of the matrix, also show marked deformation.
4. Complex but reliable methodologies for the determination of the main crack propagation direction were proposed. For brittle fracture, the method is based on a careful analysis of the river patterns along the cleavage planes. For

ductile fracture, the method is based on the measurement of the plastic deformation of the metallic matrix surrounding the graphite nodules.

References

1. Ductile Iron Data for Design Engineers (1990). Cap. II Introductions.
2. Di Cocco, F.Iacoviello, M Cavallini. *Engineering fracture Mechanics*, 2010, 77, 2016-2023.
3. D. Rajnovic, O. Eric, L. Sidjanin. *Journal of Microscopy*, 2008, 232, 605–610.
4. L.Eldoky, R.C.Voigt. Fracture of Ferritic Ductile Cast Iron. Transactions of the American Foundrymen's Society.Vol.94; Minneapolis, Minnesota; USA; 12-15, 1986. 621-630.
5. F.Iacoviello, O.Di Bartolomeo, V.Di Cocco, V.Piacente. *Materials science and Engineering A*, 2008, 478, 181-186.
6. G.L.Greno, J.L.Otegui, R.E.Boeri. *Int. J. of fatigu*e, 1999, 21, 35-43.
7. M.F. Hafiz, A. Hammouda, S. El-Gemae. AFS Transactions 2005 American Foundry Society, Schaumburg, II. USA 2-12.
8. R. Konecna, P. Lejcek, G. Nicoletto and P. Bartuska. Materials Science and Technology, 2006, 22, 1415-1422.
9. T-L.Anderson. (1995) Fracture Mechanics. Fundamentals and Applications. 2nd ed., pp. 265-305.
10. Broek D. Elementary engineering fracture mechanics. (1991) 4th ed. 101 Philip Dr., Norwell, MA 02061 USA: Kluwer Academic Publishers.
11. P.Q.Dai, Z.R.He, C.M.Zheng, Z.Y.Mao. *Materials Science and Engineering A, 2001,* 319-321, 531-534.
12. R.C.Voigt, L.M.Eldoky. Transactions of the American Foundrymen's Society. Minneapolis, Minnesota; USA; 12-15 May 1986, 94, 637-644.
13. A. Ghahremaninezhad, K. Ravi-Chandar. Acta Materialia, 2012, 60, 2359–2368
14. R.A.Martinez. *Engineering Fracture Mechanics* 2010, 77, 2749–2762.
15. V. M. Bermont, R. N. Castillo and J. A. Sikora. ISIJ International, 2002, 42, 1303–1308

Acknowledgement

The authors are grateful to CONICET and the National University of Mar del Plata for their financial support.

Modeling capabilities of phenomena in over-moisture zone existing in porous medium using the simplified simulation systems applied in foundry

P. Popielarski[1], Z. Ignaszak[1*]

[1]Poznan University of Technology, 3 Piotrowo Street, 60-965 Poznan, Poland

The problem described in the paper concerns the thermo-physical properties of the green mould material to which the cast iron most often is poured (about 50% of production). The study described in the paper includes the iron plate casting experiments poured in green bentonite-sand mould. The temperature fields of casting and in different zones of the mould were recorded. The determining of the thermo-physical properties of mould sand containing the over-moisture zone by using simulation tests (inverse problem) was the goal of this study. An originality of the related research is an attempt to take into account the effects of the global thermal phenomena occurring in the quartz sand bonded by bentonite-water binder, applying the apparent thermal coefficients. The majority of foundry simulation systems are not capable of modeling the phase transformation of water into vapor, follow by vapor transport and its condensation in the porous media (mould). In these cases, the application of apparent coefficients is an effective way.

Keywords: green sand mould, over-moisture zone, cast iron, virtualization, validation.

Introduction

About 50% of cast iron castings are made in the moulds from green bentonite sand. The physical properties of the mould material, to which the liquid cast iron is poured, have a decisive influence on the course of the physics–chemical metal–mould reactions and on the time dependent heat transfer rate from the casting especially during initial period of mould-casting thermal contact. The both determine the final casting quality. In the porous mould sand with the bentonite binder, where the amount of water added during the process does not exceed 4%, is used to activate the purely physical mechanism of binding the matrix (quartz grains) using bentonite (type of clay). An important phenomenon accompanying the heating of the green sand mould by poured metal is the production of water vapor and then its condensation in the so-called over-moisture zone (local water content in over-moisture zone exceeds the value of initial process moisture content several times) in the deeper layers of the mould. This zone of moisture condensation, which is formed from the casting–mould interface, is characterized by low strength of mould sand and is the favorable factor to form the special casting defect (scab defect). This zone gets more space and moves into the mould to its external face. Simultaneously the water evaporates increasingly when the temperature of mould is close to 100°C, the vapor is transported (presence of the pressure gradient), and further condenses in more and more distant (from casting) zones of the mould. The water vapor migration into the mould is accompanied by an additional heat transfer (parallel to conduction) related to a mass transfer (vapor). To sum up, the gradually dried and humidified zones of the mould, variable in time and space coordinates, are characterized by different local thermo-physical properties. The phenomena connected with the over-moisture zone affect obviously the dynamics of the heat transfer from the casting and the local time of solidification of its different wall sections. Dynamics of the heat transfer from the casting is of particular significance especially in the initial phase of the process of filling the mould cavity with the liquid cast iron, deciding on parameters of flow through the gating system, filling the mould cavity and distribution of temperature in the casting-mould system.

State of art – phenomena in over-moisture zone

The phenomena in the over-moisture zone were a subject of numerous studies[1,2,3,4]. These studies were mostly aimed at development of methods of measurement of humidity and temperature in the mould manufactured out of multi-component porous material, which is the mould sand. The process of simultaneous, zonal forming, movement and condensation of the water vapor in a moist, porous material is a complex problem – these phenomena should be comprised by a model of simultaneous heat and mass transfer, with taking the laws of fluid penetration through the porous medium into account. Unsteady processes of heat and moisture transfer cause local (in terms of time and space) variations of processing properties of the green sand, which in extreme cases can lead to uncapping of the sand near

* Corresponding author email: zenon.ignaszak@put.poznan.pl

moving condensation zone. Forming and movement of the over-moisture zone is described in the publications [5,6], where the authors distinguished three zones in the heated green sand: dry sand zone, transitory zone (evaporation, movement and condensation of the water vapor) and fresh (primary, external) sand zone. These zones are separated with the apparent surfaces of evaporation and condensation. On these surfaces, the characteristic temperatures correspond to phase transitions occurring in the mould space (only water boiling temperature is considered). The transient location of these surfaces are expressed as a time function (1) and (2)[5], (look Fig.1).

$$X_1^2 = K_1 \cdot t \tag{1}$$

$$X_2^2 = K_2 \cdot t \tag{2}$$

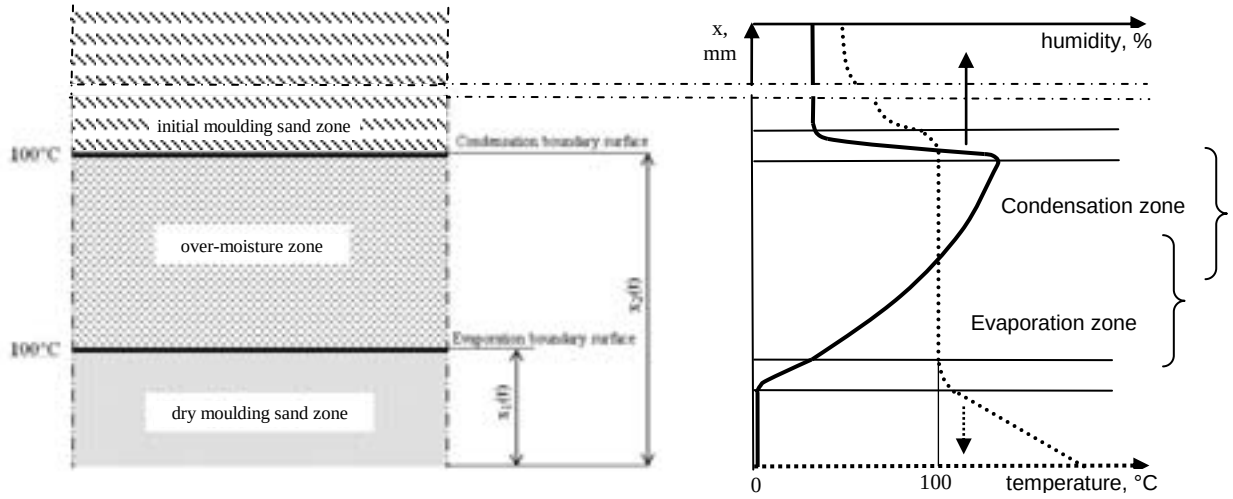

Fig.1: Cross-section through the green sand mould containing the over-moisture zone (based on [5])

However, the authors analyze only a movement of the over-moisture zone (the boundary between the dry zone and the transition zone), omitting the humidity accumulation in the transition zone. The similar relations are proposed in the [3]. Presence of water also influences the dynamics of the heat transfer out of the casting, which is of big significance especially during pouring and for thinner walls, when the decrease of temperature in canals of the gating system and the mould cavity during its filling is considered and modeled. That is why studies of the alloy castability, besides the viscosity parameter, need to take changing properties of the moist mould in the initial stage of period of its filling with liquid metal into account. In studies carried out by Pirowski and Pysz[7], the process castability test is used to determine thermo-physical properties of an alloy, including relation between viscosity and the temperature. In the cited work, influence of the alloy overheating temperature on the castability is analyzed. The authors made castings in moulds of furan sand, in which the phenomena accompanying forming of the over-moisture zone do not occur. It means that influence of the thermal and physical parameters of the mould, including the initial humidity of the sand on the castability, was not analyzed.

In the green sands, changes in amount of moisture in particular zones of the mould are possible to identify on the basis of measurement of the sand temperature in these zones. Studies conducted in [8,9], according to the methodology shown there, allowed to trace the changes of humidity and water vapor pressure in the over-moisture zone since the first contact of metal with the mould. It also creates possibilities in the indirect way, to obtain thermo-physical characteristics of the moulding sands. Forming and movement of the water vapor in the moist, porous bodies subjected to the thermal shock (contact with the liquid cast iron) are a complex problem in terms of phenomena description using a model. The models can be formulated by expressing source of evaporation heat and water vapor penetration separately, which boils down to coupling of the fields: temperature (Fourier-Kirchhoff model) and humidity distribution (Darcy model). Also, a substitute coefficient of heat transfer in the porous body can be introduced and the problem can be reduced to the temperature field modified by the presence of the humidity. The knowledge about amounts of the water vapor flowing through the mould (stream of mass) and transferring a defined amount of heat has become a base for balanced expression of the stream of energy.

Formally, the coupled model of phenomena of appearance and movement of the over-moisture zone should include phenomena of the energy flow in the presence of negative – evaporation – and positive – condensation – sources of heat (the Fourier-Kirchhoff equation), along with equation of movement (penetration) of fluid, i.e. water vapor and water in the porous medium, caused by the pressure difference (the Darcy equation).

In the simplified approach presented in the paper, substitute thermo-physical parameters of the porous medium (moulding sand) in function of temperature were introduced. In case of the foundry simulation systems, based upon

the heat model in their "hard modeling" part, there is a possibility to enter modified thermo-physical parameters of the mould sand in function of temperature. These modifications concern considering the heat of water evaporation by changing values of apparent specific heat of the mould sand.

In the databases of the foundry simulation systems, such as Procast[10] and Nova Flow & Solid Control Volume[11] (NF&S CV), phenomena related to forming of the over-moisture zone are not considered in the simulation models. The Magmasoft[12] software allows to define the initial humidity of the mould sand and in the database, the value of the specific heat in a temperature range of approx. 100°C is increased by value of the evaporation heat of water contained in the sand. The value of the considered evaporation heat is not related to the initial humidity, which determines the amount of the water in the mould sand. The simulations performed in the Magmasoft system allow formal representation of phenomena related to forming of the over-moisture zone, while the results obtained for the various initial humidity values are not compatible with intuitive prediction. The deviations of simulated times of solidification of cast iron plates from real times determined by experiment are approximately 50% higher, which means that the energetic validation was not achieved.

Experimental Procedure

The experiment was performed in the real conditions of a cast iron casting – mould system, by casting the plates of thicknesses 16, 30 and 40 mm in a mould made out of green sand. Arrangement of the castings in the mould is shown in the Fig.2. Grey cast iron EN-GJL-250 was used. The cast iron and green sand parameters are shown in Table 1. The aim of the experiment was to measure and record the temperature in selected points of the casting and the sand mould. To conduct the experiment, special measuring cores needed to be prepared out of the studied greensand (Fig.3). In the cores, the mineral insulated thermocouples of type K were placed, in the distances of 6 mm, 15 mm, 35 mm, 75 mm and in the geometrical center of each casting. The measurement results were recorded using the CASTOR 2 – data acquisition system.

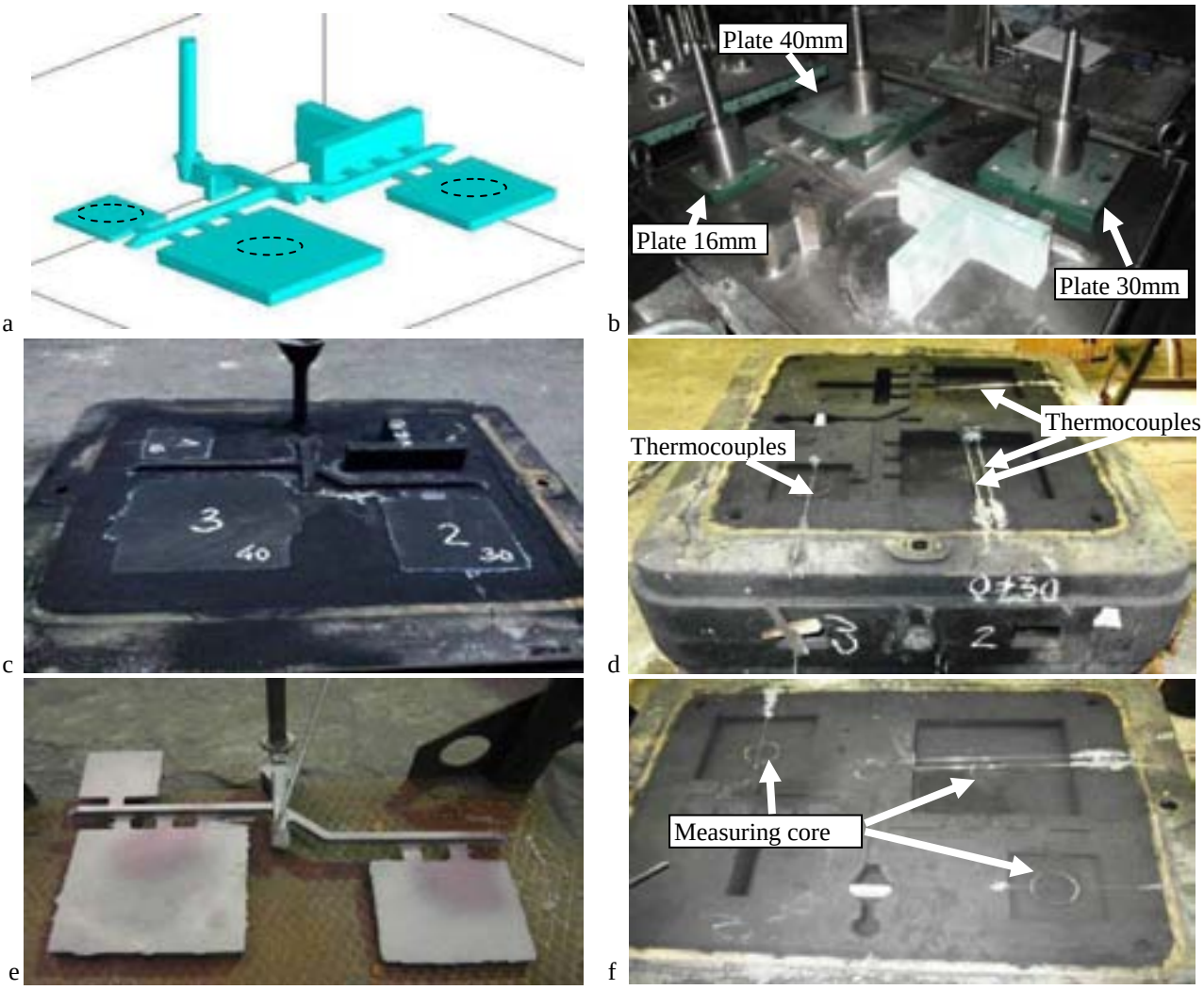

Fig.2: Casting arrangement in the mould. a – CAD model, b – pattern plate, c,d – mould instrumentation, e – mould disassembly, f – raw casting knocking out

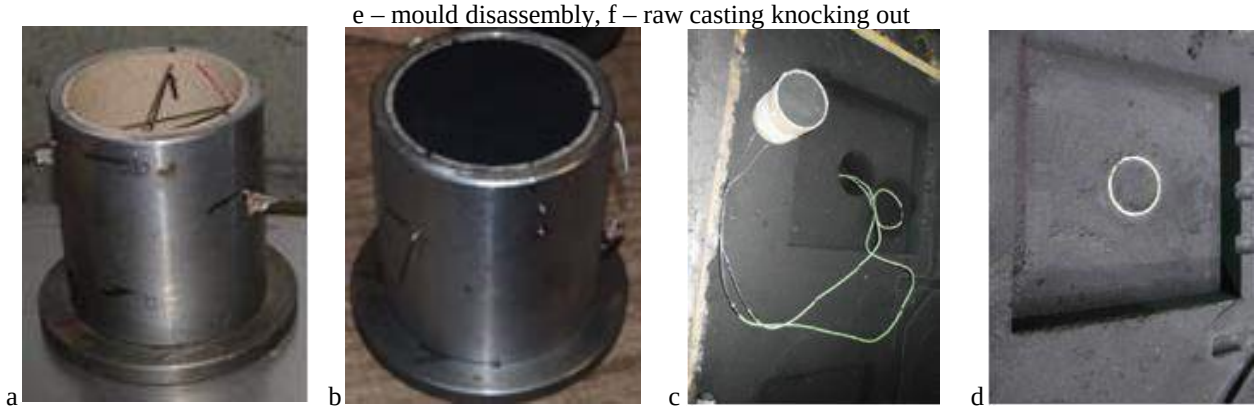

Fig.3: Measuring core – preparation procedure: a – core box with thermocouple positioning pins (6–15–35–75 mm), b – compacted core, c,d – core before and after installation in the mould cavity

Table 1: The cast iron and green sand parameters

Cast iron– final composition															
C	Si	Mn	P	S	Cr	Cu	V	Mo	Ni	Ti	Al	Co	Sn	Te	Mg
3,51	1,99	0,53	0,18	0,09	0,13	0,39	0,02	0,01	0,06	0,02	0,004	0,01	0,008	0	0
Fusion and pouring parameters															
Furnace charge: pig iron 30%, steel scrap 35%, recycle scrap 35% Ladle capacity (over lip) – 1500 kg						Superheating temperature T_{sh} = 1505°C Pouring temperature T_p = 1345°C						Tapping temperature T_{tapp} = 1450°C Pouring time T_z = 11 s			
Green bentonite-sand parameters															
Dry components: silica sand 92%, active bentonite 7,0% coal dust 1,0% + water 3,5%						Density (wet state): ρ = 1540 kg/m^3						Mechanical/technological parameters: compression strength 0,24 MPa, permeability 195 10^{-8} m^2/Pa/s, humidity 3,5%, compactibility 40%, calcination losses 3,55%			

The simulation studies were conducted using the NF&S CV system, according to the following scheme:
- virtual thermocouples were placed as in the experiment,
- simulation of filling, solidification and cooling to the 600°C was carried out,
- validation was based on assumptions resulting from the scheme presented in the Fig.4:
  - energetic validation – on the basis of comparative analysis of solidification times determined from the cooling curves of the casting,
  - dynamic validation of temperature, based on comparative analysis of the heating curves, recorded in the mould sand.

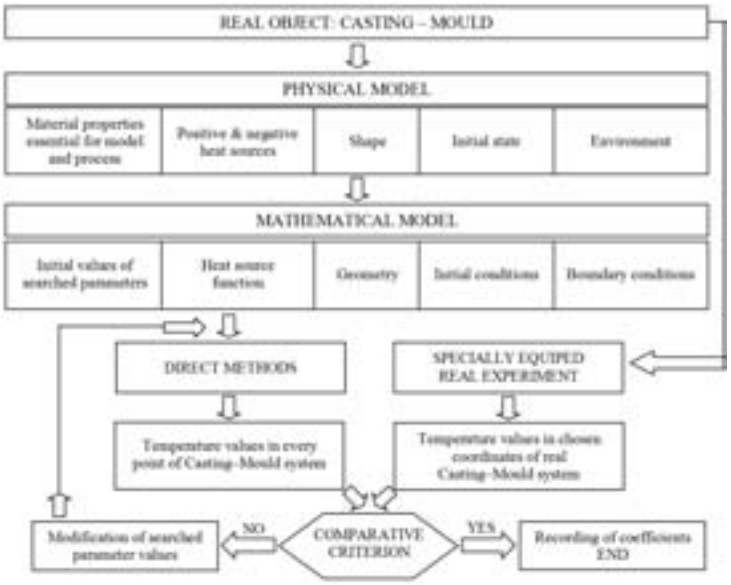

Fig.4: Scheme of validation with the comparison criterion

Results

Results of experimental studies in form of cooling curves of castings and their derivatives, along with curves of heating in the mould are presented in the Fig.5. On the basis of the minimum of the first derivative, the plate solidification times were determined. Times of solidification were used to carry out the energetic validation. On the basis of the measurements of the real thermocouple locations in the mould sand, appropriate corrections were made after casting knocking out. It was taken into consideration during the simulation calculations.

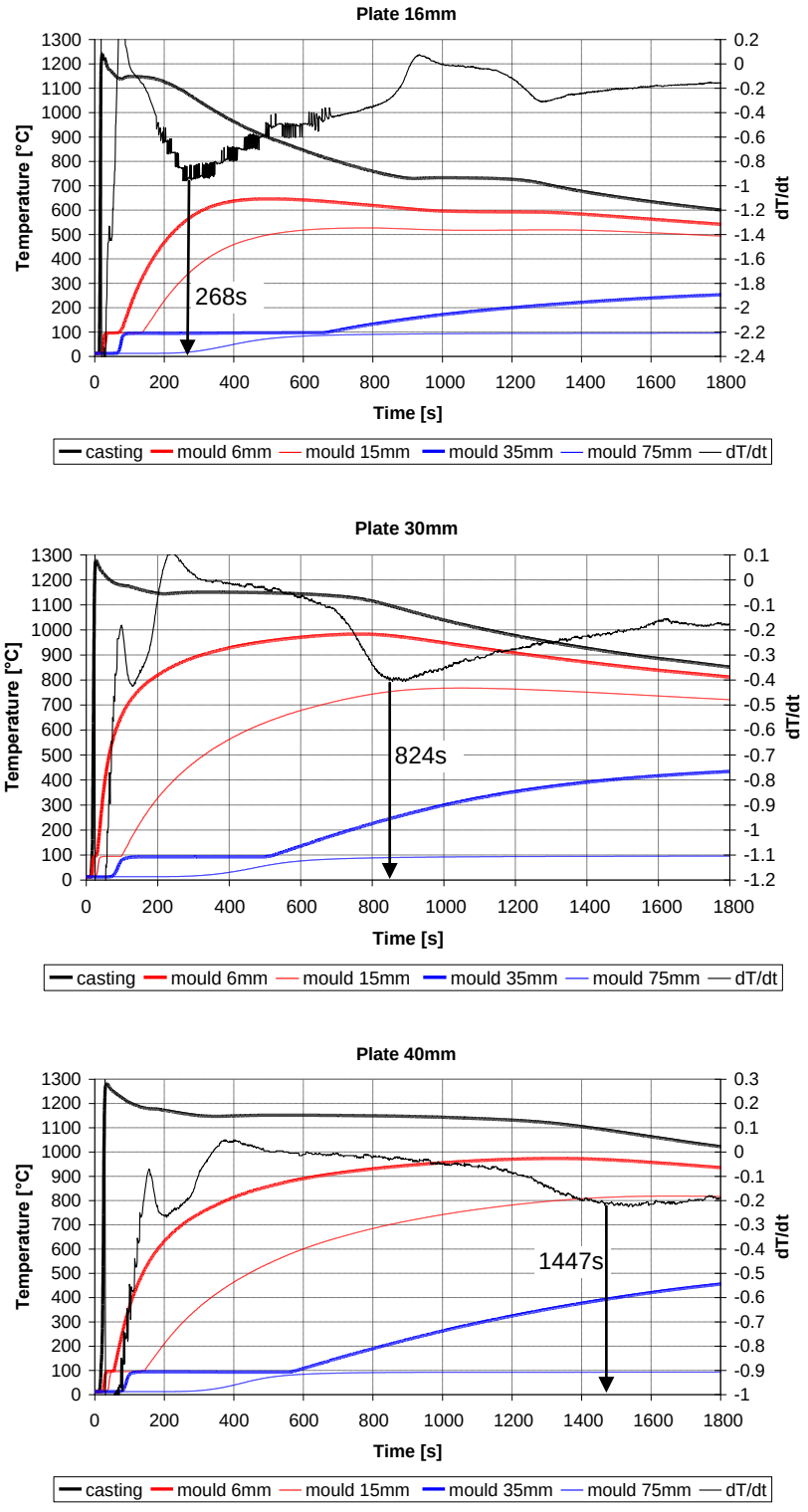

Fig.5: Results of the experimental studies (with solidification times identified by minimum of cooling curves first derivative)

As a result of the validation studies, carried out according to the scheme shown in the Fig.4, satisfying compatibility between curves from the simulation and from the experiment was achieved. The results of the simulation are shown in the Fig.6. The good agreement between times of solidification in the experiment and in the simulation was obtained. The values of obtained solidification times are shown in the graphs.

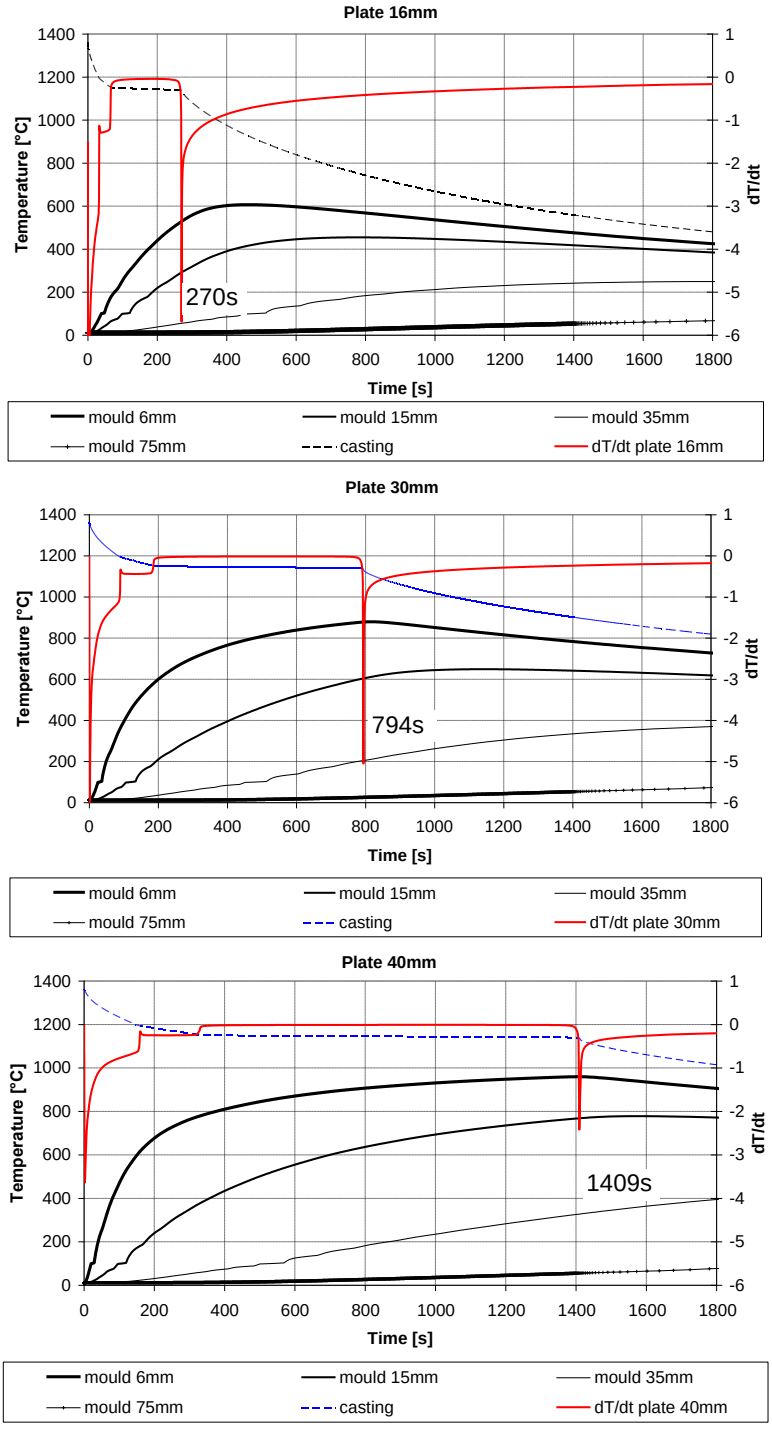

Fig.6: Results of the simulation studies (with solidification times identified by minimum of cooling curves first derivative)

Applying the rule resulting from the scheme presented in the Fig.4, thermo-physical parameters of the moist mould sand were determined. In these parameters, phenomena of appearance and movement of the over-moisture zone in the mould sand are taken into account. The specific heat was modified, considering heat of evaporation of the water contained in the sand, assuming temperature range of 98-102°C. It is presented in the graph of relation between the specific heat and the temperature for the tested sand mould (Fig.7). The thermal conductivity was adopted from NF&S and others

databases as λ=f(T) – selected values: λ=1,05 W/m/K for 20 ºC, λ=0,96W/m/K for 100ºC, λ=0,67 W/m/K for 500ºC, λ=1,04W/m/K for 1000ºC.

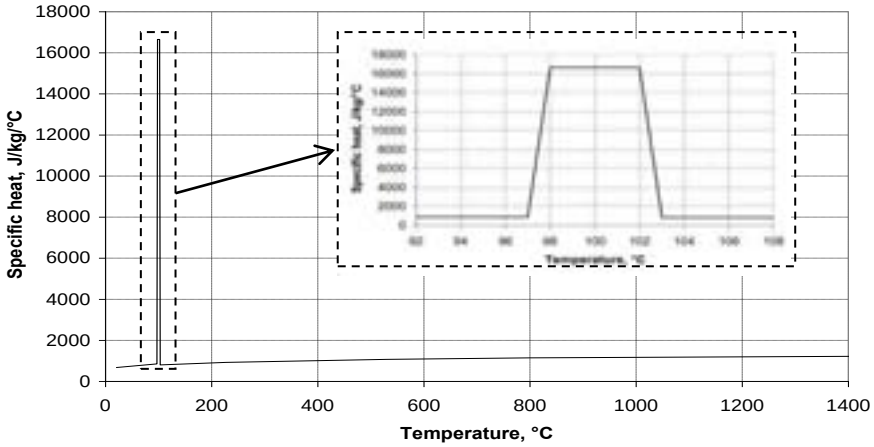

Fig.7: Substitute specific heat parameter of green sand mould determined by simplified inverse problem solution.

The thermo-physical parameters of the green mould sand determined on the basis of the validation studies were used in a simulation of castability trial[13] for cast iron EN-GJL-250 (look Table 1 – casting process parameters). The castability depends on fluidity of metal poured into standard mould cavity made of tested sand. In foundry practice this is the ability of alloy to flow through the gating system and filling the casting walls. The castability value as complex property combining both alloy and mould characteristics, is quantitatively defined by maximum length of the obtained casting (often on spiral shape). The filling of spiral canal is done without a refresh of stream front which is stopped by the local crystallization process. The results of two simulations of pouring process were compared; in the first one, data for the green sand was taken from the database of the NF&S CV system, in the second one – data determined in the described validation studies was used. The results of simulation are presented in the Fig.8 witch show an evident influence of presence of the over-moisture zone in the mould sand on filling of the castability trial.

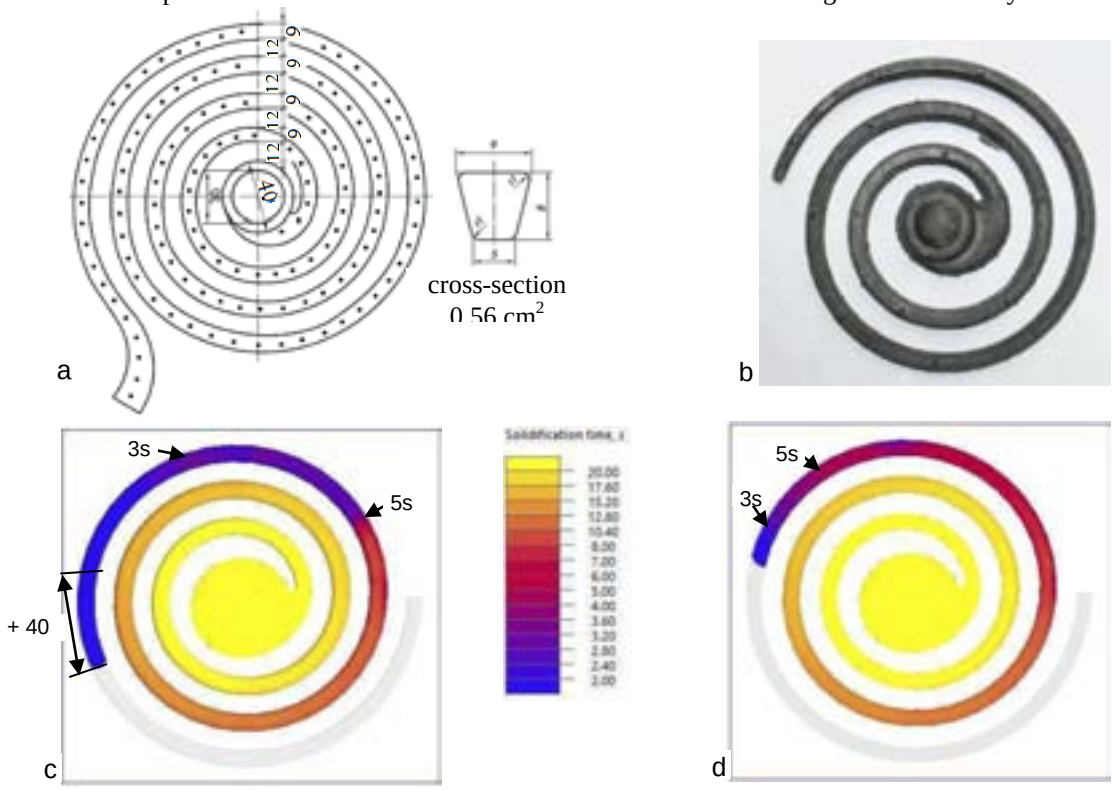

Fig.8: The comparison of filling process results: a – castability trial (spiral shape), b – result as real casting
c – simulation using mould sand parameters from the NF&S CV database, d – simulation using mould sand parameters (specific heat) determined by the validation studies

Conclusions

1. The described simulation-experimental studies allowed to estimate the thermo-physical properties of the moist mould sand, according to assumptions made in the paper. The presence of the over-moisture zone was taken into consideration (the specific heat data was modified by increasing its value about heat of evaporation of the water contained in the mould sand in the assumed temperature range of 98 – 102°C).
2. The results of simulation calculations using the determined thermo-physical data of the mould sand are similar to the experiment results.
3. The good compatibility of times of solidification of the plates castings was obtained (energetic validation condition was fulfilled). Also, a proper shape of heating curves was obtained from the simulation, in comparison with those recorded in the mould. On the heating curves from the simulation, the effect of presence of the over-moisture zone was obtained in form of short arrest in the temperature range around 100°C. The length of simulated arrest is significantly shorter than obtained in real experiment. This is caused by doesn't taking into consideration of vapor transfer and its condensation (assumed model simplification).
4. The handled data allowed to conduct a virtual experiment of castability trial. In such a way, a necessity of taking the parameters allowing re-creation of the over-moisture zone in the model into consideration was confirmed, when the cast iron casting is manufactured in the green sand. It is of great significance especially during simulation of filling of the canals of the gating system and thin walls of the casting.

References

1. T. Szmigielski: *Archives of Mechanical Technology and Automation,* 2004, 3, 163-171.
2. H.Wolff, S.Engler, A.Schrey, G.Wolf: *Giessereiforschung*, 4, 2002.
3. M. Rzeczkowski: Analysis of water circulation phenomena in the green sand moulds influenced by temperature (in Polish), *Scientific Letters* of WSInz, 1977 (book).
4. Z. Ignaszak, P. Popielarski, L. Graczyk: *Archives of Foundry*, 2006, 6, 216-223.
5. M.P.Chowdiach: *Giesserei*, 19, 1971, 582-590.
6. C.T.Marek: *Modern Casting*, 2, 1968.
7. Z. Pirowski, S. Pysz: *Journal of Research and Applications in Agricultural Engineering*, 2013, 1, 151-156.
8. T. Szmigielski: *Archives of Foundry*, 2003, 8, 267-272.
9. T. Szmigielski: *Proceedings of X Foundry Conference TECHNICAL (in Polish),* 2007.
10. https://www.esi-group.com/software-services/virtual-manufacturing/casting/procast-quikcast
11. http://novacast.se/products/novaflowsolid/
12. http://www.magmasoft.com/en/
13. BN-79/4051-17 – Polish Industy Standard: Technological castability trial for alloys.

Acknowledgement

The research was partially supported by 7FP-2012-7-NMP-ICT-FoF-314540 project

Production of a Heavy Section Ductile Iron Grinding Table

Ming You, Xiaogang Diao*
CITIC Heavy Industries Co., Ltd. Luoyang 471039, China

Production process of an extra-large ductile iron grinding table with weight of 142 t was introduced in the present paper. Solidification process of the grinding table was simulated with finite element software ProCAST. Defects, especially porosity, of the casting during solidification were predicted and hence casting process optimization has been performed based on the simulation results. In manufacturing period of the ductile iron grinding table, the following measures were adopted to avoid casting defects and improve its mechanical properties. Firstly, bottom-gated gating system was used. Secondly, chills were set on the heavy section locations. Thirdly, risers were set on the top of the casting. Besides, chemical composition was strictly controlled and raw materials with fewer impurities were used. More than 150 t molten melt was supplied using medium frequency induction furnaces. Cored wire injection nodularizing and inoculation was performed at 1360～1380℃ by two ladles with capacity of 75 t. Post–inoculation was conducted during pouring as well as low temperature and fast pouring process was adopted. The qualified heavy section ductile iron grinding table product can thus be obtained. Shrinkage and porosity was evidently decreased at thermal center of the casting. The result of casting inspection showed that mechanical properties of the casting met the requirements of EN-GJS-400-15U grade nodular iron and the UT detection didn't find any casting defect exceeding grade 3 according to EN 12680-3-2003.

Keywords: Heavy Section Ductile Iron; Grinding Table; Casting Process.

Introduction

Grinding table, whether ductile iron or cast steel, is a key part of vertical mill in the cement industry, for it affects directly the service life of vertical mill. As a result of spheroidal graphite, ductile iron possesses high castability together with improved mechanical properties, and is more economical in production in compared with cast steel. Ductile iron castings have promising applications due to a fantastic growth not only in the cement industry but also in mining, metallurgy, wind mill and nuclear industry.[1-5] In recent years an increase in the thickness of the castings has been desired due to the new requirements in the weight and size of machine parts, hence it is a challenge for manufacture factory to offer heavy section and extra large ductile iron castings with high quality and reliability.[1, 6-8]

The microstructure together with solidification defects, such as shrinkage porosity of heavy section ductile iron determines its mechanical properties. There are many factors influence the microstructure and solidification defects, such as gating system, chemical composition, cooling rate, liquid treatment and heat treatment.[9-13] Shrinkage porosity is one of the most common solidification defects.[14,15] It is often found in spheroidal graphite iron castings because of the mushy zone and special volume change during their solidification. The presence of porosity would deteriorate mechanical properties of the casting greatly. The main reason of shrinkage formation is that all metal alloys contract when it cools from the pouring temperature to the solidus. If the contraction is not compensated by supplying feed metal from the risers or the gating system, a pore will occur. Feeding system is efficient until the amount of solid phase reaches a certain level.[2] Solidification defects in heavy section ductile iron have been the subject of several research projects, but it is more difficult to fabricate such a casting with no shrinkage porosity in practice.

In this work, production of ductile iron grinding table with weight of 142 t was introduced. Casting process was optimized based on ProCAST and melt treatment with cored wire injection and inoculation in the pouring basin was used to obtain a qualified casting.

Experimental Procedure

The melting process was carried out in medium frequency induction furnaces with 60t-12t-12t and 60t-30t-12t in capacity. Furnace charges for the selected composition were pig iron, steel scrap, and carbon additive. Raw materials with fewer impurities were used. Chemical composition was strictly controlled and nominal composition of the casting is 3.6%C, 1.9%Si, <0.2%Mn, <0.025%P and <0.015%S. After melting was finished, the chemical compositions of the metal were adjusted according to the results of spectrometry analysis done on a coin sample. The melt was then heated to 1500°C—1510°C to destroy any possible pre-existing nuclei. Slag was removed from the melt surface before being poured into two preheated ladles with 75 t in capacity.

*Corresponding author, email: xgdiao@126.com

Specimen for mechanical properties is cut from a 75 mm thick block attached to the casting. Each datum was averages of three tensile tests. Metallographic samples were taken directly from the tensile test specimens. Optical microscopy was performed after standard metallographic procedure on polished and etched specimens. The matrix structure is obtained following application of a nital (4%HNO_3 in ethanol solution) etch for 20 seconds.

Results and Discussion

Simulation of casting process

Fig. 1 shows the geometry and dimensions of the ductile iron grinding table casting. Diameter of the casting is more than Φ6000 mm and height of the casting is 2456 mm. Its minimum wall thickness is 200 mm while maximum wall thickness exceeds 300 mm. The diameter of hotspot is Φ573 mm. EN-GJS-400-15U was used in place of cast steel in our practice. The casting would be rejected if any casting defect exceeding grade 3 is found after UT detection according to EN 12680-3-2003.

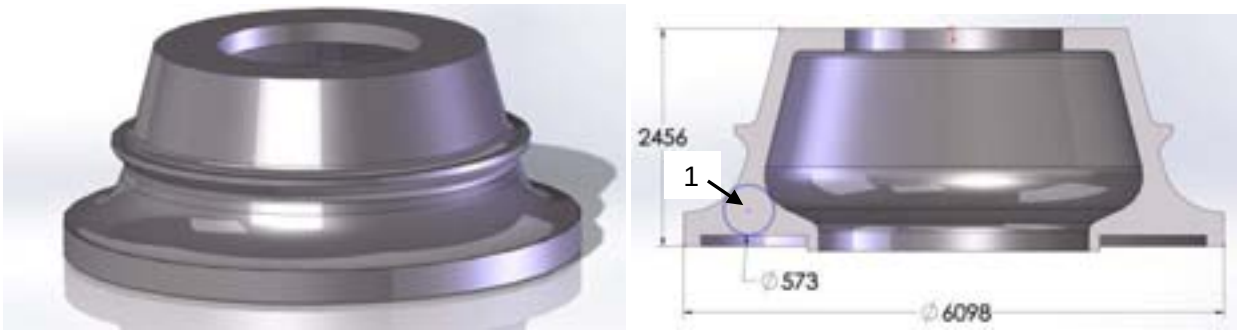

Fig.1: Geometry and dimensions of ductile iron grinding table (dimensions in mm)

Advanced simulation could be used to better understand and control such a complex solidification behavior. A commercial software ProCAST is used to predict solidification defects of the ductile iron casting. The pouring temperature at the gating inlet is 1330°C while ambient temperature is 30°C. The solidus and liquidus temperature are used as 1143°C and 1187°C, respectively. The other properties of the material, e.g. conductivity, density, viscosity, enthalpy and solid fraction are dependent upon the temperature based on ProCAST.

Fig. 2 gives simulated cooling curve of the last solidified area at the lower part of the grinding table. It is more than 28 h after the casting fully solidified, thus it leads to graphite degeneration, shrinkage porosity, etc. There exists much shrinkage porosity in the last solidified area, as confirmed in Fig. 3.

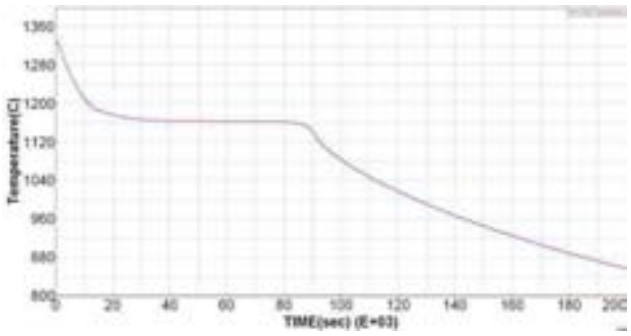

Fig.2: Simulated cooling curve of point 1 at thermal center.

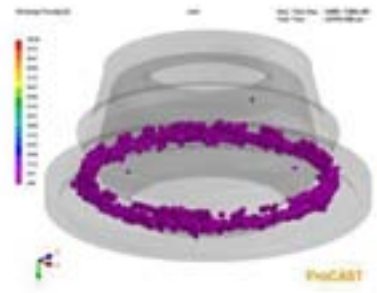

Fig.3: Shrinkage porosity prediction of the casting.

Fig.4 shows scheme diagram of an optimized casting process. Bottom-gated gating system was used and risers were set on the top of the casting. Cooling rate plays a significant role in reducing solidification time and hence shrinkage porosity of ductile iron. In order to reduce solidification time, chills are normally used, especially for a heavy section ductile iron casting. Therefore chills were set on the heavy section locations in order to make the casting solidify in sequence. Solidification time of the last solidified area (point 1 in Fig.1) reduce to about 4h, as shown in Fig.5. Short solidification time and sequence solidification help the reduction of shrinkage porosity area ratio of the casting compared with no chill used (see Fig.3 and Fig.6).

Fig.4: Schematic diagram of casting process.

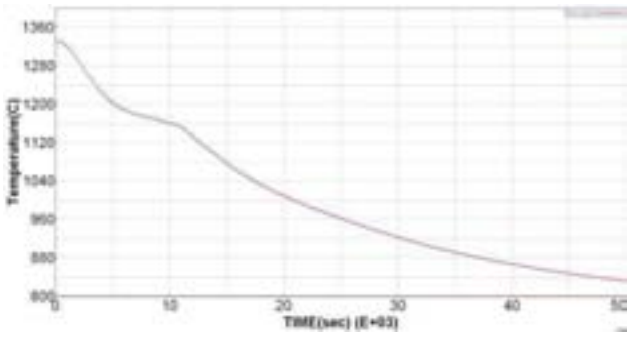

Fig.5: Cooling curve of point 1 at thermal center after casting process optimization.

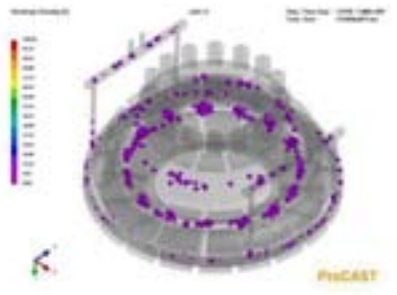

Fig.6: Shrinkage porosity prediction of the casting after casting process optimization.

Spheroidal and inoculation treatment

Heavy section ductile iron presents a unique metallurgical challenge, which can affect a casting's microstructure and shrinkage porosity. Spheroidal and inoculation treatment is very important to its microstructure and mechanical properties of ductile iron casting.

Although conventional sandwich process is used widely up to now, it is better to adopt wire feeding method instead for an extra large ductile iron casting. Fig.7 gives nodulization and inoculation treatment process with wire feeding method. They were performed at a melt temperature of 1360°C -1380°C at the same time. The amount of tapped liquid iron was more than 150 tons. The pouring temperature was 1310~1330°C.

It appears that long time after the wire feeding leads to fading of the inoculant, increasing risk of graphite degeneration and carbide formation. Therefore, additional inoculants were added in the large pouring basin to inoculate uniformly, as shown in Fig.8. The number of graphite nodules increases with increasing graphite nucleus. The addition of inoculants is beneficial to obtain high graphite grade and improve mechanical properties of the casting. The composition of cast-on sample was (wt%): 3.47C, 1.87Si, 0.17Mn, 0.011S, 0.024P, 0.061Mg and 0.013RE.

Fig.7: Spheroidal and inoculation treatment process of the casting in the cored-wire injection station.

Fig.8: Inoculant in the large pouring basin.

Microstructure and Mechanical properties

Fig.9 presents the microstructures of a cast-on sample. The nodularity of the cast-on sample was 85%-90% and graphite nodules appear almost uniform in size and evenly distributed in the matrix. It is found that solidification time has a significant effect on the morphology and size of graphite. Increasing the cooling rate leads to fine graphitization and favors spheroidal graphite formation. Hence no degenerated graphite is found in the picture with the help of chills used during solidification. Most of the matrix is nearly ferrite structure, and less than 10%-15% pearlite can be observed in the microstructure, as shown in Fig. 9(b).

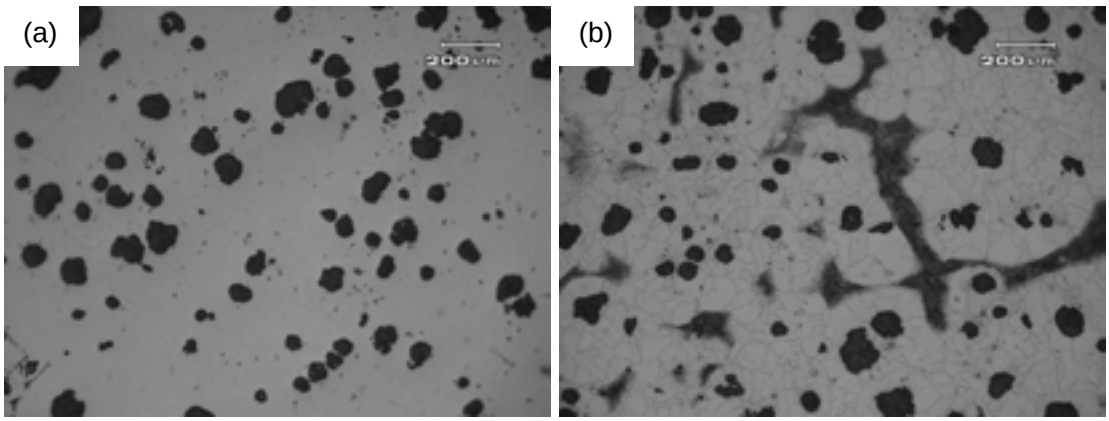

Fig.9: microstructures of ductile iron grinding table casting.
(a) unetched; (b) etched;

The mechanical properties measured are shown in Table 1. Tensile strength, elongation and hardness of the cast-on sample were above the requirements of EN-GJS-400-15U. Ultra-sonic test (UT) was performed and any casting defect exceeding grade 3 according to EN 12680-3-2003 was fully eliminated.

Table 1 Mechanical properties of the ductile iron grinding table.

	σ_b [MPa]	σ_s[MPa]	δ[%]	HB
target	≥370	≥240	≥12	120～180
No 1	412	291	14	169
No 2	407	285	16	160
No 3	405	282	15	162

Conclusions

1. Simulation is an effective way for a casting, especially extra large ductile iron casting. Both the cost and time is reduced and a qualified casting is obtained.
2. Shrinkage porosity can be reduced with the help of sequence solidification for a heavy section ductile iron casting.
3. Spheroidal and inoculation treatment is very important. Melt treatment with cored wire injection, and especially inoculation in the pouring basin is beneficial to its microstructure and mechanical properties of ductile iron casting
4. Ductile iron grinding table with good mechanical properties can replace cast steel casting.

References

1. C. Labrecque and M. Gagné: *Can. Metall. Quart.*, Vol. 1998, 37, 343-351.
2. M. You and X. Diao. *Advanced Materials Research*, 2012, 567, 141-145.
3. P. M. Cabanne, M. Gagne. Ductile Iron and Wind Energy: A Symbiotic Relationship. World Foundry Congress, Istanbul, 2004: 877-885.
4. D. M. Stefanescu, in ASM Handbook, eds. D. M. Stefanescu, N. Lillybeck (ASM International, 1998), Paper 625.
5. H. Itofuji, K. Kawamura, N. Hashimoto, H. Yamada, *AFS Transactions*, 1990, 43, 585-595.
6. K. F. Nilsson, M. Burstrom, F. Lofajand C. G. Andersson: *Eng. Fail. Anal.*, 2007, 14, 47-52
7. R. Källbom, K. Hamberg, M. Wessénand L. E. Björkegren: *Mater. Sci. Eng., A*, 2005, 413-414, 346-348
8. P. Minnebo, K. F. Nilssonand D. Blagoeva: *J. Mater. Eng. Perform*., 2007, 16, 35-41
9. M. N. Ahmadabadi, E. Niyama, M. Tanino, T. Abe, and T. Ohide: *Metall. Mater. Trans. A*, 1994, 25, 911-917
10. L. Collini, G. Nicoletto, and R. Konecna: *Mater. Sci. Eng., A*, 2008, 488, 529-534
11. K. F. Nilsson and V. Vokal: Mater. *Sci. Eng., A*, 2009, 502, 54-58
12. P. K. Basutkar, C. R. Loper, and C. L. Babu: *AFS Trans.*, 1970, 78, 429-435
13. J. Wang, P. Fu, H.Liu, D. Li and Y.Li. *Mater. and Design*. 2012, 35, 446-456.
14. B. Pustal, B. Hallstedt, W. Schafer, C. Bartels, E. Subasic, H. Siebert, J. M. Schneider, and A. Buhrig-Polaczek: *Adv. Eng. Mater*., 2010, 12, 158-169
15. D. M. Stefanescu: 'Computer simulation of shrinkage-related defects in castings - A review', 295-304; 2005, Warrendale, Minerals, Metals & Materials Soc.

Modelling of Density Changes of Nodular Cast Iron During Solidification by Cellular Automaton

D. Gurgul[1*], A. Burbelko[1], E. Guzik[1], D. Kopyciński and M. Królikowski[2]
[1]AGH University of Science and Technology, 23 Reymonta Str., 30-059 Krakow, Poland
[2]Odlewnie Polskie S.A., 70 Wyzwolenia Av., 27-200 Starachowice, Poland

Results of predictions of nodular cast iron density changes during solidification are presented. These changes were calculated by using a mathematical model which bases on a Cellular Automaton - Finite Differences (CA-FD) method. The CA-FD model takes into account, among others, the independent nucleation of graphite and austenite as a function of undercooling, the migration rate of the grains' borders, non-uniform distribution of temperature and concentration in the calculation domain, diffusion of the carbon in the liquid and the austenite. All simulation were performed at various: nucleation intensity and the eutectic saturation. It has been shown and proofed by other authors that the shrinkage phenomena take place at three stages: pre-eutectic shrinkage, eutectic expansion, and final shrinkage.

Keywords: cellular automaton, ductile iron, solidification modelling, density prediction.

Introduction

Nodular cast iron also known as ductile iron (DI) has major applications in critical engineering parts because of its mechanical and casting properties. These features of this material depend on the shape and number of graphite grains and on the structure of a metallic matrix. One of the most important thing in manufacture DI castings is the density changes during cooling and solidification.

Density of most materials increases during solidification. It means that the volume of the solid phase is smaller than the initial liquid phase. This causes in foundry engineering the need of use the feeding systems in order to eliminate the shrinkage defects. Exceptions to this rule, for example, water and bismuth are. Volume of these substances increases during the transformation from liquid state into solid state. It is caused by a specific structure of the crystal lattice. Similarly to water and bismuth the DI may behave under certain conditions. The reason for the volume expansion when cast iron solidifies (DI as well as grey cast iron – GCI) is precipitation of graphite which density is almost three times smaller than other phases. However, as the foundry practise shows, to obtain a "healthy" cast, with no shrinkage defects, made of DI is very difficult for small values of the casting's thermal module (under about 12 mm).[1]

The conditions at which graphite in DI grows are different from conditions of growth graphite in other kinds of cast iron. In GCI both primary and eutectic graphite are in permanent contact with the parent liquid phase. Additionally, the eutectic graphite grows with constant contact of three phases (graphite-austenite-liquid).

In DI the globules of the primary and the eutectic graphite, at initial stage, do not have a connection with austenite dendrites and they grow directly from the liquid.[2,3] Growing graphite particles deplete the liquid of the carbon. Such a poor carbon region is a privileged place for growing austenite. This results in acceleration of the austenite dendrite branches' growth in direction to graphite globules. After reaching the connection the austenite envelopes and isolates the graphite globules. Further growth of enclosed graphite nodules is also possible, because the carbon can diffuse from the liquid to the graphite surface through the austenite shell.

Analysed industrial castings, made of DI in one of the Polish foundry, are characterised by the same, known from literature, shrinkage defect typical for this alloy: [4]

1) the mechanism of feeders action is far more complicated than in alloys which have no expansion; sometimes elimination of feeders causes decrease of porosity,
2) minimal porosity level occurs in the eutectic alloys in which an increase of the carbon concentration in eutectic has a positive effect,
3) porosity of GCI casting is considerably smaller than in DI castings.

An example of shrinkage porosity that may occur in industrial castings made of DI is shown in Fig. 1. Such a defect has a negative effect on strength and leakproofness of castings.

* Corresponding author, email: dg@agh.edu.pl

a) b)

Fig. 1: An example of shrinkage defect in a DI casting (a); a place of the section indicated by the arrow (b).

Another examples of shrinkage defects (shrinkage cavities in feeders) in DI castings made of EN-GJS-400-18 are presented in Fig. 2. Carbon concentration was evaluated by use of Active Carbon Equivalent (ACE) which was measured by Adaptive Thermal Analysis System (ATAS). The value of ACE changed from 4.15 to 4.28 wt.%. Fig. 2 shows that the higher carbon concentration is the smaller volume of voids in the feeders is. Unfortunately, experience dictates that it does not always lead to the reduction of the level of shrinkage defects.

a) b) c) d)

Fig. 2: Influence of the ACE on the cavity shape in feeders for DI EN-GJS-400-18; ACEL values: a) 4.15 wt.%, b) 4.18 wt.%, c) 4.22 wt.%, d) 4.28 wt.%.

The mechanism of shrinkage defect formation is still under discussion, even though it is obvious that the main reason for this is the volume change of alloy during cooling and phase transformation. This paper presents assessments of the specific volume change in DI during solidification by use of the CA-FD.

The CA-FD model

Models which adopt a cellular automaton technique and the finite different method are one of the known methods used in computer modelling of solidification. They have been a subject of many studies.[5-15] All of these models are used for mono-phase transformations. Models used for two-phase solidification are also known,[3,16] but they are not as numerous as single-phase.

The CA-FD model used in this paper can calculate the microstructure of DI for binary Fe-C system during cooling of a casting at a superimposed cooling rate. The model takes into account: the continuous nucleation of austenite and graphite grains, separate non-equilibrium growth of the graphite nodules and the austenite dendrites at the initial stage of solidification, and cooperative growth of the graphite-austenite eutectic at further stage. In order to do this it is required to take into consideration, in the computational model, a number of physical phenomena such as: heat flow, carbon diffusion, interfacial energy and its influence on the crystallization front, heterogeneous nucleation, and release of latent heat.

The distinctive features of the CA-FD models is fact that the inner structure and the shape of growing grains are not superimposed at the beginning of calculations. They are effect of conditions which occur at the crystallization front during solidification. In order to obtain the satisfactory inner structure and the shape of grains (both for austenite dendrites and graphite nodules) the calculation meshes used for temperature and concentration fields should have the spatial step equal to the order of one micrometre. Such a small step limits using this method only for micro regions in two-dimensional space. It is caused by limited memory and computational power of modern computers.

The kinetic undercooling is a measure of the thermodynamic driving force of phase transformation. The total undercooling at the interface is equal to the difference between the equilibrium temperature T_{eq} (as a function of carbon

content) and the real temperature T_r at the front. On the other hand this difference is equal to the sum of the capillary undercooling ΔT_κ and the kinetic undercooling ΔT_μ:

$$T_{eq} - T_r = \Delta T_\kappa + \Delta T_\mu \tag{1}$$

where $\Delta T\kappa = \Gamma \cdot \kappa$, Γ is the Gibbs-Thomson coefficient, and κ is the front curvature.

The interface migration rate was assumed as a linear function[17] of the local kinetic undercooling ΔT_μ:

$$u = \mu \Delta T_\mu \tag{2}$$

where μ is the kinetic growth coefficient (various for austenite and graphite).

The heat flow in the computational domain was described by the Fourier equation:

$$c\frac{\partial T}{\partial \tau} = \nabla(\lambda \nabla T) + q_T + q_{cool} \tag{3}$$

where: T is the temperature, τ is the time, λ is the thermal conductivity, c is the volumetric specific heat. The terms q_T and q_{cool} are the source of latent heat generation rate and the intensity of external cooling respectively.

The carbon diffusion in the domain is similarly described to equation (3) by the following equation:

$$\frac{\partial C}{\partial \tau} = \nabla(D \nabla T) + q_C \tag{4}$$

where D is the carbon diffusion coefficient (various for liquid and austenite), and C is the carbon concentration in the appropriate phase. The term q_c is responsible for the carbon rejection by the crystallization front. This is caused by different solubility of the carbon in the liquid and the austenite.

Both equations (3) and (4) were numerically solved by using the finite differences (FD) method.

Grain nucleation in industrial alloys has a heterogeneous nature. Substrates for nuclei are randomly distributed in the bulk. The size of the substrates also has a stochastic nature. The undercooling at which a substrate becomes active is a function of substrates' size. The functional relationship between the active substrate fraction and the undercooling ΔT should be expressed by a probability distribution law.[18] The undercooling value of each phase should be calculated relatively to the appropriate liquidus line. The number n of active substrates in a domain V at undercooling ΔT below the equilibrium temperature can be calculated on the basis of a cumulative distribution function $F(\Delta T)$:

$$n = N_{\max} F(\Delta T) V \tag{5}$$

where $N_{\max}$ is the maximum specific number of substrates for nucleation.

In the CA-FD model as function $F(\Delta T)$ the Weibull cumulative distribution was assumed:[19]

$$F(\Delta T) = \exp(-b/\Delta T) \tag{6}$$

where b is an experimental coefficient.

Only one substrate is placed in the small domain V (a cell of the CA) if the n value is greater than the random number p generated with the equiprobability distribution in the (0..1] range. The undercooling of the potential nucleation in this case is estimated as an inverse function of the equation (6):

$$\Delta T = -b/\ln(p/(N_{\max} V)) \tag{7}$$

More details of stochastic nucleation are described in.[20]

The cellular automaton (CA) adopted to this model has a set of six states of cells. At the beginning of simulation all cells have the same state – liquid. When the temperature inside a cell drops down below the equilibrium temperature this cell may change its state from liquid to transitional state. The transitional state means that inside this cell a phase transformation can happen. There are three types of the transitional states: the transition from liquid into austenite $L \rightarrow \gamma$, from liquid to graphite $L \rightarrow gr$, and, when a graphite nodule grows inside austenite, the transition from austenite to graphite $\gamma \rightarrow gr$. An increment Δf of a new phase inside each transitional cell is calculated by the fallowing equation:

$$\Delta f = \frac{u \Delta \tau}{a(|\cos\theta| + |\sin\theta|)} \tag{8}$$

where: $\Delta\tau$ is the time step, a is the side length of the CA cell (for square cells), and θ the angle between the X axis and the normal direction to the front.

When a transitional cell finishes the transformation it changes its state into a solid state. There are two types of solid states. If the transformation $L \rightarrow gr$ or $\gamma \rightarrow gr$ takes place, the cell gets the graphite state. For the transformation $L \rightarrow \gamma$ the cell is changed into the austenite state.

Other details of the CA-FD model are introduced elsewhere.[21-24]

Density estimation

Density of specific phases was determined by means of CALPHAD method,[25] using Thermo-CALC® software. Obtained from Thermo-CALC® data were used for creating regression equations. For each phase the density changes ρ, kg/m^3, as a function of temperature (for liquid, austenite and graphite) and carbon concentration (only for liquid and austenite) were determined. The equations have the following forms:

– for the liquid phase:

$$\rho_L = 8192.2 - 0.5402 \cdot T - 9805.3 \cdot C \tag{9}$$

– for the austenite phase:

$$\rho_\gamma = 8238.7 - 0.48684 \cdot T - 3876.0 \cdot C - 5982.0 \cdot C^2 \tag{10}$$

– for the graphite phase:

$$\rho_{gr} = 2292.9 - 0.067442 \cdot T \tag{11}$$

where: T is temperature, K; C is carbon mass fraction.

The equations (9), (10) and (11) work in temperature range from 1010 K to 1610 K. The concentration ranges for equations (9) and (10) are from 3.9 to 4.8 mass % and from 0.5 to 2.5 mass % respectively.

Simulation results

The calculations were performed for a modelling alloy that solidifies like DI (with divorced eutectic). All simulations were conducted on a computational mesh with 640×640 cells and a spatial step equal to 2 μm. The thermophysical properties of the modelling alloy are listed in Table 1. The are adequate to the binary Fe-C alloy. Three variants of chemical composition were analysed: eutectic (C_0=4.25 wt.% C), hypoeutectic ($0.95 \cdot C_0$), and hypereutectic ($1.05 \cdot C_0$).

Samples were cooled with a cooling rate which is typical for a DI casting with 9 mm wall thickness moulded in a greensand mould:

$$q_{cool} = -5.082 \cdot c_v \cdot \exp\left(-5.307 \cdot 10^3 \cdot \tau\right) \tag{12}$$

where c_v is the mean volumetric specific heat for the alloy.

In the simulations it made an analysis for the alloy with various intensity of nucleation. In the calculations it was analysed the influence of a number of graphite spheroids on the alloy density change during solidification. A graphite nodules number depends on an amount of inoculant which is put into the alloy during so-called secondary metallurgy or out-of-furnace alloy treatment. In the simulations the change of the nucleation intensity was considered by a various number of the coefficient N_{max}: 10^9, 10^{10} and 10^{11} m^{-2}.

The obtained cooling curves presented in Fig. 3. As it can be noticed the increase of the nodule number does not impact practically on the duration process. The increase of the nodule number causes the fact that the transformation requires lower undercooling and it takes place at higher temperatures. The maximal recalescence is observed in DI samples with hypereutectic composition. In samples with hypoeutectic composition the recalescence does not appear practically.

Density changes for DI together with changes of liquid fraction are presented in Fig. 4. In this figure it is shown that independently of the eutectic level the density changes can be divided into three stages: pre-eutectic shrinkage, eutectic expansion, and final shrinkage. The presence of the pre-eutectic shrinkage, both in eutectic and slightly hypereutectic DI, has been proved by an experiment[26] carried out by using Combined Liquid Displacement and Cooling Curve Analysis (CLD CCA) method. In contrast, the final shrinkage in DI with hypoeutectic composition has been experimentally proved in. [27]

The pre-eutectic shrinkage also takes place in hypereutectic DI. The precipitation of the primary graphite slows down slightly the shrinkage at this stage of solidification, but it does not eliminate the shrinkage completely. The better a sample is inoculated, the inhibition of the shrinkage begins earlier. In this case, the transition into the eutectic expansion also happens earlier. The reason of the pre-eutectic shrinkage in hypereutectic DI is decreasing of the liquid density when the temperature of the alloy drops down. The partial expansion of DI, caused by the primary graphite solidification, only decreases the intensity of the pre-eutectic shrinkage. However, this expansion does not compensate completely for the shrinkage.

The minimal density values, at the instant when the eutectic expansion finishes and when the final shrinkage starts, are listed in the Table 2 (the numerators). The increase of the graphite nodules number results in the small density decrease. The amount of the vanishing liquid in this moment is shown in the Table 2 as the denominators. In DI with a smaller number of graphite nodules the final shrinkage begins earlier, when the liquid volume fraction is grater and equal to about 5 %.

Table 1: The thermophysical properties used in the modelling.

Heat conductivity ($W \cdot m^{-1} \cdot K^{-1}$):		
– liquid[9]	λ_L	30
– austenite[28]	λ_γ	20
– graphite[9]	λ_{gr}	20
Diffusivity of carbon in (m^2/s):		
– liquid[29]	D_L	$1.25 \cdot 10^{-9}$
– austenite[9]	D_γ	$5 \cdot 10^{-10}$
Latent heat (J/m^3):		
– liquid – austenite[30]	$L_{L\to\gamma}$	$19.7 \cdot 10^{8}$
– liquid – graphite	$L_{L\to gr}$	$16.2 \cdot 10^{5}$
– austenite – graphite	$L_{\gamma\to gr}$	$8.8 \cdot 10^{5}$
Specific heat ($J \cdot m^{-3} \cdot K^{-1}$):		
– liquid[30]	c_L	$5.6 \cdot 10^{6}$
– austenite[9]	c_γ	$5.84 \cdot 10^{6}$
– graphite[30]	c_{gr}	$1.78 \cdot 10^{6}$
Gibbs-Thomson coefficient for interface (m·K):		
– austenite – liquid[30]	$\Gamma_{L\to\gamma}$	$1.9 \cdot 10^{-7}$
– graphite – liquid	$\Gamma_{L\to gr}$	$7.0 \cdot 10^{-6}$
– graphite – austenite	$\Gamma_{\gamma\to gr}$	$9.45 \cdot 10^{-6}$
Kinetic coefficient of the interface ($m \cdot s^{-1} \cdot K^{-1}$):		
– austenite – liquid[31]	$\mu_{\gamma/L}$	10^{-3}
– graphite – liquid	$\mu_{gr/L}$	10^{-8}
– graphite – austenite	$\mu_{gr/\gamma}$	10^{-8}

The presented density, in the Table 2 and in the Fig 4, does not take into account potential shrinkage porosity. The real density can be lower which is caused by presence of discontinuity in material.

Table 2: The ratio between the minimal alloy density and the liquid fraction at the moment when the final shrinkage begins.

Alloy Composition	Graphite nucleation coefficient N_{max}, m^{-2}		
	10^9	10^{10}	10^{11}
Hypoeutectic	6959.6/5.51	6948.4/2.15	6942.0/1.60
Eutectic	6923.2/5.45	6910.7/2.17	6905.2/1.35
Hypereutectic	6884.8/4.34	6873.5/2.41	6868.0/1.20

As it follows from Table 2 and Fig. 4, better inoculation (higher N_{max}) results in the decreasing of the residual liquid phase volume at the instant of eutectic expansion termination and final shrinkage start.

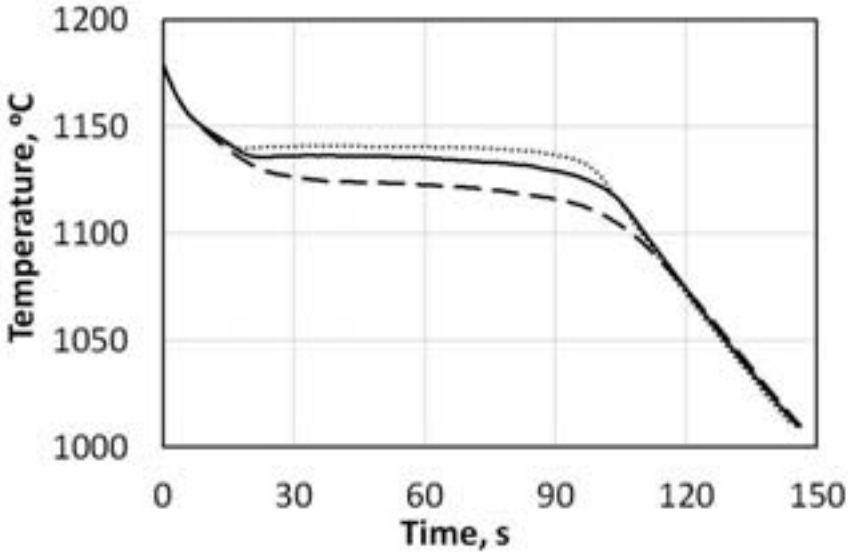

a)

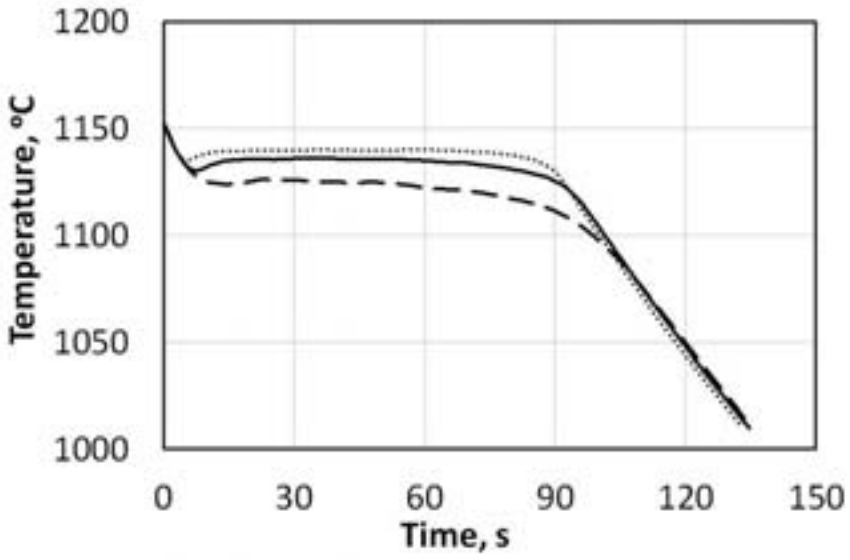

b)

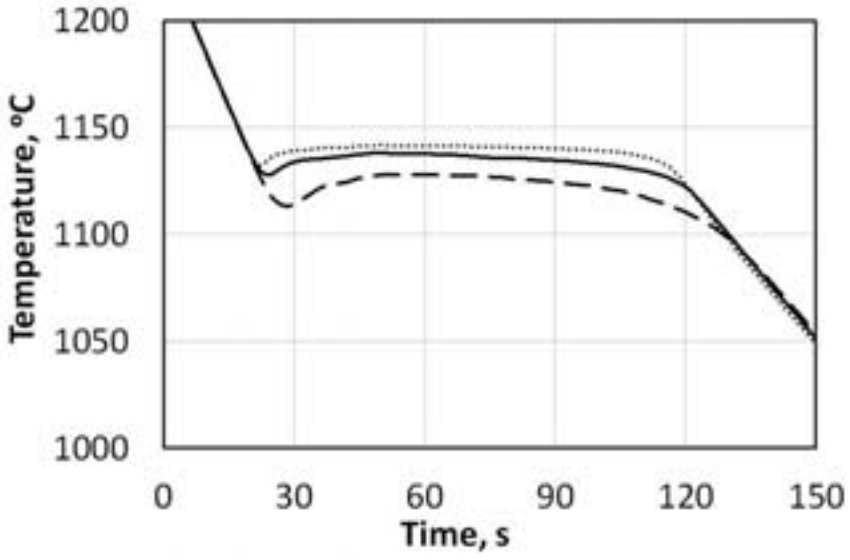

c)

Fig. 3: Cooling curves of the analysed alloys for the graphite nucleation coefficient N_{max}: 10^9, m^{-2} – the dashed lines, 10^{10}, m^{-2} – the solid lines, 10^{11}, m^{-2} –the dotted lines; a) the hypoeutectic alloy, b) the eutectic alloy, c) the hypereutectic alloy.

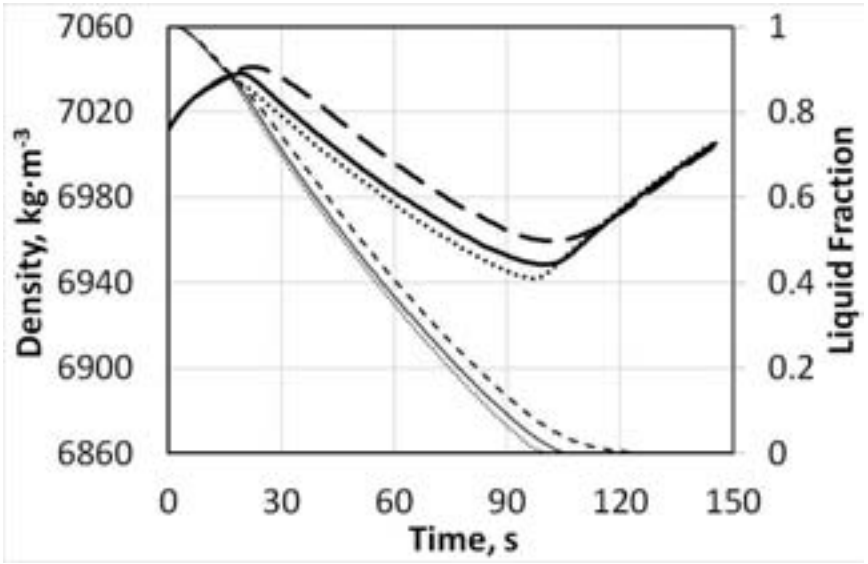

a)

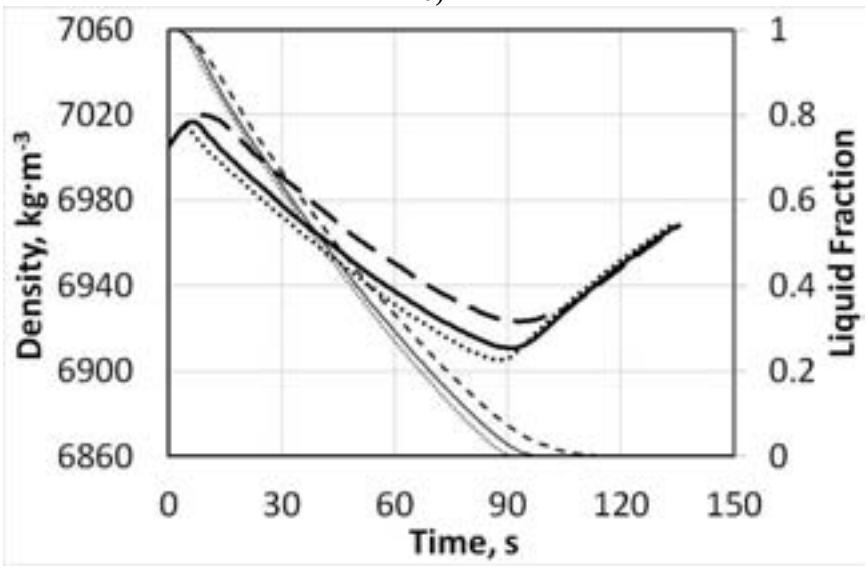

b)

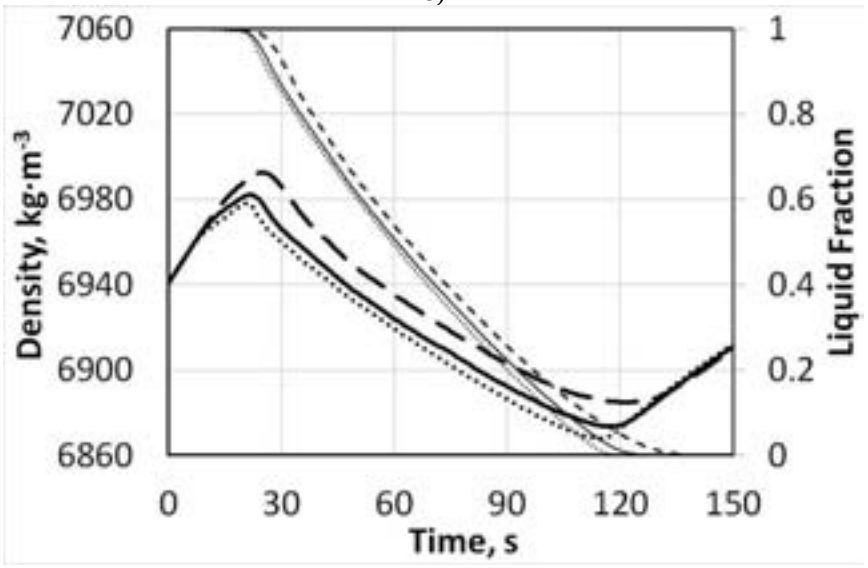

c)

Fig. 4: The density changes of DI (bold lines) and the liquid fraction (thin lines) during solidification; the graphite nucleation coefficient N_{max}: 10^9, m^{-2} – dashed lines, 10^{10}, m^{-2} – solid lines, 10^{11}, m^{-2} – dotted lines; a) hypoeutectic alloy, b) eutectic alloy, c) hypereutectic alloy.

Conclusions

1. In the paper a new tool has been tested which was designed to confirm by calculation the variability of the density of DI cast iron resulting from the additivity of precipitated phases.
2. It has been confirmed by numerical calculations that the density changes for hypoeutectic, eutectic, and hypereutectic alloys proceeds at three stages: the pre-eutectic shrinkage, the eutectic expansion, and the final shrinkage.
3. The pre-eutectic shrinkage in the DI occurs not only in the hypoeutectic or eutectic alloy. In the hypereutectic alloys it is caused by the fact that the effect of the expansion, which is generated by the primary graphite solidification, is weaker than the effect of the simultaneous liquid density increasing during the temperature dropping.
4. The observed density changes are consistent with the results obtained by use of the CLD CCA method.[26, 27]

References

1. The Sorelmetal Book of Ductile Iron. Rio Tinto Iron & Titanium, 174, 2004.
2. H. Fredriksson, J. Stjerndahl and J. Tinoco: *Mater. Sci. Eng., A*, 2005, 413-414, 363-372.
3. A. Burbelko, E. Fraś, D. Gurgul and J. Sikora: *Key Eng. Mater.*, 2011, 457, 330-336.
4. I. Ohnaka, A.Sato, A. Sugiyama and F. Kinoshita: *Int. J. Cast Met. Res*., 2008, 21, 11-16.
5. A.R. Umantsev, V.V. Vinogradov and V.T. Borisov: *Kristallografia*, 1985, 30, 455-460.
6. M. Rappaz and Ch.A. Gandin: *Acta Met. et Materialia*, 1993, 41, 345-360.
7. S. Pan and M. Zhu: *Acta Mater*., 2010, 58, 340-352.
8. G. Guillemot, Ch.A. Gandin, M. Bellet: *J. Cryst. Growth*, 2007, 303, 58-68.
9. L. Beltran-Sanchez and D.M. Stefanescu: *Metall. Mat. Trans. A*, 2004, 35, 2471-2485.
10. V. Pavlyk and U. Dilthey: *Model. Simul. Mat. Sci. Eng*., 2004, 12, 33-45.
11. M.F. Zhu and C.P. Hong: *ISIJ Int*., 2002, 42, 520-526.
12. D.S. Svyetlichnyy: *Comput. Mater. Sci*., 2012, 60, 153-162.
13. A.A. Burbelko, E. Fraś, W. Kapturkiewicz and D. Gurgul: *Mat. Sci. Forum*, 2010, 649, 217-222.
14. D.J. Jarvis, S.G.R. Brown and J.A. Spittle: *Mat. Sci. Techn*., 2000, 16, 1420-1424.
15. A.A. Burbelko, E. Fraś, W. Kapturkiewicz and E. Olejnik: *Mat. Sci. Forum*, 2006, 508, 405-410.
16. H.L. Zhao, M.F. Zhu and D.M. Stefanescu: *Key Eng. Mater.*, 2011, 457, 324-329.
17. J. Hoyt and M. Asta: *Phys. Rev. B.*, 2002, 65, 1-11.
18. Ch.A. Gandin and M. Rappaz: *Acta Metall. Mater*., 1994, 42, 2233-2246.
19. E. Fraś, K. Wiencek, M. Górny and H. Lopez: *Archives of Metallurgy*, 2001, 46, 317-333.
20. W. Kapturkiewicz, A.A. Burbelko, E. Fraś, M. Górny and D. Gurgul: *Journal of Achievements in Materials and Manufacturing Engineering*, 2010, 43, 310-323.
21. A. Burbelko, D. Gurgul, W. Kapturkiewicz and M. Górny: *Mat. Sci. Eng.*, 2012, 33, 012083, 1-9.
22. A.A. Burbelko, D. Gurgul, W. Kapturkiewicz and M. Górny: *Archives of Foundry Engineering*, 2012, 12, 11-16.
23. A. Burbelko and D. Gurgul: *Computer Methods in Materials Science*, 2011, 11, 128-134.
24. D. Gurgul and A. Burbelko: *Archives of Metallurgy and Materials*, 2010, 55, 53-60.
25. H.L. Lukas, S.G. Fries and B. Sundman: 'Computational Thermodynamics: The Calphad Method', University Press, Cambridge, 2007.
26. D.M. Stefanescu, M. Moran, S. Boonmee, and W.L. Guesser: *AFS Proceedings 2012*, American Foundry Society, Schaumbur, IL. USA, 2012, Paper 12-045, 1-9.
27. G. Alonso, D.M. Stefanescu, R. Suarez, A. Loizaga, and G. Zarrabeitia: *Int. J. Cast Met. Res.*, 2014, 27, 87-100.
28. I.K. Kikoin, ed., 'Tables of the physical parameters', 1976, Moskow, Avtomizdat, (in Russian).
29. P. Magnin, J.T. Mason and R. Trivedi; *Acta Met. et Mater.*, 1991, 39, 469-480.
30. B. Chopard and M. Droz: 'Cellular Automata Modeling of Physical Systems', 2005, Cambridge University Press.
31. A. Burbelko: 'Modeling of solidification process by cellular automata method', 2004, Krakow, UWND AGH, (in Polish).

Acknowledgement

The study was co-financed by NCBiR in the years 2012-2015 as a targeted project No. INNOTECH/IN1/13/150421/NCBR/12

Averaged Voronoi Polyhedron in the Equiaxed Solidification Modelling

A.A. Burbelko[1*], J. Początek[1], W. Kapturkiewicz[1], and M. Wróbel[1]
[1]AGH University of Science and Technology, Krakow, Poland

For the modelling of the equiaxed grain growth controlled by diffusion the spherical *Elementary Micro-Diffusion Field* (EMDF) is usually used. Unfortunately, deviation of the idealized spherical grain geometry from the real one increases with a distance from nuclei. The proposed model of the equiaxed solidification, controlled by diffusion, assumes that EMDF has non-spherical shape as a result of random contacts between the grains growing around the individual nuclei. To determine the geometry and characteristics of the proposed EMDF, Kolmogorov's principle of the statistical theory of crystallization has been used. Modelling based on the non-spherical EMDF gives more accuracy of the solidification path prediction at the last stage of solidification. The results of simulation have been compared with experimental results obtained for near-peritectic Pb-Bi alloy.

Keywords: phase transformation modelling, equiaxed growth, elementary micro-diffusion field, ductile iron, averaged Voronoi polyhedron.

Introduction

Most advanced micro-models of the equiaxed solidification take into account the diffusion field in the vanishing liquid phase, as well as back diffusion in the grains of the solid phases. They are based on the spherical shape of the *Elementary Micro-Diffusion Field* (EMDF). Very often the subject of the investigations is a ductile iron (DI).[1-6] Due to the spherical symmetry of the nodular graphite in the DI the diffusion field of components was modelled as a 1D diffusion task. Models of such type are used also for the equiaxed peritectic solidification simulation.[7-11]

In the known numerical *Spherical Models* (SM) usually the idealized geometry of the EMDF is used. Spherically symmetrical cell of R_S radius was applied:

$$R_S = \sqrt[3]{\frac{3}{4\pi n}} \tag{1}$$

where n is the number of grains per unit volume, m^{-3}.

The above approximation has a satisfactory accuracy of the concentration profile prediction in the area placed not far from the grain nucleus but doesn't take into account the distortion of the peripheral area of the EMDF. Real shape of the grains is not spherical due to the grains impingements. Moreover, more than a third of the initial area remains outside the analysed space if the n grains of R_S radius were placed in the unit volume randomly and uniformly. This estimation is obtained on the base of the Kolmogorov statistical theory of solidification.[12] Bigger EMDF size was used in some models[8,13] to compensate lack of volume balance mentioned above. In this case prediction of the concentration profile becomes possible for the areas more remote from the grain centre. For the accounting of the grain overlapping effect in these models the Kolmogorov equation is used. Unfortunately these solutions have the serious shortcoming, because the question of mass balance of the solute elements remains unclear.

Equiaxed alloy microstructure obtained as a result of growth with a spherical symmetry may be approximated by a Voronoi tessellation. The scheme of the 2D tessellation for the image of ductile iron microstructure is shown in Fig. 1a. Domain of the one grain consists of the points closest to the grain nucleation centre rather than any other. Outer borders of the equiaxed grains are represented by straight segments perpendicular to the line connected the centres of the neighbouring grains in its middle point.

Two-dimensional Granular Model (GM) of solidification based on the 2D Voronoi tessellation has been developed by Vernède et al.[14,15] Phillion et al.[16] have also developed a semi-solid model based on similar granular structures. Solidification and micro-segregation in 2D GM were analysed in the triangular EMDF domains generated by two segments connecting the nucleation centre and corners of Voronoi cell (Fig. 1b). The geometrical approach like above can be easily extended to three dimensions for which the Voronoi tessellation will produce tetrahedral elements as a shape of EMDF[17]. Solidification model based on Voronoi diagrams was used also for the prediction of alloy's behaviour during solidification.[18-20]

The final grain structure and the shapes of the triangular/tetrahedral EMDF in these cases are the results of the preliminary Voronoi tessellation. In this 2D and 3D elementary cells the one-dimension micro-diffusion tasks were

* Corresponding author, email: abur@agh.edu.pl

solved individually for the every pair of symmetric cells. One-dimensional diffusion flow is directed from the grain nucleation centre to the outer border of the Voronoi polygons or polyhedra.

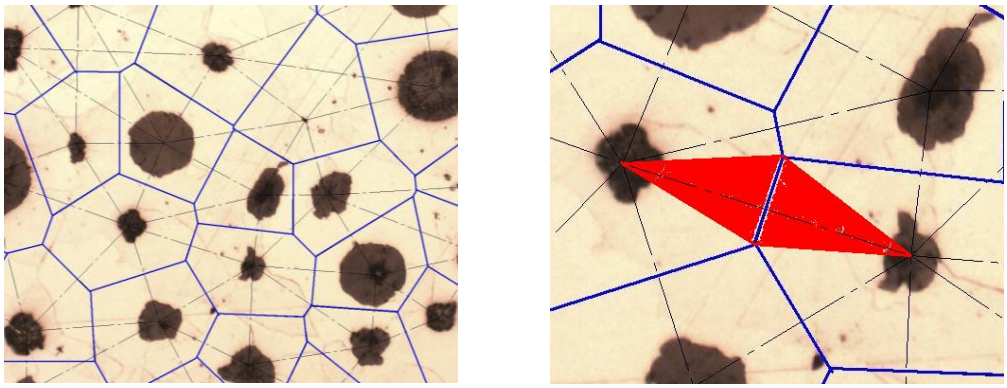

a) b)

Fig.1: Scheme of the Voronoi tessellation of the 2D microstructure of the DI (a) and fragment of the left picture with the shape of the two symmetry diffusion cells in the adjacent Voronoi polygons (b).

Description of the Mathematical Model

In the SM as well as in GM the one-dimension solute distribution $C(x,\tau)$ was obtained by numerical solution of the diffusion equation:

$$\frac{\partial C(x,\tau)}{\partial \tau} = \mathrm{div}\left[D\,\mathrm{grad}\,C(x,\tau)\right] \tag{2}$$

where: D is the solute diffusion coefficient, m^2s^{-1}; x is the distance from the EMDF centre, m; τ is time, s.

The equation (2) is solved by numerical computing in the time-varying domain of every phase with proper equilibrium solute concentration as the border conditions. Velocity of the mobile interface migration between the growing (α) and vanishing (β) phases is calculated on the base of mass conservation condition:

$$u_{\alpha/\beta}\left(\rho_\alpha C_\alpha - \rho_\beta C_\beta\right) = D_\alpha \rho_\alpha \left.\frac{\partial C_\alpha}{\partial r}\right|_\alpha - D_\beta \rho_\beta \left.\frac{\partial C_\beta}{\partial r}\right|_\beta \tag{3}$$

where: ρ is the phase density, $kg\cdot m^{-3}$; u is the velocity of interface of α-phase migration into the direction of the β-phase, $m\cdot s^{-1}$; lower indices denote the proper phase. Proper left-hand or right-hand derivative must be used for both phases.

In the derivation of the difference equations used for the numerical solution of the equation (2) the shape of the solution domain must be taken into account. The schemes of the control volumes (CV) tracing in the EMDFs for SM and GM are presented in Fig. 2a and 2b for the elementary balance calculation. Adjacent CVs cover entire volume of the EMDF.

In this paper the EMDF with the geometry of Averaged Voronoi Polyhedron (AVP) was used.[21-23] Example scheme of the CV location in the particular Voronoi polygon is shown in Fig. 2c. In the domain of every CV the uniform solute concentration is assumed. Diffusion flux of solute crosses the inner (F_i) and outer (F_{i+1}) borders of this CV only in the radial direction. All external boundaries of the Voronoi diffusion cells are assumed as adiabatic (like in the GM). In the SM adiabatic border condition is used only at the outer border of the EMDF. Differences between the GM and AVP scheme of the EMDF are as follows. In the GM every Voronoi cell volume is divided into the sectors: one EMDF consists from two symmetric cells placed in the adjacent polyhedron (see Fig. 1b). Number of the sectors is equal to the number of neighbour Voronoi polygons/polyhedra. All inner walls between the sectors are adiabatic as well as the outer borders of the Voronoi polygon / polyhedron (Fig. 2b). Parameters of CV in the AVP are calculated as averaged values like in the SM solution. These parameters in the AVP were determined for the set of Voronoi polyhedra. In the GM the individual positions of the phase border and transformed volume fractions are obtained by modelling for every EMDF. Model, based on the AVP, gives the mean values of interface position and the transformed volume for all grains growing in the micro-volume with a similar cooling path (like SM).

According to Kolmogorov[12], in the case of an instantaneous nucleation of the n grains in a unit volume and their spherical growth at the same (not necessarily constant) speed, the average volume of the material of one grain at the maximum distance r from the nucleation sites can be determined by the following equation:

$$V(r) = n^{-1}\left(1 - \exp\left(-\frac{4}{3}\pi n r^3\right)\right) \tag{4}$$

where: n is a volumetric grain density, m^{-3}; r is a distance from grain centre, m.

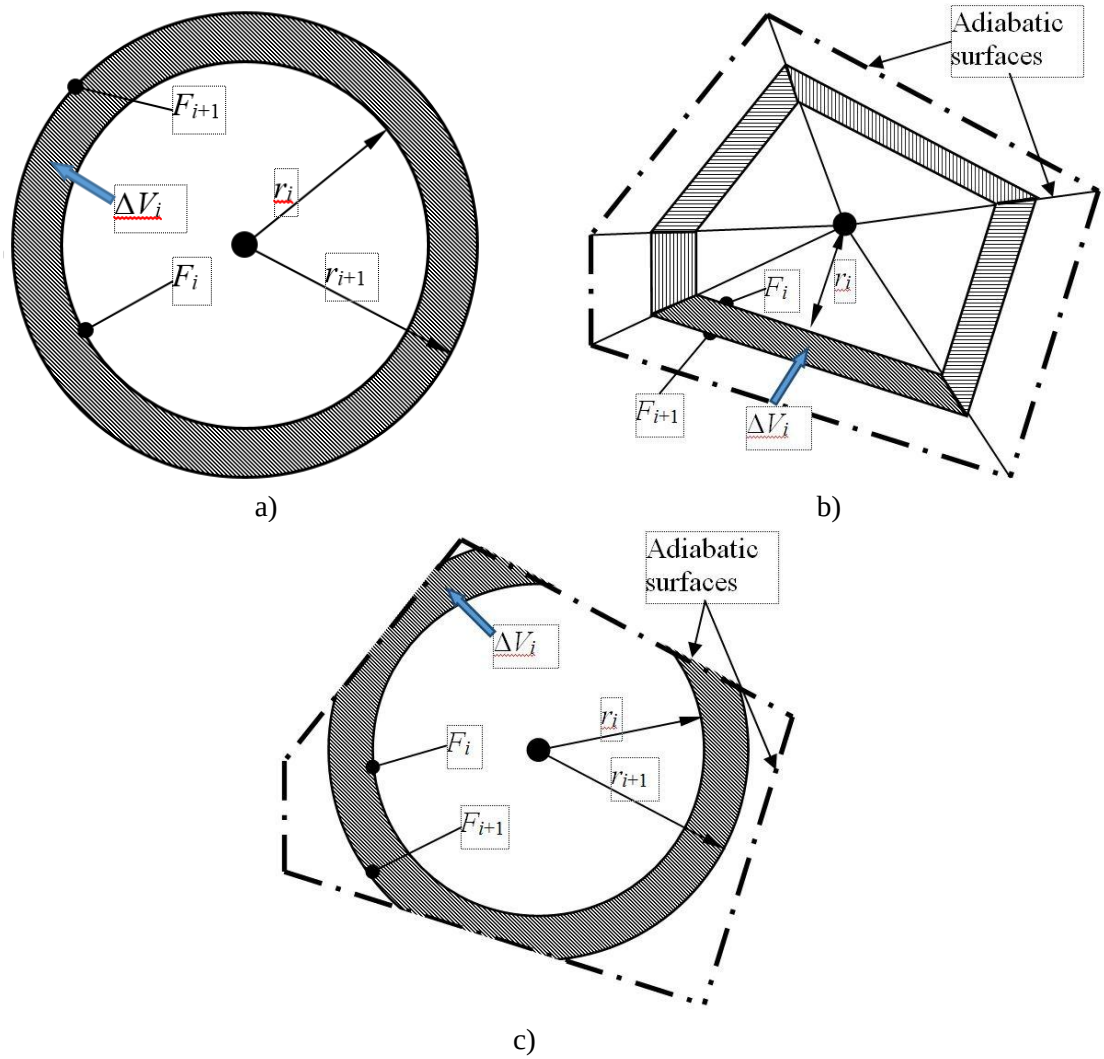

Fig.2: The schemes of the solution domain regionalisation in the case of control volume solution method for different EMDF geometry: SM (a), GM (b), and Averaged Voronoi Polyhedron (c); ΔV_i is the volume of the control element; F_i, F_{i+1} are the surfaces of the inner and outer interfaces of the control element; r_i, r_{i+1} are the positions of the inner and outer interfaces in the EMDF.

For the simplification of the used notation the following E(n,r) function is introduced:

$$E(n,r)=\exp\left(-\frac{4}{3}\pi n r^3\right) \tag{5}$$

Main advantage of the AVP scheme over the SM one is the proper choice of the EMDF size. Maximum size of the particular Voronoi Polyhedron is infinite. Shape of its body, number of faces, edges and vertices are the random values. However from equation (4) it follows that for the random set of the Voronoi polyhedra the averaged volume fraction belonging to the polyhedra and being at the distance less then r from their centres is equal to:[21]

$$\varepsilon = E(n,r) \tag{6}$$

Finishing radius of the EMDF R_{EMDF} in this case can be estimated after all grains have nucleated, on the base of grain number and desired accuracy of volume calculation ε:

$$R_{EMDF} \geq \sqrt[3]{-\frac{3\ln\varepsilon}{4\pi n}} \tag{7}$$

Size of the CV showed in Fig. 2c can be computed as follow:

$$\Delta V_i = n^{-1}\left[E(n,r_i)-E(n,r_{i+1})\right] \tag{8}$$

Inner surface of this CV can be calculated by derivation of equation (4) with respect to r:

$$F_i = 4\pi r_i^2 E(n,r_i) \tag{9}$$

The set of the difference equations for elementary balance method can be derived on the base of equations (5), (8), and (9).

Calculation of the volumetric rate of the α→β precipitation is available on the base of equation (9):

$$v_{\alpha/\beta} = 4\pi n r_{\alpha/\beta}^2 u_{\alpha/\beta} E\left(n, r_{\alpha/\beta}\right), \text{ s}^{-1} \quad (10)$$

Simulation Conditions

Modelling has been performed for two binary model alloys: eutectic Fe-C and hyperperitectic Pb-Bi (32 wt.%Bi). Diffusion coefficients used in the calculation are shown in the Table 1. Number of the eutectic cells equal to $1.96 \cdot 10^{13}$ m^{-3} was imposed for Fe-C alloy and for Pb-Bi system number of peritectic cells of $1.0 \cdot 10^{12}$ m^{-3} was chosen.

For Fe-C alloy the equilibrium concentrations for equation (3) have been computed for the given temperature by means of CALPHAD method,[24] using Thermo-Calc Software with Thermodynamic Calculation Interface (TQ-Interface). For the Pb-Bi alloy the values of equilibrium concentration were calculated by linear relations shown in Table 1. Equation parameters presented in this table are obtained on the base of binary Pb-Bi equilibrium thermodynamic system calculated by Thermo-Calc. Diffusion coefficients of the solutes used in the modelling are shown in Table 2.

Table 1: Equilibrium temperature of the Pb-Bi system.

Equilibrium Phases		Equilibrium Bi concentration, wt.%	
I	II	I phase	II phase
Liquid	Pb (FCC)	$0.85969-2.6290 \cdot 10^{-3} \cdot T$	$0.53132-1.6248 \cdot 10^{-3} \cdot T$
Liquid	ε-Pb (HCP)	$0.93469-3.0375 \cdot 10^{-3} \cdot T$	$0.71370-2.2696 \cdot 10^{-3} \cdot T$
Pb (FCC)	ε-Pb (HCP)	$0.16933-3.4678 \cdot 10^{-4} \cdot T$	$0.24491+2.8373 \cdot 10^{-4} \cdot T$

Table 2: Diffusion coefficients.

Element	Phase	Diffusion coefficient, m^{2}s^{-1}	Source
C	Liquid Fe-C (Liq)	$1.25 \cdot 10^{-9}$	25
C	Austenite (FCC)	$1.5 \cdot 10^{-10}$	25
Bi	Liquid Pb-Bi (Liq)	$1.3 \cdot 10^{-9}$	26
Bi	Pb (FCC)	$1.0 \cdot 10^{-14}$	8
Bi	ε-Pb (HCP)	$2.0 \cdot 10^{-14}$	

Modelling Results

Decreasing intensity of external cooling was assumed for Fe-C alloy solidification:

$$Q = -5.082 \cdot c \cdot \exp\left(-5.307 \cdot 10^3 \cdot \tau\right), \text{ W} \cdot \text{m}^{-3} \quad (11)$$

where: c is a volumetric specific heat of alloy, J·m^{-3}K; τ is time, s. Above heat extraction rate is typical for DI casting with 9 mm thick wall, made in the greensand mould. Results of the micro-modelling are presented in Fig. 3 and 4. Cooling curves presented in Fig. 3 were calculated with a numerical solution of the differential heat balance equation:

$$c \frac{\partial T}{\partial \tau} = Q - \sum_j \left(v_j H_j\right) \quad (12)$$

were H is the enthalpy of the phase transformation (see Table 3). Summation in the equation (12) is performed for all phase transformations j.

Table 3: Enthalpy of the precipitations.

Precipitation	Transformation Enthalpy, J·m^{-3}	Source
Austenite from Liquid	$1971.0 \cdot 10^6$	27
Graphite from Austenite	$0.88 \cdot 10^6$	

Calculations were performed by SM and AVP methods with mesh step 1 μm. For SM radius of the EMDF was obtained by equation (1) as 23 μm and for AVP by equation (7) as 44 μm (ε = 0.001). At the beginning of the eutectic

solidification the differences between temperature-time curves produced by SM and AVP method of simulation is very small. Calculated transformation rate in the SM is slightly higher than in the AVP. Accumulation of these differences over a period of the whole solidification time (88 s) results with the 5 K higher temperature of an alloy in the SM method. At that instant, the untransformed liquid fraction in the AVP model is near to the 2.5 vol.%. In the AVP modelling solidification ends near the 5 s later. Shape of the simulated cooling curve at the instant of the transformation completion obtained with the AVP confirms model assumptions in terms of quality.

Simulated changes of the graphite nodules mean size is presented in Fig. 4a as well as the position of the solid-liquid interface. Values of the interface migration velocity are shown in Fig. 4b. As it follows from these diagrams, the SM and AVP models give the similar results for the domain placed near the nodule centre, at distance shorter the half of the EMDF radius calculated for SM using equation (1). This distance is indicated in Fig. 4a by a grey line. Size of the graphite spheres and velocity of the growth are very similar in the both models. Differences between austenite envelope radii become meaningful after 20 s of solidification. Acceleration of the solid-liquid interface predicted in the AVP model at the last stage of solidification is a well-known fact.

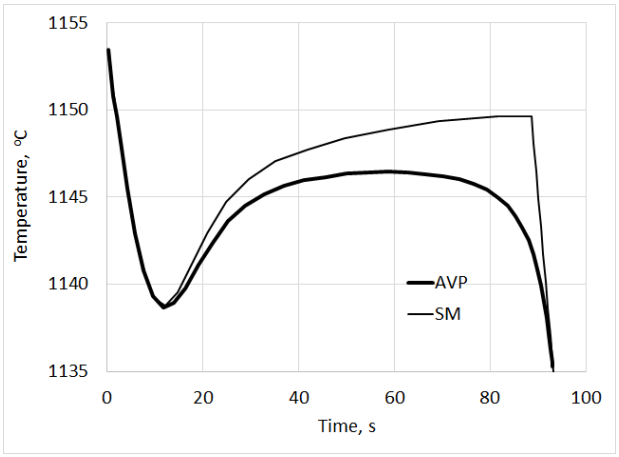

Fig.3: Calculated cooling curves obtained for eutectic Fe-C alloy with the SM and AVP models.

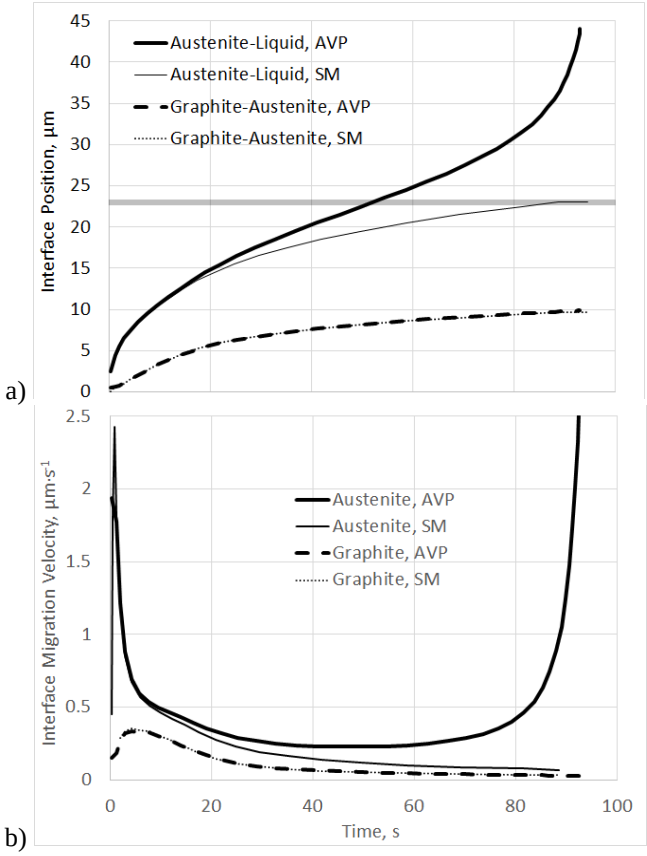

Fig.4: Changes of the interface position (a) and interface migration velocity (b) obtained in the modelling for eutectic Fe-C alloy with the SM and AVP models.

Hyper-peritectic Pb-Bi alloy has a similar shape of the EMDF scheme to eutectic DI. This alloy was used for the verification of the model correctness because of relatively simplicity to obtain the experimental results in comparison with Fe-C alloys. Modelling of the binary hyper-peritectic Pb – 32 wt.% Bi alloy solidification has been performed for the slow cooling of the sample with a furnace (cooling rate -0.011 K/s). Changes of the solid-liquid interface position for primary Pb solidification are shown if Fig. 5a together with the changes of the outer and inner interfaces positions of the peritectic ε-Pb layer in the contacts with the dissolved primary Pb and vanishing liquid phase. Changes of the phase volume fractions are presented in Fig. 5b. Modelling was performed by AVP methods with mesh step 1 μm. Radius of the EMDF was estimated by equation (7) as 188 μm (ε = 0.001).

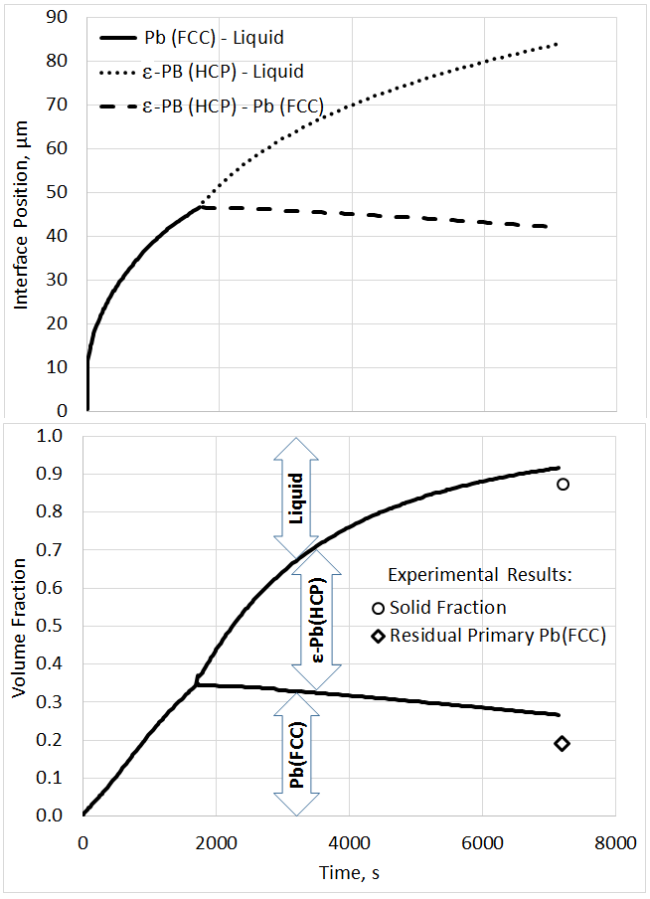

Fig.5: Changes of the interfaces positions (a) and volume fractions of the phases (b).

After cooling 5 K below the temperature of the eutectic equilibrium (120°C) the sample has been quenched in the water. Microstructure of the sample is presented in Fig. 6.

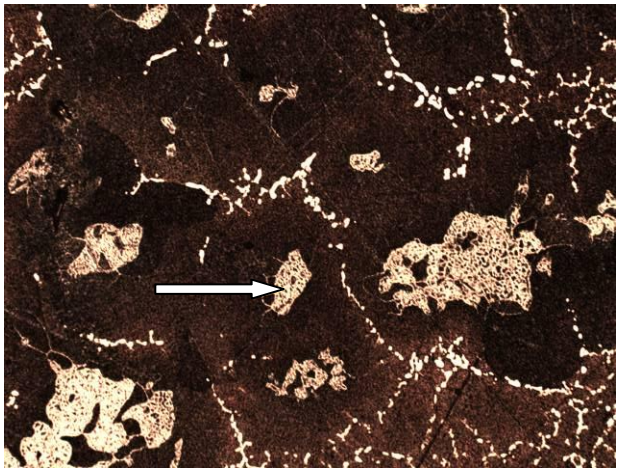

Fig.6: Microstructure of the analysed Pb-32%wt. Bi alloy, 200x.

Quantitative stereological analysis was performed for this sample. Random set of the 100 images obtained with magnification 1000x were analysed by manual point count method with using of the regular grid 11x11 points. Volume fraction of the residual primary Pb(FCC) measured by set of the 12100 points is equal to 19,15%. Measured volume fraction of the eutectic Bi is equal to 2.53%.

Chemical composition of the analysed alloy is shown in the binary Pb-Bi thermodynamic diagram in Fig. 7 by the grey vertical line. According to this diagram, in the quenching temperature this alloy has the single-phase ε-Pb structure. As it follow from Fig. 6, residual primary Pb(FCC) is observed in the sample structure (white arrow). Predicted volume fraction of this phase is in the accordance with results of quantitative metallography. Chains of the white Bi inclusion on the grain boundaries denote the eutectic composition of the liquid phase at the last stage of the sample solidification. This fact confirms the modelling results shown in Fig. 5b. On the base of the measured volume fraction of eutectic Bi, the residual volume fraction of liquid phase that solidify as the ε-Pb–Bi eutectic in the temperature of the eutectic equilibrium is estimated to be nearly 12%.

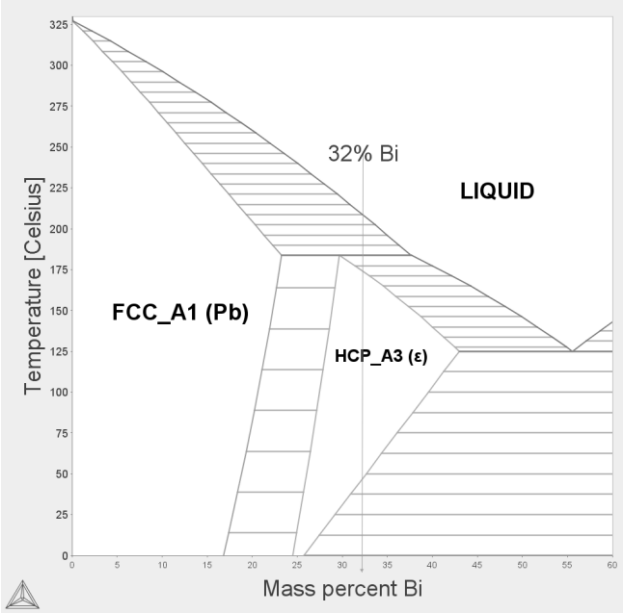

Fig.7: Fragment of the binary thermodynamic diagram Pb-Bi calculated by Thermo-Calc Software.

Discussion

Comparison of the simulation results and experimental one says about the qualitative confirmation of the AVP model rightness. It is shown that AVP model gives the better precision of the simulation for the equiaxed grain growth than SM at the final stages of the solidification. This is the result of the accounting of the actual surface area of contact between the growing solid and vanishing liquid placed in the intercrystalline space.

It is known fact that at the beginning stage the solidification of the globular graphite and austenite dendrites is not coupled: grains of both phases grow directly from liquid without common contacts. [28] Moreover, the solidification of some off-eutectic austenite is observed even in the hyper-eutectic alloys. [29] Due to this solidification mechanism the shape of the EMDF is more complicated.

The described above phenomenon was taking into account in the known models based on the SM. [5,6] To take into account the impingement of the spherical eutectic grains at the last stage of the solidification, so-called Kolmogorow-Avrami-Johanson-Mehl correction is used in these models. This is not fully accurate. Better mapping of the initial uncoupled graphite and austenite nucleation and growth as well as the transition to the stage of the coupled growth (in the eutectic, hypo- and hypereutectic alloys) gives the cellular automata technique. [30,31]

The presented version of the AVP model has a limitation and takes into account equiaxed growth only (for single primary phase as well as for few layers of solid phases). Taking into account the growth of the off-eutectic grains will be a subject of further work of the authors.

Conclusions

1. The Averaged Voronoi Polyhedron geometry for the EMDF description gets the averaged representation of the real shapes of the equiaxed grains better in comparison to known SM. Parameters of the AVP have been used for determining of EMDF in the micromodelling of the equiaxed stage of the primary, single-phase solidification (Pb in Pb-Bi), coupled stage of the eutectic solidification in the DI and peritectic solidification in the hyperperitectic Pb-Bi alloy.

2. AVP-based micromodelling gives better representation of the last stage of the equiaxed grain solidification then model with an ideal spherical shape of the EMDF because proposed characteristics of the AVP takes into account random nature of the impingements of the adjacent grains. In the DI presented version of the model doesn't take into account the possibility of the off-eutectic austenite dendrite solidification.
3. Results of the quantitative metallography for the Pb-32 wt.%Bi alloy confirm the correctness of the AVP model used for the modelling of the alloy solidification.

References

1. D. M. Stefanescu, A. Catalina, X. Guo, L. Chuzhoy, M. A. Pershing and G. L. Biltgen: Modeling of Casting, Welding and Advanced Solidification Process – VIII, The Minerals, Metals & Materials Society, Warrendale, PA, 1998, 455.
2. S. M. Yoo, A. Ludwig and P. R. Sahm: Solidification Processing, Renmor House, Univ. of Sheffield, Sheffield, 1997, 494.
3. S. Chang, D. Shangguan and D. M. Stefanescu: *Metall. Trans. A*, 1992, 23A, 1333-1346.
4. M. I. Onsoien, O. Grong, O. Gundersen and T. Skaland: *Metall. Mater. Trans. A*, 1999, 30A, 1053-68.
5. G. Lesoult, M. Castro and J. Lacaze: *Acta Mater.*, 1998, 46, 983-995.
6. J. Lacaze, M. Castro and G. Lesoult: *Acta Mater.*, 1998, 46, 997-1010.
7. A. Das, I. Manna and S.K. Pabi: *Scripta Mat.*, 1997, 36, 867-873.
8. A. Das, I. Manna and S.K. Pabi: *Acta Mater.*, 1999, 47, 1379-1388.
9. K. Matsuura, H. Maruyama, Y. Itoh, M. Kudoh and K. Ishii: *ISIJ Int.*, 1995, 35, 183-187.
10. M. El-Bealy and H. Fredriksson: *Met. and Mat. Trans. B.*, 1996, 27B, 999-1014.
11. E.P. Kalinushkin, E. Fras, W. Kapturkiewicz, A.A. Burbelko and J. Sitalo: *Mat. Sci. Forum*, 2000, 329-330, 185-190.
12. A.N. Kolmogorov: *Bull. Acad. Sci. USSR*, 1937, 3, 355-359 (in Russian).
13. E. Fraś, W. Kapturkiewicz and A.A. Burbelko: *Advanced Mat. Res.*, 1997, 4-5, 499-504.
14. S. Vernède, P. Jarry and M. Rappaz: *Acta Mater.*, 2006, 54, 4023-4034.
15. S. Vernède and M. Rappaz: *Acta Mater.*, 2007, 55, 1703-1710.
16. A.B. Phillion, S.L. Cockcroft and P.D. Lee: *Acta Mater.*, 2008, 56, 4328-4338.
17. S. Vernède and M. Rappaz: *Philosophical Magazine*, 2006, 86, 3779–3794.
18. A.B. Phillion, J.-L. Desbiolles and M. Rappaz: Modeling of Casting, Welding, and Advanced Solidification Processes – XII, TMS, 2009, 353-360.
19. S. Vernède, J.A. Dantzig and M. Rappaz: *Acta Materialia*, 2009, 57, 1554-1569.
20. A. B. Phillion, S. Vernède, M. Rappaz, S.L. Cockcroft and P. D. Lee: *Int. J. Cast Metals Research*, 2009, 22, 240-243.
21. A. Burbelko, J. Początek, D. Gurgul and M. Wróbel: *Steel Research Int.*, 2014, 6, 1010-1017.
22. A. Burbelko and J. Początek: The TMS 2013 Annual Meeting Supplemental Proceedings. TMS (The Minerals, Metals & Materials Society), John Wiley & Sons, Inc., 2013, p. 523-530.
23. A.A. Burbelko, J. Początek and M. Królikowski: *Arch. of Foundry Eng.*, 2012, 13, Iss. 1, 134-140.
24. H.L. Lukas, S.G. Fries and B. Sundman: 'Computational Thermodynamics: The Calphad Method', 2007, University Press, Cambridge.
25. P. Magnin, J.T. Mason and R. Trivedi: *Acta Met. Mat.*, 1991, 39, 469-480.
26. S. Liu and R. Trivedi: *Met. Mater. Trans. A*, 2006, 37A, 3293–3304.
27. I.K. Kikoin (Ed.): 'Tables of the physical parameters', 1976, Moscow, Atomizdat (In Russian).
28. H. Fredriksson, J. Stjerndahl and J. Tinoco: *Mat. Sci. Eng. A*, 2005, 413-14, 363-372.
29. M. Hecht and J.C. Margerie: *Memoires Scientifiques De La Revue De Metallurgie*, 1971, 68, 325.
30. A. Burbelko, E. Fraś, D. Gurgul, W. Kapturkiewicz and J. Sikora: *Key Eng. Mater.*, 2011, 457, 330-336.
31. A.A. Burbelko, D. Gurgul, W. Kapturkiewicz and E. Guzik: *Mat. Sci. Forum*, 2014, 790-791, 140-145.

Acknowledgement

This research was supported by Polish NCN grant DEC-2011/01/B/ST8/01689.